UNIVERSITAT DE BARCELONA

Nuevas técnicas de imagen en dermatología: Tomografía de Coherencia Óptica de Campo Lineal y Microscopía Confocal Ex vivo

Javiera Pérez-Anker

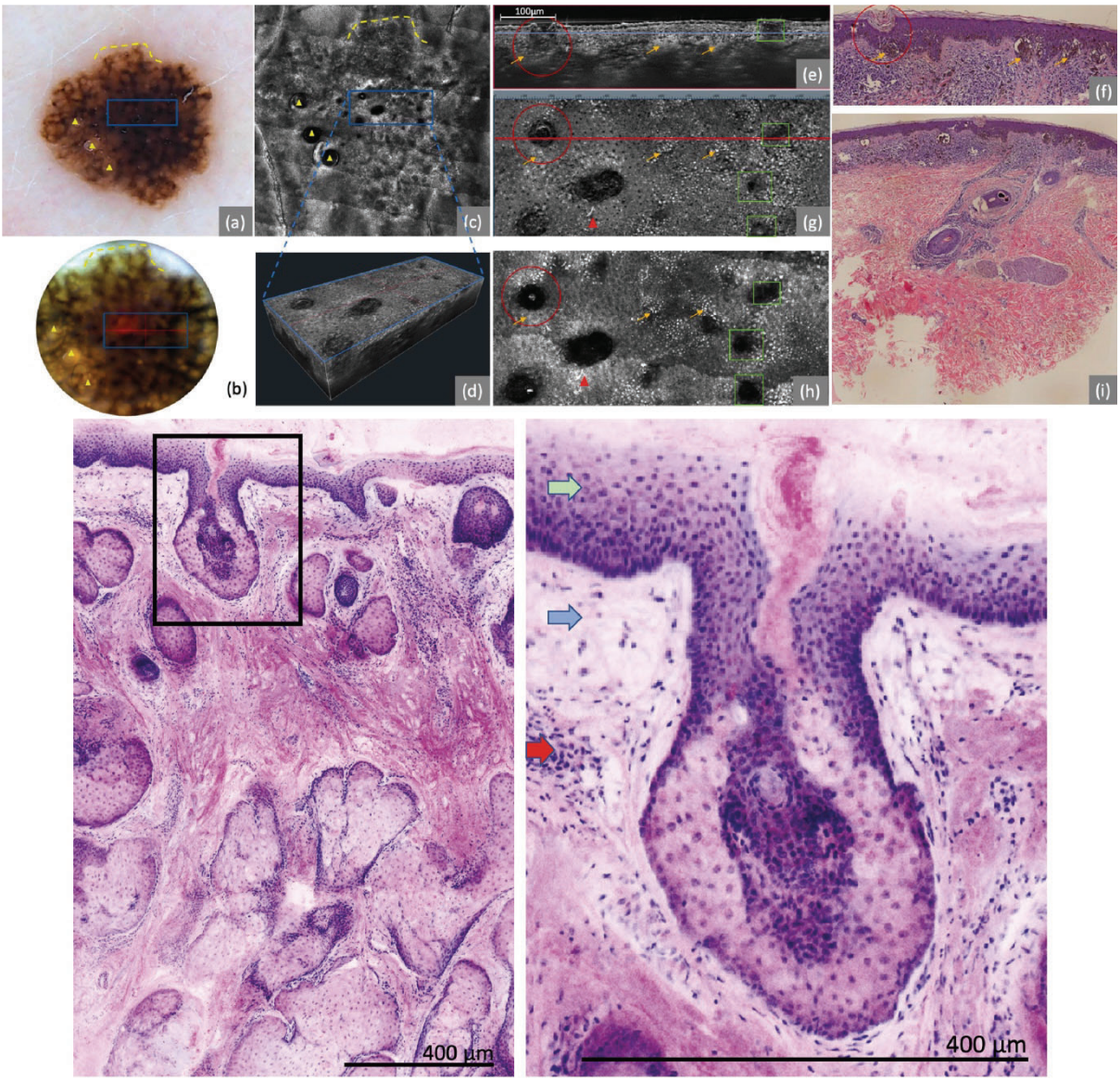

NUEVAS TÉCNICAS DE IMÁGEN EN DERMATOLOGÍA: LC-OCT Y MICROSCOPÍA CONFOCAL EX VIVO

TESIS DOCTORAL:
Dra. Javiera Pérez Anker

TUTORA:
Dra. Susana Puig Sardà

DIRECTORES:
Dra. Susana Puig Sardà
Dr. Josep Malvehy Guilera

Doctorat en Medicina i Reserca Translacional

Facultad de Medicina i Ciències de la Salut

Barcelona, 2024

Clínic Barcelona | Universitat de Barcelona

Nuevas técnicas de imagen en dermatología:

Tomografía de Coherencia Óptica de Campo Lineal y Microscopía Confocal *Ex vivo*

Doctoranda: Javiera Pérez-Anker

UNIVERSITAT DE BARCELONA

A lo más importante de la vida…a aquello que se desprecia por no verse y se minimiza para no molestar, pero que, al sentirlo, inflama el alma y percibimos que todo diseña, crea y guía en silencioso y profundo amor…

A mi familia, lugar de amor, perdón y arrepentimiento. Lugar de reposo y de tormenta, de luz y oscuridad. Donde todo se gesta y luego nace, lugar perpetuo en nuestros corazones.

A cada paciente, a cada lágrima y sufrimiento escondido, silencioso. A cada sonrisa y alegría. A cada uno de los que ha pasado a mi lado en estos 30 años de profesión.

A mis maestros, tutores y directores, a todos aquellos que me han enseñado en silencio, con acciones, con su ejemplo. A los que me han inspirado a sacar de dentro de mí lo que ni yo mismo sabía ser capaz de hacer.

A mi hijo, Gabriel Pérez Hargreaves, por su valioso aporte en la diagramación de esta tesis.

.

A Clothilde Raoux, Maxime Casals, Philipp Andre y Giuseppe Solomita por su invaluable colaboración y dedicación a lo largo de innumerables horas de trabajo conjunto en este proyecto. Sin su apoyo incondicional, esta tesis no habría sido posible.

PRESENTACIÓN

El desafío de estudiar e investigar, luego de tantos años de carrera, es semejante a volver a nacer. Es un proceso lento y algunas veces doloroso, que empieza donde no hay nada y debe ser llenado y fertilizado día a día, aprendiendo no solo de libros y de literatura publicada en revistas, sino que también de cada colega (senior o principiante) con los que interactuamos cada día.

Las técnicas de imagen complementarias al diagnóstico clínico han abierto un impresionante campo de ayuda a mejorar la calidad asistencial y al mismo tiempo una nueva frontera en investigación con potenciales cambios en la forma de estudiar a nuestros pacientes de una manera más rápida y eficiente.

Este estudio ha sido desarrollado desde una idea inicial de aprender las técnicas de diagnóstico por imagen innovadoras en dermatología y se ha transformado paulatinamente en el desarrollo de nuevas versiones de esas mismas tecnologías, el descubrimiento de nuevas indicaciones y, al mismo tiempo, ampliando su incorporación y conocimiento en otras especialidades médico-quirúrgicas.

En este trabajo de investigación revisamos la evidencia existente en las versiones tecnológicas previas de las principales técnicas de microscopía diagnóstica en dermatología, *in vivo* y *ex vivo*. Por otro lado, presentamos los estudios originales que realizamos en el campo de la dermatología en estas áreas diagnósticas, que han ayudado a generar nueva evidencia en cuanto al diagnóstico *in vivo* y *ex vivo* de los tumores. Así mismo, mostramos los estudios realizados en otras especialidades, destacando la aplicación de las nuevas tecnologías diagnósticas en patología general.

RESUMEN

Se llevó a cabo una investigación sobre la utilidad de dos novedosas técnicas de imagen, la tomografía de coherencia óptica de campo lineal (TCO-CL) y la microscopía confocal ex vivo (MCev), en el diagnóstico de tumores cutáneos.

El objetivo fue describir las características morfológicas de las lesiones tumorales cutáneas mediante TCO-CL y MCev, y relacionarlas con las estructuras observadas en dermatoscopia, microscopía confocal de reflectancia (MCR) e histología convencional.

Se detallaron los hallazgos morfológicos y citológicos de las lesiones melanocíticas observadas en TCO-CL, y se estableció una correlación entre los elementos dermatoscópicos y las estructuras identificadas en esta técnica. Asimismo, se describieron criterios diagnósticos y se desarrollaron algoritmos de inteligencia artificial para la diferenciación de lesiones (como el campo de cancerización) con TCO-CL.

En el caso de MCev, se logró mejorar la calidad de visualización de los nidos de carcinoma basocelular mediante la implementación de un nuevo protocolo de tinción. Además, se diseñó un dispositivo y se estableció un protocolo estandarizado para la obtención de muestras en MCev, contribuyendo así a una mayor eficacia en el proceso. Se evaluó la precisión diagnóstica de MCev en biopsias de lesiones equívocas y se describieron las características diagnósticas de diferentes tumores cutáneos utilizando MCev de cuarta generación. También se desarrolló un algoritmo de inteligencia artificial para la visualización de imágenes escaneadas en MCev.

Además de estos avances específicos, se llevaron a cabo comparaciones entre MCev y la tinción de H&E en patología general, ampliando así el alcance del estudio a otros campos de la medicina.

ABSTRACT

An investigation was conducted on the utility of Lineal Confocal Optical Coherence Tomography (LC-OCT) and ex vivo confocal microscopy (evCM), two novel imaging techniques, in the diagnosis of skin tumors, establishing correlations between morphological characteristics and findings in dermoscopy, Reflectance confocal microscopy (RCM), and conventional histology.

The objective was to describe the morphological characteristics of cutaneous tumor lesions using LC-OCT and evCM, and to relate these findings to those obtained in dermoscopy, MCR, and conventional histology.

The morphological and cytological findings of melanocytic lesions observed in LC-OCT were detailed, establishing connections between dermoscopic elements and the morphological and cytological structures identified in this technique. Likewise, diagnostic criteria were described, and artificial intelligence algorithms were developed for the differentiation of lesions in LC-OCT.

In the case of evCM, the visualization quality of basal cell carcinoma nests was improved by implementing a new staining protocol. Additionally, a device was designed, and a standardized protocol was established for obtaining samples in evCM, thus contributing to a greater efficiency in the process. The diagnostic accuracy of evCM in biopsies of equivocal lesions was evaluated, and the diagnostic characteristics of different skin tumors using fourth generation evCM were described. An artificial intelligence algorithm was also developed for the visualization of scanned images in evCM. In addition to these specific advancements, comparisons between evCM and H&E staining in general pathology were conducted, expanding the scope of the study to other fields of medicine.

ÍNDICE DE CAPÍTULOS

PUBLICACIÓN 3: Criterios diagnósticos para lesiones melanocíticas en Tomografía de Coherencia Óptica Lineal.

PUBLICACIÓN 4: Hendidura: ¿un nuevo predictor de malignidad e invasión en lesiones melanocíticas?

PUBLICACIÓN 5: Puntuación no invasiva de atipia celular en imágenes de tomografía de coherencia óptica de campo lineal en 3 dimensiones de tumores queratinizantes utilizando aprendizaje profundo.

PUBLICACIÓN 6: Caracterización del carcinoma basocelular mediante microscopía confocal *ex vivo* de fusión: un cambio prometedor en la histopatología cutánea.

PUBLICACIÓN 7: Una opción rápida y eficaz para el aplanamiento de tejidos: eficacia y optimización del tiempo en microscopia confocal *ex vivo*. Desarrollo de una patente

PUBLICACIÓN 8. Seis pasos para la obtención de un escaneo óptimo en la microscopía confocal *ex vivo*.

PUBLICACIÓN 9. Precisión diagnóstica de microscopia confocal ex vivo con tinción digital en el diagnóstico del carcinoma escamoso mediante biopsias.

PUBLICACIÓN 10: Tinción digital de las imágenes de la microscopía confocal utilizando aprendizaje profundo.

V. DISCUSIÓN

V.1. Estructuras morfológicas de las lesiones melanocíticas en tomografía de coherencia óptica de campo lineal.

V.1.1. Principales diferencias entre dispositivos.

V.1.2. Estructuras morfológicas de las lesiones melanocíticas en tomografía de coherencia óptica de campo lineal y su comparación con la microscopía confocal de reflectancia e histología.

V.2. Correlación de los hallazgos dermatoscópicos en las lesiones melanocíticas en tomografía de coherencia óptica de campo lineal.

V.3. Criterios diagnósticos de las lesiones melanocíticas en tomografía de coherencia óptica de campo lineal.

V.4. Presencia de "hendidura peritumoral " como marcador de malignidad.

V.5. Aplicaciones de la inteligencia artificial en el estudio campo de cancerización cutáneo en tomografía de coherencia óptica de campo lineal.

V.6. Limitaciones y otras aplicaciones de la tomografía de coherencia óptica de campo lineal.

V.7. Caracterización del carcinoma basocelular en microscopía confocal ex vivo.

V.7.1. Principales diferencias entre los dispositivos de microscopía confocal ex vivo.

V.7.2. Diferencias entre tinciones en el carcinoma basocelular.

V.7.3. Diferencias entre láseres en el carcinoma basocelular. Criterios diagnósticos.

ABREVIATURAS Y ACRÓNIMOS

3D	3 dimensiones
AP	Aprendizaje profundo
CBC	Carcinoma basocelular
CEC	Carcinoma escamoso
EC	Ecografía cutánea
H&E	Hematoxilina y Eosina
IA	Inteligencia Artificial
IC	Intervalo de confianza
MCev	Microscopía confocal *ex vivo*
MCFu	Microscopía confocal de fusión
MCR	Microscopía confocal de reflectancia
MM	Melanoma maligno
P.E.	Por ejemplo
TCO	Tomografía de coherencia óptica
TCO-CL	Tomografía de coherencia óptica de campo lineal
VPN	Valor predictivo negativo
VPP	Valor predictivo positivo

I. INTRODUCCIÓN

Uno de los objetivos principales del médico es realizar un diagnóstico preciso, en el tiempo oportuno que permita la estrategia terapéutica más adecuada en cada enfermedad y considerando las características y preferencias del paciente. Para lograr el primer objetivo, el diagnóstico correcto, es fundamental en primer lugar, una anamnesis completa y detallada. El médico debe ser capaz de obtener detalles precisos y "pistas indirectas" que, conectados en orden cronológico, nos guiaran hasta una hipótesis diagnóstica. Como complemento a la anamnesis, recogeremos preciosas evidencias realizando un examen físico de piel, mucosas y faneras (tratándose de dermatología). Este nos afirmará o alejará de las primeras hipótesis planteadas y muchas veces nos proporcionará claves diagnósticas no referidas por el paciente (y algunas veces incluso negadas por este mismo paciente), orientándonos hacia un diagnóstico más preciso. A menudo "la piel habla" lo que al paciente no menciona, o el médico no pregunta, o simplemente confirma lo anteriormente sospechado en la anamnesis.

Sin embargo, con frecuencia, la anamnesis y el examen cutáneo directo aún son insuficientes para un diagnóstico certero y es necesario recurrir a maniobras semiológicas y/o diagnósticas llamadas complementarias.

En este sentido, diversas tecnologías diagnósticas han sido desarrolladas en los últimos años en dermatología, tanto sean *in vivo* como *ex vivo*. Algunas, permiten la visualización de estructuras de la superficie cutánea, sabiendo que estas se correlacionan claramente con las mismas estructuras *ex vivo* en las preparaciones histológicas. En otros casos, las técnicas de imagen permiten una visualización con mayor resolución, permitiendo el reconocimiento de estructuras a nivel celular.

La dermatoscopia es una de las técnicas diagnósticas complementarias más efectivas utilizadas en dermatología. Múltiples estudios han demostrado la evidencia de su aplicación tanto en patología tumoral, como inflamatoria o infecciosa.[1,2] Es una herramienta no invasiva de imagen que permite reconocer estructuras cutáneas de pigmento, vasculares y otras siendo de indiscutible ayuda diagnóstica.[3] Esta técnica se ha convertido en una herramienta indispensable en nuestro diagnóstico junto al examen físico.

Sin embargo, existen lesiones cutáneas dudosas o mal delimitadas en el examen dermatoscópico. En esos casos, es necesario para obtener un diagnóstico *in vivo* recurrir a otras técnicas, como la microscopia confocal *in vivo* (MCR), la tomografía de coherencia óptica confocal de campo lineal (TCO-CL), la tomografía de coherencia óptica (TCO) o la ecografía cutánea (EC), entre otras. Cada una de estas técnicas presenta ventajas y también limitaciones, y muchas veces se complementan entre sí.[4,5]

Además de mejorar la precisión diagnóstica, las técnicas de imagen no invasivas también han demostrado su aplicabilidad clínica asistiendo en el mapeo de lesiones para definir la extensión de lesiones de bordes imprecisos (como en caso de los tumores recurrentes), o de extensión subclínica (como en la definición de los bordes del lentigo maligno o de otros tumores sin pigmento antes de la cirugía). También son un complemento fundamental en la estadificación, ayudando en la evaluación del compromiso de estructuras nobles en profundidad, además de en la identificación de eventuales metástasis cutáneas o linfáticas (regionales). Finalmente, son de gran utilidad en la monitorización de los tratamientos dermatológicos quirúrgicos o de otro tipo, ya que permiten la evaluación del tejido, facilitando la

comparación objetiva y reproducible de los hallazgos antes y después de su tratamiento.

Estos métodos no pretenden sustituir el diagnóstico histológico convencional. A pesar de todos estos recursos, cuando no es posible obtener con total seguridad un diagnóstico de certeza, se deberá realizar una biopsia incisional o excisional de la lesión para su estudio histológico y molecular. En estos casos, especialmente en el caso de los tumores, se requiere la exéresis completa de la lesión y es de gran ayuda conocer si el tejido extirpado ha sido suficiente para evitar su recidiva (control de márgenes).

Para analizar estos tejidos, la única técnica diagnóstica disponible en el pasado fue el estudio histológico. Desde el inicio del estudio, hace más de 100 años, se ha realizado mediante fijación del tejido con formaldehido durante horas o días, ulterior inclusión en parafina y finalmente, realizando cortes de 5 a 10 micras que posteriormente se tiñen con hematoxilina & eosina u otras tinciones específicas, para la visualización en el microscopio. En aquellos casos donde es necesario un diagnóstico rápido, las muestras se congelan a bajas temperaturas (aproximadamente -25ªC) en un criostato, y se realizan cortes en congelado para su posterior tinción y evaluación morfológica. La inmediatez diagnóstica se requiere, sobretodo, en el campo de la patología quirúrgica.

Sin embargo, desde hace menos de 20 años, se han desarrollado nuevas formas de obtener imágenes histológicas. Estas técnicas, permiten el análisis inmediato de los tejidos extirpados (*ex vivo*) en pocos minutos. En lugar de la preparación del tejido con cortes histológicos en láminas de vidrio, se obtienen imágenes de los tejidos reproducidas en una pantalla de ordenador, utilizando un microscopio confocal. Esta técnica es llamada microscopía confocal *ex vivo* (MCev).[6,7]

En este trabajo, mostraremos de forma más detallada algunas de estas técnicas y sus aplicaciones diagnósticas, sobretodo de las que permiten resolución celular tanto *in vivo* como *ex vivo*. Discutiremos la evidencia previa y la compararemos, posteriormente, con nuestro aporte en el desarrollo y utilización de dos de estas técnicas: TCO-CL y MCev.

I.1. TÉCNICAS DE DIAGNÓSTICO *IN VIVO*

I.1.1. Dermatoscopia

La dermatoscopia (también llamada de microscopia de epiluminiscencia, dermoscopia),[8,9] es una técnica de magnificación y visualización de estructuras presentes en la superficie cutánea, de mucosas o de faneras, que utiliza un dispositivo llamado dermatoscopio. (Figura 1) Éste, tiene una lente de aumento que varía, de acuerdo con el dispositivo empleado, entre 10 x y 40 x y una fuente de luz polarizada o no polarizada.

Técnicamente, de acuerdo con el tipo de luz utilizada, podemos realizar dos tipos de dermatoscopia (visualización de estructuras): la dermatoscopia de contacto con aplicación de líquido de inmersión o la dermatoscopia de polarización cruzada que utiliza una luz polarizada y un filtro de polarización cruzada. Ambos consiguen evitar la reflexión y refracción de la capa córnea para visualizar estructuras más profundas. Las dos son similares, pero no idénticas y la utilización de ambas técnicas es complementaria. Algunos dispositivos, ofrecen la opción de visualización de ambas luces, polarizada o no polarizada, de acuerdo con las estructuras que quieran ser observadas.

Por otro lado, los dermatoscopios actuales se han incorporado de tal forma a la práctica clínica diaria, que algunos de estos aparatos pueden integrarse a los dispositivos móviles, permitiendo el registro fotográfico instantáneo. Estas pueden ser enviadas a teleconsulta o ser almacenadas para realizar un estudio comparativo posterior. (Figura 1B)

Figura 1. Dermatoscopios. A. Ejemplo de uno de los diferentes tipos de dermatoscopio de mano; B. Dermatoscopio acoplado a teléfono móvil. (Fuente: Dermlite www.dermlite.com)

La visualización de estructuras en dermatoscopia se realiza gracias a la presencia de cromóforos. El principal es la melanina que ofrecerá, por el efecto Tyndall, un color distinto según la profundidad: negro en capa córnea, marrón en epidermis y unión dermoepidérmica, gris en dermis papilar y azul en dermis reticular. El segundo cromóforo es la hemoglobina que variará su color dependiendo si es sangre arterial o venosa, el tamaño del vaso, la profundidad y si está coagulado dando tonalidades de rojo vivo a pardo, violeta o incluso azul o negro. Otros cromóforos de la piel son la queratina (color blanco, amarillento o marronáceo), los lípidos (colores amarillos o naranjas), el hierro de la hemosiderina (tonalidades verdes) o el colágeno (blanco).

Con el dermatoscopio, podemos visualizar directamente estructuras de la epidermis, unión dermoepidérmica y dermis superficial de una forma accesible y no invasiva. Éstas tienen una muy buena correlación con estructuras anatómicas que pueden observarse en la histopatología, permitiendo una mejora en la precisión

diagnóstica y en la toma de decisiones en diferentes lesiones y/o patologías de la piel.

De esta forma, para cada estructura dermatoscópica visualizada, existe una o varias correlaciones a nivel histopatológico. Ésto no solo permite inferir el diagnóstico (muchas veces sin necesidad de biopsia), sino que también nos orienta a elegir el mejor sector para biopsiar. Tal es el grado de correlación, que ya hay diversos estudios en los que la utilización de la dermatoscopia en el laboratorio de histopatología mejora la inclusión de lesiones. [1,10,11]

A lo largo del tiempo se han descrito diferentes criterios dermatoscópicos y se han desarrollado distintos métodos o algoritmos diagnósticos. La aproximación diagnóstica suele realizarse en dos etapas para definir primero si la lesión es melanocítica o no. Si la lesión tiene criterios de lesión melanocítica se aplican distintos algoritmos o métodos diagnósticos.[11,12] Algunos ejemplos de estos métodos son: el análisis de "patrones", la regla del "ABCD", el método de "Menzies", el de "7-point checklist" (Argenziano), entre otros. A pesar de todos estos métodos, los dermatoscopistas expertos utilizan, de una forma casi intuitiva, el método de patrones, siendo capaces de diagnosticar lesiones en aproximadamente un segundo. [12-17] En él se analiza la lesión globalmente en cuanto al patrón global (simetría o asimetría en color y estructuras), colores presentes (marrón, rojo, blanco, azul, negro) y patrón global (homogéneo, reticular, globular, combinaciones de dos, multicomponente o inespecífico). Posteriormente, si es necesario, se analiza en detalle las distintas estructuras y su distribución. (Figura 2)

Se han descrito diferentes patrones dermatoscópicos para la gran mayoría de tumores cutáneos (melanocíticos y no melanocíticos). Un ejemplo de patrones

dermatoscópicos encontrados en el tumor más frecuente a nivel mundial, el carcinoma basocelular, son la presencia de "hojas de arce", "ruedas de carro", "glóbulos azul-grises", "nidos ovoides azul-grisáceos", "ulceración", "telangiectasias arborescentes", entre otros.[3,9] (Figura 3) En lesiones melanocíticas, estos criterios diagnósticos pueden variar de acuerdo con la localización corporal. En topografías especiales, como por ejemplo la cara, las palmas, las plantas y las mucosas, otros criterios dermatoscópicos específicos han sido descritos.[15-17] En lesiones melanocíticas faciales, uno de los principales criterios diagnósticos para el diagnóstico de melanoma temprano, es la presencia de "puntos" que se van agregando en el área peri-folicular. (Figura 2)[3,14]

Diferentes metanálisis y revisiones han mostrado que la dermatoscopia, dependiendo de la experiencia del observador,[18-19] ha mejorado la sensibilidad diagnóstica para melanoma en más de 25%, comparada con el ojo desnudo. Con relación a otros tumores malignos cutáneos, como el carcinoma basocelular, metanálisis han mostrado una sensibilidad de 91.2% y especificidad del 95% con el uso de la dermatoscopia.[20] Además, cuando ésta ha sido comparada al ojo desnudo, la sensibilidad aumentó de 66.9% a 85% (P = 0.0001) y la especificidad de 97.2% a 98.2% (P = 0.006).[20] La sensibilidad, al igual que en lesiones melanocíticas, aumentó en observadores expertos comparados con inexpertos.[14,20]

Los primeros estudios se enfocaron en diferenciar las lesiones melanocíticas benignas de las malignas. Sin embargo, en la actualidad es utilizada no solamente en todos los tipos de patología tumoral cutánea, si no que, además, en patologías inflamatorias, infecciosas o cualquier otro tipo de dolencia cutánea.[21]

Por su pequeño tamaño, precio y practicidad, esta técnica ha revolucionado el ámbito de la dermatología, transformándose en un complemento imprescindible durante el examen físico del paciente dermatológico.[1] La dermatoscopia digital se incorpora en muchos de los dispositivos innovadores de microscopía no invasiva de la piel para "navegar" y localizar las áreas de la lesión exploradas y finalmente combinar la información diagnóstica obtenida con estos dispositivos.

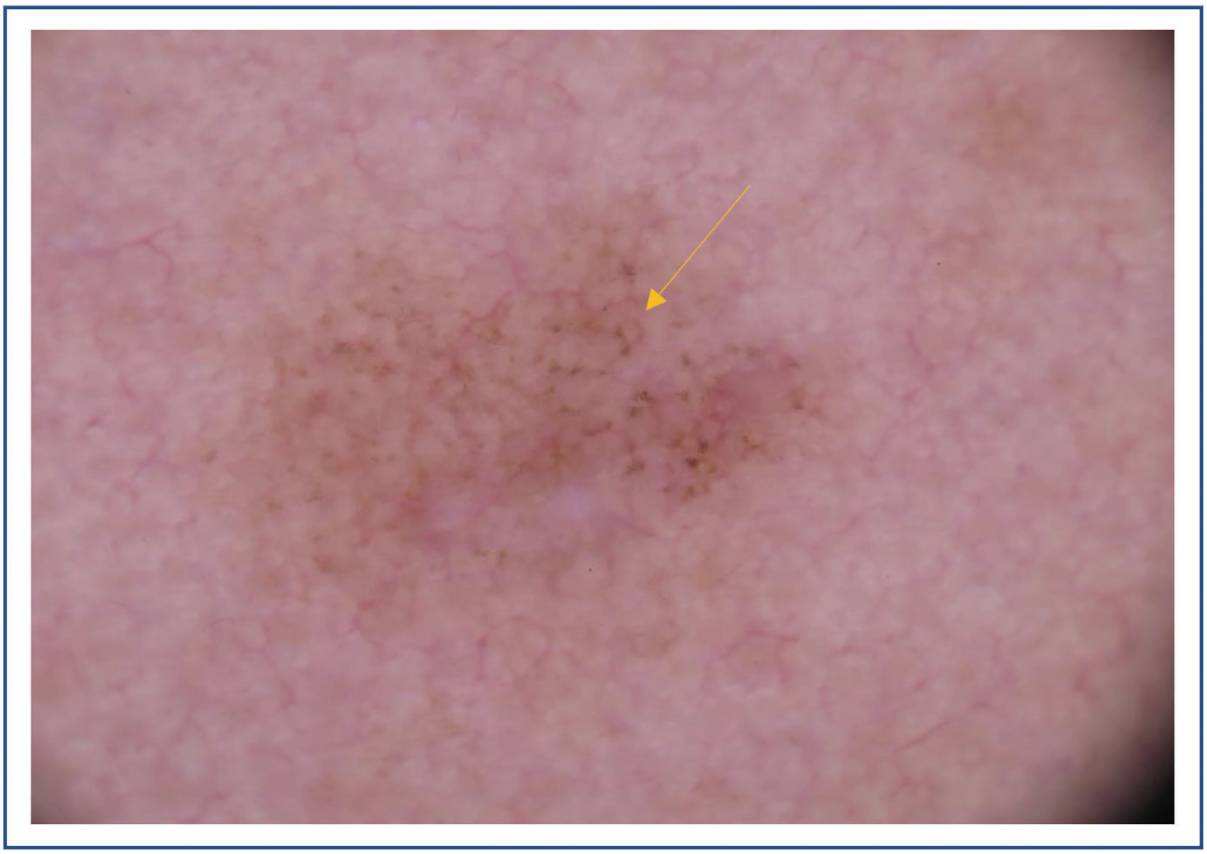

Figura 2. Dermatoscopia de lentigo maligno facial incipiente. Presencia de puntos marrones perifoliculares, caracterizado por puntos que se disponen alrededor de las aberturas foliculares (fecha amarilla) en una mácula marrón. Los márgenes de este tumor son difíciles de determinar con esta técnica. (Fuente: Dra. Cristina Carrera)

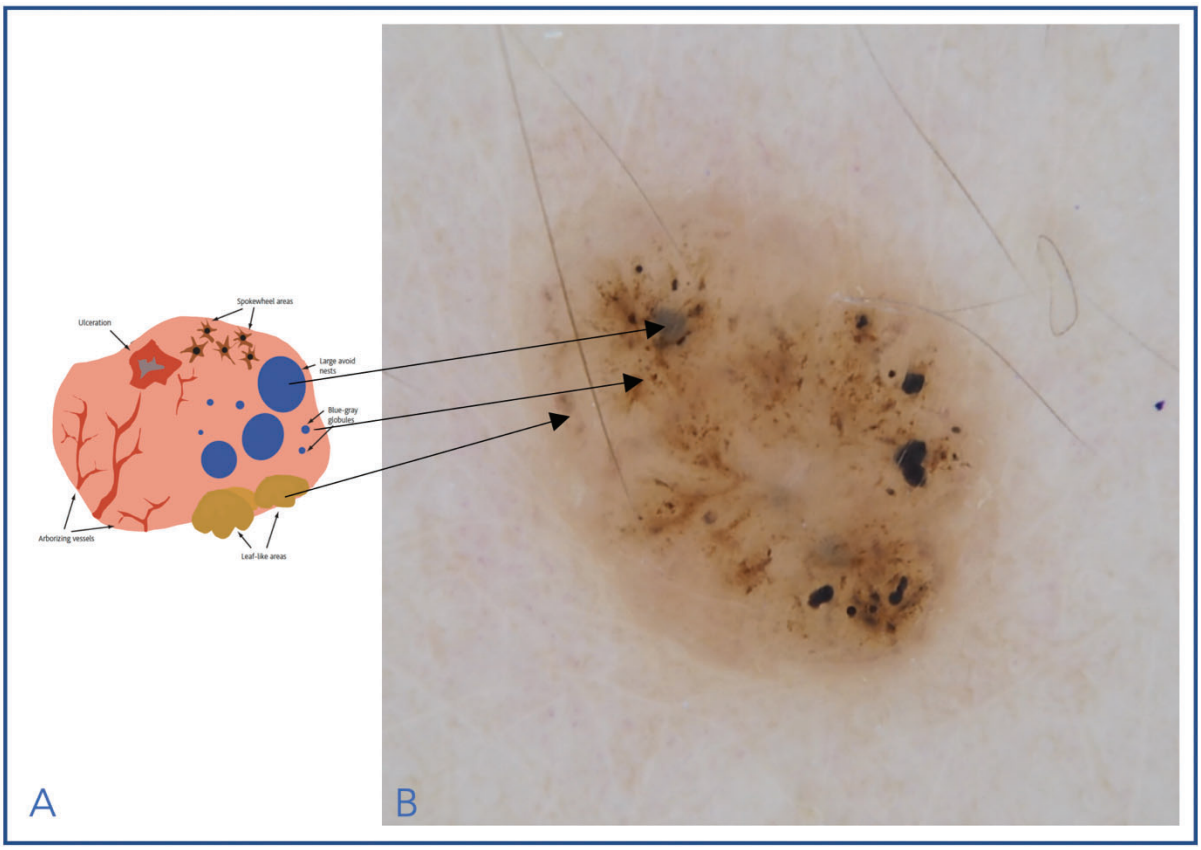

Figura 3. Dermatoscopia de carcinoma basocelular. A. Esquema de los principales patrones dermatoscópicos encontrados en un carcinoma basocelular. (Adaptado de Malvehy et al., 2006);[9] B. Dermatoscopia de carcinoma basocelular con patrones como "nidos ovoides azul-grises", "glóbulos azul-gises", "ruedas de carro", entre otros. (Fuente: Dra. Javiera Pérez-Anker)

I.1.2 Microscopia confocal *in vivo*

Esta técnica de imagen no invasiva, llamada microscopía de reflectancia confocal *in vivo*, permite la visualización de tejidos con una resolución aún mayor que la de la dermatoscopia. Por medio de este dispositivo, podemos visualizar la epidermis, la unión dermoepidérmica y la dermis papilar con resolución celular, en tiempo real.[22] (Figura 4)

El microscopio confocal amplifica el área examinada mediante un sistema de lentes (incluyendo un divisor de haz) que aumentan y direccionan la luz reflejada de un láser de diodo de 830 nm. El láser es emitido por el dispositivo y reflejado por la piel, que regresa a través de un divisor de rayo y golpea el detector. Esta luz reflejada pasa por un diafragma de muy pequeño diámetro, resultando en la visualización instantánea del tejido en un punto en foco (confocal). Tanto la fuente de luz, como el punto iluminado en la piel, como la apertura del detector, están en planos focales ópticamente conjugados (interconectados confocalmente). (Figura 4)

La resolución a nivel celular es de 0,5 µm a 1,0 µm lateralmente y de 4 µm a 5 µm en profundidad. Las imágenes se reproducen en una escala del gris siendo las estructuras con más reflectividad de color blanco y la ausencia de reflectividad de color negro. La mayor reflectividad se produce por la melanina, seguido por los gránulos de queratina, algunas organelas citoplasmáticas, el colágeno que contrastan con la ausencia de reflectividad en el agua. Sin embargo, una limitación de la microscopia confocal *in vivo*, es que la penetración del láser en profundidad alcanza la dermis papilar (aproximadamente entre 200 µm y 250 µm).[22,23] La imagen final ("mosaico") que es obtenida por algunos confocales, se debe a la unión de imágenes individuales ("frame by frame"), que se van agregando horizontalmente, uno al lado

de otro, hasta componer la imagen final. Cada "imagen individual" varía entre 500 µm a 750 µm, dependiendo del dispositivo utilizado. (Figura 5) Recientemente se ha desarrollado un algoritmo que permite la fusión de imágenes de video para producir una imagen de mayores dimensiones en un video mosaico.[23]

Existen actualmente dos tipos de microscopios confocales *in vivo* comercializados para el uso en pacientes, y ambos pertenecen a la misma empresa: el VIVASCOPE (VS) 1500® y el Vivascope (VS) 3000®. El mecanismo de obtención de las imágenes es el mismo (láser de reflectancia de 830 µm, con resolución óptica horizontal de < 1,25 µm y vertical de < 5,0 µm, en el centro de la imagen). La diferencia principal entre ambos está en el cabezal para obtención de imágenes. Uno de ellos presenta un cabezal que se fija a la piel mediante un adhesivo desechable y realiza un escaneo automático (VS 1500), mientras que el otro presenta un cabezal libre y el escaneo se realiza de manera manual por el operador (VS 3000). Este último, es más apropiado para explorar localizaciones específicas, como facial, mucosas o acrales. El VS 3000 adquiere imágenes individuales de superficie igual a 750 µm x 750 µm y no tiene límites respecto al tamaño del área a escanear puesto que depende del operador. El VS 1500, en cambio, adquiere imágenes de 500 µm x 500 µm pero realiza un barrido en superficie que abarca un área cuadrangular máxima de 8.0 mm x 8.0 mm componiendo así un mosaico de superficie mayor compuesto por las diferentes imágenes individuales. A diferencia del V3000 el equipo V1500 con fijación en la piel incorpora una cámara de dermatoscopia adicional para navegar y correlacionar las estructuras diagnósticas de ambas técnicas. Ambos equipos de MCR tienen la misma resolución óptica de 1024 x 1024 píxels y la pantalla de visualización de las imágenes escaneadas, es táctil de 23" (1920 x 1080 de resolución). (Figura 5)

La 4ª generación de estos aparatos ha incorporado la tecnología de "streapping". Por medio de ésta, la imagen se obtiene en tiras verticales que incluye el total del eje vertical del plano a medida que avanza por el eje horizontal. En esta nueva generación, la obtención de imágenes se realiza de manera vertical y no horizontal como previamente. Como resultado obtenemos una adquisición de imágenes con mayor rapidez y con desaparición del artefacto creado en la unión entre las imágenes de imagen que conforman el mosaico (imagen final). (Figura 5).[23]

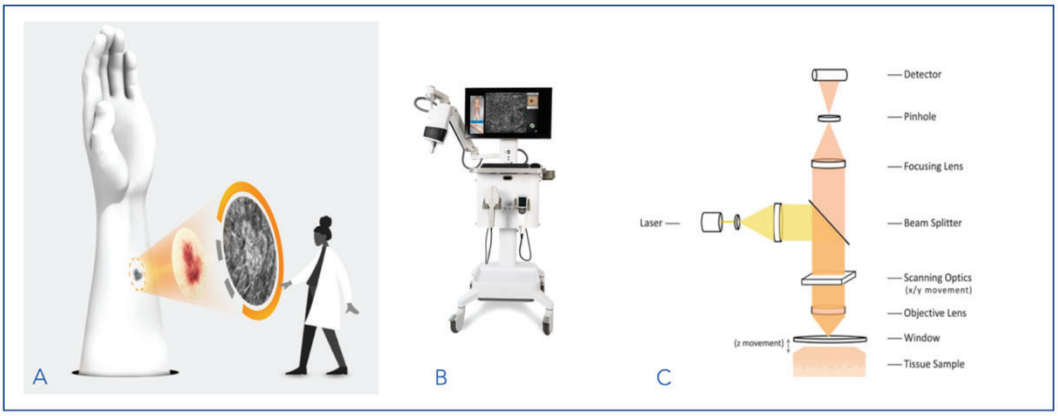

Figura 4. A. Microscopio confocal in vivo: visualización instantánea de la piel con resolución celular; B. VIVASCOPE 1500 y 3000®; C. Mecanismo de funcionamiento del confocal. (Fuente: VivaScope www.vivascope.de)

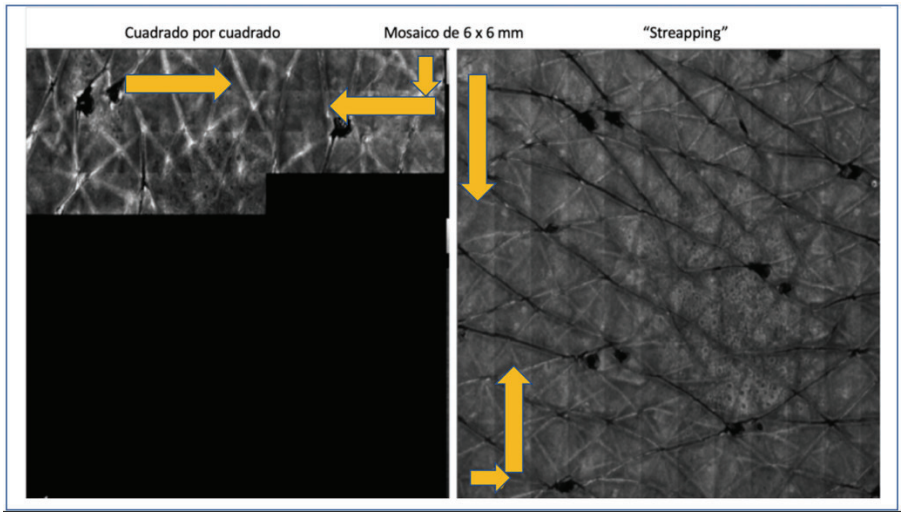

Figura 5. Formación de "mosaicos", comparación en tiempo real. Izquierda: 3ª generación. La imagen es formada "imagen por imagen", por la unión "horizontal" de una imagen con la siguiente. Derecha: 4ª generación. La imagen es más rápida y se genera una imagen lineal vertical. El mosaico final resultante es más homogéneo, sin el artefacto creado por las uniones entre las imágenes individuales (Fuente: VivaScope www.vivascope.de)

Las estructuras visualizadas en las imágenes de confocal se correlacionan con elementos morfológicos o celulares, vistos en cortes histológicos horizontales. De esta forma, se pueden observar imágenes instantáneas, *in vivo*, de secciones horizontales (con resolución celular) de diferentes niveles de la piel. (Figuras 6 y 7)

Múltiples criterios diagnósticos han sido descritos tanto en patologías malignas como benignas de la piel. Una de sus aplicaciones más reconocidas ha sido en la diferenciación de lesiones melanocíticas dudosas de las malignas. Con esta finalidad, se describieron diferentes patrones que pueden ser encontrados en los distintos niveles de la piel como, por ejemplo, en epidermis: "epidermis en panal de abejas", "en empedrado", "epidermis desestructurada", o hallazgos citológicos como la presencia de "células pagetoides". En dermis, algunos de los criterios visualizados son: "papilas dérmicas visibles" (que pueden ser bien o mal delimitadas), "nidos dérmicos" (regulares y densos, no homogéneos o cerebriformes), o la presencia de "células atípicas" a nivel de unión dermoepidérmica o bien "células atípicas nucleadas". (Figuras 6 y 7)[24-28]

Con el objetivo de diferenciar lesiones melanocíticas de no melanocíticas y nevus atípicos de melanomas tempranos, se ha validado el "algoritmo de dos pasos".[29] En el primer paso, la presencia de papilas dérmicas visibles, patrón en empedrado, presencia de células pagetoides y de nidos dérmicos, se relacionan con

lesiones melanocíticas. Con la sospecha de lesión melanocítica, se evalúa el segundo paso donde la presencia de células redondas supra basales (pagetoides epidérmicas) y de células nucleadas atípicas en la unión dermoepidérmica o dermis se asocian a melanoma, y, la presencia de papilas bien delimitadas, con células típicas en la unión dermoepidérmica, se ha asociado con nevus melanocítico benigno. (Figura 6)[29]

Por otro lado, en otros tumores muy frecuentes, como el carcinoma basocelular, se observan criterios como "nidos dérmicos híper refráctiles", "siluetas oscuras", "empalizada", "clefting" y "células dendríticas peri tumorales". (Figura 7) Además, es posible la diferenciación entre distintos subtipos tumorales. Los criterios como la presencia de nidos tumorales en el carcinoma basocelular en las capas superiores de la superficie epidérmica o la polarización de los núcleos (streaming), nos permiten inferir la sospecha del subtipo tumoral "superficial". (Figura 7)

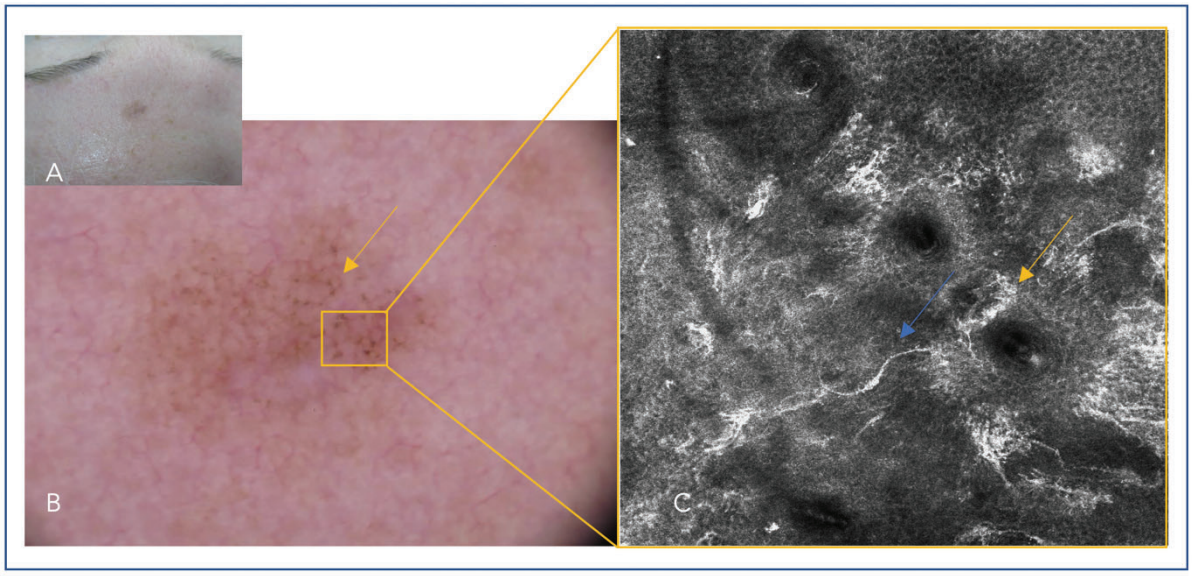

Figura 6. Correspondencia de técnicas de imagen en lentigo maligno facial. A. Foto clínica; B. Dermatoscopia mostrando patrón granular anular gris (fecha amarilla); C. MCR con presencia de células dendríticas (flecha azul) a nivel epidérmico y refuerzo perifolicular con células nucleadas atípicas (flecha amarilla). (Fuente: Dra. Cristina Carrera)

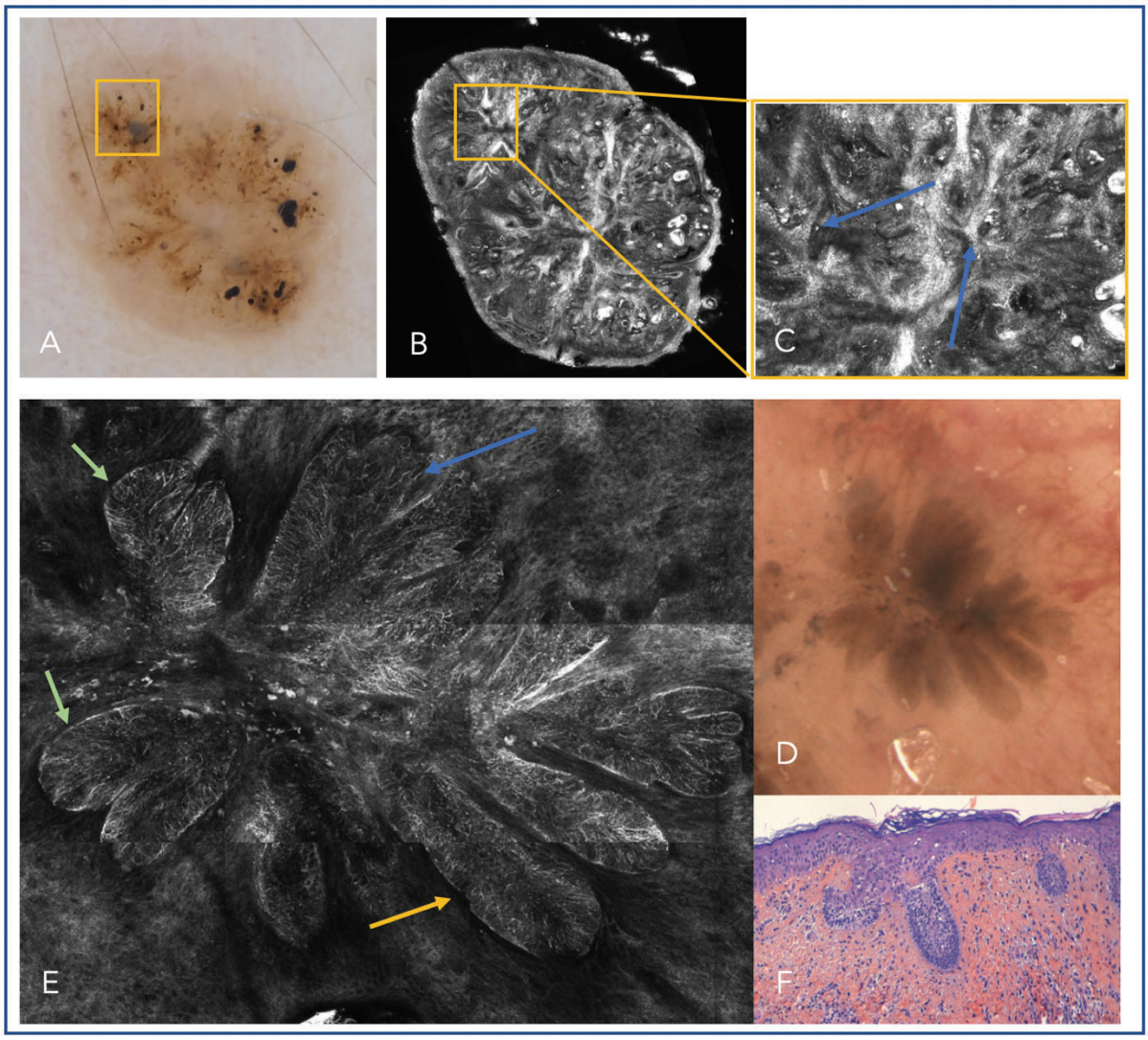

Figura 7. Correspondencia de técnicas de imagen en carcinoma basocelular. A. Dermatoscopia de carcinoma basocelular; B. Microscopia confocal *in vivo* del mismo carcinoma. Los patrones dermatoscópicos de "nidos ovoides azul-grises", "glóbulos azul-gises", "ruedas de carro", se corresponden con nidos de carcinoma basocelular (C: cuadrado amarillo); D. Dermatoscopia de una "hoja de arce" y su correlación exacta con MCR (E); F. Correlación histológica (carcinoma basocelular superficial) de la misma estructura dermatoscópica. Los criterios de MCR observados son "islas/nidos tumorales blanco brillantes" (flecha azul), la "hendidura peri-tumoral" (flecha amarilla) y la "empalizada periférica" (flecha verde). (Fuente: Dra. Javiera Pérez-Anker, Dra. Puig y Dr. Josep Malvehy)

En patología inflamatoria, distintos estudios describen los patrones asociados a otros diagnósticos como en el eccema y la psoriasis.[30']

En el campo de las lesiones melanocíticas, los estudios han alcanzado tasas de sensibilidad de 98.15% y especificidad del 98.89%.[31-38] En un estudio reciente prospectivo, multicéntrico, liderado por el grupo de la Universidad de Módena, Italia, se incluyeron más de 3000 lesiones dermatoscópicamente dudosas, que fueron randomizadas en dos grupos, con y sin el uso de la MCR. Los autores demostraron que, mediante el uso de la MCR, el número de biopsias realizadas disminuyó a la mitad en las lesiones con un diagnóstico equívoco, con un aumento significativo de la precisión diagnóstica en las lesiones benignas respecto a la dermatoscopia. Por otro lado, se demostró que las lesiones melanocíticas con atipia, que se recomendaron controlar después de la MCR, y que fueron extirpados posteriormente en un control con un diagnóstico de malignidad, eran melanomas "finos", con un Breslow menor que respecto al grupo sin confocal (MCR: SD 0.19, rango 0.24, 0-0.8 mm de Breslow en promedio, vs NO MCR: SD 0.15, rango 0.22, 0-0.8 mm de Breslow en promedio, con un p value de 0.02).[39]

Con respecto al cáncer cutáneo no melanoma, la sensibilidad ronda casi el 100% en algunas series en el diagnóstico de carcinoma basocelular.[33, 40] Sin embargo, los tumores queratinizantes pueden ser menos accesibles a su visualización con esta técnica cuando presentan gran hiperqueratosis, debido a que la señal de la escama interfiere en la visualización de estructuras en profundidad. [33]

Este dispositivo, no sólo es un complemento necesario para mejorar la capacidad diagnóstica y el reconocimiento de áreas dudosas, si no que, además,

ayuda en la delimitación de márgenes pre operatorios, en la monitorización de tratamientos y en el diagnóstico de lesiones complejas como el melanoma amelanótico.[5] Su uso en el diagnóstico diferencial de lesiones dermatoscópicamente equivocas, ha cambiado significativamente el diagnóstico no invasivo en dermatología, aportando evidencia histológica de forma instantánea, evitando exéresis innecesaria de estas lesiones.

I.1.3 Tomografía de coherencia óptica confocal de campo lineal (TCO-CL)

El principio físico que se aplica a las técnicas de imagen diagnósticas establece que cuanto mayor la capacidad de penetración de fuentes de luz en el tejido, menor resolución de estructuras es observada.

Con la necesidad de lograr un dispositivo que logre mayor visualización morfológica en profundidad que la MCR, sin perder resolución celular, aparece la tomografía de coherencia óptica de campo lineal. Esta técnica une conceptos y tecnología de microscopia confocal *in vivo* (como los filtros espaciales) y de tomografía de coherencia óptica (como la interferometría). Así siendo, se logra que dos fuentes de luz diferentes, que pasan por dos objetivos (a diferencia del confocal, con solo una fuente de luz y un solo objetivo), penetren en los tejidos de forma vertical y en oblicuo, respectivamente. Esto proporciona no solo una mayor visualización de estructuras profundas, sino que también la obtención de imágenes en 3 dimensiones (3D) en tiempo real. La penetración en profundidad alcanza las 450 µm de estructuras morfológicas, conservando la resolución celular hasta una profundidad de ± 350 µm. [41,42] (Figura 8)

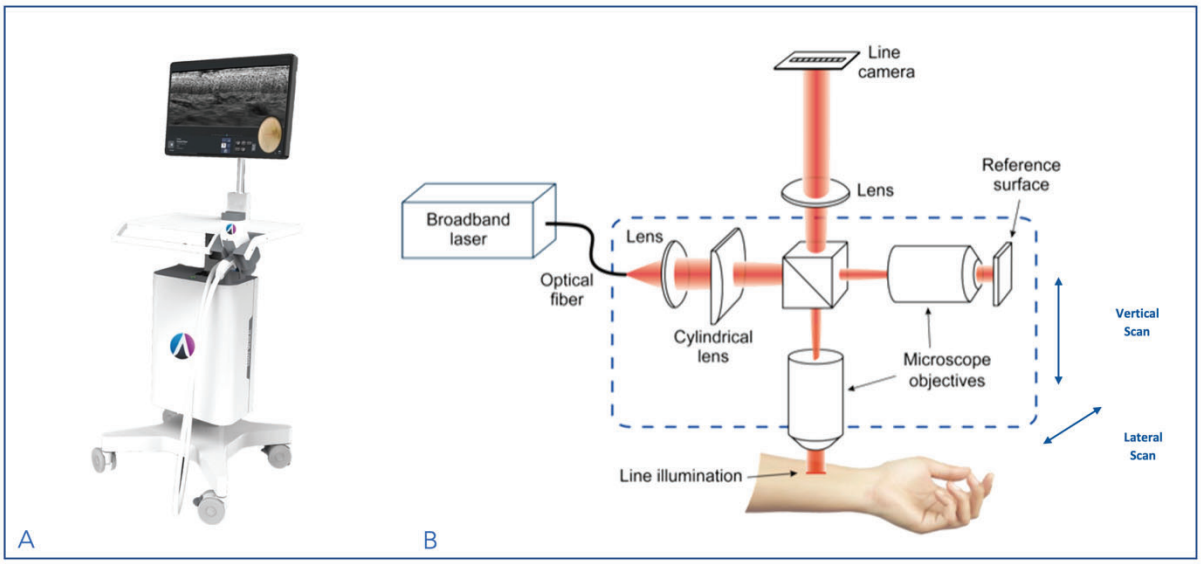

Figura 8. Tomografía de coherencia óptica confocal de campo lineal. A. DeepLive®; B. Mecanismo de captura de imágenes. A diferencia del confocal, hay dos fuentes de luz y dos objetivos que conducen la fuente de luz. (Fuente: Damae-medical https://damae-medical.com). Tecnología inventada por Pr. Arnaud Dubois (CNRS, IOGS, UPSUD), licenciado exclusivamente para DAMAE Medical, fundada en septiembre de 2014)[41,42]

Este dispositivo presenta tres grandes ventajas: la imagen dermatoscópica integrada (por primera vez, se identifica el punto exacto de la imagen dermatoscópica que está siendo escaneado, con las imágenes de TCO-CL, en tres dimensiones); la piel es observada en cortes verticales con resolución celular y, por último, la formación de cubos de piel escaneada en 3 D, que mantienen resolución celular. (Figura 9)

La imagen vertical tiene un área de 1.2 mm x 0.4 mm, con resolución óptica de 1.3 µm x 1.1 µm. La imagen horizontal, es de 1.2 mm x 0.5 mm (mayor que cada "imagen individual (frame)" del microscopio confocal, pero inferior a los mosaicos de 8x8 mm de la MCR), con resolución óptica de 1.3 µm x 1.3 µm. El cubo de 3D, es comprendido por la unión de las otros dos secciones vertical y horizontal. (Figura 9)

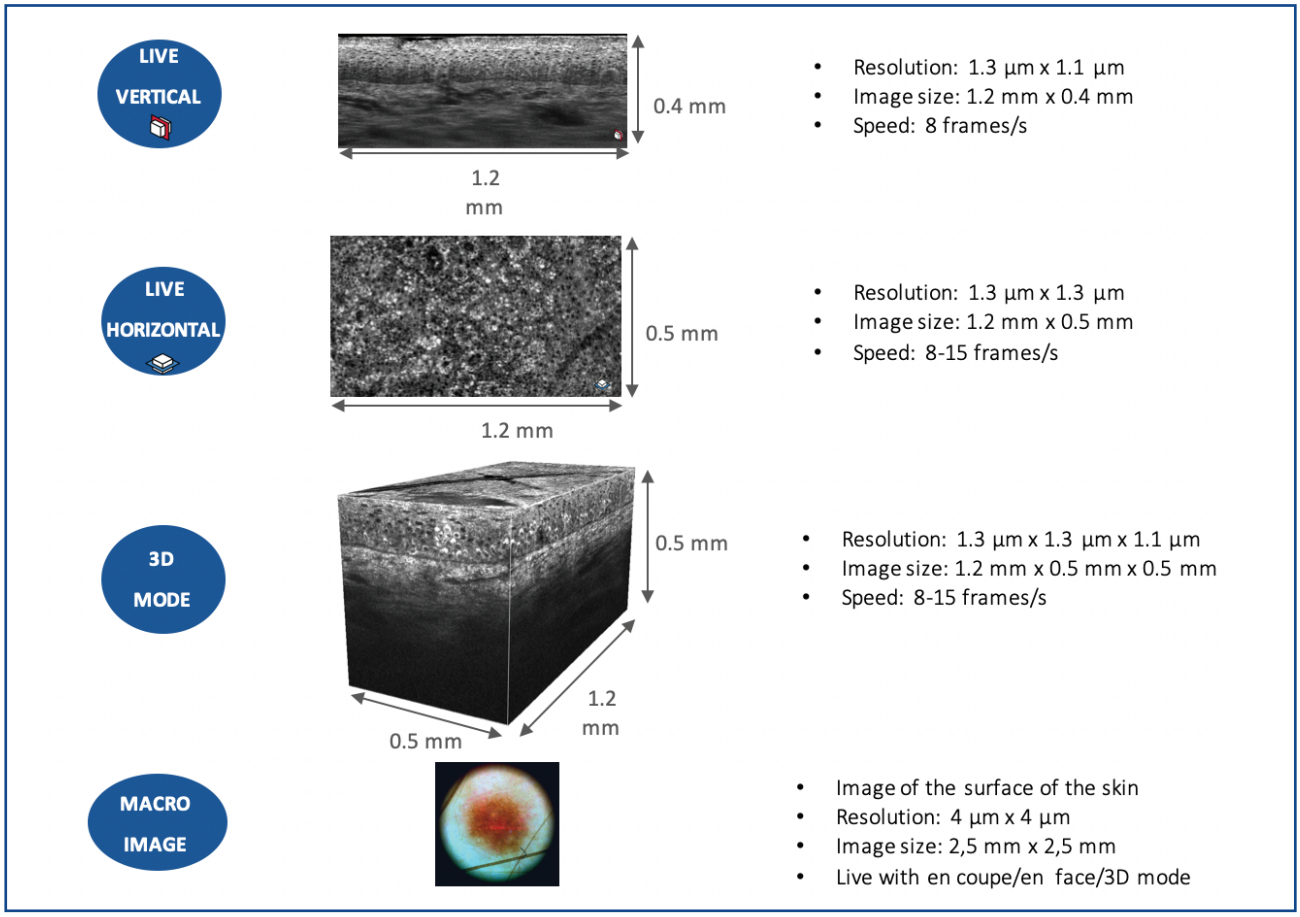

Figura 9. Tomografía de coherencia óptica confocal de campo lineal. Rango de resolución y de penetración. Estructuras cutáneas observadas en vertical, horizontal y en 3D, con la correlación dermatoscópica a nivel celular. (Fuente: Damae-medical https://damae-medical.com). Tecnología inventada por Pr. Arnaud Dubois (CNRS, IOGS, UPSUD), licenciado exclusivamente para DAMAE Medical, fundada en septiembre de 2014)[41,42]

El mecanismo de obtención de las imágenes es semejante al de la microscopía confocal de reflectancia. La fuente de luz refleja en los tejidos que, por su índice de reflectancia natural, brillarán con más o menos intensidad.

En el momento actual, esta tecnología se encuentra patentada (inventada por el Dr. Arnau Dubois), por lo que aún no existen otros dispositivos en el mercado con semejantes características. Mediante la formación de un consorcio europeo de investigación entre Italia, Bélgica, Francia y España, y también de otros grupos a nivel internacional, se han realizado diferentes estudios en distintos tipos de tumores y de patologías cutáneas en los últimos años. [43,44]

Aun no se han descrito algoritmos diagnósticos para guiar el diagnóstico de diferentes tumores con esta técnica. Sin embargo, se han descrito los criterios diagnósticos para algunos de ellos, como, por ejemplo, el carcinoma basocelular.[45,46] Los criterios más frecuentemente encontrados por los autores fueron: la presencia de "lóbulos", "vasos sanguíneos" y "células pequeñas y brillantes en la epidermis o en la periferia de los lóbulos" (que pueden corresponder a células dendríticas). El subtipo superficial se asoció a la presencia de "lóbulos hemisféricos unidos a la epidermis"; el nodular, con "lóbulos grandes, hemisféricos, sin conexión con la epidermis" y, por último, el subtipo infiltrante, con "glóbulos ramificados", rodeados por estroma.[45] (Figuras 10 y 11)

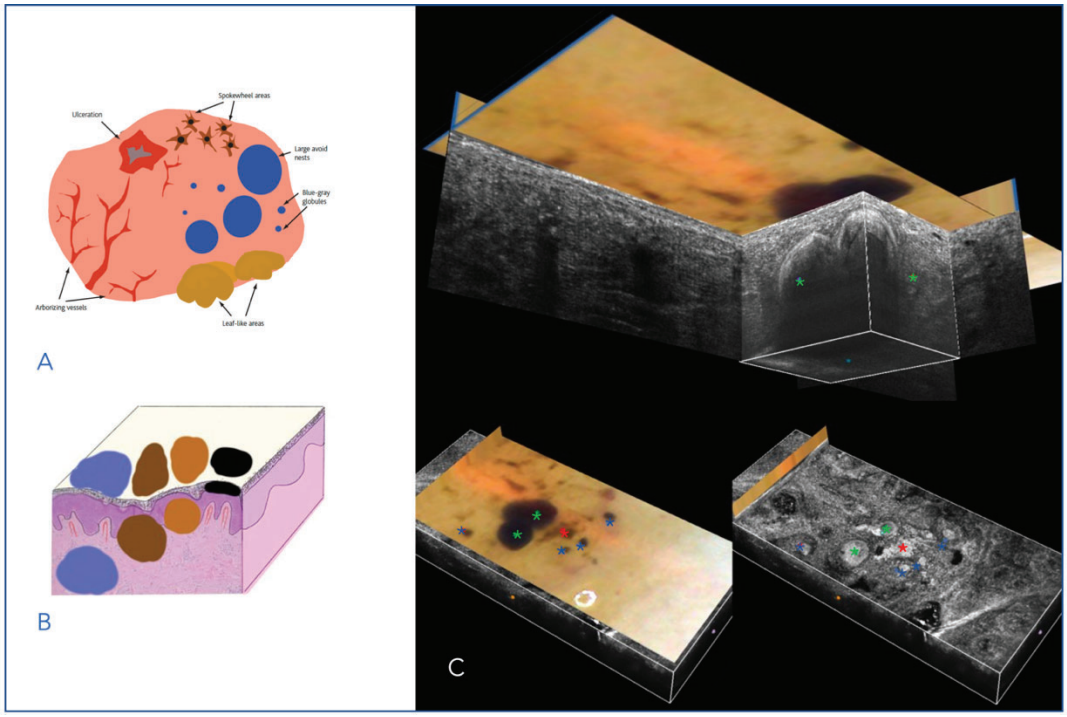

Figura 10. Correlación dermatoscópica con TCO-CL. A. Esquema de los principales patrones dermatoscópicos encontrados en un carcinoma basocelular. (Adaptado de Malvehy et al., 2006);[9] B. La coloración varía de acuerdo con la profundidad de las estructuras. (Adaptado de Malvehy et al., 2006);[9] C. Cada estructura vista en dermatoscopia tiene una precisa correlación morfológica tanto en vertical, como en horizontal. Asteriscos verdes: "nidos ovoides". Asteriscos azules: "nidos ovoides azul-grises". Asterisco rojo: nido de carcinoma basocelular superficial. (Fuente: Javiera Pérez-Anker)

Otros autores también han caracterizado el carcinoma basocelular con esta tecnología,[46] pero con descripciones morfológicas, más próximas a la histología. De esta forma, han encontrado que los carcinomas basocelulares nodulares, presentaban "queratinocitos atípicos", con la "unión dermoepidérmica alterada", con la presencia de "nidos de células tumorales en dermis", "hendidura peri tumoral", "aumento de vascularización "y la presencia de un "estroma característico". Los carcinomas basocelulares superficiales, presentaban una "epidermis engrosada" por la evidente

presencia de nidos tumorales conectados a la epidermis. Los carcinomas basocelulares infiltrantes, fueron vistos por "nidos alargados hiporefráctiles", rodeados por un denso "estroma brillante".[46] (Figura 11)

En el mismo estudio, la concordancia entre el TCO-CL y la histología entre los diferentes subtipos, fue de 90.4% (95% CI 79.0-96.8). Con respecto a la precisión diagnóstica,[46] en el caso del diagnóstico de carcinomas basocelulares equívocos con la dermatoscopia, la confianza diagnóstica mejoró en un 22% con el uso de la nueva tecnología (48% dermatoscopia vs 70% TCO-CL). La sensibilidad fue de 98% y la especificidad del 80%, cuando fueron comparados con la histología. La concordancia inter observador fue del 95%. Cuando se analizó la combinación de TCO-CL con dermatoscopia, la sensibilidad aumentó al 100% y la especificidad al 94.9%.

Esta herramienta, sin duda, ha venido a abrir fronteras respecto a la compresión tridimensional de la piel normal y patológica. En los próximos años, más estudios permitirán una compresión morfológica totalmente distinta a la actualmente descrita.

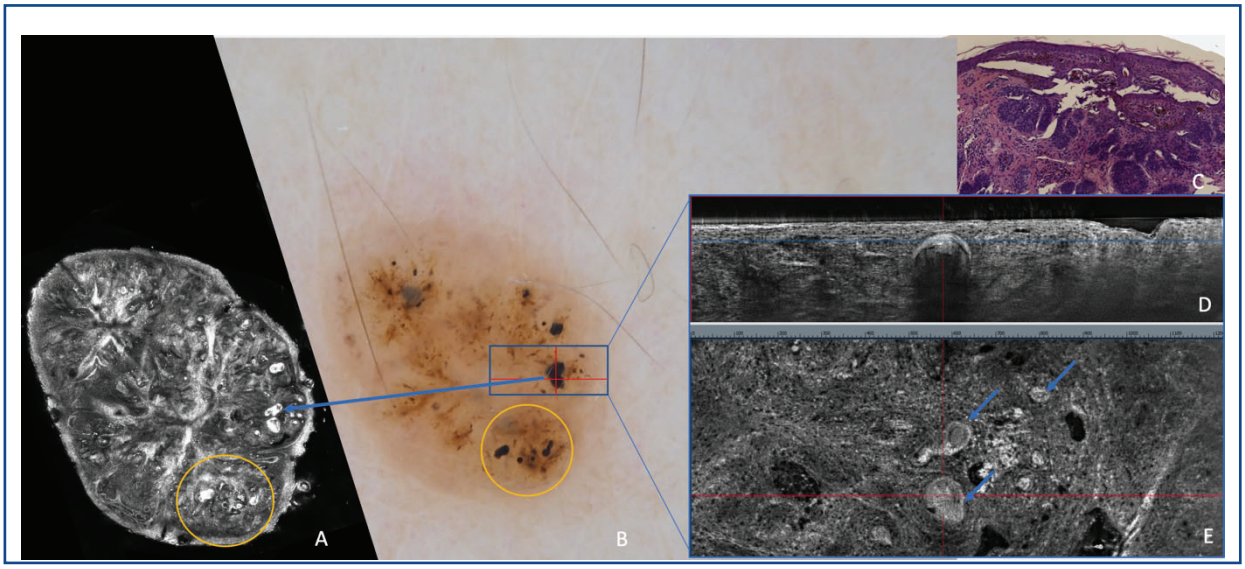

Figura 11. Tomografía de coherencia óptica confocal de campo lineal de un carcinoma basocelular nodular. El mismo tumor visto en las diferentes técnicas de diagnóstico *in vivo*. Cada estructura vista en dermatoscopia tiene una precisa correlación morfológica tanto en vertical, como en horizontal y un hallazgo histológico correspondiente. A. MCR de carcinoma basocelular; B. Dermatoscopia del mismo tumor; C. Correspondencia histológica; D. TCO-CL corte vertical; E. TCO-CL corte horizontal. Las flechas azules indican los nidos de carcinoma basocelular y su correspondiente visualización encada técnica. El cuadro amarillo, muestra la correspondencia de las mismas estructuras en dermatoscopia y MCR. (Fuente: Javiera Pérez-Anker)

I.1.4. Tomografía de coherencia óptica (TCO)

La TCO de ha usado para el estudio en oftalmología y otras especialidades desde hace décadas. Esta técnica posee una mayor penetración en la piel que la MCR y la TCO-CL, permitiendo la visualización morfológica a 1 mm-2 mm en profundidad. Existe un equipo con marca CE aprobado por la EMA y la FDA para su uso de dermatología (Vivosight Dx^{R}; Michaelson diagnostics. UK). Las imágenes escaneadas son de 6 mm x 6 mm y se presentan en cortes verticales (sin resolución celular). La TCO es una técnica que utiliza una fuente de luz cercana a la infrarroja y en este equipo se utiliza una fuente de luz central de 1305 nm de longitud de onda y un barrido de un rango de 147 nm. Su alcance en profundidad permite la visualización de estructuras morfológicas en dermis en 15 segundos, o en 30 segundos (si además se captura la vascularización de los tejidos). Este sistema usa una tecnología con 4 diferentes haces de luz, cada uno enfocado a diferentes profundidades, que mejora la resolución en profundidad.

Este equipo produce 500 cortes transversales (fotogramas) por escaneo, lo que le confiere la capacidad de reconstruir los tejidos en 3D. La resolución axial varía entre de 3 µm - 15 µm (7.5 µm en profundidad). La imagen final resultante puede ser vista tanto en un corte vertical, como en un video continuo, o en 3D (sólo en el modo de patrón de vascularización). Tiene una cámara macroscópica integrada que permite la correlación clínica instantánea de lo que está siendo escaneado (Figura 12)

Las imágenes son producidas por la refracción de la luz cuando la misma contacta con los tejidos de diferentes densidades ópticas, utilizando una técnica llamada interferometría,[47] midiendo la profundidad de acuerdo con la cantidad de disrupción de cada tejido a medida que la fuente de luz pasa por el mismo.[47] Cuatro

haces de luz, donde cada uno se enfoca en una profundidad diferente, brindan no sólo una resolución más alta, sino también un aumento en la profundidad de penetración de la luz en el tejido (comparados con un sistema de un solo haz).

Dentro de sus principales aplicaciones, se encuentran el diagnóstico y monitorización de tratamiento de carcinomas basocelulares,[48] y, sobre todo, la caracterización de lesiones vascularizadas. Por medio del análisis del patrón de vascularización, es posible determinar la persistencia de lesiones o la profundidad de estas. (Figura 13) Algunos de los patrones descritos para carcinoma basocelular son:[49] la disminución del espesor epidérmico, la presencia de costras, la ulceración y la disminución de los folículos pilosos. Los nidos de carcinoma basocelular son observados como un "patrón lobular" y tienen una reflectividad menor que la del área perilesional. La hendidura peri tumoral es visualizada como un "halo negro" en la periferia del tumor. (Figura 13)

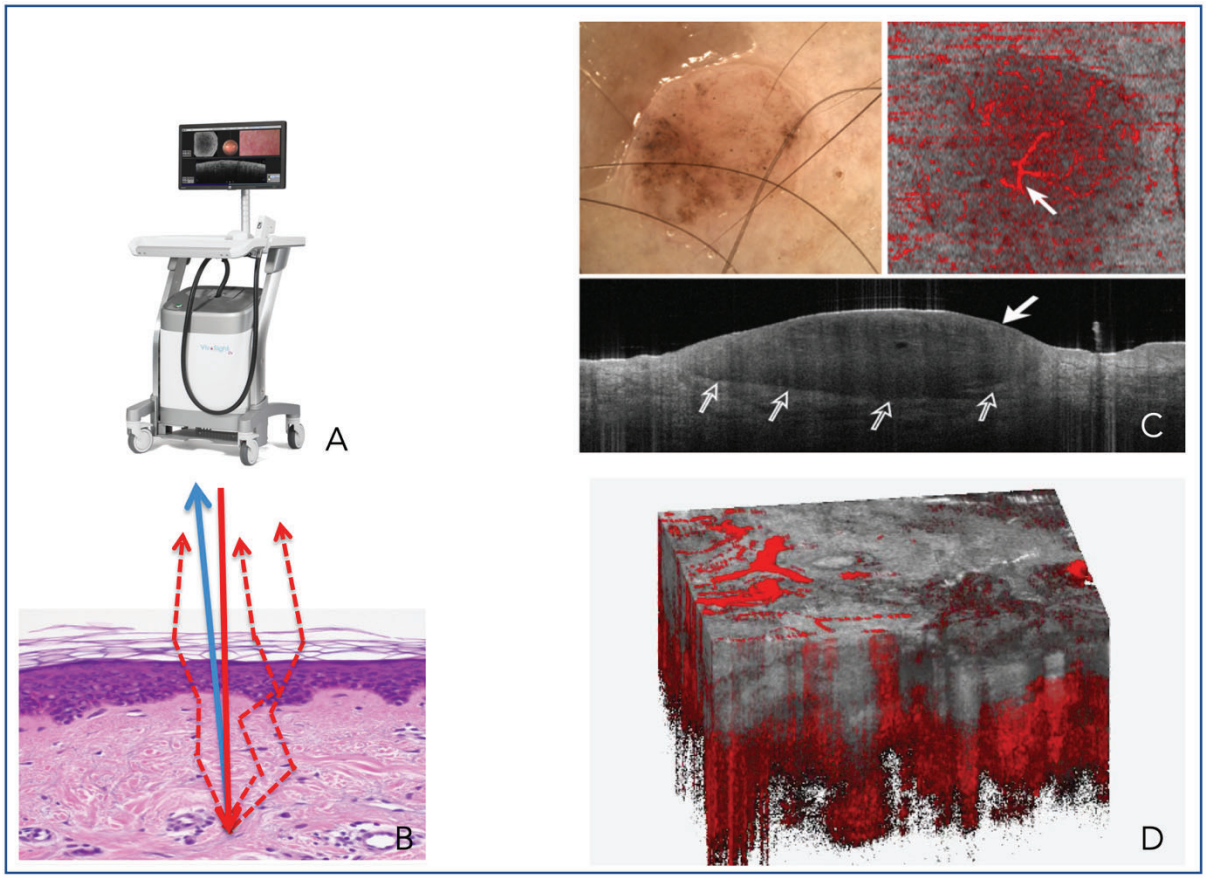

Figura 12. TCO. A. Dispositivo de TCO comercializado (Vivosight®; Michelson Diagnostics Limited, UK); B. Mecanismo de acción: el TCO filtra la luz directamente reflejada (flecha azul) de la luz dispersa (flecha discontinua roja) formando una imagen; C. Carcinoma basocelular nodular. Foto clínica (superior izquierda), patrón vascular (superior derecha) e imagen de TCO (inferior). Nido de CBC con reflectividad menor que la periferia (patrón lobular), consumo epidérmico (flecha blanca) y hendidura peri tumoral (flechas claras). Alcance de 1 mm en profundidad; D. Reconstrucción 3D, con patrón de vascularización. (Fuente: VivoSight www.vivosight.com)

Nueve estudios, con un total de 1386 lesiones analizadas, han reportado la capacidad diagnóstica para CBC.[50] La sensibilidad agrupada encontrada fue de 92.4% (95% CI: 0.90 a 0.94, I2=71.7%) y la especificidad del 86.9% (95% CI: 0.84 a

0.89, I2=89.4%); el VPP y el VPN agrupados fueron, respectivamente, de 6.07 (95% CI: 3.27 a 11.26, I2=88.9%) y de 0.12 (95% CI: 0.07 a 0.23, I2=80.3%).[48]

Respecto al diagnóstico de los CEC, tres estudios demostraron una sensibilidad agrupada del 92.3% (95% CI: 0.79 a 0.98, I2=71.2%) y una especificidad de 99.5% (95% CI: 0.97 a 1.00, I2=0.0%), con un VPP y VPN respectivos de 68.01 (95% CI: 17.01 a 272.4, I2=0.0%) y de 0.11 (95% CI: 0.01 a 1.20, I2=82.0%).[48]

En el diagnóstico de melanoma, se obtuvo una sensibilidad agrupada del 81.0% (95% CI: 0.66 a 0.91, I2=62.3%) y una especificidad del 93.8% (95% CI: 0.87 a 0.98, I2=0.0%) (PPV de 11.82 (95% CI: 5.16 a 27.09, I2=3.4%) y NPV de 0.18 (95% CI: 0.05 a 0.71, I2=54.0%).[48]

Sin embargo, por la falta de resolución celular,[48] esta técnica no ha demostrado ser capaz de mejorar la capacidad diagnóstica en lesiones melanocíticas con un diagnóstico dermatoscópico dudoso. Tampoco en disminuir el número de estadios en la cirugía de Mohs, cuando se aplica en el mapeo prequirúrgico de los márgenes tumorales.[48]

Una de sus mejores aplicaciones, además de en el diagnóstico de CBC, es en la monitorización del tratamiento, incluyendo el de lesiones inflamatorias.[50] No sólo por los hallazgos morfológicos, sino también por la reconstrucción tridimensional del patrón vascular, es posible valorar de forma objetiva la actividad del tumor o de la patología inflamatoria. (Figura 13)

De una forma global, el uso de esta técnica se ve potenciada cuando es combinada con otras técnicas con una resolución celular, como la MCR o TCO-CL.

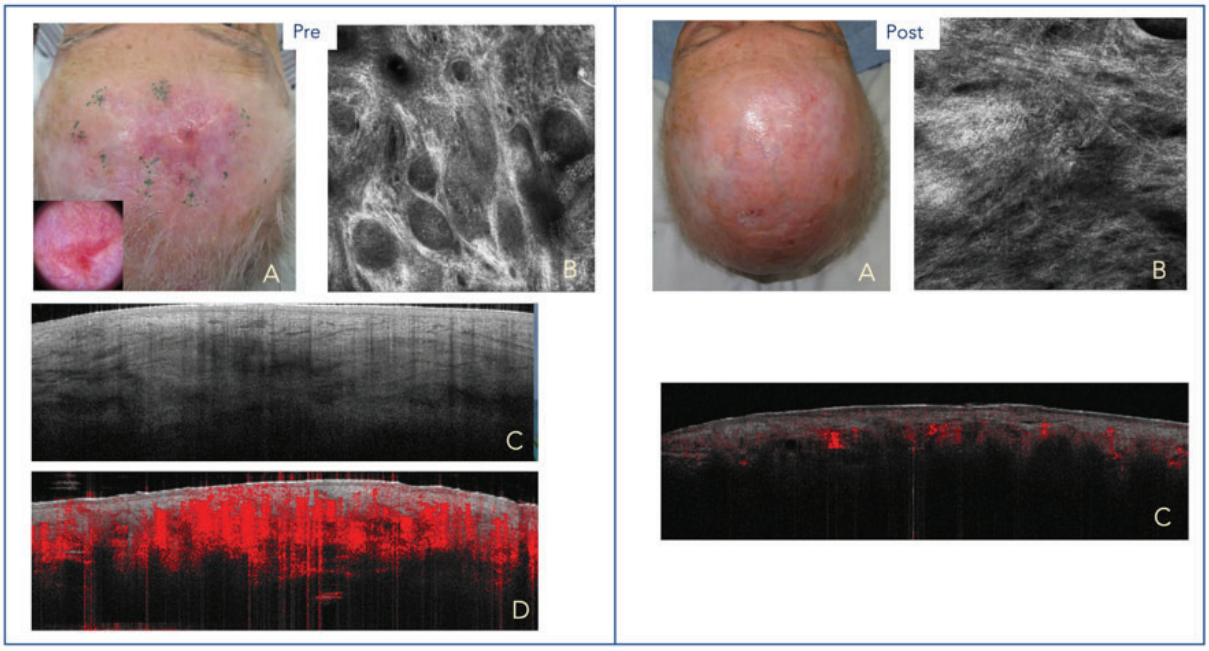

Figura 13. Diagnóstico y valoración de respuesta terapéutica a inhibidores de vía Hedgehog con técnicas de imagen en CBC recurrente e infiltrante. Izquierda: pré tratamiento. A. Foto clínica y dermatoscópica (cuadrado menor), donde es difícil apreciar el remanente tumoral; B. MCR. Presencia de "siluetas oscuras" confirmando la presencia de CBC infiltrante; C. TCO. Cordones finos tumorales que confirman morfológicamente la persistencia de tumor; D. TCO. Patrón vascular compatible con actividad tumoral. Derecha: post tratamiento; A. MCR. Foto clínica; B. MCR. Presencia de cicatriz; C. TCO con franca disminución del patrón vascular, sin apreciar criterios de carcinoma basocelular remanente. (Fuente: Dra. Susana Puig)

I. 2. TÉCNICAS DE DIAGNÓSTICO *EX VIVO*

I. 2.1. Microscopía confocal *ex vivo*

La microscopia confocal *ex vivo* es una técnica de imagen que permite el análisis del tejido fresco, inmediatamente después de la extirpación, utilizando un microscopio confocal específico para esta función: el microscopio confocal *ex vivo*. Este microscopio confocal, produce una imagen del tejido extirpado en lugar de los cortes en parafina o en congelado, utilizados tradicionalmente para el diagnóstico histológico, permitiendo un diagnóstico inmediato intraoperatorio.

A diferencia del microscopio confocal *in vivo*, dos láseres de diodo de diferentes longitudes de onda son utilizados para producir las imágenes del tejido: el láser de reflectancia y el de fluorescencia (actualmente de 638 ηm y de 488 ηm respectivamente).

Sus mecanismos de captura de imagen son semejantes a los del microscopio confocal *in vivo*. Los dos haces de luz del láser emitidos por el dispositivo se concentran en un mismo punto focal interconectado, después de pasar por un pequeño diafragma, y de que la luz reflejada por el tejido escaneado regrese y alcance el detector, pasando por un sistema de lentes y espejos que concentran los haces de luz.

La resolución celular actual es de 1024 x 1024 pixeles, llegando hasta menos de 200 micras en profundidad (visualización óptima a 4 micras), con posibilidad de magnificación hasta alcanzar los 540 x por zoom digital. Las imágenes también se reproducen en una escala del gris por las diferentes reflectividades de los tejidos,

tanto en el láser de reflectancia como en el de fluorescencia. Sin embargo, en las imágenes obtenidas por el láser de fluorescencia, se aprecia un brillo intenso de los tonos de gris, diferente al obtenido por el de reflectancia (siendo este último más sutil). La superficie escaneada puede tener un tamaño de hasta 2.5 -3 cms x 2.5-3 cms. Se han usado diferentes longitudes de onda y tecnologías a lo largo del tiempo para el análisis de los tejidos *ex vivo*, hasta llegar a la 4ª generación de estos aparatos en el año 2018 (posteriormente al inicio de nuestro estudio en esta tesis).

El primer dispositivo usado en el año 2000 fue el VivaScope 2000® (Lucid Inc.) que tenía apenas un láser de reflectancia de 1064 ηm, descrito por González S. y colaboradores.[51,52] Posteriormente, el láser fue sustituido por un dispositivo de iluminación de 830 ηm, en el año 2003. Sin embargo, las imágenes obtenidas a partir del láser de reflectancia no eran adecuadas para diferenciar las estructuras histológicas de forma óptima. Los tumores no se destacaban fácilmente del estroma circundante y las diferentes estructuras presentes en el tejido no podían ser reconocidas.[52,53] Finalmente, en el año 2009, se introduce por primera vez el uso de un segundo láser, el láser de fluorescencia. Este dispositivo tenía fuentes de luz de 658 ηm y de 445 ηm, para mejorar el contraste entre los tejidos. En el año siguiente, el láser de 445 ηm fue sustituido por uno de 488 ηm, permaneciendo así hasta el año 2017. A partir del año 2018, la tecnología ha experimentado cambios significativos, lo cual es el tema central de nuestra tesis. Uno de los avances destacados ha sido la implementación de la tecnología de "streapping", la cual ha posibilitado el escaneo simultáneo de tumores utilizando láseres de fluorescencia y de reflectancia. (Figura 14, Tabla 1)

Otro láser de microscopía confocal utilizado en dermatología es el HistoLog scanR MCF®.[54] Este dispositivo tiene un solo láser de fluorescencia, de 488 ηm, y

escanea una superficie mayor, de 8 x 8 cm lo que puede ser una ventaja en el estudio rápido de muestras de tumores de mayores dimensiones como en el cáncer de mama. Sin embargo, a diferencia del equipo multi-láser, la imagen final es de un único color púrpura. No existen estudios que comparen ambas técnicas.

Dispositivo	Año	Laser	Modo	Área	Adquisición	Objetivo	FOV	Tiempo
VS2000®	2001	1064ηm	Reflectancia		Mosaico	10, 20, 30, 60, 100X	150-2000 µm	5-6.5 min
VS2000®	2003	830 ηm	Reflectancia	10x10mm	Mosaico	30X	750µm	
VS2500 Gen2®	2009	830 ηm 658 ηm 445 ηm	Reflectancia Fluorescencia Fluorescencia	16x16mm	Mosaico	25X	750µm	9 min
VS2500 Gen2®	2010	830 ηm 658 ηm 488 ηm	Reflectancia Fluorescencia Fluorescencia	16x16mm	Mosaico	25X	750µm	
VS2500 Gen3®	2014	830 ηm 658 ηm 488 ηm	Reflectancia Fluorescencia Fluorescencia	20x20mm	Mosaico	25X	635µm	
VS2500 Gen4®	2018	785 ηm 488 ηm	Reflectancia Fluorescencia	25x25mm	Líneas	38X	500µm	
VS2500 Gen4®	2020	638 ηm 488 ηm	Reflectancia Fluorescencia	25x25mm	Líneas	38X	500µm	2-3 min

Tabla 1. Evolución de microscopios confocales Vivascope®. No es hasta la 4ª generación que se obtienen imágenes con H&E digital y tecnología de "streapping." (Adaptado de Pérez-Anker et al., 2022)[55]

,

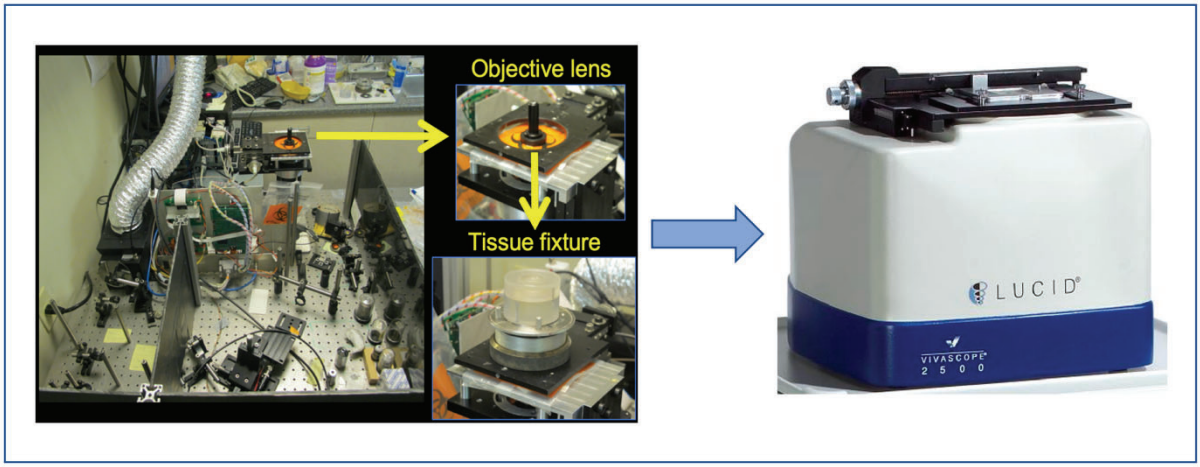

Figura 14. Primeros prototipos (izquierda) creados por el doctor Milind Rajadhyaksha y colaboradores. Primeros dispositivos de uso clínico (derecha) de confocal *ex vivo* Vivascope®. (Fuente: imágenes cedidas por Milind Rajadhyaksha)

En la MCev, a diferencia del MCR, es necesario utilizar un agente de tinción antes de escanear el tejido, para destacar los núcleos y diferenciarlos del estroma circundante, facilitando el diagnóstico de las muestras. En este sentido, se han descrito diferentes protocolos de tinción. El ácido acético fue la primera tinción utilizada en el pasado por los pioneros en el desarrollo y aplicación clínica de esta técnica, el equipo de González S. y colaboradores.[53] Desafortunadamente, ésta limitaba la visualización de imágenes monocromáticas, especialmente de pequeños remanentes tumorales como los micronódulos de CBC.[53,56]

Con el fin de superar este inconveniente, se ha probado teñir con naranja de acridina a una concentración de 1 mmol L, desde la introducción del láser de fluorescencia.[57] Esta, se utiliza como un agente de contraste fluorescente que penetra con afinidad nuclear, marcando selectivamente el ácido nucleico (fluorescencia verde)

y el ARN (fluorescencia roja), permitiendo que los mismos se destaquen de resto del tejido, brillando en el modo de fluorescencia. (Figura 15)[57-63]

Se han propuesto otras tinciones con el objetivo de lograr una mejor visualización de los núcleos: la fluoresceína al 0,4%, azul nilo al 0,2 mg/mL en etanol 70%, el azul patente al 0,4mg/ml y el azul de metileno a 2 mg/mL, el cloruro de aluminio, entre otros. Sus resultados, sin embargo, aún no han superado al de la naranja de acridina.[54]

Una de las principales ventajas de la microscopía confocal *ex vivo*, es el análisis rápido de la morfología celular del tejido extirpado sin ningún procedimiento estándar de histopatología convencional previo al procesamiento de la pieza. Ha sido aplicada y fundamentalmente descrita para la cirugía de Mohs, sobre todo para los carcinomas basocelulares desde 2003.[64] Su utilización en cirugía de Mohs ha permitido ahorrar al menos 1/3 del tiempo comparado con el Mohs tradicional.[62]

Se han descrito en distintos trabajos los criterios diagnósticos para algunos tumores en el modo de Fluorescencia. En el carcinoma basocelular, se observa la presencia de empalizada, hendidura peri tumoral, pleomorfismo nuclear, aumento de la relación núcleo/citoplasma y la presencia de estroma peri tumoral.[58] (Figura 15)

Posteriormente, se han descrito los hallazgos morfológicos encontrados en otros tipos de cáncer de piel como el carcinoma espinocelular y en lesiones melanocíticas.[54,60] También se ha aplicado para el control de tratamientos no quirúrgicos de carcinoma basocelular, para la diferenciación de lesiones orales potencialmente malignas, para la diferenciación de tumores no melanocíticos de uñas

en el intraoperatorio y para describir lesiones inflamatorias, como la infección por virus del Herpes.[6]

Se han reportado tasas de sensibilidad del 88% y de especificidad del 99% en cirugía de Mohs, para carcinoma basocelular.[54,58,60] Sin embargo, una de las mayores dificultades evidenciadas es la diferenciación de pequeños remanentes de tumor con estructuras normales de la piel, como la unidad pilosebácea, en colores monocromáticos. Otro gran desafío es poder lograr un aplanamiento correcto de la muestra a ser escaneada, siendo esta etapa fundamental para lograr la representación completa de todo el espécimen y, por lo tanto, un diagnóstico correcto.

Por todas estas aplicaciones en el ámbito de la patología, así como por la adecuada representación morfológica de los tejidos, esta técnica de imagen se presenta, por primera vez, como una alternativa potencial para el análisis histológico. Puede, en un futuro, llegar a ser un método alternativo a los histológicos tradicionales realizados en congelado o en parafina en la rutina asistencial.

Por otro lado, en la última generación de dispositivos VS 2500 4G se ha conseguido la fusión de imágenes y la tinción digital reproduciendo la tinción histológica de H&E. La técnica de fusión de MCeV tiene como objeto facilitar la identificación de las características citológicas y arquitecturales de los tejidos y mejorar el diagnóstico. Este trabajo de tesis ha permitido desarrollar y en última instancia, validar esta tecnología.

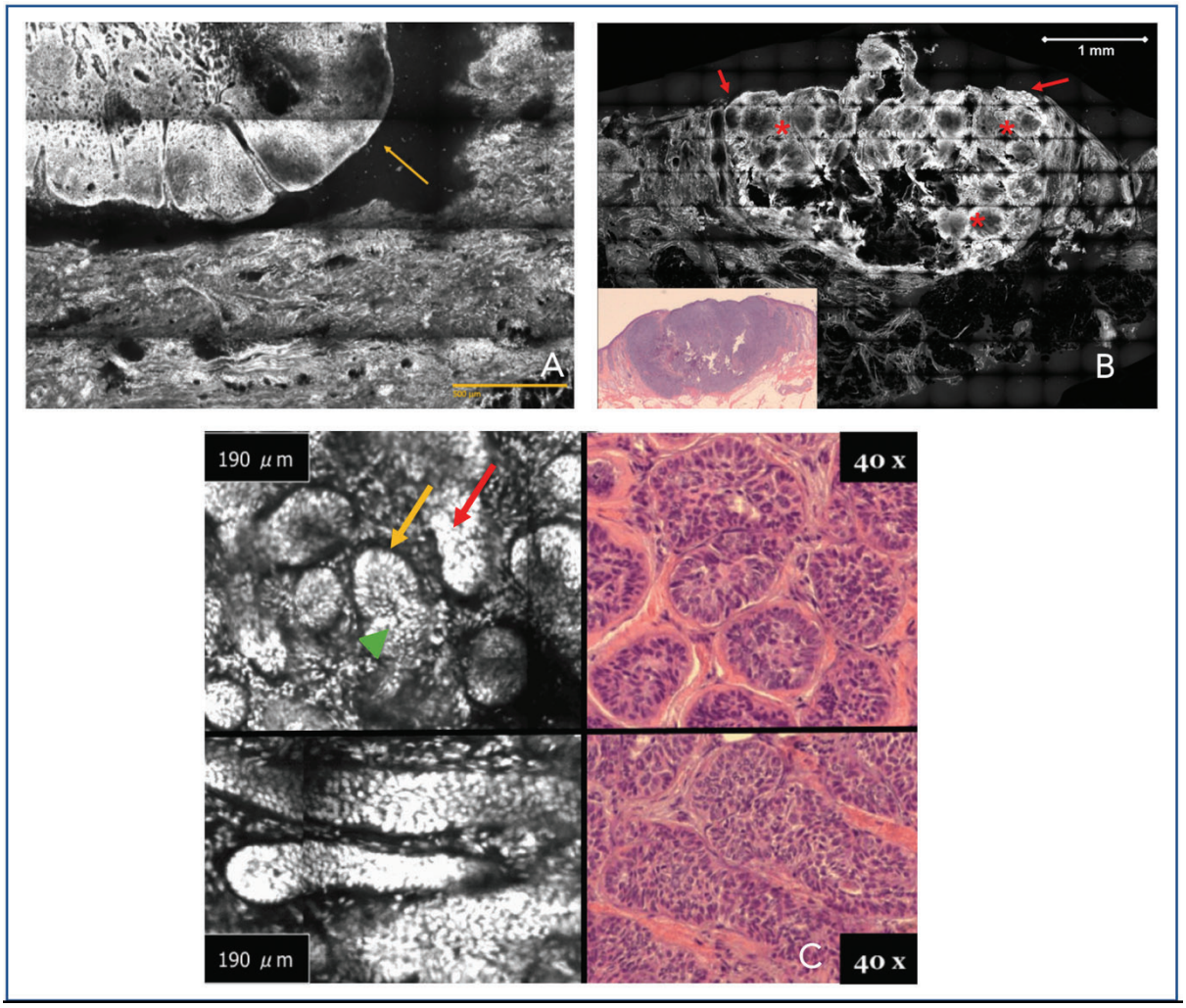

Figura 15. Imágenes de carcinoma basocelular con MCeV, obtenida con láser de fluorescencia, teñido con naranja de acridina 1 mmol L. Flecha amarilla: Hendidura peri tumoral y empalizada periférica. Flecha roja: Islas tumorales. Asterisco rojo: Fluorescencia. Triangulo verde: Aumento de relación núcleo citoplasma. A. La hendidura peri tumoral y la empalizada periférica son marcadas; B. Isla tumoral bien delimitada, con presencia de fluorescencia característica, de diferente intensidad en relación con el estroma; C. Detalles de carcinoma basocelular micronodular. Se observa empalizada, hendidura peri tumoral y aumento de la relación núcleo-citoplasmática. (Fuente: (A) Javiera Pérez-Anker; (B y C) Adaptado de Bennàssar et al., 2013)[58]

I.3. FUNDAMENTOS DEL ESTUDIO

El desarrollo de estas tecnologías descritas no sólo ha permitido mejorar la precisión diagnóstica, si no que, además, ha permitido realizar diagnósticos rápidos instantáneos que antaño requerían necesariamente un procesado de laboratorio laborioso. Por otro lado, han demostrado ayudar en el mapeo y delimitación de lesiones, en la estadificación y en la monitorización, estandarización y comparación de los tratamientos.

Estas técnicas, han abierto un campo totalmente nuevo de estudio en diferentes áreas de la dermatología y de la patología. Las imágenes morfológicas y citológicas han permitido entender procesos de respuesta al tratamiento y patrones de "comportamiento" patológico *in vivo*, antes incomprendidos.

Esta tesis se centra en el estudio de dos de las tecnologías mencionadas: la TCO-LC y la MCeV y su correlación con la dermatoscopia, la MCR y la histopatología. Por todo esto, se ha hecho necesario ampliar el conocimiento en las últimas tecnologías de imagen, investigando nuevas aplicaciones y describiendo los hallazgos en patologías aun no descritas. Asimismo, ha sido fundamental aprender a conocer sus límites actuales y de proponer soluciones y aplicaciones futuras.

II. HIPÓTESIS

Las técnicas de tomografía de coherencia óptica de campo lineal y de microscopía confocal ex vivo son útiles en el diagnóstico de tumores de la piel y las características morfológicas encontradas en estas técnicas se correlacionan con los hallazgos en dermatoscopia, microscopía confocal de reflectancia e histología convencional.

III. OBJETIVOS

OBJETIVO GENERAL

Describir las características morfológicas de lesiones tumorales cutáneas (epiteliales y melanocíticas) en tomografía de coherencia óptica de campo lineal y microscopía confocal ex vivo y correlacionar estos hallazgos con los encontrados en dermatoscopia, microscopía confocal de reflectancia e histología convencional.

OBJETIVOS ESPECIFICOS

TCO-CL:

- Describir las principales estructuras morfológicas de las lesiones melanocíticas benignas, atípicas y malignas en la TCO-CL y compararlas con las encontradas en MCR e histología convencional.
- Describir los hallazgos dermatoscópicos encontrados en lesiones melanocíticas, y correlacionarlos con sus respectivos hallazgos morfológicos en la TCO-CL.
- Describir los criterios diagnósticos de la TCO-CL para el reconocimiento de lesiones melanocíticas benignas, atípicas y malignas.
- Desarrollar un algoritmo de IA para el reconocimiento y diferenciación a nivel celular, entre campo de cancerización y queratosis actínicas, en la TCO-CL.

MCev:

- Describir un nuevo protocolo de tinción para la MCev y compararlo con los ya existentes.
- Desarrollar un algoritmo en AI para mejorar la tinción digital en MCev.
- Diseñar un dispositivo que permita aplanar las muestras que serán escaneadas por la MCev, de forma más eficaz.
- Desarrollar un protocolo estandarizado de trabajo para obtener imágenes reproducibles y de mejor calidad en la MCev.

IV. MATERIAL Y MÉTODOS, RESULTADOS, PUBLICACIONES

PUBLICACIÓN Nº 1:[65]

Evaluación morfológica de lesiones melanocíticas con tomografía de coherencia óptica de campo lineal en 3 dimensiones: correlación con histología y microscopía confocal de reflectancia. Un estudio piloto.

Morphologic evaluation of melanocytic lesions with three-dimensional line-field confocal optical coherence tomography: correlation with histopathology and reflectance confocal microscopy. A pilot study.

Javiera Pérez-Anker, Susana Puig, Llucia Alos, Adriana García, Beatriz Alejo, Elisa Cinotti, Carmen Orte Cano, Linda Tognetti, Clement Lenoir, Jilliana Monnier, Natalia Machuca, Paola Castillo, Pau Rosés Gibert, Pietro Rubegni, Mariano Suppa, Jean Luc Perrot, Veronique del Marmol, Josep Malvehy.

Clinical and Experimental Dermatology (2022) 47, pp2222-2233.

Factor de impacto: 3.47

Resumen

Antecedentes: La TCO-CL es una nueva técnica de diagnóstico *in vivo* que proporciona, en tiempo real, imágenes con resolución celular. Alcanza una profundidad aproximada de 400 µm, tanto en el plano horizontal, como en el vertical y en 3D. Las características morfológicas encontradas en los diferentes subtipos de

lesiones melanocíticas (benignas, atípicas y malignas) y su correlación con la histopatología y la MCR todavía no se han estudiado.

Objetivos: Describir las características morfológicas de las lesiones melanocíticas en TCO-CL y correlacionarlas con los correspondientes hallazgos en la histología (en las imágenes verticales) y en MCR (en las imágenes horizontales).

Métodos: Se tomaron imágenes, *in vivo*, de lesiones melanocíticas seleccionadas benignas, atípicas y de diferentes tipos de melanomas con MCR y TCO-CL, en el Hospital Clínic de Barcelona. El área mínima escaneada con MCR fue de 4 mm x 4 mm (Vivablocks) y en 4 profundidades (estrato granuloso, suprabasal, unión dermoepidérmica y dermis superior). En TCO-CL, se escanearon, como mínimo, 3 cubos en 3D. Las secciones horizontales, verticales y los cubos 3D de TCO-CL fueron comparados con los obtenidos con MCR e histopatología. La comparación entre TCO-CL, histología y MCR fue realizada a nivel celular, con una precisión de ~5 µm (los mismos núcleos se midieron en X, Y y Z). Las imágenes fueron evaluadas por tres observadores con experiencia en MCR e histopatología.

Resultados: Doce tumores melanocíticos (2 melanomas in situ, 2 melanomas invasivos, 4 nevus atípicos, 2 nevus intradérmicos, un nevus compuesto y un nevus de la unión) fueron incluidos. Se observó una alta correlación entre MCR, histología y TCO-CL en cada tumor. Se obtuvieron imágenes en 3D de lesiones melanocíticas, con resolución celular, que permitieron, por primera vez, una comprensión de la arquitectura tridimensional de las mismas. Se observaron similitudes entre TCO-CL y MCR respecto a los criterios diagnósticos previamente descritos en la literatura, tanto en la arquitectura (nidos de células melanocíticas, patrón en anillas y patrón en malla), cuanto en detalles celulares (como células dendríticas y pagetoides). La principal ventaja del diagnóstico por MCR fue la capacidad de producir escaneos más grandes de la lesión, usando mosaicos (con una sonda fija) en comparación a la sonda portátil del TCO-CL. Respecto a los cortes verticales, las principales características

morfológicas y citológicas también fueron observadas en TCO-CL y comparadas con la histología convencional.

Conclusiones: La TCO-CL nos permitió la descripción arquitectural y celular de diferentes tipos de lesiones melanocíticas en vertical, horizontal y en 3D. Además, mostró una alta correlación con la histopatología (cortes verticales) y la MCR (secciones horizontales) en lesiones melanocíticas. Los criterios diagnósticos en MCR fueron similares a los encontrados en TCO-CL.

Original Article

CED
Clinical and Experimental Dermatology

Morphological evaluation of melanocytic lesions with three-dimensional line-field confocal optical coherence tomography: correlation with histopathology and reflectance confocal microscopy. A pilot study

Javiera Perez-Anker,[1,2] Susana Puig,[2,3] Llucia Alos,[4] Adriana García,[4] Beatriz Alejo,[1] Elisa Cinotti,[5,6] Carmen Orte Cano,[7] Linda Tognetti,[5] Clement Lenoir,[7] Jilliana Monnier,[8] Natalia Machuca,[9] Paola Castillo,[4] Pau Rosés Gibert,[2] Pietro Rubegni,[5] Mariano Suppa,[6,7,10] Jean Luc Perrot,[11] Veronique del Marmol[7] and Josep Malvehy[2,3]

[1]*Fundación Hospital Clinic;* [2]*Melanoma Unit, Department of Dermatology, Hospital Clínic de Barcelona, IDIBAPS, Universitat de Barcelona;* [3]*Centro de Investigación Biomédica en Red de Enfermedades Raras (CIBERER) Instituto de Salud Carlos III;* [4]*Department of Pathology, Hospital Clínic de Barcelona, Universitat de Barcelona, Barcelona, Spain;* [5]*Dermatology Unit, Department of Medical, Surgical and Neurological Sciences, University of Siena, Siena, Italy;* [6]*Groupe d'Imagerie Cutanée Non Invasive (GICNI) of the Société Française de Dermatologie; (SFD), Paris, France;* [7]*Department of Dermatology, Hôpital Erasme, Université Libre de Bruxelles, Brussels, Belgium;* [8]*Dermatology Department, AP-HM, Aix-Marseille University, Marseille, France;* [9]*Department of Bioengineering, Universitat Internacional de Catalunya, Sant Cugat del Vallès, Barcelona, Spain;* [10]*Department of Dermatology, Institut Jules Bordet, Université Libre de Bruxelles, Brussels, Belgium; and* [11]*Department of Dermatology, University Hospital of Saint-Etienne, Saint-Etienne, France*

doi:10.1111/ced.15383

Abstract

Background. Line-field confocal optical coherence tomography (LC-OCT) is a new *in vivo* emerging technique that provides cellular resolution, allows deep imaging (400 µm) and produces real-time images in both the horizontal and vertical plane and in three dimensions. No previous description of different subtypes of melanocytic lesions and their correlation with histopathology and reflectance confocal microscopy has been reported.

Aim. To describe the features of melanocytic lesions by LC-OCT and their correlation with histopathology and reflectance confocal microscopy (RCM) findings.

Methods. Selected melanocytic benign lesions and melanomas were imaged *in vivo* with RCM and LC-OCT at the Fundación Hospital Clinic (Barcelona, Spain). A minimum area of 4 × 4 mm (block image) at four depths (stratum granulosum, suprabasal, layer dermoepidermal junction and upper dermis) were acquired with RCM and a minimum of three cubes with LC-OCT. Horizontal, vertical sections and three-dimensional (3D) cubes of LC-OCT were matched with RCM (Vivablock two-dimensional composite mosaic) and histopathology, with ~5 µm lateral resolution accuracy (the same cell nuclei were measured in X, Y and Z) and evaluated by three observers experienced in using RCM and histopathology.

Results. In total, 12 melanocytic tumours (2 *in situ* melanomas, 2 invasive melanomas, 4 atypical naevi, 2 intradermal naevi, 1 compound naevus and 1 junctional naevus) were included. High correlation with 5 µm accuracy between RCM and LC-OCT was observed for each tumour. The 3D images of melanocytic lesions were obtained with cellular resolution and correlated with both RCM and histopathology, allowing an understanding of the architecture and precise correlation at the cellular level with RCM. Similarities between LC-OCT and RCM for the described diagnostic

Correspondence: Dr Javiera Pérez-Anker, Melanoma Unit, Department of Dermatology Hospital Clinic Barcelona, Villarroel 170, 08036 Barcelona, Spain
E-mail: javiperezanker@gmail.com

Accepted for publication 19 August 2022

features and architecture (nests of melanocytic cells, ringed and meshwork pattern, and cellular details of tumour cells as dendritic and pagetoid cells) were confirmed. The main advantage of diagnosis by RCM fixed probe was the ability to produce larger scans of the lesion using mosaicing compared with an LC-OCT handheld probe.
Conclusion. LC-OCT allows the architectural and cellular description of different types of melanocytic lesions. LC-OCT showed high correlation with histopathology (vertical sections) and RCM (horizontal sections) in melanocytic lesions. Diagnostic criteria for RCM were similar to those for LC-OCT.

Introduction

Line-field confocal optical coherence tomography (LC-OCT) is an innovative skin imaging technology, combining optical coherence tomography (OCT) and reflectance confocal microscopy (RCM),[1,2] with 1.2 μm axial resolution and 1.3 μm lateral resolution,[3] 1.2 mm field of view and ~500 μm penetration depth.[3] It enables skin visualization in real time with cellular resolution, reaching the deep papillary dermis. The features of basal cell carcinoma (BCC), actinic keratosis, squamous cell carcinoma, sebaceous hyperplasia, xanthogranuloma, herpes, scabies, Kaposi sarcoma, aquagenic keratoderma, bullous diseases and normal skin have been described with this technology.[2–14]

RCM and OCT are two other noninvasive technologies, which have different resolutions and depths of penetration into the skin. RCM enables an *en face* view with cellular resolution (spatial lateral resolution of 1 μm, similar to histology and axial resolution of < 5 μm).[15–23] Its main limitation is the large depth of penetration, down to ~250 μm. OCT allows two-dimensional (2D) and three-dimensional (3D)[2,24–27] images at a lower resolution but at a deeper penetration of 0.15–1.5 mm at a 1310 nm resolution and 1.8 mm at 1700 nm.[28] Dynamic OCT or OCT angiography (OCT-A) is a technique that allows the identification of vascular patterns in the skin tissue. OCT and OCT-A are useful in the diagnosis, treatment planning and monitoring of nonmelanoma skin cancers.[10,24,25,29,30] Although OCT and OCT-A both allow deep skin penetration, neither technique has the cellular resolution that is fundamental to the diagnosis of melanocytic lesions.

Recent studies have demonstrated the advantages of integrating RCM and OCT in another new prototype tested in the USA, with a deep penetration of ~400 μm. The depth penetration of BCCs using this technique compared with the histopathologically measured depth had high correlation ($R = 0.86$); however, cellular resolution, which is fundamental to the diagnosis of melanocytic lesions, was not observed.[31]

To overcome the depth limitations of RCM and the lack of cell resolution of OCT, LC-OCT was introduced. The main advantage of LC-OCT is that it permits 3D analysis of skin lesions,[2,31–35] allowing an appreciation of both the architectural morphology and cytological aspects. Moreover, LC-OCT enables deeper imaging than RCM, with comparable cellular resolution.

The aim of this study on melanocytic lesions was to describe the morphological and cellular correlation between LC-OCT vertical sections with histopathology and LC-OCT horizontal sections with *in vivo* RCM, in order to compare the cellular definition and resolution (which is fundamental to the diagnosis of melanocytic lesions) and the main differences between these gold-standard techniques. The 3D anatomy of different melanocytic lesions is also described for the first time.

Methods

We prospectively evaluated patients with melanocytic lesions from January to February 2021 with the following inclusion criteria: age ≥ 18 years and melanocytic lesions on the trunk, limbs or scalp. Acral, facial or mucosal/submucosal melanocytic lesions were excluded. We collected clinical, dermoscopic, RCM, LC-OCT and histopathological images of different types of melanocytic lesions.

Acquisition methods

Collection of clinical, dermoscopic, reflectance confocal microscopy and line-field confocal optical coherence tomography images in horizontal view. For each lesion, a clinical and a dermoscopic (Olympus OM-D E-M10 Mark-II; Dermlite Foto XTM, 3Gen Inc., San Juan Capistrano, CA, USA) image was obtained. An image of the lesion was then taken with an imaging device (Vivascope 1500™; Mavig Corp., Munich, Germany) with a dermoscopic image integrated into the device for navigation (which allows for perfect correlation between the dermoscopy image and the corresponding confocal image)

and multiple mosaics (Vivablocks) of confocal images (4 × 4 mm), at 3–5 different depths from the stratum corneum (SC) to the papillary dermis. The same lesion was then imaged with an LC-OCT handheld probe (deepLive™, DAMAE Medical, Paris, France). LC-OCT 3D images (1.2 × 0.5 × 0.4 mm) of two to three regions of interest were acquired, including one in the centre of the tumour and others selected within the lesion based on their dermoscopic appearance, using an integrated videodermoscopy camera that allows precise navigation within the lesion. Finally, an LC-OCT 3D image including the horizontal section that best matched the confocal image was selected. A final adjustment was then applied based on features common to both the LC-OCT horizontal image and RCM.

Collection of histopathological and line-field confocal optical coherence tomography images in vertical view. All melanocytic lesions included in the study were excised for histopathological study. Histological sections were guided by the correlated morphological findings in the serial routine slides (one taken every 2 mm of tissue), comparing and matching the most representative features in both techniques. For each lesion, histopathological slides were digitized and reviewed using QuPath software (V0. 2.3; https://qupath.github.io/).[36] Navigating within the LC-OCT volume using dedicated software (deepLive V1.4.0; DAMAE Medical), the LC-OCT vertical image that best matched the histopathological picture was compared on the same scale. Horizontal sections were not performed, because of ethical concerns, as these would cause problems in the final diagnosis and estimation of Breslow thickness in melanocytic lesions.

Reflectance confocal microscopy, line-field confocal optical coherence tomography and histopathological criteria. The 2D and 3D LC-OCT images were searched for features based on the established RCM and histopathological diagnostic criteria for melanocytic lesions,[2–4,18,19,37] using a side-by-side, quantitative (micrometric) comparison performed by three investigators (JP, SP, JM) (Fig. 1), with any disagreement resolved by consensus between them.

For LC-OCT horizontal images, the presence/absence of the following RCM criteria was evaluated at three different levels (Fig. 2): (i) epidermis: honeycomb pattern, cobblestone pattern, epidermal disarray, pagetoid cells, cellular atypia, morphology of melanocytic cells (roundish, dendritic, pleomorphic) and visibility of nuclei; (ii) dermal–epidermal junction (DEJ): visible dermal papilla, edged papilla, nonedged papilla, typical

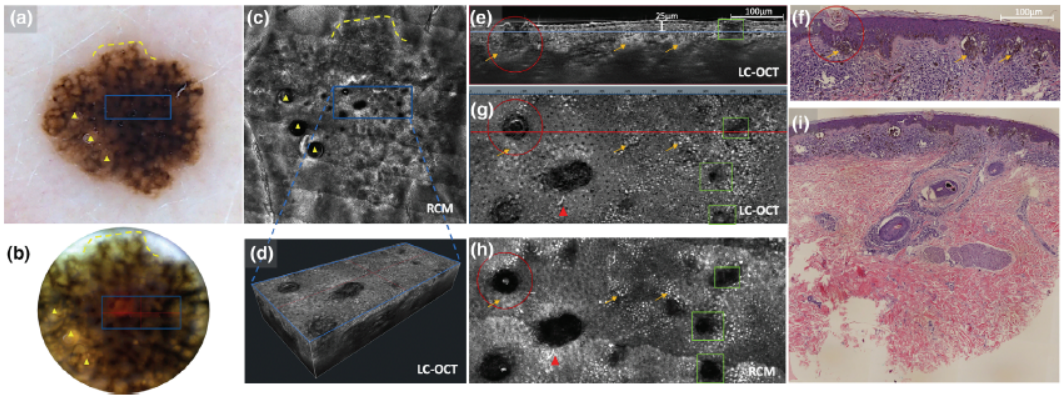

Figure 1 (a–i) Image collection method: comparison between line-field confocal optical coherence tomography (LC-OCT), reflectance confocal microscopy (RCM) and histopathology (haematoxylin and eosin staining) in an atypical naevus. (a) Dermoscopic image (Vivacam™) including the area selected for comparison between RCM, LC-OCT and histopathology. (b) Dermoscopic image (integrated dermoscopic camera of DeepLive™ LC-OCT) showing the selected area in detail. (c) RCM Vivablock™ mosaic including the selected area. (d) LC-OCT three-dimensional (3D) cube image of the selected area. (e) LC-OCT vertical image of the selected area and (f) corresponding histopathological image (original magnification × 20). (g) LC-OCT horizontal image, (h) corresponding RCM image and (i) complete histopathological overview of the lesion (macro view). Yellow landmarks and triangles: macroscopic guides to precisely select the same area to be compared in dermoscopy and RCM. Blue rectangle: selected area for comparison of LC-OCT and RCM. Blue line: location of the horizontal plane [represented in (g)] on the corresponding vertical plane [represented in (e)]. Red line: location of the vertical plane [represented in (e)] on the corresponding horizontal plane [represented in (g)]. Orange arrows: nest of atypical melanocytes (cobblestone). Red circles: pseudocysts. Green squares: follicular openings. Red triangles: dendritic cells.

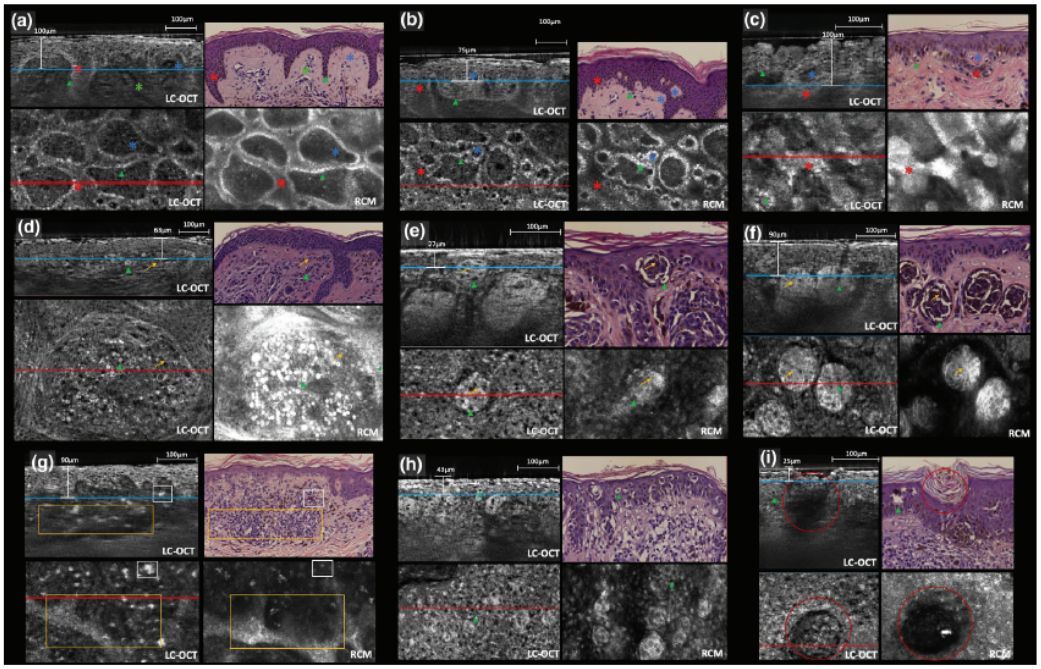

Figure 2 (a–f) Benign and malignant features of melanocytic lesions: comparison between line-field confocal optical coherence tomography (LC-OCT), reflectance confocal microscopy (RCM) and histopathology (haematoxylin and eosin staining) of the same area and depth. For each panel: superior left is vertical LC-OCT; superior right is histopathology; inferior left is horizontal LC-OCT; and inferior right is RCM. Blue line: location of the horizontal LC-OCT plane (inferior left) on the corresponding vertical LC-OCT plane (superior left). Red line: location of the vertical LC-OCT plane (superior left) on the corresponding horizontal LC-OCT plane (inferior left). (a) Normal ringed pattern. Red asterisks: typical elongated ridges, with an increased number of melanocytes (green triangles). Blue asterisk: dermal papillae. Green asterisks: vessels in the papillae. (b) Nonedged papillae indicate the junctional thickening. Red asterisks: atypical, elongated ridges, with an increased number of atypical melanocytes (green triangles). Blue asterisk: dermal papillae. (c) Clod pattern indicates the regular dermal dense and sparse nests with monomorphous melanocytes. Orange arrows: large sparse dermal nests. Green triangles: large, roundish monomorphic melanocytes. (d) Orange arrows: atypical dense nests within the papillae. Green triangles: atypical melanocytes. (e) Atypical nests within the epidermis. Orange arrows: atypical dense nest within the epidermis and dermoepidermal junction with atypical melanocytes (green triangles). (f) Pagetoid spread. Green triangles: atypical melanocytes (pagetoid isolated and clustered cells within the epidermis).

and atypical basal cells, sheetlike structures and junctional nests (regular dense nests, heterogeneous nests, cerebriform nests); and (iii) papillary dermis: dermal nests (regular dense nests, heterogeneous nests, cerebriform nests), atypical cells, plump bright cells, bright hyper-reflectant spots and enlarged dermal vessels.

For LC-OCT vertical images, a comparison with known histopathological diagnostic features was made for each lesion.

Results

In total, 12 melanocytic lesions from 12 patients (6 women, 6 men; mean age 45 years, range 28–83 years) were assessed (Table 1). Most of the histological morphological and cytological features were observed equally in vertical sections of LC-OCT of benign, atypical and malignant melanocytic lesions. Moreover, most of the melanocytic features were observed equally with LC-OCT and RCM in horizontal views with a micrometre comparison.

Benign junctional, compound and dermal naevus

Histopathology and line-field confocal optical coherence tomography in vertical sections. With LC-OCT examination, the SC appeared as a hyper-reflective band, 10–30 µm thick. The nuclei of keratinocytes were

Table 1 Characteristics of patients and melanocytic lesions.

Patient	Sex	Age, years	Anatomical site of lesion	Histology
1	F	54	Forearm	SSM (in situ)
2	M	63	Back	SSM (in situ)
3	M	70	Scalp	SSM (Breslow thickness 0.5 mm)
4	M	83	Arm	Lentigo maligna melanoma
5	M	28	Back	Atypical naevus
6	F	35	Leg	Atypical naevus
7	F	37	Chest	Atypical naevus
8	F	47	Breast	Atypical naevus
9	F	33	Back	Dermal naevus
10	F	69	Scalp/ forehead	Dermal naevus
11	M	44	Leg	Compound blue naevus
12	F	68	Abdomen	Junctional naevus

SSM, superficial spreading melanoma.

seen as hyporeflective dots of different shapes depending on the examined epidermal layer: flat in the stratum granulosum (SG), roundish and smaller in the stratum spinosum (SS). At the basal layer, nuclear details were more difficult to visualize, especially in compound and junctional naevi, owing to the concomitant presence of melanocytes and pigmented keratinocytes, which appeared hyper-reflective. In common naevi, a clear clefting between the basal layer and papillary dermis could be seen.

Cytoplasms in melanocytes were bright with roundish dark nuclei. Naevocytes, observable as bright roundish cells with dark nuclei, could be seen, either as isolated cells or in groups arranged in dense nests at the DEJ in both junctional and compound naevi. Dermal nests with discernible nuclei were observed down to the upper dermis (~250 μm depth) whereas they appeared to be homogeneous in deeper layers. Adnexal structures and rete ridges were identified with similar morphology to that seen in histopathology.

The Grenz zone was also observed with LC-OCT as a dark space between the epidermis and the dermal naevus component. In the dermis, LC-OCT allowed the observation of hyper-reflective linear structures corresponding to collagen and elastic fibres, and hyporeflective linear structures corresponding to vessels in the dermal papillae.

Vertical sections of LC-OCT showed hyper-reflective structures corresponding to the ridge of melanocytic strands/cords/nests, separated by hyporeflective spaces of varying thickness ('wave-like' pattern, as previously described).[33] Large sparse dermal nests with large roundish monomorphic melanocytes were also evident (Fig. 2; Video S1).

Reflectance confocal microscopy and line-field confocal optical coherence tomography in horizontal sections.. A typical honeycomb pattern of the epidermis was observed in all lesions in the SG and SS (Fig. 2; Video S1). At the suprabasal layer, a stereotypical cobblestone pattern was recognized with the two microscopes. Similarly, a ring-like pattern and meshwork pattern were similar with RCM and LC-OCT. Nests of naevocytes were seen with both techniques, appearing as oval structures either homogeneously dense or characterized by bright small roundish cells of 10–15 μm in diameter with visible nuclei. However, at deeper layers, nuclear details were better seen with LC-OCT than with RCM, as LC-OCT showed homogeneous nests already appearing at a depth of 150–200 μm.

Three-dimensional view. The advantage of the 3D view (vertical and horizontal imaging modes combined to reconstruct a 3D cube) is that it allows precise determination of the size, shape, location and distribution of each structure or feature. Nests of benign melanocytes were visualized surrounded by thin collagen and could be easily differentiated from normal structures such as hair follicles, eccrine glands and adnexal structures (Video S1).

Atypical naevi

Histopathology and line-field confocal optical coherence tomography in vertical sections. The analysis at the SC showed the presence of grey/whitish dots in some lesions, corresponding to pigment parakeratosis in histopathology (Fig. 3, Video S1). A typical honeycomb pattern was recognized in vertical sections of LC-OCT, corresponding to epidermal keratinocytes, which were similar to those seen in common naevi.

Sparse and focal atypical melanocytes were observed at the DEJ in some atypical naevi with both LC-OCT and histopathology. Melanocytic hyperplasia, corresponding to nests of melanocytes in histopathology, was detected as bright roundish cells within grey nests in the DEJ and upper dermis. Some irregularly shaped melanocytes with dark irregular nuclei were apparent, whereas nuclear structures such as chromatin, nucleoli and mitoses were not visible with LC-OCT. Fusion of rete ridges was visible with both histopathology and LC-OCT. In some of the melanocytic lesions showing inflammation and regression, melanophages were seen as bright plump cells with a median diameter of

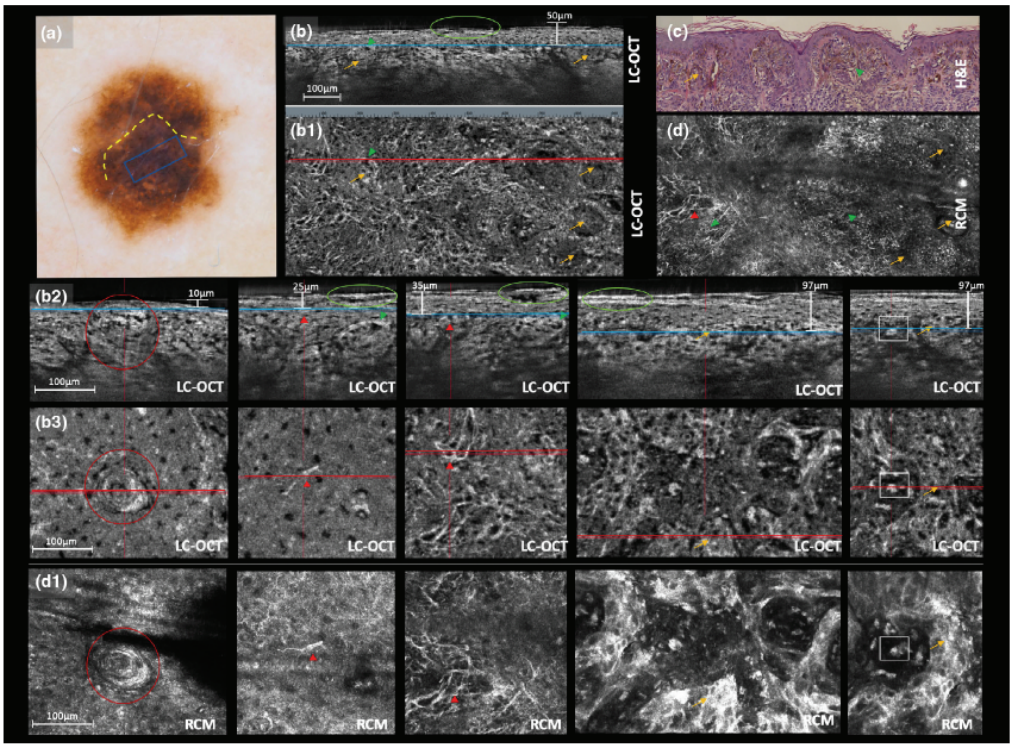

Figure 3 (a–d) Naevus with severe atypia: comparison between line-field confocal optical coherence tomography (LC-OCT), reflectance confocal microscopy (RCM) and histopathology (haematoxylin and eosin staining). (a) Dermoscopic image. (b) LC-OCT in (b,b2) vertical, (b1,b3) horizontal and (b4) three-dimensional (3D) modes. (c) Histopathology. (d) RCM. Focal architectural losses and the presence of atypical cells are shown in the lower part of the figure for parts b2–b4 and d1. Blue rectangle: selected area for comparison of LC-OCT and RCM. Blue line: location of the horizontal LC-OCT plane on the corresponding vertical LC-OCT plane. Red line: location of the vertical LC-OCT plane on the corresponding horizontal LC-OCT plane. Green circles: pigment within the stratum corneum. Red triangles: dendritic cells. Orange arrows: meshwork pattern indicating the nest fusion within the epidermis and upper dermis with atypical melanocytes (green triangle). Red asterisks: melanophages.

20 µm, without prominent nuclei. Interestingly, LC-OCT allowed better visualization of dendritic melanocytes (seen as bright cells with visible nuclei at the DEJ and suprabasal layers) compared with histopathology.

Reflectance confocal microscopy and line-field confocal optical coherence tomography in horizontal sections. In some atypical naevi, at the SG and SS layers, melanin was visible as bright small discs ~8 µm in diameter with both RCM and LC-OCT, but the contrast of these structures was higher in the RCM image. White dots ~2 µm in diameter (possibly correlating with inflammatory infiltrate) were visible within the epidermis under both RCM and LC-OCT. With LC-OCT, the contrast of keratinocytes with black nuclei was higher than with RCM.

Moreover, in one of the atypical naevi, epidermal pseudocysts of 60–150 × 40–110 µm filled with pigmented parakeratosis appeared as black round/oval structures in the horizontal section image acquired with LC-OCT. These structures were misidentified in horizontal sections with RCM as follicular openings and dermal papillae.

A smaller number of suprabasal bright keratinocytes (cobblestone pattern) were observed with LC-OCT compared with RCM.

Regarding the DEJ, it appeared brighter in the RCM image, whereas nuclei of melanocytes were better

distinguished using LC-OCT. With LC-OCT, dendritic cells were less apparent than with RCM; however, they were easily identified using navigation through different layers with LC-OCT (at a depth of ~10 μm). Nuclei of dendritic cells were better observed with LC-OCT.

Elongated nests of melanocytes (maximum diameter 30–150 μm) with fusion (meshwork pattern) were visualized on both RCM and LC-OCT images, and these cells showed cellular atypia (pleomorphism, including large nuclei and dendrites). In general, nests at the DEJ were brighter under RCM, but cell nuclei within the nests were more easily visible with LC-OCT. The density of the visible melanocytes nuclei within the nests was higher with LC-OCT.

In atypical naevi showing inflammation and regression, bright plump cells with a median length (approximately 25−50 μm) were visualized with both RCM and LC-OCT images.

In deeper layers (> 200 μm) of a severe atypical naevus, atypical bright cells with large black nuclei could still be observed with LC-OCT, but not with RCM.

Three-dimensional view. The 3D view enabled better understanding of the anatomy of the tumour at the DEJ and in the dermis. The nests were shallow in depth (50–70 μm thick) and budded from a wavy, bright DEJ fusion of ridges. Detached cells were also observed.

Similarly, precise representation and position of the dendritic cells within the epidermis (basal layer, SS or SG) could be determined. A very large number of dendritic cells was observed in severe atypical naevi. Unlike RCM, which is not 3D, LC-OCT showed the SG and upper epidermis to have dendritic cells corresponding to atypical melanocytes with smaller and flatter nuclei (~8 μm diameter, ~2 μm thickness) and longer fine dendrites with main branches measuring about 30 μm in length and additional distal ramifications of 10 μm length. At the DEJ, dendritic cells showed roundish nuclei of ~10 μm diameter, a bright cytoplasm and three to four dendrites.

Owing to their spatial distribution/orientation, dendrites tended to be best observed on the horizontal plane of the LC-OCT 3D mode. Bright dots (~1 μm diameter), which might possibly correspond to melanosomes, were seen in some lesions.

Using LC-OCT vertical view and 3D reconstruction, the nests of melanocytic hyperplasia correlated with elongated rete ridges with varying lengths (40–100 μm), forming a network that appeared in vertical sections as a fusion of nests.

Melanoma

Histopathology and line-field confocal optical coherence tomography in vertical sections. Most of the features recognized in the atypical naevi were also present in the *in situ* melanomas (Fig. 4; Video S1). However, LC-OCT examination showed that the atypical cells at different epidermal layers (pagetoid spread) were denser and more continuous in the latter than in the former. This finding correlated well with the presence of epidermal tumour cells in histopathology.

With LC-OCT, some superficial nests containing atypical melanocytic cells were observed at ~30 μm depth from the SC below the epidermis; their size varied from ~60 μm to ~140 μm and they corresponded to superficial nests of melanomas in histopathology. Atypical melanocytes were also observed at the periphery of hair follicles.

Nests of melanocytes of different sizes were seen at the DEJ and down to a depth of 250 μm in the dermis in the case of invasive melanomas. Similar to atypical naevi, an inflammatory infiltrate and melanophages were also seen in melanomas.

Reflectance confocal microscopy and line-field confocal optical coherence tomography in horizontal sections. There were similar findings with both RCM and LC-OCT, including the presence of atypical bright cells in the epidermis, at the DEJ and in the upper dermis. The DEJ was disarranged, with nonedged papillae. Medusa-like structures[38] were observed in one of the *in-situ* melanomas with both LC-OCT and RCM.

Dyscohesive nests of different sizes and atypical melanocytes with dark nuclei were similar with LC-OCT and RCM. Pleomorphism of atypical cells in melanoma was also evident with both techniques. However, one main difference between them was that atypia of cells and nests could be visualized at 247 μm with LC-OCT, whereas nests at that level appeared homogeneous with RCM, owing to the different resolution/penetration of the two techniques. The surrounding stroma of nests and hair follicles in the superficial dermis was observed equally with both RCM and LC-OCT, but was less evident with RCM than LC-OCT at deeper levels.

Three-dimensional view. In 3D mode, dense roundish dermal nests within dermal papillae surrounded by elongated rete ridges were observed in the *in situ* melanomas. Disruption of the DEJ and dermal invasion could be easily recognized in invasive melanomas. Bright cells in the different epidermal layers and atypical nests spreading from the DEJ could be observed.

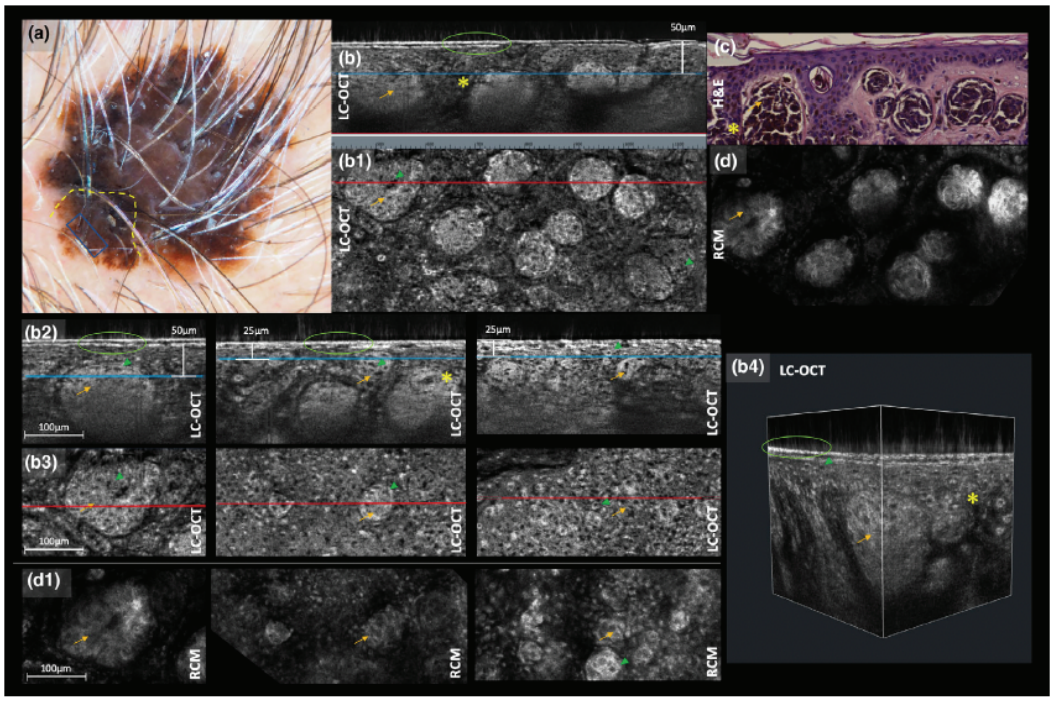

Figure 4 (a–d) Naevoid melanoma, Breslow thickness 0.5 mm: comparison between line-field confocal optical coherence tomography (LC-OCT), reflectance confocal microscopy (RCM) and histopathology (haematoxylin and eosin staining). (a) Dermoscopic image. (b) LC-OCT in (b, b2) vertical, (b1, b3) horizontal and (b4) three-dimensional (3D) modes. (c) Histopathology. (d) RCM. Details are shown in the bottom part of the figure for b2–b4 and d1. The regular architecture was disarranged and atypical cells were evident, along with typical dense nests within the epidermis, dermoepidermal junction (DEJ) and dermis. Blue line: location of the horizontal LC-OCT plane on the corresponding vertical LC-OCT plane. Red line: location of the vertical LC-OCT plane on the corresponding horizontal LC-OCT plane. Green circle: pigment within the superficial epidermis. Yellow asterisk: disruption of the DEJ. Orange arrows: irregular nest with atypical melanocytes (green triangles). Red asterisk: atypical melanocytes (pagetoid isolated and clustered cells within the epidermis).

Discussion

In this study, LC-OCT allowed observation of architectural and cytological aspects of common naevi, atypical naevi and melanoma. In a pioneering study with LC-OCT, Dubois *et al.* described findings with 2D imaging in normal skin, BCC and two melanomas.[2] The authors described key histopathological features of melanoma, and reported similar findings in this tumour with LC-OCT compared with RCM.[35] Lenoir *et al.* also described the wave-like pattern in seven compound and dermal naevi, with histopathological correlation confirmed by the presence of hyperrefractive elongated structures with darker spaces between them, corresponding to nests of melanocytes surrounded by collagen in the upper dermis.[34] In these cases, no cellular atypia was observed in the epidermis, DEJ or dermis. An additional LC-OCT feature was a thin layer of homogeneous hyper-reflective material immediately below the DE, corresponding to the upper papillary dermis, which was thinned by the growth of melanocytic nests. In our study, the dermal component of melanocytic tumours showed large nests in dermal naevi and a clear correlation with histopathology. Moreover, pink lesions were also evidenced in our series (not shown).

To our knowledge, previous OCT studies in the field of melanocytic lesions did not provide comparisons with RCM, nor did they include 3D images. Compared with histopathology, a limitation of both LC-OCT and RCM is the reduced ability to identify nuclear details of melanocytes and naevocytes, including density of nuclei, chromatin and nucleoli, which represent major diagnostic criteria in histopathology. However, some cellular details such as the morphology of dendritic cells were visible with LC-OCT; moreover, the 3D LC-OCT analysis

Table 2 Main differences between reflectance confocal microscopy and line-field confocal optical coherence tomography.

Feature	RCM	LC-OCT horizontal
Melanin contrast	++++	+++
Deep visualization, µm	200	350
Nuclear details	+++	+++[a]
Shape of dendritic cells	++	++++[b]
Cellular spatial distribution	++	++++[b]
Disruption of the DEJ	+/–	++++[b]
Size of scan, mm	8	1.5

DEJ, dermoepidermal junction; LC-OCT, line-field confocal optical coherence tomography; RCM, reflectance confocal microscopy. [a]Could still be visualized at greater depths; [b]vertical and 3D.

Table 3 Main differences between histopathology and line-field confocal optical coherence tomography.

Feature	Histo	LC-OCT vertical
Nuclear resolution	++++	+
Desmosomes	++++	–
3D representation	–	+
Vertical sections[a]	+	–
In vivo diagnosis	–	+

3D, three-dimensional; histo, histopathology; LC-OCT, line-field confocal optical coherence tomography. [a]In lower dermis and subcutaneous tissue.

allowed detailed characterization of these cells, which is not possible with vertical sections in conventional histopathology. The different optical properties of LC-OCT and RCM and their specific vertical resolution (~1 µm vs. 5 µm, respectively), may be responsible for the differences observed between LC-OCT and RCM (Tables 2 and 3). Moreover, it is important to note that all the features observed with RCM were also observed equally with LC-OCT in the horizontal view in all the cases in our sample. There were no criteria seen with RCM that were not also visualized with LC-OCT at the same depth and area (Figs 2–4).

The global architecture of the melanocytic tumours was highly correlated with the histopathological features in vertical sections. Architectural details could still be visualized at a depth of 300 µm; however, cellular details were sometimes limited to a depth of 250 µm, depending on the tissue characteristics (Figs 3b,c and 4b,c).

Previous descriptions with OCT and high-definition OCT in melanocytic lesions have had limited clinical applicability in the study of melanocytic lesions, owing to their insufficient resolution, which reduced their diagnostic sensitivity for detecting skin lesions such as melanoma.[39] Recently, dynamic OCT has been used to describe different patterns of vascularization in melanocytic tumours, which could be useful in evaluation of these lesions.[40] Moreover, Schuh *et al.* found that LC-OCT can be used to differentiate between naevi and melanoma, with 93% sensitivity and 100% specificity compared with RCM in diagnosing melanoma.[41]

RCM has gained a well-established place in the diagnostic armamentarium of melanocytic tumours.[38] However, its low penetration depth (~200 µm) can sometimes represent a limitation. In our study, most features of melanocytic tumours, including cellular details, were similarly visible with LC-OCT and RCM in the superficial layers, DEJ and superficial dermis. Compared with LC-OCT, RCM has the advantages of visualization of mosaics of the entire lesion with a diameter of 8 mm, and also a higher lateral resolution. By contrast, LC-OCT penetrates deeper into the skin, with cellular details still visible at 300 µm depth and global architecture to 400 µm depth. Furthermore, the availability of 3D reconstructions with LC-OCT seems to allow a better description of the morphology and arrangement of melanocytes, dendritic cells and nests in melanocytic lesions. This study revealed for the first time the real global 3D architecture of the epidermis, DEJ and superficial dermis in melanocytic lesions, opening a new frontier to comprehend the dynamic modifications from benign to malignant lesions. Moreover, the vertical mode with cellular resolution allowed visualization of the integrity of the dermoepidermal junction.

One of the main advantages of 3D visualization is the precise localization of each feature, which is particularly important for tumour cells within the epidermis, DEJ and dermis. The vertical visualization with cellular resolution in these skin layers helped us to precisely locate typical and atypical cells and nests, and also to clearly visualize DEJ integrity. These two findings were fundamental to the recognition of the normal, atypical and malignant melanocytic lesions, and is an indisputably useful tool for tumoral differentiation. Moreover, the atypical nests and pagetoid spreading of the naevoid melanoma, with clear disruption of the DEJ in the vertical view, were one of the clues to correct recognition of the malignancy.

Conclusion

In this study, most of the histological and RCM features in benign, atypical and melanocytic tumours could also be recognized with LC-OCT. Furthermore, new morphological aspects were comprehended with the 3D visualization mode. Future studies with a larger number of lesions are needed to validate our results and confirm the value of LC-OCT in the characterization and, ultimately, the diagnosis/management of melanocytic

tumours. Moreover, in order to obtain a reliable and specific histological correlation between LC-OCT and histology using vertical sections stained with haematoxylin and eosin to make sure that the best spatial correlation is obtained, a 2- or 3-mm punch biopsy can be taken from the specific area to be studied.

What's already known about this topic?

- LC-OCT is a new imaging technique that allows *in vivo* skin visualization with cellular resolution and the advantage of imaging in 3D and to a depth of 400 μm.
- LC-OCT features of healthy skin, BCC and dermal naevus have been described.
- In previous studies, a correlation of RCM with histopathology findings was reported and diagnostic criteria were established for melanocytic lesions.

What does this study add?

- We describe 3D *in vivo* visualization of melanocytic lesions and correlation with histopathology.
- LC-OCT findings correlated with RCM criteria in melanocytic lesions.
- We describe the advantages and limits of LC-OCT in melanocytic lesions compared with RCM.

Acknowledgement

We thank the members of the Dermatology Investigation Unit, especially Pablo Iglesias for helping to collect patient data, and the Dermatopathology Department of the Hospital Clinic Barcelona, for providing support to this project. We thank all the patients and their families, who are the main reason for our studies. We also thank Paul Hetherington for his help with the text editing. We are indebted to Maxime Cazalas and Clara Tavernier (DAMAE Medical, Paris, France) for technical assistance with the LC-OCT device. The Non-Invasive Skin Imaging Research Program of Hôpital Erasme, Université Libre de Bruxelles (Brussels, Belgium), would like to acknowledge the support of the Fonds Erasme (www.fondserasme.org).

Conflict of interest

The authors declare that they have no conflict of interest.

Funding

None.

Ethics statement

Ethics approval not applicable. Informed consent was obtained from patients for the use of their images and data for research/education.

Data availability

Data are available on request from the corresponding author.

References

1 Barut A, Dubois A, Davis A *et al.* Line-field confocal time-domain optical coherence tomography with dynamic focusing. *Opt Express* 2018; **26**: 33534–42.
2 Dubois A, Levecq O, Azimani H *et al.* Line-field confocal optical coherence tomography for high-resolution noninvasive imaging of skin tumors. *J Biomed Opt* 2018; **23**: 1–9.
3 Dubois A, Davis A, Siret D *et al.* Simultaneous dual-band line-field confocal optical coherence tomography: application to skin imaging. *Biomed Opt Express* 2019; **10**: 694–706.
4 Lenoir C, Diet G, Cinotti E *et al.* Line-field confocal optical coherence tomography of sebaceous hyperplasia: a case series. *J Eur Acad Dermatol Venereol* 2021; **35**: e509–11.
5 Lenoir C, Cinotti E, Tognetti L *et al.* Line-field confocal optical coherence tomography of actinic keratosis: a case series. *J Eur Acad Dermatol Venereol* 2021; **35**: e900–2.
6 Tognetti L, Carraro A, Cinotti E *et al.* P. Line-field confocal optical coherence tomography for non-invasive diagnosis of lichenoid dermatoses of the childhood: a case series. *Skin Res Technol* 2021; **27**: 1178–81.
7 Cinotti E, Tognetti L, Cartocci A *et al.* Line-field confocal optical coherence tomography for actinic keratosis and squamous cell carcinoma: a descriptive study. *Clin Exp Dermatol* 2021; **46**: 1530–41.
8 Tognetti L, Cinotti E, Suppa M *et al.* Line field confocal optical coherence tomography: an adjunctive tool in the diagnosis of autoimmune bullous diseases. *J Biophotonics* 2021; **14**: e202000449.
9 Suppa M, Fontaine M, Dejonckheere G *et al.* Line-field confocal optical coherence tomography of basal cell carcinoma: a descriptive study. *J Eur Acad Dermatol Venereol* 2021; **35**: 1099–110.
10 Monnier J, Tognetti L, Miyamoto M *et al. In vivo* characterization of healthy human skin with a novel, non-invasive imaging technique: line-field confocal optical coherence tomography. *J Eur Acad Dermatol Venereol* 2020; **34**: 2914–21.
11 Tognetti L, Rizzo A, Fiorani D *et al.* New findings in non-invasive imaging of aquagenic keratoderma: line-field optical coherence tomography, dermoscopy and reflectance confocal microscopy. *Skin Res Technol* 2020; **26**: 956–9.
12 Tognetti L, Ekinde S, Habougit C *et al.* Delayed tattoo reaction from red dye with overlapping clinicopathological features: examination with high-frequency ultrasound and line-field optical coherence tomography. *Dermatol Pract Concept* 2020; **10**: e2020053.

13 Tognetti L, Fiorani D, Suppa M *et al.* Examination of circumscribed palmar hypokeratosis with line-field confocal optical coherence tomography: dermoscopic, ultrasonographic and histopathologic correlates. *Indian J Dermatol Venereol Leprol* 2020; **86**: 206–8.
14 Lacarrubba F, Verzì AE, Puglisi DF, Micali G. Line-field confocal optical coherence tomography: a novel, non-invasive imaging technique for a rapid, in-vivo diagnosis of herpes infection of the skin. *J Eur Acad Dermatol Venereol* 2021; **35**: e404–6.
15 Nori S, Rius-Díaz F, Cuevas J *et al.* Sensitivity and specificity of reflectance-mode confocal microscopy for in vivo diagnosis of basal cell carcinoma: a multicenter study. *J Am Acad Dermatol* 2004; **51**: 923–30.
16 Pellacani G, Guitera P, Longo C *et al.* The impact of in vivo reflectance confocal microscopy for the diagnostic accuracy of melanoma and equivocal melanocytic lesions. *J Invest Dermatol* 2007; **127**: 2759–65.
17 Segura S, Puig S, Carrera C *et al.* Dendritic cells in pigmented basal cell carcinoma: a relevant finding by reflectance-mode confocal microscopy. *Arch Dermatol* 2007; **143**: 883–6.
18 Scope A, Benvenuto-Andrade C, Agero ALC *et al.* In vivo reflectance confocal microscopy imaging of melanocytic skin lesions: consensus terminology glossary and illustrative images. *J Am Acad Dermatol* 2007; **57**: 644–58.
19 Guitera P, Menzies SW, Longo C *et al.* In vivo confocal microscopy for diagnosis of melanoma and basal cell carcinoma using a two-step method: analysis of 710 consecutive clinically equivocal cases. *J Invest Dermatol* 2012; **132**: 2386–94.
20 Alarcon I, Carrera C, Palou J *et al.* Impact of in vivo reflectance confocal microscopy on the number needed to treat melanoma in doubtful lesions. *Br J Dermatol* 2014; **170**: 802–8.
21 Guida S, Longo C, Casari A *et al.* Update on the use of confocal microscopy in melanoma and non-melanoma skin cancer. *G Ital Dermatol Venereol* 2015; **150**: 547–63.
22 De Carvalho N, Farnetani F, Ciardo S *et al.* Reflectance confocal microscopy correlates of dermoscopic patterns of facial lesions help to discriminate lentigo maligna from pigmented nonmelanocytic macules. *Br J Dermatol* 2015; **173**: 128–33.
23 Yélamos O, Manubens E, Jain M *et al.* Improvement of diagnostic confidence and management of equivocal skin lesions by integration of reflectance confocal microscopy in daily practice: prospective study in 2 referral skin cancer centers. *J Am Acad Dermatol* 2020; **83**: 1057–63.
24 Boone MALM, Suppa M, Dhaenens F *et al. In vivo* assessment of optical properties of melanocytic skin lesions and differentiation of melanoma from non-malignant lesions by high-definition optical coherence tomography. *Arch Dermatol Res* 2016; **308**: 7–20.
25 Levine A, Wang K, Markowitz O. Optical coherence tomography in the diagnosis of skin cancer. *Dermatol Clin* 2017; **35**: 465–88.
26 Malvehy J, Pellacani G. Dermoscopy, confocal microscopy and other non-invasive tools for the diagnosis of non-melanoma skin cancers and other skin conditions. *Acta Derm Venereol* 2017; **97**: 22–30.
27 Davis A, Levecq O, Azimani H *et al.* Simultaneous dual-band line-field confocal optical coherence tomography: application to skin imaging. *Biomed Opt Express* 2019; **10**: 694–706.
28 Hibler BP, Qi Q, Rossi AM. Current state of imaging in dermatology. *Semin Cutan Med and Surg* 2016; **35**: 2–8.
29 Aleissa S, Navarrete-Dechent C, Cordova M *et al.* Presurgical evaluation of basal cell carcinoma using combined reflectance confocal microscopy-optical coherence tomography: a prospective study. *J Am Acad Dermatol* 2020; **82**: 962–8.
30 Boone MALM, Norrenberg S, Jemec GBE, Del Marmol V. High-definition optical coherence tomography imaging of melanocytic lesions: a pilot study. *Arch Dermatol Res* 2014; **306**: 11–26.
31 Iftimia N, Sahu A, Cordova M *et al.* The potential utility of integrated reflectance confocal microscopy-optical coherence tomography for guiding triage and therapy of basal cell carcinomas. *J Cancer* 2020; **11**: 6019–24.
32 Pedrazzani M, Breugnot J, Rouaud-Tinguely P *et al.* Comparison of line-field confocal optical coherence tomography images with histological sections: validation of a new method for in vivo and non-invasive quantification of superficial dermis thickness. *Skin Res Technol* 2020; **26**: 398–404.
33 Lacarrubba F, Verzì AE, Puglisi DF *et al.* Line-field confocal optical coherence tomography of xanthogranuloma: correlation with vertical and horizontal histopathology. *J Cutan Pathol* 2021; **48**: 1208–11.
34 Lenoir C, Perez-Anker J, Diet G *et al.* Line-field confocal optical coherence tomography of benign dermal melanocytic proliferations: a case series. *J Eur Acad Dermatol Venereol* 2021; **35**: 399–401.
35 Ruini C, Schuh S, Sattler E, Welzel J. Line-field confocal optical coherence tomography – practical applications in dermatology and comparison with established imaging methods. *Skin Res Technol* 2021; **27**: 340–52.
36 Bankhead P, Loughrey MB, Fernández JA *et al.* QuPath: open source software for digital pathology image analysis. *Sci Rep* 2017; **7**: 16878.
37 Pellacani G, Vinceti M, Bassoli S *et al.* Reflectance confocal microscopy and features of melanocytic lesions: an internet-based study of the reproducibility of terminology. *Arch Dermatol* 2009; **145**: 1137–43.
38 Pellacani G, Longo C, Malvehy J *et al.* In vivo confocal microscopic and histopathologic correlations of dermoscopic features in 202 melanocytic lesions. *Arch Dermatol* 2008; **144**: 1597–608.

39 Ulrich M, Themstrup L, De Carvalho N *et al.* Dynamic optical coherence tomography in dermatology. *Dermatology* 2016; **232**: 298–311.
40 Welzel J, Schuh S, De Carvalho N *et al.* Dynamic optical coherence tomography shows characteristic alterations of blood vessels in malignant melanoma. *J Eur Acad Dermatol Venereol* 2021; **35**: 1087–93.
41 Schuh S, Ruini C, Perwein MKE *et al.* Line-field confocal optical coherence tomography: a new tool for the differentiation between nevi and melanomas? *Cancers (Basel)* 2022; **14**: 1140.

Supporting Information

Additional Supporting Information may be found in the online version of this article:

Video S1 Comparison of line-field confocal optical coherence tomography (LC-OCT), reflectance confocal microscopy (RCM) and histopathology. Differences observed in benign and malignant melanocytic lesions. Artificial Intelligence segmentation of the melanocytes. Yellow landmarks: macroscopic guide to select the precise same area to be compared in dermoscopy and RCM; blue rectangle: corresponding area to be compared in both LC-OCT and RCM; red line: corresponding area of the vertical of LC-OCT image in the horizontal view of LC-OCT; blue line: same feature localized and observed both in horizontal and vertical modes; red arrow: each pattern or feature is named in the corresponding image.

PUBLICACIÓN N° 2:[66]

Comprendiendo la anatomía de la dermatoscopia de los tumores melanocíticos de la piel: correlación *in vivo* con la tomografía de coherencia óptica de campo lineal.

Understanding anatomy of dermoscopy of melanocytic skin tumors: correlation *in vivo* with line-field optical coherence tomography.

Simone Soglia *, Javiera Pérez-Anker *, Raquel Albero, LLucia Alos, Veronique Berot, Paola Castillo, Elisa Cinotti, Veronique del Marmol, A Fakih, Adriana García, Clement Lenoir, Jilliana Monnier, Jean Luc Perrot, Susana Puig, Pietro Rubegni, F Skowron, Mariano Suppa, Linda Tognetti, M. Venturini, Josep Malvehy.

J Eur Acad Dermatol Venereol. 2023 Dec 22;00:1-11.doi: 10.1111/jdv.19771. Epub ahead of print. PMID: 38131528.

Factor de impacto: 9.228

Resumen:
Antecedentes: La detección temprana del melanoma es el principal factor que afecta su pronóstico y supervivencia. Por esta razón, se han propuesto tecnologías no invasivas para obtener un diagnóstico más preciso.
Recientemente, se ha desarrollado la tomografía de coherencia óptica de campo lineal (TCO-CL), que permite ver imágenes *in vivo* con resolución celular en 3 dimensiones. Al combinar las ventajas de la TCO convencional y de la microscopía confocal de reflectancia, esta herramienta parece ser especialmente adecuada para las lesiones melanocíticas.

Objetivos: El objetivo de este estudio fue identificar y describir la correlación entre criterios dermatoscópicos específicos y características de TCO-CL en 3 dimensiones en lesiones melanocíticas.

Métodos: Se adquirieron imágenes dermatoscópicas y de TCO-CL de 126 lesiones melanocíticas en tres centros diferentes. Se consideraron los siguientes criterios dermatoscópicos: patrón reticular, puntos y glóbulos, áreas sin estructura, velo azul blanquecino, estructuras de regresión, red negativa, patrón homogéneo, proyecciones, manchas.

Resultados: Se analizaron 69 (55%) lesiones benignas y 57 (45%) lesiones malignas. Se encontró que un patrón reticular regular se asociaba en el 75% de los casos con la presencia de crestas alargadas con células pigmentadas a lo largo de la capa basal, mientras que un patrón reticular atípico mostraba una organización irregular de las crestas con una hiperplasia melanocítica, crestas ensanchadas y fusionadas y nidos alargados. Tanto los puntos y glóbulos típicos como los atípicos se asociaron con nidos melanocíticos en la dermis o en la unión dermoepidérmica (UDE), así como con quistes de queratina/pseudoquistes. Los glóbulos grises correspondían a la presencia de células inflamatorias dérmicas que contenían melanina (melanófagos) dentro de las papilas. Las áreas sin estructura marrones/negras se correlacionaron con alteraciones de la UDE. Observamos las mismas alteraciones de la UDE, pero con la presencia de melanófagos dérmicos, en el 36% de los casos de áreas sin estructura azules/blancas/grises. Se realizó una descripción de cada correlación TCO-CL/dermatoscopia.

Conclusiones: TCO-CL permitió, por primera vez, realizar una correlación *in vivo* en 3 dimensiones entre criterios dermatoscópicos y características patológicas de las lesiones melanocíticas.

Received: 3 June 2023 | Accepted: 21 November 2023

DOI: 10.1111/jdv.19771

ORIGINAL ARTICLE

Understanding the anatomy of dermoscopy of melanocytic skin tumours: Correlation in vivo with line-field optical coherence tomography

S. Soglia[1,2] | J. Pérez-Anker[1] | R. Albero[3] | L. Alós[3] | V. Berot[4] | P. Castillo[3] | E. Cinotti[5,6] | V. Del Marmol[7] | A. Fakih[4] | A. García[3] | C. Lenoir[7] | J. Monnier[8] | J. L. Perrot[4,6,9] | S. Puig[1,10,11] | P. Rubegni[5] | F. Skowron[4] | M. Suppa[6,7,12] | L. Tognetti[5] | M. Venturini[2] | J. Malvehy[1,10,11]

[1]Melanoma Unit, Dermatology Department, Hospital Clínic de Barcelona, Barcelona, Spain

[2]Department of Dermatology, University of Brescia, Brescia, Italy

[3]Pathology Department, Hospital Clinic, University of Barcelona, Barcelona, Spain

[4]Dermatology Department, University Hospital of Saint-Etienne, Saint-Etienne, France

[5]Dermatology Unit, Department of Medical, Surgical and Neurological Sciences, University of Siena, Siena, Italy

[6]Groupe d'Imagerie Cutanée Non Invasive (GICNI) of the Société Française de Dermatologie, Paris, France

[7]Department of Dermatology, Hôpital Erasme, HUB, Université Libre de Bruxelles, Brussels, Belgium

[8]Dermatology Department, AP-HM, Aix-Marseille University, Marseille, France

[9]Laboratoire de tribologie des systèmes UMR CNRS 5513, Saint-Etienne, France

[10]Universitat de Barcelona, Barcelona, Spain

[11]IDIBAPS, Barcelona, Belgium

[12]Department of Dermato-Oncology, Institut Jules Bordet, HUB, Université Libre de Bruxelles, Brussels, Belgium

Correspondence
Simone Soglia, Department of Dermatology, University of Brescia, Piazzale Spedali Civili 1, Brescia, Italy.
Email: s.soglia@unibs.it

Abstract

Background: Early melanoma detection is the main factor affecting prognosis and survival. For that reason, non-invasive technologies have been developed to provide a more accurate diagnosis. Recently, line-field confocal optical coherence tomography (LC-OCT) was developed to provide an in vivo, imaging device, with deep penetration and cellular resolution in three dimensions. Combining the advantages of conventional OCT and reflectance confocal microscopy, this tool seems to be particularly suitable for melanocytic lesions.

Objectives: The objective of this study was to identify and describe the correlation between specific dermoscopic criteria and LC-OCT features in three dimensions associated with melanocytic lesions.

Methods: Dermoscopic and LC-OCT images of 126 melanocytic lesions were acquired in three different centres. The following dermoscopic criteria have been considered: reticular pattern, dots and globules, structureless areas, blue-whitish veil, regression structures, negative network, homogeneous pattern, streaks and blotches.

Results: 69 (55%) benign and 57 (45%) malignant lesions were analysed. A regular reticular pattern was found associated in the 75% of the cases with the presence of elongated rete ridges with pigmented cells along the basal layer, while atypical reticular pattern showed an irregular organization of rete ridges with melanocytic hyperplasia, broadened and fused ridges and elongated nests. Both typical and atypical dots and globules were found associated with melanocytic nests in the dermis or at the dermoepidermal junction (DEJ), as well as with keratin cysts/pseudocysts. Grey globules corresponded to the presence of melanin-containing dermal inflammatory cells (melanophages) within the papillae. Structureless brown/black areas correlated with alterations of the DEJ. We observed the same DEJ alterations, but with the presence of dermal melanophages, in 36% of the cases of blue/white/grey structureless areas. A description of each LC-OCT/dermoscopy correlation was made.

Conclusions: LC-OCT permitted for the first time to perform an in vivo, 3D correlation between dermoscopic criteria and pathological-like features of melanocytic lesions.

S Soglia and J Pérez-Anker equally contributed to this paper.

INTRODUCTION

Dermoscopy is a non-invasive, in vivo diagnostic technique based on a magnification lens that uses incident light to make subsurface structures of the skin accessible to visual examination. It allows to look not only onto but also into the superficial skin layers, and thus permits a more detailed inspection of skin tumours.[1–3]

Since its creation, dermoscopy has become a mainstay in dermatology, capable of increasing the diagnostic accuracy of both tumour and inflammatory lesions.[3]

Each dermoscopic structure has a direct histopathologic correlate, representing the ideal clinicopathologic bridge.[4] Understanding this correlation is essential to better elucidate the in vivo behaviour of skin lesions, helping dermatologists in their management. However, there are some limitations intrinsic to the two procedures that make difficult to fully understand the anatomy of the tumours and pathological findings in skin diseases. Histopathology in vertical sections cannot be fully correlated with horizontal view of dermoscopy and some small dermoscopic structures are difficult to be identified in histopathological sections. Finally, ex vivo pathology may differ from in vivo dermoscopic observations after processing of samples (i.e. modification of cellular aspect and observation of blood vessels). With the intention to correlate dermoscopy and histopathology, some authors reported correlation of tumours in horizontal histopathological sections in a limited number of cases.[5]

Likewise, several works have been published over the years, on the correlation between pathological findings, dermoscopic structures and the other cornerstone of dermatological cancer diagnostics, reflectance confocal microscopy (RCM).[4,6]

RCM is a non-invasive imaging tool extensively used in the evaluation of equivocal cutaneous neoplasms to decrease the number of biopsies needed.[7] It allows to obtain en-face tumoural images up to 8 × 8 mm with a maximum depth of penetration of about 250 μm and with cellular resolution.[7] Despite its great utility, this method has a limited depth of penetration and does not allow to obtain 3D reconstructions, therefore it does not enable to fully understand the in vivo architecture of the analysed lesion. RCM visualizes the skin in horizontal sections similarly to dermoscopy. Therefore, a 3D observation of the anatomy of the skin is not possible with this technique.

As a response to this challenge, a new optical technique called line-field confocal optical coherence tomography (LC-OCT) has been recently developed to meet the need for an in vivo non-invasive imaging device with deep penetration and high resolution dedicated to dermatology.[8] This imaging modality combines the physical principles of time domain OCT and RCM with a penetration up to a depth of ~500 μm and with an isotropic resolution of ~1 μm. The device is composed of a handheld probe connected to a mobile chart embedding a central unit and a display. By combining the advantages of OCT (high penetration; vertical and horizontal slice imaging) and RCM (high resolution), this tool seems to be particularly suitable for understanding the anatomy of the skin. Moreover, LC-OCT offers the possibility to reconstruct a 3D volume of the lesions and, thanks to a dermoscopic camera integrated in the same probe, to indicate with accuracy the dermoscopic area of the lesion that is being analysed.

The goal of this study was to identify and describe the correlation between dermoscopic criteria associated with melanocytic lesions and LC-OCT features in three dimensions.

MATERIALS AND METHODS

A descriptive, retrospective study was performed, to identify the 3D LC-OCT features associated with the dermoscopic criteria associated with melanocytic lesions described in the literature.[9,10] Images were acquired at Hospital Clinic of Barcelona (Spain), the Hospital Erasme of Brussels (Belgium) and the University Hospital of Saint-Etienne (France), according to standard clinical practice, from June 2020 to January 2022. Only the lesions with a univocal/unambiguous clinical or histopathological diagnosis were selected.

The 2D dermoscopic camera integrated into the LC-OCT probe allowed a precise correlation of the horizontal, vertical and 3D LC-OCT images with each dermoscopic criterion (Figures 1–7, Table S1).

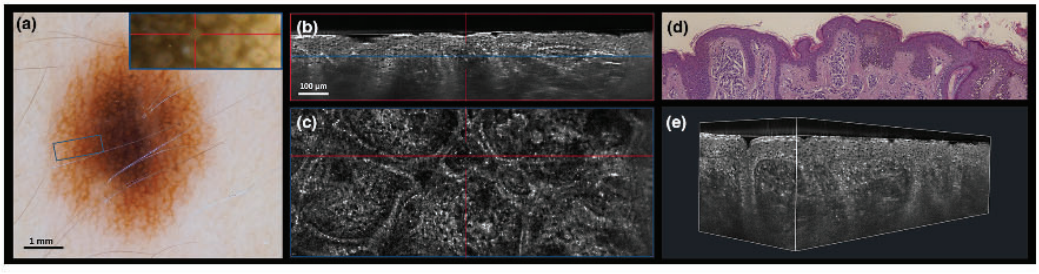

FIGURE 1 Regular pigment network. (a) Dermoscopic image of a compound nevus with moderate atypia showing a regular reticular pattern. The blue rectangle corresponds to the 3D capture area. (b) Vertical and (c) horizontal images, (d) histological image and (e) 3D reconstruction showing the presence of elongated rete ridges with pigmented cells (keratinocytes and/or melanocytes) along the basal layer.

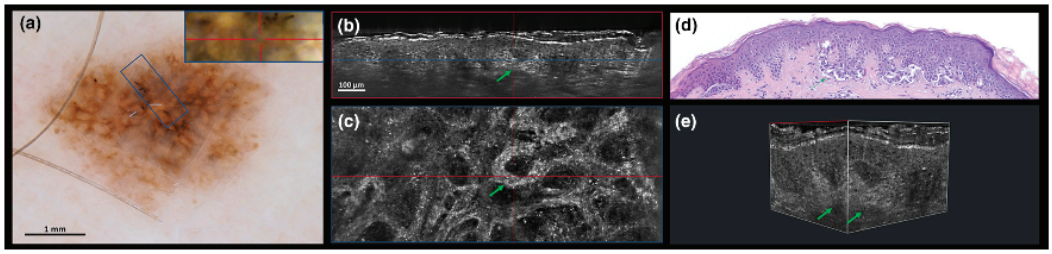

FIGURE 2 Atypical pigment network. (a) Dermoscopic image of a melanoma showing an atypical pigment network. The blue rectangle corresponds to the 3D capture area. (b) Vertical and (c) horizontal images, (d) histological image and (e) 3D reconstruction showing an irregular organization of rete ridges with a melanocytic hyperplasia, broadened and fused ridges (green arrows) and elongated nests distributed in a mesh-like horizontal pattern.

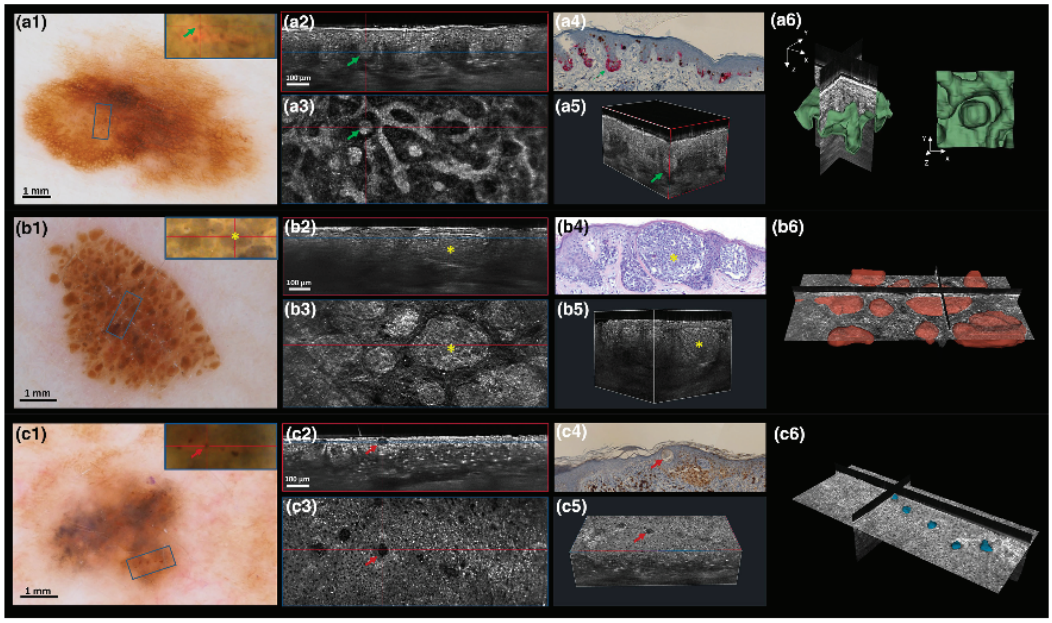

FIGURE 3 Brown dots and globules. They can correspond to the presence of junctional nests at the tip of the rete ridges (green arrows) (a1–a6), big nests of melanocytes close to the surface of the skin (asterisks) (b1–b6) or to roundish keratin structures (cysts/pseudocysts) in the epidermis (red arrows) (c1–c6). Dermoscopic image of a compound nevus with severe atypia (a1), compound melanocytic nevus with moderate atypia (b1) and of a melanocytic proliferation (c1). (a2–c2) Vertical and (a3–c3) horizontal images (a4–c4) histological image and (a5–c5) 3D reconstruction of the corresponding lesions. (a6–c6) 3D reconstruction with semi-automatic segmentation of the shape and distribution of the melanocytic nests and cysts/pseudocyst.

The following dermoscopic criteria were taken into account: reticular pattern (regular, atypical); dots and globules (typical, atypical/asymmetric); structureless areas (black/brown, white/blue/grey); blue-whitish veil (BWV); regression structures (scar-like, blue-grey); negative network; homogeneous pattern (blue, white/yellow/red); streaks (linear, bulbous projections); blotches; white structures, white-streaks, rosettes; blue dots.

These dermoscopic criteria were compared with LC-OCT findings in terms of 3D architectural organization and cellular details including size, morphology, atypia, and distribution of melanocytes, keratinocytes and inflammatory cells.

Clinical and dermoscopic evaluation were performed by two trained dermatologists expert in dermoscopy (SS and JPA). Clinical images of the skin lesions were acquired with a digital camera with at least 500×500 pixel size. Dermoscopic images were acquired at 20× magnification with a videodermoscope or a dermoscope coupled with a digital camera.

LC-OCT images were acquired with a CE-marked LC-OCT device [deepLiveTM; DAMAE Medical, Paris, France] in a standardized manner in each centre, by trained dermatologists. For each melanocytic lesion, multiple LC-OCT 3D acquisitions were performed in separate areas of the lesion. The device allows to obtain a dermoscopic image with a field of view of 2.5 mm and a resolution of 5 µm. For this reason, for the lesions with a diameter > of 2.5 mm the acquisitions

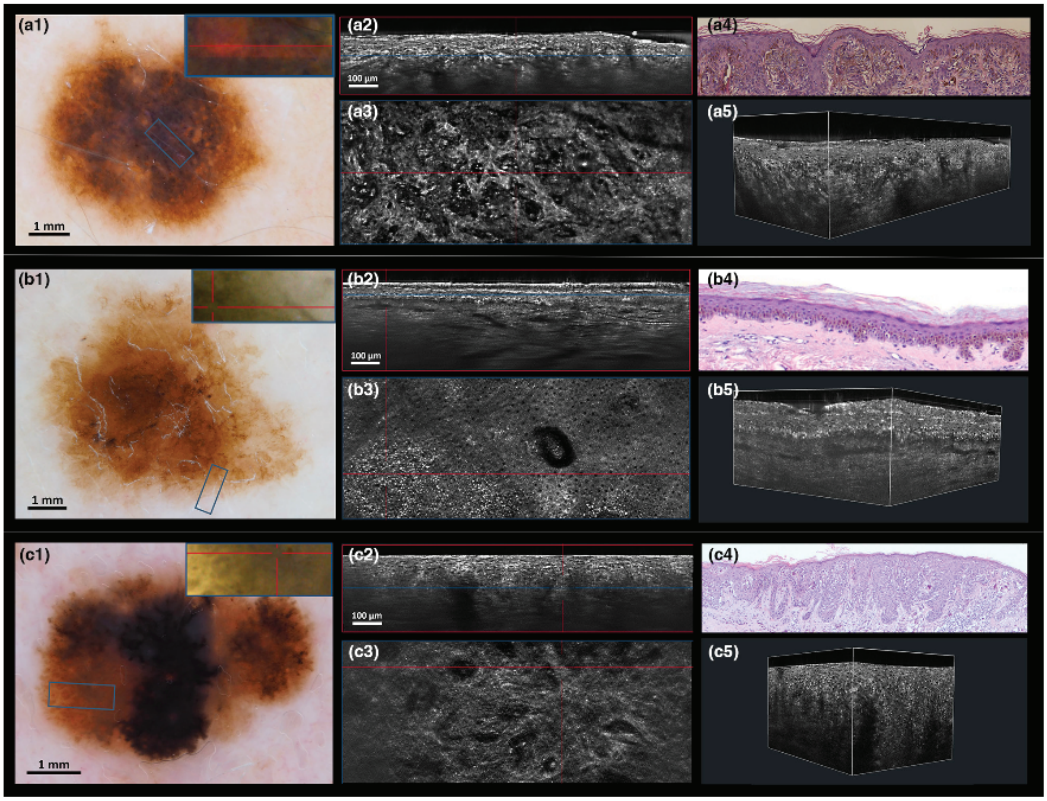

FIGURE 4 Brown/black structureless areas. They can correspond to the presence of a disrupted dermoepidermal junction (DEJ) (a1–a5), a flat DEJ (b1–b5) or of an irregular DEJ with broadened and fused rete ridges (c1–c5). Dermoscopic image of a compound nevus with moderate atypia (a1), melanocytic hyperplasia (b1) and of a melanoma in situ (c1). (a2, b2, c2) Vertical and (a3, b3, c3) horizontal images, (a4, b4, c4) histological image and (a5, b5, c5) 3D reconstruction of the corresponding lesions.

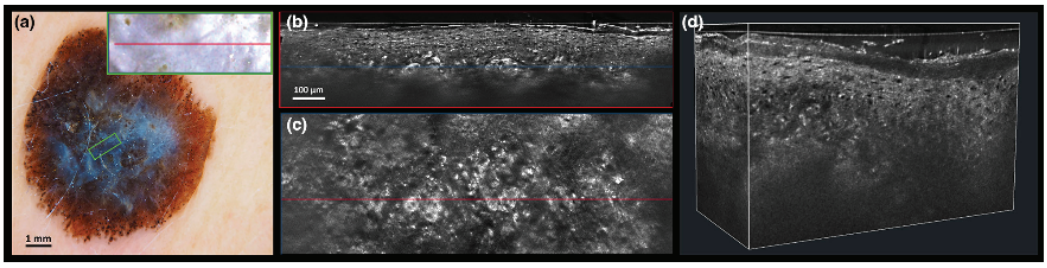

FIGURE 5 Blue-whitish veil. (a) Dermoscopic image of a superficial spreading melanoma (Breslow 0.8 mm) showing a blue-whitish veil. The green rectangle corresponds to the 3D capture area. (b) Vertical and (c) horizontal images and (d) 3D reconstruction showing the presence of bright dermal nests and hyperkeratosis.

were manually localized within the dermoscopic image under study, to ensure a precise correlation. All the acquisitions with bad image quality or with uncertain localization within the dermoscopic image were excluded from the study.

Ethical aspects

The study was conducted following the principles provided for by the declaration of Helsinki and all patients provided written informed consent.

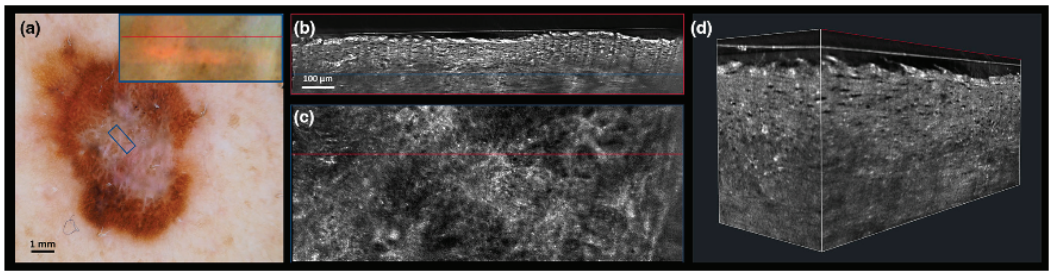

FIGURE 6 Scar-like regression structures. (a) Dermoscopic image of a melanoma in situ showing scar-like regression structures. The blue rectangle corresponds to the 3D capture area. (b) Vertical and (c) horizontal images and (d) 3D reconstruction showing the presence of melanophages in the dermis and coarse bright collagen fibres of fibrosis.

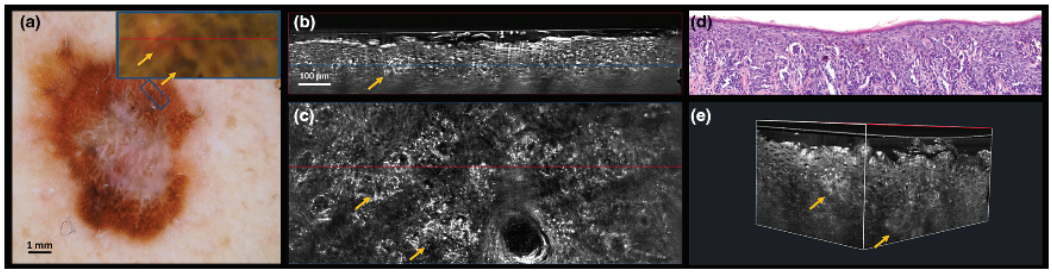

FIGURE 7 Negative of the pigment network. (a) Dermoscopic image of a melanoma in situ showing a negative of the pigment network. The blue rectangle corresponds to the 3D capture area. (b) Vertical and (c) horizontal images, (d) histological image and (e) 3D reconstruction showing the presence of broad and hypopigmented rete ridges with elongated nests of melanocytes inside the papillae (yellow arrows) in the vertical and 3D projections and thick bright rings that are spaced apart ('thick-rings pattern') in the horizontal.

Statistical analysis

Statistical analysis was performed using R software version 4.1.3 (R Foundation for Statistical Computing, Vienna, Austria). The frequency of each LC-OCT feature related to a dermoscopic feature, their associated odds ratio and their 95% confidence interval were computed. A Fisher exact test was performed to evaluate the repartition of melanoma and nevi for each criterion. A p-value <0.05 was considered as statistically significant.

RESULTS

A total of 126 melanocytic lesions were analysed, 69 (55%) benign and 57 (45%) malignant. For benign lesions, the diagnosis was based on the clinical dermoscopic assessment in 10 (14%) cases and on histopathological analysis in 59 (86%) cases; benign lesions included 8 junctional, 15 compound, 5 dermal, 32 atypical, 1 congenital, 4 Spitz/Reed nevi and 4 melanocytic hyperplasias. For malignant lesions, routine histopathology was obtained in all cases; malignant lesions included 23 in situ melanomas and 34 invasive melanomas with a mean Breslow thickness of 1.3 (0.2–5.2) mm.

The association of dermoscopic structures with LC-OCT patterns is reported in Table 1 and Table S1.

Pigment network

In 36 lesions a pigment network (PN) was present; typical in 11% and atypical in 89% of cases, respectively. A regular reticular pattern in dermoscopy was found associated with the presence of elongated rete ridges with pigmented cells (keratinocytes and/or melanocytes) along the basal layer in the 75% of the cases. The other 25% (only one case) was represented by a melanoma with melanin diffused throughout the entire epidermis and dilated/glomerular blood vessels inside regularly spaced papillae. The atypical pigment network showed an irregular organization of rete ridges with a melanocytic hyperplasia, broadened and fused ridges and elongated nests distributed in a mesh-like horizontal pattern in the 88% of the lesions with this feature (Figure 2). In four lesions the atypical PN correlated with a partial disruption of the dermoepidermal junction (DEJ) in the vertical and 3D projections. In the case of tumours with atypical PN at the dermoscopy, the absence of disruption of DEJ seen in LC-OCT was associated with benignity (OR = 0.10 [0.002; 1.49]$_{95\%,}$ p-value = 0.06).

TABLE 1 Dermoscopic features and corresponding LC-OCT pattern of melanocytic lesions: distribution across and association with benign and malignant lesions.

Dermoscopic feature/LC-OCT pattern	Overall	MM	Benign lesions	OR [95% CI]	p^*
Pigment network	**36 (28%)**	**10 (18%)**	**26 (38%)**	**0.35 [0.14; 0.87]**	**0.02**
Regular	**4 (11%)**	**1 (10%)**	**3 (12%)**	**0.86 [0.01; 12.4]**	**1**
Elongated rete ridge with pigmented cells along the DEJ	3 (75%)	0 (0%)	3 (100%)	0.00 [0.00; 13.0]	0.25
Pigmented epidermis with regularly spaced glomerular vessels	1 (25%)	1 (100%)	0 (0%)	Inf [0.08; Inf]	0.25
Atypical	**32 (89%)**	**9 (90%)**	**23 (88%)**	**1.17 [0.08; 68.4]**	**1**
Irregular, broaden and fused elongated rete ridges with pigmented cells along the DEJ	28 (88%)	6 (67%)	22 (96%)	0.10 [0.00; 1.49]	0.06
Partially disrupted DEJ	4 (13%)	3 (33%)	1 (4%)	9.99 [0.67; 600]	0.06
Dots and globules	**50 (39%)**	**21 (37%)**	**29 (42%)**	**0.81 [0.37; 1.75]**	**0.59**
Atypical/Asymmetric	**17 (34%)**	**8 (38%)**	**9 (31%)**	**1.36 [0.35; 5.20]**	**0.96**
Shallow dermal nests within the papillae	8 (47%)	5 (63%)	3 (33%)	3.09 [0.32; 37.6]	0.35
Nests at the tip of the rete ridge without bridging	6 (35%)	2 (25%)	4 (44%)	0.44 [0.03; 4.73]	1
Pseudocysts	3 (18%)	1 (13%)	2 (22%)	0.52 [0.01; 12.3]	1
Typical	**14 (28%)**	**1 (5%)**	**13 (45%)**	**0.06 [0.00; 0.51]**	**0.003**
Shallow dermal nests within the papillae	6 (43%)	1 (100%)	5 (38%)	Inf [0.03; Inf]	0.43
Nests at the tip of the rete ridge without bridging	7 (50%)	0 (0%)	7 (54%)	0.00 [0.00; 39.0]	1
Pseudocysts	1 (7%)	0 (0%)	1 (8%)	0.00 [0.00; 503]	1
Grey	**19 (38%)**	**12 (57%)**	**7 (24%)**	**4.06 [1.07; 16.9]**	**0.02**
Dermal melanocytic nests +/− inflammatory infiltrate	8 (42%)	6 (50%)	2 (29%)	2.38 [0.25; 34.7]	0.63
Junctional melanocytic nests	4 (21%)	2 (17%)	2 (29%)	0.52 [0.03; 9.18]	0.52
Melanophages within the papillae	7 (37%)	4 (33%)	3 (43%)	0.68 [0.07; 7.06]	1
Structureless area	**40 (31%)**	**19 (33%)**	**21 (30%)**	**1.14 [0.50; 2.59]**	**0.85**
Black/brown	**26 (65%)**	**15 (79%)**	**11 (52%)**	**3.30 [0.71; 18.5]**	**0.10**
Irregular and dense organization of the rete ridges	9 (35%)	6 (40%)	3 (27%)	1.74 [0.26; 14.5]	0.68
Disrupted DEJ	12 (46%)	6 (40%)	6 (55%)	0.57 [0.09; 3.46]	0.69
Flat pigmented DEJ	5 (19%)	3 (20%)	2 (18%)	1.12 [0.10; 16.1]	1
White/blue/grey	**14 (35%)**	**4 (21%)**	**10 (48%)**	**0.30 [0.05; 1.41]**	**0.10**
Low-pigmented epidermis + melanophages in the dermis	7 (50%)	1 (25%)	6 (60%)	0.24 [0.01; 4.44]	0.56
Irregular organization of the rete ridges/Flat DEJ + dermal melanocytic nests	7 (50%)	3 (75%)	4 (40%)	4.03 [0.22; 274]	0.56
Blotches	**6 (5%)**	**4 (7%)**	**2 (3%)**	**2.51 [0.34; 28.8]**	**0.41**
Parakeratosis +/− dendritic cells in the epidermis	2 (33%)	1 (25%)	1 (50%)	0.41 [0.00; 52.1]	1
Pigment ascension into the stratum corneum	1 (17%)	1 (25%)	0 (0%)	Inf [0.01; Inf]	1
Invagination of the SC with parakeratosis	3 (50%)	2 (50%)	1 (50%)	1 [0.01; 117]	1
Homogeneous pattern	**6 (5%)**	**1 (2%)**	**5 (7%)**	**0.23 [0.01; 2.15]**	**0.22**
Blue	**3 (50%)**	**1 (100%)**	**2 (40%)**	**Inf [0.03; Inf]**	**1**
Compact nest of melanocytes in the dermis	1 (33%)	0 (0%)	1 (50%)		
White/yellow/red	**3 (50%)**	**0 (0%)**	**3 (60%)**	**0.00 [0.00; 39.0]**	**1**
Wave pattern	3 (100%)	0 (0%)	3 (100%)		
Blue-Whitish Veil	**17 (13%)**	**14 (25%)**	**3 (4%)**	**7.06 [1.82; 40.5]**	**0.001**
Melanophages in the dermis	7 (41%)	5 (36%)	2 (67%)	0.30 [0.00; 7.15]	0.54
Dermal nests with hyperkeratosis +/− clefting	6 (35%)	6 (43%)	0 (0%)	Inf [0.23; Inf]	0.51
Dermal nests with thin or low-pigmented epidermis +/− clefting	4 (24%)	3 (21%)	1 (33%)	0.57 [0.02; 42.8]	1

TABLE 1 (Continued)

Dermoscopic feature/LC-OCT pattern	Overall	MM	Benign lesions	OR [95% CI]	p*
Regression structures	**36 (28%)**	**23 (40%)**	**13 (19%)**	**2.89 [1.22; 7.10]**	**0.01**
Scar-like	**12 (33%)**	**8 (35%)**	**4 (31%)**	**1.19 [0.23; 7.05]**	**1**
Melanophages in the dermis	1 (8%)	1 (13%)	0 (0%)	Inf [0.01; Inf]	1
Fibrosis without melanophages	1 (8%)	0 (0%)	1 (25%)	0.00 [0.00; 19.5]	0.33
Fibrosis with melanophages	10 (83%)	7 (88%)	3 (75%)	2.16 [0.02; 208]	1
Blue-grey	**22 (61%)**	**14 (61%)**	**8 (62%)**	**0.97 [0.19; 4.78]**	**1**
Inflammation with melanophages in the dermis	21 (95%)	13 (93%)	8 (100%)	0.00 [0.00; 68.2]	1
Melanophages + fibrosis	1 (5%)	1 (7%)	0 (0%)	Inf [0.01; Inf]	1
Peppering	**2 (6%)**	**1 (4%)**	**1 (8%)**	**0.56 [0.01; 46.4]**	**1**
Big isolated pigmented cells in the dermis	2 (100%)	1 (100%)	1 (100%)		
Negative network	**4 (3%)**	**2 (4%)**	**2 (3%)**	**1.22 [0.09; 17.3]**	**1**
Melanocytic nests within papillae	3 (75%)	1 (50%)	2 (100%)	0.00 [0.00; 39.0]	1
Melanophages and inflammation within the papillae	1 (25%)	1 (50%)	0 (0%)	Inf [0.03; Inf]	1
STREAKS	**4 (3%)**	**2 (4%)**	**2 (3%)**	**1.22 [0.09; 17.3]**	**1**
Lineal streaks	**3 (75%)**	**2 (100%)**	**1 (50%)**	**Inf [0.03; Inf]**	**1**
Confluent melanocytes in the basal layer at the periphery	3 (100%)	2 (100%)	1 (100%)		
Bulbous projection	**1 (25%)**	**0 (0%)**	**1 (50%)**	**0.00 [0.00; 39.0]**	**1**
Melanocytic nests within the papillae at the periphery	1 (100%)	0 (0%)	1 (100%)		
White structures + rosettes	**6 (5%)**	**2 (4%)**	**4 (6%)**	**0.69 [0.05; 4.32]**	**0.51**
Central hypopigmentation	**2 (33%)**	**1 (50%)**	**1 (25%)**	**2.44 [0.02; 312]**	**1**
Flat DEJ with wave pattern +/− hyperkeratosis	1 (50%)	1 (100%)	0 (0%)	Inf [0.03; Inf]	1
Melanophages in the dermis with hyperkeratosis	1 (50%)	0 (0%)	1 (100%)	0.00 [0.00; 39.0]	1
Rosettes	**1 (17%)**	**1 (50%)**	**0 (0%)**	**Inf [0.05; Inf]**	**0.33**
Keratin-filled inclusion in the epidermis	1 (100%)	1 (100%)	0 (0%)		
White globules	**1 (17%)**	**0 (0%)**	**1 (25%)**	**0.00 [0.00; 77.9]**	**1**
Melanocytic nests with balloon cells	1 (100%)	0 (0%)	1 (100%)		
Others	**2 (33%)**	**0 (0%)**	**2 (50%)**	**0.00 [0.00; 11.8]**	**0.50**
Flat DEJ with wave pattern +/− orthokeratosis	1 (50%)	0 (0%)	1 (50%)		
yperkeratosis with parakeratosis	1 (50%)	0 (0%)	1 (50%)		

Note: *N* (%) presented in each box, unless otherwise stated. Bold indicates: *p* is significant for values less than 0.05.

Abbreviations: CI, confidence intervals; DEJ, dermaoepidermal junction; LC-OCT, line-field confocal optical coherence tomography; OR, odds ratio.

*Fisher exact test.

Dots and globules

Dots/globules were found in 50 lesions and they were atypical in 34% of cases (Figure 3). Both typical and atypical dots and globules were found associated with melanocytic nests in the dermis or dermoepidermal junction. Moreover, 13% of the total number of dots that we observed, mostly atypical, correlated to keratin cysts or pseudocysts. Grey dots were found in 38% of cases and frequently associated with malignancy (OR = 4.06 $[1.07; 16.85]_{95\%}$, *p*-value = 0.02). They showed as LC-OCT counterpart, the presence of dermal melanocytic nests (42% of the cases), junctional melanocytic nests (21%) or the presence of melanin-containing dermal, roundish, inflammatory cells with an average diameter of 15 μm (melanophages) within the papillae (37%).

Structureless areas

Black/brown structureless areas in melanocytic tumours correlated with alterations of DEJ that can be irregular with broadened and fused rete ridges (35%), disrupted DEJ (46%) or flat DEJ (19%) (Figure 4). We observed the presence of melanophages in the 50% of the lesions which present dermoscopic blue/white/grey structureless areas. In 36% of the lesions with blue/white/grey structureless area, the presence of melanophages was associated with an irregular

organization and broadened rete ridge. In the other 14%, the dermoepidermal junction was flat or disrupted.

Blotches

Six melanocytic lesions showed blotches on dermoscopy. This finding correlated to the presence of parakeratosis in the 83% of the cases. In the 33% of these lesions the parakeratosis could be accompanied by the presence of dendritic cells in the epidermis, while in the remaining 50% by hypopigmented invagination in the stratum corneum. Finally, one lesion (17%) showed pigment retention in the epidermis (Table S1).

Homogeneous pattern

A blue homogeneous pattern was found associated in the 67% of the cases with the presence of a flat DEJ in the vertical and 3D projections with melanocytes deep in the dermis. The remaining 33% showed deep dermal nests with melanocytes. All the white/yellow/red homogeneous pattern analysed (three lesions) were found on benign lesions and showed a dermal 'wave pattern',[11] which probably can be considered a protective factor (Table S1).

Blue-white veil

BWV is a well-known dermoscopic feature associated with pigmented malignant lesions.[12] We observed BWV in 25% of cases corresponding to melanoma. This finding was associated with a set of epidermal and dermal findings like orthokeratosis and dermal melanocytic nests (35%) (Figure 5) or thin/ulcerated low-pigmented epidermis with dermal melanocytic nests (24%). The remaining 41% of the cases showed the presence of melanin-containing cells (melanophages and melanocytes) in the dermis. A new, in vivo finding associated with blue-white veil, frequently found in these areas was a clefting, a hyporefractile space that runs along junctional or dermal melanocytic nests.

Regression structures

In 28% of the lesions analysed, regression structures were found. Both scar-like and blue-grey regression structures were founded associated with the presence of melanophages in the dermis (respectively in the 91% and 100% of the cases). Especially the first ones showed as LC-OCT counterpart the presence of bright coarse dermal collagen fibres of fibrosis (91%) (Figure 6).

Negative of the PN

We observed this feature in 3% of tumours. The 75% of the cases showed the presence of broad and hypopigmented rete ridges with elongated nests of melanocytes inside the papillae in the vertical and 3D projections and a 'thick-rings pattern' in the horizontal[13] (Figure 7). The remaining 25% of the cases correlated to the presence of solitary melanin-containing cells (mostly melanophages) inside large papillae between undulated rete ridges in the vertical and 3D projections and a 'meshwork pattern'[13] in the horizontal.

Streaks

The 3% of the lesions examined, 50% benign and 50% malignant, showed streaks on dermoscopy. Bulbous streaks correlated to the presence of junctional melanocytic nests that radiate from the periphery of the lesions, while in the case of linear streaks it was not possible to observe melanocytic nests but rather the presence of a concentration of dendritic cells with a centrifugal pattern (Table S1).

The rest of the dermoscopic criteria analysed with the relative LC-OCT counterparts can be found in Table 1 and Table S1.

DISCUSSION

For the first time, 3D LC-OCT diagnostic features in melanocytic lesions were precisely compared to their corresponding dermoscopic structure.

Dermoscopy and histopathology are closely linked. Shape, dimension and colour of each dermoscopic structure provide us an easily accessible glimpse of what the pathologist will see during his analysis. Different dermoscopic colours, for example, depend on the type and location of the chromophores in the skin.[14,15] Melanin, keratin, blood and collagen represent the most important cutaneous chromophores and an increase or decrease in their concentration is, generally, responsible for the different presentations of skin lesions.

If dermoscopy gives us clues on the pathological aspect of dermatological lesions, with LC-OCT we can, for the first time, obtain an in vivo histological-like image without the artefacts deriving from the processing and fixation of the surgical specimens, in a 3D mode.[16,17]

Thanks to LC-OCT we could, for the first time, observe in vertical histological-like and tridimensional projections such features as the shape of the DEJ, the shape, dimension, distribution of the melanocytic nests and the vascular patterns. All this information, also thanks to the aid of artificial intelligence reconstruction systems, will play a fundamental role in the diagnosis of melanocytic lesions (Figure 3).

Several dermoscopic criteria and algorithms have been developed to help the clinician in an early detection of malignant tumours.[18–20]

Reticular pattern corresponds to a brown-black network structure associated with a large number of lesions from nevi and dermatofibromas to dysplastic nevi and melanomas.[10]

Histologically, it corresponds to elongated rete ridges with pigmented keratinocytes and melanocytes at the tips.[21] An irregular reticular pattern, with the lines of the network varying in terms of colour, thickness and size, is usually explained, histologically, with a disarrangement of the rete ridges.[22] In LC-OCT examination, atypical reticular pattern showed an irregular distribution of rete ridges that appear broadened or fused in most of the cases. The remaining 13% revealed a disrupted DEJ making it impossible to clearly distinguish the transition from epidermis to dermis. These findings were clearly related to malignancy.

Globules are round to oval well-demarcated structures, aggregated in clusters or located at the periphery of melanocytic lesions.[23] Brown/black globules correspond to melanocytic nests located at the DEJ.[4] LC-OCT showed, in these cases, melanocytic nests that could be located both at the tip of the rete ridges or within the papillae. We found atypical globules associated with nests located in the papillae, mainly in malignant lesions even though this finding did not reach statistical significance (OR 3.09 $[0.32; 37.60]_{95\%}$, p-value = 0.35). Interestingly, a rather high percentage of clinically and dermoscopically indistinguishable globules revealed keratin cysts or pseudocysts on LC-OCT examination, discriminating them from atypical globules.

As expected, we observed grey globules especially in melanomas (OR 4.06 $[1.07; 16.85]_{95\%}$, p-value = 0.02); they showed the presence of melanophages in the dermis in the 37% of the cases as compared to brown/black ones. In some cases, big melanophages seem to correspond directly to some small grey dots.

Streaks are lineal or bulbous projections at the periphery of the lesion.[14] They are a sign of a growing lesion and generally correspond histologically to confluent junctional nests of pigmented melanocytes. Interestingly, we found that in the 75% lineal streaks did not have as LC-OCT counterpart clear melanocytic nests, but the presence of numerous dendritic cells in the basal layer associated with an irregular organization of the rete ridges.

Some melanocytic lesions show structureless areas of different colours in which it is impossible to recognize any dermoscopic criteria. They are generally explained, histologically, with areas of flattening of rete ridges or with a decrease of concentration in melanin in the cases of hypopigmented ones.[14] LC-OCT showed the presence of a flat DEJ only in a minority of the lesions. In the other cases, both in brown/black and white/blue/grey structureless areas we observed a disrupted, unrecognizable DEJ or an irregular organization of rete pegs, with very elongated and dense ridges. In the case of dark brown/black areas, we can assume that the melanic pigment is so densely and irregularly arranged not to allow the recognition of the reticular pattern on dermoscopic examination, while the presence of melanin-containing cells in the dermis (deep melanocytic nests or melanophages) is responsible for the colour of the grey/blue ones.

If the dermoscopic structureless area is uniformly dark, obscuring the underlying structures, it is called blotch. These structures correspond to epidermal melanin retention or can be due to parakeratosis with or without the presence of dendritic cells in the epidermis.

Finally, homogeneous pattern is a structureless uniform area, covering uniformly the entire lesion.[14] It is a structure more frequently associated with deep benign lesions such as blue nevi. In these cases, we observed at the LC-OCT analysis deep nests of melanocytes or the presence of a wave pattern, a typical presentation of lesions with an intradermal component already described by Lenoir et al.[11]

Histologic regression can be seen dermoscopically as blue-grey dots, also called peppering, or as white scar-like areas.[24] Grey dots, sometimes densely packed (peppering) can be found in many conditions, from lichen planus-like keratosis to melanomas and correspond both histologically and in LC-OCT to melanin in dermis, inside or outside melanophages. In 5% of the cases we observed, together with these findings, the presence of dermal coarse collagen fibres of fibrosis.

White is the dermoscopic colour for collagen, indeed, 92% of the scar-like regression areas that we analysed showed the presence of fibroplasia that can be visualized via LC-OCT as bright dense dermal lines, both in vertical, horizontal and 3D projections.

Blue-whitish veil, a well-known criterion generally associated with melanoma, is described as a blue pigmentation, with an overlying white 'ground glass' haze over palpable portions of lesions.[13] This finding can be explained by the presence of heavily pigmented melanocytes or melanophages in the dermis associated with epidermal modifications such as hyperkeratosis. Our analysis confirmed these statements but, at same time, the possibility of an in vivo examination highlighted some new features. We observed a thin or ulcerated epidermis in the 24% of the lesions and, more interestingly, we described the presence of clefting not previously described in in vivo examination of melanocytic tumours (submitted elsewhere). This feature was observed in many rapidly growing melanomas and corresponded to dark, hyporefractile spaces in between the nests of melanocytes and surrounding epidermis or stroma. We assume that could be due to the role of proteolytic enzymes, pivotal in some mechanisms such as cancer cell motility and tumour cell invasion and metastasis.[25]

The negative network consists of light areas making up the 'cords' of the network, and darker areas filling the holes; it is seen as a negative of the pigmented network.[26] LC-OCT perfectly reflects this scenario showing compact nests of melanocytes or melanophages in the papillae between elongated rete ridges.

Beyond the architectural criteria explained, the LC-OCT analysis allowed to identify the presence of dendritic and pagetoid cells in the 89% of melanomas and in the 36% of benign lesions (OR = 14.6 $[5.28; 47.64]_{95}$, $p < 0.001$*). These data, which were not reported in the results section as they do not directly explain a precise dermoscopic pattern, will be pivotal in future work aimed at defining LC-OCT criteria for differentiating benign from malignant melanocytic lesions.

LC-OCT is a non-invasive easy-to-use diagnostic device which allows fast acquisition of skin images; however, the quality of the images acquired can be affected by some factors such as the use of incorrect quantities of oil or patient movement (particularly in areas of the body, such as the abdomen, subject to breathing movements). For this reasons, 18 lesions have been excluded from the study due to poor image quality.

Obtaining a precise correlation between the area investigated with LC-OCT and the histological counterpart is not always simple, particularly in large lesions. However, this limit can be easily overcome using simple expedients, such as marking the area to be investigated with substances (like white-out) that can be identified by the pathologists and that can resist the fixation process.

LC-OCT permitted for the first time to perform an in vivo, 3-D correlation between dermoscopic criteria and pathological-like features of melanocytic lesions, allowing to discover new correlations and to confirm the ones already hypothesized with other methods of non-invasive diagnostics.

The provided information, combined with the ease and speed of the technique make LC-OCT a very promising technique also for the diagnosis of melanocytic lesions.

ACKNOWLEDGEMENTS

The Non-Invasive Skin Imaging Research Team of *Hôpital Erasme, HUB, Université Libre de Bruxelles* (Brussels, Belgium) would like to acknowledge the support of the *Fonds Erasme* (www.fondserasme.org). We thank Maxime Calzalas, Clothilde Raoux and Clara Tavernier (DAMAE Medical, Paris, France) for technical assistance with the LC-OCT device.

FUNDING INFORMATION

None.

CONFLICT OF INTEREST STATEMENT

The authors report no conflict of interest.

DATA AVAILABILITY STATEMENT

The data that support the findings of this study are available from the corresponding author upon reasonable request.

ETHICS STATEMENT

The patients in this manuscript have given written informed consent to the publication of their case details.

ORCID

S. Soglia https://orcid.org/0000-0002-2882-2036
J. Pérez-Anker https://orcid.org/0000-0002-6959-7250
P. Castillo https://orcid.org/0000-0002-9284-8601
E. Cinotti https://orcid.org/0000-0002-4009-0659
S. Puig https://orcid.org/0000-0003-1337-9745
M. Suppa https://orcid.org/0000-0002-9266-0342
L. Tognetti https://orcid.org/0000-0002-6691-4310
M. Venturini https://orcid.org/0000-0001-6800-3695

REFERENCES

1. Woltsche N, Schwab C, Deinlein T, Hofmann-Wellenhof R, Zalaudek I. Dermoscopy in the era of dermato-oncology: from bed to bench side and retour. Expert Rev Anticancer Ther. 2016;16:531–41.
2. Fuller SR, Bowen GM, Tanner B, Grossman D. Digital dermoscopic monitoring of atypical nevi in patients at risk for melanoma. Dermatol Surg. 2007;33:1198–206.
3. Kittler H, Pehamberger H, Wolff K, Binder M. Diagnostic accuracy of dermoscopy. Lancet Oncol. 2002;3:159–65.
4. Yélamos O, Braun RP, Liopyris K, Wolner ZJ, Kerl K, Gerami P, et al. Dermoscopy and dermatopathology correlates of cutaneous neoplasms. J Am Acad Dermatol. 2019;80:341–63.
5. Rezze GG, Scramim AP, Neves RI, Landman G. Structural correlations between dermoscopic features of cutaneous melanomas and histopathology using transverse sections. Am J Dermatopathol. 2006;28:13–20.
6. Shahriari N, Grant-Kels JM, Rabinovitz H, Oliviero M, Scope A. Reflectance confocal microscopy: diagnostic criteria of common benign and malignant neoplasms, dermoscopic and histopathologic correlates of key confocal criteria, and diagnostic algorithms. J Am Acad Dermatol. 2021;84:17–31.
7. Shahriari N, Grant-Kels JM, Rabinovitz H, Oliviero M, Scope A. Reflectance confocal microscopy: principles, basic terminology, clinical indications, limitations, and practical considerations. J Am Acad Dermatol. 2021;84:1–14.
8. Dubois A, Levecq O, Azimani H, Siret D, Barut A, Suppa M, et al. Line-field confocal optical coherence tomography for high-resolution noninvasive imaging of skin tumors. J Biomed Opt. 2018;23:1–9.
9. Argenziano G, Soyer HP, Chimenti S, Talamini R, Corona R, Sera F, et al. Dermoscopy of pigmented skin lesions: results of a consensus meeting via the internet. J Am Acad Dermatol. 2003;48:679–93.
10. Kittler H, Marghoob AA, Argenziano G, Carrera C, Curiel-Lewandrowski C, Hofmann-Wellenhof R, et al. Standardization of terminology in dermoscopy/dermatoscopy: results of the third consensus conference of the International Society of Dermoscopy. J Am Acad Dermatol. 2016;74:1093–106.
11. Lenoir C, Perez-Anker J, Diet G, Tognetti L, Cinotti E, Trépant AL, et al. Line-field confocal optical coherence tomography of benign dermal melanocytic proliferations: a case series. J Eur Acad Dermatol Venereol. 2021;35:e399–401.
12. Lallas A, Paschou E, Manoli SM, Papageorgiou C, Spyridis I, Liopyris K, et al. Dermatoscopy of melanoma according to type, anatomic site and stage. Ital J Dermatol Venerol. 2021;156:274–88.
13. Farnetani F, Scope A, Mazzoni L, Mandel VD, Manfredini M, Magi S, et al. A comparative dermoscopic and reflectance confocal microscopy study of naevi and melanoma with negative pigment network. J Eur Acad Dermatol Venereol. 2019;33:2273–82.
14. Marghoob AA, Braun RP, Malvehy J. Atlas of dermoscopy. 2nd ed. New York: Informa Healthcare; 2012.
15. Woltsche N, Schmid-Zalaudek K, Deinlein T, Rammel K, Hofmann-Wellenhof R, Zalaudek I. Abundance of the benign melanocytic universe: dermoscopic-histopathological correlation in nevi. J Dermatol. 2017;44:499–506.
16. Suppa M, Fontaine M, Dejonckheere G, Cinotti E, Yélamos O, Diet G, et al. Line-field confocal optical coherence tomography of basal cell carcinoma: a descriptive study. J Eur Acad Dermatol Venereol. 2021;35:1099–110.
17. Cinotti E, Tognetti L, Cartocci A, Lamberti A, Gherbassi S, Orte Cano C, et al. Line-field confocal optical coherence tomography for actinic keratosis and squamous cell carcinoma: a descriptive study. Clin Exp Dermatol. 2021;46:1530–41.
18. Blum A, Rassner G, Garbe C. Modified ABC-point list of dermoscopy: a simplified and highly accurate dermoscopic algorithm for the diagnosis of cutaneous melanocytic lesions. J Am Acad Dermatol. 2003;48:672–8.
19. Zalaudek I, Argenziano G, Soyer HP, Corona R, Sera F, Blum A, et al. Three-point checklist of dermoscopy: an open internet study. Br J Dermatol. 2006;154:431–7.

20. Unlu E, Akay BN, Erdem C. Comparison of dermatoscopic diagnostic algorithms based on calculation: the ABCD rule of dermatoscopy, the seven-point checklist, the three-point checklist and the CASH algorithm in dermatoscopic evaluation of melanocytic lesions. J Dermatol. 2014;41:598–603.
21. Massi D, De Giorgi V, Soyer HP. Histopathologic correlates of dermoscopic criteria. Dermatol Clin. 2001;19:259–68.
22. Russo T, Piccolo V, Ferrara G, Agozzino M, Alfano R, Longo C, et al. Dermoscopy pathology correlation in melanoma. J Dermatol. 2017;44:507–14.
23. Malvehy J. Handbook of dermoscopy. London: Informa Healthcare; 2006.
24. Zalaudek I, Argenziano G, Ferrara G, Soyer HP, Corona R, Sera F, et al. Clinically equivocal melanocytic skin lesions with features of regression: a dermoscopic-pathological study. Br J Dermatol. 2004;150:64–71.
25. Moro N, Mauch C, Zigrino P. Metalloproteinases in melanoma. Eur J Cell Biol. 2014;93:23–9.
26. Pizzichetta MA, Talamini R, Marghoob AA, Soyer HP, Argenziano G, Bono R, et al. Negative pigment network: an additional dermoscopic feature for the diagnosis of melanoma. J Am Acad Dermatol. 2013;68:552–9.

SUPPORTING INFORMATION

Additional supporting information can be found online in the Supporting Information section at the end of this article.

How to cite this article: Soglia S, Pérez-Anker J, Albero R, Alós L, Berot V, Castillo P, et al. Understanding the anatomy of dermoscopy of melanocytic skin tumours: Correlation in vivo with line-field optical coherence tomography. J Eur Acad Dermatol Venereol. 2023;00:1–11. https://doi.org/10.1111/jdv.19771

PUBLICACIÓN N°3:[67]

Criterios diagnósticos para lesiones melanocíticas en Tomografía de Coherencia Óptica Lineal.

Criteria for melanocytic lesions in LC-OCT.

Javiera Pérez-Anker, Simone Soglia, Clement Lenoir, Raquel Albero, Llucia Alos, Adriana García, Beatriz Alejo, Elisa Cinotti, Carmen Orte Cano, Cyril Habougit, Christian Dorado Cortes, Luca Pellegrino, Lida Tognetti, Paola Castillo, Pietro Rubegni, Mariano Suppa, Jean Luc Perrot, Veronique del Marmol, Susana Puig, J. and Josep Malvehy.

J Eur Acad Dermatol Venereol., 2023, Submitted revision January 28, 2024. Under review

Factor de impacto: 9.228

Resumen

Antecedentes: La tomografía de coherencia óptica lineal de campo de línea (TCO-CL) es una novedosa herramienta de diagnóstico que permite un alcance en la profundidad de la imagen de aproximadamente ~400 µm, y la obtención de un cubo tridimensional (3D) con resolución celular. Hasta donde sabemos, solo hay un número limitado de artículos que han informado criterios diagnósticos para lesiones melanocíticas utilizando esta técnica, y ninguno de ellos ha sido multicéntrico.

Objetivos: Nuestro objetivo fue establecer los criterios diagnósticos para lesiones melanocíticas utilizando TCO-CL e identificar las características arquitectónicas y citológicas más significativas asociadas con la malignidad.

Métodos: Se realizó una evaluación retrospectiva de 80 lesiones melanocíticas consecutivas de un conjunto de datos prospectivo y multicéntrico que abarcaba tres centros europeos. Se excluyeron las lesiones faciales, acrales y mucosas del estudio. Las imágenes dermoscópicas y de TCO-CL fueron evaluadas por consenso de cuatro observadores. Se empleó una regresión logística multivariante y se desarrolló un modelo de árbol de inteligencia artificial para determinar los criterios más relevantes para distinguir nevos benignos del melanoma. Se compararon los dos métodos en cuanto a su rendimiento.

Resultados: Los principales criterios diagnósticos para el melanoma incluyen: la detección de >10 células pagetoides en la adquisición 3D, arquitectura epidérmica irregular en 3D, desorden en la unión dermoepidérmica (UDE) y hendidura. Los factores de riesgo significativos basados en ambos análisis fueron: arquitectura epidérmica irregular en 3D, >10 células pagetoides, células dendríticas en la UDE sin inflamación subyacente. Nuevos criterios de malignidad encontrados únicamente en imágenes verticales: rotura de la UDE y hendidura alrededor de los nidos de melanocitos atípicos. Las características exclusivas del melanoma fueron: nidos epidérmicos, consumo epidérmico, nidos dérmicos densos con atipia celular. Las características protectoras en ausencia de indicadores de malignidad fueron: patrón de anillo UDE, patrón en empedrado, crestas alargadas, UDE bien definida y patrón en onda (en imagen vertical).

Conclusiones: Se han establecido una serie de criterios diagnósticos para la identificación de lesiones melanocíticas con TCO-CL. La validación de estos criterios en la práctica clínica a través de futuros estudios es esencial para establecer aún más su utilidad.

JEADV JOURNAL OF THE EUROPEAN ACADEMY OF DERMATOLOGY & VENEREOLOGY

Diagnostic criteria for melanocytic lesions in Linear Confocal Optical Coherence Tomography.

Journal:	*Journal of the European Academy of Dermatology and Venereology*
Manuscript ID	Draft
Manuscript Type:	Original Article

Note: The following files were submitted by the author for peer review, but cannot be converted to PDF. You must view these files (e.g. movies) online.

Video 1.mkv

-Title: Diagnostic criteria for melanocytic lesions in Linear Confocal Optical Coherence Tomography.

-Keywords: Line-field confocal optical coherence tomography, melanoma, melanocytic, OCT, LC-OCT, diagnostic criteria.

- Running head: LC-OCT Diagnostic criteria for melanocytic tumors

- Word count of body text: 2991

- Table count: 3

- Figure count: 5

- **Video count**: 1

- Supplementary material: 1 table and 1 figure.

- Authors: J. Perez-Anker,[1,2] S. Soglia,[2] C. Lenoir,[2] Albero R,[3] L. Alos,[3] A. García,[3] B. Alejo,[1] E. Cinotti,[4,5] C. Orte Cano,[6] C. Habougit,[7] Ch. Dorado Cortes,[7] L. Pellegrino,[2] L. Tognetti,[5] P. Castillo,[3] P. Rubegni,[4] M. Suppa,[5,6,8] J.L. Perrot,[5,7,9] V. del Marmol,[6] S. Puig,[1,2,10]* J. Malvehy[1,2,10]*

* Both senior authors equally contributed to this work.

- **Affiliations:**

1. Dermatology Department, Melanoma Unit, Hospital Clínic de Barcelona, IDIBAPS, Barcelona, Spain.

2. Universitat de Barcelona, Barcelona, Spain.

3. Pathology Department, Hospital Clínic de Barcelona, Universitat de Barcelona, Barcelona, Spain.

4. Dermatology Unit, Department of Medical, Surgical and Neurological Sciences, University of Siena, Siena, Italy.

5. Groupe d'Imagerie Cutanée Non Invasive (GICNI) of the Société Française de Dermatologie (SFD), Paris, France.

6. Department of Dermatology, Hôpital Erasme, Université Libre de Bruxelles, Brussels, Belgium.

7. Department of Dermatology, University Hospital of Saint-Etienne, Saint-Etienne, France.

8. Department of Dermatology, Institut Jules Bordet, Université Libre de Bruxelles, Brussels, Belgium.

9. Lab Hubert Curien UMR CNRS 5516

10. Centro de Investigación Biomédica en red de enfermedades raras, CIBERER, Instituto de Salud Carlos III, Barcelona, Spain.

-Corresponding author:

Javiera Pérez-Anker

Melanoma Unit, Dermatology Department, Hospital Clinic Barcelona

Villarroel 170, 08036, Barcelona, Spain.

javiperezanker@gmail.com

Tel.: +34 93 2275400 ext 2422

Fax: +34 93 2275438

ORCID:

Javiera Pérez-Anker	0000-0002-6959-7250
Susana Puig	0000-0003-1337-9745
Elisa Cinotti	0000-0002-4009-0659
Carmen Orte Cano	0000-0002-1570-7856
Linda Tognetti	0000-0002-6691-4310
Mariano Suppa	0000-0002-9266-0342
Josep Malvehy	0000-0002-6998-914X

-Funding statement: The reasearch at the Melanoma Unit in Hospital Clinic Barcelona is partially financed by Centro de Investigación Biomédica en Red de Enfermedades Raras (CIBERER), of the Instituto de Salud Carlos III, Spain, co-financed by European Development Regional Fund "A way to achieve Europe" ERDF; Spanish Fondo de Investigaciones Sanitarias grants PI15/00716, PI15/00956 and PI18/00419, of the Instituto de Salud Carlos III, Spain, co-financed by European Development Regional Fund "A way to achieve Europe" ERDF; AGAUR 2017_SGR_1134 of the Catalan Government, Spain; European Commission under the 6th Framework Programme, Contract No. LSHC-CT-2006-018702 (GenoMEL), by the European Commission under the 7th Framework Programme, Diagnoptics, and the European Commision under the HORIZON2020 Framework Programme, iTobos and Qualitop; The National Cancer Institute (NCI) of the US National Institute of Health (NIH) (CA83115); a grant from "Fundació La Marató de TV3" 201331-30, Catalonia, Spain; a grant from "Fundación Científica de la Asociación Española Contra el Cáncer" GCB15152978SOEN, Spain, and CERCA Programme / Generalitat de Catalunya. Part of the work was carried out at the Esther Koplowitz Center, Barcelona.

-**Disclosures**: The authors have no disclosures or conflicts of interest to report.

Bulleted statements

What is already known on this topic

- Line-Field Optical Coherence Tomography (LC-OCT) diagnostic criteria for skin cancer, as basal cell carcinoma (BCC), has been described.
- Other imaging techniques, such as *in vivo* reflectance confocal microscopy (RCM), have been shown to be capable of reducing the number of biopsies and enabling early diagnoses in malignant melanocytic lesions.
- The morphologic and cytologic features of LC-OCT correlated with RCM.

What does this study add

- Diagnostic criteria for melanocytic lesions have been described in LC-OCT.
- Their performance has been demonstrated.
- The presence of over 10 pagetoid cells within a 3D acquisition, irregularities observed in the 3D architecture of the epidermis, disruption of the dermo-epidermal junction (DEJ), and the presence of clefting were strongly associated to melanoma.

Ethic statements

This work follows the ethical principles of Helsinki.

ABSTRACT

Background: Line-field confocal optical coherence tomography (LC-OCT) is an emerging diagnostic tool with imaging depth reaching ~400 µm and a novel 3-dimensional (3D) cube providing cellular resolution. As far as we are aware, there are only a limited number of papers that have reported diagnostic criteria for melanocytic lesions using this technique, and none of them have been multicentric.

Objectives: Our aim was to establish the diagnostic criteria for melanocytic lesions using LC-OCT and identify the most significant architectural and cytologic features associated with malignancy.

Methods: A retrospective evaluation of 80 consecutive melanocytic lesions from a prospective multicentric dataset spanning three European centers was conducted. We excluded facial, acral, and mucosal lesions from the study. Dermoscopic and LC-OCT images were evaluated by a consensus of four observers. Multivariate logistic regression with backward elimination was employed, and an artificial intelligence tree model was developed to determine the most relevant criteria for distinguishing nevus from melanoma. The two methods were compared for their performance.

Results: The main melanoma diagnostic criteria include detecting >10 pagetoid cells in 3D acquisition, irregular 3D epidermal architecture, disrupted dermo-epidermal junction (DEJ), and clefting. Significant risk factors based on both analysis: irregular 3D epidermal architecture, >10 pagetoid cells, dendritic cells at DEJ without underlying inflammation. Novel malignancy criteria in vertical view: DEJ disruption and clefting around atypical melanocyte nests. Exclusive melanoma features: epidermal nests, epidermal consumption, dense dermal nests with atypia. Protective features in the absence of any malignancy indicators: DEJ ring pattern, cobblestone, elongated rete-ridges (vertical), well-defined DEJ, and wave pattern (vertical).

Conclusions: A series of diagnostic criteria for the identification of melanocytic lesions with LC-OCT have been established. Validation of these criteria in clinical practice through future studies is essential to further establish their utility.

INTRODUCTION

LC-OCT allows real-time in vivo tissue examination, with cellular resolution until ± 350 µm and deep penetration about ~ 450 µm. The main advantage arises in the vertical cell resolution view and its capability to create three-dimensional blocks of 1.2 mm x 0.5 mm x 0.5 mm, with 1.3 µm resolution. Dermoscopy picture is included beside the scanning tissue, allowing the possibility of determining the exact scanned area and a perfect morphologic correlation.

One of its most frequent applications has been in nonmelanoma skin cancer, increasing the sensitivity and specificity of diagnosing basal cell carcinoma (BCC) [1, 2] and squamous cell carcinoma (SCC).[3,4]

Recent studies had proved that the morphological and cytological features can be similar to gold-standard techniques (reflectance confocal microscopy (RCM) in horizontal view and conventional histopathology (HP) in vertical mode).[5] The same tumor was scanned with RCM and LC-OCT and posteriorly biopsied. The same area, at the same depth was compared in each technique. Morphological and cytological aspects described showed a good association of benign, atypical, and malignant features. Ringed pattern, junctional thickenings, and meshwork pattern were well identified and recognized. Dendritic, and atypical nucleated cells were also compared with an excellent correlation. Both images (RCM and LC-OCT) showed a cellular resolution of 1µm, with +/-5µm accuracy. There are few data about the diagnostic accuracy of LC-OCT for melanocytic lesions with diagnoses based on the experience of experts.[6]

However, to achieve a precise diagnosis distinguishing atypical nevi from melanomas, it is essential to establish diagnostic criteria in this technique, which was the primary objective of this study.

MATERIAL AND METHODS

Study lesions

A multicentric dataset from Erasme University Hospital (Belgium), Hospital Clinic Barcelona (Spain), and University Hospital in Saint Etienne (France) was assessed. Facial, acral, and mucosal lesions were excluded. Most lesions underwent excision with histopathological confirmation, except clear-cut dermoscopically benign nevi monitored for months without suspicious changes.

LC-OCT acquisitions

3D acquisitions (1.2 x 0.5 x 0.4 mm^3) were obtained from suspicious lesion areas using a CE-marked LC-OCT device (deepLive, DAMAE Medical, Paris, France). The procedure involved three experienced melanocytic lesion investigators (JPA, SS, CL) and one non-expert investigator (MS or LP) from different centers (Spain, Italy, France, Belgium). Precise scan areas were manually targeted and matched to dermoscopy images using the device's integrated macroscopic view, providing a 2.5 mm-diameter skin surface image.

Sample selection

Lesion selection followed these steps: (i) Lesions lacking 3D acquisitions or those with suboptimal image quality were excluded. (ii) Dermoscopy images were reviewed by a consensus of at least 3 experienced dermatologists (JPA, SS, CL), categorizing each lesion as "clear-cut benign," "equivocal," or "clear-cut melanoma." (iii) Adequate lesion coverage, ensuring representative areas for diagnosis, was determined by consensus among them. Lesions lacking representative dermoscopic scans were excluded. The study included 124 lesions, which were then randomized, and IDs were sorted to mix database locations. Subsequently, 44 lesions were intentionally and randomly excluded to maintain a final selection of 80 lesions, ensuring a balanced distribution between clear-cut and equivocal dermoscopic cases. A total of 178 3D acquisitions were assessed.

LC-OCT criteria evaluation

Criteria selection was based on significant features from previous RCM studies[7,8] and specific LC-OCT criteria, drawn from author observations. Each criterion is detailed in **Table 1 and video 1**. Architectural and cytologic aspects were assessed in a sequence mirroring conventional histopathological examination by dermatopathologists.

Criteria were examined in every skin layer (Stratum corneum, epidermis, dermo-epidermal junction (DEJ), and dermis) on 3D acquisitions to offer a comprehensive skin representation with enhanced contrast on LC-OCT images. Depending on the criterion, it was appraised using the horizontal, vertical, or both 3D acquisition perspectives. Evaluation involved consensus among at least 4 reviewers (JM, SP, JPA, MS, SS, CL, with JPA, SS, CL, LP on the 2nd day).

Statistical analysis

Analysis gathered all acquisitions of the same lesion, assessing criteria presence per lesion. If a criterion was observed in at least one 3D acquisition of a lesion, it was deemed present.

R software (R Foundation for Statistical Computing, Vienna, Austria) was used for statistical analysis. Frequencies of nevi, melanomas, typical/atypical nevi, in situ/invasive melanomas, clear-cut/doubtful benign/melanoma cases were calculated independently for each criterion. Differences between melanoma and nevi were assessed using Pearson's Chi-squared test (Fisher's exact test for criteria with <5 lesions per category). Odd ratios (OR) with 95% confidence intervals were calculated between nevi and melanomas using maximum likelihood approximation.

A backward elimination approach was employed for multivariate logistic regression, where non-significant predictors were progressively removed until all remaining predictors were significant. All tests were two-tailed, with significance set at *: $p<0.05$, **: $p<0,01$ and ***: $p<0.001$.

An IA decision tree model consisting of three stages was constructed, incorporating all study criteria, whether significant or not. This model employed Gini coefficients to identify the optimal

attribute/criterion for segregating data between nevi and melanoma at each node. To ensure the model's generalizability, a 5-fold cross-validation was performed.

RESULTS

Dataset description

A total of 178 3D acquisitions were reviewed from 80 melanocytic lesions belonging to the multicentric dataset of consecutive melanocytic lesions from the 3 reference European hospitals (51% of Hospital Clinic Barcelona, 34% Erasme Hospital (Brussels, Belgium) and 15% University of Saint-Etienne (France)).

Data summary: 41/80 (51.2%) lesions in females, with 33.7% on the back and 17.6% on the chest/abdomen. Dermoscopy findings: 42 lesions (52.2%) deemed "equivocal." Histological diagnoses: 27 (33.7%) typical nevi, 19 (23.8%) atypical, 14 (17.5%) melanomas in situ, and 20 (25.0%) invasive melanomas. Typical nevi: 16/80 (20%) long term monitored without excision, 11/80 (14%) excised as typical nevi**. Supplementary Table 1.**

Histopathological features and their association with nevi and melanoma were compared.

Architectural criteria

All the descriptive criteria are summarized in **Table 1** and represented in **Figs.1-4**. All the descriptive statistics are shown in **Table 2**.

Epidermis - Horizontal Criteria (Figs.1-3):

'Irregular honeycomb pattern' showed a strong association with melanoma: Seen in 3 nevi cases (6.5%) and 19 melanoma cases (55.9%). OR for melanoma vs. nevi: 17.4 (95% CI: 4.28–105, $p < 0.001$). Cobblestone was linked to benign lesions: Found in 26 nevi cases (56.5%) and 11 melanoma

cases (32.4%), OR 0.37 (95% CI: 0.13–1.02, p = 0.06). DEJ ring pattern linked to benign: Observed in 24 nevi cases (52.2%) and 8 melanoma cases (23.5%), OR 0.29 (95% CI: 0.09–0.82, p = 0.02).

Epidermis - 3D Architecture (Figs.1-3):

Epidermal nests (mainly in vertical and 3D views) were strongly associated with malignancy, absent in nevi (0%) but present in 7 melanoma cases (20.6%, p = 0.002). Small nests of pagetoid cells (best in horizontal view, confirmed vertically) not observed in nevi (0%) but in 5 melanoma cases (14.7%, p = 0.01). Larger nests also not evidenced in nevi (0%) but in 5 melanoma cases (14.7%, p = 0.01). Similarly, clefting around nests (mainly in vertical and 3D views) absent in nevi (0%) but in 5 melanoma cases (14.7%, p = 0.01), and epidermal consumption: absent in nevi (0%) but in 7 melanoma cases (20.6%, p = 0.002), significantly associated with melanoma. The opposite, the acanthosis of the epidermis, was also associated with malignancy, found in 2 cases (4.3%) of nevi and 11 cases (32.4%) of melanoma (OR 10.2, 95% CI (1.99 to 103), *p-value* = 0.001.

Dermo-epidermal Junction (Figs.1-3):

DEJ disruption (seen mainly in vertical and 3D views) in 17 nevi cases (37.0%) and 30 melanoma cases (88.2%, OR 12.4, 95% CI 3.52–56.6, p < 0.001). Irregular rete ridge and papillae distribution (mainly in vertical and 3D views) in the superior part, near DEJ: 18 nevi cases (40.0%) and 25 melanoma cases (83.3%, OR 7.29, 95% CI 2.20–29.0, p = 0.005). Similar irregular distribution near the reticular dermis: 23 nevi cases (51.1%) and 27 melanoma cases (90.0%, OR 8.37, 95% CI 2.12–49.3, p = 0.01), highly linked to melanoma.

Conversely, regular elongated rete ridges (mainly in vertical and 3D views): 40 nevi cases (87.0%) and 22 melanoma cases (64.7%, OR 0.28, 95% CI 0.08–0.94, p = 0.04), associated with benign lesions.

Dermis (Figs.1-3):

Dermal nests: Nevi 10 cases (21.7%), melanoma 18 cases (52.9%, OR 3.97, 95% CI 1.39–12.1, p = 0.008). Sparse dermal nests: Nevi 3 cases (6.5%), melanoma 14 cases (41.2%, OR 7.45, 95% CI 1.10–68.2, p = 0.02). Irregular dermal nest shape: Nevi 2 cases (4.3%), melanoma 13 cases (38.2%, OR 9.42, 95% CI 1.28–122, p = 0.02), significantly linked to melanoma. Dermal clefting (mainly in vertical and 3D views): Nevi 3 cases (6.5%), melanoma 13 cases (38.2%, OR 8.62, 95% CI 2.07–52.2, p < 0.001), strongly associated with melanoma. Wave pattern (mainly in vertical and 3D views): Nevi 15 cases (32.6%), melanoma 3 cases (8.8%, OR 0.20, 95% CI 0.03–0.82, p = 0.01), linked to benign lesions.

Cytological criteria associated with melanoma: **(Figs.1,3)**

Epidermis: Pagetoid and atypical cells (roundish and/or dendritic).

Pagetoid cells: nevi 14 cases (30.4%) and melanoma 33 cases (97.1%, OR 71.0, 95% CI 9.95–3101, p < 0.001). When located at stratum granulosum, were observed in nevi 7 (15.2%) and melanoma 25 cases (73.5%), OR 14.8, 95% CI 4.56–54.9, p < 0.001). Roundish pagetoid cells: (nevi 12 cases (26.1%) and melanoma 30 cases (88.2%), OR 20.2, 95% CI 5.58–95.8, p < 0.001). Dendritic pagetoid cells (nevi 14 cases (30.4%) and melanoma 33 cases (97.1%), OR 71.0, 95% CI 9.95–3101, p < 0.001).

Moreover, more than 10 cells: nevi 6 cases (13.0%), melanoma 30 cases (88.2%, OR 45.9, 95% CI 11.3–247, p < 0.001). Roundish pagetoid cells (more than 10): nevi 5 cases (10.9%), melanoma 24 cases (70.6%, OR 18.7, 95% CI 5.36–79.3, p < 0.001).

Marked atypia: nevi 4 cases (8.7%), melanoma 21 cases (61.8%, OR 6.2, 95% CI 4.4–77.0, p < 0.001). Diffused atypia: nevi 8 cases (17.4%), melanoma 28 cases (82.4%, OR 21.0, 95% CI 6.13–85.1, p < 0.001).

Dermo-epidermal Junction:

DEJ cellular atypia: Nevi 17 cases (37.0%), melanoma 31 cases (91.2%, OR 15.5, 95% CI 3.96–90.7, $p < 0.001$). Atypical roundish cells: Nevi 13 cases (28.3%), melanoma 29 cases (85.3%, OR 14.1, 95% CI 4.23–57.4, $p < 0.001$). Dendritic cells: Nevi 14 cases (30.4%), melanoma 31 cases (91.2%, OR 21.8, 95% CI 5.48–130, $p < 0.001$), all significantly associated with melanoma. Bridging nest with atypia in 3D: Nevi 3 cases (6.7%), melanoma 12 cases (41.4%, OR 9.54, 95% CI 2.21–59.3, $p < 0.001$). Bridging nest with atypical roundish cells in 3D: Nevi 3 cases (6.7%), melanoma 12 cases (41.4%, OR 9.54, 95% CI 2.21–59.3, $p < 0.001$). Bridging nest with dendritic atypia in 3D: Nevi 1 case (2.2%), melanoma 9 cases (31.0%, OR 19.0, 95% CI 2.37–883, $p < 0.001$).

Dermis:

Atypia in dense dermal nests (brighter cells, larger and irregular nucleus): Absent in nevi (0.0%), present in 11 melanoma cases (61.1%, $p = 0.002$). Atypia in papillae/upper dermis: Nevi 3 cases (6.7%), melanoma 13 cases (38.2%, OR 8.62, 95% CI 2.07–52.24, $p < 0.001$). Atypical roundish cells in papillae/upper dermis: Nevi 1 case (2.2%), melanoma 13 cases (38.2%, OR 26.78, 95% CI 3.60–1201, $p < 0.001$). Dendritic cells in papillae/upper dermis: Nevi 2 cases (4.3%), melanoma 11 cases (32.4%, OR 10.2, 95% CI 1.99–103, $p = 0.001$).

Multivariate logistic regression

Multivariate regression, considering two key criteria strongly associated with malignancy (more than 10 pagetoid cells, and irregular 3D epidermis architecture, **Table 3**), revealed that applying these criteria to the entire database, only two melanomas were missed. One (a melanoma in situ) was due to a review error, where images contained atypical cells unnoticed by reviewers. The other was due to an error in selecting the diagnostic area, not scanned in the database selection process. Among nevi meeting at least one criterion, 8/11 (72.7%) were atypical nevi, 1/11 (9.1%) spitzoid junctional nevus, and 2/11 (18.2%) were traumatized.

IA Decision tree

AI decision tree assessed malignancy prediction (**Supplementary Fig.1**). The first key criterion was >10 pagetoid cells in the epidermis, found in 30 melanoma and 6 nevi (vs. 4 melanoma and 40 nevi without). When >10 pagetoid cells were present in a 3D acquisition, it sufficed to consider a lesion suspicious, as subsequent criteria didn't distinctly separate melanoma from nevi.

For cases with <10 pagetoid cells in 3D, the presence of dendritic cells at the dermo-epidermal junction became the second most differentiating criterion. All melanomas (4/4) and 8 nevi exhibited atypical dendritic cells, compared to 32 nevi. However, further inspection revealed that 6 of these nevi, unlike melanoma, showed underlying dermal inflammation, raising questions about whether the dendritic cells indicated epidermal inflammation.

A 5-fold cross-validation assessed model generalization and melanoma prediction on a larger dataset. It trained on 80% of the data and tested on the remaining 20%, yielding a mean AUC of 0.84 (STD=0.10) and an out-of-fold AUC of 0.84, indicating good discriminative ability.

Summary and main diagnostic criteria (**Fig.1-4, supplementary figure 1, video 1)**

- Statistical analysis identifies two primary malignancy criteria: abundant pagetoid cells and irregular epidermal architecture.
- Other easily assessable vertical view criteria strongly linked to melanoma include disrupted DEJ and clefting.
- Statistically significant criteria exclusive to melanoma: epidermal melanocyte nests without dermal connection and epidermal consumption.
- Statistically significant factors (similar to RCM): ring-pattern, cobblestone pattern; LC-OCT adds vertical view for outlined DEJ, rete-ridge visualization, and wave pattern.
- Notion of protective criteria to be specified: they must be seen everywhere + absence of malignant criteria.

DISCUSSION

Our results highlight key architectural and cytologic criteria distinguishing nevi from melanoma, encompassing patterns and structures in the epidermis, dermo-epidermal junction, and dermis in 3D.

Prior studies on LC-OCT criteria for melanocytic lesion malignancy, such as the study conducted by Schuh and colleagues,[9] have identified similar malignant and protective criteria. However, we have identified new criteria that were not previously considered. One key methodological difference that enhances the reliability of our results is our approach to ensure complete lesion coverage before evaluation, ensuring the capture of all relevant features in each individual lesion. Furthermore, we have included a more comprehensive list of criteria, including those derived from H&E analysis. Additionally, we excluded facial and mucosal lesions, which exhibit very specific diagnostic criteria and should be studied separately.

In contrast, LC-OCT findings align with established trends in cytological and architectural features, consistent with previous RCM studies.[10-14] These features demonstrated comparable diagnostic significance. Irregular honeycomb patterns favored malignancy (OR 0.37 in LC-OCT vs. 0.30 in RCM),[9-13] while regular honeycomb and cobblestone patterns indicated benign conditions. In the epidermis, characteristics such as epidermal disorganization, extension to the stratum corneum, roundish and dendritic pagetoid cells, and the presence of more than 3 (or more than 10 in LC-OCT) pagetoid cells favored malignancy.

At the dermoepidermal junction (DEJ), significant indicators included edged or non-edged papillae, cellular atypia, and junctional nests. However, criteria in the superficial dermis, such as the presence of dense nests (sparse and cerebriform), atypical cells within the papillae, inflammatory cells, macrophages, and collagen, lacked significant diagnostic value.

Including 10 pagetoid cells in LC-OCT was based on practical considerations. Given RCM's 5µm resolution, approximately 3 cells could be identified within a 25µm thickness, equivalent to around 5 cells across the entire epidermis. Considering LC-OCT's larger field of view, approximately 10 cells

per 3D image were estimated. In addition, the 5-fold validation resulted in a mean AUC of 0.84 (STD=0.10) with an out-of-fold AUC of 0.84. When compared to Pellacani et al.'s approach, they achieved an AUC of 0.827 (95% CI 0.765–0.890).[15]

LC-OCT revealed novel significant parameters, enabled by its vertical and 3D imaging capabilities: epidermal consumption, clefting, nests in the epidermis (with confirmation of no connection with the dermis), and disrupted dermo-epidermal junction, exhibiting strong statistical associations with malignant melanocytic lesions. Furthermore, the wave pattern previously described in dermal nevi[16] is indicative of benignancy.

Additionally, the vertical view facilitated distinguishing between inflammation around the DEJ and a genuine disruption of this feature. The vertical view offered improved comprehension of architectural changes across all epidermal layers, aligning with both morphological and cytological aspects akin to conventional histology, which has already proved to be a valuable asset in evaluating physiological and pathological skin.[17-22] **Fig. 4**.

The results suggest that LC-OCT can complement RCM by providing additional information, leveraging the differences in imaging technologies and the availability of the vertical view in LC-OCT. While our approach offers numerous benefits, it may have a limitation in potentially missing Vivablocks, leading to a less comprehensive lesion representation and potential diagnostic inaccuracies. To mitigate this, our study recommends implementing a diagnostic algorithm during the scanning process, as illustrated in **Fig. 5**.

The initial step involves capturing a dermoscopic image, which serves as the foundation for representing all areas targeted for 3D scanning. The primary goal is to encompass the entire lesion through a vertical view. By identifying malignancy-related features in this perspective, we can pinpoint the most representative areas requiring 3D scanning for thorough evaluation. Dermoscopy is a globally recognized tool in dermatology, and our prior research has established the correlation

between dermoscopy and LC-OCT for melanocytic lesions.[23] By leveraging dermoscopy, we can easily identify areas necessitating detailed LC-OCT examination.

Subsequently, the examination of the scanned regions in the dermoscopic image offers critical insights to ensure that no significant diagnostic area has been inadvertently overlooked or omitted during the scanning procedure.

Our study confirms the efficacy of this proposed workflow, which was exclusively applied to our dataset. We consistently detected malignant criteria in melanomas, with only one case revealing overlooked malignant features in hindsight. This validates our approach's distinctiveness and effectiveness compared to both RCM and histopathology.

In conclusion, the results suggest that LC-OCT shows promise in identifying specific architectural and cytologic criteria that are associated with melanoma. The availability of the 3D vertical view in LC-OCT allows for the detection of new significant parameters that may aid in improving the diagnostic accuracy of melanoma compared to other imaging modalities such as RCM. Nonetheless, further research and validation studies are needed to establish the clinical utility and reliability of these LC-OCT parameters in melanoma diagnosis and management.

ACKNOWLEDGEMENTS:

The authors are indebted to Maxime Cazalas and Clothilde Raoux (DAMAE Medical, Paris, France) for the technical assistance with various subjects related to the LC-OCT device. Their support has been invaluable in ensuring a comprehensive understanding of the device and its functionalities. Additionally, we extend our gratitude to Sébastien Fischman for constructing the AI tree.

We want to thank the members of the Dermatology Investigation Unit, specially Pablo Iglesias and Beatriz Alejo, for helping collect patient data and Dermatopathology Department of the Hospital Clinic Barcelona, for providing support to this project. We also want to thank all the patients and their families who are the main reason for our studies. We also thank Paul Hetherington for his help with the text editing.

The Non-Invasive Skin Imaging Research Program of Hôpital Erasme, Université Libre de Bruxelles (Brussels, Belgium), would like to acknowledge the support of the Fonds Erasme (www.fondserasme.org).

REFERENCES

1. Barut A, Dubois A, Davis A, et al. Line-field confocal time-domain optical coherence tomography with dynamic focusing. *Opt Express.* 2018; **26**:33534–42.

2. Dubois A, Levecq O, Azimani H, et al. Line-field confocal optical coherence tomography for high-resolution noninvasive imaging of skin tumors. *J Biomed Opt.* 2018; **23**:1.

3. Dubois A, Davis A, Siret D, et al. Simultaneous dual-band line-field confocal optical coherence tomography: application to skin imaging. *Biomed Opt Express.* 2019; **10**:694–706.

4. Lenoir C, Diet G, Cinotti E, et al. Line-field confocal optical coherence tomography of sebaceous hyperplasia: a case series. *J Eur Acad Dermatol Venereol.* 2021; **35**.

5. Lenoir C, Cinotti E, Tognetti L, Orte Cano C, Diet G, Miyamoto M, Rocq L, Trépant AL, Perez-Anker J, Puig S, Malvehy J, Rubegni P, Perrot JL, Del Marmol V, Suppa M. Line-field confocal optical coherence tomography of actinic keratosis: a case series. J Eur Acad Dermatol Venereol. 2021 Jul 26. doi: 10.1111/jdv.17548. Epub ahead of print.

6. Cinotti, E., Brunetti, T., Cartocci, A., Tognetti, L., Suppa, M., Malvehy, J., Perez-Anker, J., Puig, S., Perrot, J. L., & Rubegni, P. (2023). Diagnostic Accuracy of Line-Field Confocal Optical Coherence Tomography for the Diagnosis of Skin Carcinomas. Diagnostics (Basel, Switzerland), 13(3), 361. https://doi.org/10.3390/diagnostics13030361

7. Tognetti L, Carraro A, Cinotti E, Suppa M, Del Marmol V, Perrot JL, Rubegni. P. Line-field confocal optical coherence tomography for non-invasive diagnosis of lichenoid dermatoses of the childhood: A case series. Skin Res Technol. 2021 Jul 6. doi: 10.1111/srt.13075. Epub ahead of print.

8. Cinotti E, Tognetti L, Cartocci A, Lamberti A, Gherbassi S, Orte Cano C, Lenoir C, Dejonckheere G, Diet G, Fontaine M, Miyamoto M, Perez-Anker J, Solmi V, Malvehy J, Del Marmol V, Perrot JL, Rubegni P, Suppa M. Line-field confocal optical coherence tomography for actinic

keratosis and squamous cell carcinoma: a descriptive study. Clin Exp Dermatol. 2021 Jun 11. doi: 10.1111/ced.14801. Epub ahead of print.

9 Tognetti L, Cinotti E, Suppa M, Guazzo R, Habougit C, Santi F, Diet G, Fontaine M, Berot V, Monnier J, Pianigiani E, Del Marmol V, Malvehy J, Perrot JL, Rubegni P. Line field confocal optical coherence tomography: An adjunctive tool in the diagnosis of autoimmune bullous diseases. J Biophotonics. 2021May;14(5):e202000449. doi: 10.1002/jbio.202000449. Epub 2021 Feb 22.

10. Suppa M, Fontaine M, Dejonckheere G, Cinotti E, Yélamos O, Diet G, Tognetti L, Miyamoto M, Orte Cano C, Perez-Anker J, Panagiotou V, Trepant AL, Monnier J, Berot V, Puig S, Rubegni P, Malvehy J, Perrot JL, Del Marmol V. Line-field confocal optical coherence tomography of basal cell carcinoma: a descriptive study. J Eur Acad Dermatol Venereol. 2021 May;35(5):1099-1110. doi: 10.1111/jdv.17078. Epub 2020 Dec 29.

11. Monnier J, Tognetti L, Miyamoto M, Suppa M, Cinotti E, Fontaine M, Perez J, Orte Cano C, Yélamos O, Puig S, Dubois A, Rubegni P, Del Marmol V, Malvehy J, Perrot JL. In vivo characterization of healthy human skin with a novel, non-invasive imaging technique: line-field confocal optical coherence tomography. J Eur Acad Dermatol Venereol. 2020 Dec;34(12):2914-2921. doi: 10.1111/jdv.16857.Epub 2020 Aug 27.

12 Pellacani G, Cesinaro AM, Seidenari S. Reflectance-mode confocal microscopy of pigmented skin lesions--improvement in melanoma diagnostic specificity. J Am Acad Dermatol. 2005 Dec;53(6):979-85. doi: 10.1016/j.jaad.2005.08.022. Epub 2005 Oct 19. PMID: 16310058.

13. Tognetti L, Rizzo A, Fiorani D, Cinotti E, Perrot JL, Rubegni P. New findings in non-invasive imaging of aquagenic keratoderma: Line-field optical coherence tomography, dermoscopy and reflectance confocal microscopy. Skin Res Technol. 2020 Nov;26(6):956-959. doi: 10.1111/srt.12882. Epub 2020 Aug 9.

14. Tognetti L, Ekinde S, Habougit C, Cinotti E, Rubegni P, Perrot JL. Delayed Tattoo Reaction From Red Dye With Overlapping Clinicopathological Features: Examination With High-Frequency Ultrasound and Line-Field Optical Coherence Tomography. Dermatol Pract Concept. 2020 Jun 29;10(3):e2020053.

15. Pellacani G, Guitera P, Longo C, et al. The Impact of In Vivo Reflectance Confocal Microscopy for the Diagnostic Accuracy of Melanoma and Equivocal Melanocytic Lesions. *J Invest Dermatol.* 2007; **127**:2759–65.

16. Lenoir C, Perez-Anker J, Diet G, et al. Line-field confocal optical coherence tomography of benign dermal melanocytic proliferations: a case series. *J Eur Acad Dermatol Venereol.* 2021; **35**:399–401.

17. Levine A, Wang K, Markowitz O. Optical Coherence Tomography in the Diagnosis of Skin Cancer. *Dermatol Clin.* 2017; **35**:465–88.

18. Monnier J, Tognetti L, Miyamoto M, et al. In vivo characterization of healthy human skin with a novel, non-invasive imaging technique: line-field confocal optical coherence tomography. *J Eur Acad Dermatol Venereol.* 2020; **34**:2914–21.

19. Pedrazzani M, Breugnot J, Rouaud-Tinguely P, et al. Comparison of line-field confocal optical coherence tomography images with histological sections: Validation of a new method for in vivo and non-invasive quantification of superficial dermis thickness. *Skin Res Technol.* 2020; **26**:398–404.

20. Lacarrubba F, Verzì AE, Puglisi DF, et al. Line-field confocal optical coherence tomography of xanthogranuloma: Correlation with vertical and horizontal histopathology. *J Cutan Pathol.* 2021; 1–4.

21. Ruini C, Schuh S, Sattler E, Welzel J. Line-field confocal optical coherence tomography-Practical applications in dermatology and comparison with established imaging methods. *Skin Res Technol.* 2021; **27**:340–52.

22. Pellacani G, Vinceti M, Bassoli S, et al. Reflectance confocal microscopy and features of melanocytic lesions: An internet-based study of the reproducibility of terminology. *Arch Dermatol.* 2009; **145**:1137–43.

23. Soglia S, Pérez-Anker J, Albero R, et. al. Understanding anatomy of dermoscopy of melanocytic skin tumors: correlation in vivo with line-field optical coherence tomography. . *J Eur Acad Dermatol Venereol.* 2023; accepted for publication November 21, 2023.

FIGURE LEGENDS

Figure. 1. Main diagnostic criteria. Left column: malignant criteria. Right column: benign criteria. Blue square: criteria detail. (a) The presence of nucleated cells (roundish or dendritic), with dark nuclei and bright cytoplasm (red arrow) is associated to malignancy in the context of absence of inflammation. (b) Cobblestone pattern, associated to benignancy, corresponds to monomorphous, small (6 µm diameter) pigmented keratinocytes (blue circle). (c) Irregularities in the epidermis (size and shape of cells) are observed in the yellow circle. (d) Epidermic cells of homogeneous size and shape are observed in green circle. (e) The disruption of the DEJ (white triangle), in the absence of inflammation, is strongly associated to malignancy. The opposite is observed in a well-defined DEJ (blue triangle) (f). Clefting, a dark space in between the bright nucleated discohesive melanocytes (yellow arrow) is associated to malignancy. The opposite occurs with the presence of "wave pattern" (h) (green arrow), that corresponds to collagen fibers around nonpigmented nests of melanocytes.

Figure 2. Compound nevus on the right posterior thigh of a 43-years-old woman. (a) Clinical and **(b)** dermoscopic images with the LC-OCT field of view represented as a blue rectangle and the integrated dermoscopic camera of DeepLive→ LC-OCT on the lower left corner. **(c)** Histological image, **(d, e, f)** horizontal LC-OCT views of the 3D acquisitions at a depth of **(d)** 24 µm, **(e)** 34 µm and **(f)** 57 µm showing a regular honeycomb pattern, cobblestone pattern (*orange dashed circle*) and ring-pattern (*green arrows*). **(g, h)** vertical and **(i)** 3D LC-OCT views of the same acquisitions at different positions showing the pigmentation confined at the dermo epidermal junction outlining the DEJ (*green arrows*), some junctional nests at the tip of the rete ridges (*blue stars*) and their fusion creating bridging (*blue arrows*) and isolated melanocytes in the dermis (*orange arrows*).

Figure 3. Melanoma in situ on the right volar forearm of a 60 years-old woman

(a) Clinical and **(b)** dermoscopic images with the LC-OCT field of view represented as a blue rectangle and the integrated dermoscopic camera of DeepLive→ LC-OCT on the lower left corner. **(c)** Histological image, **(d, e, f)** horizontal LC-OCT views of the 3D acquisitions at a depth of **(d)** 22 µm, **(e)** 34 µm and **(f)** 72 µm showing the presence of multiple pagetoid dendritic melanocytes (*red arrows*) and an irregular honeycomb pattern with different sizes and shapes of the nuclei inside the epidermis (*yellow dashed circle*) and an irregular distribution of the papillae. **(g, h, i)** vertical and **(i)** 3D LC-OCT views of the same acquisitions at different positions showing the presence of pagetoid melanocytes (*red arrows*), a disrupted DEJ (*orange stars*) and numerous and dense junctional nests with fusion (*blue arrows*).

Figure 4. Disrupted DEJ vs inflammation.

A comprehensive understanding of this fundamental criterion is crucial. (a) The DEJ is borrowed (indicated by the orange asterisk) and cannot be visualized. (b) The presence of inflammatory cells and stromal reaction, a result of inflammation, contributes to the distinctive image observed in the vertical view (green asterisk), and is pivotal for distinguishing between malignant and benign lesions.

Figure 5. LC-OCT acquisition workflow for melanocytic lesions. 1. Find the most important dermoscopy image. 2. Cover all the lesion with the vertical video. 3. Do a 3D acquisition in the most atypical areas according to dermoscopy and video findings.

Table 1. Description of the evaluated criteria

Table 2. Descriptive statistics

Table 3. Multivariate logistic regression for the differentiation between melanoma and nevi

SUPPLEMENTARY MATERIAL

Video 1. Benign and malignant melanocytic diagnostic criteria

For a more comprehensive review, the benign and malignant described in this study have been illustrated in this video.

Figure S1. IA Decision tree

The identification of over ten pagetoid cells, coupled with the presence of dendritic cells at the DEJ in the absence of inflammation, is indicative of melanoma. Conversely, the presence of inflammation and the absence of pagetoid cells are characteristic of benign conditions, even if atypical cells at the DEJ are visualized in the epidermis.

Supplementary Table 1. Dataset information

Table 1. Description of the evaluated criteria

	Criteria	Description
	ARCHITECTURE CRITERIA	
Stratum corneum	Parakeratosis	Presence of white disk regularly spaced of ~ 12µm diameter (almost flat) within the stratum corneum
	Erosion/disruption of the stratum corneum	Loss of continuity of the stratum corneum
	Hyperkeratosis	Thickness of the stratum corneum bigger than 20 µm
	Pigment ascension into the SC	Cluster of bright nucleated cells in the stratum corneum
Epidermis – Horizontal pattern	Irregular honeycomb pattern	Irregularity in size and shape of cells nuclei (round dark structure of ~ 10µm) in the epidermis.
	Cobblestone pattern	Structure consisting of adjacent small bright disks (~ 6µm diameter) separated by a dark border
	DEJ ring pattern	Delineated ring composed of bright small disks (~ 6µm diameter) aligned around the papillae.
	DEJ meshwork pattern	Enlarged interpapillary spaces predominantly constituted by junctional thickenings. (definition from Navarrete-Dechent et al., (2021), https://doi.org/10.1016/j.jaad.2020.05.097)
	Cerebriform structures	Confluent amorphous aggregates of low reflecting cells which exhibit granular cytoplasm without evident nuclei and ill-defined borders. The aggregates have brain-like with fine hyporeflective ''fissures'' appearance.
Epidermis – 3D Architecture	Irregular 3D epidermis architecture	Irregular honeycomb in horizontal view and anormal maturation of KN in vertical view: irregular arrangement in layers without larger/flattened nuclei on the top layers.
	Nest of pagetoid melanocytes	Aggregates of bright nucleated cells in the epidermis with no connection with the dermis
	Small nest of pagetoid melanocytes	Aggregates of 5 or less bright nucleated cells (the longer axis is less than 50µm)
	Big nest of pagetoid melanocytes	Aggregates of more than 5 bright nucleated cells (the longer axis is more than 50µm)
	Epidermal clefting	Clear dark space around nest of pagetoid melanocytes with no connection with the dermis
	Consumption of the epidermis	Thinning of the epidermis with attenuation of basal and suprabasal layers and loss of rete ridges adjacent to collections of melanocytes (definition from Walters et al., Am. J. Clin. Dermatol (2007) doi: 10.1097/DAD.0b013e318156e0a7).
	Atrophic epidermis	Thickness of the epidermis (SC excluded) < 30µm
	Acanthosis	Thickness of the epidermis (SC excluded) > 100µm
Dermo-epidermal junction	Disrupted DEJ	Dermo-epidermal junction not clearly identifiable in the vertical images (0,5 x 1,2mm) on at least one area of the 3D acquisition
	Visualisation of the elongated rete-ridge	Visualization of the rete ridges with a regular distribution and a length higher than epidermis thickness.
	Bridging nest	Fusion of some junctional nest at the tip of the rete ridges which creates bridging.
	Irregular distribution of rete ridges/papillae: top	Irregularity in size, distribution, and shape of the rete ridges and the papillae in the horizontal images at the top of the papillae.
	Irregular distribution of rete ridges/papillae: bottom	Irregularity in size, distribution, and shape of the rete ridges and the papillae in the horizontal images at the bottom of the rete ridge.

Dermis	Dermal nests	Aggregates of bright nucleated cells inside the dermal papillae or below.
	Dense dermal nests	Compact aggregates of melanocytes with sharp margin in the dermis.
	Sparse dermal nests	Sparse aggregates of melanocytes in the dermis.
	Irregular shape of the dermal nests	Irregular shape (no spherical or no well-delimited boundaries) of the aggregate of melanocytes in the dermis.
	Bright regular cells in the nests	Bright monomorphous nucleated cells inside the nest
	Clefting	Clear dark space in between the bright nucleated cells and surrounding epidermis or stroma. Nest of bright nucleated cells can become discohesive from its surrounding structures.
	Melanophages	Bright plump cells, with a diameter of ~15 µm, in the dermis without a visible nucleus.
	Inflammation	Local hypo-reflective area with presence of small bright structures (around 5µm) with no visible nucleus in the superficial dermis with underlying brighter dermis
	Fibrosis	Coarse and bright collagen fibers in the superficial dermis.
	Wave pattern	Presence in the papillary and reticular dermis of alternating undulated hyper-reflective and hypo-reflective lines corresponding to melanocytic strands/cords/nests in the dermis.
CYTOLOGIC CRITERIA		
Epidermis	Pagetoid cells at stratum granulosum	Presence of nucleated (roundish or dendritic) cells, with dark nuclei and bright cytoplasms, in the stratum granulosum.
	Roundish pagetoid cells	Presence of bright roundish nucleated cells within suprabasal layers.
	Number of roundish pagetoid cells >10	Number of bright roundish nucleated cells within suprabasal layers over 10 in the whole 3D acquisition
	Dendritic pagetoid cells	Presence of bright nucleated cells, with dendritic-like branches, within suprabasal layers.
	Number of dendritic pagetoid cells >10	Number of bright nucleated cells, with dendritic-like branches, within suprabasal layers over 10 in the whole 3D acquisition
	Marked cell atypia	Presence of cells with a diameter >40µm, nuclei >20µm or/and significantly different in size/shape from all its neighbors.
	Focused cell atypia	Presence of atypical cells concentrated only on a small portion of the area of the horizontal plane (0,5 x 1,2mm).
	Diffused cell atypia	Presence of nucleated cells (roundish or dendritic) dispersed on the whole area of the horizontal plane (0,5 x 1,2mm).
Dermo-epidermal junction	Atypical roundish cells at the DEJ	Presence of atypical roundish nucleated cells at the dermo-epidermal junction.
	Dendritic cells at the DEJ	Presence of atypical dendritic nucleated cells at the dermo-epidermal junction.
	Roundish cell atypia in bridging nests	Presence of atypical roundish nucleated cells in a nest, connected to the epidermis with bridging of the rete ridges.
	Dendritic cell atypia in bridging nests	Presence of atypical dendritic nucleated cells in a nest, connected to the epidermis with bridging of the rete ridges.
Dermis	Cell atypia in dense dermal nests	Presence of nucleated cell (roundish or dendritic) in dense dermal nest.
	Nucleated roundish cells within the papillae / upper dermis	Presence of bright roundish nucleated cells within the upper dermis or papillae.
	Dendritic cells within the papillae / upper dermis	Presence of bright atypic nucleated cells, with dendritic-like branches, within the upper dermis or papillae.

Table 2. Descriptive statistics

	Criteria	Nevi (N=46)	Melanoma (N=34)	OR (95% confidence interval)	p-value
ARCHITECTURAL CRITERIA					
Stratum corneum	Parakeratosis	1 (2.2)	3 (8.8)	4.28 (0.33 - 233)	0.31
	Ulceration. disruption_stratum_corneum	0 (0.0)	1 (2.9)	Inf (0.03 - Inf)	0.43
	Hyperkeratosis	6 (13.0)	10 (29.4)	2.74 (0.79 - 10.4)	0.12
	Pigment ascension into the SC	2 (4.3)	2 (5.9)	1.37 (0.09 - 19.8)	1
Epidermis – Horizontal view	Irregular honeycomb pattern	3 (6.5)	19 (55.9)	17.4 (4.28 - 105)	**< 0.001**
	Cobblestone pattern	26 (56.5)	11 (32.4)	0.37 (0.13 - 1.02)	0.06
	DEJ ring pattern	24 (52.2)	8 (23.5)	0.29 (0.09 - 0.82)	**0.02**
	DEJ meshwork pattern	14 (30.4)	14 (41.2)	1.59 (0.57 - 4.47)	0.45
	Cerebriform structures	0 (0.0)	2 (5.9)	Inf (0.26 - Inf)	0.18
Epidermis – 3D architecture	Irregular 3D epidermis architecture	6 (13.0)	26 (76.5)	20.5 (5.97 - 83.0)	**< 0.001**
	Nest of cells in the epidermis	0 (0.0)	7 (20.6)	Inf (2.21 - Inf)	**0.002**
	Small nest of pagetoid cells within epidermis	0 (0.0)	5 (14.7)	Inf (1.33 - Inf)	**0.01**
	Big nest of pagetoid cells within epidermis	0 (0.0)	5 (14.7)	Inf (1.33 - Inf)	**0.01**
	Clefting around epidermal nest	0 (0.0)	5 (14.7)	Inf (1.33 - Inf)	**0.01**
	Consumption of the epidermis	0 (0.0)	7 (20.6)	Inf (2.21 - Inf)	**0.002**
	Atrophic epidermis	12 (26.1)	3 (8.8)	0.28 (0.05 - 1.17)	0.08
	Hypertrophic epidermis	2 (4.3)	11 (32.4)	10.2 (1.99 - 103)	**0.001**
Dermoepidermal junction	Disrupted DEJ 3D	17 (37.0)	30 (88.2)	12.4 (3.52 - 56.6)	**< 0.001**
	Elongated rete-ridge	40 (87.0)	22 (64.7)	0.28 (0.08 - 0.94)	**0.04**
	Bridging nest 3D (junctionnal nest)	37 (80.4)	22 (64.7)	0.45 (0.14 - 1.38)	0.19
	Irregular distribution of rete ridges 3D and papillae : top	18 (40.0)	25 (83.3)	7.29 (2.20 - 29.0)	**0.005**
	Irregular distribution of rete ridges 3D and papillae : bottom	23 (51.1)	27 (90.0)	8.37 (2.12 - 49.3)	**0.01**
Dermis	Dermal nests	10 (21.7)	18 (52.9)	3.97 (1.39 - 12.1)	**0.008**
	Dense dermal nests	8 (17.4)	12 (35.3)	0.51 (0.04 - 3.91)	0.12
	Sparse dermal nests	3 (6.5)	14 (41.2)	7.45 (1.10 - 68.2)	**0.02**
	Irregular shape of the dermal nests	2 (4.3)	13 (38.2)	9.42 (1.28 - 122)	**0.02**
	Bright cells in the nests	2 (4.3)	5 (14.7)	1.52 (0.19 - 19.5)	1
	Clefting	3 (6.5)	13 (38.2)	8.62 (2.07 - 52.2)	**< 0.001**
	Melanophages	20 (43.5)	21 (61.8)	2.08 (0.78 - 5.74)	0.16
	Inflammation	16 (34.8)	13 (38.2)	1.16 (0.42 - 3.21)	0.93
	Fibrosis	10 (21.7)	9 (26.5)	1.29 (0.40 - 4.13)	0.82
	Wave pattern	15 (32.6)	3 (8.8)	0.20 (0.03 - 0.82)	**0.01**
CYTOLOGIC CRITERIA					
Epidermis	Pagetoid cells	14 (30.4)	33 (97.1)	71.0 (9.95 - 3101)	**< 0.001**
	Pagetoid cells at stratum granulosum	7 (15.2)	25 (73.5)	14.8 (4.56 - 54.9)	**< 0.001**
	Roundish pagetoid cells	12 (26.1)	30 (88.2)	20.2 (5.58 - 95.8)	**< 0.001**
	Dendritic pagetoid cells	14 (30.4)	33 (97.1)	71.0 (9.95 - 3101)	**< 0.001**
	Number of pagetoid cells >10	6 (13.0)	30 (88.2)	45.9 (11.3 - 247)	**< 0.001**
	Number of roundish pagetoid cells >10	5 (10.9)	24 (70.6)	18.7 (5.36 - 79.3)	**< 0.001**
	Number of dendritic pagetoid cells >10	6 (13.0)	30 (88.2)	45.9 (11.3 - 247)	**< 0.001**
	Marked atypia	4 (8.7)	21 (61.8)	16.2 (4.4 – 77.0)	**< 0.001**

	Focused atypia	9 (19.6)	9 (26.5)	1.47 (0.45 - 4.86)	0.65
	Diffused atypia	8 (17.4)	28 (82.4)	21.0 (6.13 - 85.1)	**< 0.001**
Dermoepidermal junction	Atypia at the DEJ	17 (37.0)	31 (91.2)	15.5 (3.96 - 90.7)	**< 0.001**
	Atypical roundish cells at the DEJ	13 (28.3)	29 (85.3)	14.1 (4.23 - 57.4)	**< 0.001**
	Dendritic cells at the DEJ	14 (30.4)	31 (91.2)	21.8 (5.48 - 130)	**< 0.001**
	Bridging nest with atypia	3 (6.7)	12 (41.4)	9.54 (2.21 - 59.3)	**< 0.001**
	Bridging nest with roundish atypia 3D	3 (6.7)	12 (41.4)	9.54 (2.21 - 59.3)	**< 0.001**
	Bridging nest with dendritic atypia 3D	1 (2.2)	9 (31.0)	19.0 (2.37 - 883)	**< 0.001**
Dermis	Atypia in dense dermal nests	0 (0.0)	11 (61.1)	Inf (2.38 - Inf)	**0.002**
	Atypia in the papillae / upper dermis	3 (6.7)	13 (38.2)	8.62 (2.07 - 52.24)	**< 0.001**
	Atypical roundish cells in the papillae / upper dermis	1 (2.2)	13 (38.2)	26.78 (3.60 - 1201)	**< 0.001**
	Dendritic cells in the papillae / upper dermis	2 (4.3)	11 (32.4)	10.2 (1.99 - 103)	**0.001**

OR corresponds to odd ratio, CI corresponds to confidence intervals, Inf. corresponds to infinity value.

Table 3. Multivariate logistic regression for the differentiation between melanoma and nevi

	Nevi (N=46)	Melanoma (N=34)	OR (95% confidence interval)	p-value
Number of pagetoid cells >10	6 (13.0)	30 (88.2)	31.4 (7.876– 169)	**< 0.001**
Irregular 3D epidermis architecture	6 (13.0)	26 (76.5)	11.8 (2.78– 63.2)	**0.001**

SUPPLEMENTARY MATERIAL

Supplementary Table 1. Dataset information

	Nevus (N=46)	**Melanoma (N=34)**	Typical nevi (N=27)	Atypical nevi (N=19)	Melanoma in situ (N=14)	Invasive melanoma (N=20)	**Total (N=80)**
Sex							
Female	**27 (58.7)**	**14 (41.2)**	18 (66.7)	9 (47.3)	7 (50.0)	7 (35.0)	**41 (51.2)**
Male	**19 (41.3)**	**20 (58.8)**	9 (33.3)	10 (52.6)	7 (50.0)	13 (65.0)	**39 (48.8)**
Body location							
Chest / Abdomen	**9 (19.6)**	**5 (14.7)**	5 (18.5)	4 (21.1)	3 (21.4)	2 (10.0)	**14 (17.6)**
Back	**15 (32.6)**	**12 (35.3)**	8 (29.6)	7 (36.8)	4 (28.6)	8 (40.0)	**27 (33.7)**
Upper extremities	**7 (15.2)**	**10 (29.4)**	4 (14.8)	3 (15.8)	5 (35.7)	5 (25.0)	**17 (21.2)**
Lower extremities	**13 (28.3)**	**7 (20.6)**	8 (29.6)	5 (26.3)	2 (14.3)	5 (25.0)	**20 (25.0)**
Dermoscopy evaluation							
Clear-cut	**19 (41.3)**	**19 (55.9)**	18 (66.7)	1 (5.3)	9 (64.3)	10 (50.0)	**38 (47.5)**
Equivocal	**27 (58.7)**	**15 (44.1)**	9 (33.3)	18 (94.7)	5 (35.7)	10 (50.0)	**42 (52.5)**

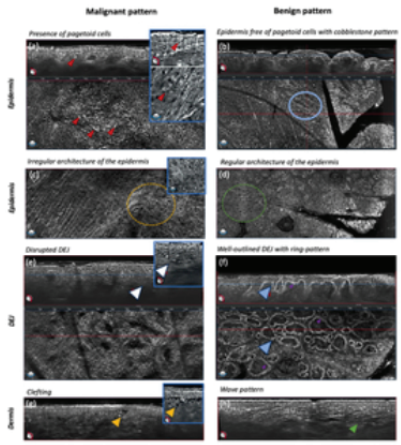

Figure. 1. Main diagnostic criteria. Left column: malignant criteria. Right column: benign criteria. Blue square: criteria detail. (a) The presence of nucleated cells (roundish or dendritic), with dark nuclei and bright cytoplasm (red arrow) is associated to malignancy in the context of absence of inflammation. (b) Cobblestone pattern, associated to benignancy, corresponds to monomorphous, small (6□□m diameter) pigmented keratinocytes (blue circle). (c) Irregularities in the epidermis (size and shape of cells) are observed in the yellow circle. (d) Epidermic cells of homogeneous size and shape are observed in green circle. (e) The disruption of the DEJ (white triangle), in the absence of inflammation, is strongly associated to malignancy. The opposite is observed in a well-defined DEJ (blue triangle) (f). Clefting, a dark space in between the bright nucleated discohesive melanocytes (yellow arrow) is associated to malignancy. The opposite occurs with the presence of "wave pattern" (h) (green arrow), that corresponds to collagen fibers around nonpigmented nests of melanocytes.

11x12mm (600 x 600 DPI)

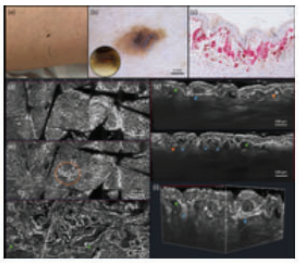

Figure 2. Compound nevus on the right posterior thigh of a 43-years-old woman. (a) Clinical and (b) dermoscopic images with the LC-OCT field of view represented as a blue rectangle and the integrated dermoscopic camera of DeepLive□ LC-OCT on the lower left corner. (c) Histological image, (d, e, f) horizontal LC-OCT views of the 3D acquisitions at a depth of (d) 24 µm, (e) 34 µm and (f) 57 µm showing a regular honeycomb pattern, cobblestone pattern (orange dashed circle) and ring-pattern (green arrows). (g, h) vertical and (i) 3D LC-OCT views of the same acquisitions at different positions showing the pigmentation confined at the dermo epidermal junction outlining the DEJ (green arrows), some junctional nests at the tip of the rete ridges (blue stars) and their fusion creating bridging (blue arrows) and isolated melanocytes in the dermis (orange arrows).

8x7mm (600 x 600 DPI)

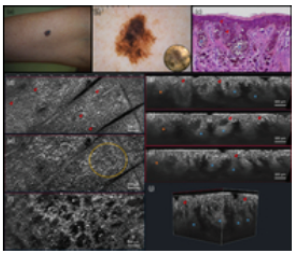

Figure 3. Melanoma in situ on the right volar forearm of a 60 years-old woman
(a) Clinical and (b) dermoscopic images with the LC-OCT field of view represented as a blue rectangle and the integrated dermoscopic camera of DeepLive□ LC-OCT on the lower left corner. (c) Histological image, (d, e, f) horizontal LC-OCT views of the 3D acquisitions at a depth of (d) 22 µm, (e) 34 µm and (f) 72 µm showing the presence of multiple pagetoid dendritic melanocytes (red arrows) and an irregular honeycomb pattern with different sizes and shapes of the nuclei inside the epidermis (yellow dashed circle) and an irregular distribution of the papillae. (g, h, i) vertical and (i) 3D LC-OCT views of the same acquisitions at different positions showing the presence of pagetoid melanocytes (red arrows), a disrupted DEJ (orange stars) and numerous and dense junctional nests with fusion (blue arrows).

8x6mm (600 x 600 DPI)

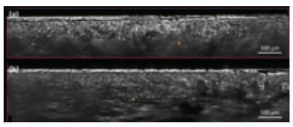

Figure 4. Disrupted DEJ vs inflammation.
A comprehensive understanding of this fundamental criterion is crucial. (a) The DEJ is borrowed (indicated by the orange asterisk) and cannot be visualized. (b) The presence of inflammatory cells and stromal reaction, a result of inflammation, contributes to the distinctive image observed in the vertical view (green asterisk), and is pivotal for distinguishing between malignant and benign lesions.

8x3mm (600 x 600 DPI)

Figure 5. LC-OCT acquisition workflow for melanocytic lesions. 1. Find the most important dermoscopy image. 2. Cover all the lesion with the vertical video. 3. Do a 3D acquisition in the most atypical areas according to dermoscopy and video findings.

8x2mm (600 x 600 DPI)

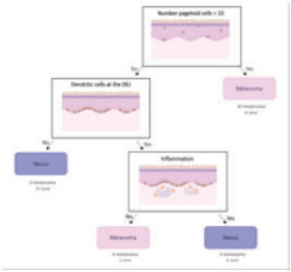

The identification of over ten pagetoid cells, coupled with the presence of dendritic cells at the DEJ in the absence of inflammation, is indicative of melanoma. Conversely, the presence of inflammation and the absence of pagetoid cells are characteristic of benign conditions, even if atypical cells at the DEJ are visualized in the epidermis.

8x7mm (600 x 600 DPI)

PUBLICACIÓN N° 4:[68]

Hendidura: ¿predictor de malignidad melanocítica?

Clefting: predictor of melanocytic malignancy?

Javiera Pérez-Anker, Simone Soglia, Susana Puig, Raquel Albero, Adriana García, Beatriz Alejo, Elisa Cinotti, Carmen Orte Cano, Cyril Habougit, François Skowron, Luca Pellegrino, Lida Tognetti, Clement Lenoir, Paola Castillo, Pietro Rubegni, Mariano Suppa, Jean Luc Perrot, Veronique del Marmol, * Llucia Alos, *Josep Malvehy.

Br J Dermatol. 2023. Submitted revision March 2024. Under review.
Factor de impacto: 10.03

Resumen

Antecedentes: La tomografía de coherencia óptica confocal de campo lineal (TCO-CL) proporciona imágenes *in vivo* con resolución celular en lesiones melanocíticas. La hendidura alrededor de los nidos de células melanocíticas aún no ha sido descrita en técnicas de imagen *in vivo* como MCR o TCO-CL, ni ha sido asociada con malignidad e invasión.

Objetivos: Nuestro objetivo fue describir la característica "hendidura" que rodea los nidos de melanocitos y correlacionarla con la histopatología y la MCR.

Métodos: Se escanearon con TCO-CL lesiones melanocíticas benignas, atípicas y malignas consecutivas, recogidas en el Hospital Clínic de Barcelona, el Hôpital Erasme y el Hospital Universitario de Saint-Etienne. Se revisaron las imágenes de lesiones corporales y faciales para describir los criterios de estudio. Sólo se seleccionaron lesiones con un diagnóstico inequívoco (clínica o histológicamente).

Resultados: Se halló una hendidura en 36 de las 200 lesiones analizadas. Estuvo presente en 28 de los 70 melanomas (40%) y en 8 de las 130 lesiones benignas (6%). La razón de probabilidad de malignidad para la presencia de hendidura en una lesión melanocítica fue de 10,03 (IC 4,07 – 27,5; $p < 0,001$). La magnitud de la fisura también mostró diferencias significativas: la fisura marcada estuvo presente en 17 de los 70 melanomas (24 %) y sólo en 2 lesiones benignas (2 %), con un OR 20,22 (IC 4,55 – 186,2; $p<0,001$). No se observaron diferencias en cuanto a la presencia de esta característica en diferentes topografías. Este criterio se asoció fuertemente a otras características malignas como: el consumo de la epidermis, nidos en la epidermis y disrupción de la unión dermoepidérmica.

Conclusiones: Este estudio demuestra, por primera vez en técnicas de imagen *in vivo*, que este criterio no es un artefacto creado por la preparación de la muestra, sino una característica específica relacionada con la malignidad. Además, la hendidura marcada aparentemente se asocia con una invasión más profunda de melanoma.

British Journal of Dermatology

Clefting: a new predictor of malignancy and invasion in melanocytic lesions?

Journal:	*British Journal of Dermatology*
Manuscript ID	Draft
Manuscript type:	Original Article
Date Submitted by the Author:	n/a
Complete List of Authors:	Pérez-Anker, Javiera; Hospital Clinic de Barcelona, Dermatology Soglia, Simone; Universitat de Barcelona Puig, Susana; Hospital Clinic Barcelona, Dermatology Department, Melanoma Unit Garcia-Herrera, Adriana; Hospital Clinic, Pathology; Universitat de Barcelona, Fonaments Clinics Albero-González, Raquel; Hospital Clinic de Barcelona, Pathology Department Alejo, Beatriz; Hospital Clinic Barcelona, Dermatology Department, Melanoma Unit Cinotti, Elisa; University Hospital of Saint-Etienne, Dermatology Orte Cano, Carmen; Hopital Erasme, Department of Dermatology Habougit, Cyril; University Hospital of Saint-Etienne, Dermatology Skowron, François; Hôpitaux Drôme Nord, Department of Dermatology Pellegrino, Luca; Universitat de Barcelona Tognetti, Linda; University of Siena, Siena (Italy), Dermatology Unit - Department of Medical, Surgical and Neuro Sciences ; Lenoir, Clement; Université Libre de Bruxelles, Dermatology Castillo, Paola; Hospital Clinic de Barcelona, Patology; IDIBAPS, Patology Rubegni, Pietro; University of Siena, Department of Clinical, Surgical and Neuro-sciences Suppa, Mariano; University of L'Aquila, Department of Dermatology Perrot, Jean; University Hospital of Saint-Etienne, Department of Dermatology del Marmol, Veronique; Université Libre Bruxelles., Dermatology Alos, Llucia; Hospital Clinic de Barcelona, Pathology Malvehy, Josep; University of Barcelona, Department of Dermatology
Keywords:	Melanoma, Dermatopathology, Melanocytes, Melanocytic nevi, Naevi, Optical coherence tomography

Abbreviated Abstract

This study demonstrates, for the first time in in vivo imaging techniques, that "clefting" is not an artifact created by the sample preparation, but is a specific feature related to malignancy. Moreover, marked clefting is apparently associated with a deeper invasion of melanoma

-**Title:** Clefting: a new predictor of malignancy and invasion in melanocytic lesions?

- **Running head:** LC-OCT for melanocytic tumors

- **Word count of body text:**

- **Table count:** 2 (and 1 supplementary table)

- **Figure count:** 4 (and 4 supplementary images)

- Video count: 0

- **Authors:** J. Perez-Anker,[1,2] S. Soglia,[2] S. Puig, [1,2,3]A. García,[4] R. Albero,[4] B. Alejo,[1] E. Cinotti,[5,6] C. Orte Cano,[7] Cyril Habougit,[9] François Skowron,[9] L. Pellegrino, [2] L. Tognetti,[5] C. Lenoir,[7] P. Castillo,[4] P. Rubegni,[5] M. Suppa,[6,7,8] J.L. Perrot,[6,9] V. del Marmol,[7] *L. Alos,[4] *J. Malvehy[1,2,3]

- Affiliations:

1. Dermatology Department, Melanoma Unit, Hospital Clínic de Barcelona, IDIBAPS, Barcelona, Spain.

2. Universitat de Barcelona, Barcelona, Spain.

3. Centro de Investigación Biomédica en red de enfermedades raras, CIBERER, Instituto de Salud Carlos III, Barcelona, Spain.

4. Pathology Department, Hospital Clínic de Barcelona, Universitat de Barcelona, Barcelona, Spain.

5. Dermatology Unit, Department of Medical, Surgical and Neurological Sciences, University of Siena, Siena, Italy.

6. Groupe d'Imagerie Cutanée Non Invasive (GICNI) of the Société Française de Dermatologie (SFD), Paris, France.

7. Department of Dermatology, Hôpital Erasme, Université Libre de Bruxelles, Brussels, Belgium.

8. Department of Dermatology, Institut Jules Bordet, Université Libre de Bruxelles, Brussels, Belgium.

9. Department of Dermatology, University Hospital of Saint-Etienne, Saint-Etienne, France.

- Both senior authors contributed equally to this study.

-Corresponding author:

Susana Puig

Melanoma Unit, Dermatology Department, Hospital Clinic Barcelona

Villarroel 170, 08036, Barcelona, Spain.

susipuig@gmail.com

Tel.: +34 93 2275400 ext 2422

Fax: +34 93 2275438

ORCID:

Javiera Pérez-Anker	0000-0002-6959-7250
Susana Puig	0000-0003-1337-9745
Elisa Cinotti	0000-0002-4009-0659
Carmen Orte Cano	0000-0002-1570-7856
Linda Tognetti	0000-0002-6691-4310
Mariano Suppa	0000-0002-9266-0342
Josep Malvehy	0000-0002-6998-914X

-**Keywords**: Line-field confocal optical coherence tomography, melanoma, melanocytic, LC-OCT, RCM, nevus, clefting

-**Funding statement:** The research at the Melanoma Unit in Barcelona is partially funded by CIBER de Enfermedades Raras of the Instituto de Salud Carlos III, Spain, co-financed by European Development Regional Fund "A way to achieve Europe" ERDF; AGAUR

-**Disclosures**: The authors have no disclosures or conflicts of interest to report.

Bulleted statements

What is already known on this topic?

- Line-Field Optical Coherence Tomography (LC-OCT) is an imaging technique that allows in vivo skin visualization with cellular resolution.
- LC-OCT features of melanocytic lesions have been described.
- In melanocytic lesions, LC-OCT horizontal features correlated with Reflectance Confocal Microscopy (RCM) criteria, and vertical features correlated to histopathology.

What does this study add?

- We described new criteria in LC-OCT, RCM, and their histopathology correlation for melanocytic lesions.
- Clefting was associated with malignancy in melanocytic tumors
- Clefting was easily recognized in the vertical view of LC-OCT.

ABSTRACT

Background: Line-field confocal optical coherence tomography (LC-OCT) can provide in vivo images with a cellular resolution for melanocytic lesions. No previous description of clefting has been reported and associated with malignancy for melanocytic lesions in *in vivo* imaging techniques as RCM or LC-OCT.

Objectives: We aimed to describe the feature of "clefting" surrounding the melanocytic nests and its correlation with histopathology and RCM.

Methods: Consecutive benign, atypical, and malignant melanocytic lesions were scanned with LC-OCT, collected at the Hospital Clinic of Barcelona, Hôpital Erasme, and University Hospital of Saint-Etienne. The body and facial lesions images were reviewed for the study criteria. Only lesions with a univocal or unambiguous diagnosis (clinically or histologically) were selected.

Results: Clefting was found in 36 of the 200 analyzed lesions. It was present in 28 of the 70 melanomas (40%) and in 8 of the 130 benign lesions (6%). The odd ratio for malignancy for the presence of clefting in a melanocytic lesion was 10.03 (CI 4.07 – 27.5; $p < 0.001$). The magnitude of the clefting also showed significant differences: Marked clefting was present in 17 of the 70 melanomas (24%) and in only 2 benign lesions (2%), with an OR 20.22 (CI 4.55 – 186.2; $p<0.001$). No differences were observed regarding the presence of this feature in different locations. It was strongly associate to other malignant features as: the consumption of the epidermis, nest in the epidermis and disruption of the dermo-epidermal junction.

Conclusions:

This study demonstrates, for the first time in *in vivo* imaging techniques, that this criterion is not an artifact created by the sample preparation, but is a specific feature related to malignancy. Moreover, marked clefting is apparently associated with a deeper invasion of melanoma.

INTRODUCTION

Since the 1990s, dermatology is transformed by the emergence of new imaging techniques. By offering insights into the morphology and cytological aspects of skin neoplasms, *in vivo* imaging techniques provide complementary information to dermoscopy and improve diagnosis accuracy[1,2]. In addition to reducing the number of biopsies, it also allows the determination of the subtype of certain tumors,[3] leading to more suitable management of lesions. Furthermore, imaging modalities have been shown to be useful in monitoring the effectiveness of topical treatment[4,5] and in delineating margins, especially in areas where surgery may be particularly invasive.[6,7]

Line-field confocal optical coherence tomography (LC-OCT) is an imaging modality that combines optical coherence tomography (OCT) and reflectance confocal microscopy (RCM),[8,9] providing *in vivo* real time images with cellular resolution, both with vertical and horizontal view. LC-OCT use has been investigated in benign and malignant tumors, as well as in some inflammatory skin diseases.[9–22]

In melanocytic lesions, LC-OCT diagnostic features have been described in both benign, atypical and malignant tumours, along with their correlation with RCM (i.e., horizontal mode) and histopathology (i.e., vertical mode).[23] Since LC-OCT highlights the same features as RCM, it can be assumed that the diagnostic criteria are comparable for both techniques:[23] this was also confirmed by Schuh *et al.* who found similar diagnosis performances on RCM and LC-OCT.[24] However, LC-OCT's superior axial resolution enables the visualisation of cellular details in the vertical view, allowing a more precise evaluation of certain criteria such as the disruption of the dermo-epidermal junction (DEJ)[23] and bringing out new diagnosis criteria like wave-pattern.[25] Moreover, identifying cleaving criteria between malignant and benign lesions remains crucial as it increases the confidence rate of the diagnosis and could provide information on the prognosis of the lesion.

Cleft formation is a histopathological criterion defined as a separation between the epidermis and

in the diagnosis of melanocytic lesions.[26,27] Though traditionally considered as an artifact due to sample fixation, "clefting" seems to be often associated with epidermal consumption[28] – an histopathological criterion which shows a good correlation with Breslow thickness and ulceration[29]- suggesting that it is an important prognostic indicator for melanoma. *In vivo*, clefting has only been observed around peripheral nests using RCM[30] but the presence of *in vivo* clefting in the centre of melanocytic lesions and its links with malignancy has not yet been reported.

MATERIAL AND METHODS

Patients with melanocytic lesions were prospectively collected from January 2021 to November 2022 at the Hospital Clinic of Barcelona, Hôpital Erasme of Bruxelles, and University Hospital of Saint-Etienne. The presence of the "clefting criteria" was retrospectively reviewed in all the melanocytic images obtained. Body and also facial lesions were included. Only the lesions with a univocal or unambiguous diagnosis, clinically or histologically, were selected. 3D acquisitions with insufficient image quality were excluded. Spitzoid lesions were also included.

The presence of "clefting" was evaluated by at least three dermatologists by consensus (JPA, JM, MS, SP, SS, CL, LP). Three of them were present in all the evaluations (JPA, SS, CL).

Clefting definition

Clefting was considered a space around a melanocytic nest. Mild and marked clefting were distinguished. It was considered as mild clefting when a dark thin (~10µm) linear separation was seen around melanocytic nests and marked clefting corresponds to a bigger dark space with often the presence of discohesive cells inside the corresponding clefting area, which probably is related to a discohesive nest.

The correspondence with the histology image was observed and compared. (Figures 1 and 2).

Lesions from the Hospital Clinic of Barcelona were also compared with RCM images captured of the same lesion area, as it was the only center with the appropriate technology and/or the technical conditions to do so. (Figure 3).

Statistical analysis

The statistical analysis was performed using R software version 4.1.3 (R Foundation for Statistical Computing, Vienna, Austria). Fisher's exact test was performed to evaluate differences between benign lesions and melanomas. Odds ratios and their 95 % confidence intervals were also calculated.

Rho (Spearman test) was calculated to compare the correlation between clefting and other criteria. A p-value < 0.05 was considered statistically significant.

Acquisition methods

Lesions were imaged with an LC-OCT handheld probe (DeepLive®, DAMAE Medical, Paris, France). LC-OCT 3D images (1.2 mm x 0.5 mm x 0.4 mm) were captured of the most dermoscopically represented areas to diagnose the malignancy in each lesion.

RCM images were captured with a Vivascope 1500™ device (Mavig corp. Munich. Germany; Caliber, Rochester.US) with a dermoscopic image integrated into the device for navigation and multiple mosaics (Vivablocks®) of confocal images (4 mm x 4 mm), at a minimum of 3 to 5 different depths from *stratum corneum* to the papillary dermis.

Histology slides were digitized and reviewed using QuPath v0. 2.3.

RESULTS

A total of 200 pigmented lesions from 200 patients were evaluated. The mean age was 54.6 years old and 53% of the patients were women. One hundred forty-one lesions were histologically confirmed and the others were dermoscopically unequivocal lesions. RCM was also performed in 133 lesions. (Table 1).

Regarding the distribution of the lesions, 68 were at the trunk (34%), 71 at the face (36%), 26 at the upper limbs (13%), 33 at the lower limbs (17%), and 2 at the palm/sole (1%).

There were 59 lesions with a clinically (including dermoscopy) clear diagnosis, and 141 lesions suspicious of malignancy. Of the suspicious lesions ones, seventy were histopathological diagnosed as melanomas, and additional 71 excised lesions were benign. Of the 70 melanomas, 35 were in situ

and 35 invasive, while the rest 130 benign lesions imaged corresponded to nevus (79), lentigos (30), melanocytic hyperplasia (7), and pigmented actinic keratosis (14). (Table 1).

Criteria prediction of malignancy

Results are summarized in table 2. The feature "clefting" was found in 36 of the 200 analyzed lesions. Twenty-eight of the 70 melanomas had this feature present (40%) and it was also found in 8 of the 130 benign lesions (6%), odd ratio 10.03 (4.07 – 27.5 CI; $p < 0.001$). When the magnitude of the clefting was analyzed, mild clefting was present in 11 melanomas (16%) and 6 benign lesions (5%), odd ratio 3.82 (1.23 -13.2 CI; p=0.01). Marked clefting was present in 17 of the 70 melanomas (24%) and in only 2 benign lesions (2%), OR 20.22 (4.55 – 186.2 CI; $p<0.001$).

Regarding the comparison between melanoma in situ and invasive melanoma, clefting was found in 11 of the *in situ* melanoma (31% of all, 6 (17%) had mild clefting, and 5 (14%) had marked clefting); in 17 (49%) of the 35 invasive melanomas (5 (14%) mild clefting while 12 (34%), marked clefting; and in 6 (8%) of the benign nevi (4 (5%) mild clefting and 2 (3%), marked clefting.

Concerning nevi presenting clefting, 2 of them were in typical nevi (5%, one mild and the other marked clefting (2% each)), and four (10%) in atypical nevi (3 (8%) mild and 1(3%), marked clefting). (Supplementary figures 1-3).

Only one of the 30 SL/SK/Lentigo had clefting, and it was mild clefting. One of the 7 melanocytic hyperplasia/melanosis, had a mild clefting. None of the rest of the 14 other lesions had this feature. (Supplementary figure 4).

Location clefting`s occurrence

Regarding the location, results are summarized in table 1. No statistical differences were observed between the different locations (p=0.9952). No statistical differences were also observed concerning the mild (p=0.9325), or the marked clefting (p=0.8085) in different locations. The majority of the lesions which presented clefting were on the trunk (N=13 (19%)), while 13 were localized on the face (18%), 4 on upper limbs (15%), 6 in lower limbs (18%) and none of them on palms/soles. The distribution was practically the same between both subgroups in all the different parts of the body: 6 (9%) and 7 (10%) on the trunk; 6 (8%) and 7 (10%) on the face; 3 (12%) and 1 (4%) on upper limbs; and 2 (6%) and 4 (12%) on lower limbs, respectively between mild and marked clefting.

Clefting correlation with other LC-OCT criteria in body location (supplementary table 1, figure 4)

A strong association was observed when correlating this feature with other diagnostic melanocytic features in LC-OCT associated with malignancy (published elsewhere) as the presence of nests in the epidermis (Rho 0.3981, p<0.001), sparse nests (Rho 0.5806, p<0.001), cerebriform structures (Rho 0.3203, p=0.004), irregular honeycomb pattern (Rho 0.3219, p=0.004), disruption of the DEJ (Rho 0.292, p=0.009), with the absence of elongation of the rete ridges (Rho -0.3293, p=0.003), consumption of the epidermis (Rho 0.2875, p=0.01) and ulceration/disruption of the stratum corneum (Rho 0.225, p=0.04).

It was also associated with morphological features as dermal nests (Rho 0.5052, p<0.001(dense (0.5052, p<0.001), shape 3D (Rho 0.6405, p<0.001)), and the absence of ring pattern at the DEJ (Rho -0.2807, p=0.01).

When correlated to the cytologic criteria of atypia (published elsewhere), it was strongly associated with dermal dense atypical nests (Rho 0.5263, p<0.001), dendritic cells in the papilla/upper dermis (Rho 0.3727, p<0.001), pagetoid cells at stratum granulosum (Rho 0.3572, p=0.001),

atypical/roundish cells in the papilla/upper dermis (Rho 0.3454, p=0.002), dendritic cells at the DEJ (Rho 0.3034, p=0.006), more than 10 dendritic pagetoid cells (Rho 0.3015, p=0.007), more than 10 roundish pagetoid cells (Rho 0.3015, p=0.007), presence of morphologic atypia in the papilla/upper dermis (Rho 0.2969, p=0.007), presence of pagetoid cells (any type) (Rho 0.292, p=0.009) and also the global presence of atypia (marked, diffused and at the DEJ) (Rho 0.2697, p=0.02; Rho 0.2387, p=0.03; Rho 0.2694, p=0.02).

Clefting visualization in vertical and horizontal views

When compared with the horizontal visualization in RCM only in 13/36 (36%) of the lesions in which the same criteria were observed in LC-OCT (7/19 with marked and 5/17 with mild clefting). In this technique, the clefting was also observed with the same morphologic characteristics described and visualized in LC-OCT. However, sometimes it was harder to be founded, and the darker areas were not clearly distinguished from the surrounding tissue with this technique. (Figure 3 and supplementary figure 3).

On the other hand, the vertical view and the axial resolution of LC-OCT permit us to clearly identify this criterion as a dark space close to the dermo-epidermal junction or inside the epidermis, in the periphery of the dense melanocytic nests, sometimes with discohesive melanocytes inside it. This visualization made easier and faster the recognition of the criteria.

DISCUSSION

In this study, we have described, for the first time to our knowledge, the criterion of clefting on *in vivo* imaging techniques for melanocytic lesions. Moreover, we demonstrated that it is a reliable predictor of malignancy by itself (observed in 24% of melanomas, and only in 2% of benign lesions)

In 2012, AbdullGaffar *et al*. also described a list of cutaneous neoplasms in which this feature was observed, but they did not find this feature in their series of 4 melanomas, but they found it in 3% of their analyzed nevi (in a total of 93 melanocytic nevi analyzed), in agreement with our results of marked clefting.[31]

For all these reasons, it seems that clefting is an interesting criterion that could offer information associated to the diagnosis, invasiveness and prognosis of the lesion.

In LC-OCT, it was easily recognized and visualized in vertical sections in the periphery of the atypical melanocytic nests, due to the clear space visualization similar to the histology slides and/or inside the skin (in the disrupted epidermis), with atypical melanocytes inside this area. In the same lesions, it was harder to visualize clefting in RCM, probably because this criterion is more easily identified in the vertical view and it also showed a better contrast in LC-OCT at the same depth.

Some lesions had not been biopsied due to their clearly benign dermoscopy and 4 lesions presented this feature. (supplementary figures 1-4). Because of that, it is not possible to determine if some other phenomenon could be confused with clefting. When reviewing these cases, one of them (supplementary figure 1), which had marked clefting arising in a typical nevus, we observe a possible presence of a large vessel around a nest, that probably has been interpreted as clefting. No other malignant criteria were observed in the rest of the images. The second benign lesion (supplementary figure 2), had non-other malignant criteria associated, and it was a mild clefting around the nest. Doing the association with the dermoscopy, we can also hypothesize that it could be a spitzoid nevus. The third case, a lentigo/SL/SK with clefting, was associated with other malignancy criteria. When reviewing the dermoscopy and the images, the diagnosis of lentigo maligna was suspected and it was decided to perform a biopsy. This lesion was arising in a patient with previous history of melanoma (supplementary figure 3). The results haven't been obtained until the submission of the paper. The last one, it was an atypical nevus with a marked clefting (supplementary figure 4), when reviewing the rest of criteria, the lesion had enough criteria to suspect of a melanoma, and we decided also to remove the lesion. More studies need to be done to determine the differentiation of this feature with

and even stronger when associated with other diagnostic criteria for malignancy in melanocytic lesions as, for example, consumption of the epidermis.

In 2005, Markus Braun-Falco *et al*. described this histological feature for the first time, as a diagnostic marker for melanoma.[27] Clefting was considered as a "separation between the epidermis and underlying melanocytic cells at the dermo-epidermal junction, with a length of at least 0.3mm". Clefting was visualized in 24% of the 503 melanomas they analyzed, in agreement with our results (important clefting visualized in 24% of the melanomas). In addition, clefting was observed in <1% (9 over 939) of the benign melanocytic lesions included, in concordance with our study which was 2%. Comparing both datasets, those authors had 26% of benign lesions represented and we had 35% of atypical benign lesions.

It is also an important clue concerning the invasiveness of the lesion. Marked clefting was observed in 34% of invasive melanomas and 14% of melanomas in situ. This link with invasiveness has already been reported in histology in 2007 by Walters *et al.,* showing that the consumption of the epidermis was a reliable criterion in differentiating melanomas from dysplastic nevi and, moreover, that it was associated with an increasing Breslow thickness and ulceration. Additionally, the authors explained that clefting was a complementary criterion of the consumption of the epidermis, helping in the identification of invasive melanomas.[29] The correlation of the presence of this feature with other morphologic and cytologic diagnostic features of malignancy, to our knowledge, hasn't been described before.

Markus Braun-Falco *et al*. also described different types of clefting as linear, single-nest, and multi-nest clefting. But they did not describe these subtypes as related to more superficial or invasive melanomas. They observed a slight predilection for the back of this feature and a slightly higher prevalence in the superficial spreading type of melanoma, and for tumors with a Breslow thickness between 1 and 2 mm. We didn't find any differences regarding the location and the presence of this feature.

other conditions. Probably, some inflammation at the epidermis/DEJ or even edema could be confounded with clefting.

Furthermore, to investigate the composition of this substrate, histological slides of some cases in which clefting were seen with LC-OCT were stained with Alcian blue. It reveals no mucin deposit, contrary to the observations on the clefting present in BCC.[32] Although the origin of this clefting remains unclear, three explanations have been suggested: a mechanophysical response to friction or rapid tumors growth, an immulogic reaction similar the one in pemphigus and a molecular process that implies cross-talk and adhesion between keratinocytes and melanocytic cells during melanogenesis.[33]

This study demonstrates, for the first time in *in vivo* imaging techniques, that this criterion is not an artifact created by the sample preparation, but is a specific feature related to malignancy. Moreover, it seems that marked clefting is associated with a deeper invasion of melanoma. The strong association with other malignant diagnostic features (published elsewhere) demonstrated that this technique reveals a precise approach to detecting early malignancy.

ACKNOWLEDGEMENTS:

We want to thank the members of the Dermatology Investigation Unit, specially Pablo Iglesias for helping collect patient data and Dermatopathology Department of the Hospital Clinic Barcelona, for providing support to this project. We also want to thank all the patients and their families who are the main reason for our studies. We also thank Paul Hetherington for his help with the text editing.

The authors are indebted to Clothilde Raoux and Maxime Cazalas (DAMAE Medical, Paris, France) for the technical assistance with the research and LC-OCT device.

REFERENCES

1 Pezzini C, Kaleci S, Chester J, *et al.* Reflectance confocal microscopy diagnostic accuracy for malignant melanoma in different clinical settings: systematic review and meta-analysis. *J Eur Acad Dermatol Venereol* 2020; **34**:2268–79.

2 Holmes J, von Braunmühl T, Berking C, *et al.* Optical coherence tomography of basal cell carcinoma: influence of location, subtype, observer variability and image quality on diagnostic performance. *Br J Dermatol* 2018; **178**:1102–10.

3 Sinx KAE, van Loo E, Tonk EHJ, *et al.* Optical Coherence Tomography for Noninvasive Diagnosis and Subtyping of Basal Cell Carcinoma: A Prospective Cohort Study. *J Invest Dermatol* 2020; **140**:1962–7.

4 Ulrich M, Krueger-Corcoran D, Roewert-Huber J, *et al.* Reflectance Confocal Microscopy for Noninvasive Monitoring of Therapy and Detection of Subclinical Actinic Keratoses. *Dermatology* 2010; **220**:15–24.

5 Verzì AE, Micali G, Lacarrubba F. Line-Field Confocal Optical Coherence Tomography May Enhance Monitoring of Superficial Basal Cell Carcinoma Treated with Imiquimod 5% Cream: A Pilot Study. *Cancers* 2021; **13**:4913.

6 Champin J, Perrot J-L, Cinotti E, *et al.* In Vivo Reflectance Confocal Microscopy to Optimize the Spaghetti Technique for Defining Surgical Margins of Lentigo Maligna. *Dermatol Surg* 2014; **40**:247–56.

7 De Carvalho N, Schuh S, Kindermann N, *et al.* Optical coherence tomography for margin definition of basal cell carcinoma before micrographic surgery-recommendations regarding the marking and scanning technique. *Skin Res Technol* 2018; **24**:145–51.

8 Dubois A, Levecq O, Azimani H, *et al.* Line-field confocal time-domain optical coherence tomography with dynamic focusing. *Opt Express* 2018; **26**:33534–42.

9 Dubois A, Levecq O, Azimani H, *et al.* Line-field confocal optical coherence tomography for high-resolution noninvasive imaging of skin tumors. *J Biomed Opt* 2018; **23**:1–9.

10 Davis A, Levecq O, Azimani H, *et al.* Simultaneous dual-band line-field confocal optical coherence tomography: application to skin imaging. *Biomed Opt Express* 2019; **10**:694–706.

11 Lenoir C, Diet G, Cinotti E, *et al.* Line-field confocal optical coherence tomography of sebaceous hyperplasia: a case series. *J Eur Acad Dermatol Venereol JEADV* 2021. doi:10.1111/jdv.17251.

12 Lenoir C, Cinotti E, Tognetti L, *et al.* Line-field confocal optical coherence tomography of actinic keratosis: a case series. *J Eur Acad Dermatol Venereol* 2021; :jdv.17548.

13 Tognetti L, Carraro A, Cinotti E, *et al.* Line-field confocal optical coherence tomography for non-invasive diagnosis of lichenoid dermatoses of the childhood: A case series. *Skin Res Technol* 2021; **n/a**. doi:10.1111/srt.13075.

14 Cinotti E, Tognetti L, Cartocci A, *et al.* Line-field confocal optical coherence tomography for actinic keratosis and squamous cell carcinoma: a descriptive study. *Clin Exp Dermatol* 2021; :ced.14801.

15 Tognetti L, Cinotti E, Suppa M, *et al.* Line field confocal optical coherence tomography: An adjunctive tool in the diagnosis of autoimmune bullous diseases. *J Biophotonics* 2021. doi:10.1002/jbio.202000449.

16 Suppa M, Fontaine M, Dejonckheere G, *et al.* Line-field confocal optical coherence tomography of basal cell carcinoma: a descriptive study. *J Eur Acad Dermatol Venereol JEADV* 2021; **35**:1099–110.

17 Monnier J, Tognetti L, Miyamoto M, *et al.* In vivo characterisation of healthy human skin with a novel, non-invasive imaging technique: line-field confocal optical coherence tomography. *J Eur Acad Dermatol Venereol* 2020; **n/a**. doi:10.1111/jdv.16857.

18 Tognetti L, Rizzo A, Fiorani D, *et al.* New findings in non-invasive imaging of aquagenic keratoderma: Line-field optical coherence tomography, dermoscopy and reflectance confocal microscopy. *Skin Res Technol* 2020; :srt.12882.

19 Tognetti L, Ekinde S, Habougit C, *et al.* Delayed Tattoo Reaction From Red Dye With Overlapping Clinicopathological Features: Examination With High-Frequency Ultrasound and Line-Field Optical Coherence Tomography. *Dermatol Pract Concept* 2020; **10**. doi:10.5826/dpc.1003a53.

20 Tognetti L, Fiorani D, Suppa M, *et al.* Examination of circumscribed palmar hypokeratosis with line-field confocal optical coherence tomography: Dermoscopic, ultrasonographic and histopathologic correlates. *Indian J Dermatol Venereol Leprol* 2020; **86**:206.

21 Lacarrubba F, Elisa Verzì A, Francesco Puglisi D, Micali G. Line-field confocal optical coherence tomography: a novel, non-invasive imaging technique for a rapid, in-vivo diagnosis of herpes infection of the skin. *J Eur Acad Dermatol Venereol* 2021; :jdv.17182.

22 Verzì A e., Broggi G, Micali G, *et al.* Line-field confocal optical coherence tomography of psoriasis, eczema and lichen planus: a case series with histopathological correlation. *J Eur Acad Dermatol Venereol*; **n/a**. doi:10.1111/jdv.18293.

23 Perez-Anker J, Puig S, Alos L, *et al.* Morphologic evaluation of melanocytic lesions with three-dimensional line-field confocal optical coherence tomography: correlation with histopathology and reflectance confocal microscopy. A pilot study. *Clin Exp Dermatol* 2022; :ced.15383.

24 Schuh S, Ruini C, Perwein MKE, *et al.* Line-Field Confocal Optical Coherence Tomography: A New Tool for the Differentiation between Nevi and Melanomas? *Cancers* 2022; **14**:1140.

25 Lenoir C, Perez-Anker J, Diet G, *et al.* Line-field confocal optical coherence tomography of benign dermal melanocytic proliferations: a case series. *J Eur Acad Dermatol Venereol* 2021; **n/a**. doi:https://doi.org/10.1111/jdv.17180.

26 Ackerman AB, Jacobson M, Vitale PA. Clues to diagnosis in dermatopathology. Chicago, American Society of Clinical Pathologists Press, 1991.

27 Braun-Falco M, Friedrichson E, Ring J. Subepidermal cleft formation as a diagnostic marker for cutaneous malignant melanoma. *Hum Pathol* 2005; **36**:412–5.

28 Hantschke M, Bastian BC, LeBoit PE. Consumption of the Epidermis: A Diagnostic Criterion for the Differential Diagnosis of Melanoma and Spitz Nevus. *Am J Surg Pathol* 2004; **28**:1621–5.

29 Walters RF, Groben PA, Busam K, *et al.* Consumption of the Epidermis: A Criterion in the Differential Diagnosis of Melanoma and Dysplastic Nevi That is Associated With Increasing Breslow Depth and Ulceration. *Am J Dermatopathol* 2007; **29**:527–33.

30 Benati E, Zalaudek I, Piana S, *et al. In vivo* detection of peripheral clefting in melanocytic lesions. *Br J Dermatol* 2015; **173**:1525–6.

31 AbdullGaffar B. The prevalence and importance of clefts in cutaneous neoplasms. *Pathology (Phila)* 2012; **44**:267–70.

32 Ulrich M, Roewert-Huber J, González S, *et al.* Peritumoral clefting in basal cell carcinoma: correlation of in vivo reflectance confocal microscopy and routine histology. *J Cutan Pathol* 2011; **38**:190–5.

33 Braun-Falco M. Cleft formation and consumption of the epidermis in cutaneous melanocytic lesions—reply. *Hum Pathol* 2006; **37**:247.

FIGURE LEGENDS

Figure 1. Clefting presentation. Invasive SSM (Breslow 0.3 mm) on the scapular region of a 44-year-old man. Yellow triangles: clefting areas. Red triangle: atypical cells. Melanocytic nests: green triangle. Blue line: location of the horizontal LC-OCT plane on the corresponding vertical LC-OCT plane. Red line: location of the vertical LC-OCT plane on the corresponding horizontal LC-OCT plane.

a. Dermoscopic image (Vivacam®) with the 3D capture area in green, **b.** 3D-Cube of the section with DeepLive® LC-OCT, **c.** Histopathological vertical section of the area imaged with LC-OCT (H&E magnification 10x), **d.** LC-OCT vertical section, **e.** LC-OCT horizontal section. The vertical view shows the clefting areas with atypical nucleated cells at the periphery or inside the discohesive nest.

Figure 2. Correlation between LC-OCT and histopathology. Yellow triangles: clefting areas. Red triangle: atypical cells. Melanocytic nests: green stars.

a. Melanoma in situ on the outer arm of a 41-year-old woman, b. Invasive SSM (Breslow 0.8 mm) on the thigh of a 41-year-old woman, c. Lentigo Maligna on the helix of a 66-year-old man, d. Invasive SSM (Breslow 0.8 mm) on the chest of a 47-year-old man. [a-d]1. Dermoscopic image, [a-d]2. DeepLive® LC-OCT vertical, [a-d]3. Histopathological images of the same area (H&E magnification 10x). The vertical view shows clefting areas with atypical nucleated cells at the periphery or inside which are also present in the histopathological image. Clefting is considered as mild in melanoma in situ (a) and marked for the three other melanomas (b-d).

Figure 3. Correlation between LC-OCT and RCM. Melanoma recurrence on the temple of a 69 year-old woman. **a.** DeepLive® LC-OCT vertical view, **b.** LC-OCT horizontal view, **c.** Vivascope RCM images of the same area. Clefting is darker on the LC-OCT horizontal images than in RCM.

The vertical helps to distinguish clefting from the area above the skin. Yellow triangles: clefting areas; blue stars: outer layer of the epidermis.

Figure 4. Correlation with other criteria. Rho (Spearman test). * = *p-value* (* 0.01 – 0.04; **0.002 – 0.009; ***<0.001)

Figure S1. Monitored nevus of a 31-year-old man. a. Clinical image, **b.** dermoscopic image, **c.** LC-OCT vertical and **d.** LC-OCT horizontal images showing marked clefting (yellow arrows) between dermal melanocytic nests (green stars) and the dermo-epidermal junction around a keratinized follicle (orange stars). **e.** LC-OCT vertical and **f.** LC-OCT horizontal images of the same lesion showing some atypical melanocytes in the epidermis (red arrows). Blue line: location of the horizontal LC-OCT plane on the corresponding vertical LC-OCT plane. Red line: location of the vertical LC-OCT plane on the corresponding horizontal LC-OCT plane.

Figure S2. Compound nevus of a 32-year-old woman. a. Clinical image, b. dermoscopic image, **c-e.** LC-OCT vertical and **d-f.** LC-OCT horizontal images showing mild clefting (yellow arrows) around some melanocytic nests (green stars). The dermal component of the lesion is represented by the wave pattern on the dermis. Blue line: location of the horizontal LC-OCT plane on the corresponding vertical LC-OCT plane. Red line: location of the vertical LC-OCT plane on the corresponding horizontal LC-OCT plane.

Figure S3. Compound nevus with moderate atypia of a 28-year-old man. a. Clinical image, **b.** dermoscopic image, **c-f.** LC-OCT vertical (top) and LC-OCT horizontal images (bottom), **h-i.** Histopathological images of 2 different areas of the lesion and **j-k.** RCM images (Vivascope 1500) showing marked clefting (yellow arrows) and the presence of numerous atypical melanocytes (red arrows) in the epidermis and at the dermo epidermal junction. Blue line: location of the horizontal

LC-OCT plane on the corresponding vertical LC-OCT plane. Red line: location of the vertical LC-OCT plane on the corresponding horizontal LC-OCT plane.

Figure S4. Monitored seborrheic keratosis of a 77-year-old woman. a. Clinical image, **b-d.** dermoscopic images, **e-i.** LC-OCT vertical (top) and LC-OCT horizontal images (bottom), showing mild clefting (yellow arrows) and the presence of atypical melanocytes (red arrows) in the epidermis, at the dermo epidermal junction and around the follicles. Blue line: location of the horizontal LC-OCT plane on the corresponding vertical LC-OCT plane. Red line: location of the vertical LC-OCT plane on the corresponding horizontal LC-OCT plane.

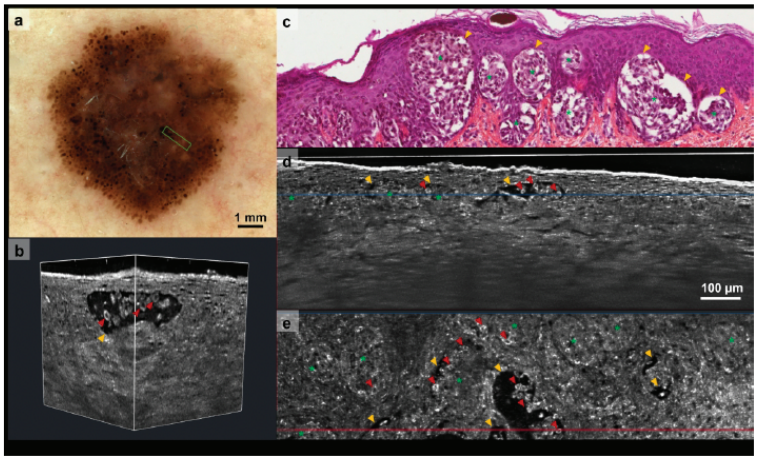

Figure 1. Clefting presentation. Invasive SSM (Breslow 0.3 mm) on the scapular region of a 44-year-old man. Yellow triangles: clefting areas. Red triangle: atypical cells. Melanocytic nests: green triangle. Blue line: location of the horizontal LC-OCT plane on the corresponding vertical LC-OCT plane. Red line: location of the vertical LC-OCT plane on the corresponding horizontal LC-OCT plane.
a. Dermoscopic image (Vivacam□) with the 3D capture area in green, b. 3D-Cube of the section with DeepLive□ LC-OCT, c. Histopathological vertical section of the area imaged with LC-OCT (H&E magnification 10x), d. LC-OCT vertical section, e. LC-OCT horizontal section. The vertical view shows the clefting areas with atypical nucleated cells at the periphery or inside the discohesive nest.

297x179mm (300 x 300 DPI)

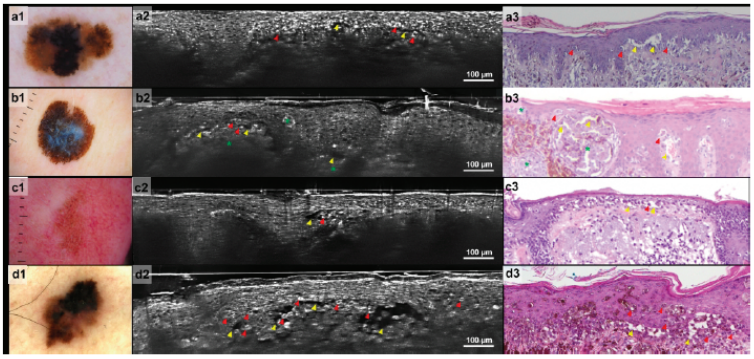

Figure 2. Correlation between LC-OCT and histopathology. Yellow triangles: clefting areas. Red triangle: atypical cells. Melanocytic nests: green stars.
a. Melanoma in situ on the outer arm of a 41-year-old woman, b. Invasive SSM (Breslow 0.8 mm) on the thigh of a 41-year-old woman, c. Lentigo Maligna on the helix of a 66-year-old man, d. Invasive SSM (Breslow 0.8 mm) on the chest of a 47-year-old man. [a-d]1. Dermoscopic image, [a-d]2. DeepLive□ LC-OCT vertical, [a-d]3. Histopathological images of the same area (H&E magnification 10x). The vertical view shows clefting areas with atypical nucleated cells at the periphery or inside which are also present in the histopathological image. Clefting is considered as mild in melanoma in situ (a) and marked for the three other melanomas (b-d).

341x160mm (300 x 300 DPI)

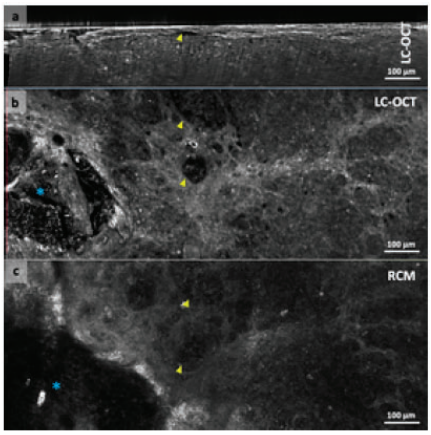

Figure 3. Correlation between LC-OCT and RCM. Melanoma recurrence on the temple of a 69 year-old woman. a. DeepLive□ LC-OCT vertical view, b. LC-OCT horizontal view, c. Vivascope RCM images of the same area. Clefting is darker on the LC-OCT horizontal images than in RCM. The vertical helps to distinguish clefting from the area above the skin. Yellow triangles: clefting areas; blue stars: outer layer of the epidermis.

11x12mm (600 x 600 DPI)

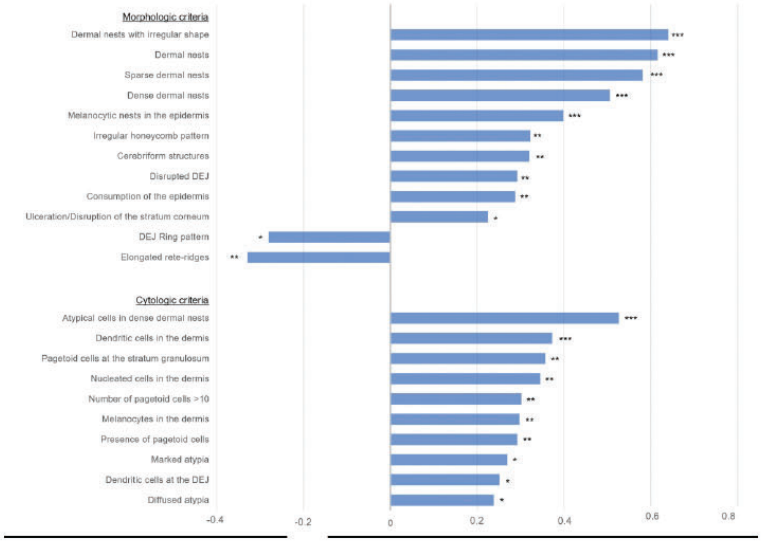

Figure 4. Correlation with other criteria. Rho (Spearman test). * = p-value (* 0.01 – 0.04; **0.002 – 0.009; ***<0.001)

241x175mm (300 x 300 DPI)

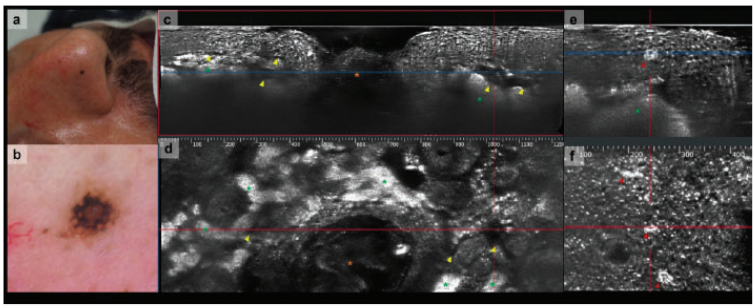

Figure S1. Monitored nevus of a 31-year-old man. a. Clinical image, b. dermoscopic image, c. LC-OCT vertical and d. LC-OCT horizontal images showing marked clefting (yellow arrows) between dermal melanocytic nests (green stars) and the dermo-epidermal junction around a keratinized follicle (orange stars). e. LC-OCT vertical and f. LC-OCT horizontal images of the same lesion showing some atypical melanocytes in the epidermis (red arrows). Blue line: location of the horizontal LC-OCT plane on the corresponding vertical LC-OCT plane. Red line: location of the vertical LC-OCT plane on the corresponding horizontal LC-OCT plane.

339x135mm (300 x 300 DPI)

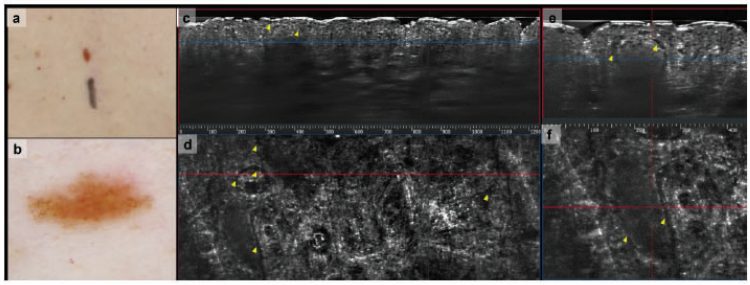

Figure S2. Compound nevus of a 32-year-old woman. a. Clinical image, b. dermoscopic image, c-e. LC-OCT vertical and d-f. LC-OCT horizontal images showing mild clefting (yellow arrows) around some melanocytic nests (green stars). The dermal component of the lesion is represented by the wave pattern on the dermis. Blue line: location of the horizontal LC-OCT plane on the corresponding vertical LC-OCT plane. Red line: location of the vertical LC-OCT plane on the corresponding horizontal LC-OCT plane.

339x126mm (300 x 300 DPI)

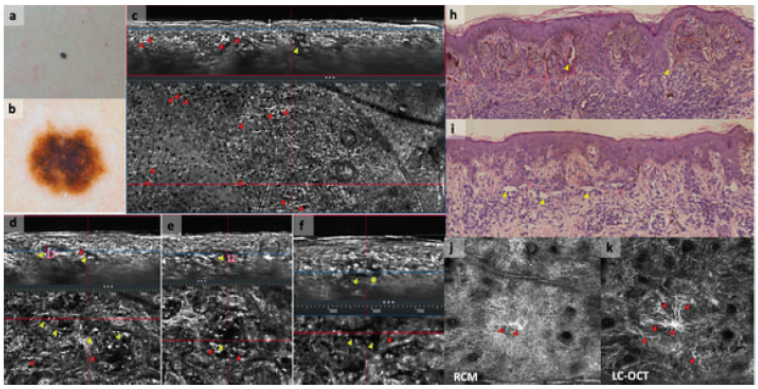

Figure S3. Compound nevus with moderate atypia of a 28-year-old man. a. Clinical image, b. dermoscopic image, c-f. LC-OCT vertical (top) and LC-OCT horizontal images (bottom), h-i. Histopathological images of 2 different areas of the lesion and j-k. RCM images (Vivascope 1500) showing marked clefting (yellow arrows) and the presence of numerous atypical melanocytes (red arrows) in the epidermis and at the dermo epidermal junction. Blue line: location of the horizontal LC-OCT plane on the corresponding vertical LC-OCT plane. Red line: location of the vertical LC-OCT plane on the corresponding horizontal LC-OCT plane.

24x12mm (600 x 600 DPI)

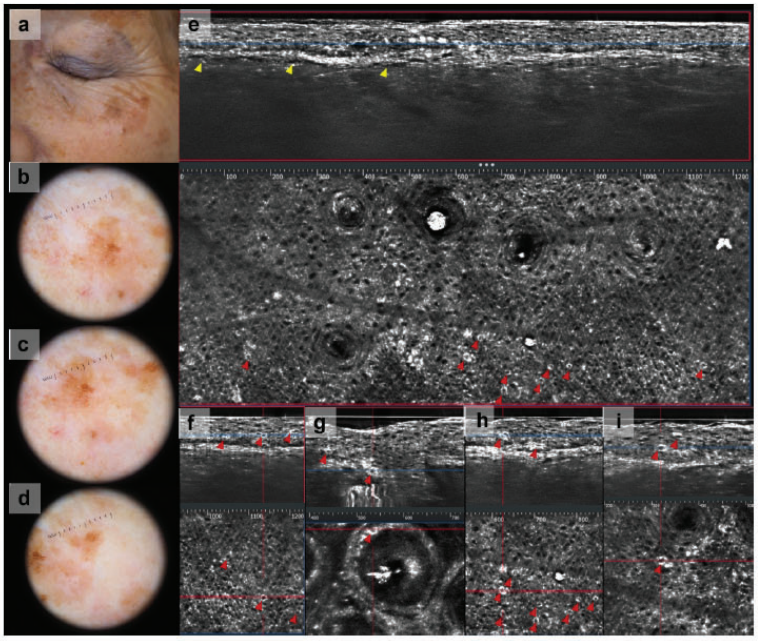

Figure S4. Monitored seborrheic keratosis of a 77-year-old woman. a. Clinical image, b-d. dermoscopic images, e-i. LC-OCT vertical (top) and LC-OCT horizontal images (bottom), showing mild clefting (yellow arrows) and the presence of atypical melanocytes (red arrows) in the epidermis, at the dermo epidermal junction and around the follicles. Blue line: location of the horizontal LC-OCT plane on the corresponding vertical LC-OCT plane. Red line: location of the vertical LC-OCT plane on the corresponding horizontal LC-OCT plane.

227x191mm (300 x 300 DPI)

PUBLICACIÓN N° 5:[69]

Puntuación no invasiva de atipia celular en imágenes de TCO-CL en 3D de tumores queratinizantes utilizando Deep Learning

Non-invasive scoring of cellular atypia in keratinocyte cancers in 3D LC-TCO images using Deep Learning

Sébastien Fischman, Javiera Pérez-Anker, Linda Tognetti, Angelo Di Naro, Mariano Suppa, Elisa Cinotti, Théo Viel, Jilliana Monnier, Pietro Rubegni, Veronique del Marmol, Josep Malvehy, Susana Puig, Arnaud Dubois, Jean-Luc Perrot.

Sci Rep. 2022 Jan 10;12(1):481. doi: 10.1038/s41598-021-04395-1
Factor de impacto: 5.133

Resumen
Antecedentes: El diagnóstico histopatológico es el "método estándar" para la detección del cáncer de piel y se basa en la presencia o ausencia de biomarcadores y de atipia celular. Sin embargo, alguno de los inconvenientes es que requiere una gran experiencia y mucho tiempo en su ejecución. Además, la noción de atipia o de displasia celular usadas para el diagnóstico es muy subjetiva, habiendo poca concordancia entre evaluadores reportada en la literatura. Por último, la histología requiere la realización de una biopsia, que es un procedimiento invasivo y que además obtiene solo una pequeña muestra de la lesión, siendo insuficiente en el contexto de grandes campos de cancerización.
Objetivos: Demonstrar que los criterios de atipia celular se pueden definir y cuantificar objetivamente, con métodos *in vivo*, no invasivos, en 3D.

Métodos: Entrenar un algoritmo de aprendizaje profundo (AP) para segmentar núcleos de queratinocitos (KC) a partir de imágenes 3D de TCO-CL. Para esto, se realizaron segmentaciones y se obtuvieron parámetros métricos cuantitativos, reproducibles y biológicamente relevantes para describir los núcleos de los KC individualmente.

Resultados: Mostramos que, usando esos parámetros métricos cuantitativos, se pudieron derivar definiciones simples y otras más complejas de atipia, para discriminar entre pieles sanas y patológicas, logrando puntajes de área bajo la curva ROC (AUC) superiores a 0.965, superando en gran medida a los expertos médicos en la misma tarea con un ABC de 0,766.

Conclusiones: En conjunto, nuestro enfoque y hallazgos abren la puerta a un control cuantitativo preciso de las lesiones cutáneas y de la evaluación de tratamientos, ofreciendo una herramienta no invasiva prometedora para estudios clínicos, ayudando a determinar la potencial gravedad de una lesión o incluso para observar la evolución de las lesiones precancerosas a cancerosas a lo largo del tiempo.

scientific reports

Check for updates

OPEN

Non-invasive scoring of cellular atypia in keratinocyte cancers in 3D LC-OCT images using Deep Learning

Sébastien Fischman[1✉], Javiera Pérez-Anker[2,3], Linda Tognetti[4], Angelo Di Naro[4], Mariano Suppa[5,6,7], Elisa Cinotti[4,6], Théo Viel[1], Jilliana Monnier[6,8], Pietro Rubegni[4], Véronique del Marmol[5], Josep Malvehy[2,3], Susana Puig[2,3], Arnaud Dubois[9] & Jean-Luc Perrot[10]

Diagnosis based on histopathology for skin cancer detection is today's gold standard and relies on the presence or absence of biomarkers and cellular atypia. However it suffers drawbacks: it requires a strong expertise and is time-consuming. Moreover the notion of atypia or dysplasia of the visible cells used for diagnosis is very subjective, with poor inter-rater agreement reported in the literature. Lastly, histology requires a biopsy which is an invasive procedure and only captures a small sample of the lesion, which is insufficient in the context of large fields of cancerization. Here we demonstrate that the notion of cellular atypia can be objectively defined and quantified with a non-invasive in-vivo approach in three dimensions (3D). A Deep Learning (DL) algorithm is trained to segment keratinocyte (KC) nuclei from Line-field Confocal Optical Coherence Tomography (LC-OCT) 3D images. Based on these segmentations, a series of quantitative, reproducible and biologically relevant metrics is derived to describe KC nuclei individually. We show that, using those metrics, simple and more complex definitions of atypia can be derived to discriminate between healthy and pathological skins, achieving Area Under the ROC Curve (AUC) scores superior than 0.965, largely outperforming medical experts on the same task with an AUC of 0.766. All together, our approach and findings open the door to a precise quantitative monitoring of skin lesions and treatments, offering a promising non-invasive tool for clinical studies to demonstrate the effects of a treatment and for clinicians to assess the severity of a lesion and follow the evolution of pre-cancerous lesions over time.

Histopathology is the gold standard to confirm a diagnosis in all tissues. The advent of numerical technologies facilitate the access of physicists to digital imaging. However, diagnoses and prognoses with whole slide images still suffer from the subjectivity and level of experience of the specialist, even when some grading scales systems exist[1,2].

The recent progress in computer vision with Deep Learning techniques has opened up new opportunities to create more reliable quantitative metrics based on physical segmentations to help pathologists. Specifically, metrics based on cell nuclei spatial distributions have gained recent interest as cell nuclei are essential markers for the diagnosis and study of cancer[3]. Due to the large amount of cells visible in medical images at microscopic level, their global geometry is especially hard to understand for the human eye, making automated segmentation of nuclei particularly helpful and promising. Waliszewski et al.[4] tried to quantify the spatial distribution of cancer cell nuclei with a fractal geometrical model to automate Gleason scoring. Kendall et al.[5] introduced geoscience

[1]DAMAE Medical, Paris, France. [2]Melanoma Unit, Hospital Clinic Barcelona, University of Barcelona, Barcelona, Spain. [3]CIBER de enfermedades raras, Instituto de Salud Carlos III, Barcelona, Spain. [4]Dermatology Unit - Department of Medical, Surgical and Neurological Sciences, University of Siena, Siena, Italy. [5]Department of Dermatology, Université Libre de Bruxelles, Hôpital Erasme, Brussels, Belgium. [6]Groupe d'Imagerie Cutanée Non Invasive (GICNI) of the Société Française de Dermatologie (SFD), Paris, France. [7]Institut Jules Bordet, Université Libre de Bruxelles, Brussels, Belgium. [8]Department of Dermatology and skin cancer, la Timone hospital, Assistance Publique-Hôpitaux de Marseille, Aix-Marseille University, Marseille, France. [9]Université Paris-Saclay, Institut d'Optique Graduate School, Laboratoire Charles Fabry, Palaiseau, France. [10]Department of Dermatology, University Hospital of Saint-Etienne, Saint-Etienne, France. ✉email: sebastien@damae-medical.com

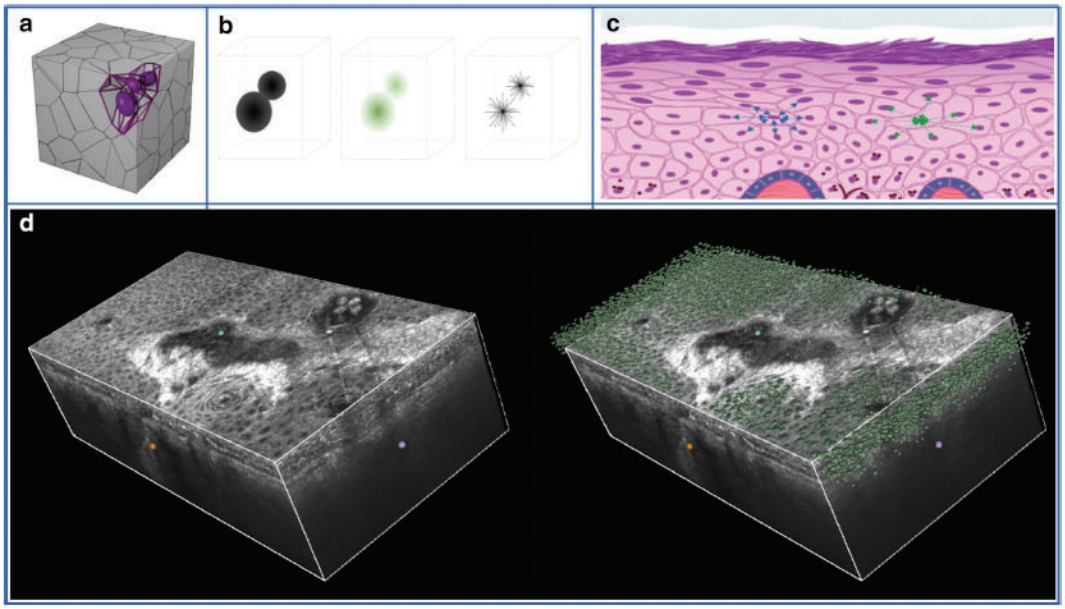

Figure 1. (**a**) Representation of a 3D Voronoi Diagram in a cube. (**b**) Scheme of a StarDist inputs, probability predictions and rays predictions. (**c**) Representation of skin structure, center to center distance (in green) and border to border distance (in blue). (**d**) Example of 3D visualisation of StarDist nuclei detection in LC-OCT 3D images.

frameworks and a two dimensional space (2D) graph-based approach for digital pathology in order to quantitatively differentiate lesional and non-lesional images. Lu et al.[6] also used automated cell nuclei segmentations and a local nuclear graph approach to create complex, hardly interpretable but reproducible metrics, useful for predicting lung cancer survival of patients. Jiao et al.[7] proposed a 2D distribution analysis of spatial organisation of cell nuclei in brain tumors using Voronoi statistics. Zhou et al.[8] applied a graph neural network approach from nuclei segmentation in order to automatically grade colorectal cancer histology images.

All these studies tried to capture the complexity of the spatial distribution of cell nuclei from histology slides into a few quantitative metrics to demonstrate predictive or discriminative power. But histology slides cannot perfectly reflect the actual physical changes of tissues. In fact, slide preparation pipeline (including biopsy, tissue fixation, processing, sectioning and staining) creates physical deformation and results in a 2D representation that cannot fully capture the spatial complexity of a 3D reality, which is a known issue[9–11].

LC-OCT is a new in-vivo non-invasive medical imaging technology that combines deep penetration and cellular resolution in 3D[12]. It allows to study cell nuclei distributions without the sliding procedure deformation and renders information in 3D. With a resolution of 1 µm, LC-OCT is more accurate than standard Optical Coherence Tomography (OCT)[13] and presents an ideal resolution for nuclei segmentation. Reflectance Confocal Microscopy (RCM) images are very similar to LC-OCT images, except that they don't allow imaging in 3D. Pellacani et al.[14] showed that two by two comparisons of 2D RCM images could allow specialists to rank actinic keratosis by atypia in a similar order than with histopathology images. Such an approach does not allow to objectively define atypia nor systematically reproduce the results, and no absolute atypia score is generated, only a relative score among a fixed set of images.

This study proposes a novel automated approach based on deep learning segmentation applied to 3D LC-OCT images, capable of accurately assessing the amount of atypia in keratinocyte cancers. Our approach overcomes many of the limitations of existing studies. Our pipeline is non-invasive and therefore does not require biopsies. Atypia scores are calculated on 3D LC-OCT images and therefore do not suffer from the distortions and limitations of a 2D histology slide which is also a time consuming process whereas a 3D LC- OCT image can be acquired in 30 seconds. All features used to define cellular atypia are physically robust and easy to interpret, making the final score more reliable than that provided by "black box" algorithms.

Material

Line-field confocal optical coherence tomography (LC-OCT). Images of the study were collected using LC–OCT devices (DAMAE Medical, Paris) which produce—painlessly and non-invasively— vertically-oriented (histology-like) and horizontally-oriented (similar to Reflectance Confocal Microscopy (RCM)) sectional images as well as full 3D volume block images (Fig. 1). The LC-OCT technology uses a two-beam interfer-

	Healthy	Pathological	Subclinical AK	AK	Bowen
Number of patients	38	34	18	22	7
Number of woman (percentage)	38 (100%)	10 (29%)	2 (11%)	6 (27%)	2 (28%)
Number of lesions	114	71	34	30	7
Age (average ± standard deviation)	49.6±10.0	75.6±9.8	77.5±7.6	74.7±11.0	66±13.3
Positions					
Head/neck	90 (78%)	62 (88%)	34 (100%)	26 (87%)	2 (29%)
Trunk	12 (11%)	4 (6%)	0 (0%)	2 (7%)	2 (29%)
Upper extremities	12 (11%)	0 (0%)	0 (0%)	0 (0%)	0 (0%)
Lower extremities	0 (0%)	4 (6%)	0 (0%)	1 (3%)	3 (42%)

Table 1. Demographics of the healthy and pathological populations.

ence microscope with a supercontinuum laser as a class 1 light source at the center wavelength of 800 nm and a line-scan camera as a detector. LC-OCT measures the time of flight and amplitude of light backscattered from the tissue microstructures illuminated by a line of light. This new technology combines the OCT interferometry principle with the confocal spatial filtering of RCM. The vertical and horizontal sectional images are produced in real time at 8 frames per second. 3D stacks can be acquired for 3D reconstruction in approximately 30 s per stack. The images can be acquired up to a depth of ~ 500 µm. They have an axial resolution of 1.1 µm, a lateral resolution of 1.3 µm and a field of view of 1.2 mm × 0.4 mm (vertical) and 1.2 mm × 0.5 mm (horizontal). Complete technical details are described elsewhere[15–17].

Patients and volunteers. In order to compare healthy skin with pathological skin we retrospectively analyzed a total of 185 LC-OCT 3D images (Table 1). For lesional skin, we retrospectively collected consecutive cases of 35 patients from 4 hospitals—Hôpital Erasme (Belgium), Hospital Clinic Barcelona (Spain), University Hospital of Saint-Etienne (France), University of Siena (Italy)—imaged with LC-OCT 3D between January 2020 and May 2021 with an histopathologically confirmed diagnosis of Actinic Keratosis (AK), subclinical AK (SAK)—area surrounding the AK lesion within the field of cancerization—or Bowen disease and for which image quality was judged appropriate regarding KC visibility (entire epidermis visible without too thick hyperkeratosis). Healthy skin images have been acquired between February 2020 and January 2021 on healthy volunteers in Paris for DAMAE Medical internal research. All patients and volunteers gave informed consent for their images to be anonymously used in this study.

From a clinical standpoint Bowen's disease (Bowen) is the most severe pathology, followed by Actinic Keratosis (AK) and then the subclinical AK. Even though Bowen and AK are different diseases they present similarities and may represent the same disease process at different stages[18].

3D keratinocytes nuclei segmentation with Deep Learning. In order to detect cells and segment them individually, we used an instance segmentation approach. We trained a 3DStarDist[19] model, a deep learning architecture well suited for this problem as it learns directly on 3D images thanks to 3D convolutions and detects star-convex polyhedras similar to cell nuclei.

Each 3D LC-OCT image was segmented using our trained model as visualized in Fig. 1. In the combined images of this study, a total of more than 3.7 million nuclei were detected by the Deep Learning model with 2.5 millions nuclei from healthy images, 491000 in AK, 630000 in fields of cancerization and 95000 in Bowens. The predictions of the model have been reviewed and validated by an expert in LC-OCT image interpretation to ensure both good image quality and correct segmentation. More information about the training procedure and parameters can be found in the "Methods" section.

Physical and biological metrics based on 3D nuclei segmentation. Based on keratinocyte nuclei segmentations we can compute different physical, quantitative and reproducible metrics in order to analyse the differences between healthy and pathological skins. Being able to easily interpret those metrics is important for building trust in the final results for practitioners, as explainable Artificial Intelligence is now largely preferred to black-box models when it comes to anatomic pathology[20].

Graph based approach. Even though only cell nuclei are segmented from the LC-OCT images, the entire epidermis is actually filled with cells which closely adjoin each other[21]. A common modelization of this biological fact is done using Voronoi graphs. A Voronoi diagram[22,23] partitions the space into 3D regions (also called Voronoi cells) where each nucleus center is the closest center to its own region (see Fig. 1 for illustration). The Voronoi graph is created using Delaunay triangulation[24]. Nodes are defined as the centers of the nuclei, and edges connect each cell to its neighbours closer than 50 µm.

Cell level metrics. From the raw segmentations and the Voronoi graph, we created 13 cell level features described in Table 2. These biologically and physically relevant, easy to interpret features are taking advantage of the 3D structures of the segmentations. They allow a more complex and trustful representation than previous similar

Metric (feature name)	Description	Unit
Nucleus volume (volume)	Volume of the star-convex polyhedra detected by the StarDist model.	mm^3
Nucleus compactness (compactness)	A score that captures how close to a perfect sphere the detected nucleus is. It computes the area of a perfect sphere with the same volume as the detected nuclei and divides it by the actual area of the polyhedra: $\text{compactness} = \frac{(36 * \pi * V^2)^{1/3}}{A}$ A value close to 1 indicates that the nucleus is very close to a sphere, while a lower value indicates a nucleus with a flatter shape.	None
Volume over compactness ratio (volume_over_compactness)	Ratio between volume and compactness.	mm^3
Number of neighbours (nb_neighbours)	Inside the Voronoi graph, this is the number of edges for the node. This is the number of adjacent neighbours for the considered cell.	None
Average center to center distance from neighbours (neighbor_dist)	Average distance to cell neighbours, from center to center. This is also a proxy for the entire cell diameter, as the distance between two adjacent cells is the sum of both radiuses, and we perform over multiple neighbours in all directions. (see Fig. 1).	μm
Average border distance to neighbours (border_dist)	Average distance to neighbours, from border of the nucleus to border of the neighbour nucleus. This is a proxy for the cytoplasm thickness(see Fig. 1).	μm
Average border distance over center distance ratio (border_over_neigh_distances)	Accounts for the ratio of the volume taken by the nucleus within the entire cell. A small value indicates a comparatively large nucleus compared to the cytoplasm.	None
Neighbours average volumes (neighbours_avg_volumes)	Accounts for the average volume of the surrounding cells.	mm^3
Neighbours average compactness (neighbours_avg_compactness)	Accounts for the average compactness of the surrounding cells.	None
Neighbours standard deviation of volumes (neighbours_std_volumes)	Measures the differences in sizes of the neighbouring cells.	μm
Neighbours standard deviation of compactness (neighbours_std_compactness)	Measures differences in compactness of the neighbouring cells.	None
Neighbours volume ratio (volume_neigh_ratio)	Ratio of the nucleus volume to the average volume of its neighbours.	None
Neighbours compactness ratio (compactness_neigh_ratio)	Ratio of the nucleus compactness to the average compactness of its neighbours.	None

Table 2. Cell level metrics, list and descriptions.

work[7,25]. Furthermore, they are entirely derived from the 3D geometry of the detection of StarDist and do not use direct information from the original 3D image.

Image level metrics. The cellular level metrics can be aggregated to create image level metrics:

- *Cell density* (mm^{-2}): total number of cells divided by the en-face area, which corresponds to skin surface.
- *Average volumes, compactness and distance to neighbours*: the overall averages for volumes, compactness and distances to neighbours are computed for the entire image.
- *Standard deviations for volumes and compactness*: the overall standard deviations for volumes and compactness are computed on the entire image.

Cell level atypia definitions. To define atypia at the cellular level, we considered four approaches based on the quantitative metrics we obtained from deep learning segmentation (Table 2), extending previous qualitative studies on grading KC atypia with Reflectance Confocal Microscopy 2D images[14]. One simple, rule-based, expert definition is analysed while three Machine Learning based methods are also proposed.

All the approaches presented here share the same principle: atypia scores can be defined at cellular level thanks to the metrics derived from segmentations. Averaging these cell level atypia scores then gives a global atypia score to an entire 3D image. As we have the labels from histology for all the images, we can then compute a meaningful performance score at separating healthy versus pathological skins.

Rule based definition. Being able to segment and derive quantitative features at cellular level enable the use of rule-based definition for nucleus atypia. As an example of a simple rule, we define the following three criteria:

- Nuclei larger than 2.8×10^{-7} µm are potential atypia (top 10% of the largest detected nuclei in our data).
- Nuclei with a compactness smaller than 0.592 are potential atypia (top 10% of the least compact detected nuclei in our data).
- Nuclei with neighbours larger than 1.56×10^{-7} µm on average are potential atypias (top 10% of the largest detected neighbours in our data).

A cell will then be considered atypical if it meets at least two of these 3 criteria simultaneously.

Machine learning definitions. From the Machine Learning point of view, atypia detection can be seen as outlier detection[26]. The input features representing a nucleus are the feature derived from the segmentation and the output of the model is a binary score indicating whether a nucleus is atypical or not. Algorithms learn their own definition of atypia based on statistical evidence from the data. In this study, we consider two different approaches:

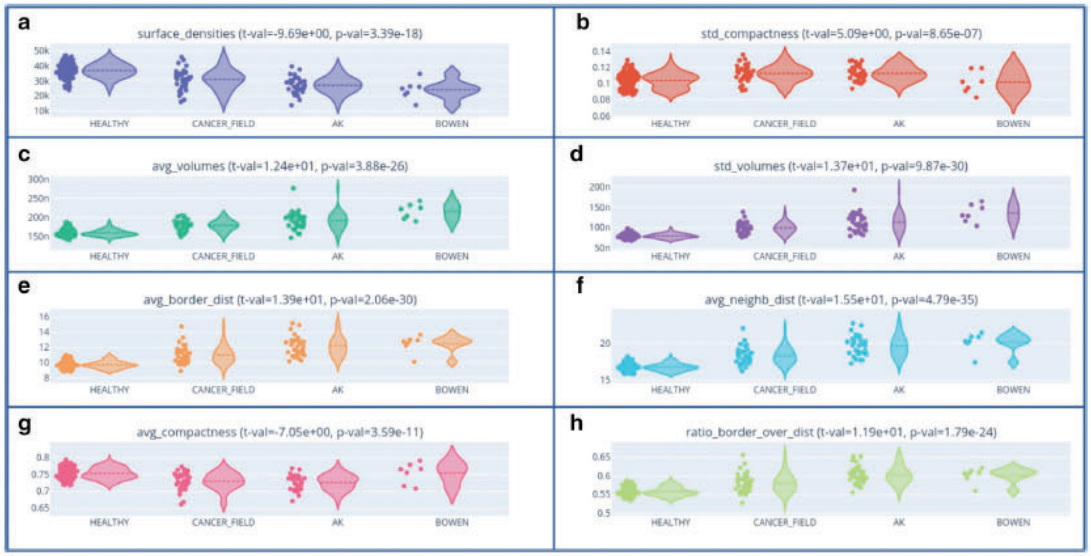

Figure 2. Global metrics per image with their corresponding t-values and p-values for the T-test for the means of two independent samples of scores.

- An unsupervised approach with the Isolation Forest algorithm[27], where atypia are simply considered as cells that look different from the majority of cells. No labels are needed for training the algorithm.
- A weakly-supervised approach, where the main assumption is that atypia mostly appear in pathological skin. During the training phase, all nuclei from pathological skin are considered atypical while all nuclei from healthy skin are considered healthy. Two different models are trained following this paradigm: a Logistic Regression[28] and a XGBoost[29].

Detailed explanations about the different algorithms, training procedures and outputs analysis can be found in the "Methods" section.

Reader study. To compare the automated models to medical experts, we asked three dermatologists, highly experienced in non-invasive imaging, to review and assess an atypia score for each 3D image. The images are presented to the experts as two short videos, en-face and en-coupe views, spanning the entire 3D image.

Experts were asked to assess 3 criteria both on horizontal and vertical images (atypia related to the shape, size and spatial spread of atypia nuclei) using a scale from 0 to 4 (0 meaning no irregularities, 1 if less than 25%, 2 if between 25 and 50%, 3 between 50 and 75% and 4 if more than 75% of nuclei are irregular).

In total, 6 scores were given for each of the 185 LC-OCT 3D images of the study. For each score, a higher value indicates a higher degree of atypia. When summing all the scores, this gives a global atypia score ranging from 0 to 24. The score is normalized between 0 and 1 and compared to the Machine Learning based scores. A medical consensus score is computed by averaging the scores of each reviewer.

Statistical tools. Classical statistical tools were used to analyse the different results of the study. To compare metrics between the healthy and pathological skins we used a T-test for the means of two independent samples of scores using scipy[30]. To compute the correlation between the scores of the different methods we used the Pearson correlation also using scipy.

Results

Statistically significant differences at image level. A T-test analysis of the image level metrics shows statistically significant differences between healthy and pathological populations (Fig. 2). Positive t-values indicate larger values for the pathological population than the healthy population while negative value indicate the opposite.

Healthy skins have a higher cell density than pathological ones (Fig. 2a : t-value = 9.69, p-value = 3.39×10^{-18}) and larger nuclei compared to their cytoplasm as shown by a lower border to border distance over center to center distance ratio. (Fig. 2h: t-value = 11.9, p-value = 1.79×10^{-24}).

However pathological skins have larger nuclei in terms of volumes (Fig. 2c : t-value = 1.24, p-value = 3.88×10^{-26}). Moreover smaller and larger nuclei coexist in pathological skins while volumes are more uniform in

	XGBoost	Simple Rule	Logistic Regression	Isolation Forest	Medical Consensus	Expert 1	Expert 2	Expert 3
Healthy vs pathological	0.982	0.965 (0.92, $p = 4e \times 10^{-78}$)	0.970 (0.98, $p = 1.7 \times 10^{-128}$)	0.971 (0.88, $p = 3.7 \times 10^{-62}$)	0.766 (0.66, $p = 4 \times 10^{-24}$)	0.715 (0.45, $p = 9 \times 10^{-11}$)	0.745 (0.54, $p = 2 \times 10^{-15}$)	0.708 (0.47, $p = 8 \times 10^{-12}$)
Healthy vs AK and Bowen	0.991	0.968 (0.92, $p = 3 \times 10^{-67}$)	0.979 (0.98, $p = 9.9 \times 10^{-112}$)	0.978 (0.89, $p = 9.5 \times 10^{-54}$)	0.952 (0.75, $p = 1 \times 10^{-29}$)	0.828 (0.52, $p = 4 \times 10^{-12}$)	0.924 (0.63, $p = 5 \times 10^{-18}$)	0.839 (0.53, $p = 2 \times 10^{-12}$)
Healthy vs subclinical AK	0.972	0.962 (0.84, $p = 1 \times 10^{-40}$)	0.960 (0.96, $p = 8 \times 10^{-84}$)	0.964 (0.78, $p = 2 \times 10^{-31}$)	0.563 (0.27, $p = 6 \times 10^{-4}$)	0.592 (0.12, $p = 1 \times 10^{-1}$)	0.550 (0.21, $p = 1 \times 10^{-2}$)	0.564 (0.18, $p = 1 \times 10^{-2}$)

Table 3. AUC scores for different subsets of the data for different methods (and their Pearson correlation to XGBoost and p-values).

healthy skins as shown by a higher standard deviation of volumes (Fig. 2d: t-value = 13.7, p-value = 9.87×10^{-30}). Pathological cells are also less compact (spherical) on average than healthy cells (Fig. 2g: t-value = 7.05, p-value = 3.59×10^{-11}) with more diversity in terms of compactness as shown by standard deviation of compactness (Fig. 2b: t-value = 5.09, p-value = 8.65×10^{-7}). Distances between nuclei from border to border (Fig. 2e: t-value = 13.9, p-value = 2.06×10^{-30}) and from center to center (Fig. 2f: t-value = 15.5, p-value = 4.79×10^{-35}) are greater for pathological skins.

Discrimintative power of automated cell level atypia definitions. By averaging the individual nuclei scores by 3D images for each method, we can compare the discriminative powers of the rule-based, the unsupervised and the weakly-supervised models to differentiate between healthy skin on one hand and pathological skin (AK, SAK or Bowen) on the other. These scores are computed at image level and compared to histopathology groundtruth results. As shown in Fig. 4, all Machine Learning approaches show a better discriminative power than the rule-based approach (AUC = 0.965), with an AUC of 0.970 for the Logistic Regression, 0.971 for the Isolation Forest and 0.982 for XGBoost. Overall, the weakly-supervised models are outperforming the unsupervised one.

Automated methods outperform medical experts assessing an atypia score. The medical consensus of experts from the reader study achieves an AUC score of 0.766 for the entire dataset (while individual expert have scores ranging from 0.708 to 0.745), under-performing automated scores by more than 20 points of AUC (Fig. 4). Nevertheless statistically significant positive Pearson correlations of 0.647 ($p = 2.7 \times 10^{-23}$), 0.592 ($p = 6.7 \times 10^{-19}$) and 0.657 ($p = 4.1 \times 10^{-24}$) can be observed with the Logistic Regression, the Isolation Forest and XGBoost respectively. In more details, as shown on Table 3, medical consensus is good at differentiating between healthy skin and AK or Bowen, where there is a clear-cut visible difference of atypia within images, with an AUC of 0.952, which is only slightly worse than the automated approaches (ranging from 0.968 to 0.991). However, medical consensus can hardly discriminate between healthy skin and field of cancerization with an AUC of 0.573. Looking at each of the 6 different scores individually yields similar results.

Discussion

In this study, we demonstrated the ability to apply deep learning models to segment nuclei on LC-OCT 3D images which is an impossible task for humans in a reasonable amount of time. The inference time of around 3 minutes of the deep learning model for a fully automated procedure could allow physician to benefit from all the results presented in this study during their daily practice.

The metrics derived from the segmentations at image level showed statistical differences which are intuitive to clinical experts : pathological skins often present larger, less spherical nuclei, with more heterogeneity. The ability to precisely measure those intuitive metrics is an important step towards objective measurements and standardized clinical decisions.

The cohort used for this study is of a moderate size but 185 3D images are sufficient to obtain significant results to compute and compare discriminative powers of the different atypia scoring methods. Even though the two populations do suffer some biases, the hypothesis validated by medical experts was that the differences between lesional and non-lesional epidermis exceed by far the variability of epidermis that may be attributed to the age, gender and localization differences in between our two cohorts. Moreover, the automated pipeline used in this study only uses the raw images without taking into account any of these parameters.

Defining what cellular atypia or dysplasia means is a difficult task since these concepts rely on the expertise of pathologists and not on quantitative metrics[31]. Nevertheless, we showed that a simple rule-based definition of atypia can quantify atypia with a better precision than medical experts.

With a similar rule-based approach, more complex rules could be defined by experts in order to get definitions of atypia with better discriminative powers. Moreover, it would be possible, as a direct extension of this work, to apply several rule-based classifications derived from expert knowledge to distinguish between different kinds of atypia. These definitions apply at cell level and can be used to highlight atypia during a clinical review as shown in Fig. 3.

Nevertheless, expert rules are not complex enough to model the interactions between 13 features and may result in an overly simplified definition of atypia. That is why data-driven definitions of atypia based on Machine Learning show better performances than rule-based methods. The more complex the model the harder it is to interpret, and there is always a trade-off between interpretability and performance. However, it is possible to

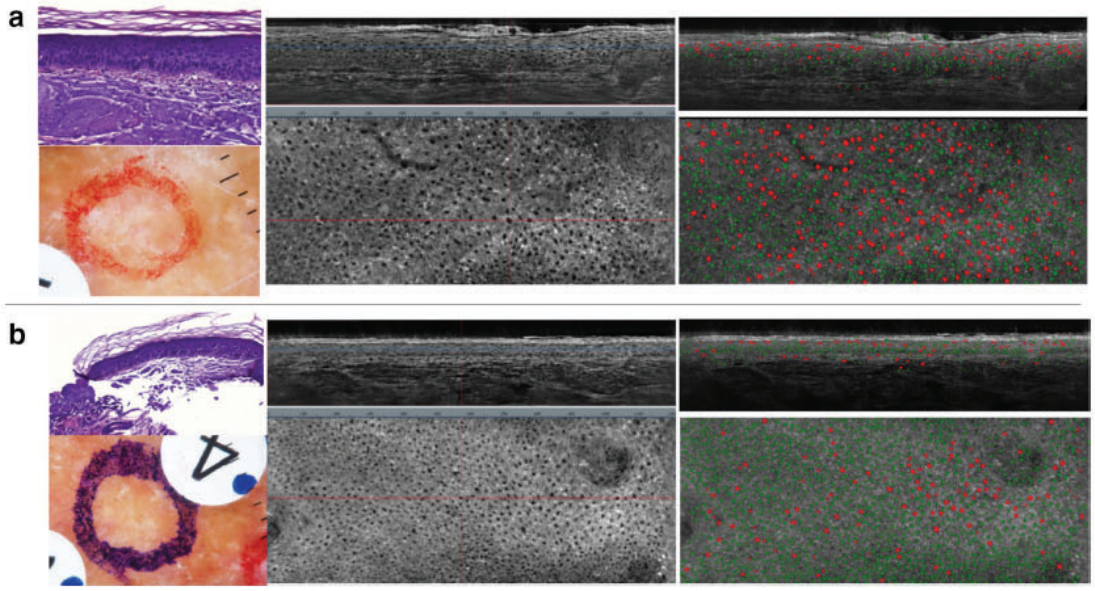

Figure 3. Example of atypia detections (in red) and normal nulcei (in green) with the simple rule-based atypia definition for one AK lesion (**a**) and its perilesional field of cancerization (**b**).

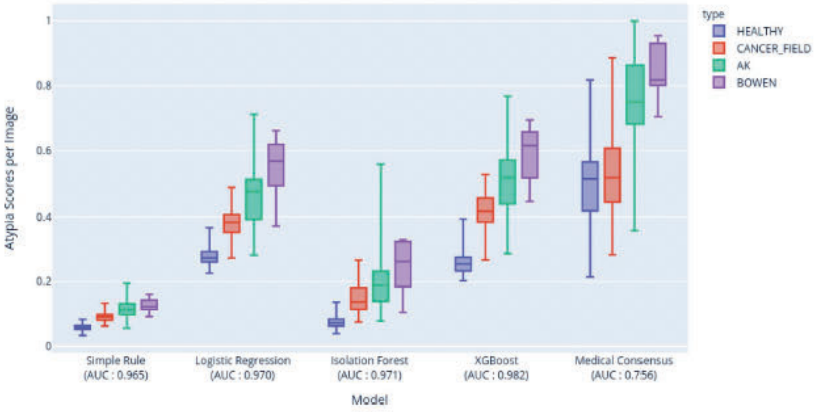

Figure 4. Box plots (min, max, median, q1, q3) of average atypia score per stack for different methods including medical consensus from the reader study. The medical consensus has a much lower AUC score than the other automated methods.

analyse the feature importance for each model as shown in Fig. 5 to give more trust to the practitioners in the automated scores.

For the Logistic Regression, the perfect prototype for an atypical cell is a large (both large nucleus volume and cytoplasm radius), non spherical (low compactness) cell, surrounded by a few large cells as neighbours. For the XGBoost algorithm, the perfect prototype for an atypical cell is also large cell surrounded by a few heterogeneous cells in terms of sizes as shown in Fig. 5c,d. For the Isolation Forest 4 features are mostly used to define atypia (Fig. 5b): the volume ratio with neighbouring cells, the distance and number of neighbouring cells and the cytoplasm size.

Even though the definitions of atypia are different for each model they are highly correlated between each other: the Logistic Regression has a Pearson correlation coefficient at the global atypia level of 0.98 and 0.95 with XGBoost and the simple rule respectively while the Isolation Forest has a correlation of 0.93, 0.88 and 0.91 with the simple rule, the Logistic Regression and XGBoost respectively. These correlations suggest that the most

Figure 5. Models atypia definition interpretability: (**a**) Logistic regression model weights (**b**) Isolation Forest global feature importance (**c**) XGBoost Shapley values (**d**) XGBoost global feature importance.

complex and best performing algorithm can be safely used without losing the general understanding of what atypia intuitively means. Moreover it is remarkable that for the four automated approaches, we see that (Fig. 4) the ranking between subclinical AK, AK and Bowen is aligned with the expected clinical output with growing scores of atypia, while no distinction was made between them during training.

The medical consensus defined in the reader study, only created from the scoring of three experts, is not designed to accurately quantify the capacity of human experts on this task. It is rather meant to give an overview of how hard it is for the human eyes to grasp information from so many nuclei in 3D and assign to it a global score of atypia. We can see from Table 3 that the medical consensus reaches a decent score when comparing clear-cut lesions: healthy skin versus AK and Bowen. The consensus has a statistically significant correlation with XGBoost scores of 0.66. However, the performances and level of correlation to XGBoost drops when comparing healthy skin versus subclinical AK which is a harder task. The same observation as for the consensus results can be made for each expert individually but averaging the scores to create medical consensus significantly improves the results compared to individual contributions, slightly lowering the gap between automated approach and individual expert scores. These results show that subtle differences are really difficult to be accurately quantified by human experts while automated methods still perform at a very high level. Since detecting cancers as early as possible is beneficial for treatment and survival chances, it's particularly important to improve on non clear-cut lesions. The fact that our methods outperform individual experts and the medical consensus show that a precise automated atypia score would be a precious piece of information for clinicians to assist them in making their diagnoses in the best interest of their patients.

We believe that this technology, able to obtain a reproducible atypia score, robust to subtle changes, in a few minutes and non-invasively brings a response to two of the currently unmet needs for AK treatments according to the International Dermatology Outcome Measures[32]: the measurement of AK in clinical practice and the outcomes of clinical trials. It opens a wide range of promising applications. For the dermatologists it will add a powerful assistance to quantify the level of atypia of a lesion but also to precisely monitor the evolution of a lesion overtime. For medical research on cancer treatment, it will allow quantitative analysis of treatment efficiency. A standardized metric can also help compare results of different treatments between each other.

Further research should focus on applying similar approach to different pathologies. In particular, targeting melanocytes instead of keratinocytes alongside with designing problem specific features (e.g. using the pixel intensity to characterize melanin) is a promising path for the assisted diagnosis of melanoma skin cancers. Another path we wish to follow is the use of our work to demonstrate the efficiency of a cancer treatment in a clinical trial.

Methods

The study was approved by the ethical committee of the university hospital of Saint-Etienne (NCT0.3731247) and was conducted in accordance with the ethical principles of the Helsinki Declaration.

Deep Learning: StarDist training procedure. A 3D image of in-vivo skin with a field of view of 0.4mm × 0.5mm × 1.2mm can contain tens of thousands of keratinocytes inside the epidermis. Annotating them in 3D is a very tedious and complicated task but is absolutely mandatory in order to train a deep learning algorithm.

A semi-automatic software developed by DAMAE Medical allowed human experts to annotate 50 healthy LC-OCT 3D images coming from different volunteers, on different body sites and 20 pathological skins so that atypical nuclei are available to the algorithm during training. All the training images are completely disjoint of the images of this study.

This amount of data might not seem huge, but there are multiple reasons why the training of a deep learning algorithm is feasible here:

- Annotated 3D images are much larger than the training patch size (60 × 128 × 128): a 3D images of size 300 × 400 × 1200 contains approximately 150 non-overlapping 60 × 128 × 128 patches. This represents more than ten thousand different training patches.
- One training patch contains hundreds of nuclei, so overlapping patches are still very different images, making the actual × 150 cropping boost much bigger.
- Data augmentations (randoms flips, intensity changes, crops and zooms) prevent overfitting and allow the model to learn essential features to detect nuclei.

We used the open source library [https://github.com/stardist/stardist] of the original StarDist[19,33] paper to train our own 3D StarDist model for LC-OCT 3D images. The model is trained for 200 epochs with a batch size of 2 and an exponential learning rate decay of 0.8 every 10 epochs, the best iteration on the validation set (20% of the stacks) is kept for the final model. The Non-Maximum-Suppression (NMS) algorithm applied at post-processing enforces the detection of non-overlapping cells. In order to allow adjacent cells to be detected, the NMS threshold was set to 0.05 (meaning that two detected cells can't overlap on more than 5% of their volumes). Each detected nucleus is represented by a central position and 96 rays of different length providing an accurate 3D representation of the nucleus with a large variety of possible shapes.

Stratified 5-fold cross validation. For all the experiments where a Machine Learning algorithm was trained to score atypia, 5-fold stratified cross-validation was performed at the image level. At first, the 185 LC-OCT 3D images are separated into 5 folds, each of them containing a similar proportion of healthy and pathological images, then a model is trained using nuclei coming from 4 folds and validated on completely unseen images belonging to the last fold. This represents a total of more than 3.7 million cells to be classified as normal or atypical. This approach allows to observe reliable results across the entire database limiting the risks of overfitting compared to using a predetermined subset used as hold-out validation[34].

Unsupervised approach. The unsupervised approach uses no labels and no prior assumption about cellular atypia. The idea is to analyze all the detected nuclei from both healthy and pathological skins and derive a mathematical frontier separating 'normal' nuclei from 'outliers' (or atypia).

We used the Isolation Forest algorithm to see if nuclei isolated by the algorithm were predominant in pathological 3D images. Even though this approach does not require any label, the 5 fold cross-validation scheme was used to allow a fair comparison with the weakly-supervised learning approach. We used scikit-learn's[35] implementation with default parameters.

Without supervision, the notion of outlier learnt by the model could be completely different from cellular atypia. However the high discriminative power (AUC = 0.971 as shown in Table 3) of the aggregated results at the image level gives a good guarantee that outliers detected by the model are indeed atypical cells.

In order to better understand what is considered as atypical for the model we derived the global feature importance of the model[36]. Figure 5b shows that the 4 most important features are related to neighbouring cells, giving interesting hints of its definition of atypia.

However, the Isolation Forest is a quite complex Machine Learning model (based on a Random Forest and the number of splits required to predict an instance), so its definition of atypia cannot be easily summed up in one sentence as feature interactions play an important role in the model decisions. Using a simpler model in a supervised setting is a good way to overcome this issue as discussed below.

Weakly-supervised approach. A fully supervised approach for this study would need one label per detected cell, this means more than 3.7 million labels done by human experts, which is infeasible. Moreover, no perfect ground truth could be achieved since the visual definition of atypia remains blurry. The weakly-supervised approach hence only uses a simple prior assumption: atypia must be significantly more frequent within pathological skin than healthy skin.

In this setting, nuclei from pathological images are all considered as atypia while nuclei from healthy images are considered healthy. Even though this might seem a very naive proxy for atypia, this kind of weakly-supervised approach have already been successfully used for detection of visual anomalies in histology images[37]. Since we have the clinical diagnoses for each image, we can use them to create weak labels.

Logistic regression. In order to be able to easily understand the final model of the weakly-supervised approach we trained a simple Machine Learning model: a logistic regression[28]. Logistic Regression is probably the simplest yet powerful algorithm for binary classification. It has the advantage of being easily comprehensible thanks to its closed form prediction function

$$p = \sigma(\beta_0 + \beta_1 x_1 + \cdots + \beta_n x_n)$$

with p being the probability of being an atypia, x_i the input features, σ the sigmoid function and β_i the learnt parameters. Before training, features are normalized to get 0-mean and standard deviation of 1. This is done following the safe cross validation procedure in order to get reliable results : standardization is done with training statistics and the validation set is transformed accordingly. As we have weak labels, the default scikit-learn's[35] parameters are used without need for hyper-parameter tuning nor risks of overfitting.

Using 5 fold cross-validation at image level, we can predict for each nucleus an atypia score between 0 and 1. Having a continuous probability as atypia score allows to set up a binary threshold to detect atypia. The choice of this threshold could allow us to sharpen our definition of atypia, for example a threshold of 0.5 will consider more nuclei as atypical when a threshold of 0.9 will only detect the most atypical nuclei. The results shown in Fig. 4 are obtained using a simple averaging of all cells predictions, without thresholding.

Moreover, we can use the fitted parameters of the logistic regression to understand what atypia means for the trained model. Figure 5a shows the model weights: the larger the absolute value the more impact the feature has on the final decision. Positive weights mean positively correlated impact (a larger value of the feature means a larger atypia score) while negative weights mean the opposite. We can understand in depth how atypia is defined by the model. Cytoplasm ratio (border to border distance divided by center to center distance), nucleus volume and neighbours volumes are positively correlated to atypia while neighbours distance, number of neighbours and volume over compactness are negatively correlated to atypia.

XGBoost. XGBoost[29] is based on gradient boosted trees method and is one the best algorithm to solve tabular data tasks. It has a much bigger modeling capacity than a logistic regression and heavily relies on feature interactions. It outperformed all other approaches for this study with an AUC score of 0.982 . Because of the weak labels paradigm, no tuning has been performed and a simple model with 200 estimators (no early stopping), a depth of 5 and sub sample rate of 0.5 was used.

Despite the complexity of the model, it is interpretable thanks to shapley values[38] as shown in Fig. 5c. This graph allows a similar interpretation as a logistic regression, although more sophisticated. We can see that cytoplasm ratio, volumes and standard deviations of neighbours are positively correlated to atypia score while distance to neighbours, compactness and number of neighbours are negatively correlated to atypia score.

Received: 12 October 2021; Accepted: 22 December 2021
Published online: 10 January 2022

References

1. Geetha, K., Leeky, M., Narayan, T., Sadhana, S. & Saleha, J. Grading of oral epithelial dysplasia: Points to ponder. *J. Oral Maxillofac. Pathol.* **19**, 198 (2015).
2. Bulten, W. *et al.* Automated deep-learning system for gleason grading of prostate cancer using biopsies: A diagnostic study. *Lancet Oncol.* **21**, 233–241 (2020).
3. Hou, L. *et al.* Dataset of segmented nuclei in hematoxylin and eosin stained histopathology images of ten cancer types. *Sci. Data* **7**, 1–12 (2020).
4. Waliszewski, P., Wagenlehner, F., Gattenlöhner, S. & Weidner, W. On the relationship between tumor structure and complexity of the spatial distribution of cancer cell nuclei: A fractal geometrical model of prostate carcinoma. *The Prostate* **75**, 399–414 (2015).
5. Kendall, T. J., Duff, C. M., Thomson, A. M. & Iredale, J. P. Integration of geoscience frameworks into digital pathology analysis permits quantification of microarchitectural relationships in histological landscapes. *Sci. Rep.* **10**, 1–16 (2020).
6. Lu, C. *et al.* A prognostic model for overall survival of patients with early-stage non-small cell lung cancer: A multicentre, retrospective study. *Lancet Digit. Health* **2**, e594–e606 (2020).
7. Jiao, Y., Berman, H., Kiehl, T.-R. & Torquato, S. Spatial organization and correlations of cell nuclei in brain tumors. *PLoS ONE* **6**, e27323 (2011).
8. Zhou, Y. *et al.* Cgc-net: Cell graph convolutional network for grading of colorectal cancer histology images. In *Proceedings of the IEEE/CVF International Conference on Computer Vision Workshops* (2019).
9. Jansen, I. *et al.* Histopathology: Ditch the slides, because digital and 3d are on show. *World J. Urol.* **36**, 549–555 (2018).
10. Newton, V. *et al.* Novel approaches to characterize age-related remodelling of the dermal-epidermal junction in 2d, 3d and in vivo. *Skin Res. Technol.* **23**, 131–148 (2017).
11. Kiemen, A. *et al.* In situ characterization of the 3d microanatomy of the pancreas and pancreatic cancer at single cell resolution. *bioRxiv* https://doi.org/10.1101/2020.12.08.416909 (2020).
12. Ogien, J., Daures, A., Cazalas, M., Perrot, J.-L. & Dubois, A. Line-field confocal optical coherence tomography for three-dimensional skin imaging. *Front. Optoelectron.* **13**, 381–392 (2020).
13. Adabi, S. *et al.* Universal in vivo textural model for human skin based on optical coherence tomograms. *Sci. Rep.* **7**, 1–11 (2017).
14. Pellacani, G. *et al.* Grading keratinocyte atypia in actinic keratosis: A correlation of reflectance confocal microscopy and histopathology. *J. Eur. Acad. Dermatol. Venereol.* **29**, 2216–2221 (2015).
15. Dubois, A. *et al.* Line-field confocal time-domain optical coherence tomography with dynamic focusing. *Optics express* **26**, 33534–33542 (2018).
16. Dubois, A. *et al.* Line-field confocal optical coherence tomography for high-resolution noninvasive imaging of skin tumors. *J. Biomed. Opt.* **23**, 106007 (2018).
17. Ogien, J., Levecq, O., Azimani, H. & Dubois, A. Dual-mode line-field confocal optical coherence tomography for ultrahigh-resolution vertical and horizontal section imaging of human skin in vivo. *Biomed. Opt. Express* **11**, 1327–1335 (2020).
18. Cockerell, C. J. Histopathology of incipient intraepidermal squamous cell carcinoma (actinic keratosis). *J. Am. Acad. Dermatol.* **42**, S11–S17 (2000).
19. Weigert, M., Schmidt, U., Haase, R., Sugawara, K. & Myers, G. Star-convex polyhedra for 3d object detection and segmentation in microscopy. *IEEE Winter Conf. Appl. Comput. Vis.* https://doi.org/10.1109/WACV45572.2020.9093435 (2020).
20. Tosun, A. B. *et al.* Explainable ai (xai) for anatomic pathology. *Adv. Anat. Pathol.* **27**, 241–250 (2020).
21. Boer, M., Duchnik, E., Maleszka, R. & Marchlewicz, M. Structural and biophysical characteristics of human skin in maintaining proper epidermal barrier function. *Adv. Dermatol. Allergol./Postepy Dermatologii Alergologii* **33**, 1 (2016).
22. Virtanen, P. *et al.* fundamental algorithms for scientific computing in python. Scipy 1.0. *Nat. Methods* **17**, 261–272 (2020).

23. Aurenhammer, F. & Edelsbrunner, H. An optimal algorithm for constructing the weighted Voronoi diagram in the plane. *Pattern Recogn.* **17**, 251–257 (1984).
24. Delaunay, B. *et al.* Sur la sphere vide. *Izv. Akad. Nauk SSSR, Otdelenie Matematicheskii i Estestvennyka Nauk* **7**, 1–2 (1934).
25. Chang, C.-K. *et al.* Segmentation of nucleus and cytoplasm of a single cell in three-dimensional tomogram using optical coherence tomography. *J. Biomed. Opt.* **22**, 036003 (2017).
26. Hodge, V. & Austin, J. A survey of outlier detection methodologies. *Artif. Intell. Rev.* **22**, 85–126 (2004).
27. Liu, F. T., Ting, K. M. & Zhou, Z.-H. Isolation forest. In *2008 Eighth IEEE International Conference on Data Mining* 413–422, https://doi.org/10.1109/ICDM.2008.17 (2008).
28. Kleinbaum, D. G., Dietz, K., Gail, M., Klein, M. & Klein, M. *Logistic Regression.* (Springer, 2002).
29. Chen, T. & Guestrin, C. XGBoost: A scalable tree boosting system. In *Proceedings of the 22nd ACM SIGKDD International Conference on Knowledge Discovery and Data Mining*, KDD '16, 785–794. https://doi.org/10.1145/2939672.2939785 (ACM, 2016).
30. Virtanen, P. *et al.* Fundamental algorithms for scientific computing in python. SciPy 1.0. *Nat. Methods* **17**, 261–272. https://doi.org/10.1038/s41592-019-0686-2 (2020).
31. Sanfrancesco, J., Jones, J. S. & Hansel, D. E. Diagnostically challenging cases: What are atypia and dysplasia?. *Urol. Clin. North Am.* **40**, 281 (2013).
32. Kohn, A. H. *et al.* International dermatology outcome measures (ideom): Report from the 2020 annual meeting. *Dermatology.* https://doi.org/10.1159/000518966 (2021).
33. Schmidt, U., Weigert, M., Broaddus, C. & Myers, G. Cell detection with star-convex polygons. In *International Conference on Medical Image Computing and Computer-Assisted Intervention* 265–273 (Springer, 2018).
34. Bengio, Y. & Grandvalet, Y. No unbiased estimator of the variance of k-fold cross-validation. *J. Mach. Learn. Res.* **5**, 1089–1105 (2004).
35. Pedregosa, F. *et al.* Scikit-learn: Machine learning in Python. *J. Mach. Learn. Res.* **12**, 2825–2830 (2011).
36. Carletti, M., Masiero, C., Beghi, A. & Susto, G. A. Explainable machine learning in industry 4.0: Evaluating feature importance in anomaly detection to enable root cause analysis. In *2019 IEEE International Conference on Systems, Man and Cybernetics (SMC)* 21–26 (IEEE, 2019).
37. Campanella, G. *et al.* Clinical-grade computational pathology using weakly supervised deep learning on whole slide images. *Nat. Med.* **25**, 1301–1309 (2019).
38. Lundberg, S. M. & Lee, S.-I. A unified approach to interpreting model predictions. In *Advances in Neural Information Processing Systems 30* (eds Guyon, I. *et al.*) 4765–4774 (Curran Associates Inc, New York, 2017).

Author contributions

S.F. conducted the experiments, implemented the features, trained the algorithms and wrote the article. T.V. discussed and validated the machine learning approaches. J.L.P, J.P.A, M.S, E.C and L.T acquired the LC-OCT images and collected histologic diagnosis. J.M., E.C., L.T., J.P.A., M.S. and J.L.P designed the reader study and validated the results. L.T., J.P.A. and A.D.N. performed the reader study. All authors discussed the results and commented on the manuscript.

Competing interests

A.D is co-founder of DAMAE Medical. S.F. and T.V are employed by DAMAE Medical. V.M received a grant from DAMAE Medical in April 2019 not related to this work. All other authors declare no competing interests.

Additional information

Correspondence and requests for materials should be addressed to S.F.

Reprints and permissions information is available at www.nature.com/reprints.

Publisher's note Springer Nature remains neutral with regard to jurisdictional claims in published maps and institutional affiliations.

PUBLICACIÓN N° 6:[70]

Caracterización del carcinoma basocelular mediante microscopía confocal *ex vivo* de fusión: un cambio prometedor en la histopatología cutánea.
Basal cell carcinoma characterization using fusion *ex vivo* confocal microscopy: a promising change in conventional skin histopathology.

Javiera Pérez-Anker, Simone Ribero, Oriol Yélamos, Adriana García-Herrera, Llúcia Alos, Beatriz Alejo, Marc Combalia, David Moreno-Ramírez, Josep Malvehy, Susana Puig

Br J Dermatol. 2020 Feb;182(2):468-476. doi: 10.1111/bjd.18239.
Factor de impacto: 9.302

Resumen
Antecedentes: La MCev trabaja bajo dos modos de visualización, la fluorescencia y la reflectancia, lo que permite la visualización de diferentes estructuras en cada láser. El láser de fluorescencia (MCF) requiere un agente de contraste y se ha utilizado para el análisis de carcinomas basocelulares (CBC) durante la cirugía de Mohs. Por el contrario, el láser de reflectancia (MCR) se usa principalmente para el diagnóstico *in vivo* de tumores cutáneos equívocos. Recientemente, se ha desarrollado un nuevo microscopio confocal *ex vivo* más rápido, que utiliza simultáneamente ambos láseres (modo de fusión).
Objetivos: Describir las características del CBC identificadas en los modos de reflectancia, fluorescencia y fusión, utilizando este novedoso dispositivo. Determinar

el mejor modo de identificar las características del CBC. Desarrollar un nuevo protocolo de tinción para mejorar la visualización del CBC en los diferentes modos.
Métodos: Desde septiembre de 2016 hasta junio de 2017, incluimos prospectivamente CBCs consecutivos, que fueron extirpados mediante cirugía de Mohs en nuestro servicio. Las lesiones se evaluaron usando MCev después de la cirugía de Mohs. Las muestras se tiñeron primero con naranja de acridina y luego se tiñeron con ácido acético y naranja de acridina para ser comparadas.
Resultados: Incluimos 78 CBCs (35 infiltrantes, 25 nodulares, 12 micronodulares, 6 superficiales). La mayoría de las características se visualizaron mejor con el modo de fusión, utilizando la doble tinción. También identificamos nuevas características MCev, como las células dendríticas y los macrófagos, que no se habían informado anteriormente en esta técnica.
Conclusiones: Nuestros resultados sugieren que las características de los núcleos se visualizan mejor en MCF, pero el citoplasma y el estroma circundante se visualizan mejor en MCR. Así, la evaluación simultánea de reflectancia y fluorescencia parece ser beneficiosa debido a su efecto complementario y la doble tinción permite la percepción de estructuras antes no observadas.

GENERAL DERMATOLOGY

BJD
British Journal of Dermatology

Basal cell carcinoma characterization using fusion *ex vivo* confocal microscopy: a promising change in conventional skin histopathology

J. Pérez-Anker,[1] S. Ribero,[1,2] O. Yélamos,[1] A. García-Herrera,[3] L. Alos,[3] B. Alejo,[1] M. Combalia,[1] D. Moreno-Ramírez,[1] J. Malvehy[1,4] and S. Puig[1,4]

Departments of [1]Dermatology (Melanoma Unit) and [3]Pathology; Hospital Clinic of Barcelona, IDIBAPS, University of Barcelona, Villarroel 170, 08036, Barcelona, Spain

[2]Medical Sciences Department, Section of Dermatology, University of Turin, Turin, Italy

[4]Centro de Investigación Biomédica en Red (CIBER) de enfermedades raras, Madrid, Spain

Summary

Background Ex vivo confocal microscopy (CM) works under two modes, fluorescence and reflectance, allowing the visualization of different structures. Fluorescence CM (FCM) requires a contrast agent and has been used for the analysis of basal cell carcinomas (BCCs) during Mohs surgery. Conversely, reflectance CM (RCM) is mostly used for in vivo diagnosis of equivocal skin tumours. Recently, a new, faster ex vivo confocal microscope has been developed which simultaneously uses both lasers (fusion mode).

Objectives To describe the BCC features identified on reflectance, fluorescence and fusion modes using this novel device. To determine the best mode to identify characteristic BCC features. To develop a new staining protocol to improve the visualization of BCC under the different modes.

Methods From September 2016 to June 2017, we prospectively included consecutive BCCs which were excised using Mohs surgery in our department. The lesions were evaluated using ex vivo CM after routine Mohs surgery. The specimens were first stained with acridine orange and then stained using both acetic acid and acridine orange.

Results We included 78 BCCs (35 infiltrative, 25 nodular, 12 micronodular, 6 superficial). Most features were better visualized with the fusion mode using the double staining. We also identified new CM ex vivo features, dendritic and plump cells, which have not been reported previously.

Conclusions Our results suggest that nuclei characteristics are better visualized in FCM but cytoplasm and surrounding stroma are better visualized in RCM. Thus, the simultaneous evaluation of reflectance and fluorescence seems to be beneficial due to its complementary effect.

Correspondence

Susana Puig.
E-mail: susipuig@gmail.com; spuig@clinic.cat

Accepted for publication

17 June 2019

Funding sources

The research at the Melanoma Unit at the Hospital Clinic of Barcelona is partially funded by Spanish Fondo de Investigaciones Sanitarias grants PI15/00716 and PI15/00956; CIBER de Enfermedades Raras of the Instituto de Salud Carlos III, Spain, co-financed by the European Development Regional Fund 'A way to achieve Europe'; AGAUR 2014_SGR_603 of the Catalan Government, Spain; European Commission under the 6th Framework Programme, Contract No. LSHC-CT-2006-018702 (GenoMEL) and by the European Commission under the 7th Framework Programme, Diagnoptics; The National Cancer Institute (NCI) of the U.S. National Institutes of Health (NIH) (CA83115); a grant from 'Fundació La Marató de TV3' 201331-30, Catalonia, Spain; a grant from 'Fundación Científica de la Asociación Española Contra el Cáncer' GCB15152978SOEN, Spain, and CERCA Programme / Generalitat de Catalunya. Part of the work was carried out at the Esther Koplowitz Center, Barcelona. The whole-exome sequencing analysis was in part supported by the intramural research programme of the NIH, NCI, Division of Cancer Epidemiology and Genetics.

Conflicts of interest

None declared.

DOI 10.1111/bjd.18239

What's already known about this topic?

- Ex vivo fluorescent confocal microscopy (FCM) is an imaging technique that allows histopathological analysis of fresh tissue.
- FCM is faster – at least one-third of the time – than conventional methods.
- FCM has a sensitivity of 88% and a specificity of 99% in detecting basal cell carcinomas (BCCs).

What does this study add?

- Reflectance and fluorescence modes can be used simultaneously in a new ex vivo CM device.

- Each mode complements the other, resulting in an increase in the detection of BCC features in fusion mode.
- A combined staining using acetic acid and acridine orange enhances the visualization of tumour and stroma without damaging the tissue for further histopathological analysis.

Paraffin-embedded blocks have been used in conventional histopathology for a century.[1] Imaging technologies such as confocal microscopy (CM) have made definitive changes in dermatological and histopathological diagnosis in recent decades. Reflectance CM (RCM) has been shown to provide high diagnostic accuracy in diagnosing skin cancers.[2–4] In addition, CM using fluorescence has also been used to evaluate excised specimens (*ex vivo* FCM) showing correct identification of residual tumour after Mohs surgery.[5] In this setting, high-resolution *ex vivo* CM allows for fresh tissue analysis immediately after excision.[6] In order to improve the detection of residual tumour, specimen staining protocols have been described. The first stain was 5% acetic acid (AA), which induced whitening of the epithelium and brightening of the nuclei by chromatin compaction.[7] Acridine orange (AO) was also used, resulting in an increase of the nuclei brightness by selectively highlighting nucleic acid (green fluorescence) and RNA (red fluorescence) in fluorescence mode.[8] Other stains have been tested such as Nile blue, methylene blue or patent blue, but results have not improved on those obtained with AO in *ex vivo* CM.[9]

Ex vivo CM saves at least one-third of the time while processing basal cell carcinoma (BCC) Mohs samples, providing a sensitivity of 88% and a specificity of 99%, while not affecting posterior staining of permanent sections.[5,7,10]

The first *ex vivo* confocal microscope, the VivaScope 2500® (Lucid Inc, Henrietta, NY, U.S.A.), had two different diode lasers: one for RCM with a wavelength of 830 nm, and another for FCM with a laser wavelength of 488 nm. However, the simultaneous acquisition in both modes was not possible and it was relatively slow, taking ~30 min. Recently, a novel confocal microscope (VivaScope 2500 4th Gen®, MAVIG GmbH, Munich, Germany) has been developed which allows the visualization with reflectance and fluorescence simultaneously, providing high-resolution images in both modes separately and in combination (fusion mode).

Herein, we present the first results using this new device and we describe the features encountered in a series of consecutive BCCs. Moreover, we describe a new staining protocol which combines AO and AA to enhance the visualization of structures in both reflectance and fluorescence, thus allowing a better definition of both stroma and tumour characteristics.

Material and methods

After approval by the Ethics Committee at the Hospital Clínic de Barcelona, we conducted a prospective, descriptive and exploratory study in order to describe different staining and laser modes of *ex vivo* CM. The main objective was to describe the criteria visualized with each protocol and compare between different protocols (combination of staining and mode). From September 2016 to June 2017, we included consecutive BCCs, which were excised using Mohs surgery in our centre. Lesions included in the study were at least 1 cm in their maximum diameter and complied with the indications for Mohs surgery. We excluded basosquamous BCCs and BCCs which were removed using conventional excision.

Patients who agreed to participate gave informed signed consent. All procedures performed in studies involving human participants were in accordance with the ethical standards of the institutional research committee and with the 1964 Helsinki Declaration and its later amendments or comparable ethical standards.

Tissue processing

The tissue used was obtained after Mohs surgery, both from the debulking and the lateral and deep margins. The tissue used in the study was obtained from the specimen remaining after frozen sections were obtained for standard-of-care Mohs surgery. Initially, the tissue was processed for visualization using CM after Mohs surgery, and later processed for routine histopathology analysis (vertical sections for the debulking and the lateral margins, and horizontal sections for the deep margins) (Fig. S1; see Supporting Information).

In order to compare both staining effects, two separate fusion images were obtained for each specimen: the first image was taken after AO staining and the second after AO+AA staining. The samples were first immersed for 20 s in 1 mmol L^{-1} AO and subsequently washed with saline solution for 20 s as described in the literature.[10] They were then scanned using *ex vivo* CM in fusion mode with both fluorescence and reflectance lasers. Then, the same sample was stained again with AO at the same concentration for 10 s to avoid the bleaching effect, and after washing in saline solution for 20 s, it was immersed in AA for 20 s, washed again in saline solution for 20 s, and finally re-scanned in the CM with the same setting as the first imaging.[11]

In order to analyse 100% of the lesion using CM, the specimen was placed on a slide, two small pieces of reusable adhesive putty (Blu Tack, Bostik Inc.; Paris, France) were placed on each side of the specimen, and an additional slide was placed on top in order to flatten the specimen. Later, the slides

were placed in the 4th Gen® VivaScope 2500 (MAVIG GmbH) to capture images of RCM and FCM *ex vivo*. This device uses two laser sources with a resolution image of 1024 × 1024 pixels, and an objective lens of 38× with a numerical aperture of 0·85. Mosaics of individual horizontal images and stacks of vertical images were obtained to render a three-dimensional approximation of the sample. The field of view of single images is 550 × 550 μm and the maximum mosaic area is 25 × 25 mm.

After CM acquisition, the specimens were placed in the exact same position in a processing cassette for paraffin section and haematoxylin and eosin staining to demonstrate the viability of the samples for routine histopathological analysis after all the manipulations for *ex vivo* CM.

After optimization of the technique, we developed an optimized standard operating procedure which can be used either for fresh tissue or after frozen tissue has been thawed (Fig. S1, Methods S1; see Supporting Information).

Data management and analysis

The images were stored on a secure drive within our centre. The patient's age and sex, tumour location, initial and final histopathological diagnoses were recorded. All CM images were evaluated by consensus by two Mohs surgeons, one an expert in *ex vivo* CM, and one an expert in *in vivo* CM. Histopathology slides from frozen sections and haematoxylin and eosin were evaluated by consensus by two dermatopathologists.

For the evaluation of BCC using RCM, we used the previously described criteria for *in vivo* RCM:[11–14] bright tumour islands, dark silhouettes, palisading, peritumoral clefting, peritumoral stromal reaction, thickened/distorted collagen bundles, horizontal blood vessels, dendritic cells and plump cells. For the evaluation using fluorescence CM we looked at: delimitation of the tumour, crowding, nuclear pleomorphism, increased nucleus/cytoplasm ratio and presence of fluorescence in the cell nuclei. Later, we compared the findings in fluorescence, reflectance and fusion obtained with AO as well as AA+AO.

Statistical analysis

The study variables were formally tabulated into descriptive variables and treated as paired binomial variables for each one of the experiments and stain protocols. The exact P-values of the McNemar test, which is especially suited for paired nominal data, was used to assess the statistical differences between the results before and after staining the samples with AA. All P-values have also been adjusted for multiple comparisons using the Benjamini–Hochberg[15] procedure to control the false discovery rate. Finally, the exact confidence intervals (CIs) of the binomial variables were computed and plotted and adjusted for multiple comparisons (97·7% CI).[16] All tests were performed with a significance level of $P = 0{\cdot}05$ with PASW statistical software (SPSS Corp., Chicago, IL, U.S.A.). Each of the structures analysed in this manuscript are well described and used for diagnosis using CM. This paper proposes to help guide technicians to decide when to use a given staining technique to visualize each one of the particular structures of interest.

Results

Clinical features

A total of 78 BCCs from 78 patients [41 males; mean age 63 (SD 38–93) years] were imaged. The face was the most frequent location (80%), followed by the limbs (10·5%) and the trunk (9·5%). Fifty-seven cases were primary and the remaining 21 had received prior treatment. Regarding BCC subtype, 35 were infiltrative, 25 were nodular, 12 were micronodular and 6 were superficial.

Confocal microscopy results

The results of the confocal findings comparing AO with AO+AA in fluorescence, reflectance or fusion are summarized in Figure 1(a–c), respectively, and Table S1 (see Supporting Information). The results of the different laser modes for the best stain for feature visualization are summarized in Figure 1(d) and Table S2 (see Supporting Information). The mean time required to scan each skin sample, including the stain protocol, was 7 (range 3–15) min depending on the size of the specimen. In addition, our final histology evaluation confirmed that the specimens were not damaged after the staining or CM scanning processes. The most relevant results are summarized therein.

Results in fluorescence mode

The double stain increased the visualization of most features. Statistical differences were found between the results before and after staining with AA and, especially, changes were found in the visualization of nuclear pleomorphism (61 vs. 75, $P < 0{\cdot}001$), visualization increased nuclear/cytoplasm ratio (61 vs. 74, $P = 0{\cdot}001$) and crowding (67 vs. 76, $P = 0{\cdot}01$). There were also statistical differences in the visualization of stroma (26 vs. 35, $P = 0{\cdot}01$) and thickened collagen bundles (19 vs. 26, $P = 0{\cdot}04$). The visualization of palisading, bright tumour islands, fluorescence, clefting and linear blood vessels also showed differences with the double stain; however, no statistically significant differences were found between AO vs. AA+AO for the these features. Tumour demarcation was identified in all cases using both stain protocols, while dark silhouettes, dendritic cells and plump cells were not identified in the fluorescence mode with any stain (Figs 1a, 2, 3 and Table S1; see Supporting Information).

Results in reflectance mode

The double stain showed significant differences and improved the visualization of nuclear pleomorphism (17 vs. 74, P <

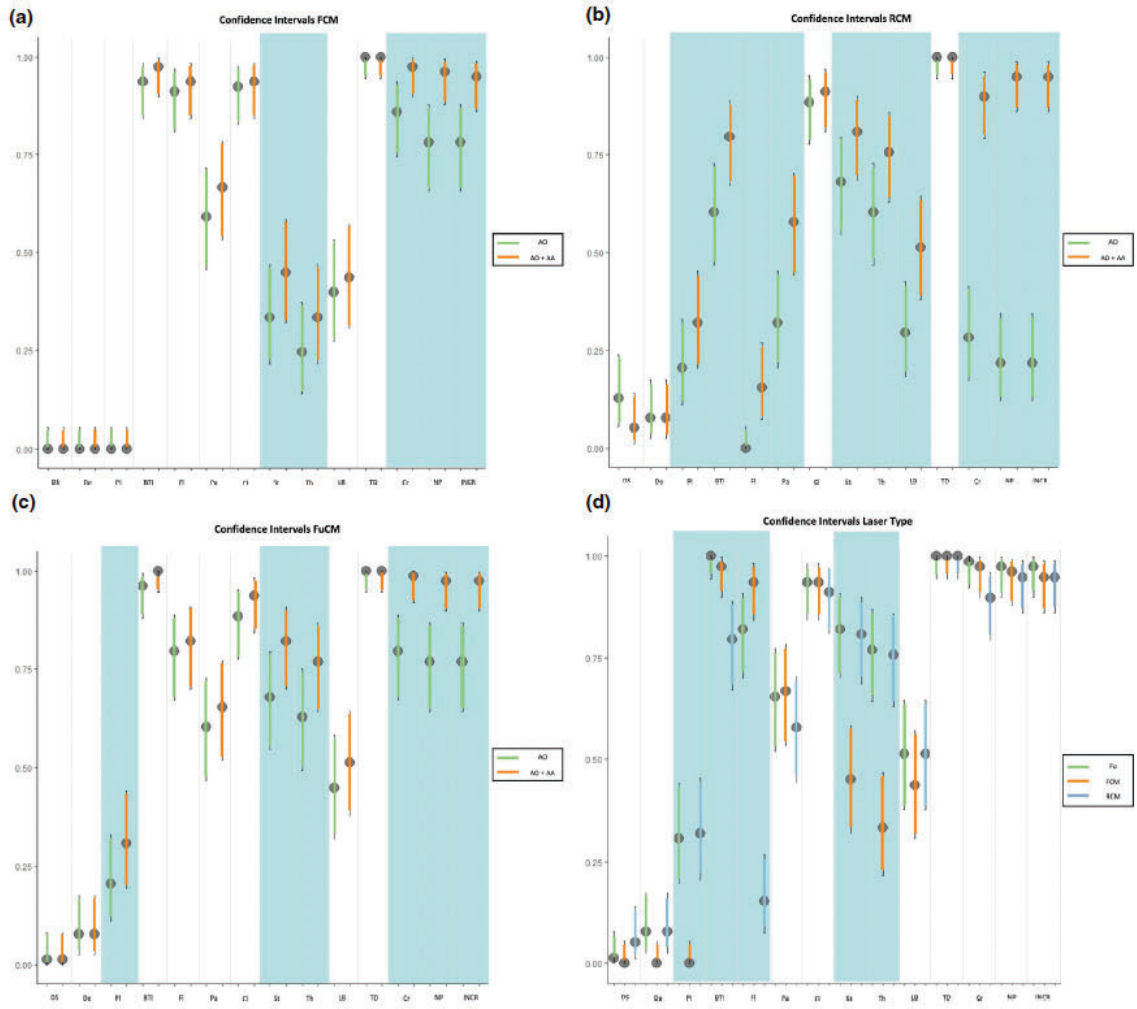

Fig 1. Confidence intervals between different laser and staining procedures. (a) Comparison of staining in FCM; (b) comparison of staining in RCM; (c) comparison of staining in fusion mode of confocal microscopy; (d) comparison between different laser modes with the best staining (AO+AA). Grey colour for significant comparisons for P-McNemar.

AA, acetic acid; AO, acridine orange; BTI, bright tumour islands; Cl, clefting; Cr, crowding; De, dendritic cells; DS, dark silhouettes; FCM, fluorescent confocal microscopy; Fl, fluorescence; FuCM, fusion confocal microscopy; INCR, increased nucleus/cytoplasm ratio; LB, linear blood vessels; NP, nuclear pleomorphism; Pa, palisading; Pl, plump cells; RCM, reflectance confocal microscopy; St, stroma; TD, tumour demarcation; Th, thickened collagen bundles.

0·001), nuclear/cytoplasm ratio (17 vs. 74, $P < 0·001$) and crowding (22 vs. 73, $P < 0·001$). The same stain also significantly differentiated the visualization of plump cells (16 vs. 25, $P = 0·01$), bright tumour islands (47 vs. 62, $P < 0·001$), fluorescence (0 vs. 12, $P = 0·002$), palisading (25 vs. 45, $P < 0·001$), stroma (53 vs. 63, $P = 0·02$), thickened collagen (47 vs. 59, $P = 0·006$) and linear blood vessels (23 vs. 40, $P < 0·001$). Clefting visualization did not change significantly with the addition of AA (69 vs.71, $P = 0·91$). Conversely, the visualization of dark silhouettes in RCM decreased with the double stain (10 vs. 4, $P = 0·14$) (Figs 1b and 3; Table S1 and Fig. S2; see Supporting Information). Dendritic cells and tumour demarcation were observed independently of the stain protocol ($P > 0·99$).

Results in fusion mode

Similar to reflectance and fluorescence, the double stain showed differences and improved the visualization of nuclear pleomorphism (60 vs. 76, $P < 0·001$), nuclear/cytoplasm ratio (60 vs. 76, $P < 0·001$) and crowding (62 vs. 77, $P < 0·001$) in fusion mode. It also showed significant differences ($P < 0·05$) in the visualization of stroma ($P = 0·004$), thickened collagen bundles ($P = 0·004$) and plump cells ($P =$

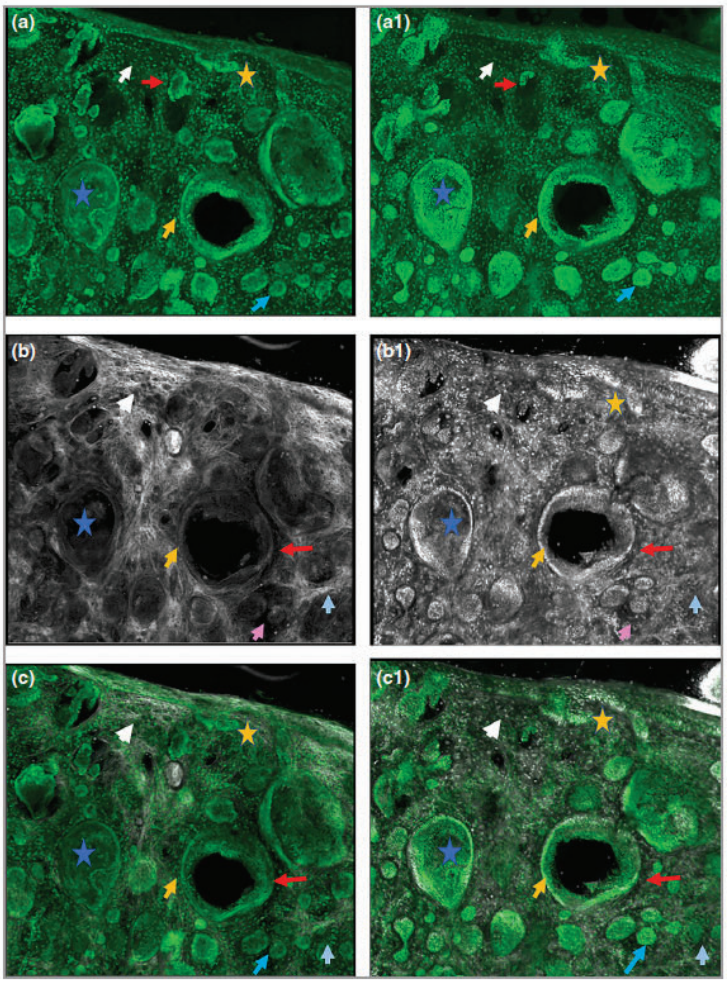

Fig 2. Micronodular basal cell carcinoma. Feature differences in distinct lasers and stain protocols. Left column (a, b, c): acridine orange. Right column (a1, b1, c1): acridine orange + acetic acid. (a, a1) Fluorescence confocal microscopy. (b, b1) Reflectance confocal microscopy. (c, c1) Fusion confocal microscopy. Differences between stroma reactions can be observed (white arrow); clefting (red arrow); palisading (yellow arrow); thickened collagen bundles (sky blue arrow); well-delineated and bright tumour islands (blue arrow); dark silhouettes (pink arrows); presence of fluorescence (yellow star); nuclear features: crowding, nuclear pleomorphism, increased nucleus/cytoplasm ratio (blue star).

0·02). The visualization of dark silhouettes, dendritic cells, bright tumour islands, fluorescence, palisading, clefting, linear blood vessels and tumour demarcation did not significantly change with the double stain protocol (Figs 1c and 2, Table S1; see Supporting Information).

Overall laser results using acetic acid plus acridine orange

When comparing fluorescence and reflectance modes using the double stain, statistical differences were found in the visualization of plump cells (0 vs. 25, $P < 0·001$), bright tumour islands (76 vs. 62, $P = 0·005$), fluorescence (73 vs. 12, $P < 0·001$), stroma reaction (35 vs. 63, $P < 0·001$) and thickened collagen bundles (26 vs. 59, $P < 0·001$). It slightly improved the observation of the linear blood vessels (34 vs. 40, $P = 0·07$). No differences between FCM and RCM were noted when evaluating palisading (52 vs. 45, $P = 0·14$), clefting (73 vs. 71, $P = 0·74$), tumour demarcation (78 vs. 78, $P > 0·99$), crowding (76 vs. 73, $P = 0·63$), nuclear pleomorphism (75 vs. 74, $P > 0·99$) and increased nuclear/cytoplasm ratio ($P > 0·99$). Conversely, in FCM, dark silhouettes (0 vs. 4, $P = 0·23$) and dendritic cells (0 vs. 6, $P = 0·07$) could not be observed.

Overall, FCM improved the visualization of bright tumour islands and fluorescence and RCM was better for identifying dark silhouettes, dendritic and plump cells (Figs 1d, 2 and 3), whereas fusion CM was also good compared with the other lasers for identifying the remaining features observed in Table S2 (see also Figs 1–4 and Fig. S2; see Supporting Information).

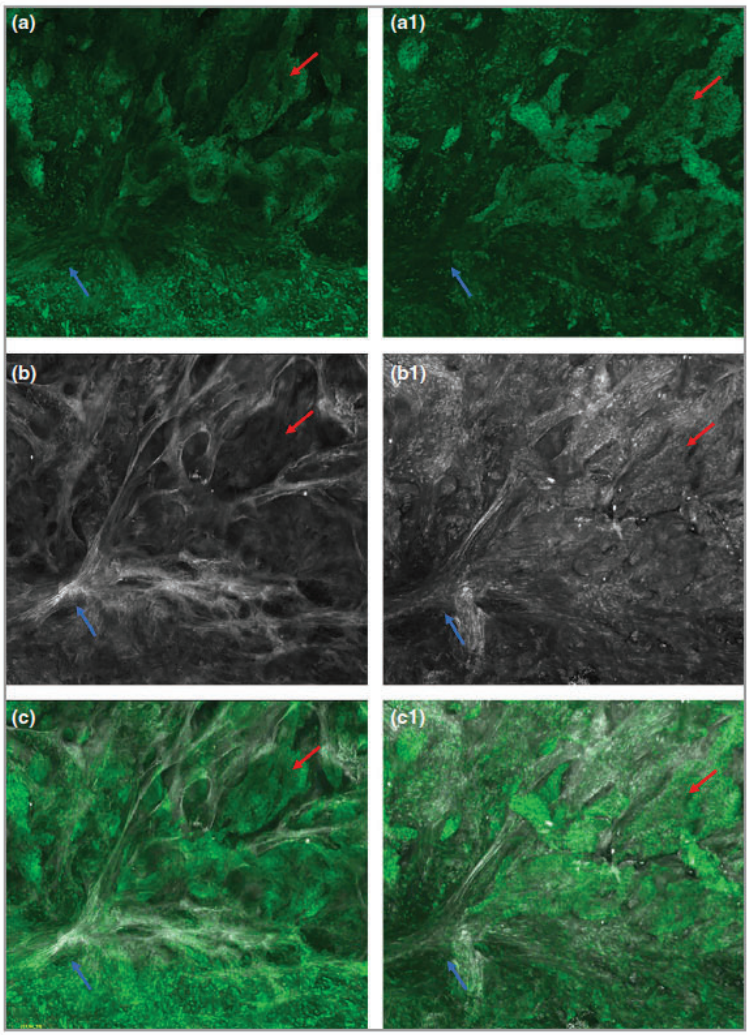

Fig 3. Infiltrating basal cell carcinoma. Feature differences: distinct lasers and stain protocols. Left column (a, b, c: acridine orange. Right column (a1, b1, c1): acridine orange + acetic acid. (a, a1) Fluorescence confocal microscopy. (b, b1) Reflectance confocal microscopy. (c, c1) Fusion confocal microscopy. Dark silhouettes are better observed without the nuclear enhancement of the acetic acid. They are poorly visualized in fluorescence mode and better observed in reflectance mode. When the acetic acid is applied, bright and well-delineated tumour islands can be observed instead of dark silhouettes (red arrow). Collagen bundles are poorly observed in fluorescence mode (blue arrow). Clefting is not always observed in infiltrating tumours.

Discussion

In this study we present the first results in skin using a novel confocal microscope which combines reflectance and fluorescence modes simultaneously. To date, most studies using *ex vivo* CM to diagnose BCC describe features using the fluorescence mode and only a few criteria have been described for *ex vivo* in RCM. Some authors have described the use of *in vivo* CM for intraoperative margin control.[5,10,17–19]

Both RCM and FCM have advantages and disadvantages when evaluating BCCs. Reflectance improves the visualization of the stromal and cytoplasmic features while fluorescence also enhances the visualization of the nuclei. Therefore, a combined approach may improve the visualization of nuclear, cytoplasmic and stromal details. Our results support this statement, because fusion CM resulted in an improvement of the visualization of most BCC features such as bright tumour islands, crowding, nuclear pleomorphism or stromal reaction (Table S2; see Supporting Information). However, for select features such as fluorescence or dark silhouettes, FCM or RCM individually seem to perform better than fusion CM. This may be due to a sharper visualization of such features when assessed using only one laser. We therefore do not believe fusion should be used alone, but we advocate for the parallel

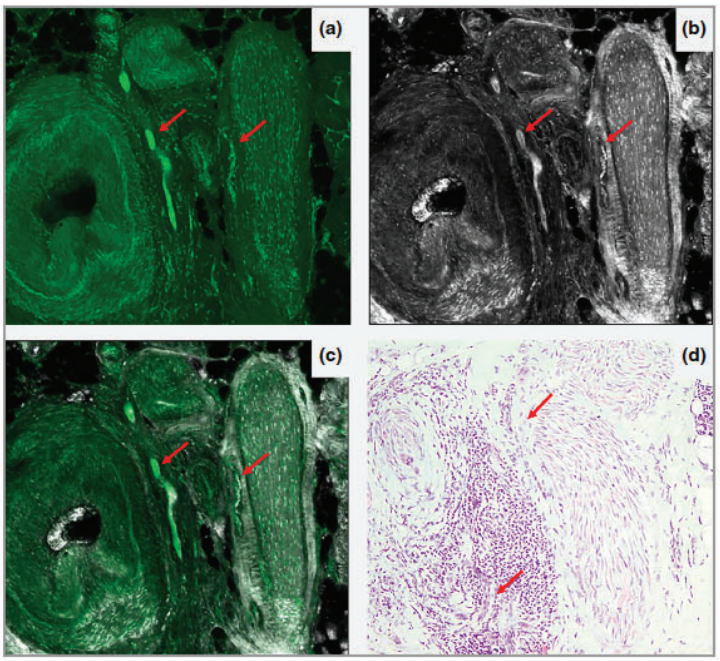

Fig 4. Three-dimensional perivascular and perineural infiltrating basal cell carcinoma (red arrow). (a) Fluorescence mode; (b) reflectance mode; (c) fusion mode; (d) haematoxylin and eosin, original magnification × 10. Even small amounts of tumour can be detected by this method, but not always clearly by conventional pathology.

use of RCM, FCM and fusion when performing *ex vivo* CM because they allow a more comprehensive evaluation of the different cellular and stromal features. A similar scenario occurs in dermoscopy, where controversy has arisen when assessing whether polarized or nonpolarized dermoscopy is better. Indeed, many advocate for the integration of both light sources in the same device in order to toggle from polarized to nonpolarized to identify certain structures not visible with both modes (blink sign).[20,21] Hence, this could be the same scenario in *ex vivo* CM, where one could toggle from fluorescence to reflectance and vice versa, and get the complete image in fusion in order to help identify residual tumour areas that may facilitate the surgical procedure.

In addition, because multiple staining methods exist to improve tumour visualization in both fluorescence and reflectance CM, we have developed a staining method which combines AA and AO to improve the visualization of the tumour (nucleus and cytoplasm) and the stroma at the same moment (Fig. S1, Methods S1; see Supporting Information).[8,22] Our results suggest that, overall, the majority of BCC features are better visualized in both reflectance and fluorescence when using the double stain with AA+AO compared with AO alone. However, the visualization of dark silhouettes in RCM decreased with the double stain. This seems logical because AA compacts the chromatin and improves the visualization of nuclear details.[14] It is also the case in our study where, in the cases where dark silhouettes were poorly visualized with the double stain, they enhanced the identification of bright tumour islands, crowding and other nuclear details. Therefore, the combination of AA+AO gives an efficient contrast with clear and sharper differentiation between cellular structures and the surrounding stroma. This may facilitate the interpretation of confocal images potentially leading to a more widespread use of the technology. However, further studies comparing novices vs. experts are needed, as well as reviewing the published criteria, which occasionally may have little clinical applicability (i.e. fluorescence feature in fluorescence mode).

Another advantage of our approach is that the entire process is faster than previous ones. Because the new generation of *ex vivo* CM is faster and the different staining phases are performed sequentially, the entire process of staining and scanning in both lasers requires 7 min on average, compared with 15–30 min using previous methods.[10] Therefore, fast margin assessment allows almost simultaneous reconstruction in case of negative margins. The main advantage of the commercial model of this device is the possibility of the visualization of the fusion mode with a digital stain similar to haematoxylin and eosin, which needs to be the main focus of another study (Fig. S3; see Supporting Information).[23]

However, our approach also has limitations. As reported previously, factors that could interfere in staining samples in *ex vivo* CM might be the lifetime of the fluorescence.[7,24] We also presume that not only the thickness of the tumour, but also the compaction of its cells in solid tumours does not

allow for sufficient stain penetration in some BCCs. In these cases, 20 s of AO stain is probably not enough to stain the tissue and more time might be required. The complete flattening of the tissue and reaching the correct depth before scanning are also the main interfering factors for perfect imaging. In addition, in the current manuscript we did not intend to assess the diagnostic accuracy of this novel CM device. Finally, we also acknowledge the fact that this novel CM device may be present in select centres only and, therefore, the results of our current study may not be generalizable to previous iterations of the device.

To sum up, we have described BCC features using a novel *ex vivo* CM which uses fluorescence and reflectance simultaneously. Our results suggest that nuclei characteristics are better visualized in FCM but cytoplasm and surrounding stroma are better visualized in RCM. Thus, the simultaneous evaluation of reflectance and fluorescence seems to be beneficial due to its complementary effect. The adjunct use of multiple stains such as AA and AO also seemed beneficial to highlight the different tumour characteristics and seems to be promising to help identify residual tumour.

Acknowledgments

We want to thank the members of Surgery Unit and Dermatopathology Department of the Hospital Clínic de Barcelona, for providing technical support to this project. We also want to thank our patients and their families who are the main reason for our studies, and the nurses from the Melanoma Unit of Hospital Clínic de Barcelona, Daniel Gabriel, Pablo Iglesias and Maria E. Moliner, for helping to collect patient data. We also thank Helena Kruyer for her help with text editing.

References

1 Forkner C. A method for supravital staining of animals with neutral red and its preservation in paraffin sections. *J Exp Med* 1930; **52**:379–84.
2 Alarcon I, Carrera C, Palou J *et al.* Impact of *in vivo* reflectance confocal microscopy on the number needed to treat melanoma in doubtful lesions. *Br J Dermatol* 2014; **170**:802–8.
3 Pellacani G, Pepe P, Casari A, Longo C. Reflectance confocal microscopy as a second-level examination in skin oncology improves diagnostic accuracy and saves unnecessary excisions: a longitudinal prospective study. *Br J Dermatol* 2014; **171**:1044–51.
4 Stevenson AD, Mickan S, Mallett S, Ayya M. Systematic review of diagnostic accuracy of reflectance confocal microscopy for melanoma diagnosis in patients with clinically equivocal skin lesions. *Dermatol Pract Concept* 2013; **3**:19–27.
5 Bennàssar A, Vilata A, Puig S, Malvehy J. *Ex vivo* fluorescence confocal microscopy for fast evaluation of tumour margins during Mohs surgery. *Br J Dermatol* 2014; **170**:360–5.
6 Longo C, Ragazzi M, Rajadhyaksha M *et al.* *In vivo* and *ex vivo* confocal microscopy for dermatologic and Mohs surgeons. *Dermatol Clin* 2016; **34**:497–504.
7 Rajadhyaksha M, Menaker G, Flotte T *et al.* Confocal examination of nonmelanoma cancers in thick skin excisions to potentially guide Mohs micrographic surgery without frozen histopathology. *J Invest Dermatol* 2001; **117**:1137–43.
8 Karen JK, Gareau DS, Dusza SW *et al.* Detection of basal cell carcinomas in Mohs excisions with fluorescence confocal mosaicing microscopy. *Br J Dermatol* 2009; **160**:1242–50.
9 Welzel J, Kästle R, Sattler EC. Fluorescence (multiwave) confocal microscopy. *Dermatol Clin* 2016; **34**:527–33.
10 Bennàssar A, Carrera C, Puig S *et al.* Fast evaluation of 69 basal cell carcinomas with *ex vivo* fluorescence confocal microscopy: criteria description, histopathological correlation, and interobserver agreement. *JAMA Dermatol* 2013; **149**:1–8.
11 Nori S, Rius-Díaz F, Cuevas J *et al.* Sensitivity and specificity of reflectance-mode confocal microscopy for *in vivo* diagnosis of basal cell carcinoma: a multicenter study. *J Am Acad Dermatol* 2004; **51**:923–30.
12 Segura S, Puig S, Carrera C *et al.* Dendritic cells in pigmented basal cell carcinoma: a relevant finding by reflectance-mode confocal microscopy. *Arch Dermatol* 2007; **143**:883–6.
13 Gonzalez S, Tannous Z. Real-time, *in vivo* confocal reflectance microscopy of basal cell carcinoma. *J Am Acad Dermatol* 2002; **47**:869–74.
14 Tannous Z, Torres A, Gonzalez S. *In vivo* real-time confocal reflectance microscopy: a noninvasive guide for Mohs micrographic surgery facilitated by aluminum chloride, an excellent contrast enhancer. *Dermatologic Surg* 2003; **29**:839–46.
15 And YB, Hochberg Y. Controlling the false discovery rate: a practical and powerful approach to multiple testing. *J R Stat Soc* 1995; **57**:289–300.
16 Benjamini Y, Yekutieli D, Edwards D *et al.* False discovery rate-adjusted multiple confidence intervals for selected parameters. *J Am Stat Assoc* 2005; **100**:71–93.
17 Villarreal-Martinez A, Bennàssar A, Gonzalez S *et al.* Application of *in vivo* reflectance confocal microscopy and *ex vivo* fluorescence confocal microscopy in the most common subtypes of basal cell carcinoma and correlation with histopathology. *Br J Dermatol* 2018; **178**:1215–17.
18 Sierra H, Damanpour S, Hibler B *et al.* Confocal imaging of carbon dioxide laser-ablated basal cell carcinomas: an *ex-vivo* study on the uptake of contrast agent and ablation parameters. *Lasers Surg Med* 2016; **48**:133–9.
19 Sierra H, Larson BA, Chen CS, Rajadhyaksha M. Confocal microscopy to guide erbium:yttrium aluminum garnet laser ablation of basal cell carcinoma: an *ex vivo* feasibility study. *J Biomed Opt* 2013; **18**:095001.1–095001.5.
20 Benvenuto-Andrade C, Dusza SW, Agero ALC *et al.* Differences between polarized light dermoscopy and immersion contact dermoscopy for the evaluation of skin lesions. *Arch Dermatol* 2007; **143**:329–38.
21 Liebman TN, Jaimes-Lopez N, Balagula Y *et al.* Dermoscopic features of basal cell carcinomas: differences in appearance under non-polarized and polarized light. *Dermatologic Surg* 2012; **38**:392–9.
22 Bini J, Spain J, Nehal K *et al.* Confocal mosaicing microscopy of human skin *ex vivo*: spectral analysis for digital staining to simulate histology-like appearance. *J Biomed Opt* 2011; **16**:076008.
23 Yélamos O, Pérez-Anker J. Avances en el manejo del cáncer cutáneo: videomosaicos y microscopía confocal de fusión. *Rev Chil dermatología* 2018; **34**:6–8.
24 Galletly NP, McGinty J, Dunsby C *et al.* Fluorescence lifetime imaging distinguishes basal cell carcinoma from surrounding uninvolved skin. *Br J Dermatol* 2008; **159**:152–61.

Supporting Information

Additional Supporting Information may be found in the online version of this article at the publisher's website:

Methods S1 Optimized standard operating procedure for dual staining in fusion *ex vivo* confocal microscopy (Vivascope 2500 4th Gen®).

Fig S1. Schematic diagram of the final optimized protocol proposed for fusion *ex vivo* confocal microscopy.

Fig S2. Peritumoral stromal reaction. Stromal differences in distinct lasers and stain protocols. Right column acridine orange + acetic acid. Left column: acridine orange. (a, a1) Fluorescence confocal microscopy. (b, b1) Reflectance confocal microscopy. (c, c1) Fusion confocal microscopy.

Fig S3. Basal cell carcinoma in fusion mode previously processed with acetic acid and acridine orange stain protocol. Visualized with digital staining.

Table S1 Detection of different confocal microscopy features using different stains and confocal laser modes.

Table S2 P-values for the different laser modes with acridine orange + acetic acid.

Supplementary material

Supplementary document:

Optimised Standard Operating Procedure for Dual Staining in Fusion *Ex vivo* Confocal Microscopy (Vivascope 2500 4Gen)

Supplementary figure 1:

Schematic diagram of the final optimised protocol proposed for fusion *ex vivo* confocal microscopy.

Abbreviations: AO, acridine orange, AA, acetic acid; MCF, fluorescence confocal microscopy; MCR, reflectance confocal microscopy; s, seconds.

Supplementary Figure 2. Infiltrating basal cell carcinoma. Digital stain.

Fig S1. Schematic diagram of the final optimized protocol proposed for fusion *ex vivo* confocal microscopy.

Fig S2. Peritumoral stromal reaction. Stromal differences in distinct lasers and stain protocols. Right column acridine orange + acetic acid. Left column: acridine orange. (a, a1) Fluorescence confocal microscopy. (b, b1) Reflectance confocal microscopy. (c, c1) Fusion confocal microscopy.

Fig S3. Basal cell carcinoma in fusion mode previously processed with acetic acid and acridine orange stain protocol. Visualized with digital staining.

Table S1. Detection of different confocal microscopy features using different stains and confocal laser modes.

Table S2. P-values for the different laser modes with acridine range + acetic acid.

Optimised Standard Operating Procedure for Dual Staining in Fusion *Ex vivo* Confocal Microscopy (VivaScope 2500 4Gen)

1. Excise the tissue from the patient. The fresh specimen can be directly processed for confocal microscopy or frozen if needed for Mohs surgery. If frozen, thaw the specimen before processing and scanning the sample
2. Immerse the specimen in 1 mmol L-1 Acridine Orange for 20 seconds
3. Wash the tissue in saline solution for 20 seconds
4. Immerse the specimen in acetic acid 50% for 20 seconds
5. Wash the tissue in saline solution for 20 seconds
6. Place the specimen in a conventional histopathology slide
7. Apply two pieces of reusable adhesive putty in each border of the slide
8. Place a thick coverslip or a clean slide on top of the specimen in order to flatten the tissue. The specimen should be in the middle of the two glasses and between the two pieces of adhesive putty
9. Scan the specimen in the *ex vivo* confocal microscope (VivaScope 2500 4th Gen) in fusion mode (with both simultaneous fluorescence and reflectance lasers)
10. Once scanned, if conventional histopathology techniques are necessary, the specimen can be placed directly in a container with 10% formalin and processed according to clinical practice

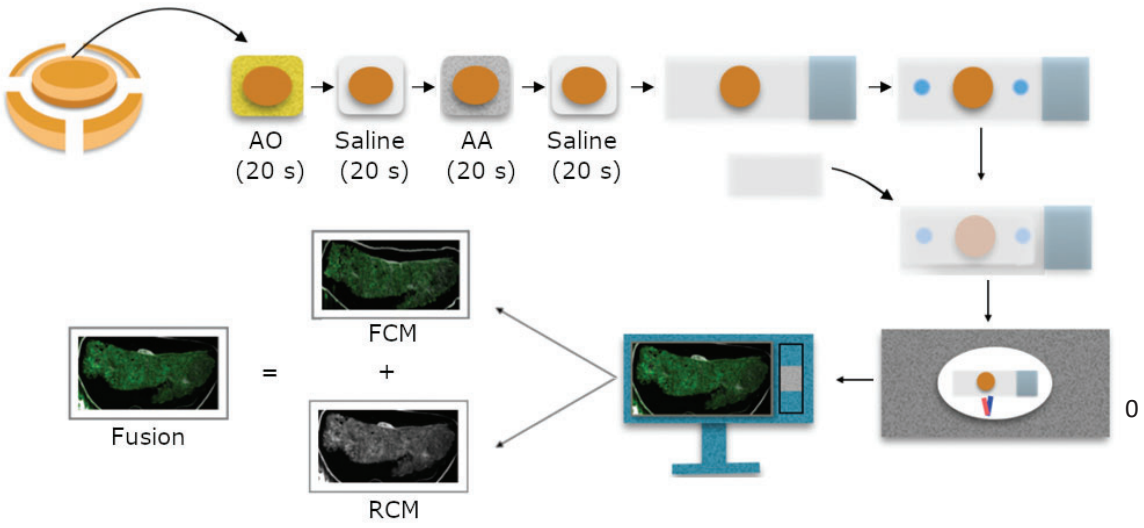

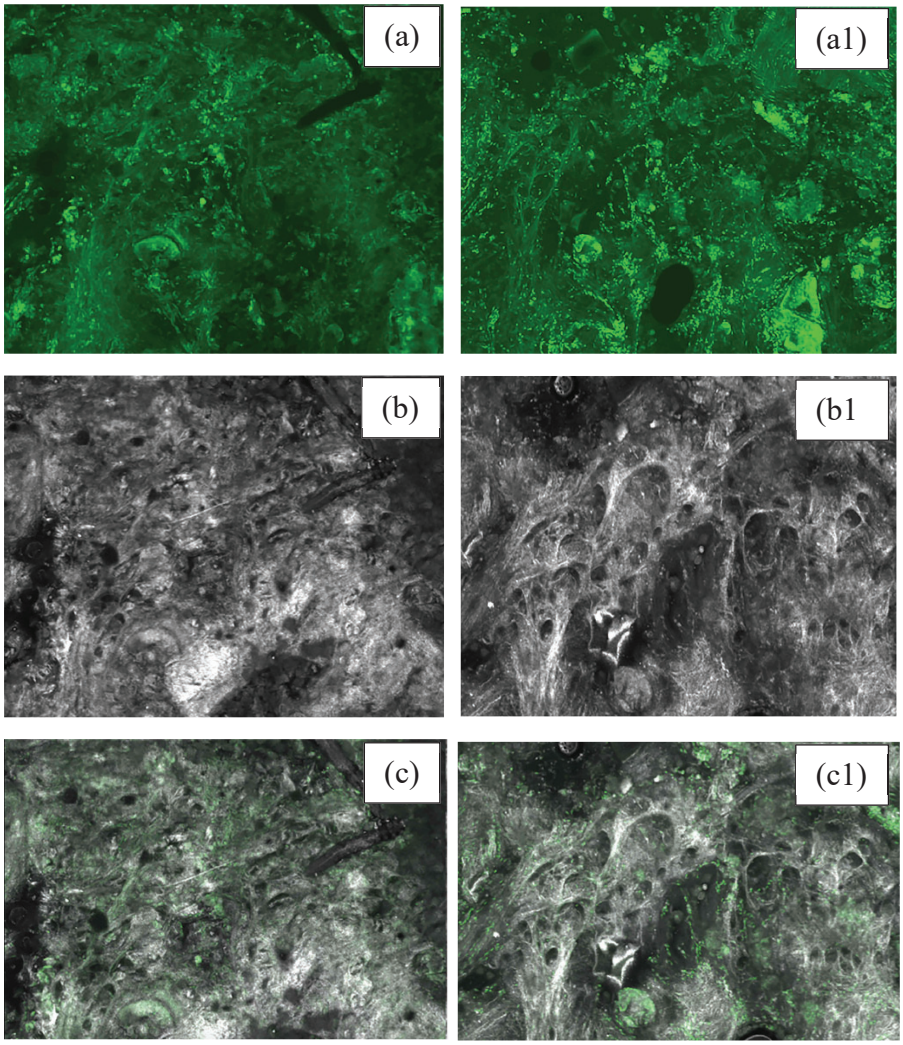
(a)
(a1)
(b)
(b1
(c)
(c1)

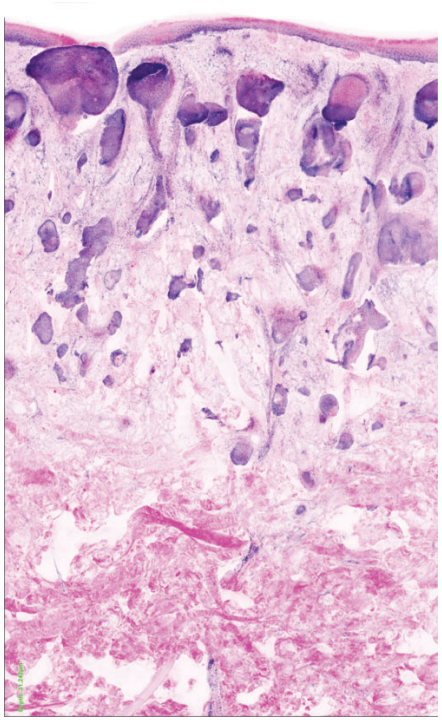

Supplementary Table 1: Detection of different CM features using different stain and confocal laser modes (R=RCM, F=FCM, Fu=Fusion technique, AO=acridine orange, AA=acetic acid). Green colour for significant comparisons.

BCC feature	FCM AO N (%)	FCM AA+AO N (%)	P	Adjusted P	RCM AO N (%)	RCM AA+AO N (%)	P	Adjusted P	FuCM AO N (%)	FuCMAA +AO N (%)	P	Adjusted P
Dark silhouettes	0 (0)	0 (0)	>0.99	>0.99	10 (13)	4 (5)	0.07	0.14	1 (1)	1 (1)	>0.99	>0.99
Dendritic	0 (0)	0 (0)	>0.99	>0.99	6 (8)	6 (8)	>0.99	>0.99	6 (8)	6 (8)	>0.99	>0.99
Plump cells	0 (0)	0 (0)	>0.99	>0.99	16 (21)	25 (32)	0.004	0.01	16 (21)	24 (31)	0.008	0.02
Bright tumour islands	73 (94)	76 (97)	0.25	0.43	47 (60)	62 (79)	<0.001	<0.001	75 (96)	78 (100)	0.25	0.43
Fluorescence	71 (91)	73 (94)	0.50	0.74	0 (0)	12 (15)	<0.001	0.002	62 (8)	64 (82)	0.69	0.98
Palisading	46 (59)	52 (66.7)	0.03	0.07	25 (32)	45 (58)	<0.001	<0.001	47 (60)	51 (65)	0.12	0.23
Clefting	72 (92)	73 (94)	>0.99	>0.99	69 (88)	71 (91)	0.62	0.91	69 (89)	73 (94)	0.12	0.23
Stroma	26 (34)	35 (45)	0.004	0.01	53 (67)	63 (81)	0.006	0.02	53 (68)	64 (82)	<0.001	0.004
Thickened	19 (24)	26 (33)	0.02	0.04	47 (60)	59 (76)	0.002	0.006	49 (63)	60 (77)	<0.001	0.004
Linear blood	31 (40)	34 (43.6)	0.25	0.43	23 (29)	40 (51)	<0.001	<0.001	35 (45)	40 (51)	0.06	0.14
Tumour demarcation	78 (100)	78 (100)	>0.99	>0.99	78 (100)	78 (100)	>0.99	>0.99	78 (100)	78 (100)	>0.99	>0.99
Crowding	67 (86)	76 (97)	0.004	0.01	22 (28)	73 (94)	<0.001	<0.001	62 (80)	77 (99)	<0.001	<0.001
Nuclear Pleomorp	61 (78)	75 (96)	<0.001	<0.001	17 (22)	74 (95)	<0.001	<0.001	60 (77)	76 (97)	<0.001	<0.001
Increased NCR	61 (78)	74 (95)	<0.001	0.001	17 (22)	74 (95)	<0.001	<0.001	60 (77)	76 (97)	<0.001	<0.001

Supplementary Table 2: p-values for the different laser modes with Acridine Orange plus Acetic Acid (R=RCM, F=FCM, Fu=Fusion CM). Green colour for significant comparisons.

BCC feature/frequency	FCM AA + AO	RCM AA + AO	FuCM AA + AO	FCM Vs RCM		FCM Vs FuCM		RCM Vs FuCM	
	N (%)	N (%)	N (%)	P	Adjusted P	P	Adjusted P	P	Adjusted P
Dark silhouette	0(0)	4(5)	1(1)	0.12	0.23	>0.99	>0.99	0.25	0.43
Dendritic	0(0)	6(8)	6(8)	0.03	0.07	0.03	0.07	>0.99	>0.99
Plump cells	0(0)	25(32)	24(31)	<0.001	<0.001	<0.001	<0.001	>0.99	>0.99
Bright tumour islands	76(97)	62(79)	78(100)	0.001	0.005	0.50	0.74	<0.001	<0.001
Fluorescence	73(94)	12(15)	64(82)	<0.001	<0.001	0.06	0.14	<0.001	<0.001
Palisading	52(67)	45(58)	51(65)	0.07	0.14	>0.99	>0.99	0.03	0.07
Clefting	73(94)	71(91)	73(94)	0.50	0.74	>0.99	>0.99	0.50	0.74
Stroma	35(45)	63(81)	64(82)	<0.001	<0.001	<0.001	<0.001	>0.99	>0.99
Thickened	26(33)	59(76)	60(77)	<0.001	<0.001	<0.001	<0.001	>0.99	>0.99
Linear blood	34(44)	40(51)	40(51)	0.03	0.07	0.03	0.07	>0.99	>0.99
Tumour demarcation	78(100)	78(100)	78(100)	>0.99	>0.99	>0.99	>0.99	>0.99	>0.99
Crowding	76(97)	73(94)	77(99)	0.38	0.63	>0.99	>0.99	0.12	0.23
Nuclear Pleomorphism	75(96)	74(95)	76(97)	>0.99	>0.99	>0.99	>0.99	0.50	0.74
Increased NCR	74(95)	74(95)	76(97)	>0.99	>0.99	0.50	0.74	0.50	0.74

PUBLICACIÓN N° 7:[71]

Una opción rápida y eficaz para el aplanamiento de tejidos: eficacia y optimización del tiempo en microscopia confocal *ex vivo*.

A fast and effective option for tissue flattening: Optimizing time and efficacy in *ex vivo* confocal microscopy.

Javiera Pérez-Anker, Susana Puig, Josep Malvehy.

J Am Acad Dermatol. 2020 May;82(5):e157-e158. doi: 10.1016/j.jaad.2019.06.041. Epub 2019 Jun 28.
Factor de impacto: 11.527

Resumen
Antecedentes: Uno de los grandes desafíos en microscopía confocal *ex vivo* es lograr la visualización y representación completa del tejido a ser escaneado. Si el tejido no contacta totalmente con el portaobjetos, la pieza no queda 100% representada durante el escaneo. Hasta el momento ningún dispositivo era capaz de lograr esto de forma rápida y eficaz.
Objetivos: Proponer un dispositivo que permita aplanar la pieza de forma rápida y eficaz.
Métodos: Se desarrolló un modelo de dispositivo experimental, mediante imanes adheridos a un portaobjeto, complementado con el uso de esponjas, para aplanar las piezas a ser escaneadas por microscopía confocal *ex vivo*.

Resultados: Las piezas pudieron ser aplanadas rápidamente y el tejido contactó con la superficie del portaobjetos, utilizando imanes de diferentes fuerzas y esponjas de diferentes densidades, de acuerdo con el tejido a ser escaneado.

Conclusiones: Se logró demostrar que el dispositivo propuesto era capaz de aplanar las piezas a ser escaneadas de forma rápida y eficaz.

JAAD ONLINE: TECHNOLOGY PEARL

A fast and effective option for tissue flattening: Optimizing time and efficacy in ex vivo confocal microscopy

Javiera Pérez-Anker, MD, MSc, Susana Puig, MD, PhD, and Josep Malvehy, MD, PhD
Barcelona, Spain

Key words: digital stain; ex vivo confocal microscopy; Mohs microscopic surgery; optimizing time; skin cancer surgery; tissue flattening device.

TECHNOLOGY CHALLENGE

Ex vivo confocal microscopy has opened the door to rapid, intraoperative diagnosis of tissue specimens. However, to avoid false-negative diagnosis, it is critical to optically visualize the whole specimen. To achieve that, the tissue specimen should be in full contact with the glass slide. Because of variability in sample density and constitution, perfect flattening is a real challenge.[1]

Several devices have been developed to achieve this aim; for example, compression of the specimen between 2 glass slides attached together with silicon glue or modeling clay has been suggested.[2] However, both techniques are time consuming and only partially effective.

THE SOLUTION

To meet this challenge, we have developed a system of magnets of different sizes and strengths attached to the slide and the cover (Fig 1). The first step is to remove all air bubbles from the sample and slide. A sponge is then placed on the sample and the cover. The slide and cover are then secured together by the magnets, which are glued to both slide and cover. The sponges and magnets vary to fit different samples. With thicker samples, thicker and denser sponges are required, and stronger magnets are needed to ensure stability. The technique of correct flattening and scanning is shown in the explanatory Video 1.

In case of thick specimens, the epidermis and dermis can also be separated from the fat with a surgical scalpel. In summary, we describe a novel tissue-flattening device that enhances optical scanning of the entire surgical specimen.

From the Melanoma Unit, Dermatology Department, Hospital Clínic de Barcelona, Institut d'investigacions Biomèdiques August Pi i Sunyer, Universitat de Barcelona.
Funding sources: None.
Conflicts of interest: This device is protected with the patent number 10 2019 101 035.7, January, 16, 2019.
Reprint requests: Javiera Pérez-Anker, MD, MSc, Dermatology Department, Hospital Clínic—IDIBAPS, University of Barcelona, Carrer de Villarroel, 170, 08036 Barcelona, Spain. E-mail: javiperezanker@gmail.com, perez12@clinic.cat.
J Am Acad Dermatol 2020;82:e157-8.
0190-9622/$36.00

https://doi.org/10.1016/j.jaad.2019.06.041

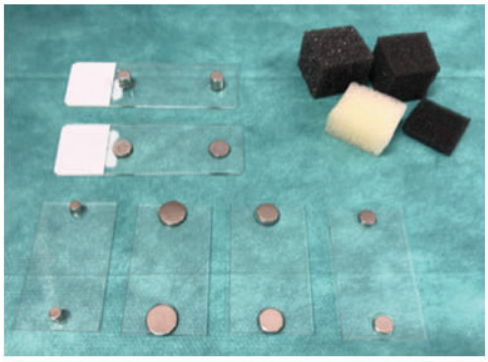

Fig 1. Magnets of different sizes and strength. Sponges of different sizes and densities.

REFERENCES

1. Pérez-Anker J, Malvehy J, Moreno-Ramírez D. Microscopia confocal ex vivo con método de fusión y tinción digital: cambiando paradigmas en el diagnóstico histológico. *Actas Dermosifiliogr*. In press.
2. Cinotti E, Grivet D, Labeille B, et al. The 'tissue press': a new device to flatten fresh tissue during ex vivo confocal microscopy examination. *Skin Res Technol*. 2017;23(1):121-124.

PATENTE DEL DISPOSITIVO PROPUESTO:[72]

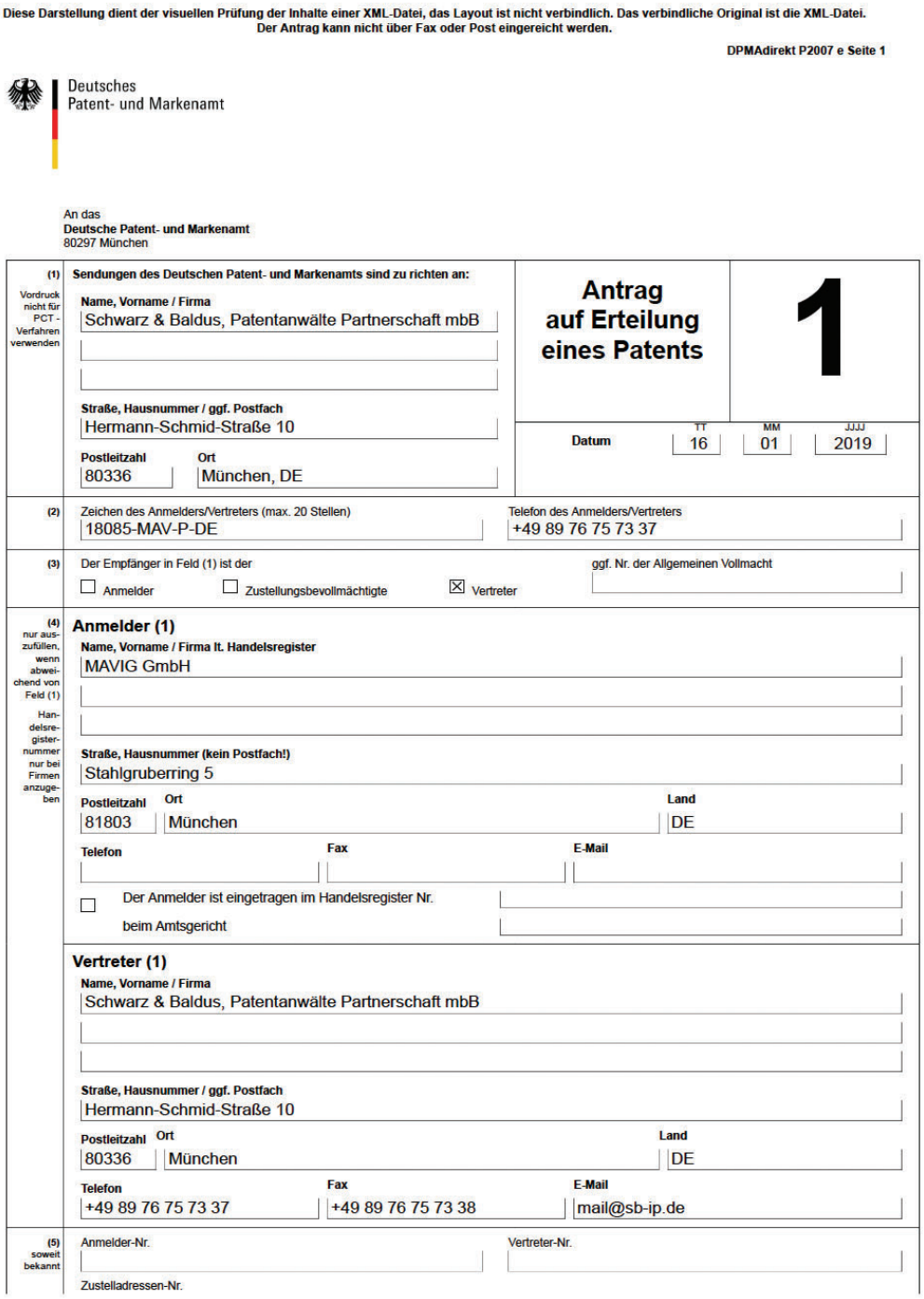

Diese Darstellung dient der visuellen Prüfung der Inhalte einer XML-Datei, das Layout ist nicht verbindlich. Das verbindliche Original ist die XML-Datei.
Der Antrag kann nicht über Fax oder Post eingereicht werden.

DPMAdirekt P2007 e Seite 1

Deutsches
Patent- und Markenamt

An das
Deutsche Patent- und Markenamt
80297 München

(1) Vordruck nicht für PCT-Verfahren verwenden

Sendungen des Deutschen Patent- und Markenamts sind zu richten an:

Name, Vorname / Firma
Schwarz & Baldus, Patentanwälte Partnerschaft mbB

Straße, Hausnummer / ggf. Postfach
Hermann-Schmid-Straße 10

Postleitzahl 80336 **Ort** München, DE

Antrag auf Erteilung eines Patents **1**

Datum TT 16 MM 01 JJJJ 2019

(2) Zeichen des Anmelders/Vertreters (max. 20 Stellen): 18085-MAV-P-DE
Telefon des Anmelders/Vertreters: +49 89 76 75 73 37

(3) Der Empfänger in Feld (1) ist der
☐ Anmelder ☐ Zustellungsbevollmächtigte ☒ Vertreter
ggf. Nr. der Allgemeinen Vollmacht

(4) nur auszufüllen, wenn abweichend von Feld (1)

Anmelder (1)

Name, Vorname / Firma lt. Handelsregister
MAVIG GmbH

Handelsregisternummer nur bei Firmen anzugeben

Straße, Hausnummer (kein Postfach!)
Stahlgruberring 5

Postleitzahl 81803 **Ort** München **Land** DE

Telefon **Fax** **E-Mail**

☐ Der Anmelder ist eingetragen im Handelsregister Nr.
beim Amtsgericht

Vertreter (1)

Name, Vorname / Firma
Schwarz & Baldus, Patentanwälte Partnerschaft mbB

Straße, Hausnummer / ggf. Postfach
Hermann-Schmid-Straße 10

Postleitzahl 80336 **Ort** München **Land** DE

Telefon +49 89 76 75 73 37 **Fax** +49 89 76 75 73 38 **E-Mail** mail@sb-ip.de

(5) soweit bekannt
Anmelder-Nr.
Vertreter-Nr.
Zustelladressen-Nr.

Diese Darstellung dient der visuellen Prüfung der Inhalte einer XML-Datei, das Layout ist nicht verbindlich. Das verbindliche Original ist die XML-Datei.
Der Antrag kann nicht über Fax oder Post eingereicht werden.

(6) IPC-Vorschlag ist unbedingt anzugeben, sofern bekannt

Bezeichnung der Erfindung

IPC-Vorschlag des Anmelders

Probenhalter für eine Gewebeprobe

(7)

Sonstige Anträge

Aktenzeichen der Hauptanmeldung (des Hauptpatents)

☐ Die Anmeldung ist **Zusatz** zur Patentanmeldung (zum Patent)
☒ **Prüfungsantrag** - Prüfung der Anmeldung **mit** Ermittlung der öffentlichen Druckschriften (§ 44 Patentgesetz)
☐ **Rechercheantrag** - Ermittlung der öffentlichen Druckschriften **ohne** Prüfung (§ 43 Patentgesetz)
☐ **Aussetzung** des Erteilungsbeschlusses auf __ Monate (§ 49 Abs. 2 Patentgesetz)
(Max. 15 Mon. ab Anmelde- oder Prioritätstag)

(8)

Erklärungen

Aktenzeichen der Stammanmeldung

☐ **Teilung/Ausscheidung** aus der Patentanmeldung
☐ an **Lizenzvergabe** interessiert (unverbindlich)
☒ **Nachanmeldung im Ausland** beabsichtigt (unverbindlich)

(9)

☐ Inländische **Priorität** (Datum, Aktenzeichen der Voranmeldung)
☐ Ausländische **Priorität** (Datum, Land, Aktenz. der Voranmeldung; vollständige **Abschrift(en) der ausländischen Voranmeldung(en)** beifügen)

(10)

Gebührenzahlung in Höhe von 390,00 EUR

☒ **Einzugsermächtigung** *elektr. Formular ist beigefügt.*
☐ **Überweisung** *(nach Erhalt der Empfangsbescheinigung)*

Wird die Anmeldegebühr nicht innerhalb 3 Monaten nach dem Tag des Eingangs der Anmeldung gezahlt, so gilt die Anmeldung als zurückgenommen!

(11)

Anlagen

1.		Vertretervollmacht
2.	1	Erfinderbenennung (P 2792e)
3.	1	Zusammenfassung(ggf. mit Zeichnung Fig. 1)
4.	9	Seite(n) Beschreibung (ggf. mit Bezugszeichenliste)
5.	2	Seite(n) Patentansprüche
	10	Anzahl Patentansprüche
6.	3	Figuren
7.		Abschrift(en) der Voranmeldung(en)
8.		Zitierte Nichtpatentliteratur
9.		Sequenzprotokoll
10.		Angabe des geografischen Herkunftortes gemäß § 34a Patentgesetz
11.		Übersetzung(en)
12.		Sonstiges

P 2007e 1.08

Unterzeichner (1)

Dr. Oliver Baldus

(12) Unterschrift

Patentanwalt

(13) Funktion des Unterzeichners

PUBLICACIÓN N° 8:[73]

Seis pasos para la obtención de un escaneo óptimo en microscopía confocal *ex vivo*.

Six steps to reach optimal scanning in *ex vivo* confocal microscopy.

Javiera Pérez-Anker, Agustí Toll, Susana Puig, Josep Malvehy.

J Am Acad Dermatol. 2022 Jan;86(1):188-189. doi: 10.1016/j.jaad.2021.01.044. Epub 2021 Jan 19.
Factor de impacto: 11.527

Resumen

Antecedentes: La microscopía confocal *ex vivo* permite el escaneo de tejido en tiempo real, con resolución celular. Sin embargo, no siempre se logran imágenes que permitan esta resolución.

Objetivos: Proponer una secuencia de pasos consecutivos a seguir, para lograr un método estandarizado de escaneo de muestras.

Métodos: Se propusieron 6 pasos a ser realizados: extirpar el tejido de forma adecuada, preparar el tejido a ser escaneado, teñir el espécimen de acuerdo con el tejido a ser escaneado, aplanar la muestra de forma precisa, encontrar el punto "cero" correctamente y ajustar el tono y color apropiados para el escaneo.

Resultados: Se escanearon tejidos con el método sugerido y las muestras lograron su adecuada representación, obteniendo imágenes de forma rápida, estandarizada y con resolución celular.

Conclusiones: Se demostró que, siguiendo la secuencia propuesta, se pudo lograr un método estandarizado de escaneo de tejidos con microscopía confocal *ex vivo*.

Malignant Hematology, H. Lee Moffitt Cancer Center, Tampa, Florida.[8]

Authors Malachowski and Moy contributed equally to this article.

Funding sources: None.

IRB approval status: Reviewed and approved by the University of South Florida Institutional Review Board (Pro00035409).

Reprints not available from the authors.

Correspondence to: Lucia Seminario-Vidal, MD, PhD, 13330 USF Laurel Dr, 6th Floor, Tampa, FL 33612

E-mail: luciasem@usf.edu

Conflicts of interest
None disclosed.

REFERENCES

1. Korgavkar K, Xiong M, Weinstock M. Changing incidence trends of cutaneous T-cell lymphoma. *JAMA Dermatol*. 2013; 149:1295-1299.
2. Ghazawi FM, Netchiporouk E, Rahme E, et al. Distribution and clustering of cutaneous T-cell lymphoma (CTCL) cases in Canada during 1992 to 2010. *J Cutan Med Surg*. 2018;22: 154-165.
3. Litvinov IV, Tetzlaff MT, Rahme E, et al. Identification of geographic clustering and regions spared by cutaneous T-cell lymphoma in Texas using 2 distinct cancer registries. *Cancer*. 2015;121:1993-2003.
4. Moreau JF, Buchanich JM, Geskin JZ, Akilov OE, Geskin LJ. Non-random geographic distribution of patients with cutaneous T-cell lymphoma in the Greater Pittsburgh Area. *Dermatol Online J*. 2014;20(7):13030/qt4nw7592w.
5. Clough L, Bayakly AR, Ward KC, et al. Clustering of cutaneous T-cell lymphoma is associated with increased levels of the environmental toxins benzene and trichloroethylene in the state of Georgia. *Cancer*. 2020;126: 1700-1707.

https://doi.org/10.1016/j.jaad.2021.01.041

Six steps to reach optimal scanning in ex vivo confocal microscopy

To the Editor: Ex vivo confocal microscopy allows an immediate histologic analysis of excised tissues, with images of microscopic cellular detail. However, reaching an optimal scanning could be challenging.[1,2] This is why some steps are crucial to obtain a correct scan at the first attempt, regardless of the type of tissue to be scanned. These measures, with few adaptations, can be applied to scan punch biopsy specimens, Mohs micrographic surgery specimens (<2.5 cm diameter), or even smaller samples such as from needle biopsies.[3,4] As an example, ex vivo confocal microscopy with a specimen from a Mohs micrographic surgical procedure is presented in the Video 1 (available at http://www.jaad.org).

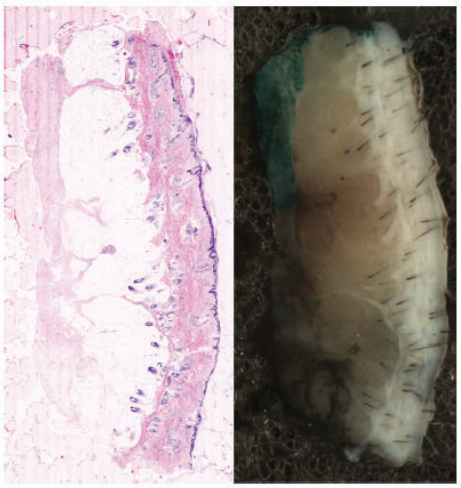

Fig 1. Perfect "zero point" and colors in the specimen with the correspondent macro image.

- First step: Properly excise the tissue.[2] When the excised tissue has a homogeneous thickness in the entire sample, the major part of the effort to obtain a correct image from the first scan is achieved, independently of the sample to be scanned. A difference in the thickness of the specimen will require a balance in the pressure applied due to the surface of the sample, and it may be necessary to use an extra sponge specifically cut for this purpose (Video 1). The excised tissue should ideally be about as thick as a dollar coin, and a double scalpel is recommended for the excision of the lateral margins when a skin specimen is going to be scanned during Mohs micrographic surgery.[2]
- Second: Prepare the tissue to be scanned. Remove blood from the surface to be scanned to avoid possible interference. Orient the sample as if it were a regular specimen from Mohs micrographic surgery in the case of scanning a Mohs specimen.
- Third: Stain the tissue. Many staining methods have been described. We demonstrated that the combination of acetic acid and acridine orange is effective in most skin samples.[5]
- Fourth: Flatten the tissue correctly. Flatten the epidermis and remove all of the bubbles. Relaxing cuts can be made to allow the epidermis or dermal component to achieve a

uniform flattened profile. If any bubbles remain, wash again in the stain solution to completely remove them (Video 1). Using an adequate flattening device increases the effectiveness of scanning because the pressure on the whole specimen is homogeneous. We have previously explained this step.[2] When more pressure is needed to reduce the sample thickness and to allow the laser to penetrate deeper into the tissue, the pressure must be increased using an extra sponge. This also reduces the irregularity of the surface. If the epidermis is folded, it can be positioned correctly with forceps or a scalpel. Choose an adequate sponge and magnet adapted to tissue thickness and consistency.

- Fifth: Find the perfect "zero point." A sharp focus of the structures will only be obtained by achieving adequate, deep laser penetration—a perfect "zero" (Fig 1).
- Sixth: Adjust the intensity of the colors in the whole specimen. The colors may be perfectly observed in some areas but may not have the correct intensity in others. A color average, between at least 3 different areas, should be obtained by increasing or decreasing both (fluorescence and reflectance) laser powers.

Javiera Pérez-Anker, MD, MSc, Agustí Toll, MD, PhD, Susana Puig, MD, PhD, and Josep Malvehy, MD, PhD

From the Dermatology Department, Melanoma Unit, Hospital Clínic de Barcelona, Instituto de Investigaciones Biomédicas August Pi i Sunye, Universitat de Barcelona, Barcelona, Spain.

Funding sources: None.

IRB approval status: Not applicable.

Correspondence and reprint requests to: Javiera Pérez-Anker, MD, MSc, Dermatology Department, Hospital Clínic—IDIBAPS, University of Barcelona, Carrer de Villarroel, 170, 08036 Barcelona, Spain

E-mail: javiperezanker@gmail.com; perez12@clinic.cat

Conflicts of interest

Dr Pérez-Anker is responsible for the ex vivo confocal microscopy training courses for CALIBER-MAVIG. Drs Toll, Puig, and Malvehy have no conflicts of interest to declare.

REFERENCES

1. González S, Swindells K, Rajadhyaksha M, Torres A. Changing paradigms in dermatology: confocal microscopy in clinical and surgical dermatology. *Clin Dermatol.* 2003;21(5):359-369.
2. Pérez-Anker J, Puig S, Malvehy Guilera J. A fast and effective option for tissue flattening: optimizing time and efficacy in ex vivo confocal microscopy. *J Am Acad Dermatol.* 2020;82(5):e157-e158.
3. Villarreal JZ, Pérez-Anker J, Puig S, et al. Ex vivo confocal microscopy performs real-time assessment of renal biopsy in non-neoplastic diseases. *J Nephrol.* 2021;34(3):689-697.
4. Puliatti S, Bertoni L, Pirola GM, et al. Ex vivo fluorescence confocal microscopy: the first application for real-time pathological examination of prostatic tissue. *BJU Int.* 2019;124:469-476.
5. Anker JP, Ribero S, Yélamos O, et al. Basal cell carcinoma characterisation using fusion ex vivo confocal microscopy: a promising change in conventional skin histopathology. *Br J Dermatol.* 2020;182(2):468-476.

https://doi.org/10.1016/j.jaad.2021.01.044

Usefulness of high-frequency Doppler ultrasound skin thickness measurement for disease staging and assessing treatment response in patients with scleredema: A case-control study

To the Editor: Scleredema, a rare disease characterized by increased collagen and mucin deposits in the dermis, has been associated with diabetes mellitus, monoclonal gammopathy, and infections.[1] The thickness of the dermis in the back can even be multiplied 3- to 4-fold, mainly because of acid mucopolysaccharides deposition.[1] The course is unpredictable, with surprising abrupt resolutions or dull persistence for years. The diagnosis is often delayed for months or years.[2] Increased body volume due to obesity can simulate the skin's stiffness and thickening in patients with scleredema and delay the diagnosis.[3] High-frequency ultrasound of skin (HFUS) is a technique that is increasingly used in dermatology.[4,5] The objective of this study was to quantify dermal infiltration and evaluate the response to treatment in patients with scleredema using HFUS.

This prospective case-control study included all scleredema patients (n = 8) at the Hospital Clínic of Barcelona and the Complejo Hospitalario Universitario de Santiago de Compostela, Spain. Three healthy controls were recruited for each case. The thickness of the dermis was measured by HFUS in 3 regions: posterior neck, upper back, and arms. After the initial assessment, long-term clinical and ultrasound follow-up was at 6 months and 1 year. Further methodologic details are provided in the Supplemental Material (via Mendeley at https://data.mendeley.com/datasets/cst2n8fpmy/1).

Demographic and ultrasonographic characteristics of the patients are described in Table I, and Table II describes the characteristics of cases and controls with

PUBLICACIÓN Nº 9.[74]

Precisión diagnóstica de microscopia confocal *ex vivo* con tinción digital en el diagnóstico del carcinoma escamoso mediante biopsias.

Diagnostic accuracy of ex vivo confocal microscopy with digital stain for squamous cell carcinoma in skin biopsies

Nelson Lobos-Guede, Carlos Toloza Salech, Raquel Albero-González, Paola Castillo, Shirley Zamora, Edgard Larotta, Llucia Alós, Adriana García, Simone Soglia, Agusti Toll, Susana Puig, Josep Malvehy and Javiera Pérez-Anker

Eur Acad Dermatol Venereol. 2024. Under Review.
Factor de impacto: 9.228

Resumen

Antecedentes: La microscopía confocal ex vivo permite el examen del tejido recién extirpado peri operatoriamente y proporciona imágenes rápidas de alta resolución comparables a la histopatología convencional.
Objetivos: Evaluar la precisión diagnóstica del diagnóstico de carcinoma de células escamosas cutáneas (CSCC) y describir algunas de sus características diagnósticas histológicas críticas en biopsias recién extirpadas con un nuevo método de microscopía confocal ex vivo en modo de fusión (MCFu) utilizando tinción digital.
Métodos: Se biopsiaron tumores cutáneos consecutivos sospechosos de CSCC por examen clínico y dermoscópico y se analizaron con MCFu. Las características diagnósticas más representativas se compararon con su imagen correspondiente de

hematoxilina y eosina (H&E) en parafina convencional. Las imágenes fueron evaluadas por dos patólogos sin experiencia previa en MCFu y por un cirujano de Mohs con más de cinco años de experiencia en MCFu. Se evaluó la precisión diagnóstica de los mosaicos de MCFu, tanto diagnóstica como de cada característica de H&E presente.
Resultados: Se incluyeron 59 CSCC confirmados histológicamente con 223 mosaicos de 41 pacientes y 55 mosaicos de 7 lesiones benignas/premalignas confirmadas histológicamente en 16 pacientes. La precisión diagnóstica del CSCC por parte de los patólogos y el cirujano de Mohs fue respectivamente: Sensibilidad (SE) 91%/96%, Especificidad (SP) 85%/94%, Valor Predictivo Positivo (PPV) 95%/98% y Valor Predictivo Negativo (NPV) 75%/89%. Las características diagnósticas de H&E también tuvieron una alta SE y SP con un valor de p <0,05 en todas ellas. Otras variables, como la desmoplasia, la disqueratosis y las figuras mitóticas, tuvieron una correlación deficiente con los hallazgos histopatológicos.
Conclusiones: Los mosaicos de MCFu mostraron un rendimiento similar al de H&E en el diagnóstico de CSCC, capturando eficazmente la mayoría de las características diagnósticas clave. Además, los patólogos sin experiencia lograron una fuerte concordancia con los diagnósticos de histología convencional.

-Diagnostic accuracy of ex vivo confocal microscopy with digital stain for squamous cell carcinoma in skin biopsies

Journal:	*British Journal of Dermatology*
Manuscript ID	Draft
Manuscript type:	Original Article
Date Submitted by the Author:	n/a
Complete List of Authors:	Lobos-Guede, Nelson; Universidad de Chile, Dermatology; Hospital Clinic de Barcelona Salech, Carlos Toloza; Universitat de Barcelona, Dermatology Department Albero-González, Raquel; Hospital Clinic de Barcelona, Pathology Department Castillo, Paola; Hospital Clinic de Barcelona, Patology; IDIBAPS, Patology Zamora, Shirley; Universitat de Barcelona, Dermatology Department Larotta, Edgard; Universitat de Barcelona, Dermatology Department Soglia, Simone; Universitat de Barcelona, Dermatology Department Puig, Susana; Universitat de Barcelona, Dermatology Department Malvehy, Josep; University of Barcelona, Department of Dermatology Pérez-Anker, Javiera; Hospital Clinic de Barcelona, Dermatology Alos, Llucia; Hospital Clinic de Barcelona, Pathology Garcia-Herrera, Adriana; Hospital Clinic, Pathology; Universitat de Barcelona, Fonaments Clinics Toll, Agusti; Hospital Clinic de Barcelona, Dermatology; Dermatology
Keywords:	Squamous cell carcinoma, Standardized skin surface biopsy, Confocal microscopy, Dermatopathology

Abbreviated Abstract

Ex vivo confocal microscopy using digitally stained FuCM mosaics demonstrated performance comparable to H&E staining in diagnosing cutaneous squamous cell carcinoma and effectively capturing critical diagnostic features. Inexperienced pathologists also achieved strong agreement with conventional histology diagnoses for CSCC.

-Title: Diagnostic accuracy of ex vivo confocal microscopy with digital stain for squamous cell carcinoma in skin biopsies

-Running head: Diagnostic accuracy of fusion ex vivo confocal microscopy with digital stain in cutaneous SCC and identification of architectural and cellular features in comparison with conventional standard haematoxylin and eosin histopathology.

-Word count of body text: 3457

-Table count: 1

- Figure count: 4

- Supplementary material: 2 figures and 6 tables

-**Authors**: Nelson Lobos-Guede[1*], Carlos Toloza Salech[1*], Raquel Albero-González[2], Paola Castillo[2], Shirley Zamora[1], Edgard Larotta [1], Llucia Alós[2], Adriana García[2], Simone Soglia[1], Agusti Toll[1], Susana Puig[1,3], Josep Malvehy[1,3]± and Javiera Pérez-Anker[1]±

[*] The authors equally contributed to this work

± The senior authors equally contributed to this work

- **Affiliations:**

[1]Dermatology Department, Hospital Clínic de Barcelona, IDIBAPS, Universitat de Barcelona, Barcelona, Spain.

[2]Pathology Department, Hospital Clínic de Barcelona, Universitat de Barcelona, Barcelona, Spain.

[3]Centro de Investigación Biomédica en Red (CIBER) de enfermedades raras, Spain

-Corresponding author:

Javiera Pérez Anker, MD

Melanoma Unit, Dermatology Department, Hospital Clinic Barcelona

Villarroel 170, 08036, Barcelona, Spain.

javiperezanker@gmail.com

Tel.: +34 93 2275400 ext 2422

Fax: +34 93 2275438

ORCID:

Susana Puig 0000-0003-1337-9745

Javiera Pérez-Anker 0000-0002-6959-7250

Nelson Lobos 0000-0003-0818-023X

Josep Malvehy 0000-0002-6998-914X

-Keywords:

Fluorescence confocal microscopy, fusion confocal microscopy, ex vivo confocal microscopy, skin cancer, squamous cell carcinoma, non-melanoma skin cancer, digital stain, digital staining ex vivo confocal

-Funding statement: The research at the Melanoma Unit in Barcelona is partially funded by Spanish Fondo de Investigaciones Sanitarias grants PI15/00716 and PI15/00956; CIBER de Enfermedades Raras of the Instituto de Salud Carlos III, Spain, co-financed by European Development Regional Fund "A way to achieve Europe" ERDF; AGAUR 2014_SGR_603 of the Catalan Government, Spain; European Commission under the 6th Framework Programme, Contract No. LSHC-CT-2006-018702 (GenoMEL) and by the European Commission under the 7th Framework Programme, Diagnoptics; The National Cancer Institute (NCI) of the US National Institute of Health (NIH) (CA83115); a grant from "Fundació La Marató de TV3" 201331-30, Catalonia, Spain; a grant from "Fundación Científica de la Asociación Española Contra el Cáncer" GCB15152978SOEN, Spain, and CERCA Programme / Generalitat de Catalunya. Part of the work was carried out at the Esther Koplowitz Center, Barcelona.

The whole exome sequencing analysis was in part supported by the intramural research program of the National Institutes of Health, National Cancer Institute, Division of Cancer Epidemiology and Genetics.

-**Disclosures**: The authors have no disclosures or conflicts of interest to report.

Bulleted statements

What is already known on this topic

- Fluorescence and reflectance lasers can be used simultaneously in ex vivo confocal microscopy and different features can be visualized with each laser.
- Ex vivo fluorescence confocal microscopy has been used to evaluate margins in basal cell carcinoma, cutaneous squamous cell carcinoma, dermatofibrosarcoma protuberans and syringomatous carcinoma excised with Mohs micrographic surgery.
- A better stain protocol has demonstrated superiority in observing tumoral and stromal features in basal cell carcinoma.

What does this study add

- Digital stain is accurate to observe morphological and cellular features with colours similar to conventional haematoxylin and eosin in digital staining ex vivo confocal microscopy.
- Classical histopathological diagnostic features were observed in digital staining with ex vivo fusion confocal microscopy. Nuclear features as mitosis and dendritic cells were also observed.
- Pathologists without experience in fusion ex vivo confocal microscopy were able to diagnose squamous cell carcinoma in skin biopsies and also to differentiate them of other suspected lesions.

ABSTRACT

Background: Ex vivo confocal microscopy enables the examination of freshly excised tissue perioperatively and provides rapid high-resolution images comparable to conventional histopathology.

Objectives: Assess cutaneous squamous cell carcinoma (CSCC) diagnostic accuracy and describe some of its critical histological diagnostic features in freshly excised biopsies with a new method of ex vivo confocal microscopy in a fusion mode (FuCM) using digitally staining.

Methods: Consecutive cutaneous tumors suspicious of CSCC by clinical and dermoscopic examination were biopsied and analyzed with FuCM. Most representative diagnostic features were compared to their corresponding image of conventional paraffined hematoxylin and eosin (H&E). Images were evaluated by two pathologists with no previous training in FuCM and by a Mohs surgeon with more than five years of experience in FuCM. Diagnostic accuracy of the FuCM mosaics were assessed, both diagnostic and of each H&E feature present.

Results: 59 histology confirmed CSCC with 223 mosaics of 41 patients and 55 mosaics from 7 histologically confirmed benign/premalignant lesions of 16 patients were included. CSCC diagnostic accuracy by pathologists and Mohs surgeon were respectively SE 91%/96%, SP 85%/94%, PPV 95%/98%, and NPV 75%/89%. H&E diagnostic features also had a high SE and SP with a p-value <0.05 in all of them. Other variables, such as desmoplasia, dyskeratosis, and mitotic figures, were poorly correlated with histopathology findings.

Conclusions: FuCM mosaics showed a performance similar to H&E in diagnosing CSCC, effectively capturing most key diagnostic features. In addition, inexperienced pathologists achieved strong agreement with conventional histology diagnoses.

INTRODUCTION

Cutaneous squamous cell carcinoma (CSCC) is a common skin cancer, second only to basal cell carcinoma (BCC), arising from keratinocytes in the stratified squamous epithelium[1,2]. Accurately estimating global CSCC incidence and mortality is challenging due to its exclusion from many national tumor registries, but Europe has seen a recent increase in CSCC incidence, with rates rising with age [3]. While diagnosing CSCC is generally straightforward, some cases can be challenging. Dermoscopy and noninvasive imaging techniques have been explored to aid differentiation from mimicking conditions, but histologic examination remains necessary for confirmation[4-9]. Recent advancements in medical technology have introduced in vivo (ivCM) and ex vivo confocal microscopy (evCM), enhancing dermatological diagnostics and therapeutic efficacy[10-15].

Recent advances in evCM devices combine reflectance (evRCM) and fluorescence (evFCM) lasers in a fusion mode (FuCM) and with the processing of these images with dedicated software, a real-time high-resolution image with digital staining is obtained [4,13], like conventional H&E. The scanned image allows the visualization of cellular and architectural details comparable to those observed in standard pathology analysis, either in paraffin-embedded or frozen samples[16,17]. It is important to mention that the EvCM fusion modality with digital staining, has allowed changing from grayscale into a color scale reproducing the colors and structures in H&E histology. This has allowed to obtain superior histopathological correlation compared with old devices, with a higher resolution at the cellular level and better stromal characterization[13].

Ex vivo confocal microscopy has demonstrated accuracy in diagnosing BCC and has been mainly used in nonmelanoma skin cancer surgeries, such as Mohs micrographic surgery. Some studies have validated its use in diagnosing CSCC, showing high sensitivity and specificity [18-19]. Deep learning models have also shown potential in detecting CSCC using digitally stained evCM images. Additionally, evCM has been utilized in characterizing normal skin structures, melanocytic lesions, and non-pigmented nail tumors. However, much of this research relied on earlier technology versions and the use of acridine orange as a contrast agent[30-35]. Currently, there is a lack of studies assessing the diagnostic accuracy of CSCC using the new fusion evCM technology with specific staining methods, such as FuCM.

Shavlokhova V. and coworkers have previously characterized oral SCC using FuCM[36], but, to our knowledge, no studies have assessed the diagnostic accuracy of CSCC using this new technology of fusion evCM with a particular staining method.

MATERIAL AND METHODS

1.1. Study population

We conducted a cross-sectional validation study to assess CSCC diagnostic capacity and some of its key histological diagnostic features with FuCM mosaics in freshly excised biopsies. Moreover, to compare these findings to those observed in their corresponding conventional H&E paraffined sections and the diagnostic concordance of both methods.

Patients with consecutive lesions with clinical and dermoscopic features of CSCC (both in situ and invasive) scheduled for incisional biopsies from January 2019 to May 2019 were included. Also, we added FuCM mosaics of benign and premalignant lesions of some patients from our image bank.

1.2. Sample processing and photographing

Each area of the tumor where the biopsy was performed was demarcated, and clinical and dermoscopic images were obtained. Biopsies were performed with a 3-4 mm punch or doing a deep shave. Each biopsy was vertically sectioned after the extraction, and then a previously described stain protocol was applied to each tissue before scanning with FuCM, according to the protocol and steps previously described in the literature[22,37,38]. All samples were scanned with the 4th Gen VivaScope 2500 (MAVIG GmbH, Munich) in fusion mode and digital staining visualization[16,38]. Afterward, each scanned side was correctly positioned in a tissue cassette for conventional histopathology analysis for image comparison with FuCM.

1.3. Study variables, images assessment, and data collection

Independent variables

We gathered data from our database and medical records, including information on sex, age, immune status, lesion location, biopsy type, tumor size, histopathological subtype, and CSCC features. Primary tumor locations were categorized as face, scalp, trunk, limbs, and genitalia. Reported histopathological features of CSCC (WHO Classification of Skin

Tumours criteria) included the presence or absence of CSCC, invasive status, keratinization, intercellular bridges, nuclear pleomorphism, stromal inflammation (peritumoral inflammatory infiltrate), dyskeratosis, parakeratosis, desmoplasia, loss of granular layer, mitotic figures, and infiltrative borders. All these histological features are shown in figures 2-4 and supplementary figures 1 and 2.

Images assessment and data collection

After the histopathological report, the resulting FuCM mosaics obtained were randomly distributed into two groups (by an independent investigator). In addition, for this accuracy study, we added FuCM mosaics of benign and premalignant lesions from our image bank, and they were added to the pool of images to be evaluated. Two independent pathologists (PTs) (at the same time) without training in FuCM (RA and PC) and a Mohs surgeon (MS) with experience in FuCM (JPA) evaluated each group of images. FuCM mosaics were assessed on the same day by PTs and MS blind to the histological diagnosis.

Results of CSCC diagnostic status and their histological features noted in each pathology report were considered the gold standard for comparison with the FuCM mosaics assessments.

Invasive or in situ variant was determined only in the suspected CSCC. Although tumor thickness (modified Breslow) can be measured with the new FuCM device, our study did not assess it because all samples were extracted using only partial incisional biopsies.

FuCM mosaics and their corresponding H&E were excluded when the assessed features were considered "not evaluable" due to the poor quality of the FuCM mosaics.

1.4. Outcomes

. The diagnostic accuracy of CSCC with FuCM mosaics measured in terms of sensitivity (SE), specificity (SP), positive predictive value (PPV), and negative predictive value (NPV).

. The ability of FuCM to detect diagnostic histological features of CSCC (compared to conventional histology).

. The degree of inter-rater reliability among examiners who assess FuCM mosaics.

1.5. Statistical analysis

A descriptive analysis of the qualitative variables was done according to their nature, using absolute and relative frequency measurements. Clinical outcomes such as age, sex, immunosuppression, type of biopsy performed, tumor location/size, and histologic subtype were obtained and tabulated. To assess the diagnostic accuracy, SE, SP, PPV and NPV were calculated for CSCC diagnosis and concordance of each architectural and cellular feature with the histological analysis. PTs, MS, inter-evaluator (PTs vs. MS), and multi-evaluator (PTs vs. MS vs. H&E) agreement for CSCC diagnosis, and each variable of CSCC using FuCM mosaics were calculated with Cohen's kappa (k).

Pearson's chi-squared test was used to analyze the examined variables with a confidence level of 95% (p-value < 0.05). Calculations were performed with STATA 14 (Copyright 1996–2021 Stata Corp LLC).

1.6. Ethical aspects

The study complied with the Declaration of Helsinki Principles and was approved by the Clinical Research Ethics Committee of the Hospital Clinic of Barcelona.

RESULTS

Two hundred twenty-three FuCM mosaics were obtained from 59 tumors of 41 patients (15 females and 26 males). The characteristics of the patients and the tumors are presented in Table 1. Two FuCM mosaics (0,9%) were excluded because of the poor quality (epidermis not represented to conclude the diagnosis). From the 221 resulting images, 166 FuCM mosaics and their corresponding H&E belonged to 59 histologically confirmed CSCC and 55 images from 16 confirmed benign/premalignant lesions of 16 patients. The latter corresponded to actinic keratosis (AK), seborrheic keratosis (SK), and verruca vulgaris (VV). All of them were included in the evaluation.

The mean age of CSCC patients was 81 (57-100) years. Tumors presented an average size of 1.6 cm (0.2-4.7), and they were located on the face (37.3%), scalp (28.8%), limbs (18.6%), trunk (10.2%), and genitalia (5.1%). Of the total number of CSCC patients, 5% presented immunosuppression. Biopsies were taken by 3 to 4 mm punch (84.7%) and deep shave (15.3%). The histological SCC subtypes found were conventional (89.8%), in situ (5.1%), keratoacanthoma (3.4%), and acantholytic (1.7%). Cross-tabulation of relative and

absolute frequencies obtained for all evaluators with FuCM are summarized in Supplementary Table 1.

The CSCC diagnostic accuracy and its histological features assessed in 221 FuCM mosaics (considering benign and premalignant lesions) are summarized in Figure 1. Variable "invasive status" only was assessed in CSCC FuCM mosaics (166 images). The remaining CSCC histological features were also evaluated for CSCC FuCM mosaics without considering benign and premalignant lesions (CSCC group). Key findings are summarized in Figure 1 and detailed in Supplementary Tables 2-7.

Considering 221 FuCM mosaics, FuCM showed a diagnostic accuracy of 91% for PTs and 96% for MS, with a significant association (p-value <0.05). PTs had a SE of 91%, SP of 85%, PPV of 95%, and NPV of 75%. MS had a SE of 96%, SP of 94%, PPV of 98%, and NPV of 89%. The accuracy for CSCC invasive status was 88% for PTs and 94% for MS, also with a significant association. Both PTs and MS demonstrated high PPV for this variable.

In assessing CSCC histological variables with all FuCM mosaics (221 images), MS demonstrated high capacity for mitotic figures (SE 96/81-99), stromal inflammation (SE 94/89-97), keratinization (SE 88/82-93), pleomorphism (SE 88/82-93), dyskeratosis (SE 87/73-95), loss of granular layer (SE 87/79-93), and parakeratosis (SE 83/74-90). These values slightly improved when analyzing only CSCC FuCM mosaics (166 images). PTs had slightly lower assessment capacity compared to MS but still adequate for these variables.

High positive predictive values (PPV) were observed for both PTs and MS for variables including keratinization, pleomorphism, stromal inflammation, infiltrative borders, loss of granular layer, parakeratosis, and intercellular bridges. Low PPV values were due to false positives for other variables, particularly desmoplasia, dyskeratosis, and mitotic figures.

When considering all FuCM mosaics (malignant and benign/premalignant lesions), FP values were higher for dyskeratosis, desmoplasia, parakeratosis, intercellular bridges, and mitotic figures. When analyzing only the CSCC FuCM mosaics group, FP values were similar but with a slight decrease in some variables, such as dyskeratosis, intercellular bridges, desmoplasia, mitotic figures, and parakeratosis. However, these FP values influenced low PPV only in desmoplasia, dyskeratosis, and mitotic figures.

Furthermore, when evaluating only CSCC FuCM mosaics (166 images), variables like keratinization, pleomorphism, stromal inflammation, infiltrative borders, loss of granular layer, parakeratosis, and intercellular bridges showed a significant increase in PPV for both PTs and MS.

Both PTs and MS exhibited high specificity (SP) values, with minimal differences. PTs were better at determining the absence of dyskeratosis, parakeratosis, desmoplasia, and mitotic figures when they were absent in conventional histology (GS). These values remained consistent when only CSCC FuCM mosaics were evaluated. MS was better at determining the absence of infiltrative borders, loss of granular layer, and stromal inflammation, and these values also remained consistent when analyzing only CSCC FuCM mosaics.

In the assessment of most CSCC histological variables in FuCM mosaics, excellent negative predictive values (NPV) were observed, indicating few false negatives (FN), except for keratinization assessed by PTs. When analyzing only the CSCC mosaics, PTs showed a decrease in NPV for pleomorphism and stromal inflammation. These findings were statistically significant (p-value < 0.05) (Figure 1 and Supplementary Tables 2 and 4).

Considering all FuCM mosaics (including malignant and benign/premalignant lesions) and the CSCC-only mosaics group, MS had higher FN values for evaluating infiltrative borders (percentage/absolute frequency), but this did not result in low NPV values for this variable.

For all FuCM mosaics, PTs had higher FN values for evaluating keratinization (percentage/absolute frequency) compared to MS. In the CSCC-only mosaics group, PTs had higher FN values for parakeratosis, pleomorphism, infiltrative borders, and stromal inflammation (percentage/absolute frequency). However, these FN values only led to low NPV values in PTs' analysis for keratinization (in all mosaics and CSCC-only mosaics group) and for pleomorphism and stromal inflammation (CSCC-only mosaics group) (Supplementary Table 6 and 7).

In the assessment of CSCC diagnosis using 221 FuCM mosaics (including benign and premalignant lesions), we found substantial correlation between PTs and GS (k=0.73), almost perfect correlation between MS and GS (k=0.80), perfect inter-observer agreement between PTs and MS (k=0.90), and almost perfect multi-observer agreement between PTs, MS, and GS (k=0.813) (Figure 1 and Supplementary Table 3).

When evaluating only CSCC FuCM mosaics (166 images), we observed almost perfect correlation between PTs and GS (k=0.83), almost perfect correlation between MS and GS (k=0.84), almost perfect inter-observer agreement between PTs and MS (k=0.90), and almost perfect multi-observer agreement between PTs, MS, and GS (0.82) (Figure 1 and Supplementary Table 5).

Regarding CSCC histological features, our findings revealed almost perfect inter-observer agreement between PTs and MS for intercellular bridges (k=0.84) and dyskeratosis (k=0.81). Mitotic figures (k=0.67), pleomorphism (k=0.64), parakeratosis (k=0.64), and stromal inflammation (k=0.62) showed substantial agreement. Keratinization (k=0.59), loss of the granular layer (k=0.58), infiltrative borders (k=0.47), and desmoplasia (k=0.43) demonstrated moderate agreement.

For CSCC diagnosis, multi-observer agreement was almost perfect (k=0.81), and for stromal inflammation, it was substantial (k=0.71).

We also calculated the Kappa coefficient (KC) for CSCC invasive status, which showed almost perfect agreement between PTs and GS (k=0.83), MS and GS (k=0.84), PTs and MS (k=0.80), and PTs, MS, and GS (k=0.82).

Importantly, all the mentioned kappa results were statistically significant (p-value < 0.05). No significant changes in agreement values were observed among examiners when evaluating only CSCC FuCM mosaics (166 images).

DISCUSSION

To our knowledge, there are no reports of CSCC characterization using FuCM with digital staining, except for an unpublished master's thesis carried out by the same team of researchers in June 2019. Previous studies that determined some CSCC features with evCM used evRCM and evFCM modalities separately or combined but without the new fusion mode with digital staining and without the incorporation of samples of non-CSCC submitted to diagnostic biopsies to adequately establish its diagnostic accuracy (except for the publication by Horn et al. [30] and Ruini et al.[31], who included FuCM mosaics of tumor-free areas). Authors who have described CSCC features with evFCM used descriptive terms similar to those used in histological settings but without digital staining. Longo et al.[24], using evFCM, performed Mohs diagnosis and identification of some CSCC features in 13 tumor

sections and margins: tumor silhouette, keratin pearls, nuclear pleomorphism, keratin formation, detection of residual tumor and tumor differentiation. More recently, Hartmann et al. using evRCM and evFCM lasers separately, reported features to differentiate carcinoma in situ from invasive SCC and predict their level of differentiation according to the Broder classification[25]. They described CSCC features (erosion/ulceration, hyperkeratosis, parakeratosis, architectural disarrangement, plump bright or speckled cells in the epidermis, plump bright or speckled cells in the dermis, nest-like structures in the dermis, keratin pearls and peritumoral inflammatory infiltrate) modifying in-vivo criteria previously described by Manfredini et al.[41] for the ex-vivo use.

Although in our study we considered the characterization of some of the CSCC findings observed in evRCM and evFCM in histological terms (hyperkeratosis, parakeratosis), another terminology previously described with ivCM [41-43] was also used, such as "architectural disarrangement" (dyskeratosis) or "plump, bright cells" (macrophages or inflammatory cells). In addition, they also included the level of differentiation according to Broder classification, keratin pearls, erosion/ulceration, and peritumoral inflammatory infiltrate, which in our case were not assessed because we had small incisional biopsies. Figures 2-4.

Only one publication has used FuCM mosaics with digital staining to characterize SCC features but of oral localization (OSCC). In a single-institutional observational cohort that included 38 invasive OSCCs of 35 patients, they described cellular and nuclear pleomorphism, anisocytosis, keratinization, nuclear hyperchromasia, and atypical mitotic figures, as well as the presence of necrosis and mixed inflammation [36]. Furthermore, they associated these characteristics with different degrees of tumor differentiation.

FuCM is a technique that relies on operator skill and training to accurately assess morphological and cellular features. Additionally, the choice of staining protocol used prior to scanning can significantly impact the final image quality and interpretation[16]. Regarding the FuCM accuracy in diagnosing CSCC, both PTs and MS showed high and similar values of SE, SP, PPV, and NPV. Also, significant levels of concordance were obtained for MS (almost perfect) and PTs (substantial agreement) when compared with conventional histopathology. These findings demonstrates that FuCM could be used as an alternative to conventional histology for CSCC diagnostic purposes. Separating each of the features considering only CSCC histologically confirmed (excluding benign and premalignant

lesions), the capacity of MS to assess mitotic figures, stromal inflammation, keratinization, pleomorphism, dyskeratosis, and loss of granular layer was better than PTs, showing slightly higher SE values. Previous studies have demonstrated that more research is needed to achieve better cellular details similar to conventional H&E images[44].

PTs better determined the absence of dyskeratosis, parakeratosis, desmoplasia, and mitotic figures when they were also absent in histological GS. These findings could be explained because PTs have more morphological experience in CSCC morphology than MS, regardless of previous experience with FuCM. Moreover, the sample size, which was not always enough to obtain FuCM mosaics to determine desmoplasia, among other histological features, and did not mean it was absent in the rest of the sample. At the same time, MS was better at determining the absence of infiltrative borders, loss of granular layer, and stromal inflammation. These findings are morphologically different observed between both techniques. Granules of the granular layer noticed in FuCM mosaics are usually pinkish and can be confounded with the normal cytoplasm (figures 2-4). The color of the stromal reaction is also different in FuCM mosaics, and even more, if we consider that a small amount of tumor was used for evaluation purposes if the PTs are not used to observe individual tumoral cells in FuCM mosaics, it could be dismissed by their assessments. Supplementary figures 1 and 2.

In evaluating CSCC features with FuCM mosaics, inter-observer agreement was "almost perfect" for intercellular bridges and dyskeratosis (PTs vs. MS) and for stromal inflammation (MS vs. GS). Other features had "substantial" or "moderate" inter-rater agreements, which is acceptable for a first-time evaluation. Both evaluators achieved high values of sensitivity, specificity, PPV, and NPV for CSCC invasive status, with "almost perfect" concordance with the GS and between themselves. These findings suggest that training and experience can enhance feature recognition.

Another observation previously made by this group of researchers was that AO staining reflects intensively pigmented structures such as hair shafts, melanocytes, and melanophages appearing pink and blurred in digitally stained FuCM mosaics, which could have clouded the visualization of some morphological and cellular details[13]. Moreover, a limitation of the digital stain was that only some cytological features could be assessed due to the change of tonality of the colors they produce. Dyskeratosis and mitotic figures are examples where both PTs and MS presented low NPV values due to the presence of FN.

Therefore, we must increase attention to morphological/architectural characteristics when cellular features are not visualized[45].

Limitations of this study derive from its uneccentric design, the size of the biopsy performed, the operator-dependent nature of the technique used to assess diagnostic accuracy, and the difference in the training profile of the evaluators. Moreover, the limited number of CSCC subtypes, and the absence of other morphologic and cellular features that were not evaluate due to the sample size, such as ulceration, keratin pearls, perineural and lymphovascular invasion, and invasive depth.

However, other studies, such as that of Hartmann et al., were able to characterize ulceration and corneal pearls using evFCM and evRCM, in addition to other characteristics also described in our study but adapting ivCM descriptions to those observed in evCM mosaics[25]. Longo et al. also described keratin pearls in their series of 13 cases evaluated with evFCM[24].

In contrast to other studies that have evaluated CSSC evCM mosaics where only Mohs surgeons evaluators were included [21,24,27] (none of these studies included pathologist evaluators), we compared the diagnostic accuracy between two different groups of evaluators: two PTs working together (without previous experience in FuCM) vs. a trained MS in FuCM assessment, demonstrating that PTs can perform an adequate diagnostic of CSCC with this technique and differentiate it from other benign and premalignant lesions.

This study highlights the potential of FuCM to significantly improve diagnostic accuracy for CSCC, paving the way for its practical integration into the daily routines of dermatologists and pathologists.

CONCLUSIONS

CSCC diagnostic capacity of FuCM mosaics showed similar performance to conventional histology. Its invasive status assessment with FuCM mosaics showed similar performance to conventional histology. FuCM mosaics allowed the assessment of key H&E CSCC diagnostic features with similar performance to conventional histology. The assessments of CSCC diagnosis, invasive status, and its histological features with FuCM mosaics were similar between experimented MS in FuCM and PTs with no previous experience in FuCM. FuCM mosaics allowed MS and PTs to obtain higher detection accuracy for the histological variables of keratinization, pleomorphism, and stromal inflammation. However, for the rest

of the variables, low PPV values were due to some false positives (FP). MS and PTs showed an "almost perfect" concordance for CSCC diagnostic and its invasive status when simultaneously evaluating all morphologic and cellular features. However, the agreement reached was slightly lower when each histological feature was assessed separately.

ACKNOWLEDGMENTS

We express our gratitude to the Dermatology Investigation Unit, with special acknowledgments to Pablo Iglesias and Beatriz Alejo, as well as the Dermatopathology Department of the Hospital Clinic Barcelona for their invaluable support in this project. Our heartfelt appreciation goes out to all the patients and their families, who serve as the primary motivation behind our research efforts. We extend special thanks to Oscar Urrejola for his invaluable assistance with statistical analysis.

REFERENCES

1. Que SKT, Zwald FO, Schmults CD. Cutaneous squamous cell carcinoma: Incidence, risk factors, diagnosis, and staging. J Am Acad Dermatol. 2018 Feb;78(2):237–47.
2. Cozma EC, Banciu LM, Soare C, Cretoiu SM. Update on the Molecular Pathology of Cutaneous Squamous Cell Carcinoma. Int J Mol Sci. 2023 Apr 2;24(7):6646.
3. Stang A, Khil L, Kajüter H, Pandeya N, Schmults CD, Ruiz ES, et al. Incidence and mortality for cutaneous squamous cell carcinoma: comparison across three continents. J Eur Acad Dermatol Venereol. 2019 Dec;33(Suppl 8):6–10.
4. de Giorgi V, Alfaioli B, Papi F, Janowska A, Grazzini M, Lotti T, et al. Dermoscopy in pigmented squamous cell carcinoma. J Cutan Med Surg. 2009 Dec;13(6):326–9.
5. Zalaudek I, Giacomel J, Schmid K, Bondino S, Rosendahl C, Cavicchini S, et al. Dermatoscopy of facial actinic keratosis, intraepidermal carcinoma, and invasive squamous cell carcinoma: a progression model. J Am Acad Dermatol. 2012 Apr;66(4):589–97.
6. Zalaudek I, Citarella L, Soyer HP, Hofmann-Wellenhof R, Argenziano G. Dermoscopy features of pigmented squamous cell carcinoma: a case report. Dermatol Surg. 2004 Apr;30(4 Pt 1):539–40.
7. Fagotti S, Pizzichetta MA, Corneli P, Toffolutti F, Serraino D, di Meo N, et al. Dermoscopic features of face and scalp basal and squamous cell carcinomas according to clinical histopathologic characteristics and anatomical location. J Eur Acad Dermatol Venereol. 2021 Mar;35(3):e237–9.
8. Rstom S, Abdalla B, Blumetti T, Matos L, Pinhal M, Paschoal F. Dermoscopy and Reflectance Confocal Microscopy in Actinic Keratosis, Intraepithelial Carcinoma, and Invasive Squamous Cell Carcinoma. J Drugs Dermatol. 2022 Mar 1;21(3):259–68.
9. Cornacchia L, Longo C, Piana S, Lai M, Pellacani G, Peris K, et al. "Eternal sunshine of the spotless islands": how dermoscopy may influence confocal microscopy when dealing with squamous cells carcinoma simulating basal cell carcinoma. J Eur Acad Dermatol Venereol. 2019 Aug;33(8):e277–80.
10. Kolm I, Braun R. How Reflectance Confocal Microscopy Works. In 2012. p. 7–10.
11. Pellacani G, Cesinaro AM, Seidenari S. Reflectance-mode confocal microscopy of pigmented skin lesions--improvement in melanoma diagnostic specificity. J Am Acad Dermatol. 2005 Dec;53(6):979–85.
12. Que SKT, Fraga-Braghiroli N, Grant-Kels JM, Rabinovitz HS, Oliviero M, Scope A.

Through the looking glass: Basics and principles of reflectance confocal microscopy. J Am Acad Dermatol. 2015 Aug;73(2):276–84.

13. Malvehy J, Pérez-Anker J, Toll A, Pigem R, Garcia A, Alos LL, et al. *Ex vivo* confocal microscopy: revolution in fast pathology in dermatology. Br J Dermatol. 2020 Dec;183(6):1011–25.

14. Hartmann D. [Ex vivo confocal laser scanning microscopy for melanocytic lesions and autoimmune diseases]. Hautarzt. 2021 Dec;72(12):1058–65.

15. Cinotti E, Perrot JL, Labeille B, Boukenter A, Ouerdane Y, Cosmo P, et al. Identification of a soft tissue filler by ex vivo confocal microscopy and Raman spectroscopy in a case of adverse reaction to the filler. Skin Res Technol. 2015 Feb;21(1):114–8.

16. Pérez-Anker J, Ribero S, Yélamos O, García-Herrera A, Alos L, Alejo B, et al. Basal cell carcinoma characterization using fusion *ex vivo* confocal microscopy: a promising change in conventional skin histopathology. Br J Dermatol. 2020 Feb;182(2):468–76.

17. Reggiani C, Pellacani G, Reggiani Bonetti L, Zanelli G, Azzoni P, Chester J, et al. An intraoperative study with ex vivo fluorescence confocal microscopy: diagnostic accuracy of the three visualization modalities. J Eur Acad Dermatol Venereol. 2021 Jan;35(1):e92–4.

18. Ragazzi M, Longo C, Piana S. Ex Vivo (Fluorescence) Confocal Microscopy in Surgical Pathology: State of the Art. Adv Anat Pathol. 2016 May;23(3):159–69.

19. Longo C, Ragazzi M, Rajadhyaksha M, Nehal K, Bennassar A, Pellacani G, et al. In Vivo and Ex Vivo Confocal Microscopy for Dermatologic and Mohs Surgeons. Dermatologic Clinics. 2016 Oct;34(4):497–504.

20. Longo C, Pampena R, Bombonato C, Gardini S, Piana S, Mirra M, et al. Diagnostic accuracy of ex vivo fluorescence confocal microscopy in Mohs surgery of basal cell carcinomas: a prospective study on 753 margins. Br J Dermatol. 2019 Jun;180(6):1473–80.

21. Rajadhyaksha M, Menaker G, Flotte T, Dwyer PJ, González S. Confocal Examination of Nonmelanoma Cancers in Thick Skin Excisions to Potentially Guide Mohs Micrographic Surgery Without Frozen Histopathology. Journal of Investigative Dermatology. 2001 Nov;117(5):1137–43.

22. Bennàssar A, Carrera C, Puig S, Vilalta A, Malvehy J. Fast Evaluation of 69 Basal Cell Carcinomas With Ex Vivo Fluorescence Confocal Microscopy: Criteria Description, Histopathological Correlation, and Interobserver Agreement. JAMA Dermatol. 2013 Jul 1;149(7):839.

23. Bennàssar A, Vilata A, Puig S, Malvehy J. Ex vivo fluorescence confocal microscopy for fast evaluation of tumour margins during Mohs surgery. Br J Dermatol. 2014 Feb;170(2):360–5.

24. Longo C, Ragazzi M, Gardini S, Piana S, Moscarella E, Lallas A, et al. Ex vivo fluorescence confocal microscopy in conjunction with Mohs micrographic surgery for cutaneous squamous cell carcinoma. Journal of the American Academy of Dermatology. 2015 Aug;73(2):321–2.

25. Hartmann D, Krammer S, Bachmann MR, Mathemeier L, Ruzicka T, Bagci IS, et al. Ex vivo confocal microscopy features of cutaneous squamous cell carcinoma. J Biophotonics. 2018 Apr;11(4):e201700318.

26. Chung VQ, Dwyer PJ, Nehal KS, Rajadhyaksha M, Menaker GM, Charles C, et al. Use of ex vivo confocal scanning laser microscopy during Mohs surgery for nonmelanoma skin cancers. Dermatol Surg. 2004 Dec;30(12 Pt 1):1470–8.

27. Al-Arashi MY, Salomatina E, Yaroslavsky AN. Multimodal confocal microscopy for diagnosing nonmelanoma skin cancers. Lasers Surg Med. 2007 Oct;39(9):696–705.

28. Longo C, Ragazzi M, Gardini S, Moscarella E, Argenziano G. Ex Vivo Fluorescence Confocal Microscopy of Eccrine Syringomatous Carcinoma: A Report of 2 Cases. JAMA Dermatol. 2015 Sep;151(9):1034–6.

29. Lamberti A, Cinotti E, Habougit C, Labeille B, Rubegni P, Perrot JL. Ex vivo confocal microscopy for dermatofibrosarcoma protuberans. Skin Res Technol. 2019 Jul;25(4):589–91.

30. Horn M, Gerger A, Koller S, Weger W, Langsenlehner U, Krippl P, et al. The use of confocal laser-scanning microscopy in microsurgery for invasive squamous cell carcinoma. British Journal of Dermatology. 2007 Jan 1;156(1):81–4.

31. Ruini C, Schlingmann S, Jonke Ž, Avci P, Padrón-Laso V, Neumeier F, et al. Machine Learning Based Prediction of Squamous Cell Carcinoma in Ex Vivo Confocal Laser Scanning Microscopy. Cancers (Basel). 2021 Nov 3;13(21):5522.

32. Hartmann D, Ruini C, Mathemeier L, Dietrich A, Ruzicka T, von Braunmühl T. Identification of ex-vivo confocal scanning microscopic features and their histological correlates in human skin. J Biophotonics. 2016 Apr;9(4):376–87.

33. Hartmann D, Ruini C, Mathemeier L, Bachmann MR, Dietrich A, Ruzicka T, et al. Identification of ex-vivo confocal laser scanning microscopic features of melanocytic lesions

and their histological correlates. J Biophotonics. 2017 Jan;10(1):128–42.

34. Hartmann D, Krammer S, Ruini C, Ruzicka T, von Braunmühl T. Correlation of histological and ex-vivo confocal tumor thickness in malignant melanoma. Lasers Med Sci. 2016 Jul;31(5):921–7.

35. Debarbieux S, Gaspar R, Depaepe L, Dalle S, Balme B, Thomas L. Intraoperative diagnosis of nonpigmented nail tumours with ex vivo fluorescence confocal microscopy: 10 cases. Br J Dermatol. 2015 Apr;172(4):1037–44.

36. Shavlokhova V, Flechtenmacher C, Sandhu S, Vollmer M, Hoffmann J, Engel M, et al. Features of oral squamous cell carcinoma in ex vivo fluorescence confocal microscopy. Int J Dermatol. 2021 Feb;60(2):236–40.

37. Pérez-Anker J, Toll A, Puig S, Malvehy J. Six steps to reach optimal scanning in ex vivo confocal microscopy. J Am Acad Dermatol. 2022 Jan;86(1):188–9.

38. Pérez-Anker J, Puig S, Malvehy J. A fast and effective option for tissue flattening: Optimizing time and efficacy in ex vivo confocal microscopy. J Am Acad Dermatol. 2020 May;82(5):e157–8.

39. Schmitz L, Kanitakis J. Histological classification of cutaneous squamous cell carcinomas with different severity. Journal of the European Academy of Dermatology and Venereology. 2019;33(S8):11–5.

40. McHugh ML. Interrater reliability: the kappa statistic. Biochem Med (Zagreb). 2012 Oct 15;22(3):276–82.

41. Manfredini M, Longo C, Ferrari B, Piana S, Benati E, Casari A, et al. Dermoscopic and reflectance confocal microscopy features of cutaneous squamous cell carcinoma. J Eur Acad Dermatol Venereol. 2017 Nov;31(11):1828–33.

42. Rishpon A, Kim N, Scope A, Porges L, Oliviero MC, Braun RP, et al. Reflectance confocal microscopy criteria for squamous cell carcinomas and actinic keratoses. Arch Dermatol. 2009 Jul;145(7):766–72.

43. González S, Sánchez V, González-Rodríguez A, Parrado C, Ullrich M. Confocal microscopy patterns in nonmelanoma skin cancer and clinical applications. Actas Dermosifiliogr. 2014 Jun;105(5):446–58.

44. Combalia M, Pérez-Anker J, García-Herrera A, Alos L, Vilaplana V, Marqués F, et al. Digitally Stained Confocal Microscopy through Deep Learning. In: Proceedings of The 2nd International Conference on Medical Imaging with Deep Learning [Internet]. PMLR;

2019 [cited 2022 Jan 24]. p. 121–9. Available from: https://proceedings.mlr.press/v102/combalia19a.html

45. Ramos-Ceballos FI, Ounpraseuth ST, Horn TD. Diagnostic concordance among dermatopathologists using a three-tiered keratinocytic intraepithelial neoplasia grading scheme. J Cutan Pathol. 2008 Apr;35(4):386–91.

BENEFITS OF RESEARCH, APPLICABILITY, AND VALIDITY

This study provided a better understanding of FuCM as a CSCC diagnostic tool comparable to conventional histology.

Here we demonstrated that FuCM mosaics could help us obtain an intraoperative CSCC diagnosis in freshly excised tissues and an immediate infiltration level (in situ vs. invasive). Applied to cutaneous oncological surgery, these findings may have clinical implications for improving the intraoperative workflow, helping determine staging variables, and immediately deciding the kind of treatment to be offered to the patient.

Regarding Mohs micrographic surgery, the findings shown in this study could be applied to reduce the overall duration of the procedure and the associated costs.

It is a single-center cohort study rather than population-based, limiting our findings' generalization. In addition, our results need to be validated in other studies on different cohorts.

Future studies should be carried out prospectively, including other malignant tumors in the pool of FuCM mosaics, excisional biopsies that allow us to visualize more details of the tumor features, and new staining protocols to improve cellular resolution.

FuCM mosaics with digital staining protocol present a diagnostic accuracy to evaluate the presence or absence of CSCC and its invasive status comparable to standard H&E histological analysis. In addition, assessing each morphologic and cellular feature separately is possible with good image quality, but it requires more training. Therefore, FuCM could be a faster alternative to conventional histology for CSCC diagnostic purposes.

TABLES

Table 1. Clinical characteristics of the patients and tumors studied.

Characteristic			Value (%)
Patients			N = 41
	Median age (range)		81 (57-100)
	Sex	Female	15 (36.6)
		Male	26 (63.4)
	Immunosuppression	Yes	5 (12.2)
		No	36 (87.8)
CSCC			N= 59
	Sample type	Punch	50 (84.7)
		Shave	9 (15.3)
	Tumour size (*)		1.6 (0.2 - 4.7)
	Body site (grouped)	Face	22 (37.3)
		Scalp	17 (28.8)
		Limbs	11 (18.6)
		Trunk	6 (10.2)
		Genitalia	3 (5.1)
	Histology subtype	Conventional CSCC	53 (89.8)
		In situ CSCC (Bowen)	3 (5.1)
		Keratoacanthoma	2 (3.4)
		Acantholytic CSCC	1 (1.7)
Benign/premalignant lesions		N=16	
	Benign/premalignant lesions (N=16)	Actinic keratosis	14 (87.5)
		Seborrheic keratosis	1 (6.25)
		Verruca vulgaris	1 (6.25)
*Larger diameter, cm			

FIGURE LEGENDS

Figure 1. Summary of results. Superior: Sensitivity and specificity of CSCC diagnosis and their morphological/cellular features assessed by PTs and MS using FuCM mosaics. **Inferior left:** Concordance between techniques and evaluators for CSCC diagnosis and identification of their morphological/cellular features using 221 FuCM mosaics (considering benign and premalignant lesions). **Inferior right:** Concordance between techniques and evaluators for CSCC diagnosis and identification of their morphological/cellular features using 166 FuCM mosaics (considering only CSCC).

Figure 2. Variations in the visualization of well-differentiated SCC in a shave biopsy. In the right image, H&E staining is used, while in the left image, FuCM is employed. Key features are indicated as follows: black asterisk: keratinization; brown asterisk: intercellular bridges; red circle: dyskeratosis; green asterisk: parakeratosis; blue triangle: infiltrative borders; brown triangle: loss of granular layer; yellow triangle: mitotic figures; yellow circle: pleomorphism; black triangle: dendritic cells. Subfigures (a) and (b) provide cellular details, while subfigures (c) and (d) offer a macro view.

Figure 3. Differences in the visualization of a punch biopsy of an acantholytic SCC are highlighted. Left image, FuCM (a). Right image, H&E (b). Red circle, dyskeratosis; yellow asterisk, desmoplasia; blue triangle, infiltrative borders; brown triangle, loss of granular layer; yellow triangle, mitotic figures; yellow circle, pleomorphism.

Figure 4. Infiltrative SCC. Brown asterisk, intercellular bridges; red circle, dyskeratosis; yellow asterisk, desmoplasia; yellow triangle, mitotic figures; yellow circle, pleomorphism; green triangle, stromal inflammation.

SUPPLEMENTARY MATERIAL

Supplementary Figure 1. In situ SCC. Black asterisk, keratinization; yellow asterisk, desmoplasia; brown triangle, loss of granular layer; yellow circle, pleomorphism; green triangle, stromal inflammation.

Supplementary Figure 2. Differences in the visualization of a well differentiated SCC (punch biopsy). Right image, H&E. Left image, FuCM. (a) and (b), macro view; (c) and (d), 4x; (e) and (f), cellular representation. Black asterisk, keratinization; red circle, dyskeratosis; green asterisk, parakeratosis; yellow asterisk, desmoplasia; blue triangle, infiltrative borders; brown triangle, loss of granular layer; yellow circle, pleomorphism; green triangle, stromal inflammation. Despite the morphological structures having a strong correlation, the colours can vary significantly.

Supplementary Table 1. Cross tabulation of relative and absolute frequencies observed.

Variable	Gold Standard (n=221)		Pathologists (n=221)		Mohs Surgeon (n=221)	
	Yes/No		Yes/No		Yes/No	
	Freq.	%	Freq.	%	Freq.	%
CSCC	166/55	75/25	159/62	72/28	164/37	74/36
Keratinization	153/68	69/31	136/85	62/38	147/74	67/33
Intercellular bridges	92/129	42/58	107/114	48/52	110/111	50/50
Dyskeratosis	42/179	19/81	71/150	32/68	81/146	37/63
Parakeratosis	93/128	42/58	98/123	44/56	113/108	51/49
Desmoplasia	27/194	13/87	33/188	15/85	66/155	30/70
Infiltrative borders	86/135	39/61	88/133	40/60	81/140	37/63
Loss of granular layer	102/114	46/54	109/112	49/51	109/112	49/51
Mitotic figures	27/194	13/87	38/183	17/83	51/170	23/77
Pleomorphism	144/77	65/35	134/87	61/39	141/80	64/36
Stromal Inflammation	150/71	68/32	143/78	65/35	150/71	68/32

Supplementary Table 2. CSCC and histological accuracy diagnostic features for PTs and MS with FuCM mosaics in all samples (N=221). *Statistically significant ($P < 0.05$) using the chi-square test. **Variable calculated with FuCM mosaics of histologically confirmed CSCC without considering benign/premalignant lesions (N=166)

Variable	N	SE PTs (95% IC)	SE MS (95% IC)	SP PTs (95% IC)	SP MS (95% IC)	PPV PTs (95% IC)	PPV s MS (95% IC)	NPV PTs (95% IC)	NPV MS (95% IC)	pvalue*
CSCC	221	91 (85-94)	96 (92-98)	85 (73-93)	94 (84-98)	95(90-97)	98 (94-99)	75 (63-85)	89 (78-96)	<0.001
Invasive status**	166	88(79-95)	94(86-98)	94 (88-98)	90(82-95)	92(87-95)	88(78-94)	91(84-96)	95(89-98)	<0.001
Keratinization	221	80 (73-86)	88 (82-93)	81 (69-89)	82 (71-90)	90(84-94)	91 (86-95)	65 (54-75)	77 (65-86)	<0.001
Intercellular bridges	221	76(66-84)	85 (77-92)	74 (66-81)	76 (67-83)	68(58-76)	71 (62-80)	81 (73-87)	88 (80-93)	<0.001
Dyskeratosis	221	75(59-87)	87 (73-95)	78 (71-84)	75 (68-81)	44(32-56)	44 (33-55)	93 (88-96)	96 (91-98)	<0.001
Parakeratosis	221	76(66-84)	83 (74-90)	78 (70-85)	73 (64-80)	72(62-81)	70 (60-78)	82 (74-88)	86 (78-92)	<0.001
Desmoplasia	221	77 (57-91)	81 (61-93)	93 (89-96)	77 (70-83)	63(45-79)	33 (22-46)	96 (93-98)	96 (92-98)	<0.001
Infiltrative borders	221	76 (66-85)	73 (62-82)	83 (76-89)	89 (83-94)	75(64-83)	81 (71-89)	85 (77-90)	84 (77-89)	<0.001
Loss of granular layer	221	82(73-89)	87 (79-93)	79 (70-85)	84 (76-90)	77(68-84)	82 (73-89)	83 (75-90)	88 (81-93)	<0.001
Mitotic figures	221	85(66-95)	96 (81-99)	92 (87-95)	87 (81-91)	60(43-76)	51 (36-65)	97 (94-99)	99 (96-100)	<0.001
Pleomorphism	221	84(77-90)	88(82-93)	84 (74-91)	83 (72-90)	91(84-95)	90 (84-95)	74 (64-83)	80 (69-88)	<0.001
Stromal inflammation	221	85 (78-90)	94 (89-97)	83 (72-91)	88 (79-95)	91(85-95)	94 (89-97)	72 (61-82)	88 (79-95)	<0.001

Supplementary Table 3. Inter-rater agreement between PTs, MS, and gold standard histology report diagnosing CSCC and identifying morphologic and cellular CSCC features with FuCM mosaics using all samples (N=221). *Variable calculated considering only histological confirmed CSCC (N=166)

Variable	kappa				pvalue
	PTs vs GS	MS vs GS	PTs vs MS	PTs vs MS vs GS	
CSCC	0.733	0.804	0.904	0.813	<0.001
Invasive status*	0.839	0.841	0.804	0.828	<0.001
Keratinization	0.592	0.709	0.598	0.631	<0.001
Intercellular bridges	0.517	0.601	0.84	0.654	<0.001
Dyskeratosis	0.430	0.446	0.8199	0.570	<0.001
Parakeratosis	0.548	0.567	0.6480	0.586	<0.001
Desmoplasia	0.65	0.362	0.4325	0.451	<0.001
Infiltrative borders	0.601	0.663	0.4737	0.579	<0.001
Loss of granular layer	0.610	0.719	0.5836	0.637	<0.001
Mitotic figures	0.659	0.603	0.6781	0.644	<0.001
Pleomorphism	0.671	0.713	0.6443	0.678	<0.001
Stromal inflammation	0.686	0.709	0.6258	0.714	<0.001

Supplementary Table 4. Tumor variables diagnostic capacity of PTs and MS with FuCM mosaics considering only histological confirmed CSCC (N=166)

Variable	N	SE PTs (95% IC)	SE MS (95% IC)	SP PTs (95% IC)	SP MS (95% IC)	PPV PTs (95% IC)	PPV s MS (95% IC)	NPV PTs (95% IC)	NPV MS (95% IC)	pvalue*
Keratinization	166	84(76-90)	90(83-94)	86(72-94)	93(80-98)	94(88-98)	97(92-99)	66(52-78)	76(63-87)	<0.001
Intercellular bridges	166	73(62-83)	85 (75-92)	79(69-87)	77(67-86)	76(65-85)	78(68-86)	76(66-84)	84(75-91)	<0.001
Dyskeratosis	166	77 (61-89)	90(76-97)	74(66-81)	70(61-78)	49 (36-62)	49(37-61)	91(84-95)	95(89-98)	<0.001
Parakeratosis	166	74 (63-83)	82(72-89)	79(68-87)	79(68-87)	78(68-87)	80(70-88)	74(63-83)	81(70-89)	<0.001
Desmoplasia	166	76(56-91)	80(60-93)	92(87-96)	76(68-83)	66(47-82)	38(25-53)	95(90-98)	95(89-98)	<0.001
Infiltrative borders	166	76(66-85)	76(66-85)	84(74-91)	88(80-94)	83(73-90)	87(78-94)	77(67-85)	78(68-86)	<0.001
Loss of granular layer	166	82(73-89)	87(78-93)	73(61-82)	79(68-88)	79(69-86)	84(75-90)	77(65-86)	83(72-91)	<0.001
Mitotic figures	166	84(63-95)	96(79-99)	92(86-96)	84(77-90)	65(46-81)	52(36-67)	97(92-99)	99(95-100)	<0.001
Pleomorphism	166	83(76-89)	89(82-87)	85(71-94)	85(71-94)	94(88-98)	94(89-98)	64(50-76)	73(58-85)	<0.001
Stromal inflammation	166	85(77-91)	94(88-97)	86(72-94)	93(81-98)	94(88-98)	97(92-99)	67(54-79)	85(72-93)	<0.001

Supplementary Table 5. Inter-rater agreement between PTs, MS, and gold standard histology report diagnosing CSCC and identifying its morphologic and cellular features with FuCM mosaics using only CSCC lesions (N=166).

Variable	kappa				pvalue
	PTs vs GS	MS vs GS	PTs vs MS	PTs vs MS vs GS	
CSCC	0.839	0.841	0.804	0.8281	<0.001
Keratinization	0.654	0.779	0.627	0.685	<0.001
Intercellular bridges	0.494	0.579	0.818	0.630	<0.001
Dyskeratosis	0.441	0.461	0.789	0.562	<0.001
Parakeratosis	0.530	0.626	0.639	0.598	<0.001
Desmoplasia	0.656	0.397	0.472	0.486	<0.001
Infiltrative borders	0.603	0.651	0.490	0.581	<0.001
Loss of granular layer	0.558	0.669	0.5439	0.590	<0.001
Mitotic figures	0.683	0.597	0.668	0.645	<0.001
Pleomorphism	0.626	0.713	0.680	0.671	<0.001
Stromal inflammation	0.695	0.849	0.644	0.727	<0.001

Supplementary Table 6. False positive (FP) and false negative (FN) values of the evaluations performed by PTs and MS with FuCM mosaics using all samples (N=221).

Variable	FP PTs		FN PTs		FP MS		FN MS	
	Absolut frecuency	Relative frecuency	Absolut frecuency	Relative frecuency	Absolut frecuency	Relative frecuency	Absolut frecuency	Relative frecuency
SCC	8	3,6%	15	6,8%	3	1,4%	5	2,3%
Intercelular bridges	34	15,4%	19	8,6%	31	14,0%	13	5,9%
Keratinization	12	5,4%	29	13,1%	11	5,0%	17	7,7%
Dyskeratosis	39	17,7%	10	4,5%	45	20,4%	6	2,7%
Parakeratosis	27	12,2%	22	10,0%	34	15,4%	14	6,3%
Pleomorphism	12	5,4%	22	10,0%	13	5,9%	16	7,2%
Desmoplasia	12	5,4%	6	2,7%	44	19,9%	5	2,3%
Infiltrative borders	22	10,0%	20	9,0%	15	6,8%	20	9,0%
Loss of granular layer	25	11,3%	18	8,1%	19	8,6%	12	5,4%
Mitotic figures	15	6,8%	4	1,8%	25	11,3%	1	0,5%
Stromal Inflammation	12	5,4%	19	8,6%	8	3,6%	8	3,6%

Supplementary Table 7. False positive (FP) and false negative (FN) values of the evaluations performed by PTs and MS with FuCM mosaics considering only histologically confirmed CSCC (N=166)

Variable	FP PTs		FN PTs		FP MS		FN MS	
	Absolut frecuency	Relative frecuency	Absolut frecuency	Relative frecuency	Absolut frecuency	Relative frecuency	Absolut frecuency	Relative frecuency
SCC	5	3,0%	8	4,8%	9	5,4%	4	2,4%
Intercelular bridges	24	14,5%	18	10,8%	23	13,9%	12	7,2%
Keratinization	6	3,6%	18	10,8%	3	1,8%	12	7,2%
Dyskeratosis	32	19,3%	9	5,4%	37	22,3%	5	3,0%
Parakeratosis	17	10,2%	22	13,3%	17	10,2%	14	8,4%
Pleomorphism	6	3,6%	20	12,0%	6	3,6%	13	7,8%
Desmoplasia	10	6,0%	6	3,6%	33	19,9%	5	3,0%
Infiltrative borders	13	7,8%	20	12,0%	9	5,4%	20	12,0%
Loss of granular layer	20	12,1%	16	9,6%	15	9,0%	12	7,2%
Mitotic figures	10	6,1%	4	2,4%	22	13,3%	1	0,6%
Stromal Inflammation	6	3,6%	15	9,0%	3	1,8%	7	4,2%

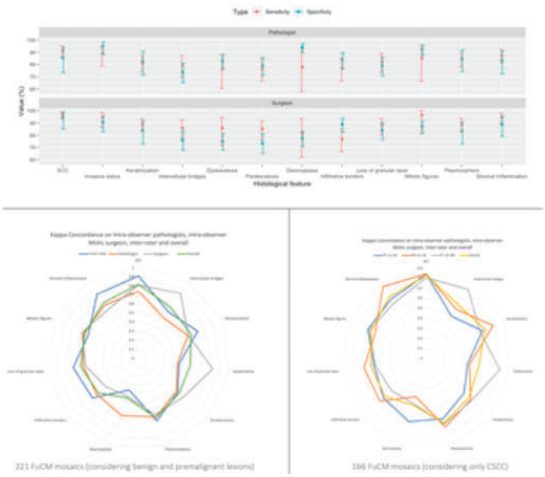

Figure 1. Summary of results. Superior: Sensitivity and specificity of CSCC diagnosis and their morphological/cellular features assessed by PTs and MS using FuCM mosaics. Inferior left: Concordance between techniques and evaluators for CSCC diagnosis and identification of their morphological/cellular features using 221 FuCM mosaics (considering benign and premalignant lesions). Inferior right: Concordance between techniques and evaluators for CSCC diagnosis and identification of their morphological/cellular features using 166 FuCM mosaics (considering only CSCC).

15x13mm (600 x 600 DPI)

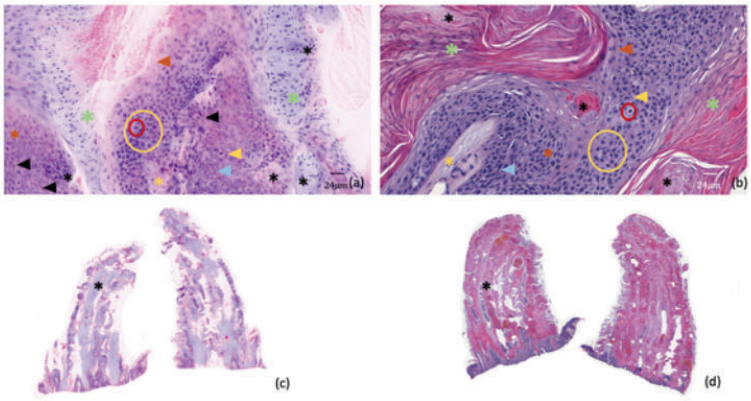

Figure 2. Variations in the visualization of well-differentiated SCC in a shave biopsy. In the right image, H&E staining is used, while in the left image, FuCM is employed. Key features are indicated as follows: black asterisk: keratinization; brown asterisk: intercellular bridges; red circle: dyskeratosis; green asterisk: parakeratosis; blue triangle: infiltrative borders; brown triangle: loss of granular layer; yellow triangle: mitotic figures; yellow circle: pleomorphism; black triangle: dendritic cells. Subfigures (a) and (b) provide cellular details, while subfigures (c) and (d) offer a macro view.

23x12mm (600 x 600 DPI)

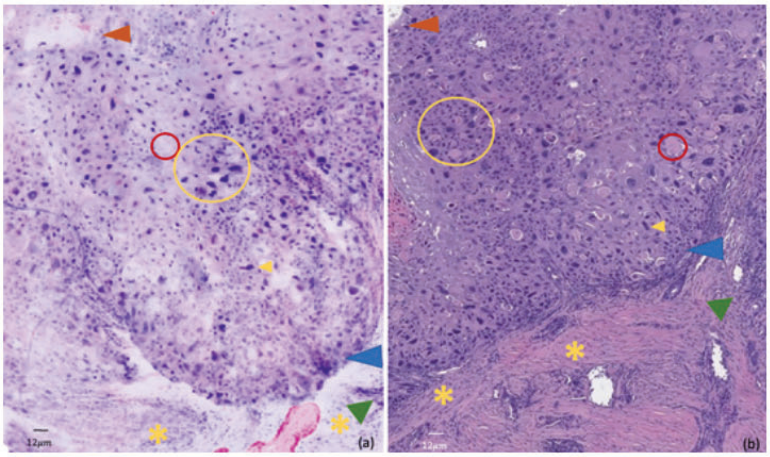

Figure 3. Differences in the visualization of a punch biopsy of an acantholytic SCC are highlighted. Left image, FuCM (a). Right image, H&E (b). Red circle, dyskeratosis; yellow asterisk, desmoplasia; blue triangle, infiltrative borders; brown triangle, loss of granular layer; yellow triangle, mitotic figures; yellow circle, pleomorphism.

22x13mm (600 x 600 DPI)

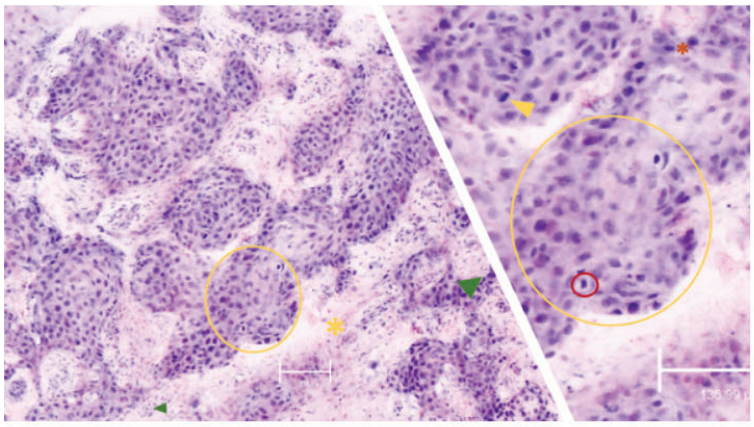

Figure 4. Infiltrative SCC. Brown asterisk, intercellular bridges; red circle, dyskeratosis; yellow asterisk, desmoplasia; yellow triangle, mitotic figures; yellow circle, pleomorphism; green triangle, stromal inflammation.

24x13mm (600 x 600 DPI)

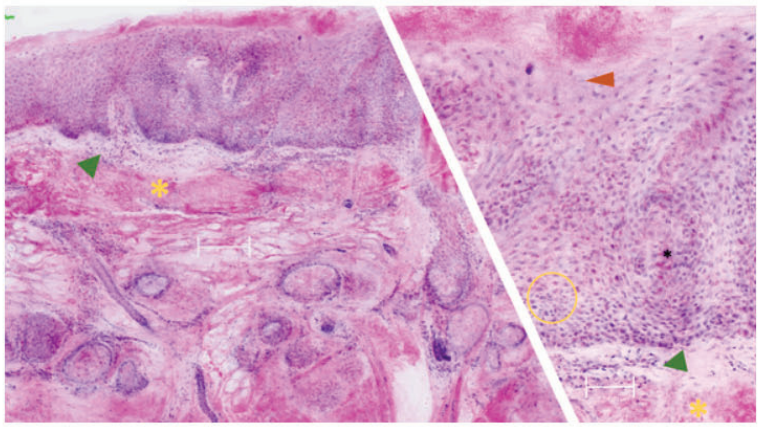

24x13mm (600 x 600 DPI)

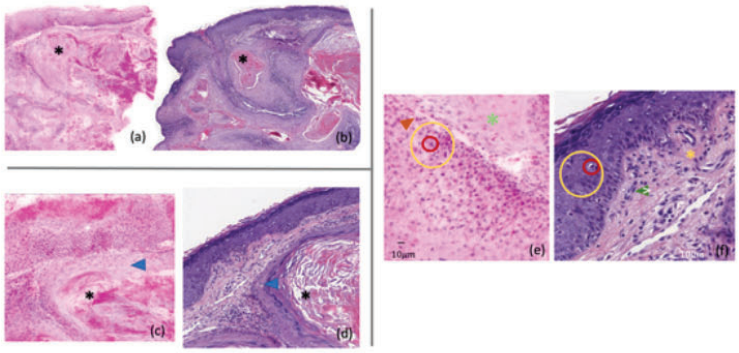

23x11mm (600 x 600 DPI)

PUBLICACIÓN N° 10:[75]

Tinción digital de microscopía confocal utilizando "aprendizaje profundo"

Digitally Stained Confocal Microscopy through Deep Learning

Marc Combalia, Javiera Pérez-Anker, Adriana García-Herrera, Llúcia Alos, Verónica Vilaplana, Ferran Marqués, Susana Puig, Josep Malvehy

Proceedings of the 2nd International Conference on Medical Imaging with Deep Learning, PMLR 102:121-129, 2019.

Resumen

Antecedentes: Los especialistas han utilizado el microscopio confocal *ex vivo* para identificar carcinomas basocelulares con una sensibilidad del 96.6% y una especificidad del 89.2%. Sin embargo, esta tecnología aún ha tardado a establecerse en la práctica clínica diaria por las dificultades de interpretación diagnóstica de las imágenes por algunos patólogos.

Objetivos: Proponer un método que permita visualizar las imágenes obtenidas por el microscopio confocal *ex vivo* de una forma más parecida a las obtenidas con la tinción convencional de H&E.

Métodos: Se utilizó de forma combinada el método de "aprendizaje profundo" y de "técnicas de visualización de ordenador" para mejorar las imágenes proporcionadas por el microscopio confocal. Se utilizó una "red adversaria generativa" para generar imágenes más parecidas a la H&E tradicional, habiendo previamente eliminado el "ruido" (despeckling) de las imágenes de microscopía confocal *ex vivo* (láser de reflectancia), mediante una red neuronal totalmente convolucional en combinación

con una conexión residual. La tinción artificial se utilizó mediante una "consistencia de ciclo de redes adversarias generativas"(CycleGAN), aplicando "generadores" (ResNet) y "discriminadores" (PatchNet), que mapean la imagen en dos sentidos, para transferir el color de la forma más parecida posible al H&E.

Resultados: 11 muestras de imágenes de confocal *ex vivo*, que fueron obtenidas con una resolución de 0.75 μm/px y un output de más de 10000 x 10000 pixeles para cada laser (reflectancia y fluorescencia). Un total de 7031 imágenes histológicas que fueron previamente transformadas a la escala de gris, para que fueran más semejantes a las del confocal. Finalmente, fueron evaluados los resultados del análisis de 1748 imágenes histológicas y de 949 imágenes de microscopia confocal de reflectancia. Se entrenó la red neuronal inicialmente en parches de 256 x 256 pixeles y luego se aumentó a 512 x 512, de manera que la arquitectura pudiera ir siendo aprendidas por el algoritmo. Las imágenes propuestas fueron evaluadas por dos patólogas expertas (LLA/AG), que confirmaron que las imágenes obtenidas eran iguales a las obtenidas en su análisis de rutina. La arquitectura entrenada con imágenes del láser de reflectancia con ruido, tuvo más dificultades para aprender la tinción digital y produjo artefactos, además de eliminar algunos núcleos presentes en las imágenes de confocal.

Conclusiones: Se demostró que, aplicando el algoritmo propuesto, las imágenes finales obtenidas tenían menos ruido y eran mejor visualizadas. Por otro lado, se pudo mejorar la tinción artificial, produciendo imágenes finales resultantes más parecidas a la H&E convencional. Son necesarios más estudios para validar estos resultados.

Proceedings of Machine Learning Research 102:121–129, 2019 MIDL 2019 – Full paper track

Digitally Stained Confocal Microscopy through Deep Learning

Marc Combalia[1] MCOMBALIA@CLINIC.CAT
Javiera Pérez-Anker[1] PEREZ12@CLINIC.CAT
Adriana García-Herrera[2] APGARCIA@CLINIC.CAT
Llúcia Alos[2] LALOS@CLINIC.CAT
Verónica Vilaplana[3] VERONICA.VILAPLANA@UPC.EDU
Ferran Marqués[3] FERRAN.MARQUES@UPC.EDU
Susana Puig[1] SPUIG@CLINIC.CAT
Josep Malvehy[1] JMALVEHY@CLINIC.CAT

[1] *Dermatology Department, Melanoma Unit, Hospital Clínic de Barcelona, IDIBAPS, Universitat de Barcelona, Barcelona, Spain.*
[2] *Pathology Department, Melanoma Unit, Hospital Clínic de Barcelona, IDIBAPS, Universitat de Barcelona, Barcelona, Spain.*
[3] *Signal Theory and Communications Department, Universitat Politècnica de Catalunya. BarcelonaTech, Spain.*

Abstract

Specialists have used confocal microscopy in the ex-vivo modality to identify Basal Cell Carcinoma tumors with an overall sensitivity of 96.6% and specificity of 89.2% (Chung et al., 2004). However, this technology hasn't established yet in the standard clinical practice because most pathologists lack the knowledge to interpret its output. In this paper we propose a combination of deep learning and computer vision techniques to digitally stain confocal microscopy images into H&E-like slides, enabling pathologists to interpret these images without specific training. We use a fully convolutional neural network with a multiplicative residual connection to denoise the confocal microscopy images, and then stain them using a Cycle Consistency Generative Adversarial Network.

Keywords: Deep learning, Neural Networks, Digital Staining, Confocal Microscopy, Speckle Noise, CycleGAN

1. Introduction

Histopathology with hematoxylin and eosin (H&E) staining is widely used as a diagnostic tool for a large variety of tissue lesions. However, it requires skilled technicians to process and stain the tissue samples, and it is very costly and time-consuming, requiring from hours to days before a pathologist can analyze the samples. These long delays often impede rapid evaluation of lesions during a surgical operation.

Confocal microscopy (CM) is a novel technique for tissue examination where a laser is focused on a microscopic target and the scattering of the light through its various structures is captured to form a two-dimensional grayscale image (Calzavara-Pinton et al., 2008). These microscopes can operate in two different modes (reflectance (RCM) and fluorescence (FCM)) which highlight different microscopic structures in the tissue. The combination of the two modes can improve the

diagnostic accuracy of the pathologist in the ex-vivo evaluation of tumour margins (Gareau, 2009). In the last years, this new technology has enabled the rapid evaluation of tissue samples directly in the surgery room significantly reducing the time of complex surgical operations in skin cancer (Cinotti et al., 2018).

CMs can obtain images with an optical resolution comparable to pathology, but their output largely differs from the standard H&E slides that pathologist use to evaluate in their clinical practise. Some researchers have focused on creating digitally stained (H&E)-like images from the output of the CMs to facilitate their interpretation by untrained pathologists and surgeons. (Gareau, 2009) has proposed a digital staining technique which linearly combines the FCM and RCM images to form an RGB output slide which resembles H&E stained pathology giving a blue color to FCM and pink to purple color to RCM. This is, in fact, the algorithm used in the last generation of the Vivascope 2500 clinical ex vivo CM device (Vivascope, 2018). This simple staining technique is good at enhancing cellular details allowing the mitosis visualization, but its colors and structures greatly vary from the ones found in the original H&E slides.

In this work, we propose a deep learning technique to combine the two modes of the CM into a (H&E)-like image. First, a fully convolutional neural network is used to remove the speckle noise present in the RCM images (Wang et al., 2017), and then a Cycle Consistency Generative Adversarial Network (CycleGAN) (Zhu et al., 2017) is used to combine the FCM and RCM modes into a digitally stained (H&E) slide.

2. Materials and Methods

In this section, we describe the architecture of the Despeckling Neural Network used in the RCM image of the CM and the Generative Adversarial Network used to create the (H&E)-like digitally stained image. Figure 1 shows the complete pipeline for CM image staining.

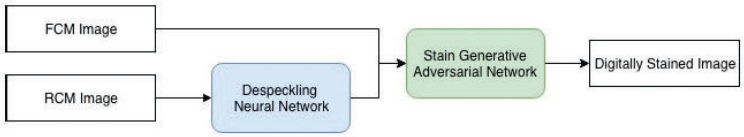

Figure 1: Diagram of the proposed architecture to transform the output of the CM to digitally stained (H&E)-like slides.

2.1. Reflectance Image Despeckling

RCM images are corrupted with a kind of multiplicative noise known as speckle (Sarode and Deshmukh, 2011). Speckle noise is due to a combination of constructive and destructive fluctuations at the input of the CM sensor which interfere with the nominal tissue structure reflectance. The presence of speckle noise limits the application of further post-processing and computer vision techniques and makes diagnosing less reliable for physicians (Gigilashvili, 2017). Hence, before digitally staining the CM images, their noise must be reduced. Figure 2 shows some RCM images extracted from the CM dataset presented in section 2.3.1.

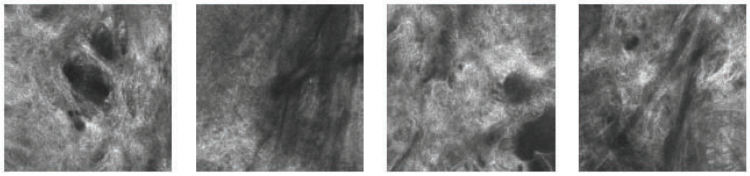

Figure 2: Reflectance images with speckle noise at the output of the CM.

In this work, similarly to (Wang et al., 2017), we use a fully convolutional neural network together with a residual connection to reduce the intensity of the noise present in the RCM images. The observed image at the output of the CM is related to real tissue reflectance by the following equation:

$$Y = X * (1 + F)$$

Where $Y \in \mathscr{R}^{WxH}$ is the observed RCM image, $X \in \mathscr{R}^{WxH}$ is the noise-free reflectance of the tissue, and $F \in \mathscr{R}^{WxH}$ is the speckle noise random variable. We include the aforementioned formulation inside the architecture of the neural network so that it is trained to estimate the inverse of the speckle noise $1/\hat{F}$ at the last convolutional layer.

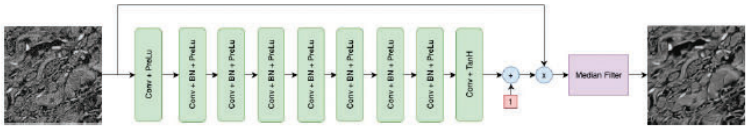

Figure 3: Architecture of the despeckling neural network used in our experiments.

The fully convolutional neural network is composed of 7 convolutional layers (PreLu activations) with 64 filters each and 1 final convolutional layer (TanH activation) with a single filter. Batch normalization is added to the intermediate layers of the neural network. We use a multiplicative residual connection between the last convolutional layer and the input image to incorporate the speckle noise formulation in the the neural network. The architecture is trained to minimize the squared error between the clean images and its output. After training, some noise may still be present in some isolated pixels (figure 6). Authors in (Wang et al., 2017) add total variation loss to the training process to remove these spurious pixel activations. Instead, we filter out the remaining noise using a 3x3 median filter. We train the neural network on a dataset of skin histology images which have been artificially contaminated, which have a similar appearance to noisy RCM images.

2.2. Confocal Microscopy Staining

Due to the impossibility to obtain paired data between the CM domain (A) and the stained H&E histology domain (B) (tissue blocks scanned with the CM need to undergo slicing before staining

with H&E), we use Cycle Consistency Generative Adversarial Networks (CycleGAN) (Zhu et al., 2017) to transfer the H&E stain appearance to the CM images. The CycleGAN architecture consists of two generator and discriminator pairs. The first pair tries to map images from domain A to domain B, while the second pair undergoes the contrary operation. The generators' task is to create images that the discriminators can't distinguish from real samples. We use a ResNet (He et al., 2016) architecture in the generators and a PatchNet (Isola et al., 2016) in the discriminators. Figure 4 shows all the components and loss functions involved in the translation from A to B.

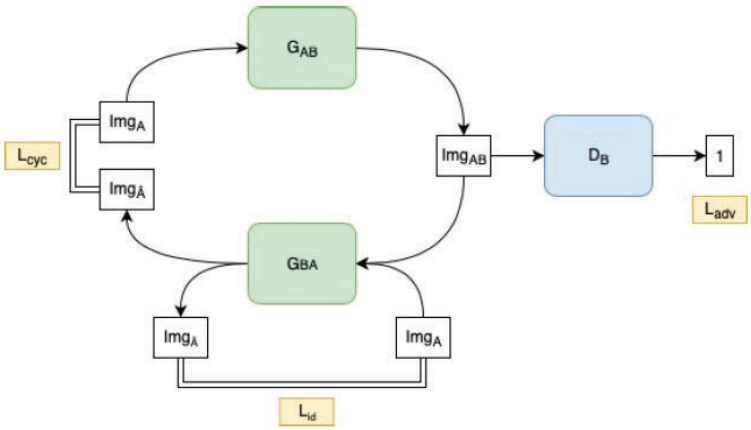

Figure 4: Components and loss functions (L_{cyc}, L_{adv}, L_{id}) involved in the domain translation from A to B. The same process is carried out on the contrary direction when translating from B to A.

It is known that CycleGANs are sensitive to their initialization, so to pose an easier task, we use the digital staining method proposed in (Gareau, 2009) as source images for domain A. Figure 5 shows this transformation.

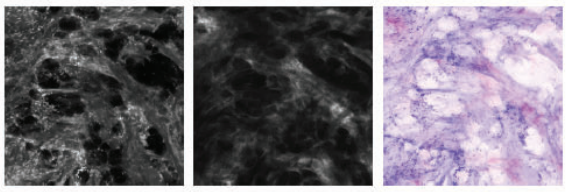

(a) (b) (c)

Figure 5: (a) FCM image, (b) RCM image, (c) Digital staining as proposed by (Gareau, 2009)

2.3. Data

2.3.1. CONFOCAL MICROSCOPY

Our CM dataset consists of 11 microscopy skin slides obtained with the Vivascope 2500 4th Generation CM (Vivascope, 2018), which captures the tissues at a resolution of 0.75 $\mu m/px$. Its output consists of two large grayscale images (more than 10000 x 10000 pixels), one for each capture mode (RCM and FCM). Both modes are normalized to cover a range from 0 to 1, and OTSU thresholding is used to determine the tissue-containing regions. Non-overlapping patches of size 1024 x 1024 pixels are extracted summing a total of 949 1024x1024 images for each mode. The patches are divided into train (80%) and validation (20 %) taking into account their origin slide.

2.3.2. H&E HISTOLOGY

Our H&E Histology dataset consists of 29 skin tissue samples obtained with a Ventana Whole Slide Image scanner captured with a resolution of 0.47 $\mu m/px$. OTSU thresholding is used to determine the tissue containing regions in each whole slide image and multiple patches of size 1630 x 1630 pixels are extracted and then resized to 1024x1024 pixels. The final resolution of each patch is the same as the CM resolution (0.75 $\mu m/px$). The processed dataset consists of a total of 8789 images (80 % for the training split and 20 % for the validation split, partitioned taking into account their origin slide).

3. Experiments and Results

In this section, we describe the results obtained for the Despeckling Neural Network used in the RCM of the CM and the Generative Adversarial Network used to create the (H&E)-like digitally stained image.

3.1. Reflectance Despeckling

Since it is not possible to obtain noise-free reflectance images at the output of the CM to train the neural network, we chose to train the despeckling neural network on histology images since the structures present in both domains are the same (Ragazzi et al., 2014). The main differences between reflectance mode confocal images and histology images are two: reflectance images are one channel only, and tissue structures appear lighter than the background. To create the dataset to train the neural network, we transformed the histology images to the YUV color space and used to the inverse of the Y channel to train the despeckling neural network (with artificial speckle noise; $noisy_{xy} = clean_{xy} * noise$ where $noise = Gauss(mean = 1, std = 0.2)$). We trained the Desplecking Neural network on 7031 histology images. We augmented the training dataset through the use of random flips and random crops of size of 256 x 256 pixels and we updated the weights of the neural network using Adam optimization with a learning rate of $5e-4$. Finally, we evaluated the results on 1758 histology images contaminated with artificial speckle noise and 949 RCM images extracted from the CM. In Table 1 we present the quantitative results obtained on the artificial dataset, and figures 6 and 7 show some images before and after going through the despeckling neural network for the artificial histology dataset and RCM dataset respectively.

Table 1: PSNR and SSIM before and after applying the proposed Despeckling Neural Network.

Error Measure	Noisy	Despeckled
PSNR (dB)	16.19	23.97
SSIM	0.438	0.727

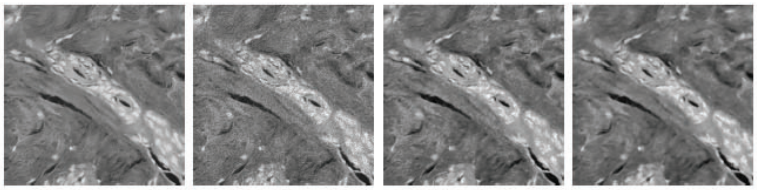

(a) (b) (c) (d)

Figure 6: (a) Original clean image from the artificial despeckling dataset, (b) Original image with artificial speckle noise, (c) Despeckled image at the output of the neural network, before the 3x3 median filter, (d) Despeckled image after the 3x3 median filter.

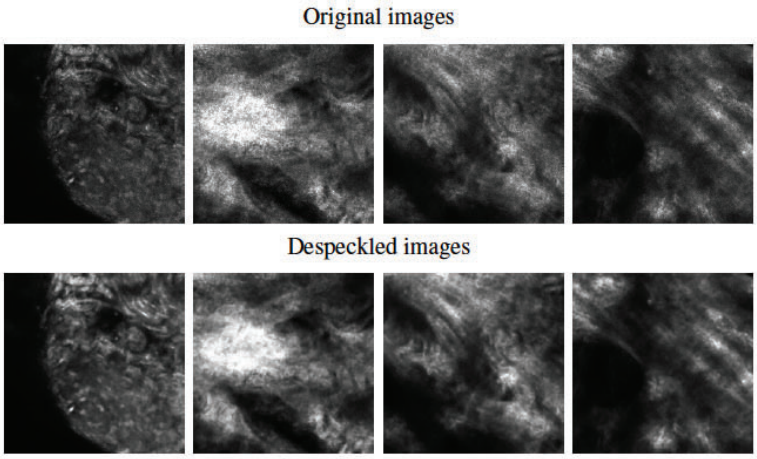

Figure 7: RCM images before and after the proposed despeckling neural network.

3.2. Confocal Image Staining

We trained the Staining CycleGAN on 759 CM images and 282 histology images extracted from a single slide (the one with the best proportion of hematoxylin and eosin stains). The CycleGAN was trained with Adam optimization and a learning rate of $2e-4$. We trained the neural network first on patches of size 256 x 256 pixels. After 50 epochs, we augmented the patch size to 512 x 512 so that the architecture could learn features seen at a higher scale and then trained it for another 50 epochs with learning rate decay. Figure 8 shows some results of a CycleGAN trained on images which

have been previously denoised with the method described in section 2.1, as well as some images from domain B. Figure 9 shows some results of a CycleGAN trained with noisy RCM images. The trained architecture can digitally stain a 15000 x 10000 pixels confocal microscopy slide in less than 3 minutes using a NVIDIA Tesla K80.

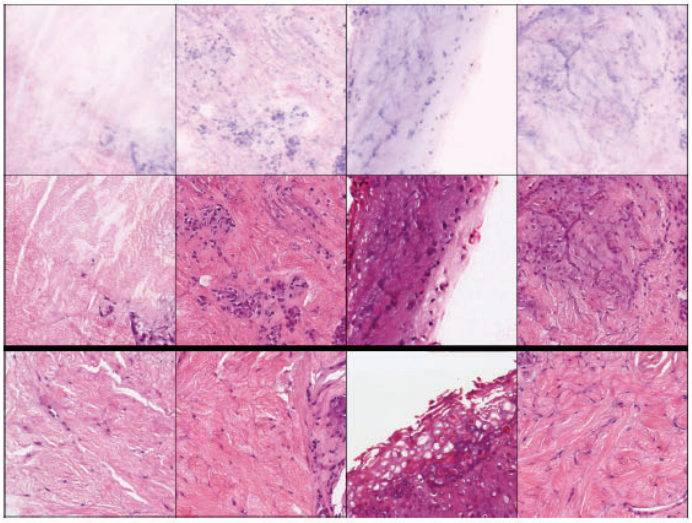

Figure 8: Results of the proposed architecture (Despeckling neural network and CycleGAN). The top row represents the input images of the CycleGAN, which have been digitally stained with the method proposed by (Gareau, 2009). Middle row is the output of the staining CycleGAN. The images in the bottom row are real H&E stained histology images extracted from the training dataset. All images are 512x512 pixels.

4. Discussion

We argue that the combination of the proposed despeckling neural network with the CycleGAN architecture for stain transfer is capable of producing realistic (H&E)-like images. Output images from the proposed algorithm were evaluated by two expert pathologists in our department (LL.A/A.G) and they confirmed that the images were similar to those in routine.

The despeckling neural network was able to successfully remove the noise from the RCM images at the output of the CM. From the results on figure 9 we conclude that the Despeckling Neural Network is crucial to obtain realistic images at the output of the CycleGAN. The architecture trained with noisy RCM images had a harder time learning to map the confocal output to the (H&E)-like appearance and produced non-desirable artifacts, as well as eliminated some nuclei present in the CM images. However, we argue that the Despeckling Neural Network could benefit from including an adversarial loss in the optimization process to produce sharper results.

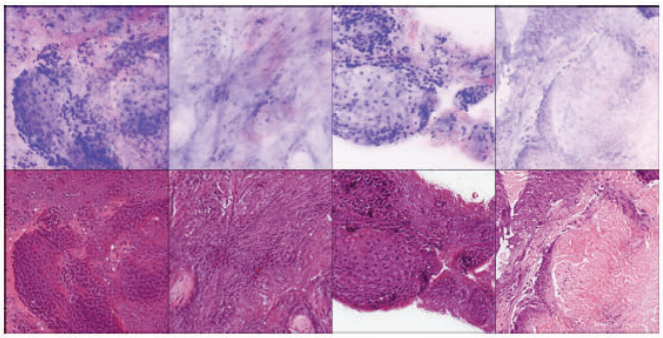

Figure 9: Results from the CycleGAN trained with RCM noisy images. Top row represents the input images of the CycleGAN, which have been digitally stained with the method proposed by (Gareau, 2009). Bottom row is the output of the staining CycleGAN. All images are 512x512 pixels.

5. Conclusions and Future Work

We have proposed an architecture which successfully addresses the problems involved in CM image staining. On the one hand, we reduce the noise present in the RCM images through the use of a denoising convolutional neural network with a multiplicative residual connection. Then, the denoised RCM image and FCM image are combined in a generative adversarial network to produce a realistic (H&E)-like output image. The methods described in this paper will undergo clinical validation and their diagnostic accuracy will be tested in the near future.

References

Piergiacomo Calzavara-Pinton, Caterina Longo, Marina Venturini, Raffaella Sala, and Giovanni Pellacani. Reflectance confocal microscopy for in vivo skin imaging. *Photochemistry and photobiology*, 84(6):1421–1430, 2008.

Vinh Q Chung, Peter J Dwyer, Kishwer S Nehal, Milind Rajadhyaksha, Gregg M Menaker, Carlos Charles, and S Brian Jiang. Use of ex vivo confocal scanning laser microscopy during mohs surgery for nonmelanoma skin cancers. *Dermatologic surgery*, 30(12p1):1470–1478, 2004.

Elisa Cinotti, Jean Luc Perrot, Bruno Labeille, Frédéric Cambazard, and Pietro Rubegni. Ex vivo confocal microscopy: an emerging technique in dermatology. *Dermatology practical & conceptual*, 8(2):109, 2018.

Daniel S Gareau. Feasibility of digitally stained multimodal confocal mosaics to simulate histopathology. *Journal of biomedical optics*, 14(3):034050, 2009.

Davit Gigilashvili. Measuring and mitigating speckle noise in dual-axis confocal microscopy images. Master's thesis, NTNU, 2017.

Kaiming He, Xiangyu Zhang, Shaoqing Ren, and Jian Sun. Deep residual learning for image recognition. In *Proceedings of the IEEE conference on computer vision and pattern recognition*, pages 770–778, 2016.

Phillip Isola, Jun-Yan Zhu, Tinghui Zhou, and Alexei A. Efros. Image-to-image translation with conditional adversarial networks. *CoRR*, abs/1611.07004, 2016. URL http://arxiv.org/abs/1611.07004.

Moira Ragazzi, Simonetta Piana, Caterina Longo, Fabio Castagnetti, Monica Foroni, Guglielmo Ferrari, Giorgio Gardini, and Giovanni Pellacani. Fluorescence confocal microscopy for pathologists. *Modern Pathology*, 27(3):460, 2014.

M.V. Sarode and P.R. Deshmukh. Reduction of speckle noise and image enhancement of images using filtering technique. *International Journal of Advancements in Technology*, 2:30–38, 01 2011.

Vivascope. Vivascope. http://www.vivascope.de/home.html, 2018. Accessed: 2018-12-13.

Puyang Wang, He Zhang, and Vishal M Patel. Sar image despeckling using a convolutional neural network. *IEEE Signal Processing Letters*, 24(12):1763–1767, 2017.

Jun-Yan Zhu, Taesung Park, Phillip Isola, and Alexei A. Efros. Unpaired image-to-image translation using cycle-consistent adversarial networks. *CoRR*, abs/1703.10593, 2017. URL http://arxiv.org/abs/1703.10593.

V. DISCUSIÓN

En esta tesis, nuestro objetivo fue expandir el conocimiento y evaluar la relevancia clínica de dos técnicas novedosas de imagen. Como principales resultados, hemos descrito criterios diagnósticos de lesiones tumorales cutáneas tanto *in vivo*, como *ex vivo*. De forma relevante, pudimos contribuir al desarrollo de la 4ª generación de MCev y del dispositivo de TCO-CL.

IN VIVO

V.1. Estructuras morfológicas de las lesiones melanocíticas en TCO-CL.

V.1.1. Principales diferencias entre dispositivos.

Debido a la robusta evidencia del uso del MCR en lesiones melanocíticas,[32,36,38] por sus tasas de sensibilidad del 98.15% y de especificidad del 98.89%, es fundamental comparar cualquier nueva técnica de microscopía *in vivo* con el "patrón de referencia", la MCR. Por lo tanto, confrontamos las imágenes obtenidas en los cortes horizontales de TCO-CL y MCR, en el espectro de las lesiones melanocíticas atípicas, benignas y malignas más comunes y evaluamos las semejanzas, las diferencias y las limitaciones de cada técnica.

Comprendimos que, en la MCR, cada imagen de corte horizontal se realiza cada 3 micras de espesor en profundidad (con resolución axial de < 5 μm, lateral de 1 μm (semejante a H&E) y ~ 250 μm de penetrancia en profundidad), mientras que las de TCO-CL, se obtienen de una en una micra (esta última, con una resolución axial de 1.2 μm y lateral de 1.3 μm – con campo de visión de 1.2 mm y ~ 400 μm de penetrancia en profundidad). En consecuencia, se observa una mejor visualización de estructuras

citológicas como las células dendríticas en MCR, ya que casi toda la extensión de estas queda representada en el espesor de 3 micras. Por otro lado, en TCO-CL, la visualización de las células dendríticas solo se logró ver completamente a medida que navegamos en los cortes horizontales o verticales, cada 3 micras. A pesar de esto, comprendimos ahora que estas células en TCO-CL se ven con gran precisión respecto a su proyección tridimensional real dentro de la epidermis, y que los "cortes más gruesos" facilitan la visualización de las estructuras citológicas.

Por otro lado, la imagen resultante del punto "focal" que concentra los haces de luz láser, permite una imagen más nítida (más "en foco") respecto a la imagen proporcionada por el TCO-CL, que está compuesta de la unión de una imagen de confocal con una de TCO (para lograr la visualización en un plano en 3D). Esta característica también resulta en que la imagen de MCR presenta mayor contraste entre las estructuras visualizadas. Sin embargo, al combinar TCO, el TCO-CL logra mayor penetración en la piel, conservando resolución celular en sectores ya no alcanzados por la MCR.

Otra desventaja observada del TCO-CL respecto al MCR, es que, en esta última, somos capaces de ver imágenes de "Vivablocks" (VS 1500), anteriormente mencionados. Los mismos, siendo imágenes de hasta 8 x 8 mm, permiten ver un gran porcentaje de lesiones melanocítica en su totalidad, facilitando el análisis de estructuras macroscópicas y microscópicas. De esta manera, se analizan los rasgos macroscópicos globales de la lesión estudiada, para luego realizar una aproximación en los sectores más relevantes, y visualizar detalles celulares (el o los sectores de mayor atipia en el contexto global de la lesión). Los "Vivablocks" son un apoyo fundamental en el estudio de lesiones melanocíticas dudosas, una de las más relevantes aplicaciones de la microscopía confocal *in vivo*.

Sin embargo, cuándo comparamos el TCO-CL al confocal de mano (VS 3000), el primer dispositivo tiene la inédita ventaja de la visualización de los cortes en vertical con resolución celular. Esta característica es, sin duda, una gran ventaja en el momento de identificar características morfológicas y citológicas de malignidad como, por ejemplo, la invasión perifolicular en el caso de lentigo maligno. También permite diferenciar campo de cancerización de queratosis actínicas, o de carcinomas escamosos avanzados. Posibilita ver la integridad de la unión dermoepidérmica (UDE), el ascenso pagetoide en lesiones melanocíticas malignas y la diferenciación entre la inflamación subepidérmica (con abundantes células dendríticas y macrófagos), de la verdadera disrupción de la UDE en el caso de una neoplasia maligna. Esta característica es también de fundamental aplicación en la diferenciación de lesiones faciales equívocas.

Otro dispositivo que nos permite ver la piel con cortes verticales es el TCO. La gran ventaja de este dispositivo es el tamaño de la pieza que puede ser estudiada y que son capturadas imágenes en 2D y 3D. La TCO dinámica (con angiografía), posibilita ver el patrón de vascularización en 3D. La penetración alcanza los ~ 2 mm. Sin embargo, por la mayor penetrancia de la fuente de luz en el tejido, posee menor resolución celular (resolución estructural a 1310 μm a 1.5 mm y de 1700 μm a 1.8 mm). A pesar de poder visualizar la unión dermo epidérmica, la resolución de los cambios arquitecturales se aprecia considerablemente mejor en TCO-CL (aunque en un campo mucho menor). Por otro lado, la comprensión y observación de fenómenos citológicos (como el ascenso de células pagetoides) no pueden ser valorados en TCO. Por este motivo, el TCO no fue comparado con las otras dos técnicas antes mencionadas, que si proporcionan definición celular. (Figura 16 y Tabla 2)

Se han publicado estudios con nuevos dispositivos, integrando en una misma sonda la MCR y la TCO, que combina las ventajas de los dos métodos, pero hasta el momento no existe ningún equipo comercializado.[76]

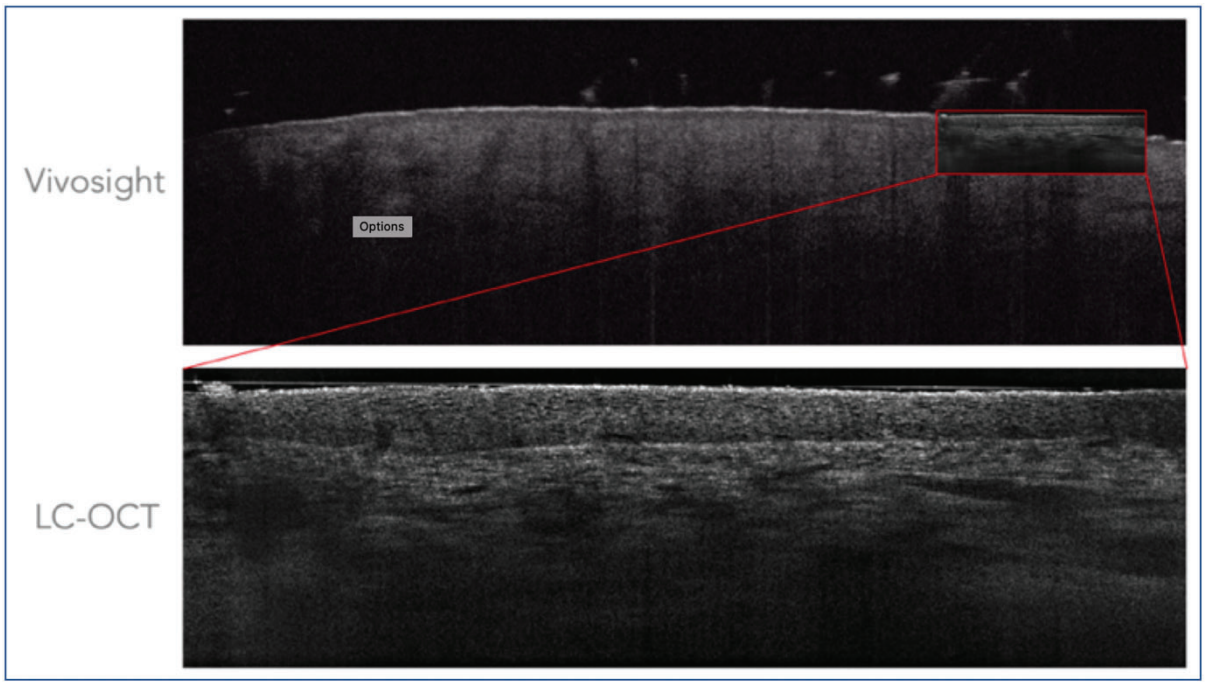

Figura 16. Imagen de piel normal con TCO (superior) y TCO-CL (inferior). El cuadrado rojo muestra la diferencia de campo de visión entre las técnicas, así como la resolución celular. En la TCO, la UDE se encuentra sutilmente visible, aunque es consistentemente más visible en la imagen de TCO-CL (inferior). De la misma manera, las células epidérmicas y las bandas de colágeno son claramente visibles en la imagen inferior, aunque el campo de visión es mucho mayor en el superior. (Fuente: Javiera Pérez-Anker)

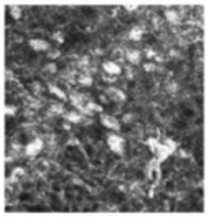
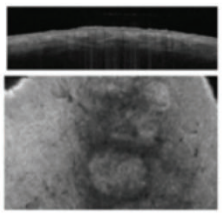
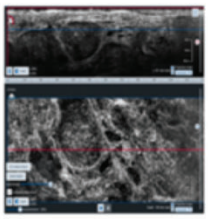

	RCM	OCT	LC-OCT
Horizontal (en face)	Si	Si	Si
Vertical (slice)	No	Si	Si
3D	No	Si	Si
Penetración (µm)	200-250 µm	1000-2000 µm	400-500 µm
Resolución lateral	1 µm	7.5 µm	1 µm
Resolución axial	3-5 µm	5-10 µm	1 µm
Resolución celular	Si	No	Si
Campo de visión	500 x 500 µm 750 x 750 µm Vivablocks 8 x 8 mm	6 x 6 mm	1.2 x 0.5 mm
Tiempo de examen	1-5 min.	1 min	1-5 min.

Tabla 2. Principales diferencias entre los dispositivos. (Adaptado y modificado de Davis et al., 2019)[77]

V.1.2. Estructuras morfológicas de las lesiones melanocíticas en TCO-CL y su comparación con MCR e histología.

Comparamos los hallazgos arquitecturales y citológicos ente TCO-CL y MCR en cortes horizontales, y TCO-CL y H&E en cortes verticales. Analizamos la definición y la resolución celular de estas técnicas, por ser fundamentales para el diagnóstico de lesiones melanocíticas equívocas. Además, analizamos estos criterios por primera vez en tres dimensiones espaciales. Los criterios diagnósticos descritos en el caso de la MCR fueron evaluados en 3 niveles: epidermis, unión dermo epidérmica y dermis superficial para ser comparados con la TCO-CL.

De acuerdo con nuestro conocimiento, hasta la fecha en que esta tesis está siendo escrita, no existen otros estudios que comparen las estructuras arquitecturales y citológicas tumorales entre TCO-CL y MCR.

De una forma global, cada estructura citológica se observó más nítida, con más brillo y con más contraste en MCR que en TCO-CL. Sin embargo, todas las estructuras vistas en MCR pudieron también ser observadas en TCO-CL. Arquitecturalmente, prácticamente no fueron encontradas diferencias entre ambas técnicas, salvo que con TCO-CL pudieron observarse cambios arquitecturales y citológicos a mayor profundidad. Otra diferencia es que, en el MCR, no pudieron ser evaluados los criterios en el plano vertical de forma similar a la histopatología convencional, ni tampoco en 3D con resolución celular con ninguna otra técnica. (Figura 17)

Diferencias en cortes horizontales

- En la MCR, el contraste de melanina fue más evidente que en TCO-CL y el tamaño de la lesión escaneada fue de 8 mm a diferencia del TCO-CL que fue de 1.5 mm. Esto permitió que sólo una superficie de 1.5 mm pudo ser comparada en ambas técnicas, causando una limitación en la comparación de la totalidad de la lesión.
- En el TCO-CL, sin embargo, por ser una técnica que incluye principios de TCO, fuimos capaces de evidenciar resolución celular hasta casi 350 μm de profundidad en comparación con el MCR, cuya resolución celular ideal se encontró hasta un máximo de 200 μm.
- Los detalles nucleares fueron igualmente observados en ambas técnicas (a profundidades de hasta 200 μm), aunque en MCR estos se observaron más brillantes y con mayor contraste.

- La forma real de las células dendríticas y su distribución espacial fue mejor comprendida en TCO-CL, pudiendo, en algunas secciones epidérmicas, visualizarse los gránulos de melanina en las dendritas, aunque eran más difíciles de ser diferenciadas del estroma. Por otro lado, el contraste evidenciado en el MCR y los cortes cada 3 μm, permitieron la visualización mucho más clara y evidente de estas estructuras en MCR en la sección horizontal.
- Los patrones diagnósticos en epidermis de MCR (panal de abejas, empedrado, desestructuración epidérmica, células pagetoides, atipia celular (células redondeadas, dendríticas y pleomorfas) y "visualización de núcleos", se encontraron en ambas técnicas, con resoluciones muy semejantes.
- A nivel de la UDE en horizontal, la presencia de papilas dérmicas (bien o mal definidas, fusionadas o no), de nidos (densos, heterogéneos o cerebriformes), de células atípicas (aisladas o en sábana), fueron igualmente observados en MCR y TCO-CL. La correlación entre lesiones malignas, atípicas y benignas siempre fue concordante en ambas técnicas.
- En la dermis papilar, la presencia de nidos, células atípicas, vasos, inflamación y macrófagos, fueron mejor observados en TCO-CL que en MCR.

Diferencias en cortes verticales

- Se observaron semejanzas arquitecturales entre la patología convencional con H&E y las secciones verticales de la TCO-CL. A pesar de la variación de colores (escalas que variaron entre el blanco, gris y negro en TCO-CL), a grandes rasgos, las estructuras morfológicas y citológicas fueron comparables.

- Se observaron en el caso de tumores con paraqueratosis pigmentada en TCO-CL la presencia de células con núcleos en la córnea (como áreas hiper refráctiles alargadas)
- Las capas de la epidermis pudieron ser reconocidas y fue fácilmente identificable cuando la arquitectura y citología normal epidérmica se había modificado por la invasión neoplásica maligna a este nivel.
- Se demostró la visualización en TCO-CL de las células dendríticas melanocíticas tumorales, sin necesidad de tinciones especiales.
- Los nidos de células melanocíticas (típicos y atípicos) fueron reconocidos y la celularidad de éstos (típica y atípica).
- Los folículos pilosos, infundíbulos y los quistes se visualizaron fácilmente en TCO-CL.
- La zona de grenz se reconocía también en TCO-CL, en los nevus benignos.
- Un hallazgo destacado ha sido observar la UDE con una resolución adecuada, en cortes verticales. La integridad de esta estructura se observaba en lesiones benignas y, al contrario, la disrupción se observó en el caso de tumores malignos en TCO-CL.
- El alargamiento de las crestas papilares, así como la fusión de ellas, y la presencia de nidos en las crestas también pudo ser observado.
- Sin embargo, la resolución de detalles nucleares, como mitosis o la visualización de nucléolos, no fue posible con TCO-CL.
- Esto también ocurrió con los desmosomas, que no pudieron ser reconocidos en TCO-CL.

Cortes en 3 D

- En relación con la distribución espacial arquitectural y celular tumoral debe destacarse el resultado de nuestro estudio. Por primera vez, fuimos capaces de observar la arquitectura en 3D de la epidermis, UDE y de la dermis superficial con resolución celular. Además, la disposición de los nidos de células melanocíticas benignas y malignas, y de las células atípicas y dendríticas, fue comprendida en el espacio tridimensional de la piel.

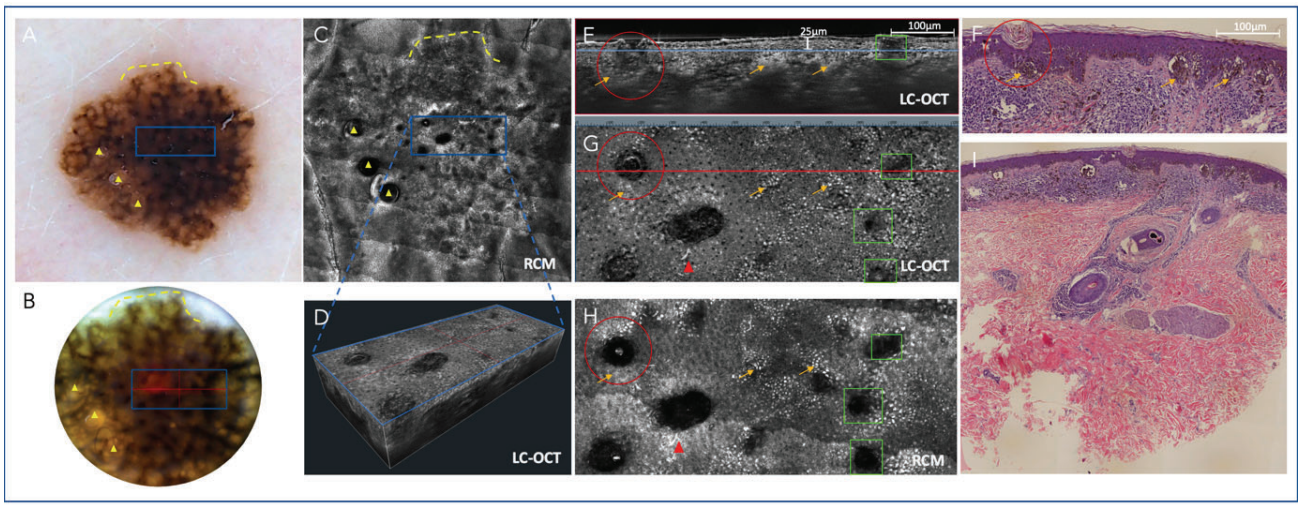

Figura 17. Nevus atípico. Comparación entre TCO-CL, MCR e histopatología.

A. Imagen dermatoscópica (Vivacam®) que incluye el área seleccionada para comparar entre MCR, TCO-CL e histopatología. B. Imagen dermatoscópica (cámara dermatoscópica integrada en DeepLive® TCO-CL) que muestra en detalle el área seleccionada a ser comparada. C. Mosaico MCR Vivablock® que incluye el área seleccionada. D. Imagen de cubo 3D TCO-CL del área seleccionada. E. Imagen vertical TCO-CL del área seleccionada. F. Imagen histopatológica (H&E) correspondiente. G. Imagen horizontal TCO-CL. H. Imagen MCR correspondiente. I. Descripción histopatológica completa (H&E) de la lesión.

Puntos de referencia y triángulos amarillos: guías macroscópicas para seleccionar con precisión la misma zona a comparar en dermatoscopia y MCR. Rectángulo azul: área seleccionada para comparar TCO-CL y MCR. Línea azul: ubicación del plano horizontal (representado en g) sobre el plano vertical correspondiente (representado en e). Línea roja: ubicación del plano vertical (representado en E) sobre el plano horizontal correspondiente (representado en G). Flechas naranjas: nido de melanocitos atípicos. Círculos rojos: pseudoquistes. Cuadrados verdes: aberturas foliculares. Triángulos rojos: células dendríticas. (Adaptado de Pérez-Anker et al., 2022)[65]

En 2018, Dubois y colaboradores llevaron a cabo estudios iniciales utilizando TCO-CL y describieron algunos hallazgos encontrados en imágenes de cortes verticales de un melanoma invasor. Observaron un desorden arquitectural de la epidermis, consumo epidérmico, disrupción de la unión dermoepidérmica, así como nidos de melanocitos atípicos y ascenso pagetoide de las células melanocíticas. Estas características se correlacionaron con los hallazgos histopatológicos. En nuestro estudio, encontramos las mismas características en las muestras de melanomas. Sin embargo, los autores no describieron hallazgos citológicos ni otras características, como la presencia de nidos intraepidérmicos. Tampoco se estudió la correlación con MCR, ni se describieron las características morfológicas y citológicas en cortes horizontales o en 3D. No se describieron hallazgos en lesiones benignas o atípicas.

Posteriormente, se describieron criterios estructurales específicos en nevus intradérmicos detectados mediante TCO-CL. (Figuras 18 y 19)[78] Los autores observaron un patrón "ondulado" compuesto por líneas hiper e hipo refráctiles en la dermis papilar y reticular, que corresponden a cordones/nidos de melanocitos y bandas de colágeno entre ellos. Además, se observó una delimitación clara de la unión dermoepidérmica, un adelgazamiento de la dermis papilar debido a la proliferación melanocítica en dermis y la ausencia de células atípicas en la epidermis/dermis. La caracterización de este patrón de benignidad ha permitido diferenciar nevus intradérmicos de lesiones clínicamente dudosas. (Figuras 18 y 19) En nuestra muestra, encontramos las mismas características en los nevus intradérmicos.

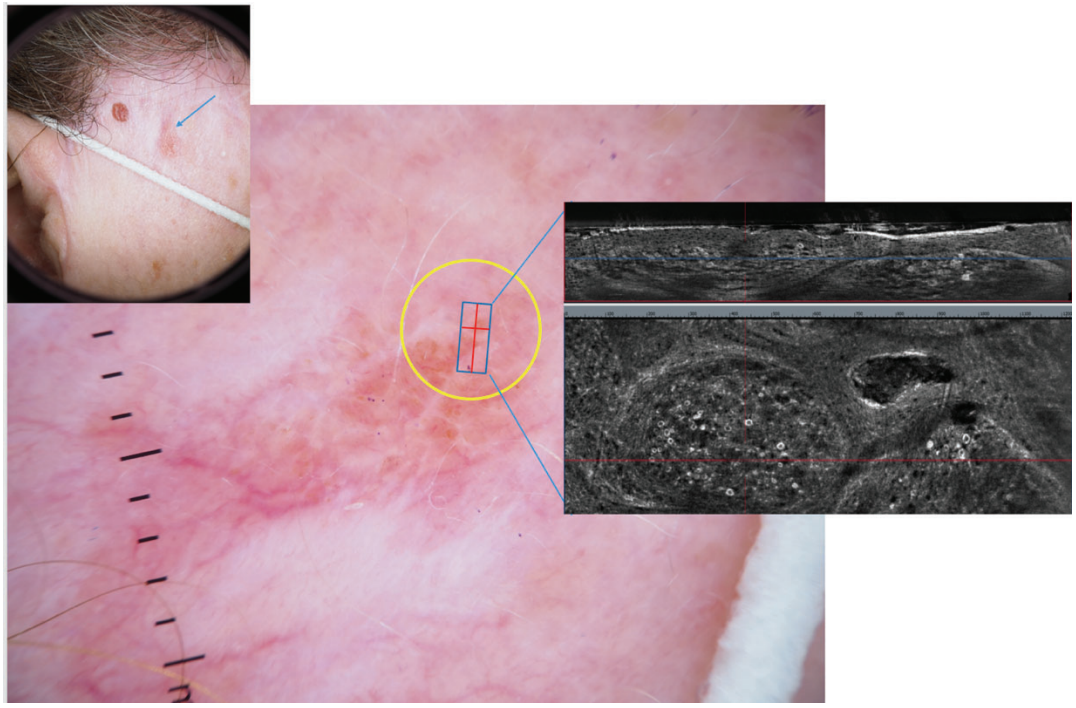

Figura 18. Imagen de una lesión discretamente pigmentada, marrón, palpable y adquirida en una paciente de 54 años, en la zona malar derecha. Imagen clínica (parte superior). Dermatoscopia con un patrón en empedrado marrón y vasos polimorfos que obligan al diagnóstico diferencial de un melanoma. Imagen de OCT-CL que confirma el diagnóstico de nevus dérmico, tanto en cortes verticales como en horizontales. La ausencia de atipia se evidencia por la presencia de nidos bien delimitados compuestos por nevocitos monomorfos, redondeados, bien delimitados, sin atipia. El cuadrado azul dentro del círculo amarillo muestra el área escaneada con TCO-CL. (Fuente: Javiera Pérez-Anker)

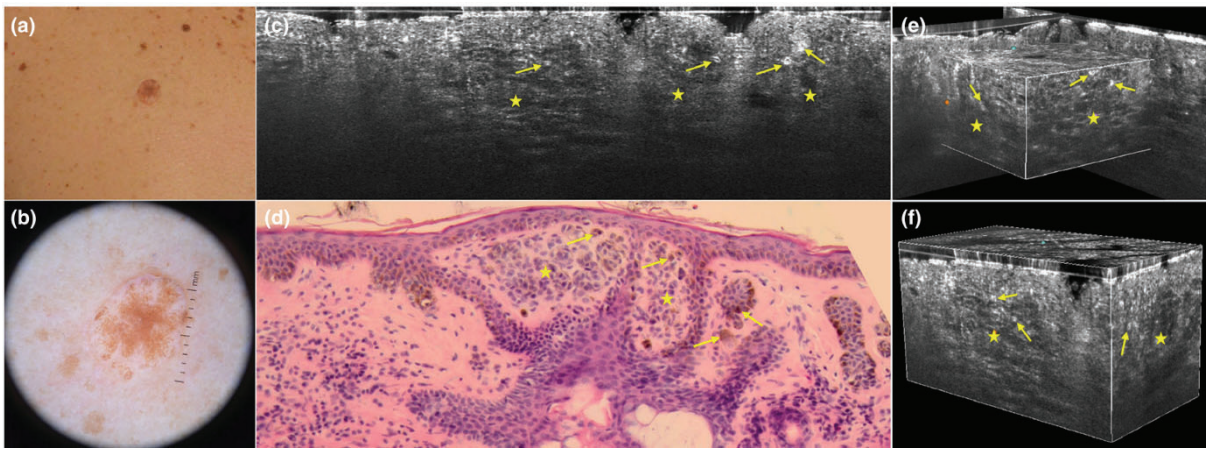

Figura 19. Nevus dérmico. (a): Clínica; (b) dermatoscopia; (c)(e)(f) tomografía de coherencia óptica de campo lineal e histología (d). Patrón típico de ondas pequeñas incluido en tres estructuras lobulillares más grandes mal definidas (c, estrellas amarillas) correspondientes a la masa de múltiples nidos melanocíticos en histopatología (d) y que contienen células redondeadas brillantes correlacionadas con la presencia de melanocitos altamente pigmentados (flechas amarillas). Las líneas brillantes son más fáciles de visualizar en el modo tridimensional (e, f). (Adaptado de Lenoir et al., 2021)[78]

Después de la publicación de nuestro estudio, se ha encontrado una correlación significativa entre las imágenes obtenidas mediante TCO-CL y los hallazgos histopatológicos en informes descriptivos de un caso en lesiones como el lentigo maligno (donde se observaron células atípicas y dendríticas peri foliculares) y los nevus de Spitz (donde, en el plano horizontal, se observaron nidos de melanocitos adyacentes a la unión dermoepidérmica y, en las imágenes verticales, nidos de melanocitos en la unión dermoepidérmica y melanófagos en la dermis papilar).[79-82]

Además, se ha explorado el uso de TCO-CL en 9 lesiones pigmentadas genitales, donde se han identificado características distintivas en melanosis dérmica benigna, un nevus genital y un melanoma invasivo.

Sin embargo, ninguno de estos estudios describió otras lesiones melanocíticas ni comparó los hallazgos con la MCR. Tampoco se mencionaron los hallazgos obtenidos en cortes horizontales y en 3D.

Por otra parte, nuestro grupo ha demostrado previamente la correlación entre las imágenes de cortes horizontales de la tinción H&E y las imágenes horizontales de la MCR.[83] En este estudio, se recopilaron un total de 44 tumores cutáneos, que incluyeron 19 lesiones melanocíticas (nueve nevos compuestos, cinco nevos junturales y cinco nevos intradérmicos), 12 carcinomas basocelulares y 13 queratosis seborreicas. Las características de la MCR que mostraron una concordancia estadísticamente significativa con las secciones horizontales histopatológicas fueron: el patrón de panal de abejas preservado y visible, la UDE bien definida, pequeñas partículas brillantes, nidos dérmicos, islas tumorales y siluetas oscuras, hendidura peri tumoral, haces de colágeno, haces de colágeno engrosados y atipia citológica. (Figura 20)

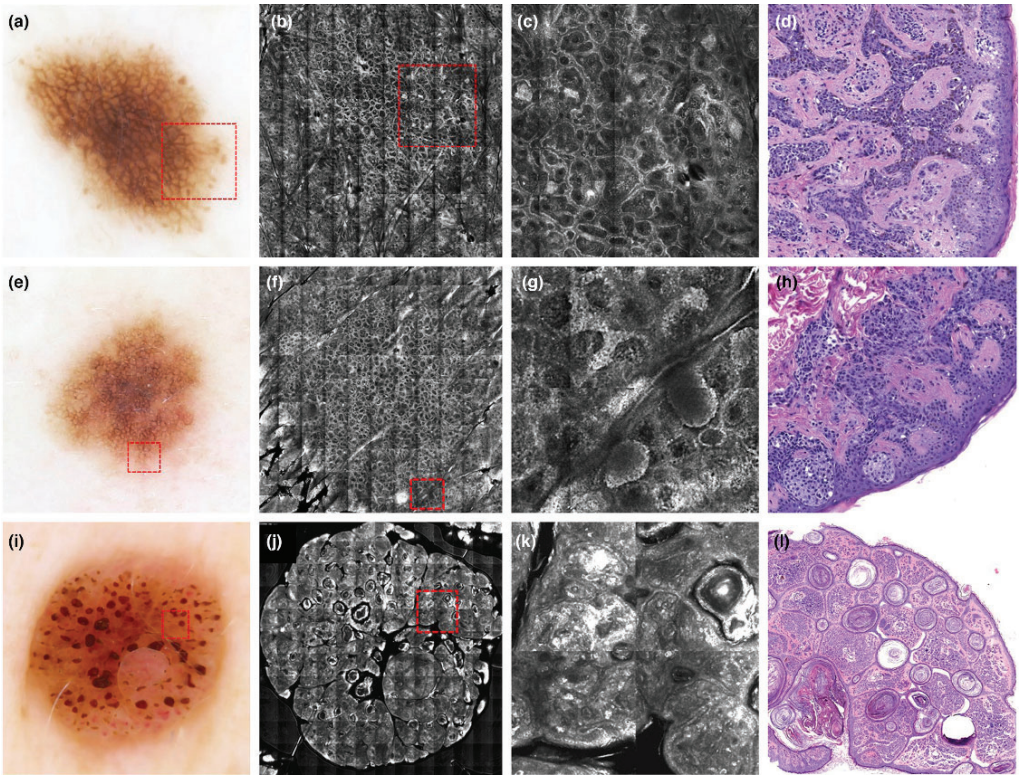

Figura 20. Imagen comparativa en melanocíticas. (a) Dermatoscopia (10×) de un nevo juncional con patrón de red regular y glóbulos periféricos. (b) MCR (5 × 5 mm) en la UDE que muestra el patrón en anillo, el patrón típico de malla y nidos homogéneos. (c) Representación del cuadrado rojo (1,5 × 1,5 mm) que exhibe las mismas características. (d) Histopatología en vista horizontal (200×) revelando el patrón de malla típico constituido por la fusión de agregados de pequeñas células melanocíticas que llevan al agrandamiento discreto de la red. Es posible individualizar algunos nidos dentro de los espacios interpapilares. (e) Dermatoscopia (10×) de un nevo juncional banal con patrón reticular y algunos glóbulos en la periferia (casi invisibles). (f) MCR (5,5 × 5,5 mm) en la UDE que muestra el patrón en anillo y el patrón típico de malla con nidos homogéneos en la periferia. (g) Representación de un cuadrado rojo (1,5 × 1,5 mm) que exhibe la fusión de agregados de pequeñas células melanocíticas formando el patrón de malla y los nidos homogéneos en la periferia. (h) Histopatología en vista horizontal (200×) que muestra los nidos de células melanocíticas en la periferia y los agregados de células melanocíticas dentro de los espacios interpapilares formando el patrón de malla típico. (i) Dermatoscopia de un nevo intradérmico papilomatoso con patrón globular y pseudoquistes. (j) RCM (7 × 7 mm) en la UDE que muestra los

pseudoquistes y nidos de células melanocíticas en las papilas. (k) Representación de un cuadrado rojo (1 × 1 mm) que muestra células melanocíticas brillantes densas y dispersas dentro de las papilas y un pseudoquiste con una intensa luminosidad en el centro. (l) Histopatología (100×) que exhibe depósitos redondos de queratina laminar dentro de la epidermis y la presencia de proliferación de nidos que agrandan las papilas. (Adaptado de Perino et.al.,2023)[83]

V.2. Correlación de los hallazgos dermatoscópicos en las lesiones melanocíticas en TCO-CL.

Debido a que la dermatoscopia es una técnica que ha revolucionado y cambiado la forma de analizar los pacientes dermatológicos, por toda la consistente evidencia generada, resultaba necesario describir de forma sistemática las principales estructuras dermatoscópicas en TCO-CL. Al comprender que los hallazgos morfológicos y citológicos de la MCR y de la H&E se correlacionaron con los de la TCO-CL, y de que somos capaces de observar las lesiones en 3D con esta tecnología, fue necesario comprender mejor las estructuras dermatoscópicas diagnósticas de las lesiones melanocíticas. (Figuras 21 y 22)

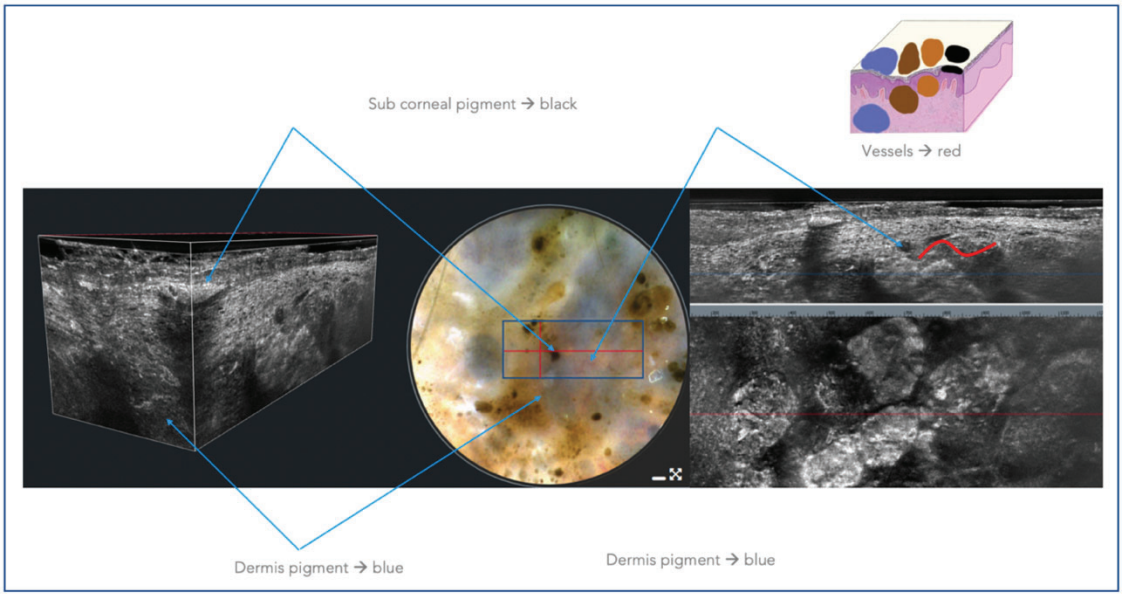

Figura 21. Melanoma. Izquierda (3D); centro (dermatoscopia); Derecha (TCO-CL en corte vertical (superior) y horizontal (inferior). Las estructuras y células son visualizadas, en tiempo real *in vivo* en 3D. El color negro corresponde a el color en capas superficiales de la piel, mientras que los diferentes tonos de marrón se correlacionan con el pigmento en diferentes partes de la epidermis. Por otro lado, el color azul corresponde a pigmento profundo, subepidérmico. Las estructuras vasculares pueden observarse en tiempo real. (Fuente: Javiera Pérez-Anker) (Esquema superior derecho, adaptado de Malvehy et al., 2006)[9]

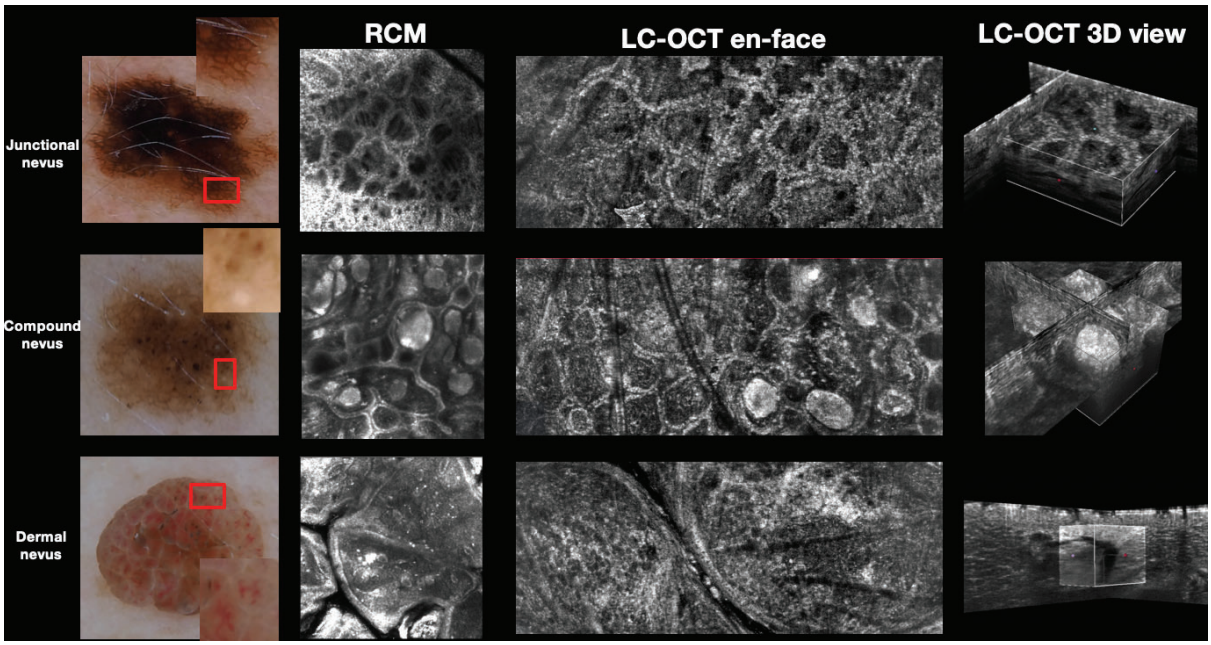

Figura 22. Nevus melanocíticos: Visualización de Estructuras Dermatoscópicas en 2D y 3D con Comparación de MCR. En el panel superior horizontal, se aprecia el patrón reticular. En esta estructura, el patrón de anillas (que se corresponde a la red) observado en MCR se relaciona directamente con el mismo patrón en TCO-CL, ofreciendo una resolución superior a una mayor profundidad. Asimismo, se distingue una trama simétrica y uniforme en 3D de este patrón. En el segundo panel horizontal, se presenta el nevus compuesto, donde se pueden apreciar los nidos ubicados entre las anillas. En términos dermatoscópicos, estos nidos se asocian a glóbulos relacionados con el patrón reticular. En el panel inferior horizontal, se visualizan nidos simétricos y redondeados de considerable tamaño en ambas técnicas, lo cual concuerda con el patrón dermatoscópico globular. Además, se destaca la identificación precisa del vaso en coma en la representación 3D. (Fuente: Javiera Pérez-Anker)

En una muestra de 126 lesiones melanocíticas (57 malignas), con representación de nevus de la unión, nevus compuestos, nevus dérmicos, nevus atípicos, nevus congénito, nevus de Spitz/Reed, hiperplasias melanocíticas, melanomas in situ y melanomas invasivos, se analizaron sus criterios dermatoscópicos.

Los patrones estudiados fueron: patrón reticular (regular o atípico), puntos y glóbulos (típicos o atípicos/asimétricos), áreas sin estructura (negras/marrones o blancas/azules/grises), velo azul blanquecino, estructuras de regresión (similares a cicatrices o azul-gris), red negativa, patrón homogéneo (azul, blanco/amarillo/rojo), líneas (proyecciones lineales o bulbosas), manchas, estructuras blancas, líneas blancas y rosetas, y puntos azules. Estos criterios dermatoscópicos se compararon con los hallazgos de TCO-CL en términos de la organización arquitectónica tridimensional y de detalles celulares (que incluían el tamaño, la morfología, la atipia y la distribución de melanocitos, queratinocitos y de células inflamatorias).

Por primera vez, se pudo observar cada criterio dermatoscópico en 3D e *in vivo*, mediante una imagen similar a la histología en corte vertical, sin los artefactos derivados del procesamiento y la fijación de las muestras. Se lograron visualizar, en proyecciones histológicas verticales tridimensionales, características como la forma de la UDE, la dimensión, forma y distribución de los nidos melanocíticos y los patrones vasculares, con la ayuda de sistemas de reconstrucción de inteligencia artificial. Hasta el momento de escribir esta tesis, no existen otros estudios semejantes.

Estructuras observadas:

- Patrón Reticular: Se relacionó con prolongaciones epidérmicas, asociadas con lesiones benignas y malignas. Se observó que un patrón reticular irregular se

correlacionó con desórdenes arquitecturales de las crestas epidérmicas, ensanchadas o unidas entre sí.

- Patrón Globular: Aunque se describe que los patrones globulares corresponden a nidos melanocíticos en la UDE, se observaron nidos ubicados tanto en la punta de las crestas dérmicas como dentro de las papilas dérmicas. También se notó que algunos glóbulos clínicamente similares en dermatoscopia tenían contrapartes en TCO-CL correspondientes a quistes queratinocitos o pseudoquistes, lo que requiere más estudios para su comprensión.

- Glóbulos Grises: Los glóbulos grises, especialmente en el melanoma, se caracterizaron por la presencia de melanófagos en la dermis. Estos melanófagos grandes parecen corresponder directamente a algunos pequeños puntos grises.

- Líneas en Dermatoscopia: proyecciones lineales o bulbosas en la periferia de la lesión. Correspondieron a nidos de melanocitos pigmentados en la UDE. Sin embargo, se encontró que en el 75% de los casos con TCO-CL, no se observaban nidos melanocíticos claros en estas proyecciones lineales, sino la presencia de células dendríticas en la capa basal y una organización irregular de las crestas dérmicas.

- Áreas sin Estructura: se relacionaron con aplanamiento de las crestas dérmicas o una disminución en la concentración de melanina. En TCO-CL, se observó que la UDE estaba interrumpida o irreconocible en la mayoría de los casos, lo

que fue crucial para la diferenciación entre benignidad y malignidad en estas áreas.

- Manchas: Las manchas se debieron a la retención de melanina en la epidermis o a la paraqueratosis, con o sin células dendríticas.

- Patrón Homogéneo: se evidenciaron nidos profundos de melanocitos o la presencia de un "patrón de olas", una presentación típica de las lesiones con un componente intradérmico. (Figuras 18 y19)[78]

- Áreas de Regresión: Se observaron puntos azul-grisáceos o áreas blancas similares a cicatrices, que correspondieron a melanina en la dermis o fibroplasia. Estos criterios se observaron en melanomas y lesiones benignas, y su interpretación requiere análisis conjunto con otros criterios.

- Color Blanco: El color blanco se asoció con el colágeno, y se observó que las áreas de regresión tipo cicatriz mostraban fibroplasia en TCO-CL, caracterizada por líneas dérmicas densas y brillantes.

- Velo Azul Blanquecino: Se observóuna epidermis delgada o ulcerada en algunas lesiones, así como la presencia de "hendiduras" entre los nidos de melanocitos y la epidermis o el estroma circundante.

- Red Negativa: consistieron en nidos compactos de melanocitos o melanófagos entre los nidos alargados, con elongación de los procesos interpapilares.

- Rosetas: Se observaron inclusiones de queratina en la epidermis en TCO-CL, lo que difiere de estudios previos que las asociaban a hiperqueratosis

infundibular. Se requieren más estudios para comprender estas estructuras blanco-brillantes.

Además de los criterios arquitectónicos previamente mencionados, el análisis de TCO-CL reveló la presencia de células dendríticas y pagetoides en un 89% de los casos de melanoma y en un 36% de las lesiones benignas (OR=14.6 [IC del 95%: 5.28; 47.64], p<0.001*). Estos datos no se incluyeron en la sección de resultados debido a que no explican directamente un patrón dermatoscópico específico, y se requerirán estudios adicionales para abordar este aspecto en detalle.

Las imágenes tridimensionales obtenidas mediante TCO-CL, proporcionaron una visión más detallada de las estructuras dermatoscópicas, permitiendo identificar detalles adicionales y establecer relaciones espaciales entre dichas estructuras. Esta mayor comprensión facilitará la selección del lugar óptimo para la captura de imágenes *in vivo*, tanto en TCO-CL como en otras técnicas, enfocándose en las áreas de mayor agresividad e invasión. Además, permitirá una identificación más precisa de la ubicación adecuada para llevar a cabo una biopsia o guiar el corte histológico, lo que podría tener un impacto significativo en la detección temprana y el manejo adecuado de los melanomas.

V.3. Criterios diagnósticos de las lesiones melanocíticas en tomografía de coherencia óptica

Una vez que identificamos los principales hallazgos morfológicas arquitecturales y citológicos en lesiones melanocíticas, se hizo necesario establecer sus criterios diagnósticos en TCO-CL e identificar las características más significativas asociadas con la malignidad.

Nuestros resultados revelaron criterios arquitectónicos y citológicos fundamentales para distinguir los nevos del melanoma, tanto en patrones arquitecturales como citológicos en epidermis, unión dermoepidérmica y dermis en 3D. Algunos de ellos fueron vistos por primera vez en nuestro estudio, y solo pudieron ser visualizados en las imágenes verticales de TCO-CL.

Criterios diagnósticos:

- Criterios de malignidad:
    - Más de 10 células pagetoides e irregularidad en la arquitectura epidérmica.
    - Disrupción de la unión dermoepidérmica (en ausencia de inflamación debajo de la unión. (Figura 23) Solo visto en cortes verticales.
    - Formación de hendidura alrededor de los nidos de células atípicas. Fundamentalmente visto en cortes verticales.
    - Nidos de melanocitos epidérmicos sin conexión dérmica. Solo visto en cortes verticales.
    - Consumo epidérmico. Solo visto en cortes verticales.

- Criterios de benignidad:
    - patrón de anillas y patrón en empedrado
    - Patrón en "olas". Solo visto en cortes verticales.

- Los criterios protectores deben observarse en todas partes de la lesión, en ausencia de criterios malignos, para certificar benignidad. El patrón en olas, por ejemplo, puede asociarse a otros criterios de malignidad, sospechándose de un melanoma sobre nevus.

- > 10 células pagetoides + células dendríticas en la UDE en ausencia de inflamación, es indicativa de melanoma. Por otro lado, la presencia de inflamación y la ausencia de células pagetoides son características de condiciones benignas, incluso si se visualizan células atípicas en la UDE o en la epidermis. (Figura 24)

Un estudio previo realizados en un único centro por Schuh y colaboradores,[79] analizó imágenes de 84 lesiones melanocíticas (aunque solo 36 también se evaluaron con MCR). Se encontró que el rendimiento diagnóstico de TCO-CL no fue inferior al de MCR en la identificación de melanomas en comparación con todos los tipos de nevos (típicos y atípicos), con una sensibilidad del 93% para ambos métodos y una especificidad del 95% para MCR y del 100% para TCO-CL. Además, el estudio sugirió que los criterios más significativos para diagnosticar melanoma con TCO-CL eran un patrón irregular en forma de panal de abejas, la presencia de células pagetoides y la ausencia de nidos dérmicos, todos ellos indicativos de malignidad.

En contraste, nuestro estudio ha sido realizado también de forma retrospectiva, pero con una base de imágenes que se adquirió prospectivamente, multicéntrica, con evaluadores de 3 países (Italia, Bélgica y España). Por otro lado, balanceamos el número de lesiones melanocíticas benignas, atípicas y malignas (habiendo realizado una selección previa con dermatoscopia), para garantizar una proporción balanceada de lesiones inciertas (más de la mitad), y mismo número de lesiones típicas y claramente atípicas. Por lo tanto, nuestro enfoque metodológico mejoró la confiabilidad al asegurar cobertura completa de las lesiones, incluyendo criterios adicionales, y excluyendo lesiones faciales, acrales y mucosas con criterios específicos.

Además, los hallazgos de TCO-CL se alinearon con características citológicas y arquitectónicas demostradas en estudios previos de MCR.[46,84-87] La arquitectura

irregular de la epidermis favoreció la malignidad (OR 0.37 en TCO-CL vs. 0.30 en MCR), mientras que patrones asociados previamente a benignidad (panal de abejas regular y en empedrado) también se indicaron benignidad en TCO-CL. En la epidermis, la presencia de células pagetoides redondas y dendríticas (3 o más en MCR y 10 o más en LC-OCT), también favorecieron la malignidad. (Figura 23)

Por lo tanto, el TCO-CL puede complementar a la MCR, proporcionando información adicional, como la capacidad de obtención de imágenes verticales en TCO-CL. Sin embargo, nuestro enfoque podría tener la limitación de omitir áreas importantes de lesiones al no poder realizar Vivablocks, lo que podría resultar en una representación menos completa y posibles imprecisiones en el diagnóstico. Para abordar este desafío, proponemos un algoritmo de adquisición de imágenes que previene la pérdida de visualización de áreas críticas para un diagnóstico preciso. (Figura 25)

El primer paso es obtener una imagen dermatoscópica que sirve como base para representar todas las áreas destinadas al escaneo 3D. El objetivo principal es abarcar toda la lesión a través de una vista vertical (mediante videos), identificando características relacionadas con malignidad en esta perspectiva, determinando las áreas más representativas para un escaneo 3D. La dermatoscopia es una herramienta globalmente reconocida en dermatología, y nuestra investigación previa ha establecido una correlación entre la dermatoscopia y TCO-CL para lesiones melanocíticas. Posteriormente, la revisión de las regiones escaneadas que permanecen guardadas en la imagen dermatoscópica inicial, proporciona información crítica para garantizar que no se haya pasado por alto ninguna área diagnóstica significativa durante el proceso de escaneo,

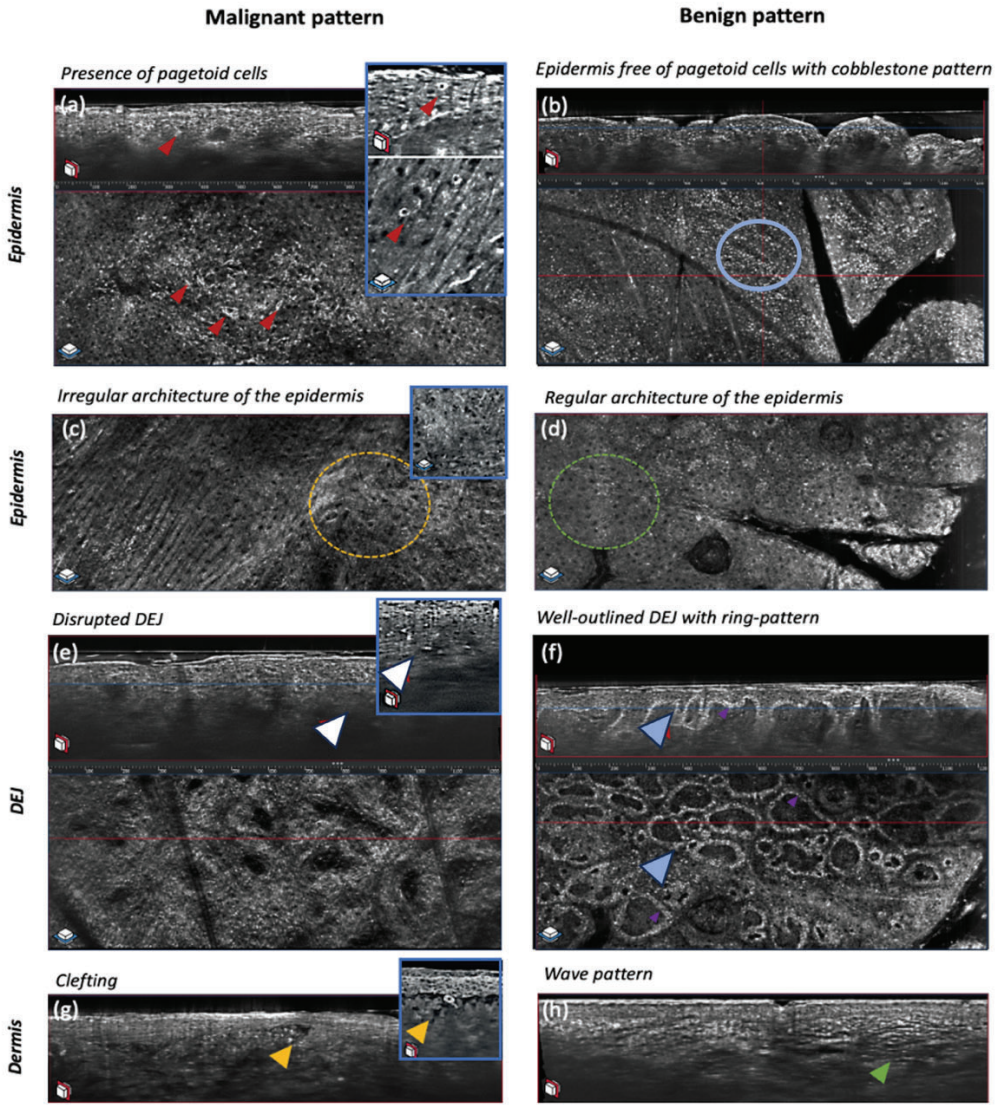

Figura 23. Criterios diagnósticos en lesiones melanocíticas asociados a malignidad y a benignidad. Columna derecha, benignidad, izquierda, malignidad. La presencia de más de 10 células pagetoides (triangulo rojo), con epidermis desestructurada (circulo amarrillo), la disrupción de la unión dermoepidérmica (triangulo blanco), en ausencia de inflamación, y la hendidura alrededor de los nidos (triangulo amarillo) han sido fuertemente asociados a malignidad. Por el contrario, una epidermis con células típicas (circulo azul), regular (circulo verde), y un patrón en anillas (triangulo azul) o en olas (triangulo verde), se asoció a benignidad, en la ausencia de criterios de malignidad. (Adaptado de Pérez-Anker et. al., 2024, en revisión)[67]

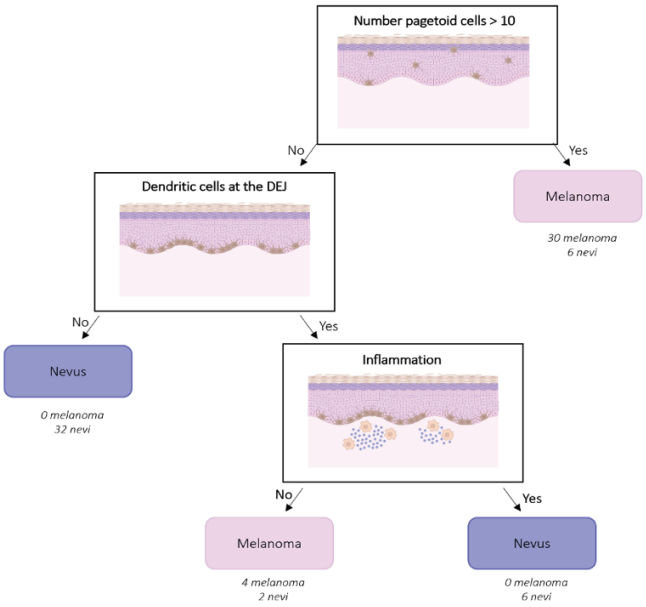

Figura 24. La identificación de más de diez células pagetoides, junto con la presencia de células dendríticas en la unión dermoepidérmica en ausencia de inflamación, es indicativa de melanoma. Por otro lado, la presencia de inflamación y la ausencia de células atípicas en la unión dermoepidérmica son características de condiciones benignas, incluso si se visualizan más de diez células pagetoides en la epidermis. (Adaptado de Pérez-Anker et. al., 2024, en revisión) [67]

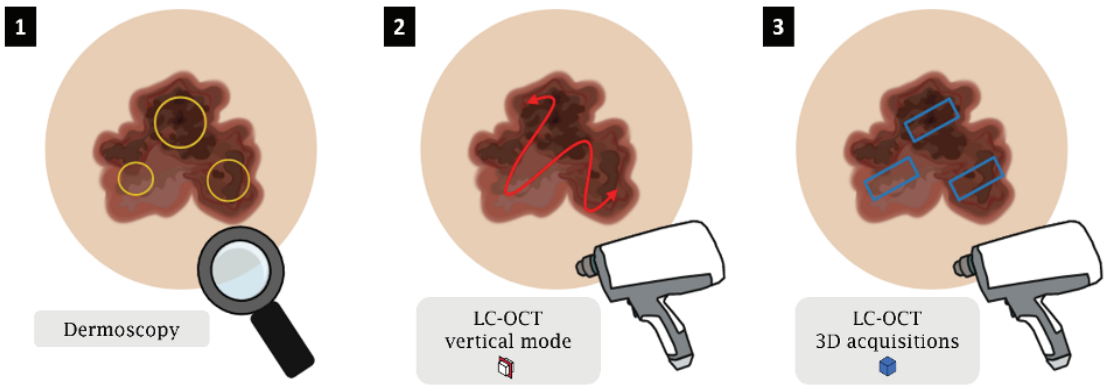

Figura 25. Flujo de adquisición de TCO-CL para lesiones melanocíticas. 1. Encuentra la imagen de dermatoscopia más importante. 2. Cubre toda la lesión con el video vertical. 3. Realiza una adquisición en 3D en las áreas más atípicas según los hallazgos de dermatoscopia y el video. (Adaptado de Pérez-Anker et. al., 2024, en revisión) [67]

V.4. Presencia de "hendidura peritumoral " como marcador de malignidad.

En este estudio, hemos ampliado, por primera vez hasta dónde llega nuestro conocimiento, el criterio de "hendidura" en técnicas de imágenes *in vivo* para lesiones melanocíticas. Además, demostramos que este criterio es un predictor confiable de malignidad por sí solo, ya que se observa en el 24% de los melanomas, y solo en el 2% de las lesiones benignas. Su capacidad predictiva es aún más sólida cuando se combina con otros criterios diagnósticos de malignidad en lesiones melanocíticas, como, por ejemplo, el compromiso de la epidermis (arquitectura irregular o adelgazamiento).

En 2005, Markus Braun-Falco et al.[88] describieron esta característica histológica por primera vez como un marcador diagnóstico para el melanoma. Definieron la fisura como una "separación entre la epidermis y las células melanocíticas subyacentes en la unión dermoepidérmica, con una longitud de al menos 0.3 mm". La fisura se observó en el 24% de los 503 melanomas que analizaron, en concordancia con nuestros resultados (fisura importante visualizada en el 24% de los melanomas). Además, la fisura se observó en <1% (9 de 939) de las lesiones melanocíticas benignas incluidas, como en nuestro estudio, en el que fue del 2%. Comparando ambos conjuntos de datos, esos autores tenían representado el 26% de las lesiones benignas, mientras que nosotros teníamos el 35% de lesiones benignas atípicas.

Este criterio también es un indicio importante en cuanto al grado de invasión de la lesión. Se observó una fisura marcada en el 34% de los melanomas invasivos y en el 14% de los melanomas in situ. Esta asociación con el grado de invasión, ya se informó en histología en 2007 por Walters et al.,[89] quienes mostraron que el

compromiso de la epidermis era un criterio confiable para diferenciar los melanomas de los nevos displásicos y, además, que se asociaba con un aumento en el grosor de Breslow y la ulceración. Además, los autores explicaron que la fisura era un criterio complementario al compromiso de la epidermis, lo que ayudaba en la identificación de melanomas invasivos. La correlación de la presencia de esta característica con otros rasgos diagnósticos morfológicos y citológicos de malignidad, hasta donde llega nuestro conocimiento, no se ha descrito antes.

Markus Braun-Falco et al.[88] también describieron diferentes tipos de fisuras, como las lineales, de nido único y de nidos múltiples, pero no las relacionaron con melanomas más superficiales o invasivos. Observaron una ligera predilección por la localización en la espalda de los melanomas que presentaban esta característica y una prevalencia ligeramente mayor en el tipo de melanoma de extensión superficial y en los tumores con un grosor de Breslow entre 1 y 2 mm. Nosotros no encontramos diferencias significativas en cuanto a la ubicación y la presencia de esta característica.

En 2012, AbdullGaffar et al.[90] también describieron una lista de neoplasias cutáneas en las que se observaba esta característica, pero no la encontraron en su serie de 4 melanomas. Sin embargo, la observaron en un 3% de los nevos melanocíticos analizados (de un total de 93 nevos melanocíticos analizados), lo que concuerda con nuestros resultados de fisura marcada.

Por todas estas razones, parece que la fisura es un criterio interesante que podría proporcionar información relacionada con el diagnóstico (como demostramos en el estudio anterior), el grado de invasión y el pronóstico de la lesión.

En la técnica de TCO-CL, fue fácilmente reconocible y visible en secciones verticales en la periferia de los nidos melanocíticos atípicos debido a la visualización clara del espacio, similar a las láminas de histología, y/o dentro de la piel (en la epidermis alterada), con melanocitos atípicos en esta área. En las mismas lesiones, fue más difícil visualizar la fisura en la MCR, probablemente porque este criterio se identifica más fácilmente en la vista vertical y también mostró un mejor contraste en TCO-CL a la misma profundidad. Sabemos que estos resultados son preliminares y ya estamos realizando estudios adicionales para comparar detalladamente ambas técnicas.

Algunas lesiones no se biopsiaron debido a su dermoscopia claramente benigna, y 4 de ellas presentaron esta característica. Por lo tanto, no es posible determinar si algún otro fenómeno podría confundirse con la fisura. Al revisar estos casos, en uno de ellos que tenía una fisura marcada en una lesión claramente benigna, observamos una posible presencia de una estructura vascular de gran calibre alrededor de un nido, que probablemente se interpretó como fisura. No se observaron otros criterios malignos en el resto de las imágenes de ese mismo caso.

La composición de la hendidura se investigó mediante tinción con Alcian blue, y no se encontraron depósitos de mucina. Aunque su origen exacto sigue siendo incierto, la fisura parece estar relacionada con el diagnóstico, la invasión y el pronóstico de las lesiones melanocíticas. Estudios adicionales se están realizando con marcadores específicos, que nos podrán indicar si este criterio se correlaciona con enzimas proteolíticas asociadas a invasión.

V.5. Aplicaciones de la inteligencia artificial en el estudio campo de cancerización cutáneo en TCO-CL.

Además de otras aplicaciones de esta tecnología, como en diagnóstico de carcinoma basocelular,[45,46,91-96]carcinoma escamoso,[91,97-,100] entre otros,[78,84,91,92,101-107] en estudios recientes se ha sugerido el potencial de la aplicación de algoritmos de inteligencia artificial en el análisis de imágenes de TCO-CL.[98] Sin embargo, hasta la fecha no se han realizado estudios semejantes con TCO-CL al que se incluye en esta tesis, validando los algoritmos entre observadores humanos y la IA en el llamado campo de cancerización y queratosis actínicas.

En nuestro estudio, aplicamos modelos de aprendizaje profundo para segmentar núcleos en imágenes 3D de TCO-CL, en un tiempo de aproximadamente 3 minutos (una tarea imposible para los humanos) en un procedimiento totalmente automatizado (Tabla 3).

Trece criterios nucleares y celulares de atipia, fueron analizados en 185 imágenes 3D (Volumen, compacidad y relación de volumen sobre compacidad de los núcleos; número de células vecinas; distancia promedio de centro a centro celular (entre células vecinas); distancia promedio del borde a borde celular (entre las células vecinas); relación de distancia promedio del borde de la célula sobre distancia del centro; volumen promedio de las células vecinas; compacidad promedio de las células vecinas; desviación estándar del volumen de las células vecinas; desviación estándar de la compacidad de las células vecinas; relación de volumen de las células vecinas; relación de compacidad de las células vecinas). (Figura 26)

En general, de forma estadísticamente significativa, las células patológicas presentaban núcleos de mayor tamaño, de forma más variable y menos esférica. Además, las distancias entre los núcleos eran notablemente mayores en las células

patológicas. El algoritmo fue capaz de diferenciar entre campo de cancerización y queratosis actínica, logrando puntuaciones en la curva ROC (AUC) superiores a 0,965, superando, en gran medida, a los expertos médicos, con un AUC de 0.766.[80] (Tabla 3).

La definición de atipia celular o displasia presenta un desafío considerable, dado que estos conceptos se fundamentan en la experiencia de los patólogos analizando criterios diagnósticos que no son criterios cuantitativos complejos como los preestablecidos en este estudio. Además, existe una variabilidad reconocida incluso entre profesionales técnicos. Por tal razón, es posible que el modelo de aprendizaje automático haya demostrado un desempeño superior en comparación con los métodos basados en criterios diagnósticos histológicos. (Figuras 26 y 27)

Por todo esto, una definición basada en reglas de atipia puede potencialmente ayudar a cuantificar la atipia con una mejor precisión que con los métodos actuales. Con un enfoque basado en definiciones celulares y nucleares, los patólogos podrían discriminar la atipia de una forma más precisa. Además, como una continuación natural de este estudio, podría considerarse una discriminación más precisa entre distintos subtipos de atipia, lo que podría ser de gran valor en el diagnóstico y la evaluación de la efectividad de tratamientos.

Las posibilidades de aplicabilidad clínica de estos resultados no se limitan únicamente a lesiones queratinocíticas, sino que también tienen el potencial de identificar cambios sutiles en lesiones melanocíticas y en otros tipos de tumores.

Métrica	Descripción	Unidad
Volumen del núcleo	Volumen de los poliedros estrellados detectados por el modelo StarDist.	mm^3
Compacidad del núcleo	Una puntuación que captura cuán cercano a una esfera perfecta es el núcleo detectado. Calcula el área de una esfera perfecta con el mismo volumen que los núcleos detectados y lo divide por el área real del poliedro. Un valor cercano a 1 indica que el núcleo está muy cerca de ser una esfera, mientras que un valor más bajo indica un núcleo con una forma más plana.	Ninguna
Relación volumen sobre compacidad	Relación entre volumen y compacidad.	mm^3
Número de vecinos	Dentro del grafo de Voronoi, este es el número de bordes para el nodo. Esto representa el número de vecinos adyacentes para la célula considerada.	Ninguna
Distancia promedio de centro a centro de los vecinos	Distancia promedio a los vecinos de la célula, desde el centro hasta el centro. Esto también es un indicador del diámetro total de la célula, ya que la distancia entre dos células adyacentes es la suma de sus radios, y lo calculamos sobre varios vecinos en todas las direcciones.	µm
Distancia promedio del borde a los vecinos	Distancia promedio a los vecinos, desde el borde del núcleo hasta el borde del núcleo del vecino. Esto es un indicador del grosor del citoplasma.	µm
Relación de distancia promedio del borde sobre distancia del centro	Representa la relación del volumen ocupado por el núcleo en la célula entera. Un valor pequeño indica un núcleo comparativamente grande en comparación con el citoplasma.	Ninguna
Volumen promedio de los vecinos	Representa el volumen promedio de las células circundantes.	mm^3
Compacidad promedio de los vecinos	Representa la compacidad promedio de las células circundantes.	Ninguna
Desviación estándar del volumen de los vecinos	Mide las diferencias en tamaños de las células vecinas.	µm
Desviación estándar de la compacidad de los vecinos	Mide las diferencias en compacidad de las células vecinas.	Ninguna
Relación de volumen de los vecinos	Relación del volumen del núcleo con el volumen promedio de sus vecinos.	Ninguna
Relación de compacidad de los vecinos	Relación de la compacidad del núcleo con la compacidad promedio de sus vecinos.	Ninguna

Tabla 3. Criterios celulares utilizados para el entrenamiento del algoritmo en el campo de cancerización cutáneo. Cada uno de estos 13 parámetros representa una medida obtenida para diferenciar, a nivel celular, las diferencias entre campo de cancerización y queratosis actínica. (Adaptado de Fischman, et al., 2022)[69]

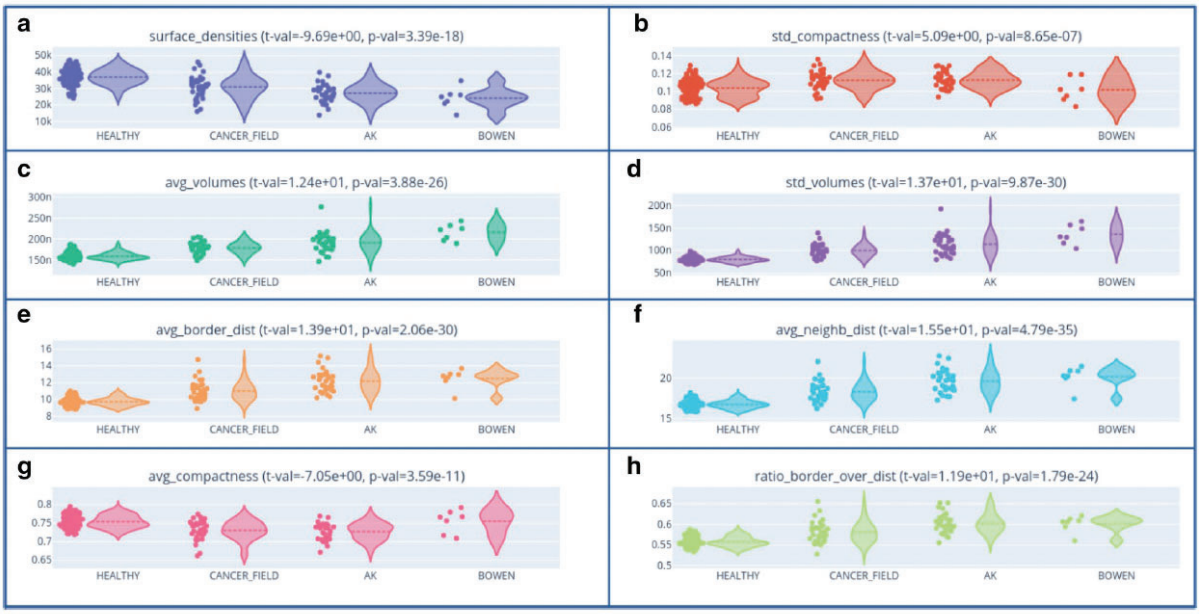

Figura 26. Visualización global de cada criterio, en piel normal, campo de cancerización, queratosis actínica y carcinoma escamoso in situ. Dos tipos de escores fueron confrontados, mostrando concordancia entre los resultados. Los algoritmos de IA fueron capaces de discriminar diferencias citológicas entre piel normal, campo de cancerización, queratosis actínica y carcinoma escamoso in situ, de forma estadísticamente significativa, en las variables indicadas. (Adaptado de Fischman, et al., 2022) [69]

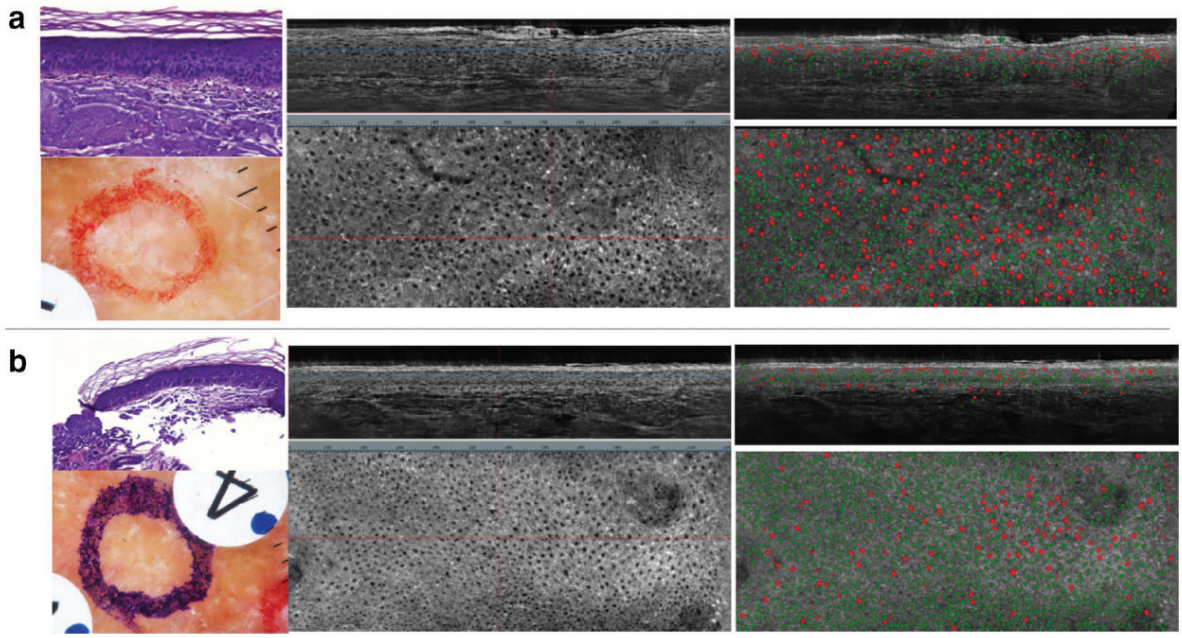

Figura 27. Diferenciación, por el algoritmo de IA, entre campo de cancerización y queratosis actínica. Panel superior: queratosis actínica. Panel inferior: campo de cancerización. Nótese las diferencias en el sector derecho, mucho más visibles por IA entre campo de cancerización y queratosis actínica. Dermatoscópicamente, sin embargo (izquierda de la figura), ambas lesiones tienen diferencias sutiles, casi imposibles de diferenciar entre ambas condiciones. (Adaptado de Fischman, et al., 2022) [69]

V.6. Limitaciones y otras aplicaciones de la TCO-CL.

Resolución axial limitada: La resolución axial de la TCO-CL está determinada por la longitud de coherencia de la fuente de luz utilizada. Aunque se ha mejorado significativamente en comparación con las técnicas de TCO convencionales, aún puede ser limitada en comparación con otras técnicas de imagen de alta resolución, como la microscopía confocal o la microscopía de excitación de dos fotones.[108-110]

Profundidad de penetración limitada: Aunque la TCO-CL puede proporcionar imágenes en secciones transversales de tejidos en profundidad, la penetración en tejidos biológicos puede verse limitada por la dispersión y absorción de la luz. Esto puede dificultar la visualización de estructuras más profundas y la obtención de imágenes de alta calidad en tejidos densos.

Artefactos de movimiento: La TCO-CL es sensible a los artefactos de movimiento, ya que los cambios en la posición o movimiento del objeto o del sistema de adquisición pueden causar distorsiones en la imagen. Esto puede ser especialmente problemático en aplicaciones clínicas donde el movimiento del paciente, como el movimiento ocular en imágenes de párpado, o del tórax durante la respiración, pueden afectar la calidad y la profundidad de la imagen. Un factor que contribuye a eso es el dispositivo de mano, que aún es muy pesado y poco práctico en áreas anatómicas complejas como en la región facial.

Dependencia del índice de refracción: La TCO-CL asume un índice de refracción "constante" en los tejidos. Sin embargo, no todos los tejidos tienen el mismo índice de refracción (como un melanoma amelanótico), o, por momentos, la imagen puede verse afectada (con variación del índice de refracción), como en un tejido inflamado.

Limitaciones en la visualización de estructuras transparentes: La TCO-CL puede tener dificultades para visualizar estructuras transparentes o mínimamente refractarias, ya que la técnica se basa en la detección de cambios en la intensidad de la luz reflejada o dispersada.

Todas estas limitaciones pueden influir en la capacidad de la TCO-CL para visualizar y analizar ciertas estructuras y procesos en tejidos biológicos. Sin embargo,

a pesar de estas limitaciones, la TCO-CL sigue siendo una técnica de imagen valiosa y pensamos que cada vez será más utilizada en diversas aplicaciones clínicas y de investigación.

EX VIVO

V.7. *Caracterización del carcinoma basocelular en microscopía confocal ex vivo.*

V.7.1. Principales diferencias entre los dispositivos de microscopía confocal ex vivo.

En la introducción, se menciona que hasta el año 2016 existía una gran variación en los dispositivos y las longitudes de onda de los láseres utilizados. Los colores de las imágenes obtenidas tenían una escala limitada de blancos, grises y negros. Esta limitación en la representación de colores dificultaba la interpretación de las imágenes adquiridas y fue uno de los factores que obstaculizó la adopción generalizada de la técnica.

Otro motivo fue que, con los equipos utilizados en ese momento, la adquisición de imágenes se realizaba con fotografías individuales, con dimensiones de 0.75-1 mm (1000 píxeles) x 0.75-1 mm (1000 píxeles). Estas imágenes individuales se unían para formar un Videomosaico, obteniendo así una vista panorámica de la muestra. Sin embargo, este proceso ralentizaba el escaneo, generando una limitación en términos de eficiencia y velocidad de diagnóstico.

Además, el proceso de obtención del Videomosaico generaba artefactos con solapamientos artificiales o áreas en las que se perdía parte de la imagen. Estos artefactos se debían a pequeñas inconsistencias o desplazamientos entre las imágenes individuales, o errores en el punto de foco de la profundidad óptima de escaneo, lo que a veces resultaba en distorsiones en la imagen final. Esto a veces dificultaba la interpretación de la imagen y la precisión del análisis. Las Figuras 5 y 15 ilustran visualmente estas limitaciones.

A partir del 2016, nuestros orientadores de tesis participaron en un proyecto de investigación financiado por el programa FP7 de la Unión Europea, en el marco del programa Diagnoptics. Dentro de este proyecto, se desarrolló un nuevo equipo de MCeV que permitía un escaneo de imágenes mucho más rápido. (Figura 28) Este nuevo sistema utilizaba la técnica de "streapping", desarrollada en 2009 pero que aún no se había utilizado clínicamente. Con esta tecnología, se lograba escanear de manera simultánea con ambos láseres de fluorescencia y reflectancia, lo que permitía obtener imágenes de "microscopia confocal de fusión" (MCFu) de una forma mucho más rápida y sin las limitaciones explicadas anteriormente. (Figura 29)

Mediante un software integrado al sistema confocal, las imágenes obtenidas por el láser de reflectancia y el de fluorescencia se combinaban de inmediato. (Figura 29) Este avance, no solo permitió obtener imágenes de tejido fresco escaneado en un tiempo de 1 a 3 minutos, sino que también ofreció la posibilidad de visualizar la imagen fusionada de ambos láseres (MCFu) o de cada imagen por separado (MCR o MCF). Las imágenes se presentan en color verde para la fluorescencia y en escala de grises para la reflectancia. La morfología celular en estas imágenes era muy similar a la observada en la histología convencional, y gracias a esta nueva tecnología, los detalles celulares eran más evidentes comparado con la tecnología anterior de MCeV.

En el año 2018, se introduce la 4ª generación de MCev, incorporando dos láseres de MCR 758 ηm y de MCF de 488 ηm. A través del uso de un software específico,[110] se logró un cambio en la representación de los colores en las imágenes. El color gris, que antes se utilizaba en la reflectancia, se cambió a un tono rosado cuando se utilizaba el láser de MCR. Por otro lado, el gris brillante de la MCF se transformó en un tono violeta. Este cambio en la representación de colores se basó en el algoritmo descrito por Gareau et al. en el año 2009.[110] (Figuras 30 a 32) Estas

mejoras permitieron obtener imágenes inmediatas con una tinción virtual muy similar y comparable a las imágenes reales obtenidas mediante la técnica de tinción Hematoxilina y Eosina, ampliamente utilizada en histología. Estos avances se han acompañado de la aplicación de esta técnica en diversos campos de la medicina y la investigación. (Figuras 30 a 32)

Las Figuras 29 a 32 muestran ejemplos visuales de estas imágenes obtenidas mediante la técnica MCFu, donde se pueden apreciar los detalles celulares y la morfología en color verde (MCF) y escala de grises (MCR) y, posteriormente, la tinción digital. Estas diferencias fueron ampliamente detalladas en otros estudios.

Posteriormente, en el año 2020, se decidió realizar un cambio en el láser utilizado en la MCev. En lugar de utilizar un láser de 785 nm, se optó por utilizar un láser de 638 nm. Esta modificación tuvo como objetivo mejorar aún más la calidad de las imágenes obtenidas.

En los próximos apartados, se hará referencia a la evidencia descrita en el pasado y se comparará con los estudios realizados, teniendo en cuenta los diferentes dispositivos utilizados. Los dispositivos anteriores a 2016 se mencionan en la literatura como "microsopía confocal de reflectancia"(MCR) o "microscopía confocal de fluorescencia "(MCF), mientras que los dispositivos del período 2016-2018 se denominarán como "prototipos", y, a partir del año 2018, la técnica que utiliza los dispositivos actuales de la cuarta generación de MCeV, se denomina "microscopía confocal de fusión" (MCFu). Esta distinción permitirá hacer una comparación adecuada entre los diferentes estudios y dispositivos utilizados. (Figura 32)

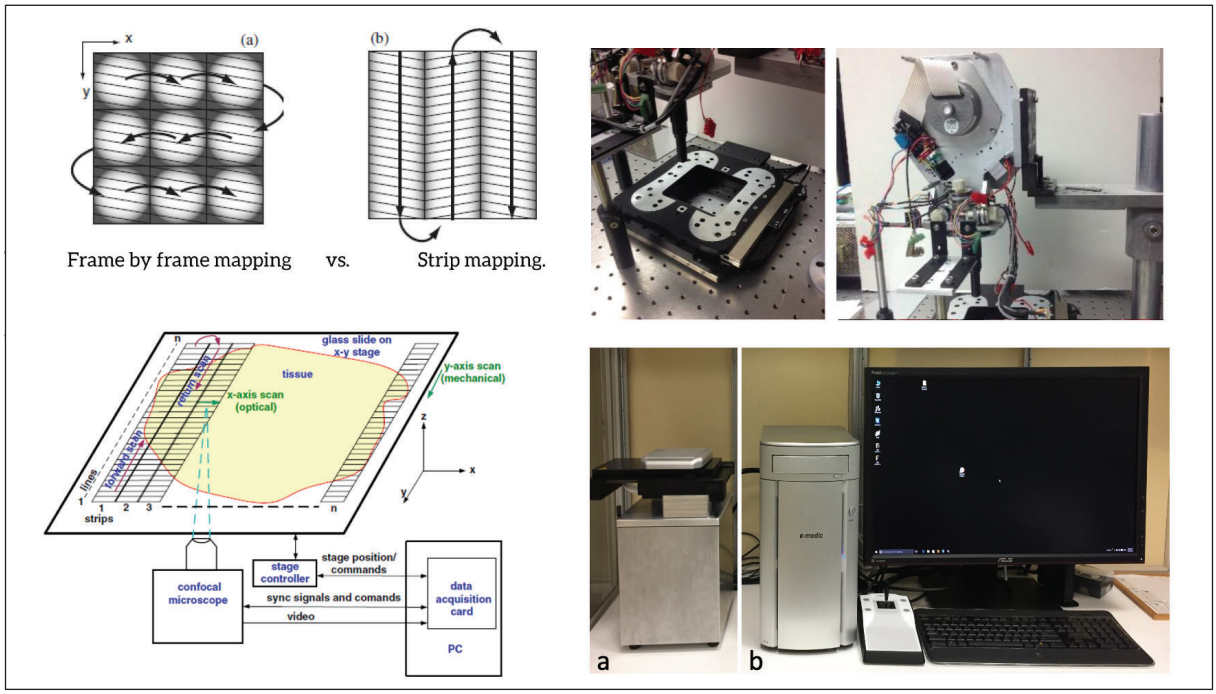

Figura 28. Representación del videomosaico ("strip mapping") y comparación con la composición de la técnica a partir de imágenes individuales ("frame by frame") (izquierda). Prototipo de MCFu desarrollado en el proyecto Diagnoptics: (a) dispositivo de posicionamiento del tejido y escaneo; (b) Espación de Pc, pantalla y "joystick" para navegación. (Fuente: Dr. Josep Malvehy)

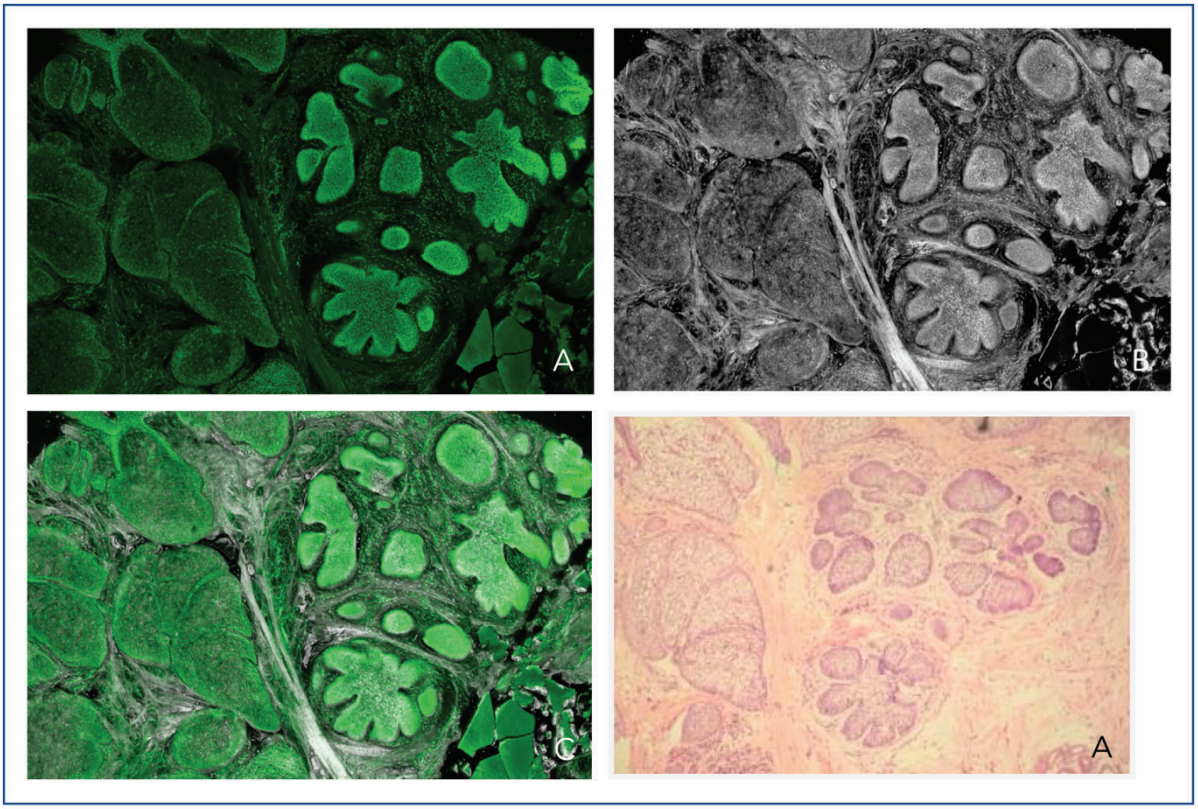

Figura 29. Carcinoma basocelular nodular. Magnificación 4x. Imagen obtenida con prototipo de 4ª generación de microscopio *ex vivo*. Tecnología de "streapping" y fusión de ambos láseres en una sola imagen. Tinción: ácido acético y naranja de acridina. A. Fluorescencia. B. Reflectancia. C. Fusión. D. Hematoxilina y Eosina. (Adaptado de Pérez-Anker J, et al.,2020).[111]

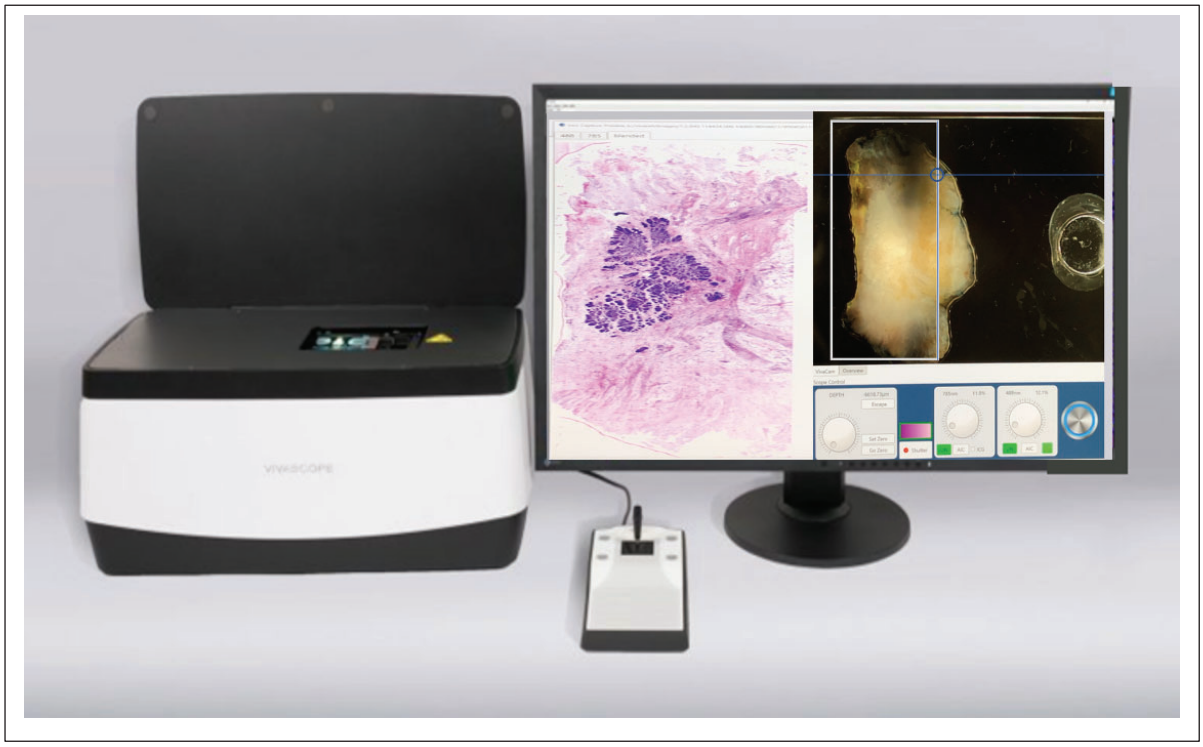

Figura 30. Cuarta generación de microscopio confocal. A la izquierda de la imagen unidad de posicionamiento y escaneo de la muestra con láseres y ópticas y motores del microscopio; a la derecha de la imagen aparecen la pantalla y el joystick de navegación. En la imagen a la izquierda se observa la imagen de fusión con tinción digital de H&E de un carcinoma basocelular. En la pantalla a la derecha se observa la imagen de la pieza de tejido y el recuadro que corresponde al área seleccionada por el operador para escanear; en la parte inferior derecha de la pantalla menús de software para calibración y modos de laser (Fluorescencia; reflectancia y imagen de fusión). (Fuente: VivaScope www.vivascope.de)

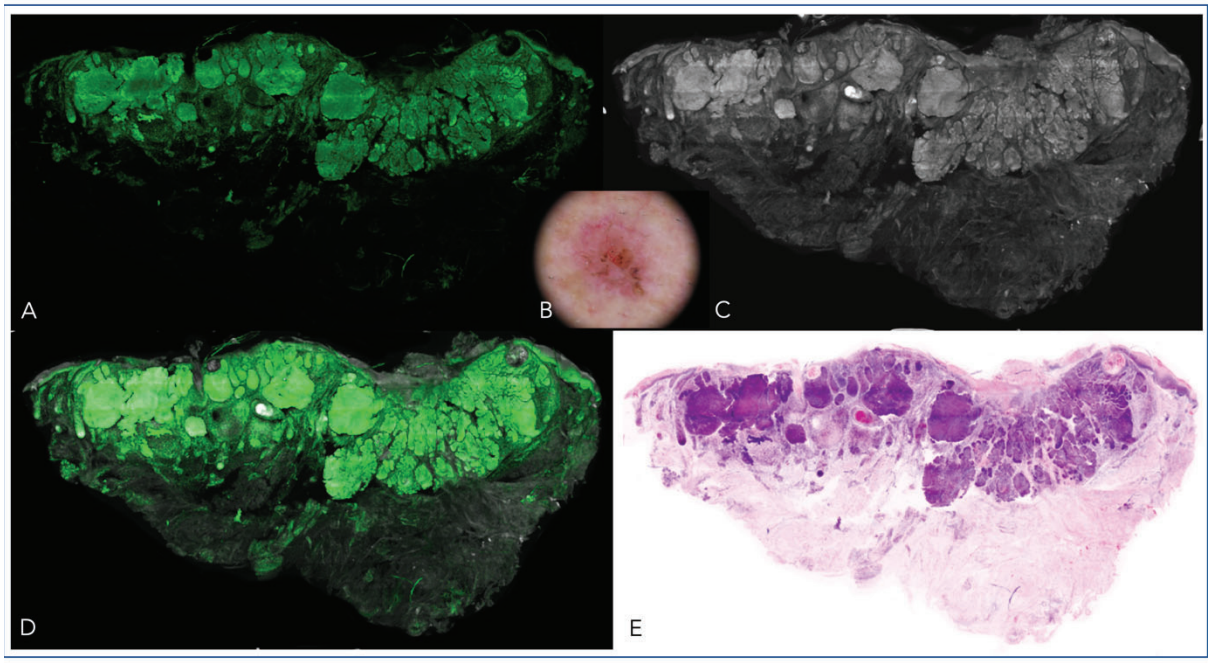

Figura 31. Carcinoma basocelular nodular. 4ª generación de microscopio confocal. A. Fluorescencia. B. Dermatoscopia de este tumor. C. Reflectancia. D. Fusión. E. Tinción hematoxilina y eosina digital. Observamos la imagen del mismo tumor en los diferentes modos de visualización. En el modo de fluorescencia (A), las islas tumorales destacan del resto del estroma, que es muy poco visualizado. En el modo de reflectancia, aunque con la tinción de ácido acético y naranja de acridina los nidos se destacan, el estroma es más evidente (C), observándose claramente el tejido adyacente al tumor. La unión de ambos láseres (D), permite la observación de lo mejor de ambas técnicas e, incluso, gracias al doble método de tinción, los núcleos destacan aún más que en el modo de fluorescencia solo (A). Esto permite que, cuando se realiza el cambio de modo a H&E digital (E), la imagen se asemeje mucho a la H&E real. (Adaptado de Pérez-Anker J, et al.,2020).[111]

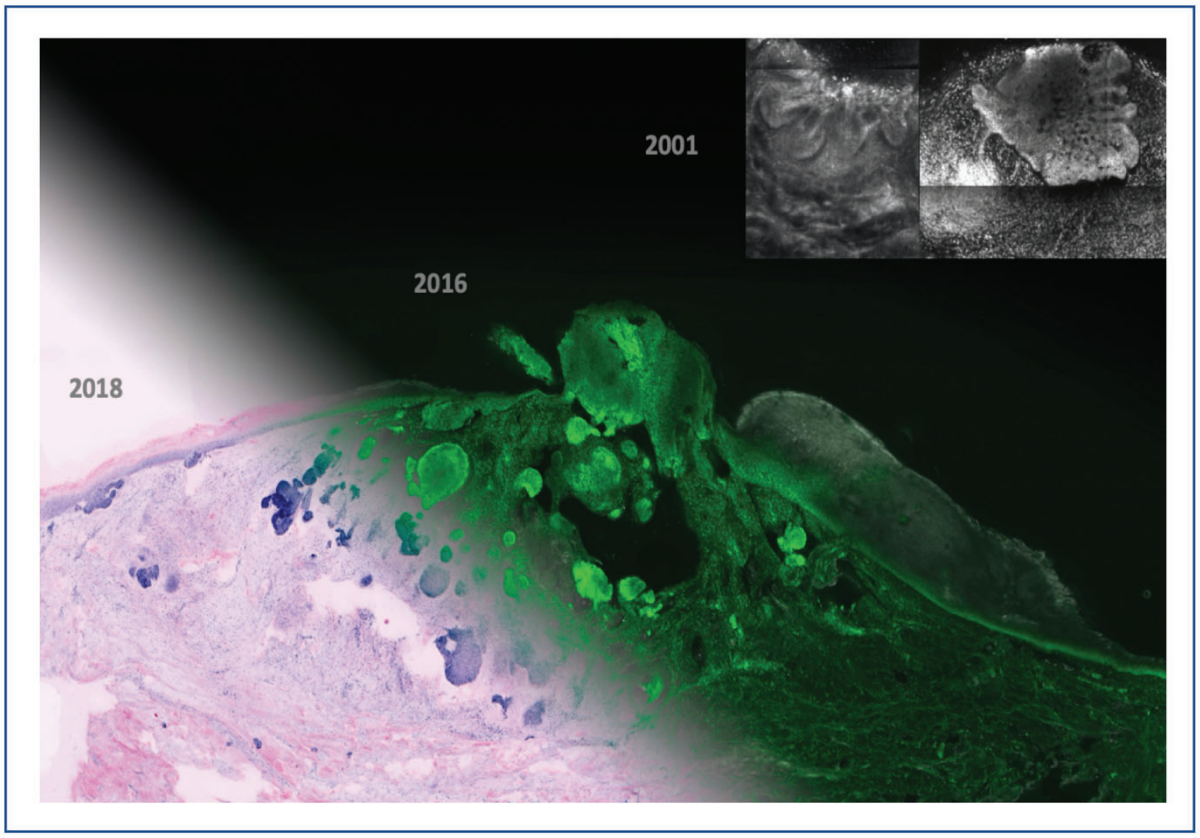

Figura 32. Imagen de carcinoma basocelular nodular y focos superficiales. Figura representativa de este subtipo tumoral mostrando la progresión de las diferentes tecnologías de microscopio confocal *ex vivo*. 2001: en los primeros dispositivos era necesario escanear la muestra dos veces para obtener imágenes en reflectancia (izquierda) y fluorescencia (derecha). Las imágenes eran vistas en negro, gris y blanco. Cada fotografía individual (cuadrado) era combinada en un videomosaico; 2016: Con el prototipo del proyecto "Diagnoptics", aparece por primera vez la imagen de fusión (unión de láseres de fluorescencia y reflectancia). Los colores pasan a verse en gris y verde. Con la novedosa tecnología de "streapping", no se observan las uniones de los submosaicos; 2018: Nace la 4ª generación de confocales *ex vivo*. Los colores simulan la hematoxilina y eosina tradicional, se introduce la tecnología de streapping y el escaneo es mucho más rápido que en el caso de los dispositivos previos. (Fuente: Javiera Pérez-Anker y VivaScope www.vivascope.de)

V.7.2. Diferencias entre tinciones en el carcinoma basocelular.

Como mencionamos anteriormente, en la literatura anterior al año 2016, la tinción más utilizada en MCev era el naranja de Acridina 0.01 mM en el modo de MCF. [57-63] Esta tinción se destacaba por resaltar los núcleos de las células, lo que facilitaba el diagnóstico de condiciones como el carcinoma basocelular. Dado que se requerían aproximadamente de 8 a 10 minutos para escanear una muestra en cada tipo de láser, obtener las dos imágenes correspondientes a ambos láseres llevaría casi 20 minutos, lo mismo que un promedio de corte en congelado en un criostato y su tinción. Por esta razón, se abandonó prácticamente por completo el láser de MCR que se consideraba que no aportaba información relevante al diagnóstico, duplicando el tiempo de adquisición, y los estudios se centraron en el láser de MCF. (Figura 33)

Por otro lado, el hecho de proporcionar imágenes en escala de grises (desde blanco hasta negro) dificultaba su correcta apreciación, especialmente en el campo de la patología general, a pesar de reproducir los aspectos arquitecturales y algunos citológicos similares a la histología convencional. Además, esto dificultaba que los nuevos usuarios de esta tecnología pudieran efectuar diagnósticos basados únicamente en imágenes de MCev sin una extensa capacitación previa. (Figuras 33 y 34)

Por todo esto, la aplicación principal de esta técnica, durante muchos años, fue prácticamente de forma exclusiva en la cirugía de Mohs utilizando mayormente el láser de MCF.

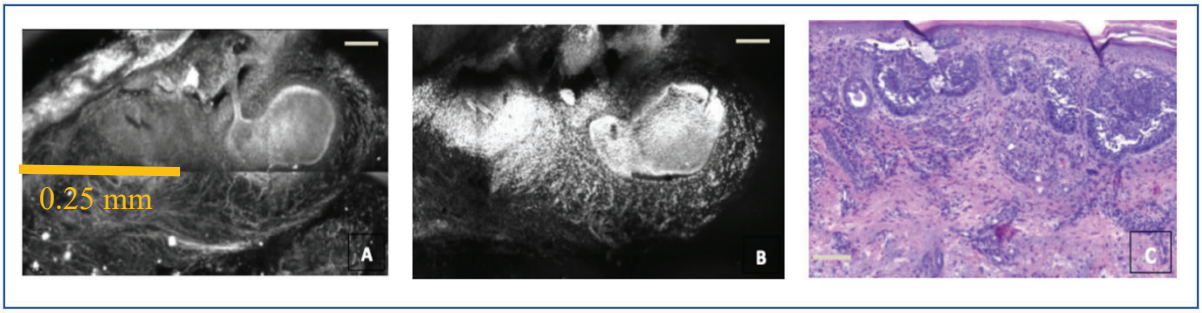

Figura 33. Imagen de carcinoma basocelular superficial, teñido con naranja de acridina y ácido acético, y su correspondiente imagen en hematoxilina y eosina. A. Láser de reflectancia; B. Láser de fluorescencia; C. Hematoxilina y eosina. Diferentes aspectos del tumor y del estroma son observados en cada tipo de láser. El mismo tumor debe ser escaneado nuevamente para ser apreciado en otro láser (Adaptado de Pérez-Anker et al.,2022).[55]

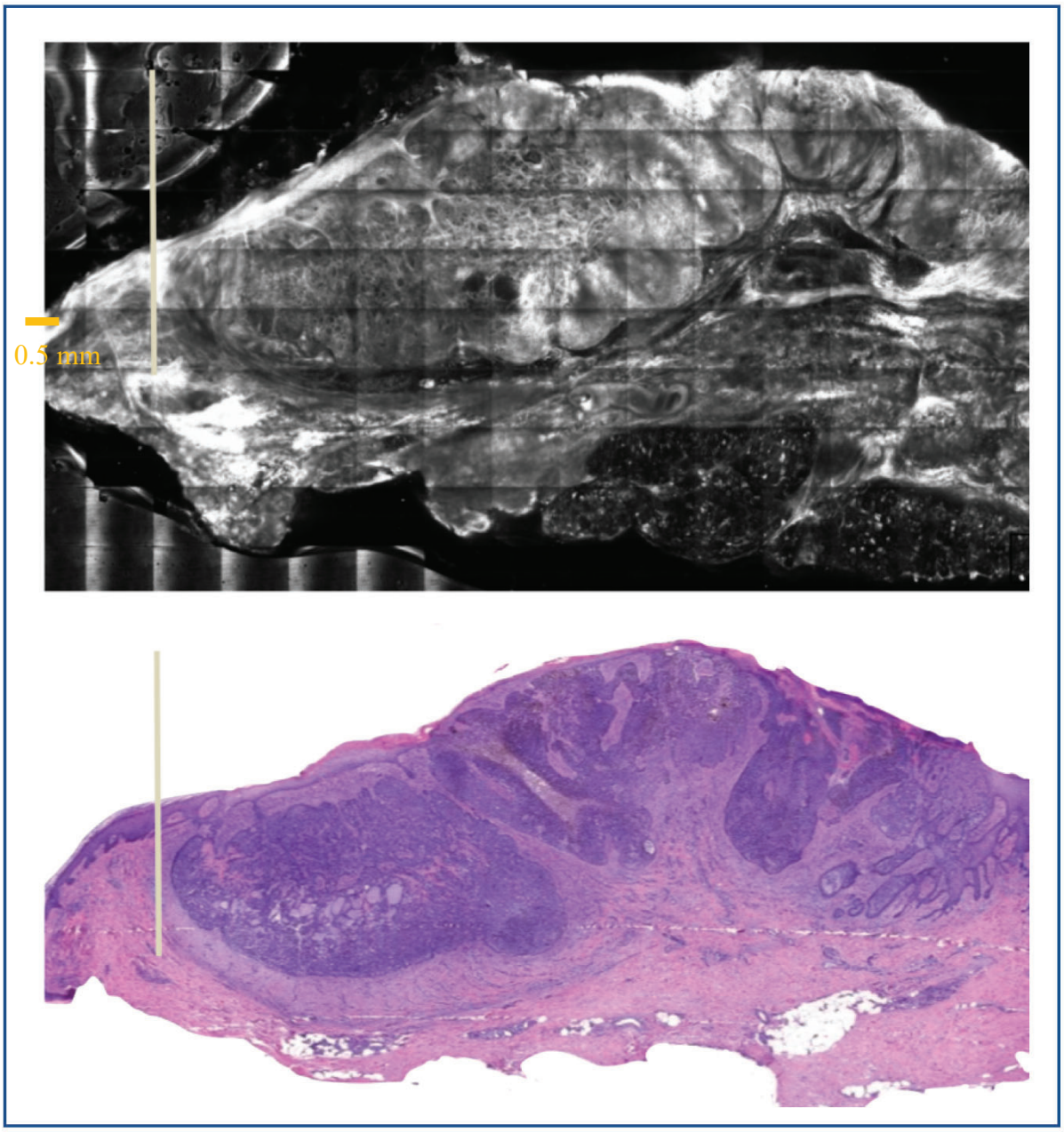

Figura 34. Imagen de carcinoma basocelular nodular obtenida con MCR (superior), teñido con ácido acético y. naranja de acridina y su correspondiente imagen en hematoxilina y eosina (inferior). Cada cuadrado que compone un mosaico tiene 1 x 1 mm. Detalles de la imagen global pueden perderse por la unión visible de los cuadrados (Adaptado de Pérez-Anker et al.,2022).[55]

Por este motivo, han sido propuestas diferentes alternativas de tinción, como el cloruro de aluminio (en MCR), el ácido cítrico (MCR y MCF), el azul de metileno, el azul de toluidina (ambos en MCR y MCF), la fluoresceína, el azul Nilo (MCF) y el azul patente V (MCF).[54] Sin embargo, hasta el momento no se habían llevado a cabo estudios sistemáticos para comparar estas tinciones en la misma muestra y determinar si proporcionan imágenes estables y de mejor calidad que las obtenidas con naranja de acridina.

En los primeros trabajos de MCev realizados por el Dr. Salvador González[64] y sus colaboradores, utilizando ácido acético al 5% y MCR, no lograron el objetivo de realzar los núcleos con esta tinción. Por el contrario, los mismos autores describen en sus trabajos que con esta tinción se obtuvieron imágenes donde los detalles del estroma fueron realzados.

Esta interesante observación nos condujo al desarrollo del trabajo de nuestra tesis de máster en esta universidad,[112] estudiando las diferencias observadas en ambos láseres (MCR y MCF), con la combinación de ácido acético y naranja de acridina. La doble tinción mejoró la visualización de detalles del estroma, como las bandas de colágeno o la reacción estromal peri tumoral.[112]

Por este motivo, en nuestro primer estudio de MCev (en el contexto de esta tesis doctoral), evaluamos la combinación de ácido acético y naranja de acridina y la comparamos con la tinción más utilizada en la literatura hasta ese momento, el Naranja de Acridina, en una serie prospectiva de carcinomas basocelulares.[70,111]

Al emplear el protocolo de doble tinción, observamos que se lograba un contraste más definido entre los tejidos tumorales y el estroma circundante,

principalmente respecto a la visualización de los núcleos, generando un aspecto morfológico semejante a la formalización de tejidos. La concentración del acético al 50% (una concentración mayor que la anteriormente publicada que era del 2%), no dañó el tejido, de forma a interferir en las imágenes histológicas finales. (Figuras 33 a 36)

Por otro lado, el proceso de doble tinción no supuso un tiempo significativo adicional ya que, con los nuevos equipos, este es mucho menor que el anteriormente descrito por Bennàssar y colaboradores. (Figura 15)[58,62]

Un aspecto interesante, es que la naranja de acridina puede presentar limitaciones en la tinción de los núcleos en ciertos casos, especialmente en tumores muy compactos con una alta densidad nuclear. En estas situaciones, presenta dificultades para penetrar en los núcleos y, por lo tanto, su capacidad para realzar las estructuras nucleares se ve comprometida. (Figura 35) En tales casos, la combinación de diferentes agentes de tinción, como el ácido acético, puede ser especialmente útil.

En el curso de nuestras investigaciones, hemos observado que, al aplicar ácido acético durante solo 1 segundo, en lugar de los habituales 20 segundos, antes del segundo agente de tinción y seguirlo con alcohol al 95% durante 20 segundos, logramos descomprimir los tejidos de manera efectiva, lo que facilita una mayor penetración de la naranja de acridina en los núcleos tumorales. En ocasiones, es necesario repetir este proceso. (Figuras 36 y 37)

Es por este motivo que, posteriormente a esta publicación invertimos el orden del proceso de tinción y comenzamos a aplicar primero ácido acético 50% (por apenas un segundo), luego alcohol 95% (20 segundos) y, por último, naranja de Acridina (20

segundos). Este cambio en el protocolo casi eliminó por completo el número de casos donde la tinción no teñía los núcleos.

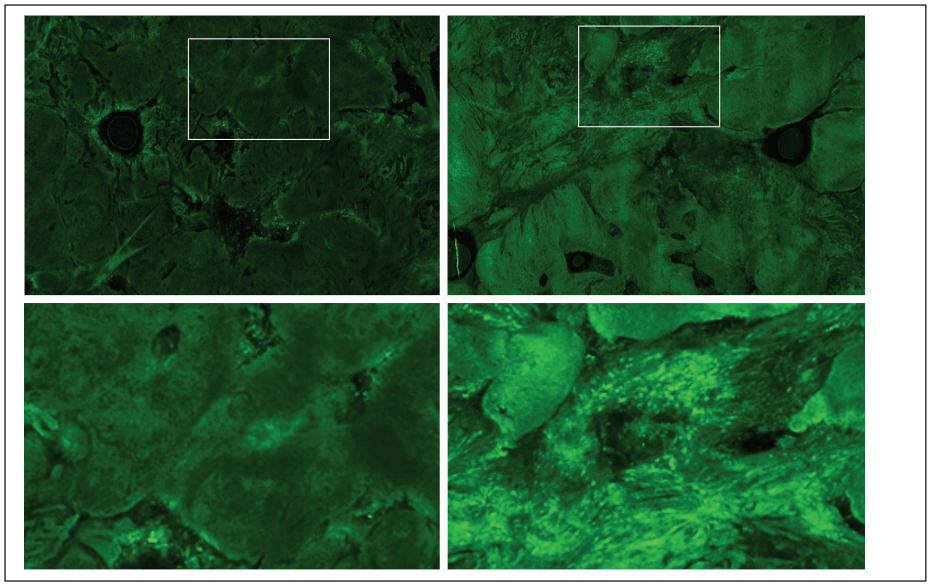

Figura 35. Carcinoma basocelular nodular. Magnificación 10x. A: Microscopia confocal de fusión (láser de fluorescencia y de reflectancia, simultáneos). Derecha: naranja de acridina y ácido acético. Izquierda: naranja de acridina. La penetración del naranja de acridina en tumores muy compactos es escasa y no siempre los núcleos son fácilmente reconocidos. (Fuente: Javiera Pérez-Anker).

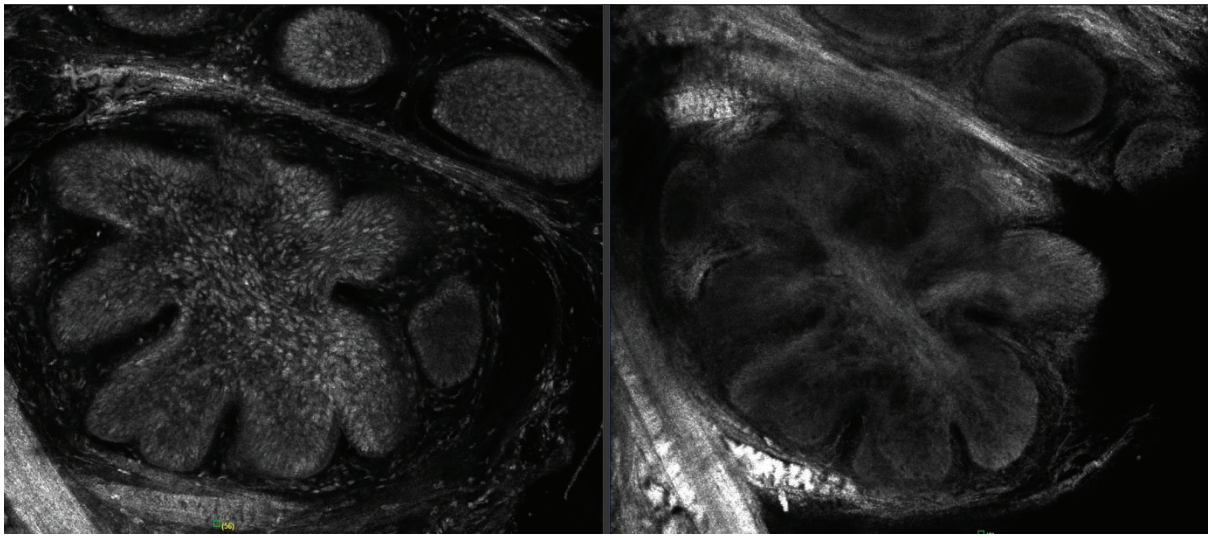

Figura 36. Carcinoma basocelular nodular. Magnificación 10x. A: Microscopia confocal de reflectancia. Derecha: naranja de acridina. Izquierda: ácido acético y naranja de acridina. Utilizando una tinción que permita la fijación del tejido, como el ácido acético, los núcleos de las estructuras son realzados. Los núcleos de la reacción peri tumoral también son visualizados. (Adaptado de Pérez-Anker et al.,2022).[55]

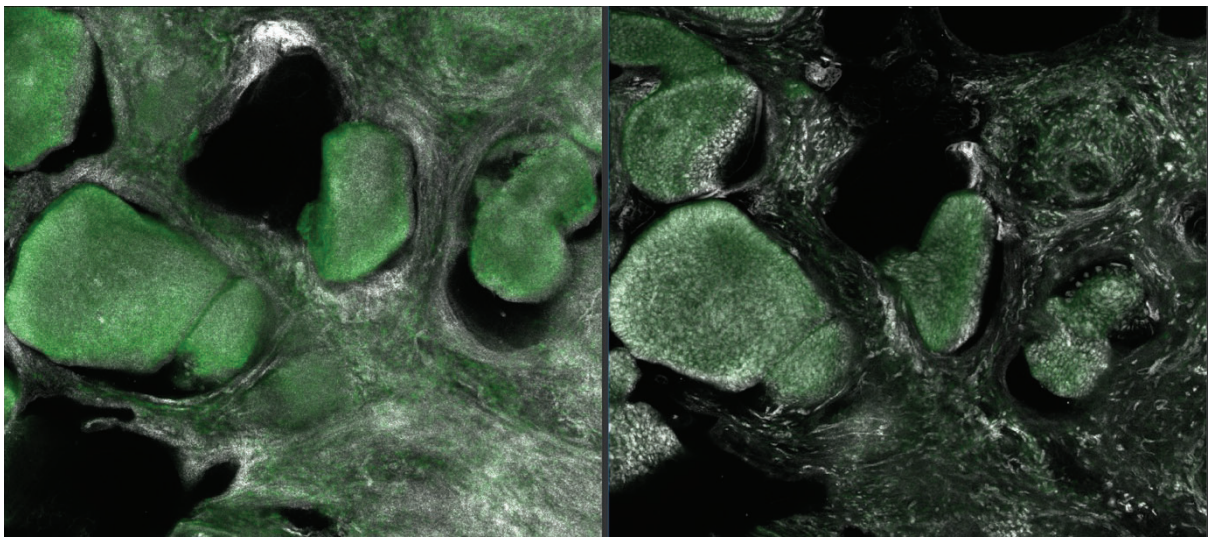

Figura 37. Carcinoma basocelular nodular. Magnificación 10x. A: MCFu (láser de MCF y MCR, simultáneos). Derecha: naranja de acridina y ácido acético. Izquierda: naranja de acridina. Las estructuras tumorales y del estroma son realzadas con el uso de la doble tinción. La imagen final es más parecida morfológicamente a la de hematoxilina y eosina. (Fuente: Javiera Pérez-Anker)

Después de nuestro estudio, se han propuesto otras combinaciones de tinciones, en reportes de casos, como el uso de naranja de acridina con el bromuro de etidio,[113] proporcionando una imagen de gran interés en 3 colores, siendo muy específica para CBC. Sin embargo, se ha observado que esta última tinción tiene ciertas limitaciones que dificultan introducción en el diagnóstico clínico.[114] Aunque el bromuro de etidio muestra una afinidad por el carcinoma basocelular es importante tener en cuenta que esta sustancia tiene mayor potencial cancerígeno que el mencionado para el naranja de acridina, según la comparación realizada de la ficha técnica de ambos productos. Su manipulación requiere de protocolos más estrictos de seguridad y manipulación,[114] como campanas de extracción de flujos incluso para su almacenamiento y el uso de doble guante, lo que limita algo más su uso generalizado en la práctica clínica y en estudios de investigación. A pesar de que el naranja de acridina también tiene afinidad nuclear, en su protocolo de manipulación no está descrita la necesidad de la utilización de campana de extracción de flujo ni doble guante. En general, el bromuro de etidio puede ser preferiblemente utilizado en situaciones donde se necesita mayor sensibilidad y menor cantidad de colorante, pero siempre siguiendo las normas de seguridad adecuadas.

Hasta el momento no se ha realizado un estudio sobre el uso de esta combinación de tinciones en otros tipos de tumores y su eficacia y aplicabilidad en diferentes tumores aún no ha sido completamente investigada y comprendida.

Aunque ambos tiñen ácidos nucleicos, nombramos algunas diferencias clave entre ambas tinciones:[114]

-Mecanismo de tinción: El bromuro de etidio se une al ADN y al ARN por intercalación, lo que significa que se inserta entre las bases nitrogenadas de las cadenas de ácidos nucleicos. La naranja de acridina se une de manera similar por

intercalación en las cadenas de ADN y ARN, permitiendo la emisión de fluorescencia cuando se ilumina con luz ultravioleta (UV).

- Espectro de Emisión: El bromuro de etidio emite fluorescencia roja cuando se ilumina con luz UV y la naranja de acridina emite fluorescencia naranja cuando se expone a la luz UV.

- Sensibilidad: El bromuro de etidio es menos sensible que la naranja de acridina, lo que significa que se necesita una mayor cantidad de bromuro de etidio para obtener una señal de fluorescencia detectable en geles de agarosa o poliacrilamida. La naranja de acridina: Es más sensible y requiere menos cantidad para obtener una señal de fluorescencia fuerte.

- Toxicidad: El bromuro de etidio es conocido por ser carcinogénico y mutagénico, por lo que se debe manipular con precaución en un entorno de laboratorio y cumplir con las normas de seguridad. La naranja de acridina también es un compuesto químico que requiere precaución, aunque es menos tóxica que el bromuro de etidio, según sus fichas técnicas.

Recientemente Sahu y colaboradores[115] han investigado PARPi-FL, un agente de contraste fluorescente exógeno dirigido al polímero de poli (adenosina difosfato ribosa) polimerasa (PARP1) nuclear, en tejidos *in vivo* (usando MCR) y *ex vivo* (usando MCev) y demostraron que mejoraron el diagnóstico no invasivo de los CBCs. PARP1 demostró una expresión consistentemente más alta de PARP1 en todos los subtipos de CBC que en las estructuras normales de la piel. En su muestra, el 90% de los CBC presentaron tinción homogénea de PARP1, especialmente en los subtipos superficiales e infiltrantes. Se observó cierta expresión heterogénea de PARP1 en algunos CBC nodulares (menos del 10%), específicamente en las variantes con cambios nodulares quísticos y diferenciación escamosa, en tejido *in vivo*. Por otro lado, en tejidos *ex vivo*, la sensibilidad diagnóstica aumentó con el uso de este

contraste conjugado con un fluoróforo, principalmente en el modo de MCeV de fluorescencia. Sin embargo, en este trabajo, no fue así con el modo de láser de reflectancia. Aunque los autores postulan que pueda ser por la variabilidad anatómica del tejido, nuestra opinión es que la tinción nuclear específica para el láser de fluorescencia no es igualmente captada por el de reflectancia. Efectivamente, en las fotografías de la publicación de este trabajo no se observa la misma calidad de la tinción en ambos láseres. Debido al alto costo y a la necesidad de realizar secciones finas para el análisis de esta tinción en MCeV, esta técnica podría ser un excelente medio de contraste para diferenciar el CBC de otros tumores en muestras *ex vivo*, similar a una técnica de inmunohistoquímica específica para CBC.[115] (Figura 38)

Otros marcadores de inmunohistoquímica han sido propuestos para MCev tumoral: anticuerpos S-100, melan-A y anti-Ver-EP4, conjugados con FITC; NPs10@D1_ICR_Alexa647_DOTAGA Fe^{3+} (MCF);[54,116-118] En enfermedades inflamatorias de la piel se han descrito resultados con: anticuerpos IgG y C3 (conjugados con fluorescencia) para pénfigo vulgar (MCR y MCF), IgG, IgM, IgA, C3 y fibrinógeno (MCR y MCF) para vasculitis cutánea, el anticuerpo anti-fibrinógeno marcado con FITC para liquen plano (MCF).[54,116]

Por otro lado, Cinotti y colaboradores[6] también han demostrado que la MCF puede detectar los efectos citopáticos virales del Herpes Simplex Virus (HSV) 1, incubando las muestras por 20 minutos con anticuerpos monoclonales anti-HSV-1 y anti-HSV-2 (MCF). También probaron el modo de reflectancia mostró queratinocitos acantolíticos grandes, y erosión, lo que sugiere una infección por HSV-1.[6]

Estos resultados confirman que la combinación de tinciones es una alternativa para mejorar la visualización y la interpretación de las imágenes de MCev en dermatología y otros campos de la patología.

No obstante, es importante destacar que se requieren estudios adicionales para validar y optimizar los protocolos de tinción, así como compararlas entre sí y con otros métodos de tinción existentes. Estudios multicéntricos de estandarización son necesarios. Es posible que, en un futuro, podamos utilizar tinciones específicas para diferentes tejidos.

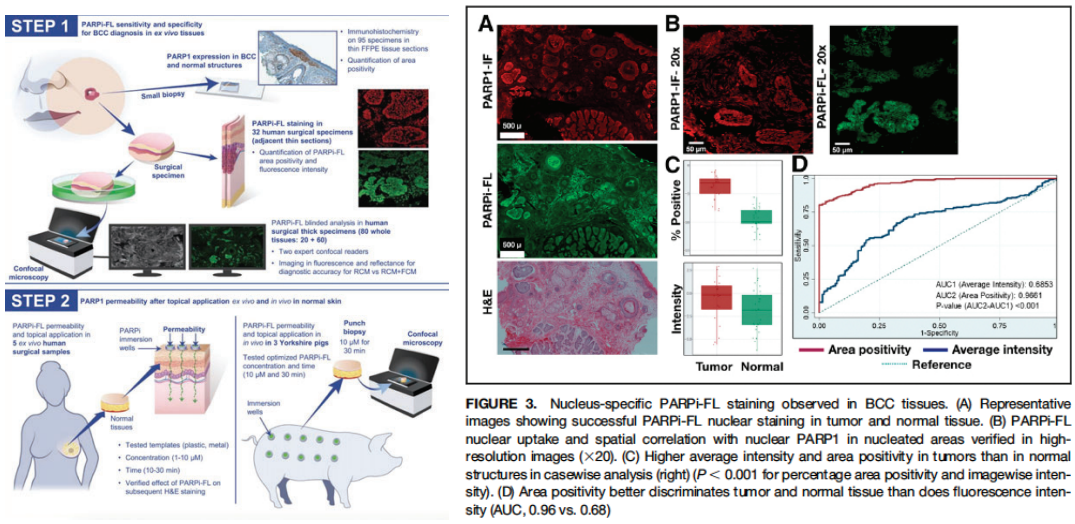

FIGURE 3. Nucleus-specific PARPi-FL staining observed in BCC tissues. (A) Representative images showing successful PARPi-FL nuclear staining in tumor and normal tissue. (B) PARPi-FL nuclear uptake and spatial correlation with nuclear PARP1 in nucleated areas verified in high-resolution images (×20). (C) Higher average intensity and area positivity in tumors than in normal structures in casewise analysis (right) ($P < 0.001$ for percentage area positivity and imagewise intensity). (D) Area positivity better discriminates tumor and normal tissue than does fluorescence intensity (AUC, 0.96 vs. 0.68)

Figura 38. Protocolo de actuación de PARPi-FL. Izquierda: PARPi-FL en MCeV. La sensibilidad diagnóstica aumentó con el uso de este contraste conjugado con un fluoróforo, principalmente en el modo de MCeV de fluorescencia. Derecha: Resultados con la misma tinción en piel normal y CBC. PARP1 demostró una expresión consistentemente más alta de PARP1 en todos los subtipos de CBC que en las estructuras normales de la piel. 90% de los CBC presentaron tinción homogénea de PARP1. (Adaptado de Aditi Sahu, et.al., 2022)[115]

V.7.3. Diferencias entre láseres en el carcinoma basocelular. Criterios diagnósticos.

Considerando que la mayoría de los estudios previos sobre el CBC se centraban en la MCF, este trabajo propuso analizar las diferencias entre el uso de láseres MCF y MCR en la MCFu, utilizando la doble tinción anteriormente mencionada. Confirmamos que criterios diagnósticos ya existentes en FCM también podían ser aplicados en la MCFu, además de añadir nuevos criterios diagnósticos.[70]

Fueron analizados y comparados en los diferentes láseres: siluetas oscuras, células dendríticas, células grandes y brillantes, células tumorales luminosas, presencia de fluorescencia, empalizada, hendidura peri-tumoral, reacción estromal peri-tumoral, bandas de colágeno engrosadas peritumorales, islas tumorales bien definidas, núcleos aglomerados, pleomorfismo nuclear y aumento de la relación núcleo/citoplasma. [58,62,112](Figuras 39 a 43)

Como era de esperar, cada uno de estos criterios se observó con mayor claridad en la MCFu, que combina los láseres de fluorescencia y reflectancia, permitiendo apreciar las características distintivas de ambos tipos de láser en una sola imagen. Algunas estructuras, como los núcleos aglomerados, el pleomorfismo nuclear y el aumento de la relación núcleo/citoplasma, se resaltaron más con el láser de fluorescencia debido al contraste proporcionado por la tinción de naranja de acridina. Aunque esta tinción no permite visualizar detalles nucleares como el nucléolo, permite diferenciar claramente los aglomerados de núcleos de otras estructuras.

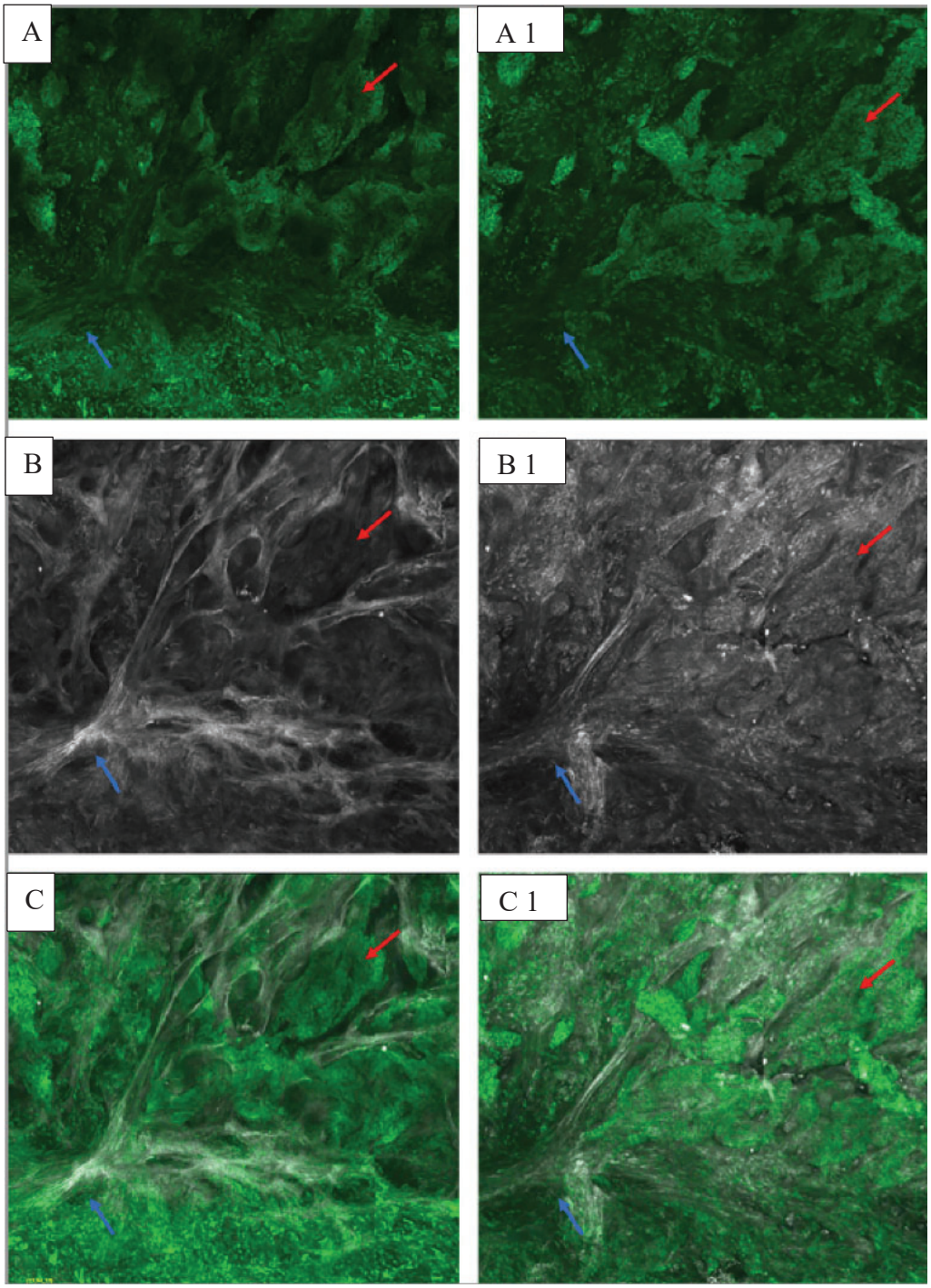

Figura 39. Carcinoma basocelular infiltrante. Magnificación 10x. A, A1: Láser fluorescencia; B, B1: Láser reflectancia. C, C1: Fusión. Izquierda: naranja de acridina. Derecha: ácido acético y naranja de acridina. La reacción estromal y las siluetas oscuras son vistas diferentemente con la doble tinción. (Adaptado de Pérez-Anker et al., 2020)[70]

La reacción estromal peri-tumoral, que también resalta las células inflamatorias circundantes al tumor, se visualizó más claramente con el láser de reflectancia. Asimismo, las bandas de colágeno engrosadas peri tumorales, las células dendríticas y los macrófagos. (Figuras 39- 43) Las reacciones estromales varían según el subtipo histológico observado. En los subtipos infiltrantes, la reacción estromal tiende a ser más densa y compacta, mientras que, en el subtipo superficial, la reacción estromal es más laxa.[54]

Al comparar los modos de fluorescencia y reflectancia con la tinción doble, la fluorescencia mejoró la visualización de las islas de tumor brillantes, mientras que la reflectancia fue más adecuada para identificar el resto de los criterios.

Por otro lado, observamos que, a pesar de la doble tinción, la presencia de células dendríticas sigue siendo más frecuentemente visualizada solo con el láser de reflectancia. Por otro lado, el criterio de siluetas oscuras fue mejor visto en reflectancia, solo con una tinción. Esto se debe a que cuando se aplicaba la doble tinción, como ya hemos mencionado, estas últimas pasaban a ser islas tumorales brillantes. Esto ha demostrado que, efectivamente, las siluetas oscuras corresponden a nidos de carcinoma basocelular infiltrante que invade en forma de cordones. (Figuras 39 y 43)

Después de nuestro estudio, Hartmann y colaboradores[119] propusieron que, utilizando la tecnología previa de MCev con FCM, era posible realizar un diagnóstico de CBC basado en 3 criterios: la presencia de masas tumorales, empalizada y clefting, obteniendo una alta sensibilidad diagnóstica del 98% y una especificidad del 95%, con un valor predictivo positivo del 92% y un valor predictivo negativo del 99%.

Es importante mencionar que, en muchos estudios de reproducibilidad diagnóstica del CBC en MCev, las islas tumorales a menudo se confunden con los folículos pilosos o los conductos de glándulas sudoríparas,[58-60] lo que subraya la importancia de incluir criterios como los núcleos aglomerados y la reacción estromal peritumoral para diferenciar eficazmente un CBC de otras estructuras en la MCev y, a su vez, ayudar a distinguir entre los subtipos tumorales. Por lo tanto, proponemos el uso de "la regla de los 5 criterios" para el diagnóstico de CBC en MCev (masas tumorales con núcleos aglomerados, empalizada, clefting y reacción estromal peritumoral).

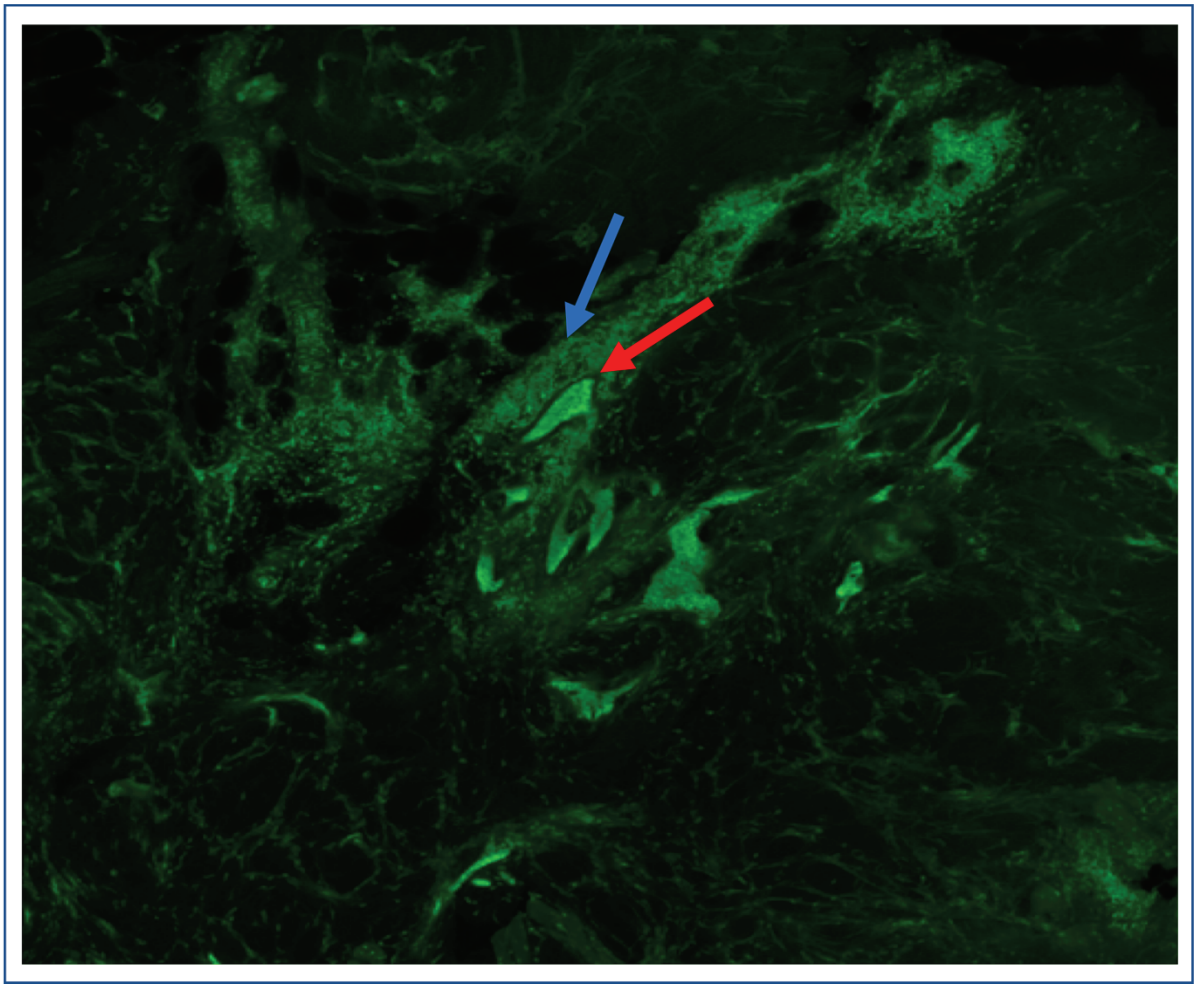

Figura 40. Carcinoma basocelular infiltrante. Prototipo Diagnoptics. Láser de florescencia. Tinción: Naranja de acridina. Magnificación 4x. Las masas tumorales con núcleos aglomerados, empalizada y clefting (flecha roja) se destacan de la reacción estromal realzan y estructuras circundantes por la unión selectiva de la tinción al núcleo (flecha azul). Son menos visibles las bandas de colágeno engrosadas peri tumorales con este láser (flecha azul). (Fuente: Javiera Pérez-Anker).

Respecto a las células dendríticas (que corresponden a células de Langerhans cargadas de pigmento y a melanocitos, conforme observamos en la figura 44), se destaca que su núcleo y su citoplasma no se tiñen con el naranja de acridina.[70,112]Aunque no podemos explicar el motivo de este fenómeno, es posible

que exista alguna característica específica en las células dendríticas que evita la unión del naranja de acridina. Es interesante destacar que las células dendríticas son evidentes en los basocelulares pigmentados incluso sin la realización de tinciones adicionales en MCev, lo que añade un criterio útil para el diagnóstico de este subtipo de carcinoma basocelular.

Las diferencias entre las estructuras visualizadas en los láseres de MCF y MCR, también pudieron ser observadas por otros autores no solo en el carcinoma basocelular, sino también en lesiones melanocíticas, carcinomas escamosos y otros tumores, utilizando el modo de láser de fluorescencia o de reflectancia. En cada uno de ellos, a semejanza de nuestro estudio, ambos láseres se complementaban para proporcionar diferentes detalles morfológicos.[120-122]

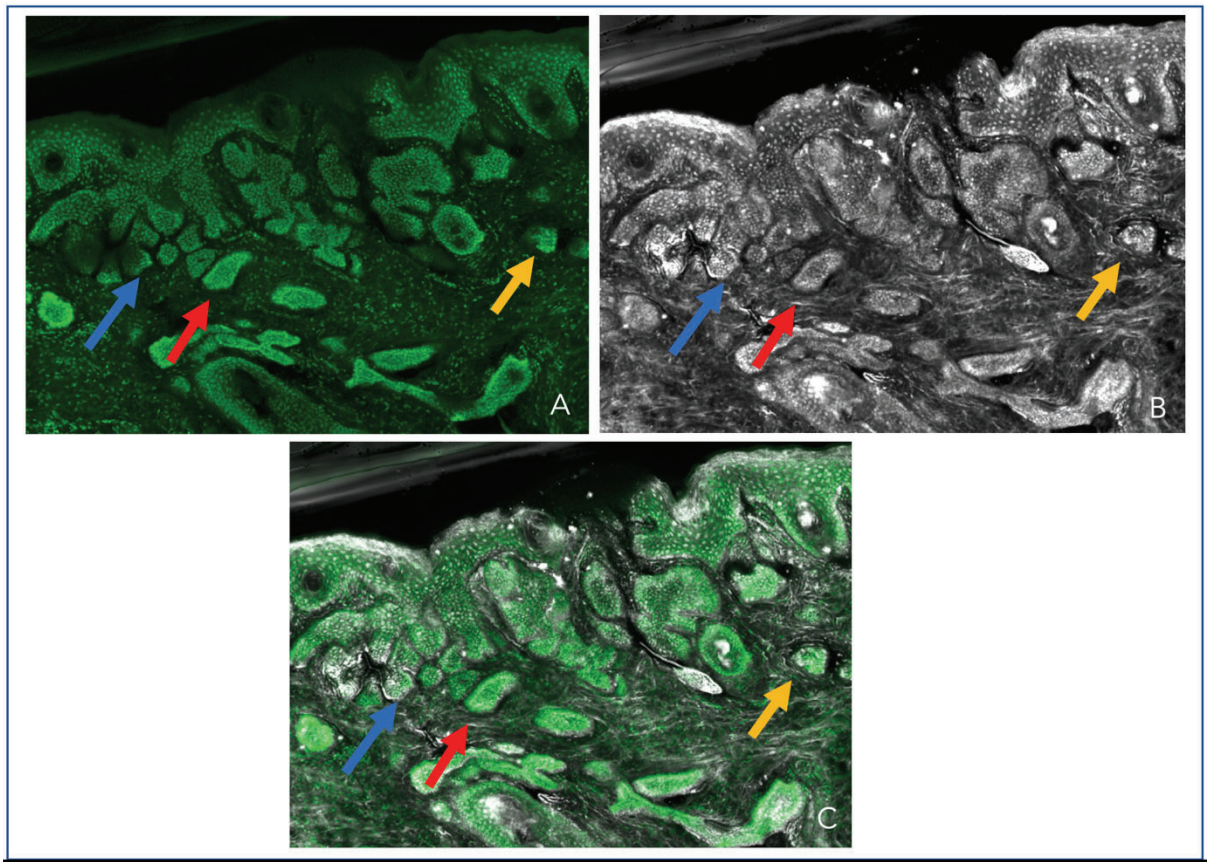

Figura 41. Carcinoma basocelular micronodular. Criterios diagnósticos. Magnificación 10x. A. Láser fluorescencia; B. Láser reflectancia. C. Fusión. Tinción naranja de acridina y ácido acético. Nidos bien delimitados de carcinoma basocelular presentando empalizada, hendidura peri-tumoral, núcleos aglomerados, pleomorfismo nuclear, aumento de la relación núcleo/citoplasmática (fecha roja), reacción estromal peri-tumoral, bandas de colágeno engrosadas peritumorales (flecha amarilla). Las células dendríticas no son visualizadas en el modo de iluminación de láser de fluorescencia (flecha azul). (Fuente: Javiera Pérez-Anker).

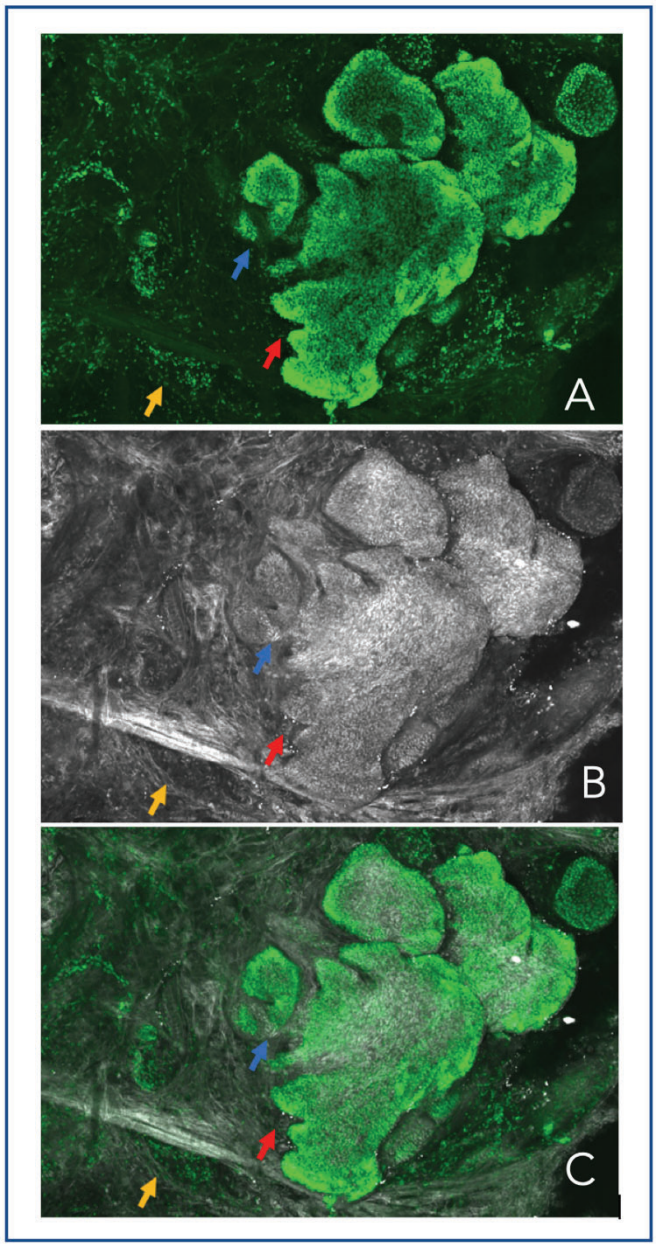

Figura 42. Carcinoma basocelular nodular. Criterios diagnósticos. Magnificación 10x. A. Láser fluorescencia; B. Láser reflectancia. C. Fusión. Tinción naranja de acridina y ácido acético. Nidos bien delimitados de carcinoma basocelular presentando empalizada, hendidura peri-tumoral, núcleos aglomerados, pleomorfismo nuclear, aumento de la relación núcleo/citoplasmática (fecha roja), reacción estromal peri-tumoral, bandas de colágeno engrosadas peritumorales (flecha amarilla). Las células dendríticas no son vistas en el láser de fluorescencia (flecha azul). (Fuente: Javiera Pérez-Anker).

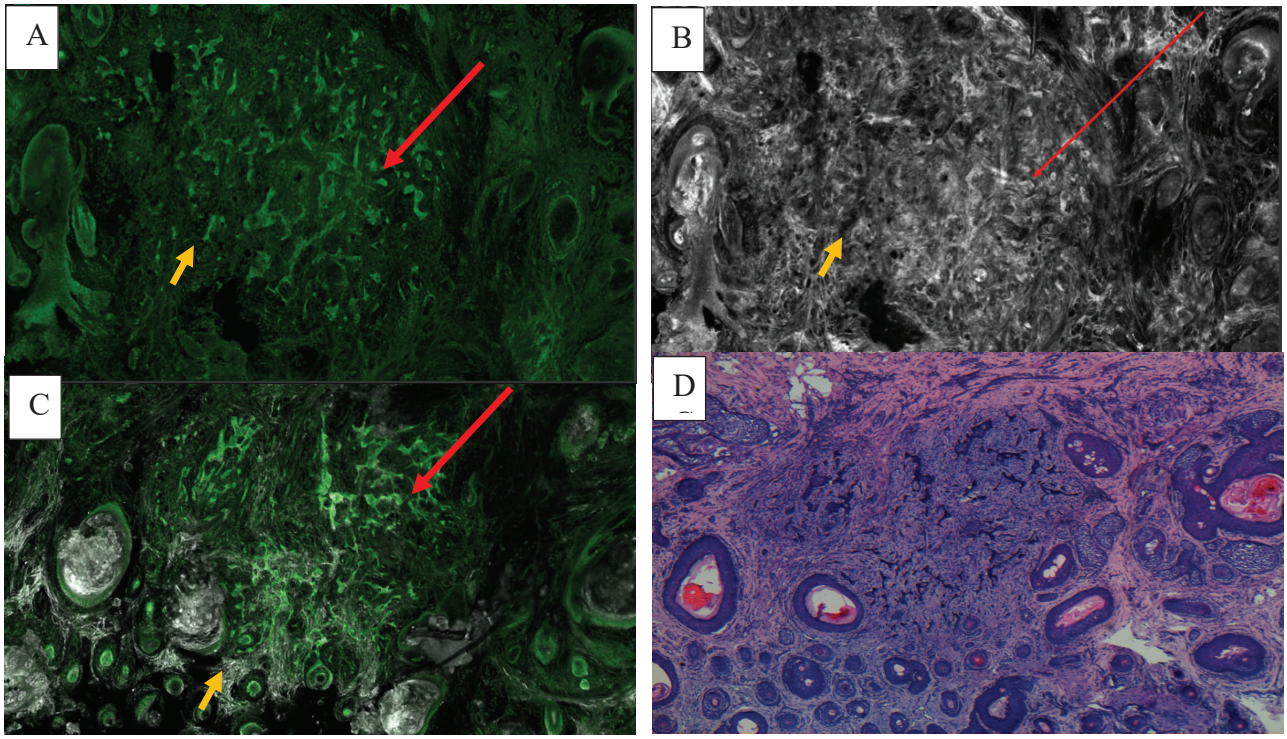

Figura 43. Carcinoma basocelular infiltrante. Tinción naranja de acridina y ácido acético. Criterios diagnósticos. Magnificación 10x. A. Láser fluorescencia; B. Láser reflectancia. C. Fusión. D. Tinción de H&E en histología convencional. En la figura se observan los nidos bien delimitados del carcinoma basocelular presentando empalizada, hendidura peri-tumoral, núcleos aglomerados, pleomorfismo nuclear, aumento de la relación núcleo/citoplasmática (fecha roja), reacción estromal peri-tumoral, bandas de colágeno engrosadas peritumorales (flecha amarilla). Los núcleos y la reacción estromal son mucho mejor visualizados con la doble tinción. (Adaptado de Pérez-Anker et.al., 2020)[70]

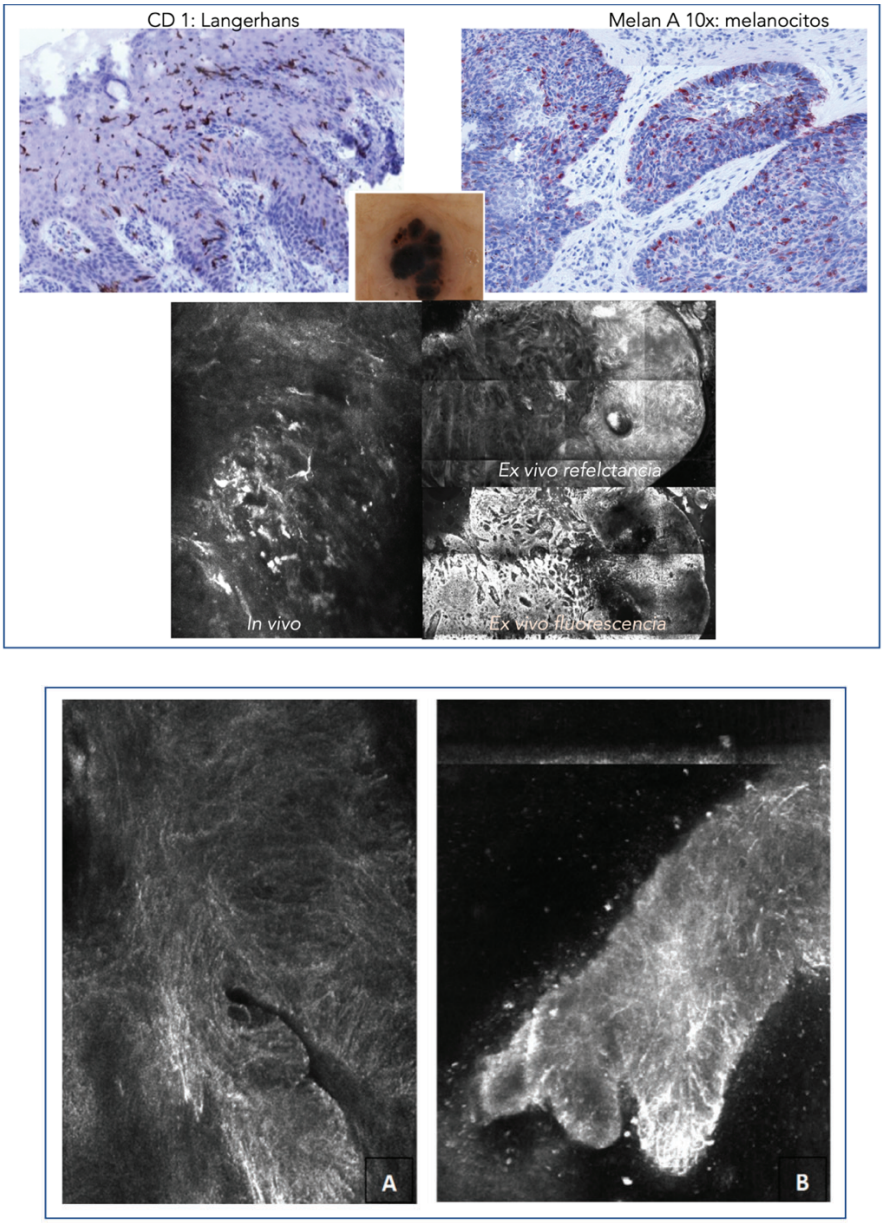

Figura 44. Carcinoma basocelular pigmentado. Visualización de células dendríticas (células de Langerhans y melanocitos). Superior: Ambas magnificaciones a 10x. Centro. Dermatoscopia. Tinción histológica de CD1, tiñendo selectivamente las células dendríticas y melan A, tiñendo melanocitos presentes en los nidos de CBC. Ambas, son fácilmente vistas con el láser de reflectancia, tanto *in vivo* como *ex vivo*. Agregar el ácido acético en la tinción de *ex vivo* ayuda a la visualización de estructuras en este láser, no siendo vistas en el láser de fluorescencia. Inferior: A. Detalle de células dendríticas visualizada con MCR. B. Detalle de células dendríticas visualizada con MCev, con el láser de reflectáncia (Fuente: Javiera Pérez-Anker).

V.7.4. Estandarización del método de obtención de imágenes en MCFu.

El procesamiento adecuado del tejido antes de la adquisición de imágenes confocales es crucial para obtener resultados de buena calidad y evitar posibles falsos negativos. La correcta preparación del tejido incluye tanto el método de tinción adecuado, como la correcta adaptación y colocación del tejido en la lámina.

Los estudios publicados en MCeV en diversos centros presentan una significativa variabilidad en cuanto al tipo de muestras, dispositivos, técnicas y terminología utilizada. Ante la necesidad de estandarizar este procedimiento, y la falta de estudios en la literatura en este sentido, esta tesis propone un protocolo integral que abarca desde la preparación de las muestras hasta la tinción, el escaneado y el control de calidad. Estos protocolos dieron lugar a diversas publicaciones.

El enfoque estandarizado tiene como objetivo no solo mejorar la calidad de las imágenes, sino también establecer un protocolo uniforme que garantice la confiabilidad y la comparabilidad de los resultados de forma multicéntrica.[55,71-73,111]

El proceso de obtención de las imágenes tiene distintas etapas:

1-Preparación y tinción de las muestras;

2-Colocación y aplanamiento de la muestra;

3-Obtención de las imágenes.

Explicamos previamente que el proceso de tinción publicado anteriormente (Figura 45), ha sido modificado con la finalidad de obtener imágenes aún más parecidas morfológicamente a la del H&E convencional.[70]

Una vez teñida, se coloca la pieza en un portaobjetos y se procede al escaneo. Estos pasos se explicarán detalladamente en los apartados siguientes, con los estudios complementarios realizados.[71-73]

Finalmente, en aquellos casos en los que sea necesario obtener una evaluación más detallada o para confirmar los hallazgos, se puede remitir la pieza a estudio histológico convencional, o para realización de técnicas de inmunohistoquímica. (Figura 41)

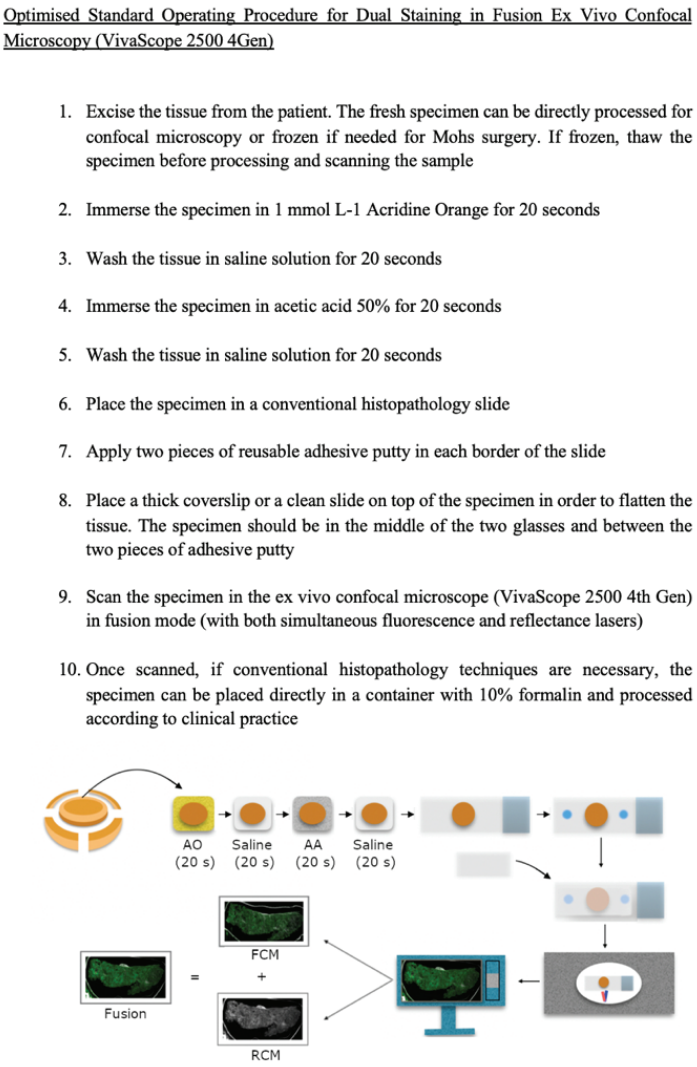

Optimised Standard Operating Procedure for Dual Staining in Fusion Ex Vivo Confocal Microscopy (VivaScope 2500 4Gen)

1. Excise the tissue from the patient. The fresh specimen can be directly processed for confocal microscopy or frozen if needed for Mohs surgery. If frozen, thaw the specimen before processing and scanning the sample
2. Immerse the specimen in 1 mmol L-1 Acridine Orange for 20 seconds
3. Wash the tissue in saline solution for 20 seconds
4. Immerse the specimen in acetic acid 50% for 20 seconds
5. Wash the tissue in saline solution for 20 seconds
6. Place the specimen in a conventional histopathology slide
7. Apply two pieces of reusable adhesive putty in each border of the slide
8. Place a thick coverslip or a clean slide on top of the specimen in order to flatten the tissue. The specimen should be in the middle of the two glasses and between the two pieces of adhesive putty
9. Scan the specimen in the ex vivo confocal microscope (VivaScope 2500 4th Gen) in fusion mode (with both simultaneous fluorescence and reflectance lasers)
10. Once scanned, if conventional histopathology techniques are necessary, the specimen can be placed directly in a container with 10% formalin and processed according to clinical practice

Figura 45. Propuesta de método estandarizado de trabajo. (Adaptado de Pérez-Anker et.al,2020)[70]

V.8. Aplanamiento de la muestra en microscopía confocal ex vivo.

Una vez que la muestra ha sido sometida al proceso de tinción, es crucial garantizar un contacto uniforme y completo del tejido con el portaobjetos. Esto es fundamental para asegurar la representatividad integral de la muestra. Cualquier espacio o irregularidad entre el tejido y el portaobjetos puede dar lugar a la omisión de esa zona en la imagen final. Esta consideración adquiere una relevancia especial en situaciones como el control de márgenes en la cirugía de Mohs o en la cirugía tumoral, dado que la falta de visualización de una región puede conllevar a resultados de falsos negativos en la evaluación de los márgenes quirúrgicos.

Esta dificultad ha sido observada y reportada por varios investigadores, y es una de las principales razones detrás de los falsos negativos en tumores como el carcinoma basocelular superficial o el carcinoma escamoso in situ

Asimismo, cualquier sustancia que se interponga entre el tejido y el portaobjetos, como sangre o tinta, puede afectar la calidad de la imagen o incluso impedir la visualización del tejido en esa zona específica. Por lo tanto, es necesario asegurarse de eliminar cualquier material no deseado antes de realizar la adquisición de imágenes. (Figura 46 y 47)

Por otro lado, durante el proceso de fijación y preparación de las muestras *ex vivo*, es posible que se produzca una contracción o distorsión de la epidermis y/o dermis, como también pérdida de fluidez, lo que puede dificultar el escaneo por exceso de rigidez.

Además, al escanear muestras de piel, a diferencia de otros tejidos, nos enfrentamos a diversas densidades de tejido en una sola muestra. Esto requiere la aplicación de presión externa en la muestra para asegurar que toda la superficie a escanear mantenga contacto con el vidrio. (Figuras 48 a 50)

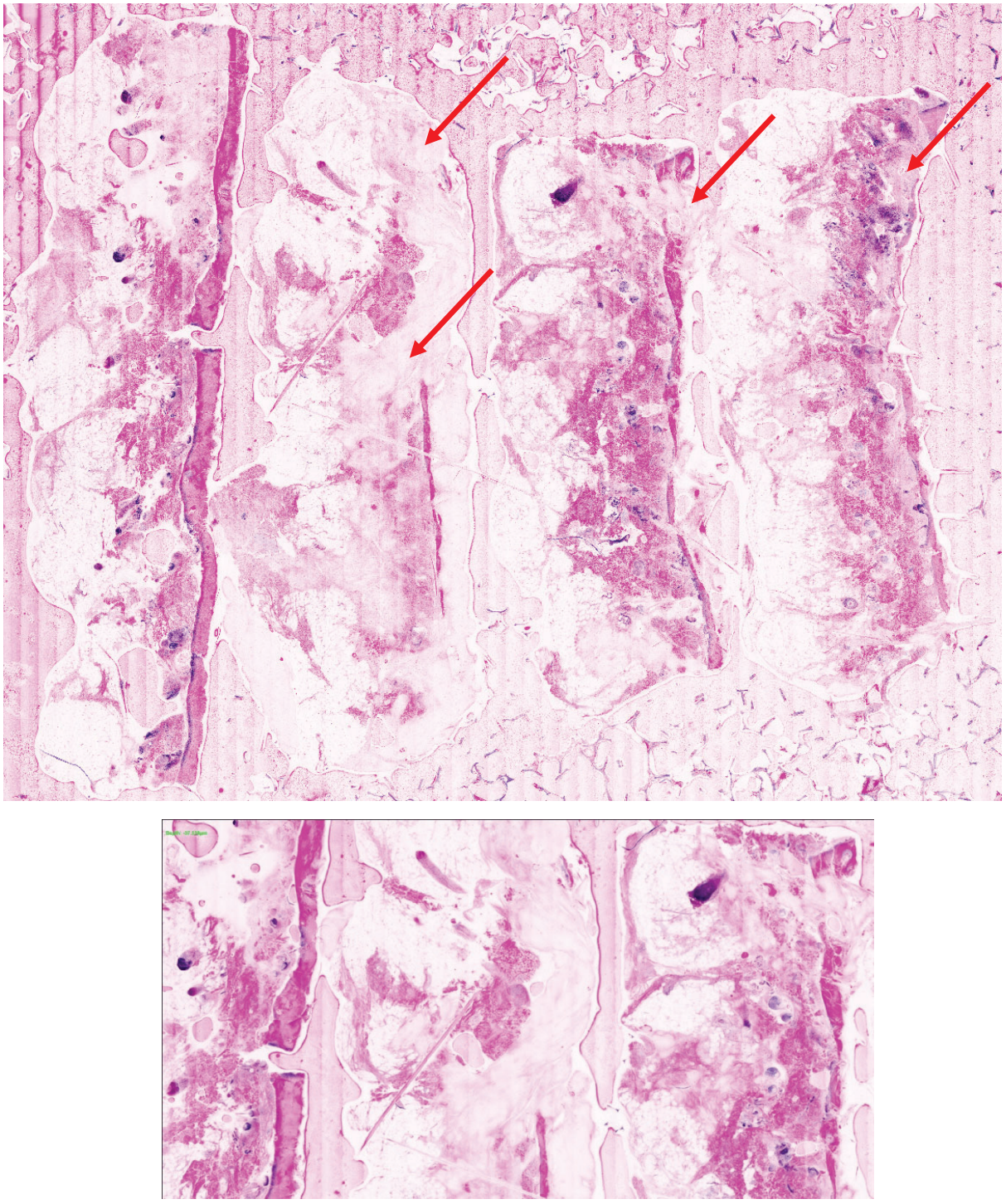

Figura 46. Varias muestras pueden ser escaneadas de forma simultánea. Sin embargo, si la epidermis no está totalmente representada, podemos encontrar falsos negativos. Flecha roja: epidermis no visualizada, en este caso, debido al acumulo de sangre. (Fuente: Javiera Pérez-Anker).

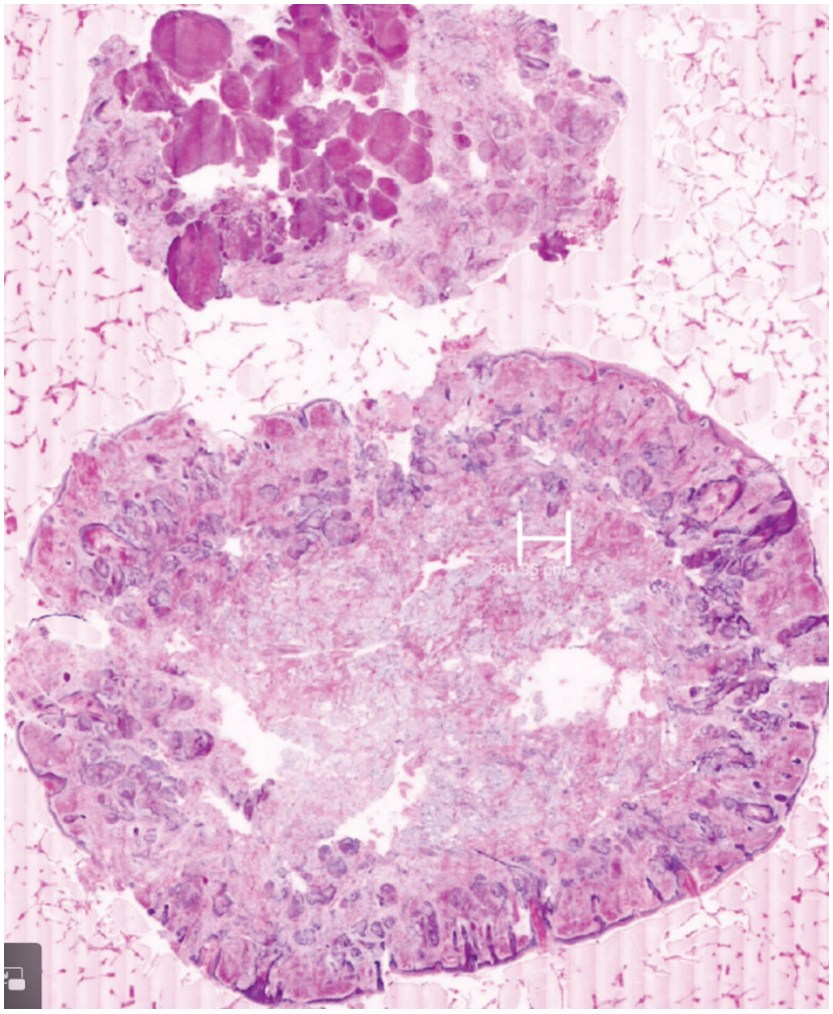

Figura 47. Si el tejido no contacta 100% con la superficie del vidrio, espacios vacíos residuales no permiten diferenciar la presencia o ausencia del tumor, dando lugar a posibles falsos negativos. Por lo tanto, es fundamental aplicar presión para lograr un contacto perfecto entre el tejido y el vidrio. (Adaptado de Pérez-Anker, et. al.,2022)[73]

Diferentes y complejos métodos de apoyo habían sido utilizados sin resultados adecuados,[123] para intentar lograr la adaptación perfecta del tejido. Sin un dispositivo adecuado, toda la rapidez de la tecnología era enlentecida por el proceso de la preparación de la muestra. (Figuras 48 y 49)

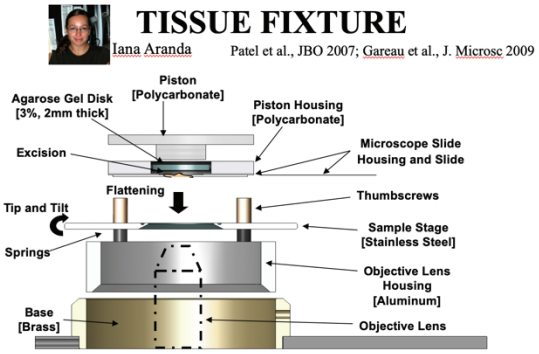

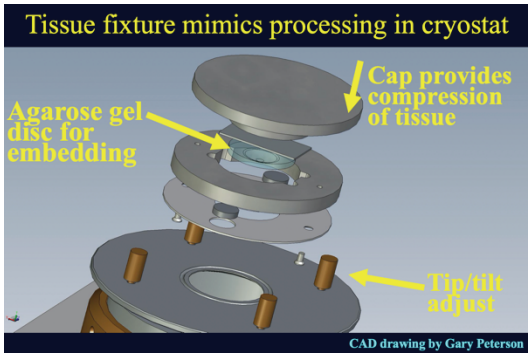

Figura 48. Diferentes métodos utilizados para aplanar la muestra. La presión externa es importante para lograr la perfecta adaptación del tejido al vidrio (Fuente: imágenes cedidas por Milind Rajadhyaksha).

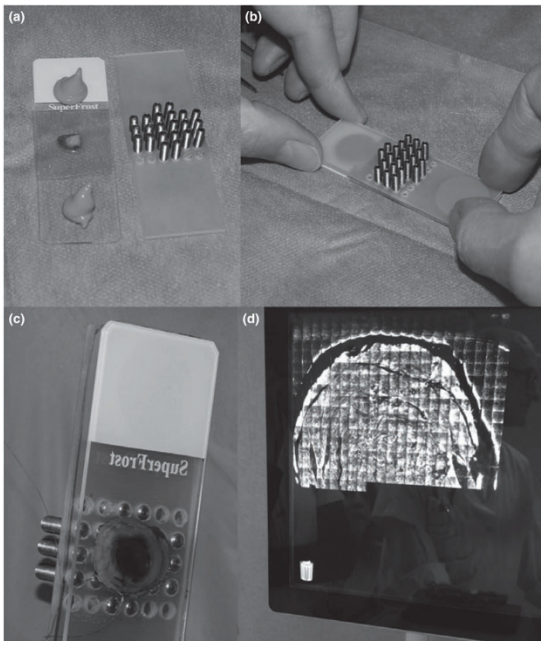

Figura 49. Diferentes métodos utilizados para aplanar la muestra. En este dispositivo diferentes tornillos especialmente diseñados encajan en un portaobjetos para intentar lograr la presión externa necesaria. (Adaptado de Cinotti et al.,2017)[123]

El desarrollo y patentado del dispositivo de "aplanamiento de la pieza"[71,72] para mejorar la técnica de contacto del tejido con el cubreobjetos es un avance significativo en la optimización de la adquisición de imágenes en MCev. Este dispositivo, denominado "flattening device", utiliza imanes de diferentes tamaños y fuerzas magnéticas, junto con esponjas de diferentes tamaños e intensidades para adaptarse a una variedad de muestras con diferentes características.[71,72] (Figura 50)

La utilización de estos imanes y esponjas permite aplicar una presión adecuada sobre la muestra, asegurando un contacto uniforme entre el tejido y el cubreobjetos. Esto es especialmente importante en muestras que varían desde citologías, punción por aguja fina, hasta grandes piezas de tejido mamario. Ajustando la combinación de imanes y esponjas según las necesidades de cada muestra, se logra un aplanamiento óptimo y homogéneo del tejido sobre el cubreobjetos, facilitando la estandarización.

Posteriormente a nuestro estudio, Sendín y colaboradores[124] han propuesto una sumatoria de las capas escaneadas para lograr la representatividad de toda la epidermis. Sin embargo, además de ser un proceso lento (ya que es necesario unir varios mosiacos para obtener la muestra adecuada, las imágenes obtenidas no logran un parecido con la H&E convencional, perdiéndose la definición de los detalles nucleares. [124] (Figura 51)

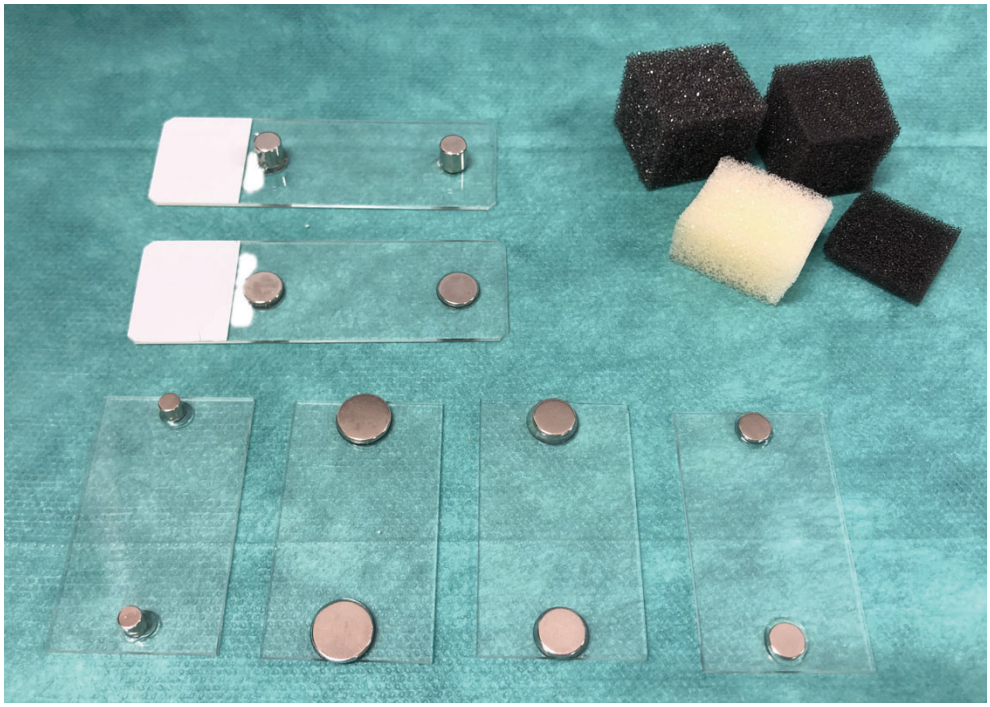

Figura 50. Imanes con distinta potencia y esponjas de diferentes densidades se combinan para lograr un contacto perfecto entre el tejido y el vidrio. (Adaptado de Pérez-Anker, Pérez-Anker et al.,2019)[71,72]

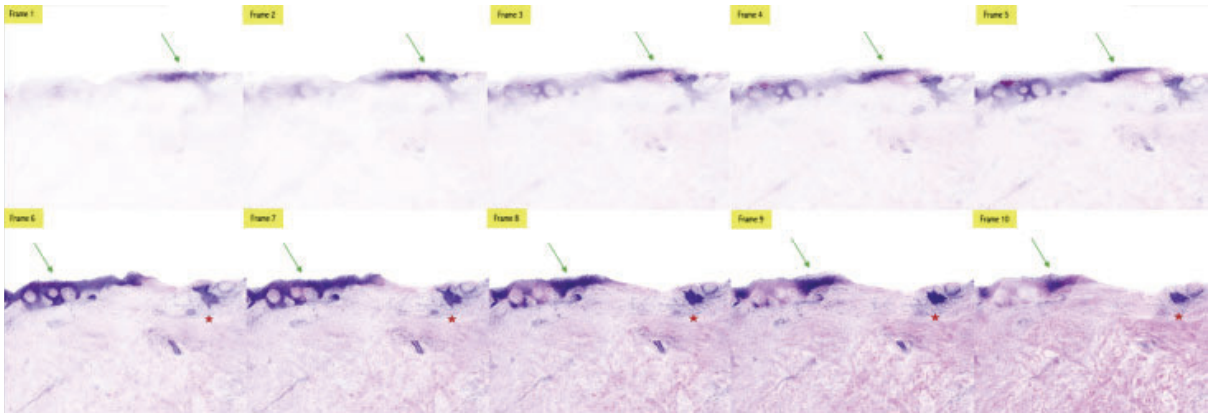

Figura 51. Capas de escaneo a diferentes profundidades se van superponiendo de manera a intentar obtener la representación de toda la epidermis. (Adaptado de Sendín-Martín et al.,2022)[124]

V.9. Nuevo protocolo estandarizado de trabajo en MCev.

A pesar de los esfuerzos para lograr una estandarización (tinción y aplanamiento), el protocolo estandarizado de trabajo propuesto por nosotros anteriormente[70] no logró ser eficaz para que los diferentes centros del mundo obtuvieran imágenes homogéneas. Observábamos frecuentemente errores en la metodología y, por consiguiente, subóptima calidad de muestras, no comparables entre los diferentes centros.

Con ese objetivo, describimos 6 pasos para lograr un escaneo adecuado en MCev:[73] (Figuras 52 y 53)

1. Extirpar adecuadamente el tejido: Es fundamental realizar una correcta extracción del tejido de interés, asegurando su integridad y preservación para el posterior escaneo. Se deben tomar las precauciones necesarias para evitar daños o deformaciones en el tejido durante este proceso. Sobre todo, es fundamental que el tejido extirpado tenga un espesor homogéneo en toda la muestra (tratándose de piel). En caso de tumores de piel, sugerimos el uso del bisturí doble: este permite un espesor homogéneo de toda la epidermis extirpada, independientemente del entrenamiento del cirujano. Por otro lado, si la muestra no es homogénea, es preciso aplicar una doble esponja (para aumentar la presión sobre la lámina) o, adaptar y recortar una esponja hasta lograr una perfecta adaptación.

2. Preparar el tejido para ser escaneado: Antes del escaneo, es necesario preparar el tejido eliminando cualquier resto de sangre u otros

contaminantes que puedan afectar la calidad de las imágenes. En el caso de cirugías de Mohs, también se pueden aplicar tinciones para orientar adecuadamente la pieza durante el escaneo, pero estas deben aplicarse en la parte superior del tejido y nuca en la superficie de apoyo con la lámina, ya que esta interfiere con la calidad de la imagen final. El espray de ácido acético al 50% (o sumergir la pieza durante un segundo en este medio, facilita la realización de este paso).

3. Aplicar protocolos de tinción: Dependiendo de los objetivos del estudio, se deben aplicar los protocolos de tinción adecuados para realzar las estructuras de interés. Esto puede incluir el uso de agentes de tinción específicos que resalten ciertos componentes celulares o estructuras del tejido.

4. Aplanar la pieza de forma adecuada: Utilizando el dispositivo de "aplanamiento de la pieza" descrito previamente, se debe asegurar un contacto uniforme y completo del tejido con el cubreobjetos. Esto garantiza que todas las áreas del tejido sean escaneadas y evita la falta de visualización de zonas que no estén en contacto con el cubreobjetos.

5. Encontrar el punto "cero": El punto "cero" hace referencia al punto de inicio del escaneo en el tejido. Es necesario encontrar este punto exacto para asegurar un escaneo sistemático y completo de toda el área de interés. Esto se logra mediante el ajuste de la posición del escáner confocal en

relación con el tejido. Un punto cero inadecuado imposibilita el reconocimiento de estructuras nucleares.

6. Ajustar la intensidad y el color de los láseres: Es importante ajustar adecuadamente la intensidad y el color de los láseres utilizados en el escaneo. Esto permitirá obtener imágenes de buena calidad, con contraste óptimo y sin distorsiones en la representación de las estructuras celulares y tisulares. Un exceso de tinción borra los detalles celulares y, por el contrario, la falta de esta no permite el reconocimiento de la citología.

Al seguir estos 6 pasos de manera consecutiva, incluso una persona sin experiencia previa en el escaneo con microscopía confocal *ex vivo* podrá obtener imágenes de alta calidad, estandarizadas, que puedan ser interpretadas correctamente.

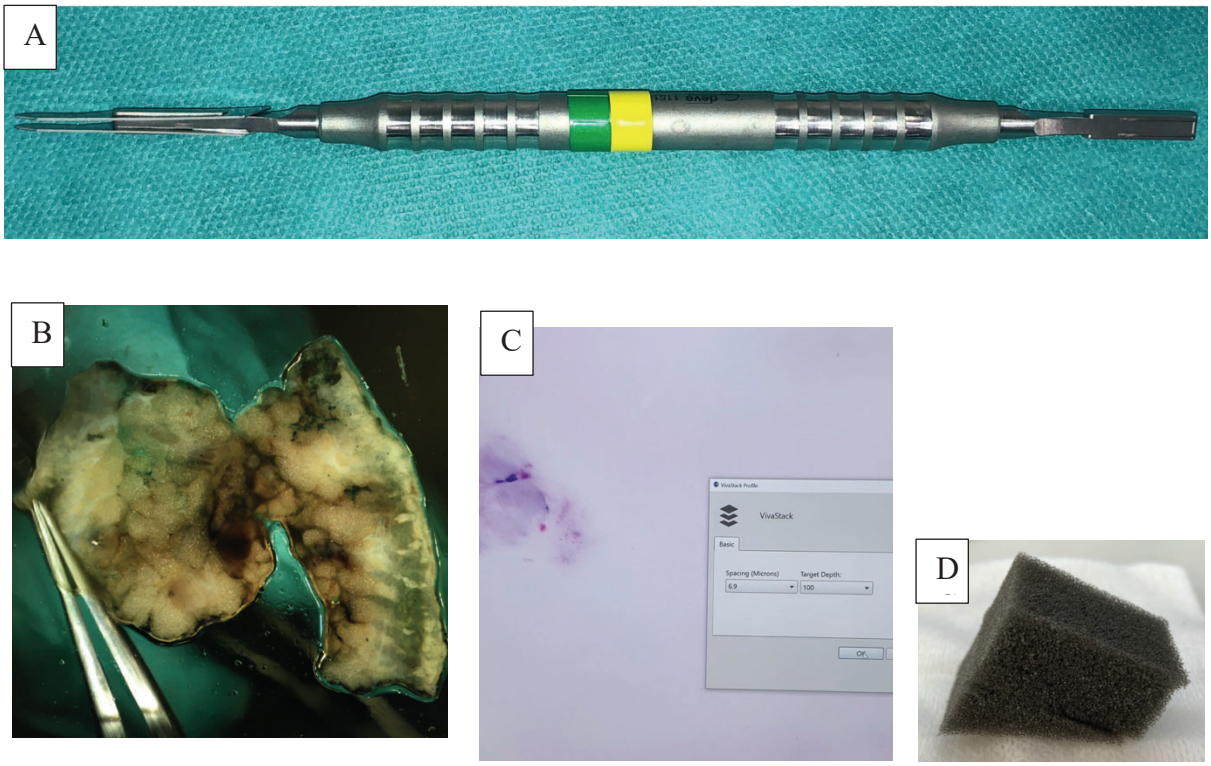

Figura 52. Técnicas aplicadas para que el tejido contacte con la superficie del vidrio. A. Bisturí de doble hoja. B. Posicionar la epidermis mediante el uso de pinzas. C. Realizar un "stack" profundizar el escaneo en el tejido. D. Apoyar esponjas cortadas especialmente para el tejido extirpado. (Adaptado de Pérez-Anker et.al., 2022)[73]

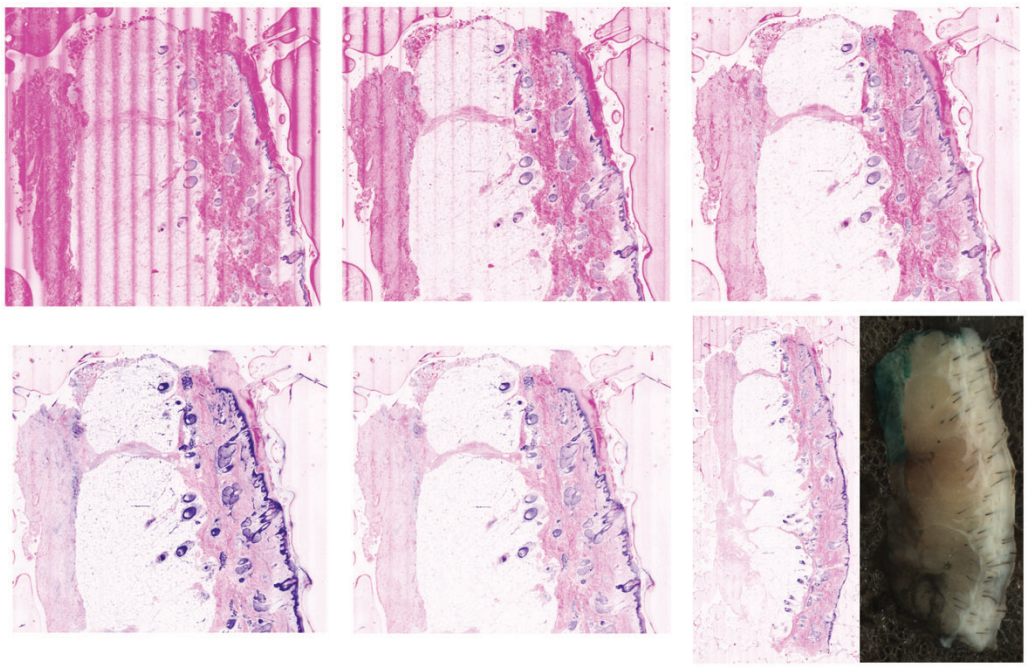

Figura 53. Encontrando el "punto cero". 4ª generación de microscopio confocal. Tinción con ácido acético y naranja de acridina. Encontrar este punto (fila superior) y ajustar los tonos de la imagen (fila inferior), son parte de las claves de un correcto escaneo. (Fuente: Javiera Pérez-Anker).

V.10. Precisión diagnóstica de la microscopía confocal ex vivo en el diagnóstico del carcinoma escamoso.

La ausencia de investigaciones previas sobre criterios diagnósticos para el CEC cutáneo mediante MCev con la nueva generación de MCFu, así como la falta de estudios de precisión diagnóstica en lesiones ambiguas, ha motivado la realización de este estudio.[74,125]

Para diagnosticar este tipo de tumor, resulta absolutamente necesario que la epidermis esté completamente representada en las imágenes obtenidas mediante MCev; de lo contrario, no sería posible visualizar los criterios diagnósticos necesarios.

Con respecto a la precisión diagnóstica del patólogo y el cirujano de Mohs fue, respectivamente: Sensibilidad 91%/96% y Especificidad (SP) 85%/94%, con un Valor Predictivo Positivo de 95% y Valor Predictivo Negativo de 75%/89%. Las características diagnósticas observadas en las muestras de H&E (queratinización, puentes intercelulares, pleomorfismo nuclear, inflamación estromal, paraqueratosis, pérdida de la capa granular y bordes infiltrantes, variante invasiva o in situ) también mostraron una alta sensibilidad y especificidad, con un valor de $p < 0.001$ en todos los casos. Otras variables, como desmoplasia, disqueratosis y figuras mitóticas, mostraron una correlación deficiente con los hallazgos histopatológico.

Observamos que las alteraciones de la queratinización en la epidermis, la paraqueratosis, la disqueratosis, la pérdida de la granulosa, la presencia de puentes intercelulares, el pleomorfismo celular, la presencia de mitosis, los bordes infiltrantes y la presencia de reacción estromal peri tumoral son claramente distinguidas en la MCFu, inclusive por observadores inexpertos.

Sin embargo, para un observador con poca experiencia en microscopia confocal *ex vivo*, la desmoplasia y las células disqueratósicas no fueron fácilmente reconocidas debido al cambio de coloración respecto a la hematoxilina y eosina en parafina (como luego discutiremos). (Figura 54) Así mismo, las figuras de mitosis requieren una curva de aprendizaje para ser observadas. (Figura 54 a 57)

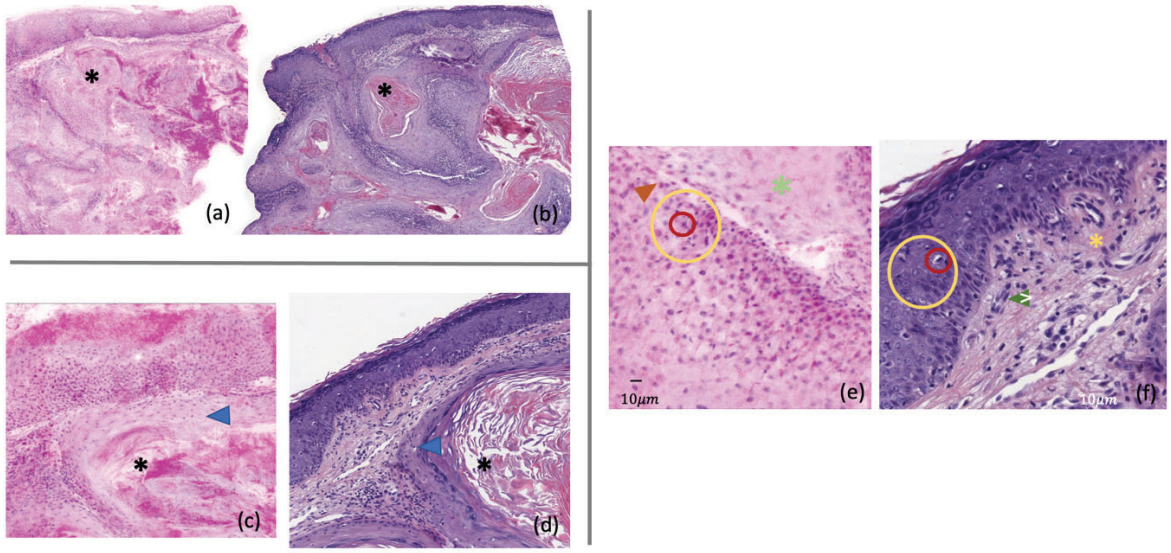

Figura 54. Diferencias en la visualización de un CEC bien diferenciado (biopsia por punch). Imagen de la derecha, H&E. Imagen de la izquierda, MCFu. (a) y (b), vista macroscópica; (c) y (d), 4x; (e) y (f), representación celular. Asterisco negro, queratinización; círculo rojo, displasia; asterisco verde, paraqueratosis; asterisco amarillo, desmoplasia; triángulo azul, bordes infiltrativos; triángulo marrón, pérdida de la capa granulosa; círculo amarillo, pleomorfismo; triángulo verde, inflamación estromal. A pesar de que las estructuras morfológicas tienen una fuerte correlación, los colores pueden variar significativamente. (Adaptado de Lobos-Guedes et al., under review 2024)[74]

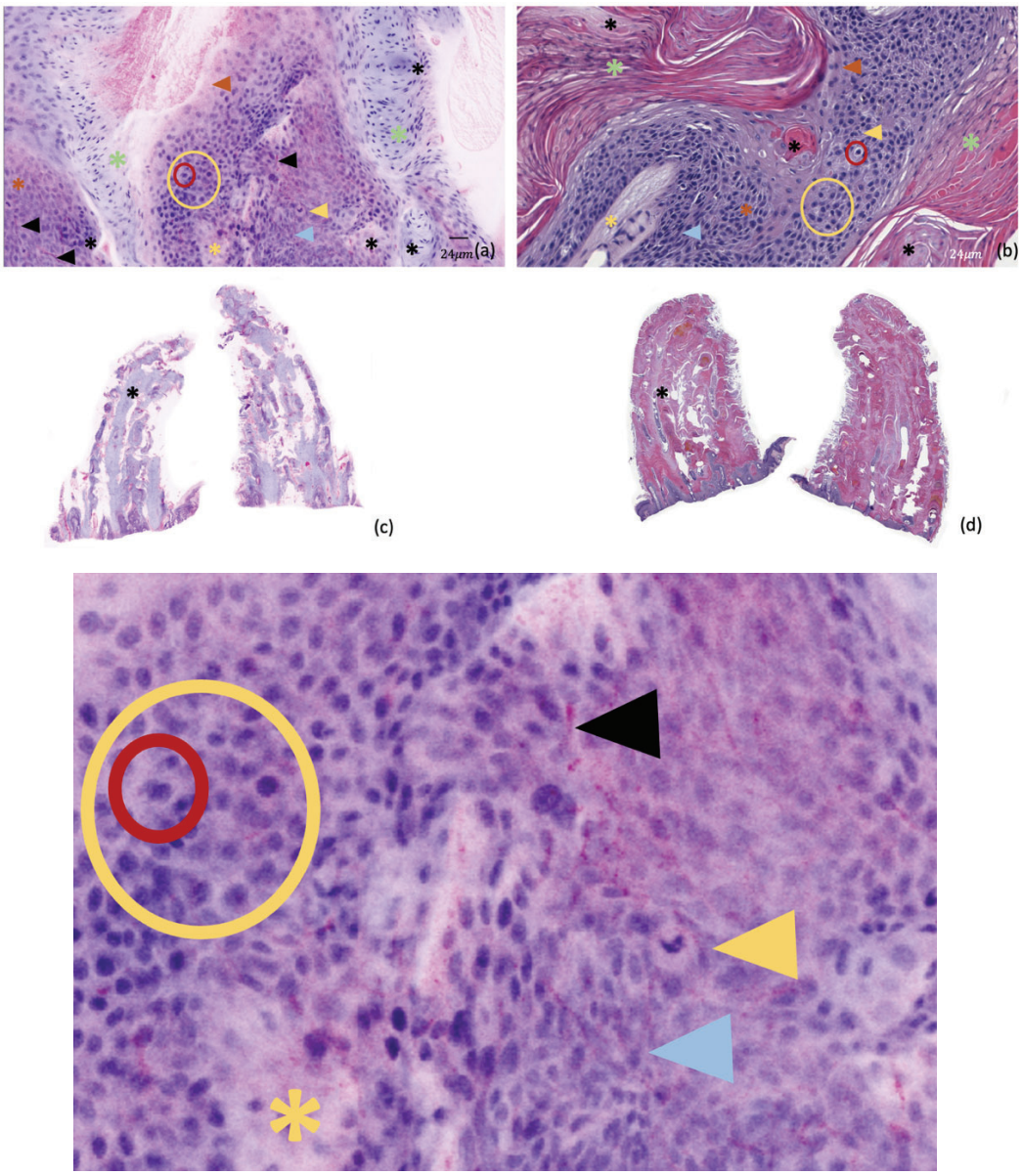

Figura 55. Variaciones en la visualización de un CEC bien diferenciado en una biopsia por afeitado. En la imagen de la derecha, se utiliza tinción H&E, mientras que, en la imagen de la izquierda, se emplea MCFu. Las características clave se indican de la siguiente manera: asterisco negro: queratinización; asterisco marrón: puentes intercelulares; círculo rojo: displasia; asterisco verde: paraqueratosis; triángulo azul: bordes infiltrativos; triángulo marrón: pérdida de la capa granular; triángulo amarillo: figuras mitóticas; círculo amarillo: pleomorfismo; triángulo negro: células dendríticas. Las subfiguras (a) y (b) ofrecen detalles celulares, mientras que las subfiguras (c) y (d) ofrecen una vista macroscópica. (Adaptado de Lobos-Guede et al., under review 2024)[74]

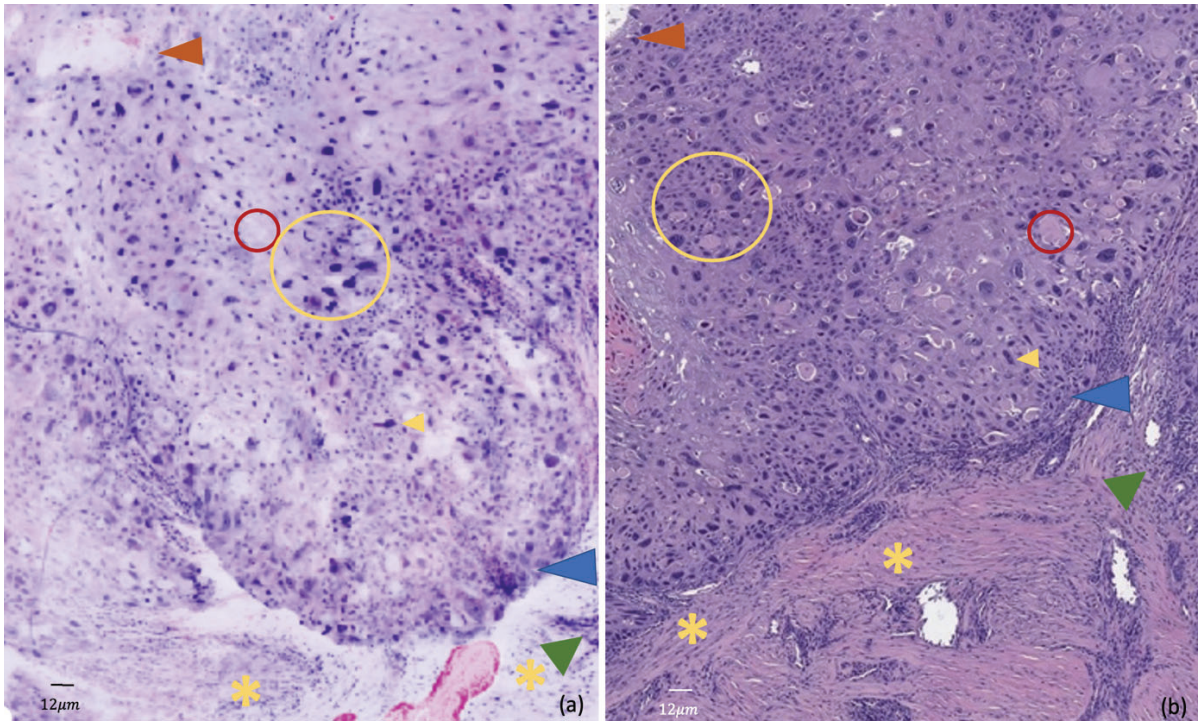

Figura 56. Se destacan las diferencias en la visualización de una biopsia de punch de un SCC acantolítico. Imagen izquierda, MCFu (a). Imagen derecha, H&E (b). Círculo rojo, displasia; asterisco amarillo, desmoplasia; triángulo azul, bordes infiltrativos; triángulo marrón, pérdida de la capa granular; triángulo amarillo, figuras mitóticas; círculo amarillo, pleomorfismo. (Adaptado de Lobos-Guede et al., under review 2024)[74]

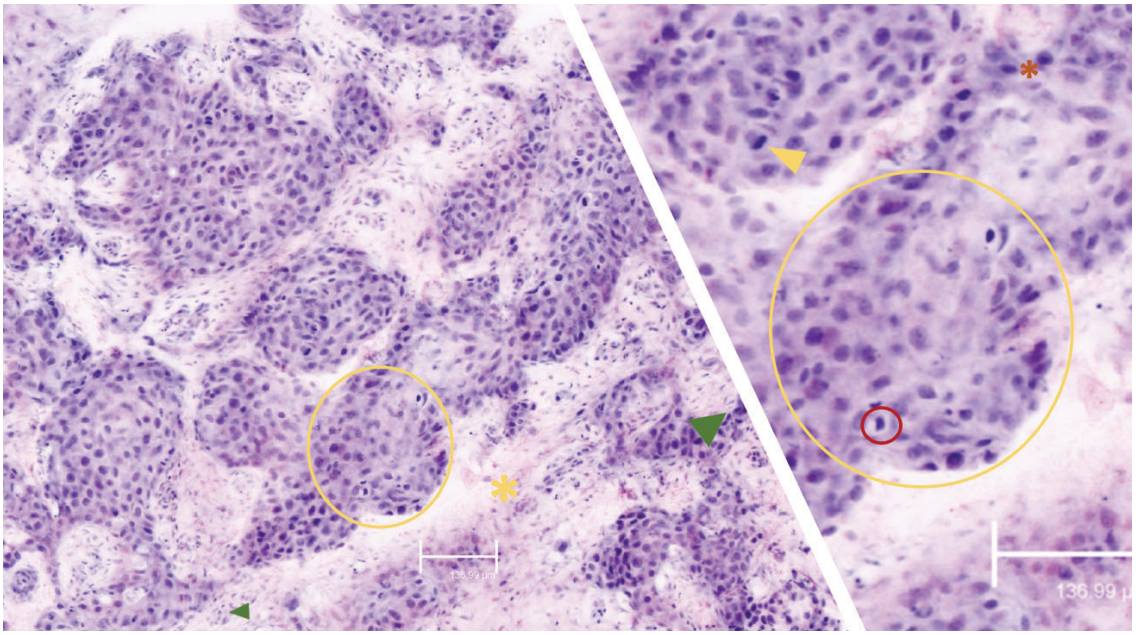

Figura 57. SCC infiltrante. Asterisco marrón, puentes intercelulares; círculo rojo, displasia; asterisco amarillo, desmoplasia; triángulo amarillo, figuras mitóticas; círculo amarillo, pleomorfismo; triángulo verde, inflamación estromal. (Adaptado de Lobos-Guede et al., under review 2024)[74]

Estudios previos habían utilizado tecnologías anteriores, y analizado las estructuras mediante MCF o MCR, ya sea por separado o combinadas, pero sin la nueva modalidad de fusión con tinción digital y sin la inclusión de muestras de lesiones equívocas dermatoscópicamente para establecer su precisión diagnóstica.[122,126]

Algunas de las características del CEC que previamente se habían descrito utilizaban términos descriptivos similares a los empleados en entornos histológicos, mientras que otros se limitaban a descripciones morfológicas sin utilizar técnicas de tinción digital. Entre estos términos se incluyen: erosión/ulceración, hiperqueratosis, paraqueratosis, desorganización arquitectural, presencia de células redondas y

brillantes en la epidermis, células redondas y brillantes en la dermis, estructuras en forma de nido en la dermis, perlas de queratina e infiltrado inflamatorio peritumoral (Figura 58).[122] Además, se evaluaron estos criterios en relación con el grado de invasión o diferenciación. La erosión se asoció más frecuentemente con la ausencia de diferenciación, mientras que las perlas de queratina estuvieron más presentes en los CEC bien diferenciados (Tabla 4). [122]

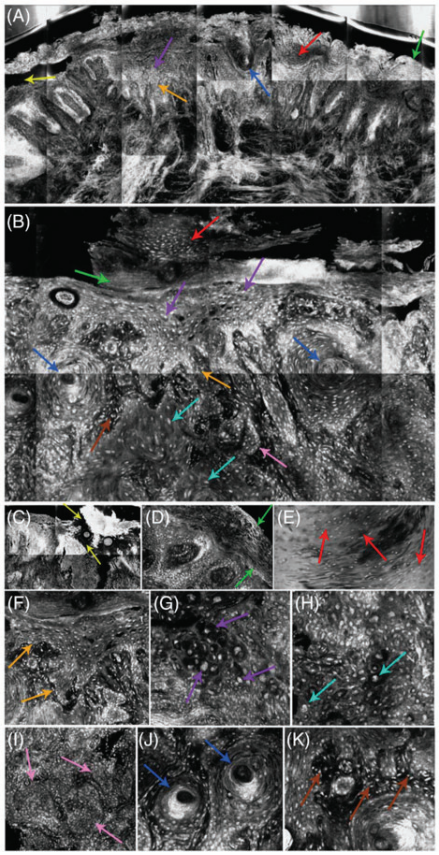

Figura 58. Ejemplos de patrones estudiados por Hartmann y colaboradores en microscopía confocal ex vivo. (A) CEC in situ, (B) CEC invasor, (C) erosión/ ulceración (fleche amarilla), (D) hiperqueratosis (fleche verde), (E) paraqueratosis (fleche roja), (F) desorganización arquitectural (fleche naranja), (G) células redondas y brillantes en la epidermis (flecha violeta), (H) células redondas y brillantes en la dermis (flecha turquesa), (I) estructuras en forma de nido en la dermis (flecha rosa), (J) Perlas de queratina (flecha azul), (K) Infiltrado inflamatorio peritumoral (flecha marrón). (Adaptado de: Hartmann et al., 2018)[122]

Patrón de Microscopía Confocal Ex Vivo	Erosión/ Ulcera (%)	Hiperqueratosis (%)	Paraqueratosis (%)	Desorden Arquitectónico (%)	Células Brillantes o Punteadas en la Epidermis (%)	Células Brillantes o Punteadas en la Dermis (%)	Estructuras en Forma de Nido en la Dermis (%)	Perlas de Queratina (%)	Infiltrado Inflamatorio Peritumoral (%)
Carcinoma in situ (%)	36.7	76.7	66.7	73.3	90.0	0	0	0	0
Carcinoma Invasivo (%)	64.8	97.2	97.2	100.0	91.7	90.3	86.1	68.1	88.9
Valor P	.009*	.001*	. 000*	.000*	.787	.000*	.000*	.000*	000*
Bien o Moderadamente Diferenciado (%)	46.8	97.9	97.9	100.0	91.7	85.4	83.3	87.5	83.3
Pobremente Diferenciado o Indiferenciado (%)	100.0	95.8	95.8	100.0	91.7	100.0	91.7	29.2	100.0
Valor P	.000*	.488	.488		.906	.003**	.383	.000**	.013

Tabla 4. Diferencias entre critérios diagnósticos estudiados y el grado de diferenciación de CEC. *La diferencia entre Carcinoma Invasivo y Carcinoma in situ fue significativa (<.05) en el análisis de χ2.**La diferencia entre Pobremente Diferenciado y Otro Carcinoma Invasivo fue significativa (<.05) en el análisis de χ2. (Adaptado de: Hartmann et al., 2018)[122]

En otro estudio, Longo y colaboradores[126] estudiaron las siguientes características utilizando apenas el láser de fluorescencia y tiñendo con naranja de acridina: presencia de fluorescencia, silueta del tumor, perlas de queratina (es decir, círculos concéntricas de escamas queratinizadas de bajo brillo fluorescente), pleomorfismo nuclear (es decir, variación en el tamaño, forma y fluorescencia de los queratinocitos) y formación de queratina (es decir, escamas fluorescentes en el estrato córneo y la dermis papilar). Se relacionaron estas características con el grado de diferenciación y se verificó la correlación de positividad o negatividad de márgenes

en cirugía de Mohs. Encontrándose un falso positivo y un falso negativo en su muestra de 13 tumores y 47 mosaicos. Se observó una silueta tumoral poco definida, con escasez o ausencia de perlas de queratina y un marcado pleomorfismo nuclear en tumores poco diferenciados.[126] (Figura 59)

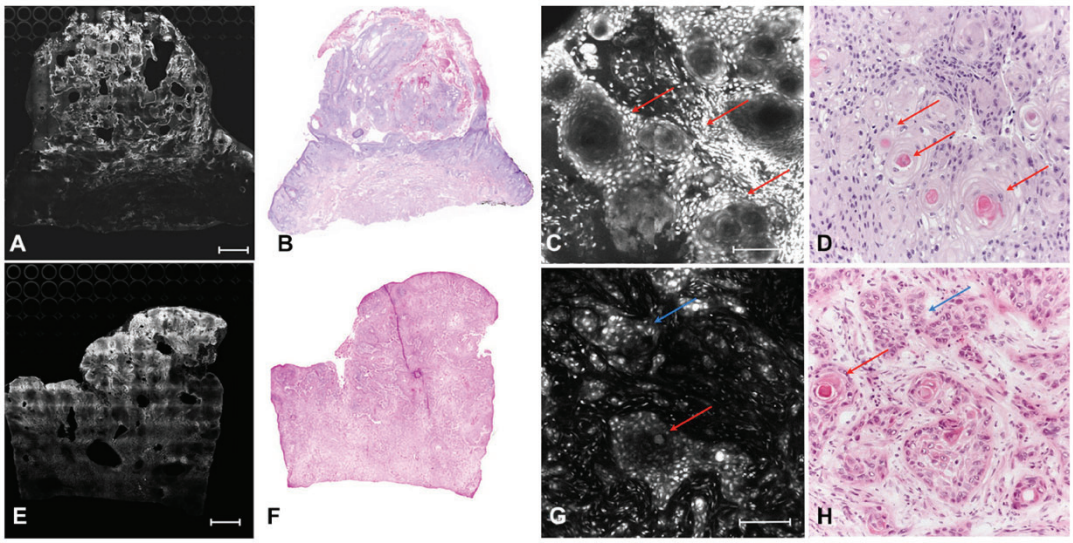

Figura 59. A, El mosaico de microscopía confocal de fluorescencia revela una silueta bien definida de un carcinoma de células escamosas cutáneas con una demarcación nítida y áreas altamente fluorescentes (barra de escala ¼ 750 µm). B, Imágenes histopatológicas correspondientes que muestran un tumor bien diferenciado. C, Detalle del tumor que muestra perlas de queratina (flechas rojas; barra de escala ¼ 150 µm). D, La evaluación histológica revela la presencia de varias perlas de queratina (flechas rojas). E, La visión general de la microscopía confocal de fluorescencia del tumor revela una silueta del tumor poco definida con un área altamente fluorescente en la parte superior y una fluorescencia menor en la parte más profunda del tejido correspondiente a la zona infiltrante (barra de escala ¼ 750 µm). F, La imagen histopatológica correspondiente muestra un tumor poco diferenciado con lenguas epiteliales irregulares. G, Se pueden detectar pocas perlas de queratina (flecha roja) junto con cordones infiltrantes de queratinocitos poco diferenciados (flecha azul; barra de escala ¼ 150 µm). H, La imagen histopatológica muestra un tumor poco diferenciado con pocas perlas de queratina (flecha roja) y cordones infiltrantes (flecha azul). (Adaptado de Longo et al.,2015)[126]

Por otro lado, un estudio previo evaluó la eficacia diagnóstica del CEC en cirugía de Mohs,[127] utilizando la tecnología previa, teñido únicamente con ácido acético al 5%, evaluados con el láser de reflectancia, en 20 pacientes. Cuatro observadores independientes recibieron instrucciones estandarizadas sobre las características diagnósticas de la microscopía confocal del CEC. Posteriormente, cada observador evaluó 120 imágenes confocales de extirpaciones frescas de CEC o piel normal, obtenidas mediante MCev. Fueron estudiadas la morfología general, la ubicación, el tamaño, la forma del área tumoral, núcleos densamente distribuidos y organizados de forma irregular, además de atipia nuclear. En general, se logró una sensibilidad del 95% y una especificidad del 96.25% por parte de los cuatro observadores (valor predictivo positivo del 96.25%, valor predictivo negativo del 95.23%).[127]

Solo una publicación anterior[128] describió las características histológicas en CEC oral (CECo) utilizando la cuarta generación de MCev. En esta, se analizaron 38 CECo invasivos de 35 pacientes, y se describieron: pleomorfismo celular y nuclear, anisocitosis, queratinización, hipercromasia nuclear y figuras mitóticas atípicas, así como la presencia de necrosis e inflamación mixta. Además, los autores asociaron estas características con diferentes grados de diferenciación tumoral. En este estudio, no se compararon las imágenes con la H&E convencional correspondiente, ni tampoco se estudió la eficacia diagnóstica. Apenas se verificó la presencia de determinadas características diagnósticas y la relación con el grado de invasión. La queratinización fue el criterio que se asoció a CEC bien diferenciado y la atipia nuclear a baja diferenciación.[128] (Figura 60)

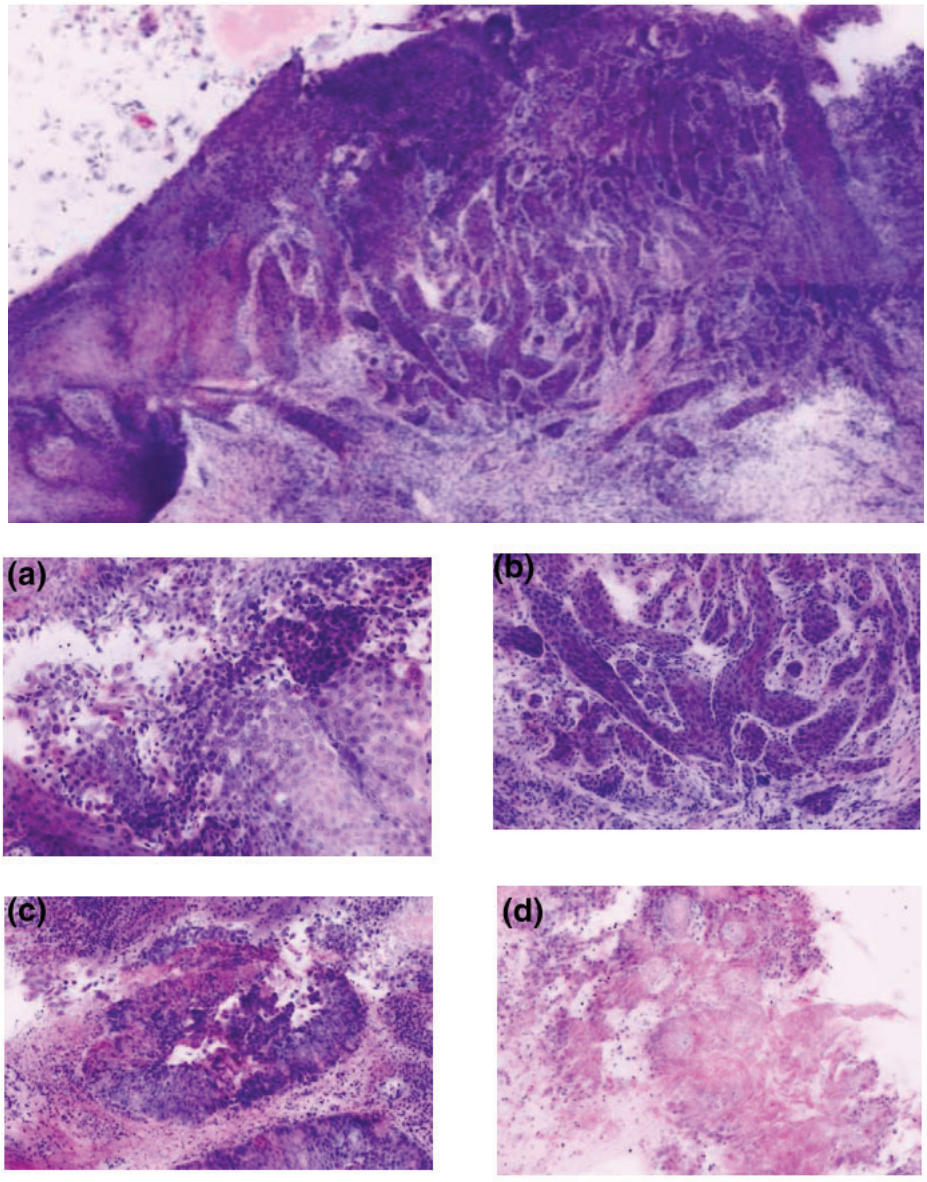

Figura 60. Mosaico CEC oral escaneado con MCev, con fluorescencia confocal, X2.5, teñido con naranja de acridina.

(a)–(d) Ejemplos de características morfológicas de CEC oral con MCev. Muestras teñidas con naranja de acridina: pérdida de adhesión celular, pleomorfismo y anisocitosis celulares, aumento de la relación núcleo citoplasma, hipercromatismo nuclear, nucléolos prominentes, necrosis, mitosis anormales y aumentadas, y queratinización. X 4.5.

(Adaptado de Shavlokhova et al.,2021)[128]

Sin embargo, debe recordarse que la tinción digital es una aproximación a la tinción H&E que pretende facilitar la interpretación de las imágenes a aquellos patólogos que no están familiarizados con las imágenes en escala de grises o de fluorescencia en verde. En la tinción digital de la MCFu los colores no siempre corresponden a los mismos que se observan en la tinción de H&E.

En la piel normal, por ejemplo, somos capaces de distinguir en la MCFu los núcleos y nucléolos, así como todas las capas epidérmicas. Sin embargo, la elastosis solar no siempre aparecerá de color violeta en la tinción digital a pesar de que morfológicamente se muestra la substitución de las fibras normales en la dermis. (Figura 61) [54,70,129]

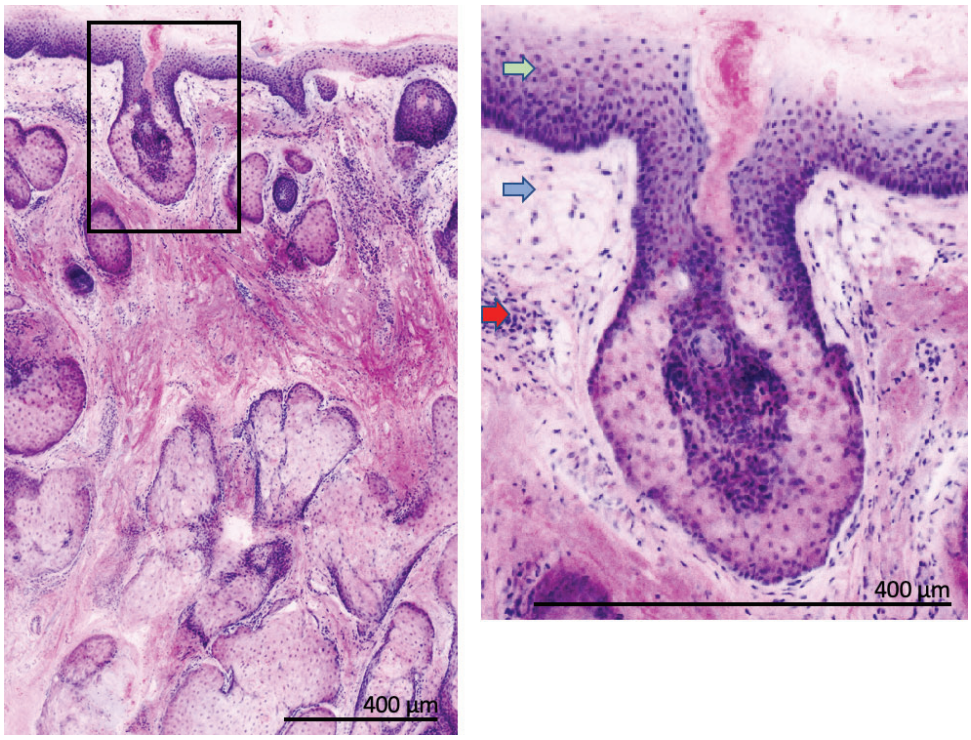

Figura 61. Piel normal. 4ª generación de microscopio confocal. Teñido con ácido acético y naranja de acridina. Flecha verde: Epidermis. Flecha azul: elastosis solar. Flecha roja: infiltrado inflamatorio. (Adaptado de Malvehy et al., 2020)[54]

En el carcinoma escamoso, los colores que se muestran en diferentes tonos de azul en la tinción con H&E a menudo aparecen en tonalidades de rosa en la técnica de MCev. La paraqueratosis presenta una variabilidad tonal, manifestándose en tonos tanto rosados como azules. Esta variación de colores, aún no completamente comprendida en los criterios diagnósticos principales de este tumor, puede dificultar su reconocimiento para el ojo no entrenado en la visualización digital de H&E. Tabla 5.[74,125] (Figuras 62 a 67)

Característica	H&E digital	H&E
Paraqueratosis	Identificable en baja magnificación	Identificable en baja magnificación
Pérdida de la granulosa	Identificable en baja magnificación	Identificable en baja magnificación
Queratinización	Varios grados de queratinización	Varios grados de queratinización
Puentes intercelulares	Observados en alta magnificación	Aparente
Disqueratosis	Queratinización prematura visible en mediana-alta magnificación	Queratinización prematura visible en baja-mediana magnificación
Pleomorfismo	Grados variables de diferenciación	Grados variables de diferenciación
Mitosis	Fácil de detectar en alta magnificación	Fácil de detectar en alta magnificación
Células dendríticas	Identificable en baja magnificación	Solo identificable con tinciones especiales
Bordes	Identificables	Identificables
Reacción estromal	Identificables	Identificables
Desmoplasia	Difícil de identificar	Fibrosis reactiva del estroma fácilmente identificable

Tabla 5. Diferencias encontradas entre las imágenes de hematoxilina y eosina en parafina y las de tinción digital de microscopía confocal *ex vivo* en el diagnóstico de carcinoma escamoso 4ª generación de microscopio confocal. Tinción comparada con ácido acético y naranja de acridina. (Adaptado de Pérez-Anker et al., 2021)[125]

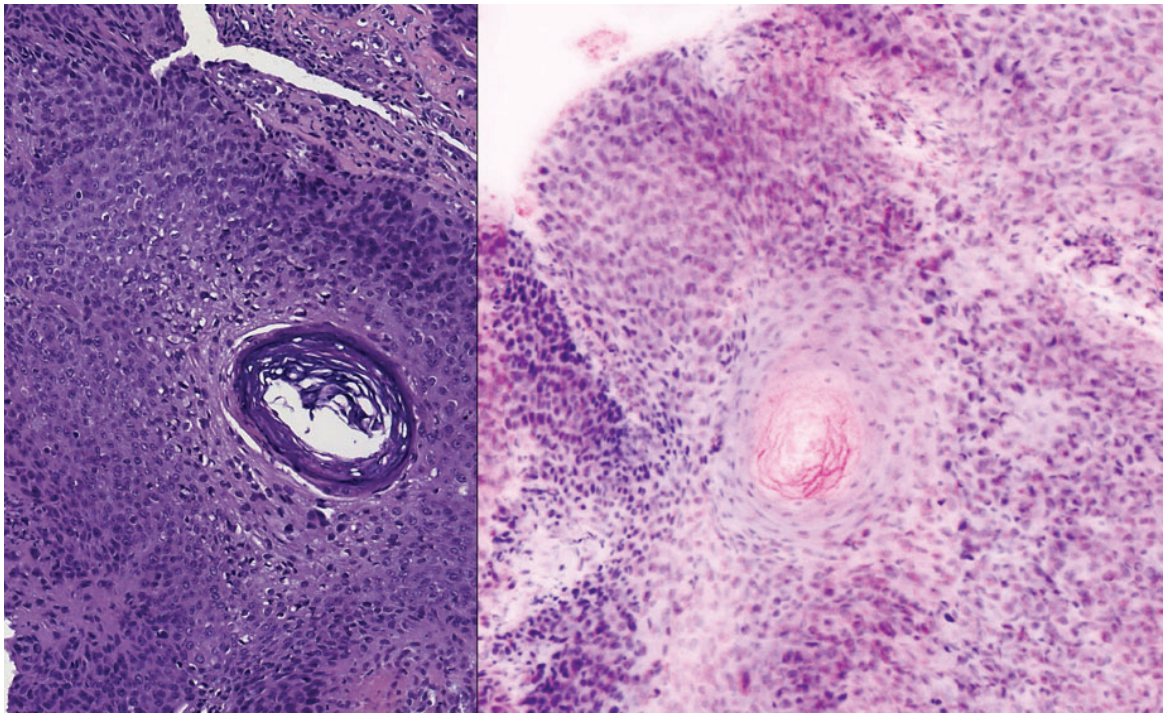

Figura 62. Detalle de la histología convencional (imagen de la izquierda) y de MCFu en un carcinoma escamoso. Los trastornos de la queratinización en la epidermis, la disqueratosis, la pérdida de la granulosa, el pleomorfismo celular, la presencia de mitosis, los bordes infiltrantes y la presencia de reacción estromal peri tumoral son en ambos casos. Se aprecian las diferencias en la tinción y los colores de ambas preparaciones de hematoxilina y eosina en parafina y las de tinción digital obtenida con MCeV de 4ª generación con ácido acético y naranja de acridina. (Adaptado de Pérez-Anker et al., 2021)[125]

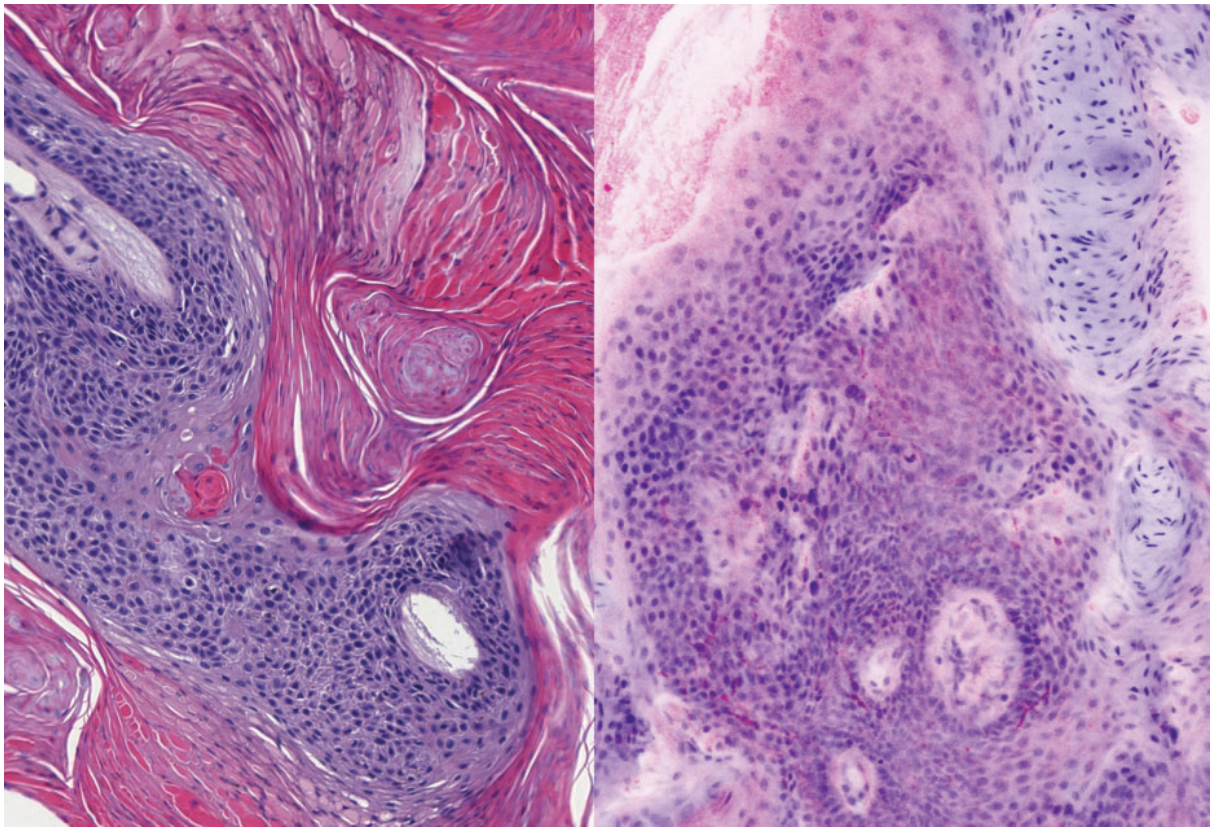

Figura 63. Diferencias encontradas entre las imágenes de hematoxilina y eosina en parafina (izquierda) y las de tinción digital de microscopía confocal *ex vivo* en el diagnóstico de carcinoma escamoso 4ª generación de microscopio confocal (derecha). Tinción comparada con ácido acético y naranja de acridina. Los trastornos de la queratinización en la epidermis, la paraqueratosis, la disqueratosis, la pérdida de la granulosa, el pleomorfismo celular, la presencia de mitosis, los bordes infiltrantes y la presencia de reacción estromal peri tumoral son observados en ambos casos. Las células dendríticas inflamatorias son evidentes sin tinciones especiales en la MCFu, adquiriendo el color rosado. Adaptado de Pérez-Anker J. et al., 2021) [125]

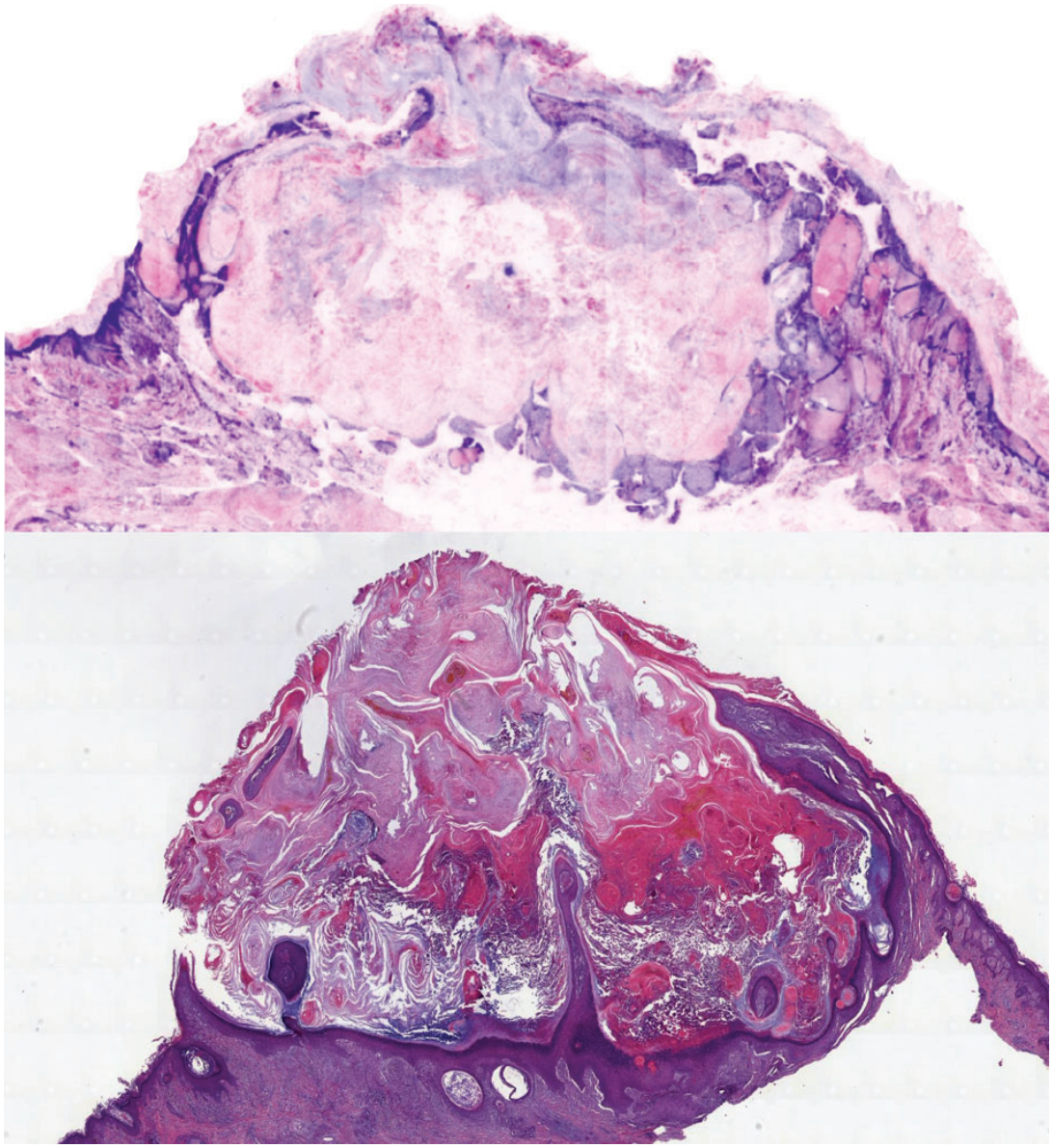

Figura 64. Diferencias encontradas entre las imágenes de hematoxilina y eosina en parafina y las de tinción digital de microscopía confocal *ex vivo* en el diagnóstico de carcinoma escamoso 4ª generación de microscopio confocal. Tinción comparada con ácido acético y naranja de acridina. Queratoacantoma. Imagen de macroscopia. (Adaptado de Pérez-Anker et al., 2021)[125]

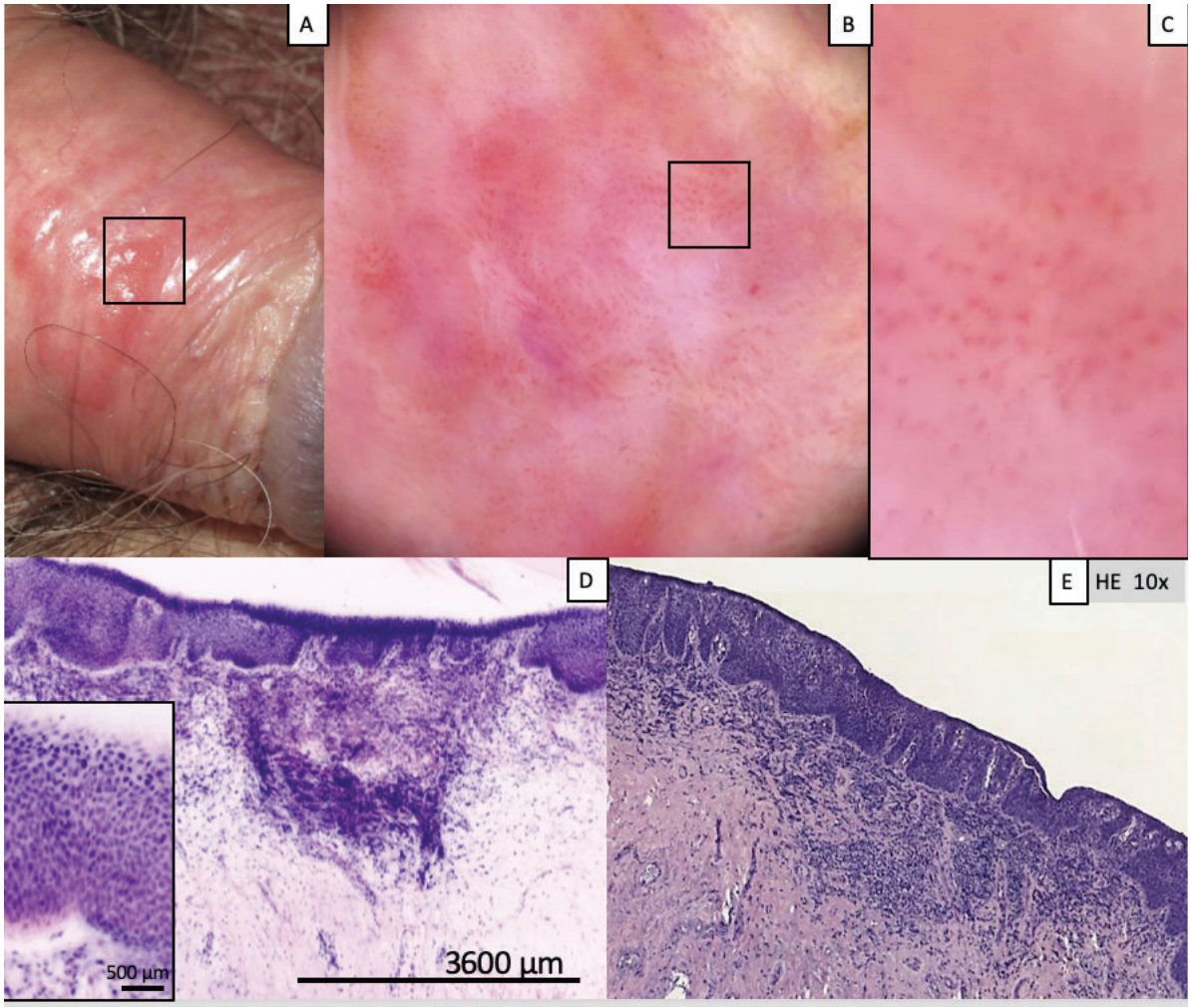

Figura 65. Carcinoma de Bowen. Foto clínica (A) y dermatoscópica (B y C). Comparación entre las imágenes obtenidas con confocal *ex vivo* (4ª generación de microscopio confocal. Tinción con ácido acético y naranja de acridina) (D) y hematoxilina y eosina (E). La acantosis psoriasiforme, la pérdida de la granulosa, el pleomorfismo celular, la presencia de mitosis, los bordes infiltrantes y la presencia de reacción estromal peri tumoral son claramente vistas. (Adaptado de Malvehy et al., 2020) [54]

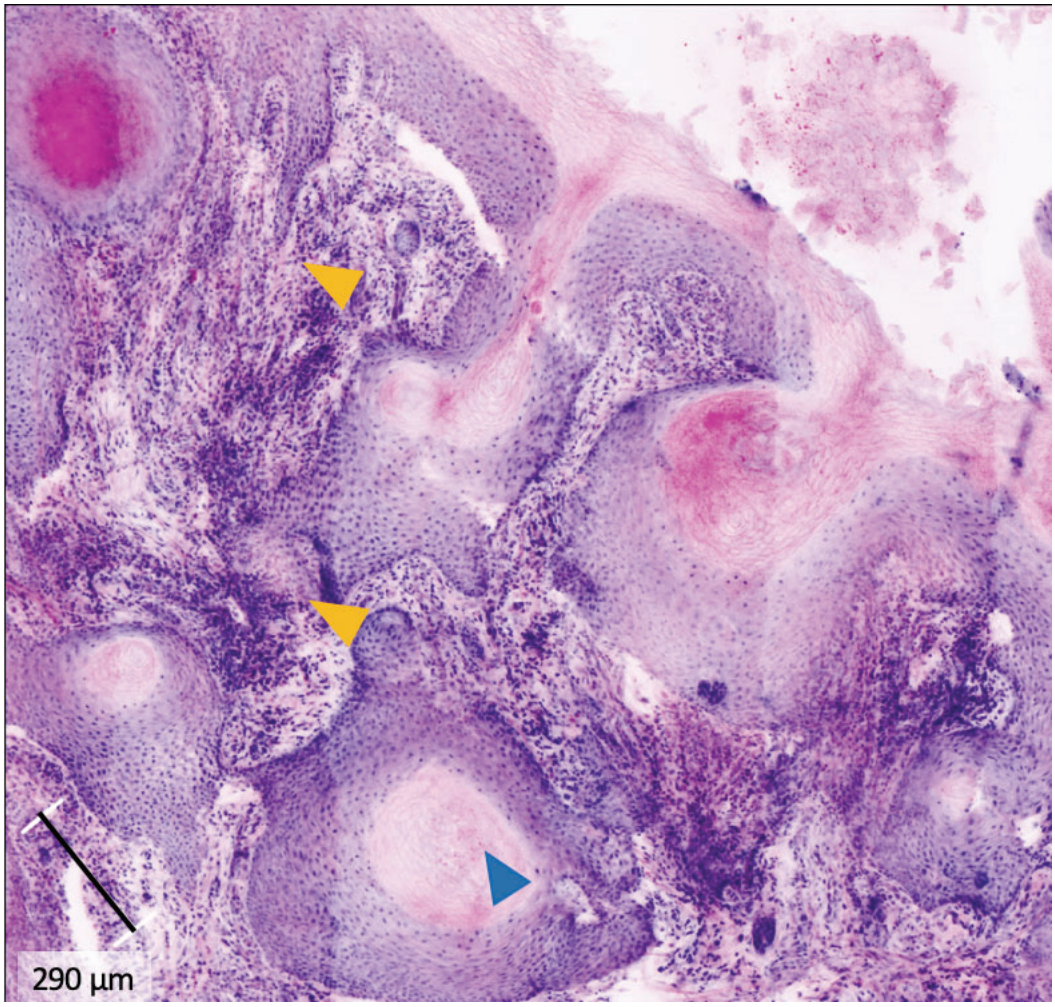

Figura 66. CEC bien diferenciado. Imagen de MCFu obtenida con un equipo de MCeV de 4ª generación de microscopio confocal. Tinción realizada con ácido acético y naranja de acridina. Los trastornos de la queratinización en la epidermis, la paraqueratosis, la disqueratosis, la pérdida de la granulosa, la presencia de puentes intercelulares, las perlas córneas, el pleomorfismo celular, la presencia de mitosis, los bordes infiltrantes y la presencia de reacción estromal peri tumoral son claramente vistas. Flecha amarilla: infiltración de CEC hacia dermis; Flecha azul: perlas de queratina. (Adaptado de Malvehy et al., 2020) [54]

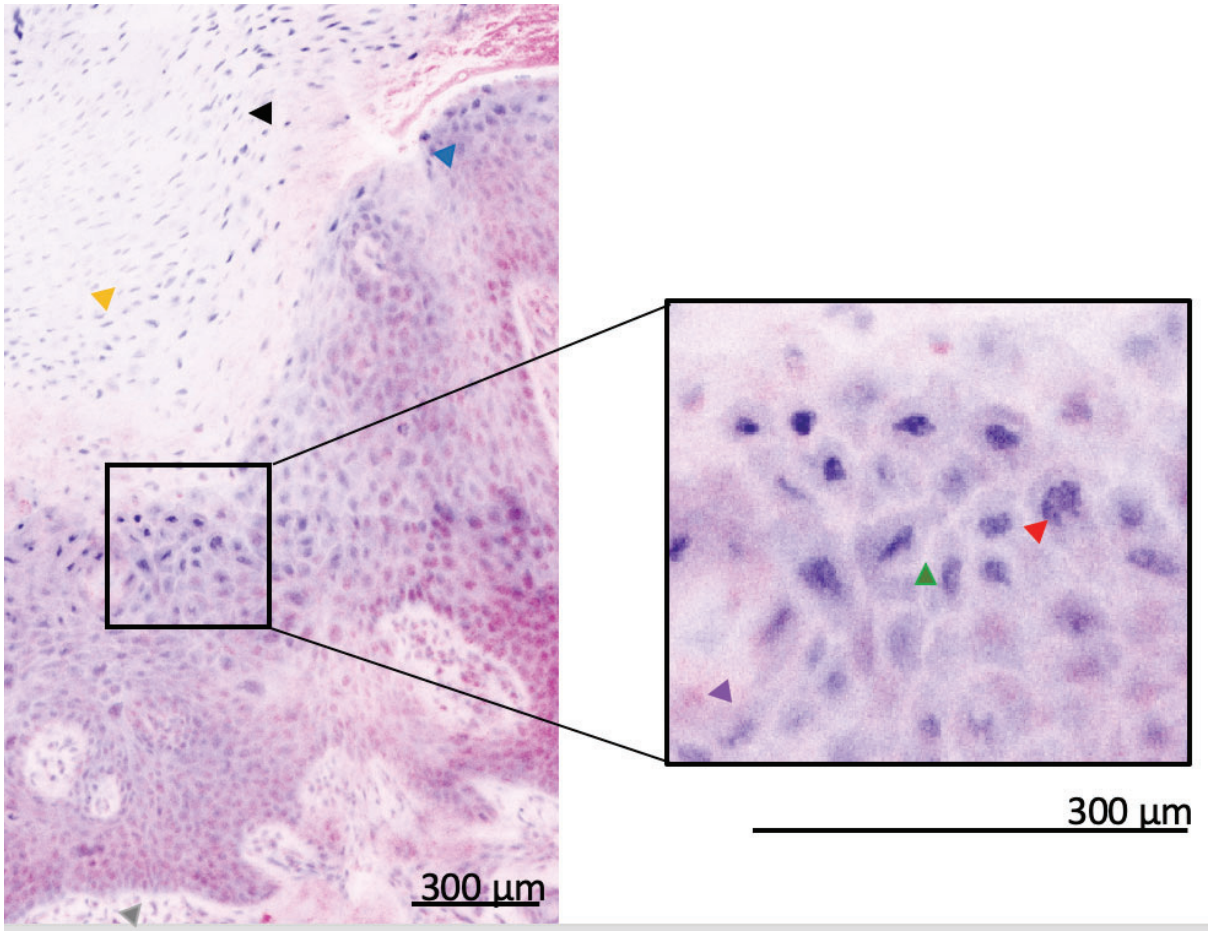

Figura 67. Alteraciones morfológicas y citológicas en un CEC. 4ª generación de microscopio confocal. Tinción con ácido acético y naranja de acridina. Flecha amarilla: paraqueratosis; flecha negra: hiperqueratosis; flecha gris: infiltrado inflamatorio peri tumoral; flecha azul: arquitectura irregular de la epidermis; flecha roja: pleomorfismo nuclear; flecha verde: puentes intercelulares; flecha violeta: disqueratosis. (Adaptado de Malvehy et al., 2020) [54]

En otros tumores, como en los diferentes subtipos de carcinoma basocelular, las características morfológicas como las islas tumorales bien delimitadas, con empalizada periférica y hendidura peri tumoral son distinguidas al igual que en la histología convencional. De la misma forma, las características citológicas y estromales se mantienen. Los carcinomas basocelulares superficiales, presentan un estroma más laxo, con abundantes células de infiltrado inflamatorio. Por otro lado, en los carcinomas basocelulares nodulares, se observan bandas de colágeno rodeando

claramente cada nido tumoral y en los infiltrantes, el estroma es denso, fibroplásico, casi acelular. Sin embargo, a pesar de estas características morfológicas semejantes, los colores del tumor tampoco son siempre equivalentes a la H&E convencional. [54,55] (Figura 68)

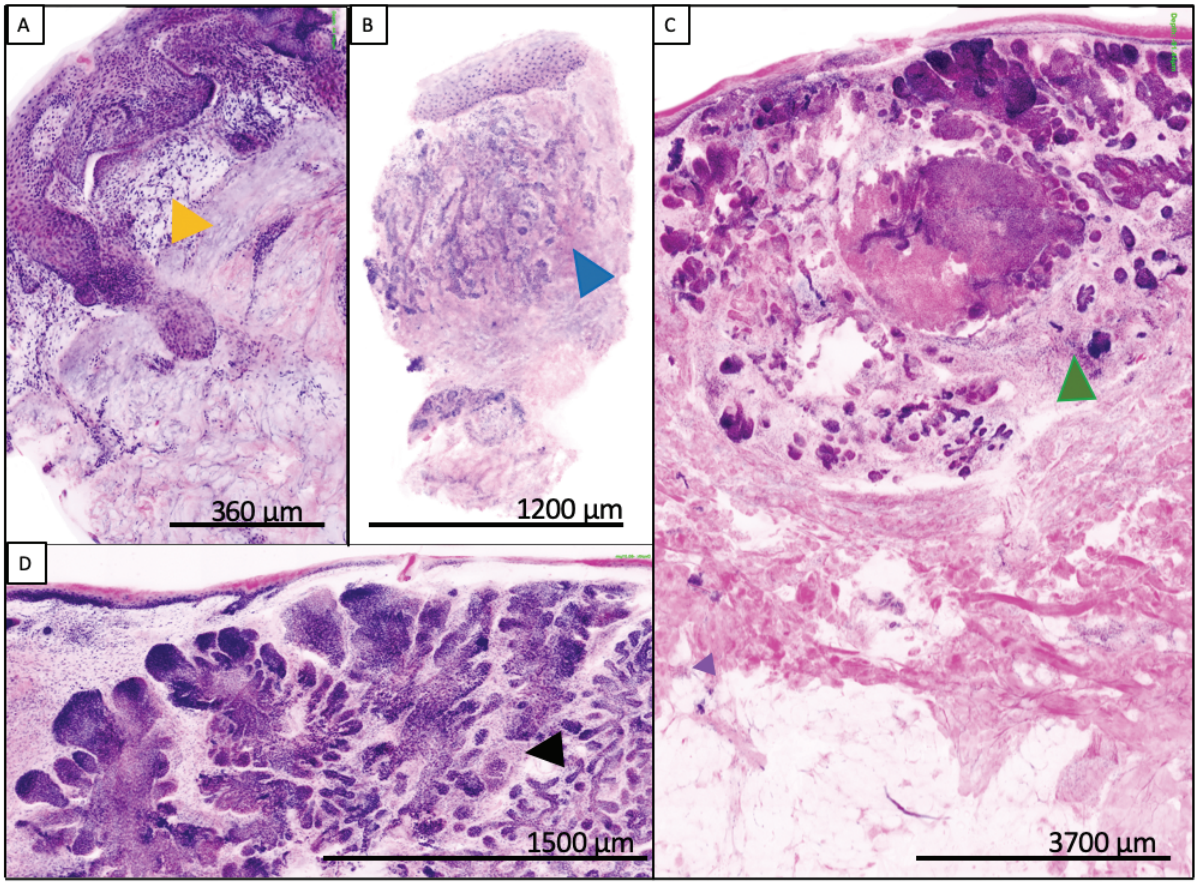

Figura 68. Diferentes subtipos de carcinoma basocelular. 4ª generación de microscopio confocal. Teñido con ácido acético y naranja de acridina. Flechas: diferentes tipos de carcinoma basocelular y su reacción estroma correspondiente. A: Superficial. B: Infiltrante. C: Nodular. D: Micronodular. (Adaptado de Malvehy et al., 2020) [54,55]

Este fenómeno no ocurre con el DFSP (Figuras 69 y 70), donde los colores se asemejan de forma considerable a los encontrados en la H&E convencional.

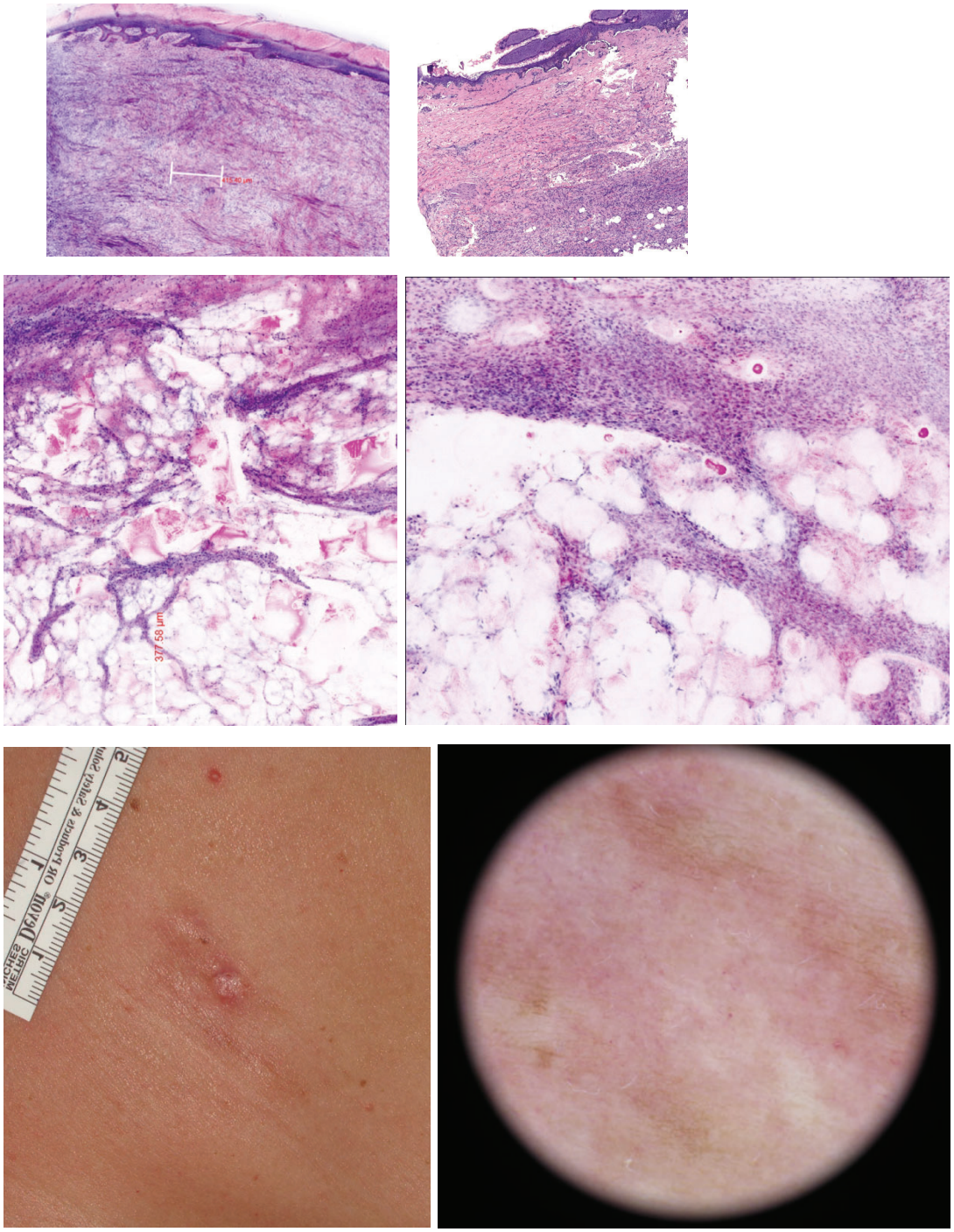

Figura 69. DFSP con MCev. Panel superior derecho, macro: H&E. Superior izquierdo: MCev: El aplanamiento de la epidermis se evidencia en ambas técnicas; Panel medio: Invasión a grasa subcutánea del DFSP evidenciado en MCev, caracterizada por celularidad fusiforme, monomorfa; Panel inferior derecho: dermatoscopia; panel inferior izquierdo: imagen clínica.

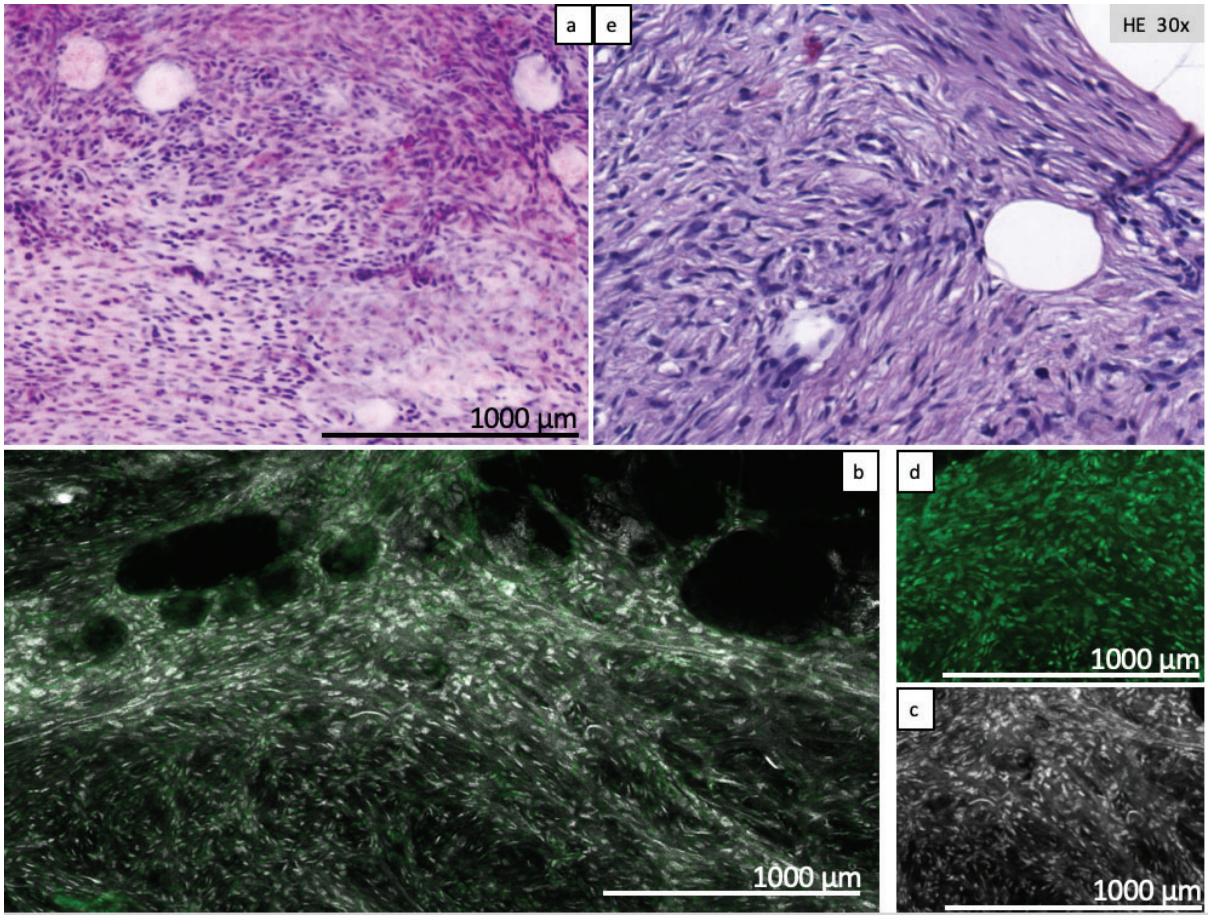

Figura 70. Dermatofibrosarcoma protuberans. 4ª generación de microscopio confocal. Tinción comparada con ácido acético y naranja de acridina. (a) Células fusiformes densas y uniformes, con núcleos grandes y alargados, con un bajo grado de variabilidad celular y poca atipia citológica, apreciadas en tinción digital de MCFu; (b) Los mismos detalles se observan con MCFu, sin la tinción digital;(c) Láser de reflectancia: se aprecia mejor la disposición linear de los agregados tumorales; (d) Láser de fluorescencia: los núcleos son mejor observados, pero se pierden detalles del estroma; (e) H&E de este tumor. (Adaptado de Malvehy et al., 2020) [54]

V.11. Algoritmo de inteligencia artificial para mejorar la tinción digital de las imágenes de la microscopía confocal ex vivo.

A pesar de los notables avances en tecnología y mejoras en la visualización de imágenes, sigue siendo esencial recibir capacitación en la técnica de MCev para garantizar la precisión en los diagnósticos. Esto se debe a las variaciones en la visualización de ciertos tejidos que aún existen, como ha sido anteriormente explicado.

Por otro lado, la aplicación de técnicas de IA para mejorar las imágenes digitales y así poder reproducir con más fidelidad una tinción semejante a la de H&E (como de cortes procesados con parafina), eliminaría la necesidad de entrenamientos específicos en imágenes de MCev.

En este trabajo de tesis, se incluyen colaboraciones con otros grupos de trabajo que participan en el desarrollo de IA. Es importante destacar que, hasta la fecha de este escrito, no se ha llevado a cabo ningún estudio similar a los que se abordan en esta propuesta.

Por medio de técnicas de aprendizaje profundo, se logró describir un algoritmo que permite retirar el ruido de las imágenes para luego obtener una imagen final mejorada casi idéntica a la H&E convencional, con respecto al color y los detalles celulares. [75,130] (Figura 71)

Sin embargo, al trabajar con algoritmos de inteligencia artificial, es fundamental analizar posibles sesgos en los resultados. Existe un riesgo inherente de que los algoritmos produzcan "alucinaciones" con el objetivo de mejorar la calidad

de la imagen, introduciendo información en la imagen que no se corresponde con el tejido. Por lo que se requieren más estudios para validar nuestro trabajo preliminar, incluyendo una gran cantidad de imágenes de alta calidad y correctamente teñidas con H&E, para entrenar al algoritmo de manera precisa.

En un primer estudio de validación, en un 20% de las veces, los observadores no fueron capaces de diferenciar entre ambas tinciones. (Figura 72)

En próximos estudios, implementaremos nuevos mecanismos de validación y verificación, con el apoyo de más expertos, para evaluar la calidad de los resultados producidos por el algoritmo. A pesar de aun ser un estudio preliminar, el desarrollo de este algoritmo ha abierto una prometedora línea de investigación, con potencial aplicación en dermatopatología y patología general.

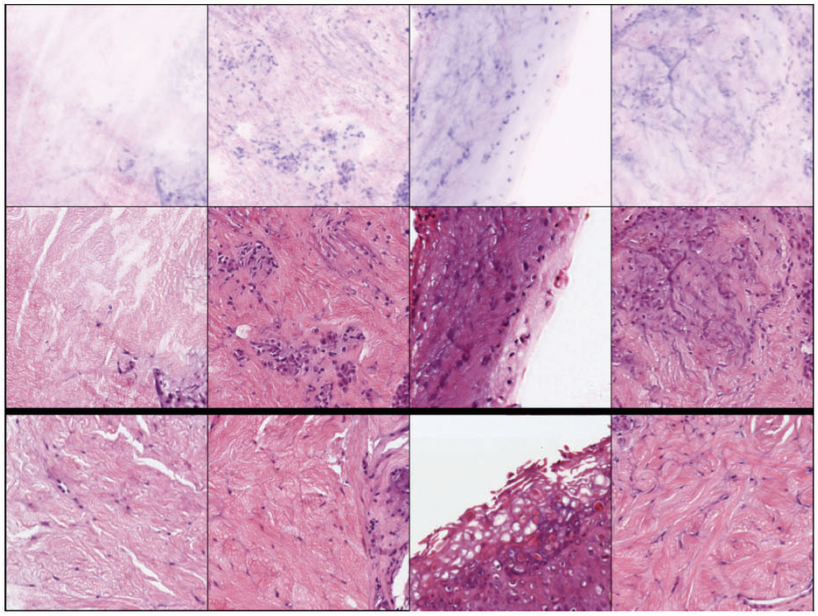

Figura 71. Mediante Deep Learning, los colores de los tejidos escaneados pueden ser modificados. Fila superior: colores de confocal *ex vivo* 4ª generación, de un tejido escaneado de forma inadecuada. Fila del medio: Colores modificados por algoritmos de Deep Learning que permitieron un aspecto mucho más real, y parecido con la tinción de hematoxilina y eosina (fila inferior). (Adaptado de Combalia M. et al., 2019).[75]

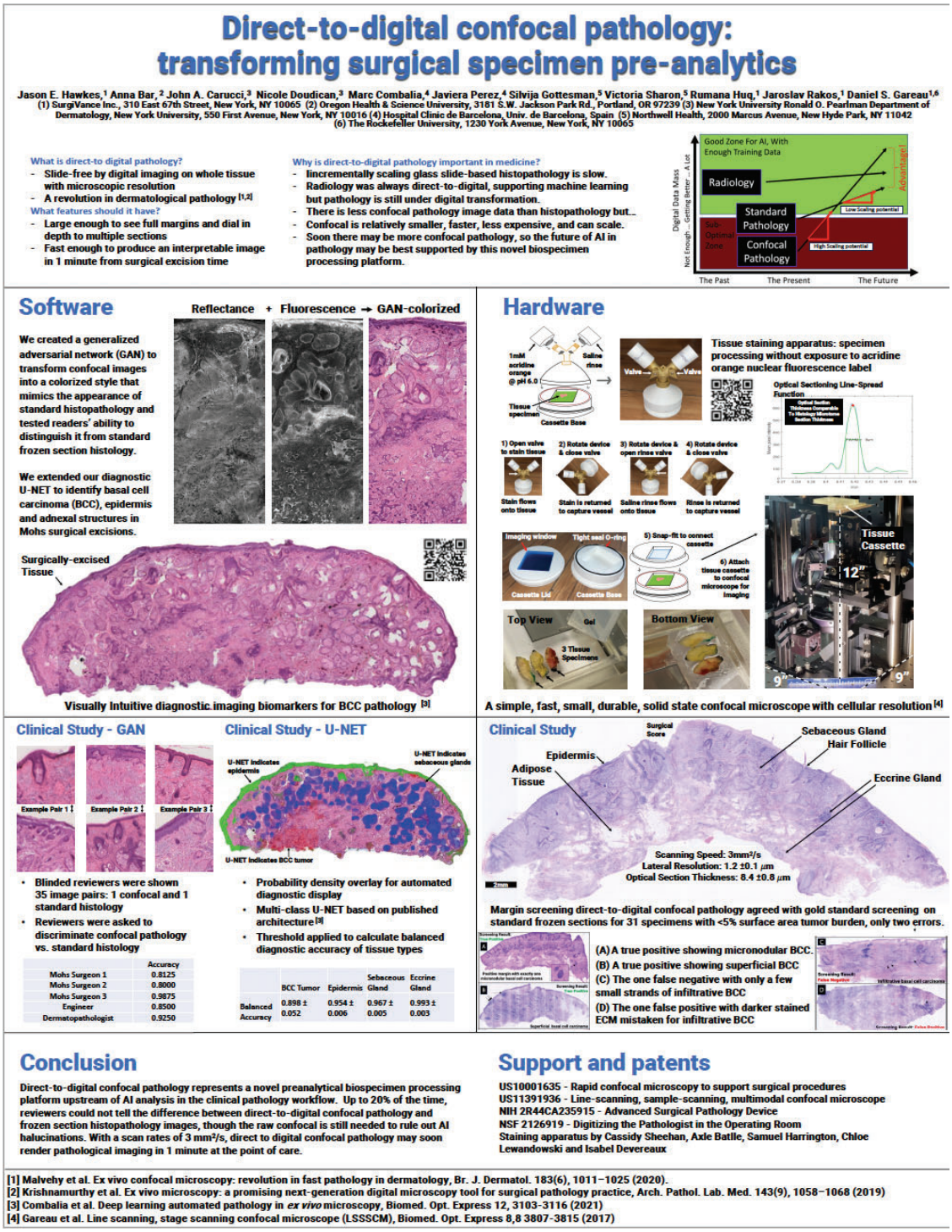

Figura 72. Poster presentado en 9th Digital Pathology & AI Congress, Junio 22 & 23, NY, USA. Por primera vez, se ha intentado validar el mecanismo de tinción digital on observadores independientes. En un 20% de las veces, los observadores no fueron capaces de distinguir entre ambas lesiones.

Con respecto al diagnóstico inmediato con inteligencia artificial, Combalia y colaboradores[130] demostraron que, por medio de IA con aprendizaje profundo, también eran capaces de, no solo mejorar la tinción digital para que fuera más fiel a los cortes histológicos en parafina, sino que también obtener diagnósticos instantáneos en esta tinción. (Figuras 73 y 74)

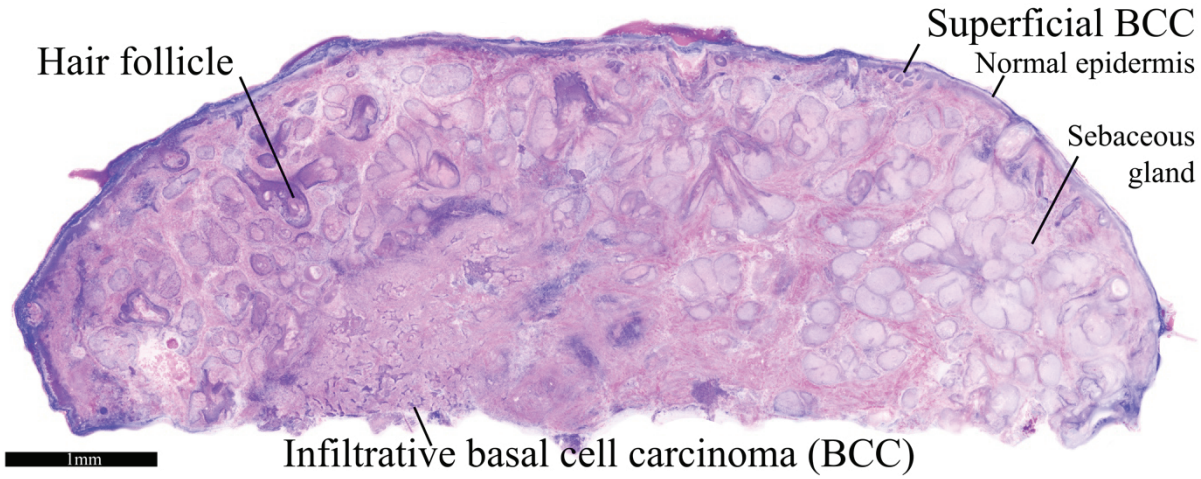

Figura 73. Diagnóstico de carcinoma basocelular mediante Deep Learning. El algoritmo propuesto pudo diferenciar entre la presencia de tumor, del resto de estructuras normales. (Adaptado de Combalia M et al., 2021)[130]

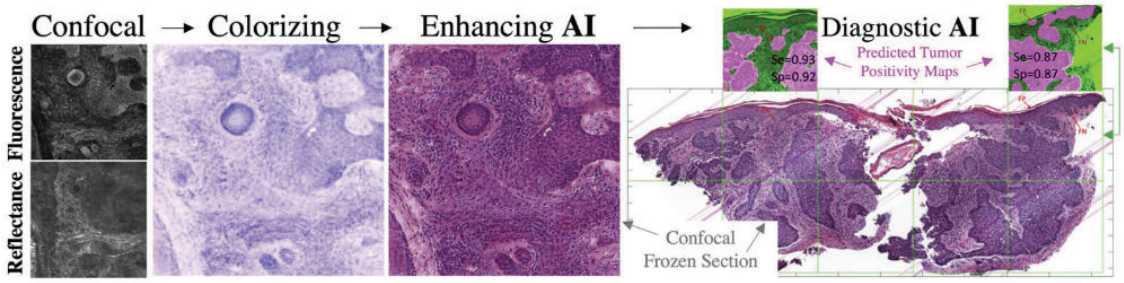

Figura 74. Diagnóstico de carcinoma basocelular mediante Deep Learning. EL Proceso de diagnóstico aplicado se ha basado en la diferenciación de estructuras macroscópicas. (Adaptado de Combalia M et al., 2021)[130]

Un estudio previo donde se estudió el diagnóstico de CEC,[131] aplicando IA sin una tinción mejorada, otro grupo de investigación que solo consideró las imágenes macroscópicas se encontró con el hecho de que el algoritmo interpretaba como tumorales, sectores que en realidad correspondían a glándulas sebáceas. (Figura 75)

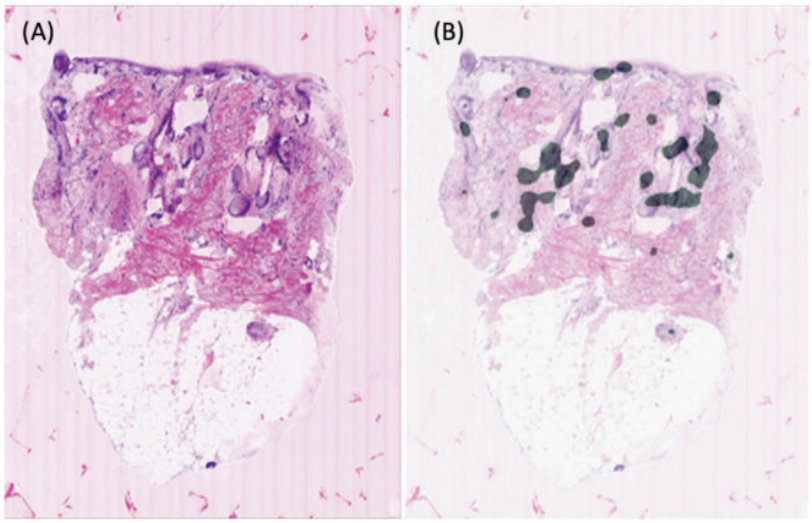

Figura 75. El algoritmo de inteligencia artificial en carcinomas escamosos ha detectado como tumor, la presencia de glándulas sebáceas. (Adaptado de Ruini et al., 2021)[131]

Otro estudio semejante a este ha sido recientemente propuesto para CBC,[132] pero, en este caso, 3 modelos fueron comparados (muestra de solo MCev, muestra de solo H&E y combinados). El algoritmo de aprendizaje profundo, entrenado con el conjunto de datos, MCev logró una precisión diagnóstica del 92%, que fue comparable a la precisión del modelo H&E del 93%. El área bajo la curva AUC-ROC fue de 0,94 para el modelo entrenado con MCEV, 0,95 para el modelo entrenado con H&E y 0,94 para el modelo entrenado con la combinación de ambos. Esto indica que el algoritmo tuvo buen desempeño en distinguir el CCB de las muestras negativas en las imágenes MCEV.

Con la realización de más estudios de validación y el desarrollo de nuevos algoritmos, es posible que, en el futuro, podamos aplicar directamente estos algoritmos a dispositivos de MCev, lo que nos permitiría una aproximación diagnóstica casi inmediata.

V.12. Fortalezas y limitaciones de la MCev

Mediante la realización de estos estudios adicionales, hemos examinado la robustez y la aplicabilidad de estos métodos en el ámbito de la patología general. Esto implicó confirmar que los procedimientos utilizados, anteriormente descritos, funcionan de manera consistente y producen resultados confiables en diferentes tipos de muestras y condiciones. Si bien existen diferencias significativas entre los diferentes campos de la medicina, también hay conceptos y principios fundamentales que pueden ser transferidos y aplicados de manera efectiva.

Si bien nuestros resultados son alentadores es importante destacar que se deben realizar estudios adicionales para respaldar aún más la efectividad y confiabilidad de nuestras investigaciones.

La implementación del diagnóstico instantáneo mediante MCev tiene un impacto clínico significativo en varios aspectos de la atención médica, permitiendo establecer conductas inmediatas, evitando consultas posteriores y la dilatación del tratamiento. Esto no solo ahorra tiempo, sino que también reduce los costos asociados con visitas y pruebas repetidas. Además, evita la incomodidad y la ansiedad causadas por la incertidumbre del diagnóstico y la espera prolongada.

Los laboratorios de anatomía patológica también experimentan un cambio significativo con la implementación de esta tecnología. Al eliminar la necesidad de procesar muestras y realizar análisis posteriores, se reducen los costos y el tiempo necesario para generar informes patológicos. Esto puede tener un impacto positivo en la capacidad del laboratorio para manejar un mayor volumen de muestras y reducir las listas de espera, lo que beneficia a los pacientes y a los médicos que dependen de los resultados patológicos para el manejo clínico. Permite, además, el uso de menos material fungible, evitando daños segundarios al medio ambiente por el excesivo descarte de materiales contaminantes.

A pesar de las enormes ventajas del análisis inmediato de una muestra por MCev, y de la definición celular que permite ver detalladamente estructuras nucleares, esta técnica también presenta algunas limitaciones:

- Limitación de la profundidad de penetración: La microscopía confocal utiliza una técnica de escaneo punto por punto, lo que significa que sólo se puede

obtener información de la capa superficial de la muestra. La luz se enfoca en un punto específico y, debido a la dispersión y absorción de la luz en los tejidos, la profundidad de penetración está limitada a unos pocos cientos de micrómetros. Esto puede ser insuficiente para examinar estructuras más profundas en la muestra.

- Artefactos de la muestra: Al analizar muestras *ex vivo*, pueden ocurrir cambios y alteraciones en la muestra debido a la manipulación, la fijación o la preparación de la muestra. Estos artefactos pueden afectar la calidad de la imagen y distorsionar la información obtenida.
- Artefactos en la obtención de la muestra: pequeñas variaciones en la intensidad de los láseres y la profundidad de escaneo pueden afectar la calidad de las imágenes. La estandarización de la técnica y la capacitación adecuada del técnico son fundamentales para minimizar estos artefactos y obtener muestras de alta calidad para su correcta interpretación.
- Necesidad de marcadores y tinciones: En muchos casos, en el estudio histológico para resaltar estructuras específicas en la muestra, se requiere el uso de marcadores fluorescentes o de tinciones específicas que se unan a ciertos componentes celulares. Es posible producir tinciones específicas celulares (nucleares o citoplasmáticas) para MCeV. Para su aplicación en la práctica clínica, estas tinciones específicas deberán estandarizarse y permitir un análisis rápido de las muestras.

- Ausencia de dinámica *in vivo*: Al examinar muestras ex-vivo del organismo, no se puede observar el tejido *in vivo* en tiempo real y el componente vascular y la interacción de los componentes celulares. Al igual que la histopatología convencional, la microscopía confocal *ex vivo* proporciona una imagen estática de la muestra en un momento específico, lo que limita la capacidad de estudiar

procesos dinámicos y en tiempo real tridimensional. Las células a menudo interactúan con su entorno y con otras células vecinas, y estas interacciones son importantes para comprender la función y el comportamiento celular (p.e.el tráfico leucocitario endotelial o transendotelial).

En resumen, la aplicación de diversas tecnologías de imagen en un único tumor muestra las diferentes perspectivas de cada técnica. (Figura 76) Ilustramos cómo un carcinoma basocelular puede presentarse de manera notablemente diferente según la técnica in vivo utilizada. Además, cada una de estas técnicas proporciona información complementaria y valiosa para el abordaje clínico del paciente en la práctica médica.[50]

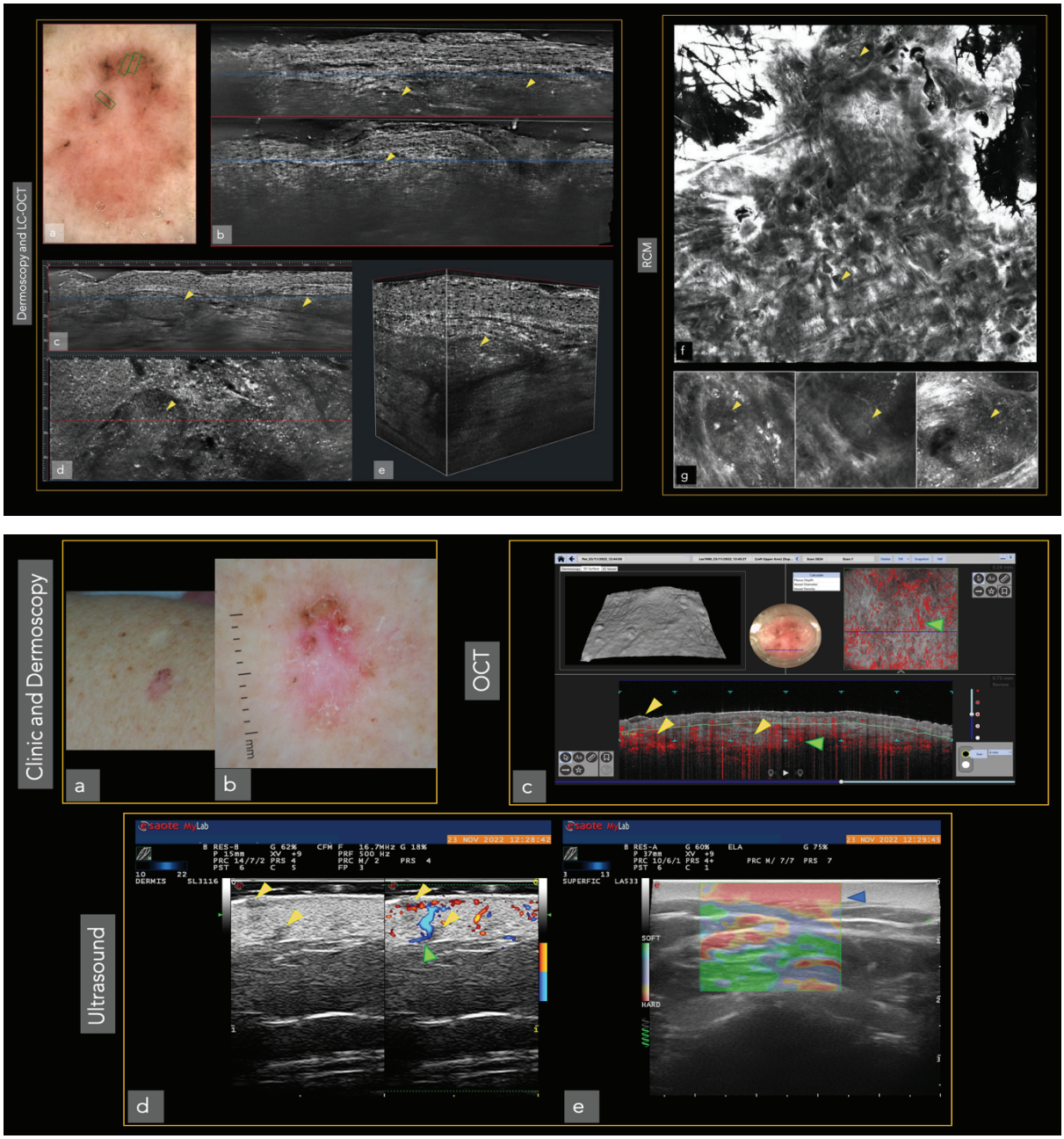

Figura 76. Resumen de técnicas de imagen más utilizadas en dermatología. Imagen macroscópica del mismo CBC en cada una de ellas: Dermatoscopia, TCO-CL, MCR, OCT, Ecografía, Ecografía con elastografía. Las técnicas se complementan entre sí, aportando diferentes detalles macroscópicos y microscópicos. (Adaptado de Soglia et al., 2022)[50]

V.13. Perspectivas futuras

- Validar la capacidad diagnóstica del MCev y del TCO-CL y la reproducibilidad de los criterios diagnósticos de patología para MCev y TCO-CL, en patología inflamatoria y tumoral.

- Evaluar la repercusión asistencial, así como la sensibilidad y especificidad diagnóstica del MCev durante 7 años en cirugía de Mohs. (Figuras 81 y 82)

- Realizar estudios multicéntricos de ambas técnicas, con muestras estandarizadas (con la misma calidad en todos los centros), de manera a evaluar resultados basados en muestras iguales.

- Validar los algoritmos de inteligencia artificial. Confrontar máquinas con especialistas, en ambas técnicas.

- Mejorar la colaboración interdisciplinaria en ambas técnicas, tal como lo hemos hecho previamente en áreas como nefrología, gastroenterología y patología mamaria.[133-137.] (Figuras 79 a 85)

- Desarrollo de nuevos protocolos de tinción específicos para diferentes tejidos y muestras en MCev y proponer tinción con IA en TCO-CL.

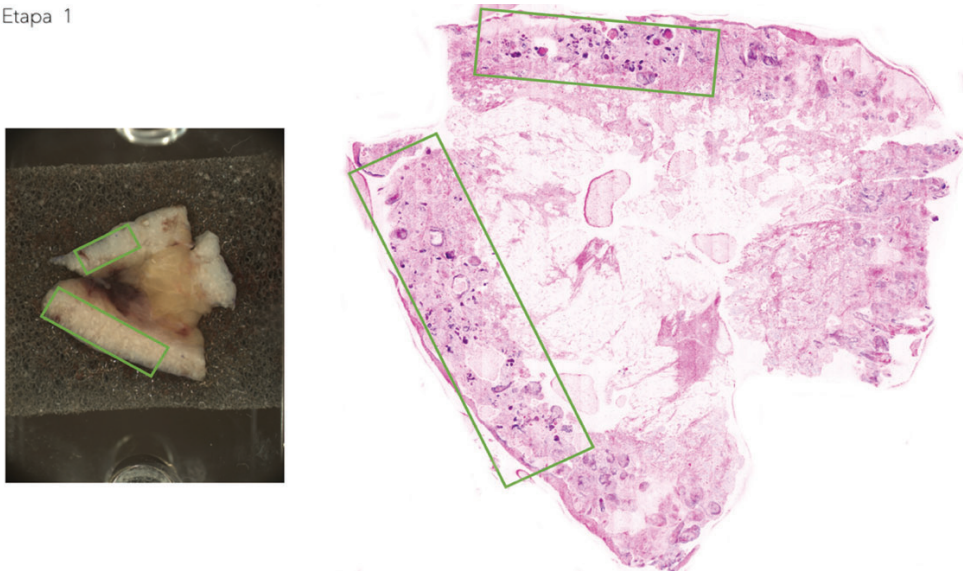

Figura 77. Imagen de una cirugía de Mohs realizada con MCev. La positividad de la imagen escaneada – cuadrado verde (derecha), se corresponde exactamente con la imagen macroscópica (izquierda), permitiendo una correlación precisa en el caso de positividad de márgenes. Corresponde a 1X de H&E. (Fuente: Javiera Pérez-Anker)

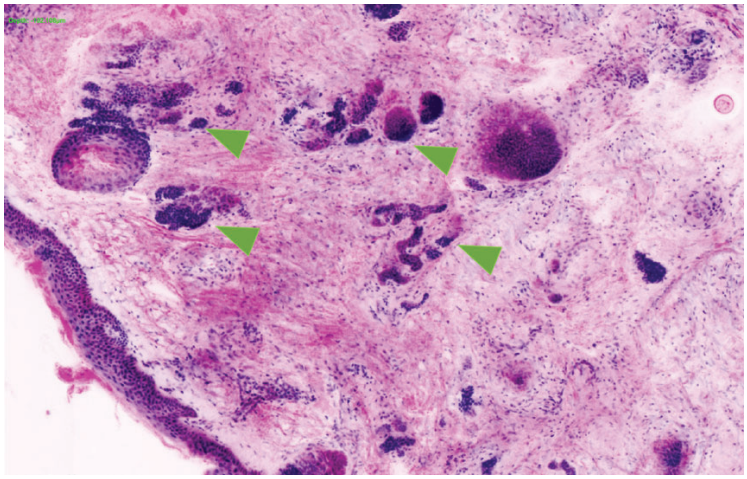

Figura 78. Carcinoma basocelular infiltrante. Cirugía de Mohs de 7 etapas, realizada en una hora y 35 minutos, incluyendo la reconstrucción mediante colgajo de avance. La aplicación de esta técnica al lado del paciente permite una inmediatez en el diagnóstico. El carcinoma basocelular micronodular puede también ser evidenciado en la periferia de los anejos. Flecha verde. (Corresponde a 4X de H&E. Fuente: Javiera Pérez-Anker).

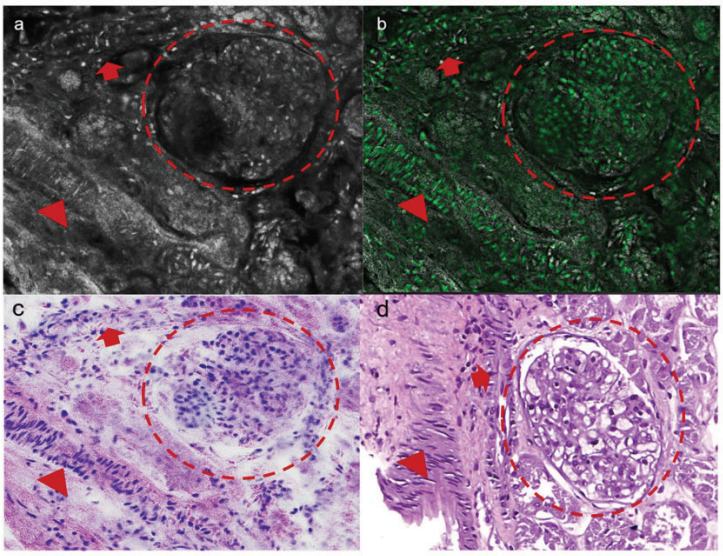

Figura 79. MCev de un glomérulo normal (círculo rojo). Arteria interlobulillar (triangulo rojo) y arteriola normal (flecha roja). 400X. (a) MCR; (b) MCFu; (c) MCFu con tinción digital; (e) H&E correspondiente. (Adaptado de Villarreal et al., 2020)[133]

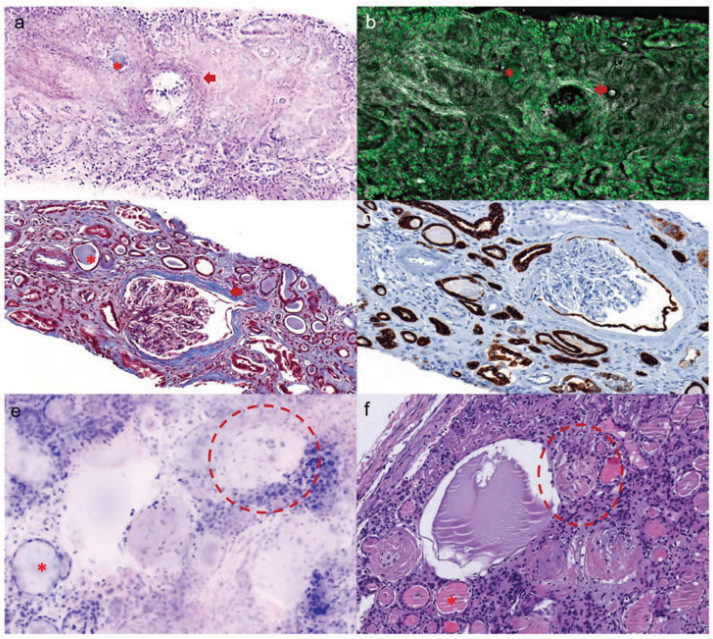

Figura 80. Primer estudio comparativo entre técnicas. (a) Lesiones crónicas pueden ser evaluadas (flecha roja); (b) Ejemplos de atrofia tubular (asterisco rojo), asociada a fibrosis intersticial; Comparación con tinción de Masson (d); (e)fibrosis peri glomerular /asterisco rojo) y glomeruloesclerosis global (círculo rojo). 200X. (Adaptado de Villarreal et al., 2020) [133]

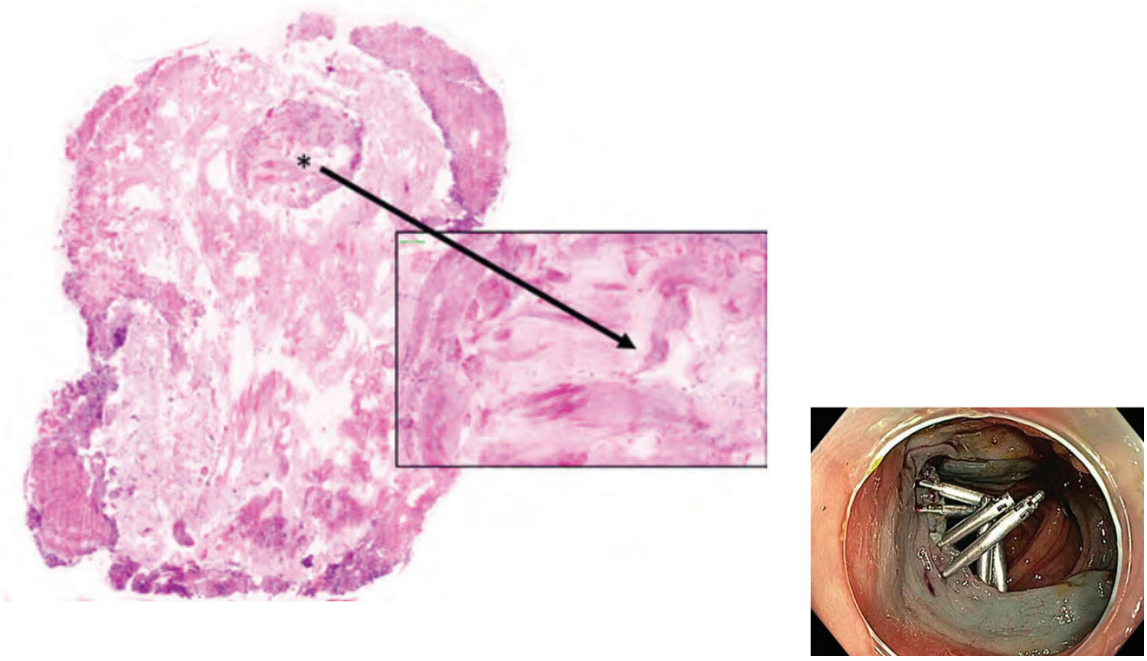

Figura 81. Muscularis propia diagnosticando una perforación durante una endoscopia. El diagnóstico inmediato ha permitido la reparación del defecto. 20X. (Adaptado de: Pérez-Anker et al., 2020) [135]

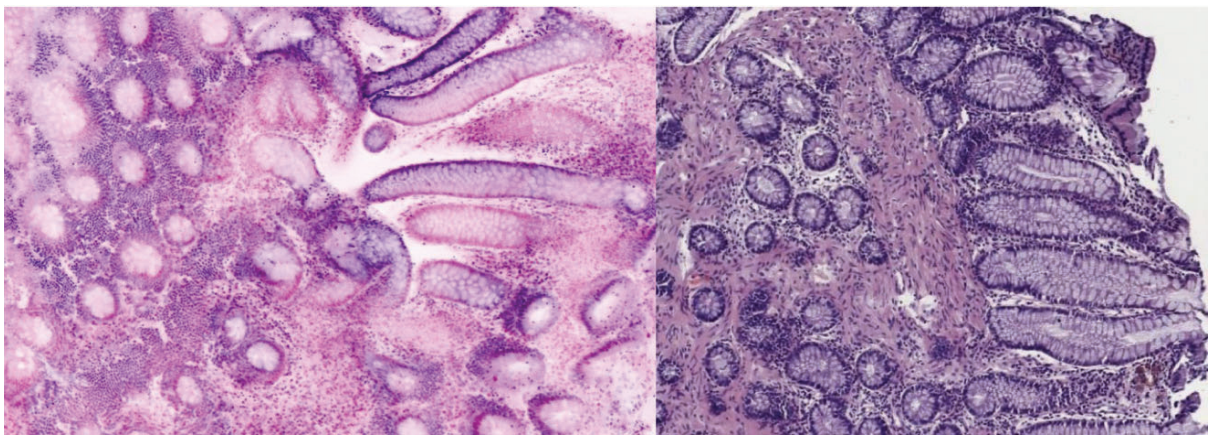

Figura 82. Mucosa normal de colon. Izquierda: microscopia confocal *ex vivo*. Derecha: hematoxilina y eosina. (Adaptado de: Guerrero et al., 2021)[136]

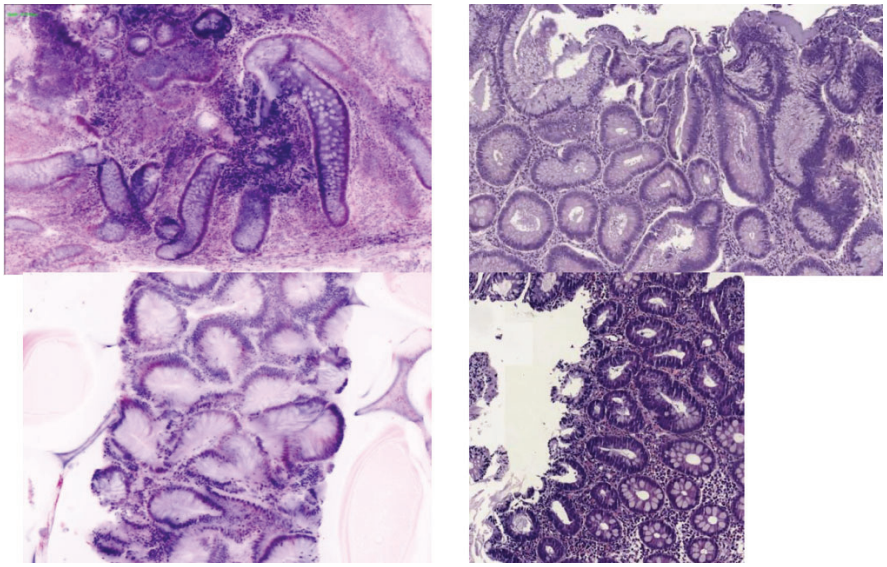

Figura 83. Displasia de bajo grado de colon. Izquierda: microscopia confocal *ex vivo*. Derecha: hematoxilina y eosina. Los detalles celulares se correlacionan de forma adecuada en ambas técnicas. 100X. (Adaptado de: Guerrero et al., 2021)[136]

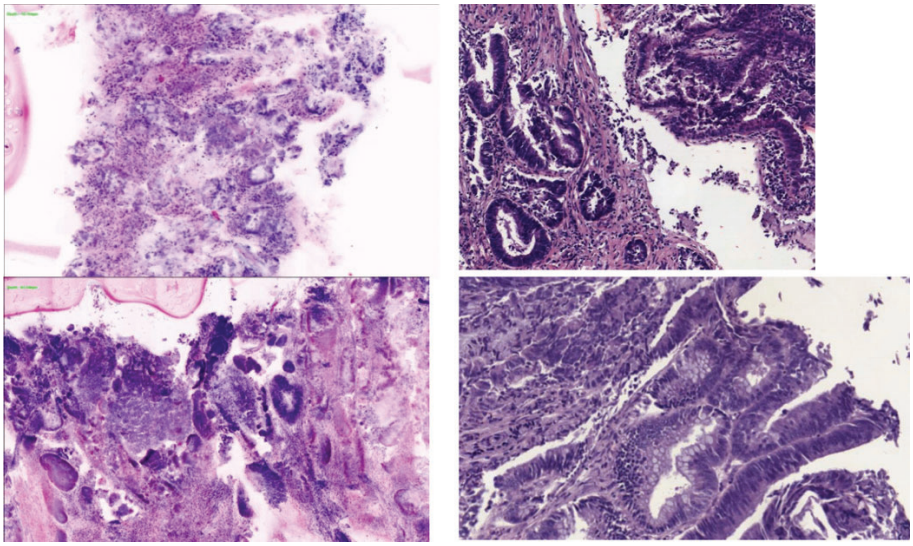

Figura 84. Displasia de alto grado de colon. Izquierda: microscopia confocal *ex vivo*. Derecha: hematoxilina y eosina. El desorden arquitectural y citológico se mantiene en ambas técnicas. 100X. (Adaptado de: Guerrero et al., 2021)[136]

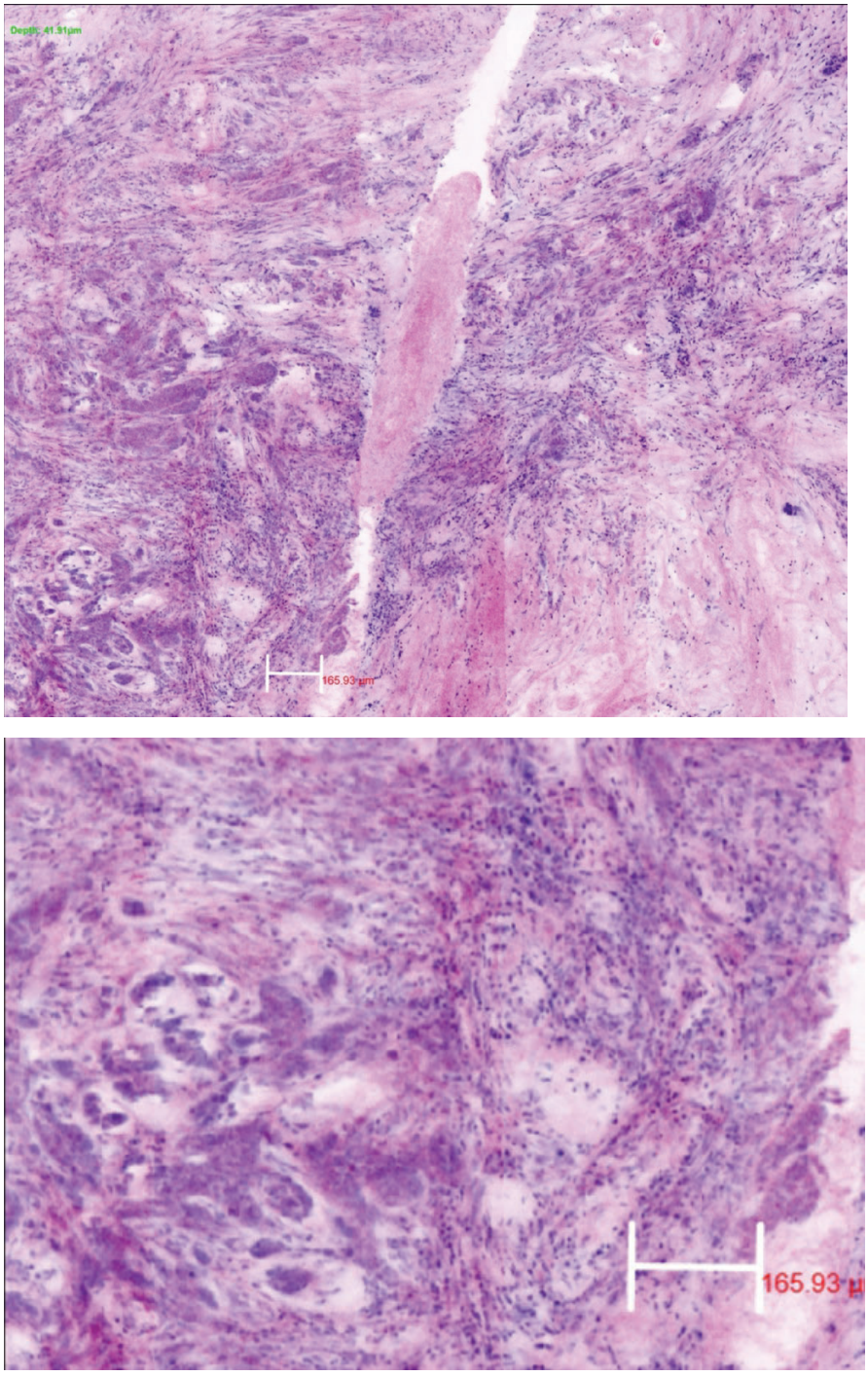

Figura 85. Vista macroscópica (superior) y microscópica (inferior) de un carcinoma ductal infiltrante de mama. Las células tumorales invaden el tejido mamario en forma de cordones. (Fuente: Javiera Pérez-Anker)

VI. CONCLUSIONES

1. Se estableció una correlación entre criterios morfológicos y citológicos en lesiones melanocíticas, utilizando diversas técnicas de imagen, incluyendo tomografía de coherencia óptica de campo lineal, microscopía confocal de reflectancia e histología convencional.

2. Logramos la visualización tridimensional de criterios dermatoscópicos en lesiones melanocíticas mediante tomografía de coherencia óptica de campo lineal, proporcionando una mejor comprensión de las estructuras morfológicas y citológicas.

3. Identificamos criterios diagnósticos, tanto estructurales como citológicos, que permiten diferenciar entre lesiones melanocíticas benignas, atípicas y malignas, destacando la importancia de la presencia de una "hendidura" como indicador de malignidad e invasión en profundidad.

4. Se desarrollaron algoritmos de inteligencia artificial para la diferenciación entre campo de cancerización y queratosis actínica, utilizando tomografía de coherencia óptica de campo lineal.

5. Propusimos un nuevo protocolo de tinción en microscopía confocal ex vivo que mejora la visualización de nidos de carcinoma basocelular y proporciona una mejor caracterización de este tipo de tumor, junto con la identificación de nuevos criterios diagnósticos.

6. Patentamos un dispositivo que facilita el aplanamiento de muestras previo al escaneo en microscopía confocal ex vivo, junto con un protocolo estandarizado para la obtención sistematizada y homogénea de muestras.

7. Evaluamos la precisión diagnóstica de la microscopía confocal ex vivo en biopsias de lesiones equívocas de carcinoma escamoso. Comparamos los criterios diagnósticos con los encontrados en histología convencional.

8. Se desarrolló un algoritmo de inteligencia artificial que permite visualizar las imágenes escaneadas en colores similares a la histología convencional, lo que facilita la interpretación de los resultados.

VII. BIBLIOGRAFIA

1 Yélamos O, Braun RP, Liopyris K, Wolner ZJ, Kerl K, Gerami P, Marghoob AA. Dermoscopy and dermatopathology correlates of cutaneous neoplasms. J Am Acad Dermatol. 2019 Feb;80(2):341-363. doi: 10.1016/j.jaad.2018.07.073. Epub 2018 Oct 13. PMID: 30321581.

2 Perino F, Suarez R, Perez-Anker J, Carrera C, Rezze GG, Primiero CA, Alos LL, Díaz A, Barreiro A, Puig S, Peris K, Malvehy J. Concordance of in vivo reflectance confocal microscopy and horizontal-sectioning histology in skin tumours. J Eur Acad Dermatol Venereol. 2024 Jan;38(1):124-135. doi: 10.1111/jdv.19491. Epub 2023 Sep 26. PMID: 37669864.

3 Álvarez-Salafranca M, Ara M, Zaballos P. Dermoscopy in Basal Cell Carcinoma: An Updated Review. Actas Dermosifiliogr (Engl Ed). 2021 Apr;112(4):330-338. English, Spanish. doi: 10.1016/j.ad.2020.11.011. Epub 2020 Nov 28. PMID: 33259816.

4 Que SKT. Research Techniques Made Simple: Noninvasive Imaging Technologies for the Delineation of Basal Cell Carcinomas. J Invest Dermatol. 2016 Apr;136(4):e33-e38. doi: 10.1016/j.jid.2016.02.012. PMID: 27012561.

5 Lan J, Wen J, Cao S, Yin T, Jiang B, Lou Y, Zhu J, An X, Suo H, Li D, Zhang Y,

Tao J. The diagnostic accuracy of dermoscopy and reflectance confocal microscopy for amelanotic/hypomelanotic melanoma: a systematic review and meta-analysis. Br J Dermatol. 2020 Aug;183(2):210-219. doi: 10.1111/bjd.18722. Epub 2019 Dec 22. PMID: 31747045.

6 Longo C, Ragazzi M, Rajadhyaksha M, Nehal K, Bennassar A, Pellacani G, Malvehy Guilera J. In Vivo and Ex Vivo Confocal Microscopy for Dermatologic and Mohs Surgeons. Dermatol Clin. 2016 Oct;34(4):497-504. doi: 10.1016/j.det.2016.05.012. PMID: 27692455; PMCID: PMC5570550.

7 Longo C, Pampena R, Bombonato C, Gardini S, Piana S, Mirra M, Raucci M, Kyrgidis A, Pellacani G, Ragazzi M. Diagnostic accuracy of ex vivo fluorescence confocal microscopy in Mohs surgery of basal cell carcinomas: a prospective study on 753 margins. Br J Dermatol. 2019 Jun;180(6):1473-1480. doi: 10.1111/bjd.17507. Epub 2019 Feb 20. PMID: 30512198.

8 Palacios-Martínez D, Díaz-Alonso RA. Dermatoscopia para principiantes (i): características generales [Dermoscopy for beginners (i): General information]. Semergen. 2017 Apr;43(3):216-221. Spanish. doi: 10.1016/j.semerg.2015.11.009. Epub 2016 Jan 4. PMID: 26762676.

9 Malvehy J., Braun, R. P., Puig, S., Marghoob, A. A., & Kopf, A. W. Handbook of Dermoscopy. London: CRC Press; 2006. doi: 10.1201/b14613.

10 Malvehy J, Aguilera P, Carrera C, Salerni G, Lovatto L, Scope A, Marghoob AA, Palou J, Alós L, Puig S. Ex vivo dermoscopy for biobank-oriented sampling of melanoma. JAMA Dermatol. 2013 Sep;149(9):1060-7. doi: 10.1001/jamadermatol.2013.4724. PMID: 23863988.

11 Weber P, Tschandl P, Sinz C, Kittler H. Dermatoscopy of Neoplastic Skin Lesions: Recent Advances, Updates, and Revisions. Curr Treat Options Oncol. 2018 Sep 20;19(11):56. doi: 10.1007/s11864-018-0573-6. PMID: 30238167; PMCID: PMC6153581.

12 Marghoob NG, Liopyris K, Jaimes N. Dermoscopy: A Review of the Structures That Facilitate Melanoma Detection. J Am Osteopath Assoc. 2019 Jun 1;119(6):380-390. doi: 10.7556/jaoa.2019.067. PMID: 31135866.

13 Carli P, De Giorgi V, Massi D, Giannotti B. The role of pattern analysis and the ABCD rule of dermoscopy in the detection of histological atypia in melanocytic naevi. Br J Dermatol. 2000 Aug;143(2):290-7. doi: 10.1046/j.1365-2133.2000.03653.x. PMID: 10951135.

14 Williams NM, Rojas KD, Reynolds JM, Kwon D, Shum-Tien J, Jaimes N. Assessment of Diagnostic Accuracy of Dermoscopic Structures and Patterns Used in Melanoma Detection: A Systematic Review and Meta-analysis. JAMA Dermatol. 2021 Sep 1;157(9):1078-1088. doi: 10.1001/jamadermatol.2021.2845.

PMID: 34347005; PMCID: PMC8339993.

15 Tanioka M. Benign acral lesions showing parallel ridge pattern on dermoscopy. J Dermatol. 2011 Jan;38(1):41-4. doi: 10.1111/j.1346-8138.2010.01128.x. PMID: 21175754.

16 Saida T, Koga H, Uhara H. Dermoscopy for Acral Melanocytic Lesions: Revision of the 3-step Algorithm and Refined Definition of the Regular and Irregular Fibrillar Pattern. Dermatol Pract Concept. 2022 Jul 1;12(3):e2022123. doi: 10.5826/dpc.1203a123. PMID: 36159128; PMCID: PMC9464531.

17 Ishihara Y, Saida T, Miyazaki A, Koga H, Taniguchi A, Tsuchida T, Toyama M, Ohara K. Early acral melanoma in situ: correlation between the parallel ridge pattern on dermoscopy and microscopic features. Am J Dermatopathol. 2006 Feb;28(1):21-7. doi: 10.1097/01.dad.0000187931.05030.a0. PMID: 16456320.

18 Vestergaard ME, Macaskill P, Holt PE, Menzies SW. Dermoscopy compared with naked eye examination for the diagnosis of primary melanoma: a meta-analysis of studies performed in a clinical setting. Br J Dermatol. 2008 Sep;159(3):669-76. doi: 10.1111/j.1365-2133.2008.08713.x. Epub 2008 Jul 4. PMID: 18616769.

19 Mayer J. Systematic review of the diagnostic accuracy of dermatoscopy in detecting malignant melanoma. Med J Aust. 1997 Aug 18;167(4):206-10. doi: 10.5694/j.1326-5377.1997.tb138847.x. PMID: 9293268.

20 Reiter O, Mimouni I, Gdalevich M, Marghoob AA, Levi A, Hodak E, Leshem YA. The diagnostic accuracy of dermoscopy for basal cell carcinoma: A systematic review and meta-analysis. J Am Acad Dermatol. 2019 May;80(5):1380-1388. doi: 10.1016/j.jaad.2018.12.026. Epub 2018 Dec 21. PMID: 30582991.

21 Sonthalia S, Pasquali P, Agrawal M, Sharma P, Jha AK, Errichetti E, Lallas A, Sehgal VN. Dermoscopy Update: Review of Its Extradiagnostic and Expanding Indications and Future Prospects. Dermatol Pract Concept. 2019 Oct 31;9(4):253-264. doi: 10.5826/dpc.0904a02. PMID: 31723457; PMCID: PMC6830565.

22 González S, Gilaberte-Calzada Y. In vivo reflectance-mode confocal microscopy in clinical dermatology and cosmetology. Int J Cosmet Sci. 2008 Feb;30(1):1-17. doi: 10.1111/j.1468-2494.2008.00406.x. PMID: 18377626.

23 Kose K, Gou M, Yélamos O, Cordova M, Rossi AM, Nehal KS, Flores ES, Camps O, Dy JG, Brooks DH, Rajadhyaksha M. Automated video-mosaicking approach for confocal microscopic imaging in vivo: an approach to address challenges in imaging living tissue and extend field of view. Sci Rep. 2017 Sep 7;7(1):10759. doi: 10.1038/s41598-017-11072-9. PMID: 28883434; PMCID: PMC5589933.

24 Pellacani G, Vinceti M, Bassoli S, Braun R, Gonzalez S, Guitera P, Longo C, Marghoob AA, Menzies SW, Puig S, Scope A, Seidenari S, Malvehy J.

Reflectance confocal microscopy and features of melanocytic lesions: an internet-based study of the reproducibility of terminology. Arch Dermatol. 2009 Oct;145(10):1137-43. doi: 10.1001/archdermatol.2009.228. PMID: 19841401.

25 Scope A, Benvenuto-Andrade C, Agero AL, Halpern AC, Gonzalez S, Marghoob AA. Correlation of dermoscopic structures of melanocytic lesions to reflectance confocal microscopy. Arch Dermatol. 2007 Feb;143(2):176-85. doi: 10.1001/archderm.143.2.176. PMID: 17309998.

26 Pellacani G, Longo C, Malvehy J, Puig S, Carrera C, Segura S, Bassoli S, Seidenari S. In vivo confocal microscopic and histopathologic correlations of dermoscopic features in 202 melanocytic lesions. Arch Dermatol. 2008 Dec;144(12):1597-608. doi: 10.1001/archderm.144.12.1597. PMID: 19075142.

27 Ahlgrimm-Siess V, Massone C, Scope A, Fink-Puches R, Richtig E, Wolf IH, Koller S, Gerger A, Smolle J, Hofmann-Wellenhof R. Reflectance confocal microscopy of facial lentigo maligna and lentigo maligna melanoma: a preliminary study. Br J Dermatol. 2009 Dec;161(6):1307-16. doi: 10.1111/j.1365-2133.2009.09289.x. Epub 2009 May 5. PMID: 19566662.

28 Abarzua-Araya A, Bañuls J, Cabo H, Carrera C, Gamo R, González S, Jaimes N, Navarrete-Dechent C, Pérez Anker J, Roldán-Marín R, Segura S, Yélamos O, Puig S, Malvehy J. Reflectance Confocal Microscopy Terminology in Spanish: A

Delphi Consensus Study. Actas Dermosifiliogr. 2023 Oct 26:S0001-7310(23)00845-1. English, Spanish. doi: 10.1016/j.ad.2023.10.014. Epub ahead of print. PMID: 37890615.

29 Segura S, Puig S, Carrera C, Palou J, Malvehy J. Development of a two-step method for the diagnosis of melanoma by reflectance confocal microscopy. J Am Acad Dermatol. 2009 Aug;61(2):216-29. doi: 10.1016/j.jaad.2009.02.014. Epub 2009 Apr 29. PMID: 19406506.

30 Batani A, Brănișteanu DE, Ilie MA, Boda D, Ianosi S, Ianosi G, Caruntu C. Assessment of dermal papillary and microvascular parameters in psoriasis vulgaris using in vivo reflectance confocal microscopy. Exp Ther Med. 2018 Feb;15(2):1241-1246. doi: 10.3892/etm.2017.5542. Epub 2017 Nov 22. PMID: 29434710; PMCID: PMC5774437.

31 Yélamos O, Manubens E, Jain M, Chavez-Bourgeois M, Pulijal SV, Dusza SW, Marchetti MA, Barreiro A, Marino ML, Malvehy J, Cordova MA, Rossi AM, Rajadhyaksha M, Halpern AC, Puig S, Marghoob AA, Carrera C. Improvement of diagnostic confidence and management of equivocal skin lesions by integration of reflectance confocal microscopy in daily practice: Prospective study in 2 referral skin cancer centers. J Am Acad Dermatol. 2020 Oct;83(4):1057-1063. doi: 10.1016/j.jaad.2019.05.101. Epub 2019 Jun 13. PMID: 31202873;

PMCID: PMC8285925.

32 Pellacani G, Farnetani F, Ciardo S, Chester J, Kaleci S, Mazzoni L, Bassoli S, Casari A, Pampena R, Mirra M, Lai M, Magi S, Mandel VD, Di Matteo S, Colombo GL, Stanganelli I, Longo C. Effect of Reflectance Confocal Microscopy for Suspect Lesions on Diagnostic Accuracy in Melanoma: A Randomized Clinical Trial. JAMA Dermatol. 2022 Jul 1;158(7):754-761. doi: 10.1001/jamadermatol.2022.1570. Erratum in: JAMA Dermatol. 2023 May 1;159(5):566. PMID: 35648432; PMCID: PMC9161119.

33 Edwards SJ, Osei-Assibey G, Patalay R, Wakefield V, Karner C. Diagnostic accuracy of reflectance confocal microscopy using VivaScope for detecting and monitoring skin lesions: a systematic review. Clin Exp Dermatol. 2017 Apr;42(3):266-275. doi: 10.1111/ced.13055. Epub 2017 Feb 20. PMID: 282184

34 Guitera P, Moloney FJ, Menzies SW, Stretch JR, Quinn MJ, Hong A, Fogarty G, Scolyer RA. Improving management and patient care in lentigo maligna by mapping with in vivo confocal microscopy. JAMA Dermatol. 2013 Jun;149(6):692-8. doi: 10.1001/jamadermatol.2013.2301. PMID: 23553208.

35 Borsari S, Pampena R, Lallas A, Kyrgidis A, Moscarella E, Benati E, Raucci M, Pellacani G, Zalaudek I, Argenziano G, Longo C. Clinical Indications for Use of

Reflectance Confocal Microscopy for Skin Cancer Diagnosis. JAMA Dermatol. 2016 Oct 1;152(10):1093-1098. doi: 10.1001/jamadermatol.2016.1188. PMID: 27580185.

36 Carrera C, Puig S, Malvehy J. In vivo confocal reflectance microscopy in melanoma. Dermatol Ther. 2012 Sep-Oct;25(5):410-22. doi: 10.1111/j.1529-8019.2012.01495.x. PMID: 23046020.

37 Pellacani G, Pepe P, Casari A, Longo C. Reflectance confocal microscopy as a second-level examination in skin oncology improves diagnostic accuracy and saves unnecessary excisions: a longitudinal prospective study. Br J Dermatol. 2014 Nov;171(5):1044-51. doi: 10.1111/bjd.13148. Epub 2014 Oct 19. PMID: 24891083.

38 Alarcon I, Carrera C, Palou J, Alos L, Malvehy J, Puig S. Impact of in vivo reflectance confocal microscopy on the number needed to treat melanoma in doubtful lesions. Br J Dermatol. 2014 Apr;170(4):802-8. doi: 10.1111/bjd.12678. PMID: 24124911; PMCID: PMC3984366.

39 Pellacani G, Guitera P, Longo C, Avramidis M, Seidenari S, Menzies S. The impact of in vivo reflectance confocal microscopy for the diagnostic accuracy of melanoma and equivocal melanocytic lesions. J Invest Dermatol. 2007 Dec;127(12):2759-65. doi: 10.1038/sj.jid.5700993. Epub 2007 Jul 26. PMID:

17657243.

40 Kadouch DJ, Schram ME, Leeflang MM, Limpens J, Spuls PI, de Rie MA. In vivo confocal microscopy of basal cell carcinoma: a systematic review of diagnostic accuracy. J Eur Acad Dermatol Venereol. 2015 Oct;29(10):1890-7. doi: 10.1111/jdv.13224. Epub 2015 Aug 19. PMID: 26290493.

41 Dubois A, Levecq O, Azimani H, Siret D, Barut A, Suppa M, Del Marmol V, Malvehy J, Cinotti E, Rubegni P, Perrot JL. Line-field confocal optical coherence tomography for high-resolution noninvasive imaging of skin tumors. J Biomed Opt. 2018 Oct;23(10):1-9. doi: 10.1117/1.JBO.23.10.106007. PMID: 30353716.

42 Ogien J, Levecq O, Azimani H, Dubois A. Dual-mode line-field confocal optical coherence tomography for ultrahigh-resolution vertical and horizontal section imaging of human skin in vivo. Biomed Opt Express. 2020 Feb 10;11(3):1327-1335. doi: 10.1364/BOE.385303. PMID: 32206413; PMCID: PMC7075601.

43 Suppa M, Palmisano G, Tognetti L, Lenoir C, Cappilli S, Fontaine M, Orte Cano C, Diet G, Perez-Anker J, Schuh S, DI Stefani A, Lacarrubba F, Puig S, Malvehy J, Rubegni P, Welzel J, Perrot JL, Peris K, Cinotti E, Del Marmol V. Line-field confocal optical coherence tomography in melanocytic and non-melanocytic skin tumors. Ital J Dermatol Venerol. 2023 Jun;158(3):180-189. doi: 10.23736/S2784-8671.23.07639-9. PMID: 37278496.

44 Donelli C, Suppa M, Tognetti L, Perrot JL, Calabrese L, Pérez-Anker J, Malvehy J, Rubegni P, Cinotti E. Line-Field Confocal Optical Coherence Tomography for the Diagnosis of Skin Carcinomas: Real-Life Data over Three Years. Curr Oncol. 2023 Sep 28;30(10):8853-8864. doi: 10.3390/curroncol30100639. PMID: 37887539; PMCID: PMC10604937.

45 Ruini C, Schuh S, Gust C, Kendziora B, Frommherz L, French LE, Hartmann D, Welzel J, Sattler E. Line-field optical coherence tomography: in vivo diagnosis of basal cell carcinoma subtypes compared with histopathology. Clin Exp Dermatol. 2021 Dec;46(8):1471-1481. doi: 10.1111/ced.14762. Epub 2021 Sep 24. PMID: 34047380.

46 Suppa M, Fontaine M, Dejonckheere G, Cinotti E, Yélamos O, Diet G, Tognetti L, Miyamoto M, Orte Cano C, Perez-Anker J, Panagiotou V, Trepant AL, Monnier J, Berot V, Puig S, Rubegni P, Malvehy J, Perrot JL, Del Marmol V. Line-field confocal optical coherence tomography of basal cell carcinoma: a descriptive study. J Eur Acad Dermatol Venereol. 2021 May;35(5):1099-1110. doi: 10.1111/jdv.17078. Epub 2020 Dec 29. PMID: 33398911.

47 Aumann S, Donner S, Fischer J, Müller F. Optical Coherence Tomography (OCT): Principle and Technical Realization. 2019 Aug 14. In: Bille JF, editor. High Resolution Imaging in Microscopy and Ophthalmology: New Frontiers in

Biomedical Optics [Internet]. Cham (CH): Springer; 2019. Chapter 3. PMID: 32091846.

48 Ferrante di Ruffano L, Dinnes J, Deeks JJ, Chuchu N, Bayliss SE, Davenport C, Takwoingi Y, Godfrey K, O'Sullivan C, Matin RN, Tehrani H, Williams HC; Cochrane Skin Cancer Diagnostic Test Accuracy Group. Optical coherence tomography for diagnosing skin cancer in adults. Cochrane Database Syst Rev. 2018 Dec 4;12(12):CD013189. doi: 10.1002/14651858.CD013189. PMID: 30521690; PMCID: PMC6516952.

49 Olmedo JM, Warschaw KE, Schmitt JM, Swanson DL. Optical coherence tomography for the characterization of basal cell carcinoma in vivo: a pilot study. J Am Acad Dermatol. 2006 Sep;55(3):408-12. doi: 10.1016/j.jaad.2006.03.013. Epub 2006 May 15. PMID: 16908344.

50 Soglia S, Pérez-Anker J, Lobos Guede N, Giavedoni P, Puig S, Malvehy J. Diagnostics Using Non-Invasive Technologies in Dermatological Oncology. Cancers (Basel). 2022 Nov 29;14(23):5886. doi: 10.3390/cancers14235886. PMID: 36497368; PMCID: PMC9738560.

51 Cunha D, Richardson T, Sheth N, Orchard G, Coleman A, Mallipeddi R. Comparison of ex vivo optical coherence tomography with conventional frozen-section histology for visualizing basal cell carcinoma during Mohs micrographic

surgery. Br J Dermatol. 2011 Sep;165(3):576-80. doi: 10.1111/j.1365-2133.2011.10461.x. Epub 2011 Jul 28. PMID: 21797838.

52 Abignano G, Laws P, Del Galdo F, Marzo-Ortega H, McGonagle D. Three-dimensional nail imaging by optical coherence tomography: a novel biomarker of response to therapy for nail disease in psoriasis and psoriatic arthritis. Clin Exp Dermatol. 2019 Jun;44(4):462-465. doi: 10.1111/ced.13786. Epub 2018 Sep 23. PMID: 30246363.

53 Rajadhyaksha M, Menaker G, Flotte T, Dwyer PJ, González S. Confocal examination of nonmelanoma cancers in thick skin excisions to potentially guide mohs micrographic surgery without frozen histopathology. J Invest Dermatol. 2001 Nov;117(5):1137-43. doi: 10.1046/j.0022-202x.2001.01524.x. PMID: 11710924.

54 Malvehy J, Pérez-Anker J, Toll A, Pigem R, Garcia A, Alos LL, Puig S. Ex vivo confocal microscopy: revolution in fast pathology in dermatology. Br J Dermatol. 2020 Dec;183(6):1011-1025. doi: 10.1111/bjd.19017. Epub 2020 May 10. PMID: 32134506.

55 Pérez-Anker J, Puig S, Malvehy J. Advances in Technology, staining Protocol, and Flattening Devices in Ex vivo Confocal Microscopy. In: Jain M, Rossi A, Nehal K, Sendín-Martín M, editors. Atlas of Ex Vivo Confocal Microscopy. New

York, NY, USA: Springer International Publishing; 2022. p. 97-105. doi:10.1007/978-3-030-89316-3.

56 Chung VQ, Dwyer PJ, Nehal KS, Rajadhyaksha M, Menaker GM, Charles C, Jiang SB. Use of ex vivo confocal scanning laser microscopy during Mohs surgery for nonmelanoma skin cancers. Dermatol Surg. 2004 Dec;30(12 Pt 1):1470-8. doi: 10.1111/j.1524-4725.2004.30505.x. PMID: 15606734.

57 Karen JK, Gareau DS, Dusza SW, Tudisco M, Rajadhyaksha M, Nehal KS. Detection of basal cell carcinomas in Mohs excisions with fluorescence confocal mosaicing microscopy. Br J Dermatol. 2009 Jun;160(6):1242-50. doi: 10.1111/j.1365-2133.2009.09141.x. Epub 2009 Mar 30. PMID: 19416248; PMCID: PMC2693082.

58 Bennàssar A, Carrera C, Puig S, Vilalta A, Malvehy J. Fast evaluation of 69 basal cell carcinomas with ex vivo fluorescence confocal microscopy: criteria description, histopathological correlation, and interobserver agreement. JAMA Dermatol. 2013 Jul;149(7):839-47. doi: 10.1001/jamadermatol.2013.459. Erratum in: JAMA Dermatol. 2013 Aug;149(8):997. PMID: 23636776.

59 Dika E, Patrizi A, Lambertini M, Scarfì F, Fanti PA. Comment on 'Diagnostic accuracy of ex vivo fluorescence confocal microscopy for Mohs surgery of basal cell carcinomas: a prospective study on 753 margins'. Br J Dermatol. 2019

Jun;180(6):1559. doi: 10.1111/bjd.17686. Epub 2019 Apr 7. PMID: 30671937.

60 Ragazzi M, Longo C, Piana S. Ex Vivo (Fluorescence) Confocal Microscopy in Surgical Pathology: State of the Art. Adv Anat Pathol. 2016 May;23(3):159-69. doi: 10.1097/PAP.0000000000000114. PMID: 27058244.

61 Reggiani C, Pellacani G, Reggiani Bonetti L, Zanelli G, Azzoni P, Chester J, Kaleci S, Ferrari B, Bellini P, Longo C, Bertoni L, Magnoni C. An intraoperative study with ex vivo fluorescence confocal microscopy: diagnostic accuracy of the three visualization modalities. J Eur Acad Dermatol Venereol. 2021 Jan;35(1):e92-e94. doi: 10.1111/jdv.16831. Epub 2020 Aug 16. PMID: 32692878.

62 Bennàssar A, Vilata A, Puig S, Malvehy J. Ex vivo fluorescence confocal microscopy for fast evaluation of tumour margins during Mohs surgery. Br J Dermatol. 2014 Feb;170(2):360-5. doi: 10.1111/bjd.12671. PMID: 24117457.

63 Kaeb S, Landthaler M, Hohenleutner U. Confocal laser scanning microscopy--evaluation of native tissue sections in micrographic surgery. Lasers Med Sci. 2009 Sep;24(5):819-23. doi: 10.1007/s10103-009-0660-9. Epub 2009 Mar 11. PMID: 19277819.

64 Tannous Z, Torres A, González S. In vivo real-time confocal reflectance microscopy: a noninvasive guide for Mohs micrographic surgery facilitated by aluminum chloride, an excellent contrast enhancer. Dermatol Surg. 2003

Aug;29(8):839-46. doi: 10.1046/j.1524-4725.2003.29219.x. PMID: 12859385.

65 Perez-Anker J, Puig S, Alos L, García A, Alejo B, Cinotti E, Orte Cano C, Tognetti L, Lenoir C, Monnier J, Machuca N, Castillo P, Gibert PR, Rubegni P, Suppa M, Perrot JL, Del Marmol V, Malvehy J. Morphological evaluation of melanocytic lesions with three-dimensional line-field confocal optical coherence tomography: correlation with histopathology and reflectance confocal microscopy. A pilot study. Clin Exp Dermatol. 2022 Dec;47(12):2222-2233. doi: 10.1111/ced.15383.Epub 2022 Oct 20. PMID: 35988042.

66 Soglia S, Pérez-Anker J, Albero R, Alós L, Berot V, Castillo P, Cinotti E, Del Marmol V, Fakih A, García A, Lenoir C, Monnier J, Perrot JL, Puig S, Rubegni P, Skowron F, Suppa M, Tognetti L, Venturini M, Malvehy J. Understanding the anatomy of dermoscopy of melanocytic skin tumours: Correlation in vivo with line-field optical coherence tomography. J Eur Acad Dermatol Venereol. 2023 Dec 22;00:1-11.doi: 10.1111/jdv.19771. Epub ahead of print. PMID: 38131528.

67 Pérez-Anker J, Soglia S, Lenoir C, Albero R, Alós L, García A, Alejo B, Cinotti E, Orte Cano C, Habougit C, Dorado Cortes Ch, Pellegrino L, Tognetti L, Castillo P, Rubegni P, Suppa M, Perrot JL, Del Marmol V, Puig S, Malvehy J. Criteria for melanocytic lesions in LC-OCT. J Eur Acad Dermatol Venereol. 2024. Under Review

68 Pérez-Anker J, Soglia S, Puig S, Albero R, García A, Alejo B, Cinotti E, Orte Cano C, Habougit C, Skowron F, Pellegrino L, Tognetti L, Lenoir L, Rubegni P, Suppa M, Perrot JL, Del Marmol V, * Alos LL, *Malvehy J. Clefting: predictor of melanocytic malignancy? J Eur Acad Dermatol Venereol. 2024. Under Review

69 Fischman S, Pérez-Anker J, Tognetti L, Di Naro A, Suppa M, Cinotti E, Viel T, Monnier J, Rubegni P, Del Marmol V, Malvehy J, Puig S, Dubois A, Perrot JL. Non-invasive scoring of cellular atypia in keratinocyte cancers in 3D LC-OCT images using Deep Learning. Sci Rep. 2022 Jan 10;12(1):481. doi: 10.1038/s41598-021-04395-1. PMID: 35013485; PMCID: PMC8748986.

70 Pérez-Anker J, Ribero S, Yélamos O, García-Herrera A, Alos L, Alejo B, Combalia M, Moreno-Ramírez D, Malvehy J, Puig S. Basal cell carcinoma characterization using fusion ex vivo confocal microscopy: a promising change in conventional skin histopathology. Br J Dermatol. 2020 Feb;182(2):468-476. doi: 10.1111/bjd.18239. Epub 2019 Oct 27. PMID: 31220341; PMCID: PMC6923630.

71 Pérez-Anker J, Puig S, Malvehy J. A fast and effective option for tissue flattening: Optimizing time and efficacy in ex vivo confocal microscopy. J Am Acad Dermatol. 2020 May;82(5):e157-e158. doi: 10.1016/j.jaad.2019.06.041. Epub 2019 Jun 28. PMID: 31255748.

72 María Javiera Pérez Anker (2019), Flattening device for ex vivo confocal

microscopy, n° 10 2019 101 035.7, Patentanwälte Partnerschaft mbB, Munich, Germany. 18085-MAV-P-DE.

73 Pérez-Anker J, Toll A, Puig S, Malvehy J. Six steps to reach optimal scanning in ex vivo confocal microscopy. J Am Acad Dermatol. 2022 Jan;86(1):188-189. doi: 10.1016/j.jaad.2021.01.044. Epub 2021 Jan 19. PMID: 33476729.

74 Lobos-Guede N, Toloza Salech C, Albero-González R, Castillo P, Zamora Sh, Larotta E, Alós Ll, García A, Soglia S, Toll A, Puig S, Malvehy, Pérez-Anker J. Diagnostic accuracy of ex vivo confocal microscopy with digital stain for squamous cell carcinoma in skin biopsies. J Eur Acad Dermatol Venereol. 2024. Under Review.

75 Combalia M, Pérez-Anker J, García-Herrera A, Alos Ll, Vilaplana V, Marqués F, Puig S, Malvehy J. Digitally Stained Confocal Microscopy through Deep Learning. Proc Mach Learn Res 2019; 102:121–9.

76 Iftimia N, Sahu A, Cordova M, Maguluri G, Gill M, Alessi-Fox C, Gonzalez S, Navarrete-Dechent C, Marghoob A, Chen CJ, Rajadhyaksha M. The potential utility of integrated reflectance confocal microscopy-optical coherence tomography for guiding triage and therapy of basal cell carcinomas. J Cancer. 2020 Aug 18;11(20):6019-6024. doi: 10.7150/jca.47026. PMID: 32922542; PMCID: PMC7477415.

77 Davis A, Levecq O, Azimani H, Siret D, Dubois A. Simultaneous dual-band line-field confocal optical coherence tomography: application to skin imaging. Biomed Opt Express. 2019 Jan 22;10(2):694-706. doi: 10.1364/BOE.10.000694. PMID: 30800509; PMCID: PMC6377879.

78 Lenoir C, Perez-Anker J, Diet G, Tognetti L, Cinotti E, Trépant AL, Rubegni P, Puig S, Perrot JL, Malvehy J, Del Marmol V, Suppa M. Line-field confocal optical coherence tomography of benign dermal melanocytic proliferations: a case series. J Eur Acad Dermatol Venereol. 2021 Jun;35(6):e399-e401. doi: 10.1111/jdv.17180. Epub 2021 Feb 28. PMID: 33594684.

79 Schuh S, Ruini C, Perwein MKE, Daxenberger F, Gust C, Sattler EC, Welzel J. Line-Field Confocal Optical Coherence Tomography: A New Tool for the Differentiation between Nevi and Melanomas? Cancers (Basel). 2022 Feb 23;14(5):1140. doi: 10.3390/cancers14051140. PMID: 35267448; PMCID: PMC8909859.

80 Verzì AE, Broggi G, Caltabiano R, Micali G, Lacarrubba F. Line-field confocal optical coherence tomography of lentigo maligna with horizontal and vertical histopathologic correlations. J Cutan Pathol. 2023 Feb;50(2):118-122. doi: 10.1111/cup.14321. Epub 2022 Sep 19. PMID: 36056910; PMCID: PMC10087826.

81 Del Río-Sancho S, Gallay C, Ventéjou S, Christen-Zaech S. Non-invasive imaging

of agminated Spitz nevi with line-field confocal optical coherence tomography. J Eur Acad Dermatol Venereol. 2023 May;37(5):e658-e659. doi: 10.1111/jdv.18863. Epub 2023 Jan 25. PMID: 36645816.

82 El Zeinaty P, Suppa M, Del Marmol V, Tavernier C, Dauendorffer JN, Lebbé C, Baroudjian B. Line-field confocal optical coherence tomography (LC-OCT): A novel tool of cutaneous imaging for non-invasive diagnosis of pigmented lesions of genital area. J Eur Acad Dermatol Venereol. 2023 Apr 16. doi: 10.1111/jdv.19120. Epub ahead of print. PMID: 37062592.

83 Perino F, Suarez R, Perez-Anker J, Carrera C, Rezze GG, Primiero CA, Alos LL, Díaz A, Barreiro A, Puig S, Peris K, Malvehy J. Concordance of in vivo reflectance confocal microscopy and horizontal-sectioning histology in skin tumours. J Eur Acad Dermatol Venereol. 2024 Jan;38(1):124-135. doi: 10.1111/jdv.19491. Epub 2023 Sep 26. PMID: 37669864.

84 Monnier J, Tognetti L, Miyamoto M, Suppa M, Cinotti E, Fontaine M, Perez J, Orte Cano C, Yélamos O, Puig S, Dubois A, Rubegni P, Del Marmol V, Malvehy J, Perrot JL. In vivo characterization of healthy human skin with a novel, non-invasive imaging technique: line-field confocal optical coherence tomography. J Eur Acad Dermatol Venereol. 2020 Dec;34(12):2914-2921. doi: 10.1111/jdv.16857. Epub 2020 Aug 27. PMID: 32786124.

85 Pellacani G, Cesinaro AM, Seidenari S. Reflectance-mode confocal microscopy of pigmented skin lesions--improvement in melanoma diagnostic specificity. J Am Acad Dermatol. 2005 Dec;53(6):979-85. doi: 10.1016/j.jaad.2005.08.022. Epub 2005 Oct 19. PMID: 16310058.

86 Tognetti L, Rizzo A, Fiorani D, Cinotti E, Perrot JL, Rubegni P. New findings in non-invasive imaging of aquagenic keratoderma: Line-field optical coherence tomography, dermoscopy and reflectance confocal microscopy. Skin Res Technol. 2020 Nov;26(6):956-959. doi: 10.1111/srt.12882. Epub 2020 Aug 9. PMID: 32776375.

87 Tognetti L, Ekinde S, Habougit C, Cinotti E, Rubegni P, Perrot JL. Delayed Tattoo Reaction From Red Dye With Overlapping Clinicopathological Features: Examination With High-Frequency Ultrasound and Line-Field Optical Coherence Tomography. Dermatol Pract Concept. 2020 Jun 29;10(3):e2020053. doi: 10.5826/dpc.1003a53. PMID: 32685273; PMCID: PMC7346588.

88 Braun-Falco M, Friedrichson E, Ring J. Subepidermal cleft formation as a diagnostic marker for cutaneous malignant melanoma. Hum Pathol. 2005 Apr;36(4):412-5. doi: 10.1016/j.humpath.2005.02.005. PMID: 15892003.

89 Walters RF, Groben PA, Busam K, Millikan RC, Rabinovitz H, Cognetta A, Mihm MC Jr, Prieto VG, Googe PB, King R, Moore DT, Woosley J, Thomas NE.

Consumption of the epidermis: a criterion in the differential diagnosis of melanoma and dysplastic nevi that is associated with increasing breslow depth and ulceration. Am J Dermatopathol. 2007 Dec;29(6):527-33. doi: 10.1097/DAD.0b013e318156e0a7. PMID: 18032946.

90 AbdullGaffar B. The prevalence and importance of clefts in cutaneous neoplasms. Pathology. 2012 Apr;44(3):267-70. doi: 10.1097/PAT.0b013e32835140d4. PMID: 22437748.

91 Ruini C, Schuh S, Sattler E, Welzel J. Line-field confocal optical coherence tomography-Practical applications in dermatology and comparison with established imaging methods. Skin Res Technol. 2021 May;27(3):340-352. doi: 10.1111/srt.12949. Epub 2020 Oct 21. PMID: 33085784.

92 Suppa M, Palmisano G, Tognetti L, Lenoir C, Cappilli S, Fontaine M, Orte Cano C, Diet G, Perez-Anker J, Schuh S, DI Stefani A, Lacarrubba F, Puig S, Malvehy J, Rubegni P, Welzel J, Perrot JL, Peris K, Cinotti E, Del Marmol V. Line-field confocal optical coherence tomography in melanocytic and non-melanocytic skin tumors. Ital J Dermatol Venerol. 2023 Jun;158(3):180-189. doi: 10.23736/S2784-8671.23.07639-9. PMID: 37278496.

93 Aktas D, Palmisano G, Cinotti E, Tognetti L, Perrot JL, Perez-Anker J, Rubegni P, Puig S, Malvehy J, Peris K, Del Marmol V, Suppa M. The role of line-field

confocal optical coherence tomography in the differential diagnosis of infiltrative basal cell carcinoma with scar-like lesions: A case series. J Eur Acad Dermatol Venereol. 2023 Dec;37(12):e1396-e1398. doi: 10.1111/jdv.19337. Epub 2023 Jul 27. PMID: 37458229.

94 Wolswijk T, Sanak D, Lenoir C, Cinotti E, Tognetti L, Rubegni P, Perez-Anker J, Puig S, Malvehy J, Perrot JL, Mosterd K, Del Marmol V, Suppa M. Line-field confocal optical coherence tomography can help differentiating melanoma from pigmented basal cell carcinoma: A case report. Skin Res Technol. 2023 Jun;29(6):e13376. doi: 10.1111/srt.13376. PMID: 37357657; PMCID: PMC10267609.

95 Palmisano G, Orte Cano C, Fontaine M, Lenoir C, Cinotti E, Tognetti L, Rubegni P, Perez-Anker J, Puig S, Malvehy J, Perrot JL, Del Marmol V, Peris K, Suppa M. Dermoscopic criteria explained by LC-OCT: Negative maple leaf-like areas. J Eur Acad Dermatol Venereol. 2023 Oct 25. doi: 10.1111/jdv.19588. Epub ahead of print. PMID: 37876332.

96 Cappilli S, Dejonckheere G, Hajjar N, Cinotti E, Tognetti L, Perez-Anker J, Rubegni P, Puig S, Malvehy J, Perrot JL, Del Marmol V, Peris K, Suppa M. Line-field confocal optical coherence tomography: a case on the importance of full-lesion examination for basal cell carcinoma. Int J Dermatol. 2022 Jul;61(7):e248-e250. doi: 10.1111/ijd.15930. Epub 2021 Sep 30. PMID: 34591332.

97 Dejonckheere G, Suppa M, Del Marmol V, Meyer T, Stockfleth E. The actinic dysplasia syndrome - diagnostic approaches defining a new concept in field carcinogenesis with multiple cSCC. J Eur Acad Dermatol Venereol. 2019 Dec;33 Suppl 8:16-20. doi: 10.1111/jdv.15949. PMID: 31833608.

98 Daxenberger F, Deußing M, Eijkenboom Q, Gust C, Thamm J, Hartmann D, French LE, Welzel J, Schuh S, Sattler EC. Innovation in Actinic Keratosis Assessment: Artificial Intelligence-Based Approach to LC-OCT PRO Score Evaluation. Cancers (Basel). 2023 Sep 7;15(18):4457. doi: 10.3390/cancers15184457. PMID: 37760425; PMCID: PMC10527366.

99 Lenoir C, Cinotti E, Tognetti L, Orte Cano C, Diet G, Miyamoto M, Rocq L, Trépant AL, Perez-Anker J, Puig S, Malvehy J, Rubegni P, Perrot JL, Del Marmol V, Suppa M. Line-field confocal optical coherence tomography of actinic keratosis: a case series. J Eur Acad Dermatol Venereol. 2021 Dec;35(12):e900-e902. doi: 10.1111/jdv.17548. Epub 2021 Aug 4. PMID: 34310768.

100 Cinotti E, Tognetti L, Cartocci A, Lamberti A, Gherbassi S, Orte Cano C, Lenoir C, Dejonckheere G, Diet G, Fontaine M, Miyamoto M, Perez-Anker J, Solmi V, Malvehy J, Del Marmol V, Perrot JL, Rubegni P, Suppa M. Line-field confocal optical coherence tomography for actinic keratosis and squamous cell carcinoma: a descriptive study. Clin Exp Dermatol. 2021 Dec;46(8):1530-1541.

doi: 10.1111/ced.14801. Epub 2021 Sep 24. PMID: 34115900; PMCID: PMC9293459.

101 Lenoir C, Perez-Anker J, Tognetti L, Cinotti E, Trépant AL, Rubegni P, Puig S, Perrot JL, Malvehy J, Del Marmol V, Suppa M. Line-field confocal optical coherence tomography of seborrheic keratosis: A case series. J Eur Acad Dermatol Venereol. 2023 Mar 28. doi: 10.1111/jdv.19075. Epub ahead of print. PMID: 36974591.

102 Soglia S, Pérez-Anker J, Ghini I, Lenoir C, Maione V, Sala R, Tonon F, Suppa M, Calzavara-Pinton PG, Malvehy J, Venturini M. Line-field confocal optical coherence tomography: A new in vivo assessment tool for cutaneous mycosis fungoides. J Eur Acad Dermatol Venereol. 2023 Nov 20. doi: 10.1111/jdv.19633. Epub ahead of print. PMID: 37983937.

103 Soglia S, Pérez-Anker J, Fraghì A, Ariasi C, La Rosa G, Lenoir C, Suppa M, Calzavara-Pinton PG, Venturini M. Line-field confocal optical coherence tomography and reflectance confocal microscopy of Merkel cell carcinoma. J Eur Acad Dermatol Venereol. 2023 Oct;37(10):e1223-e1225. doi: 10.1111/jdv.19211. Epub 2023 May 22. PMID: 37191203.

104 Cinotti E, Brunetti T, Cartocci A, Tognetti L, Suppa M, Malvehy J, Perez-Anker J, Puig S, Perrot JL, Rubegni P. Diagnostic Accuracy of Line-Field Confocal Optical Coherence Tomography for the Diagnosis of Skin Carcinomas.

Diagnostics (Basel). 2023 Jan 18;13(3):361. doi: 10.3390/diagnostics13030361. PMID: 36766466; PMCID: PMC9914674.

105 Cappilli S, Cinotti E, Lenoir C, Tognetti L, Perez-Anker J, Rubegni P, Puig S, Malvehy J, Perrot JL, Del Marmol V, Peris K, Suppa M. Line-field confocal optical coherence tomography of basosquamous carcinoma: a case series with histopathological correlation. J Eur Acad Dermatol Venereol. 2022 Aug;36(8):1214-1218. doi: 10.1111/jdv.18038. Epub 2022 Mar 8. PMID: 35224784.

106 Chauvel-Picard J, Bérot V, Tognetti L, Orte Cano C, Fontaine M, Lenoir C, Pérez-Anker J, Puig S, Dubois A, Forestier S, Monnier J, Jdid R, Cazorla G, Pedrazzani M, Sanchez A, Fischman S, Rubegni P, Del Marmol V, Malvehy J, Cinotti E, Perrot JL, Suppa M. Line-field confocal optical coherence tomography as a tool for three-dimensional in vivo quantification of healthy epidermis: A pilot study. J Biophotonics. 2022 Feb;15(2):e202100236. doi: 10.1002/jbio.202100236. Epub 2021 Oct 21. PMID: 34608756.

107 Lenoir C, Diet G, Cinotti E, Tognetti L, Orte Cano C, Rocq L, Trépant AL, Monnier J, Perez-Anker J, Rubegni P, Puig S, Malvehy J, Perrot JL, Del Marmol V, Suppa M. Line-field confocal optical coherence tomography of sebaceous hyperplasia: a case series. J Eur Acad Dermatol Venereol. 2021 Aug;35(8):e509-e511. doi: 10.1111/jdv.17251. Epub 2021 Apr 13. PMID: 33783890.

108 Wojtkowski M, Leitgeb R, Kowalczyk A, Bajraszewski T, Fercher AF. In vivo human retinal imaging by Fourier domain optical coherence tomography. J Biomed Opt. 2002 Jul;7(3):457-63. doi: 10.1117/1.1482379. PMID: 12175297.

109 Drexler W. Ultrahigh-resolution optical coherence tomography. J Biomed Opt. 2004 Jan-Feb;9(1):47-74. doi: 10.1117/1.1629679. PMID: 14715057.

110 Cho HS, Jang SJ, Kim K, Dan-Chin-Yu AV, Shishkov M, Bouma BE, Oh WY. High frame-rate intravascular optical frequency-domain imaging in vivo. Biomed Opt Express. 2013 Dec 16;5(1):223-32. doi: 10.1364/BOE.5.000223. PMID: 24466489; PMCID: PMC3891334.

110 Gareau DS. Feasibility of digitally stained multimodal confocal mosaics to simulate histopathology. J Biomed Opt. 2009 May-Jun;14(3):034050. doi: 10.1117/1.3149853. PMID: 19566342; PMCID: PMC2929174.

111 Pérez-Anker J, Malvehy J, Moreno-Ramírez D. Ex Vivo Confocal Microscopy Using Fusion Mode and Digital Staining: Changing Paradigms in Histological Diagnosis. Actas Dermosifiliogr (Engl Ed). 2020 Apr;111(3):236-242. English, Spanish. doi: 10.1016/j.ad.2019.05.005. Epub 2020 Jan 17. PMID: 31959303.

112 Pérez-Anker, J. (2016). Ex vivo confocal microscopy of basal cell carcinoma in vertical sections and histopathological correlation [Tesis de maestria, Universitt de Barcelona].

113 Sendín-Martín M, Bennàssar A, Levitsky KL, Domínguez-Cruz JJ. Ex vivo confocal microscopy of basal cell carcinoma on a 3-color scale. J Am Acad Dermatol. 2019 Apr;80(4):e91-e92. doi: 10.1016/j.jaad.2018.12.022. Epub 2018 Dec 19. PMID: 30578817.

114 Álvarez M, Urbina G, Perdomo L. Excretion Product of Shigella dysenteriae (SdyEP) Induced Cell Death in Early Larval Stage of Zebrafish (Danio rerio): Acridine Orange and Ethidium Bromide (AO/EB) in vivo Staining. Int. J. Morphol. [Internet]. 2013 Dic [citado 2024 Ene 28] ; 31(4): 1175-1180. Disponible en: http://www.scielo.cl/scielo.php?script=sci_arttext&pid=S071795022013000400005&lng=es.http://dx.doi.org/10.4067/S071795022013000400005.

115 Sahu A, Cordero J, Wu X, Kossatz S, Harris U, Franca PDD, Kurtansky NR, Everett N, Dusza S, Monnier J, Kumar P, Fox C, Brand C, Roberts S, Kose K, Phillips W, Lee E, Chen CJ, Rossi A, Nehal K, Pulitzer M, Longo C, Halpern A, Reiner T, Rajadhyaksha M, Jain M. Combined PARP1-Targeted Nuclear Contrast and Reflectance Contrast Enhance Confocal Microscopic Detection of Basal Cell Carcinoma. J Nucl Med. 2022 Jun;63(6):912-918. doi: 10.2967/jnumed.121.262600. Epub 2021 Oct 14. PMID: 34649941; PMCID: PMC9157717.

116 Bağcı IS, Aoki R, Krammer S, Vladimirova G, Ruzicka T, Sárdy M, French LE, Hartmann D. Immunofluorescence and histopathological assessment using ex vivo confocal laser scanning microscopy in lichen planus. J Biophotonics. 2020 Dec;13(12):e202000328. doi: 10.1002/jbio.202000328. Epub 2020 Oct 26. PMID: 33025741.

117 Bağcı IS, Aoki R, Krammer S, Ruzicka T, Sárdy M, French LE, Hartmann D. Ex vivo confocal laser scanning microscopy for bullous pemphigoid diagnostics: new era in direct immunofluorescence? J Eur Acad Dermatol Venereol. 2019 Nov;33(11):2123-2130. doi: 10.1111/jdv.15767. Epub 2019 Jul 22. PMID: 31265158.

118 Bağcı IS, Aoki R, Krammer S, Ruzicka T, Sárdy M, Hartmann D. Ex vivo confocal laser scanning microscopy: An innovative method for direct immunofluorescence of cutaneous vasculitis. J Biophotonics. 2019 Sep;12(9):e201800425. doi: 10.1002/jbio.201800425. Epub 2019 May 28. PMID: 31021054.

119 Hartmann D, Krammer S, Bachmann MR, Mathemeier L, Ruzicka T, von Braunmühl T. Simple 3-criteria-based ex vivo confocal diagnosis of basal cell carcinoma. J Biophotonics. 2018 Jul;11(7):e201800062. doi: 10.1002/jbio.201800062. Epub 2018 May 24. PMID: 29726112.

120 Hartmann D, Ruini C, Mathemeier L, Bachmann MR, Dietrich A, Ruzicka T, von Braunmühl T. Identification of ex-vivo confocal laser scanning microscopic features of melanocytic lesions and their histological correlates. J Biophotonics. 2017 Jan;10(1):128-142. doi: 10.1002/jbio.201500335. Epub 2016 Apr 19. PMID: 27091702.

121 Hartmann D, Ruini C, Mathemeier L, Dietrich A, Ruzicka T, von Braunmühl T. Identification of ex-vivo confocal scanning microscopic features and their histological correlates in human skin. J Biophotonics. 2016 Apr;9(4):376-87. doi: 10.1002/jbio.201500124. Epub 2015 May 21. PMID: 25996548.

122 Hartmann D, Krammer S, Bachmann MR, Mathemeier L, Ruzicka T, Bagci IS, von Braunmühl T. Ex vivo confocal microscopy features of cutaneous squamous cell carcinoma. J Biophotonics. 2018 Apr;11(4):e201700318. doi: 10.1002/jbio.201700318. Epub 2018 Jan 3. PMID: 29227042.

123 Cinotti E, Grivet D, Labeille B, Solazzi M, Bernard A, Forest F, Espinasse M, Cambazard F, Thuret G, Gain P, Perrot JL. The 'tissue press': a new device to flatten fresh tissue during ex vivo confocal microscopy examination. Skin Res Technol. 2017 Feb;23(1):121-124. doi: 10.1111/srt.12293. Epub 2016 Jun 5. PMID: 27264537.

124 Sendín-Martín M, Kose K, Harris U, Rossi A, Lee E, Nehal K, Rajadhyaksha M,

Jain M. Complete visualization of epidermal margin during ex vivo confocal microscopy of excised tissue with 3-dimensional mosaicking and intensity projection. J Am Acad Dermatol. 2022 Jan;86(1):e13-e14. doi: 10.1016/j.jaad.2020.05.044. Epub 2020 May 16. PMID: 32428611.

125 Pérez-Anker J, Albero-González R, Malvehy J. Squamous Cell Carcinoma features on Ex Vivo Confocal Imaging and Histopathologic Correlation. In: Jain M, Rossi A, Nehal K, Sendín-Martín M, editors. Atlas of Ex Vivo Confocal Microscopy. New York, NY, USA: Springer International Publishing; 2022. p. 97-105. doi:10.1007/978-3-030-89316-3.

126 Longo C, Ragazzi M, Gardini S, Piana S, Moscarella E, Lallas A, Raucci M, Argenziano G, Pellacani G. Ex vivo fluorescence confocal microscopy in conjunction with Mohs micrographic surgery for cutaneous squamous cell carcinoma. J Am Acad Dermatol. 2015 Aug;73(2):321-2. doi: 10.1016/j.jaad.2015.04.027. PMID: 26183978.

127 Horn M, Gerger A, Koller S, Weger W, Langsenlehner U, Krippl P, Kerl H, Samonigg H, Smolle J. The use of confocal laser-scanning microscopy in microsurgery for invasive squamous cell carcinoma. Br J Dermatol. 2007 Jan;156(1):81-4. doi: 10.1111/j.1365-2133.2006.07574.x. PMID: 17199571.

128 Shavlokhova V, Flechtenmacher C, Sandhu S, Vollmer M, Hoffmann J, Engel M,

Ristow O, Freudlsperger C. Features of oral squamous cell carcinoma in ex vivo fluorescence confocal microscopy. Int J Dermatol. 2021 Feb;60(2):236-240. doi: 10.1111/ijd.15152. Epub 2020 Dec 23. PMID: 33368199.

129 Yélamos O, Pérez-Anker J. Avances en el manejo del cáncer cutáneo : videomosaicos y microscopía confocal de fusión. Rev Chil Dermatología 2018; 34:6–8. doi:10.31879/rcderm.v34i1.192.

130 Combalia M, Garcia S, Malvehy J, Puig S, Mülberger AG, Browning J, Garcet S, Krueger JG, Lish SR, Lax R, Ren J, Stevenson M, Doudican N, Carucci JA, Jain M, White K, Rakos J, Gareau DS. Deep learning automated pathology in ex vivo microscopy. Biomed Opt Express. 2021 May 5;12(6):3103-3116. doi: 10.1364/BOE.422168. PMID: 34221648; PMCID: PMC8221965.

131 Ruini C, Schlingmann S, Jonke Ž, Avci P, Padrón-Laso V, Neumeier F, Koveshazi I, Ikeliani IU, Patzer K, Kunrad E, Kendziora B, Sattler E, French LE, Hartmann D. Machine Learning Based Prediction of Squamous Cell Carcinoma in Ex Vivo Confocal Laser Scanning Microscopy. Cancers (Basel). 2021 Nov 3;13(21):5522. doi: 10.3390/cancers13215522. PMID: 34771684; PMCID: PMC8583634.

132 Sendín-Martín M, Lara-Caro M, Harris U, Moronta M, Rossi A, Lee E, Chen CJ, Nehal K, Conejo-Mir Sánchez J, Pereyra-Rodríguez JJ, Jain M. Classification of Basal Cell Carcinoma in Ex Vivo Confocal Microscopy Images from Freshly

Excised Tissues Using a Deep Learning Algorithm. J Invest Dermatol. 2022 May;142(5):1291-1299.e2. doi: 10.1016/j.jid.2021.09.029. Epub 2021 Oct 23. PMID: 34695413; PMCID: PMC9447468.

133 Villarreal JZ, Pérez-Anker J, Puig S, Pellacani G, Solé M, Malvehy J, Quintana LF, García-Herrera A. Ex vivo confocal microscopy performs real-time assessment of renal biopsy in non-neoplastic diseases. J Nephrol. 2021 Jun;34(3):689-697. doi: 10.1007/s40620-020-00844-8. Epub 2020 Sep 2. PMID: 32876939.

134 Villarreal JZ, Pérez-Anker J, Puig S, Xipell M, Espinosa G, Barnadas E, Larque AB, Malvehy J, Cervera R, Pereira A, Martinez-Pozo A, Quintana LF, García-Herrera A. Ex vivo confocal microscopy detects basic patterns of acute and chronic lesions using fresh kidney samples. Clin Kidney J. 2023 Jan 27;16(6):1005-1013. doi: 10.1093/ckj/sfad019. PMID: 37260998; PMCID: PMC10229294.

135 Anker JP, Córdova H, Guerrero JA, Fernández-Esparrach G, Cuatrecasas M. Colonic perforation after piecemeal mucosectomy diagnosed by confocal microscopy. Gastrointest Endosc. 2020 Oct;92(4):971-973. doi: 10.1016/j.gie.2020.04.054. Epub 2020 May 4. PMID: 32376329.

136 Guerrero JA, Pérez-Anker J, Fernández-Esparrach G, Archilla I, Diaz A, Lopez-Prades S, Rodrigo-Calvo M, Lahoz S, Camps J, Puig S, Malvehy J, Cuatrecasas

M. Ex vivo Fusion Confocal Microscopy of Colorectal Polyps: A Fast Turnaround Time of Pathological Diagnosis. Pathobiology. 2021;88(6):392-399. doi: 10.1159/000517190. Epub 2021 Aug 18. PMID: 34407541.

137 Humaran Cozar D, Pérez-Anker J, Fernández Ruiz P, Castellà Fernández E, Pérez Roca L, Blay Aulina L, Pascual Miguel I, Puig Sardà S, Malvehy Guilera J, Julián Ibáñez JF. Ex-vivo fusion confocal microscopy for margin assessment in breast cancer surgery. Br J Surg. 2024 Jan 3;111(1):znad394. doi: 10.1093/bjs/znad394. PMID: 37992254.

X. INFORME DE LOS DIRECTORES

UNIVERSITAT DE BARCELONA

Facultat de Medicina i Ciències de la Salut – Campus Clínic

Informe director/s /tutor sobre l'autorització del dipòsit de la tesi

Dr./a.María Javiera Pérez Anker, com a director/tutor de la tesi doctoral titulada "Nuevas técnicas de imagen en dermatología:

Tomografía de Coherencia Óptica de Campo Lineal y Microscopía Confocal Ex vivo " i, d'acord amb el que s'estableix a l'article 35 Normativa reguladora del Doctorat a la Universitat de Barcelona, emeto el següent:

INFORME

(Informe detallat i motivat sobre el contingut de la tesi i sobre l'autorització de dipòsit de la tesi que s'ha demanat)

En esta tesis, se evaluó la utilidad diagnóstica de distintas técnicas de imagen para el estudio de la piel: la microscopía de coherencia óptica de campo lineal (TCO-CL) y la microscopía confocal ex vivo (MCev). En el proyecto, se han descrito las correlaciones en el diagnóstico de tumores cutáneos, en relación con sus características morfológicas y los hallazgos en dermatoscopia, MCR e histología convencional.

Se detallaron los hallazgos morfológicos y citológicos de las lesiones melanocíticas observadas en TCO-CL y la correlación de las estructuras dermatoscópicas e histológicas. Asimismo, se describieron los criterios diagnósticos de los tumores cutáneos y se desarrollaron algoritmos de inteligencia artificial para el campo de cancerización con TCO-CL.

En el caso de MCev, se desarrolla y valida una técnica de preparación del tejido que mejora la calidad de visualización de los nidos de carcinoma basocelular. Además, se diseñó un dispositivo de aplanamiento de muestras y se estableció un protocolo estandarizado en MCev, contribuyendo así a una mayor eficacia en el proceso. Se evaluó la precisión diagnóstica de MCev en biopsias de lesiones equívocas y se describieron las características diagnósticas de diferentes tumores cutáneos utilizando MCev de cuarta generación. Finalmente, se comparan los hallazgos de la MCev y la tinción de H&E en patología general, ampliando así el alcance del estudio a otros campos de la medicina.

El resultado de la tesis se ha publicado como trabajo original de investigación en revistas de alto impacto en Dermatología.

La doctoranda ha cumplido con excelencia los objetivos durante el proyecto de tesis, demostrando una gran capacidad investigadora como demuestran los resultados obtenidos en este campo.

UNIVERSITAT DE BARCELONA

Facultat de Medicina i Ciències de la Salut – Campus Clínic

Barcelona, 8 d'/de Febrero de 2024.

(signat)
Dr./a

Dr. Josep Maldehy

Un cop s'hagi emplenat l'informe, s'ha d'adjuntar i s'ha de fer arribar al doctorand o al president de la Comissió Acadèmica del programa de doctorat responsable de la tesi.